The Dissertation Committee for Michael John Hagenberger
certifies that this is the approved version of the following dissertation:

Consideration of Strand Fatigue for Load Rating Prestressed Concrete Bridges

Committee:

Sharon L. Wood, Co-Supervisor

Michael E. Kreger, Co-Supervisor

Eric B. Becker

John E. Breen

Karl H. Frank

Consideration of Strand Fatigue for Load Rating Prestressed Concrete Bridges

by

Michael John Hagenberger, B.S.C.E., M.E.

Dissertation

Presented to the Faculty of the Graduate School of
The University of Texas at Austin
in Partial Fulfillment
of the Requirements
for the Degree of

Doctor of Philosophy

The University of Texas at Austin
August 2004

Dedication

To my mom and dad, whose love and support helps make my dreams reality.

Acknowledgements

I would like to first thank the Texas Department of Transportation for sponsoring this project at the Ferguson Structural Engineering Laboratory at the University of Texas at Austin. Their generous support provided me the opportunity to further my education through research and reach my ultimate goal of an academic career. In particular, I would like to thank Mr. Keith Ramsey for his assistance in coordinating the field work performed as part of this investigation.

I would also like to thank my committee members, Dr. Sharon L. Wood, Dr. Michael E. Kreger, Dr. John E. Breen, Dr. Karl H. Frank, and Dr. Eric B. Becker, for sharing their technical knowledge, providing guidance, and sharing the wisdom they gained throughout their prestigious careers. In particular, I would like to thank Dr. Sharon L. Wood for her endless patience and guidance in helping me to be a better writer, researcher, and educator. Also, I would like to thank Dr. John E. Breen for showing me how to balance an academic career with life outside the classrooms and laboratories.

I also extend sincere thanks the laboratory staff (Blake Stassney, Dennis Fillip, and Mike Bell), for supporting my efforts in the field and in the laboratory. Without their support, I am sure I would still be testing my first bridge.

I would also like to thank Patrick Wagener for his significant contributions to the field testing portion of the project and for opening my eyes to the true Texas way of life.

I would also like to thank Bryan Heller for his significant contributions to the laboratory fatigue testing portion of the project. His energy and effort helped me to see the light at the end of the tunnel.

I would also like to thank my friends who helped make my years in Austin the best they could be and without whose support I never would have made it through. I thank Scott Witthoft for teaching me what real music is, Glenn Goldstein who helped me see the benefits of a slow paced life, Tim Phelan for always understanding and introducing me to Laura Phelan, Laura Phelan for helping me to understand myself, Cameron Sankovich for being the best physical and mental trainer I ever had, and Andrew Stark for always listening.

Finally, I would like to thank my family. I thank my brother for his unwavering support and encouragement. He is the best older brother a man can have. I thank my parents for their support and encouragement. They never doubted me and always supplied the advice I needed for every challenge that was presented to me. They have asked for nothing, but I owe them everything.

August 2004

Consideration of Strand Fatigue for Load Rating Prestressed Concrete Bridges

Publication No.______________

Michael John Hagenberger, Ph.D.
The University of Texas at Austin, 2004

Supervisors: Sharon L. Wood and Michael E. Kreger

This dissertation is an investigation of the use of fatigue of the strand in prestressed concrete beams for the load rating of prestressed concrete bridges. The criteria for load rating prestressed concrete bridges are provided by the American Association of State Highway and Transportation Officials in the Manual for Condition Evaluation of Bridges, which does not contain provisions for load rating prestressed concrete bridges for fatigue. Rather, a serviceability criterion is provided for the control of flexural cracks in prestressed members by limiting the concrete tensile stress at the extreme fiber of the member being evaluated. The initial thrust behind the research was the apparent discrepancy between the condition of bridges observed in the field, which show no significant signs of deterioration, and the expected condition from load ratings based on the current concrete tensile stress limit. To investigate this discrepancy, a research program was developed that included diagnostic load tests of five existing bridges and a series of fatigue tests on six, one-quarter scale specimens that were designed behave similarly to the beams in bridges considered in this investigation. The diagnostic load tests provided information used to evaluate the response of the bridges to applied live loads, and the results were compared with the current code provisions and the results from finite element analyses. The results of the fatigue tests provided a link between the stress range in the prestressing strand due to applied live loads and the fatigue life of the beams. Based on the results of the load tests, fatigue tests and related analyses, recommendations for improved load rating procedures with respect to the tensile stress criterion are provided and alternative criteria for load rating prestressed concrete bridges based on the fatigue of the prestressing strand are proposed.

Table of Contents

CHAPTER 6 RESULTS OF LABORATORY FATIGUE TESTS

List of Tables

List of Figures

CHAPTER 1

Introduction

1.1 GENERAL

Highways represent a critical part of the infrastructure of the United States and bridges are a key component of the highway system. Since the passage of the Federal Highway Act of 1956, the American Association of State Highway and Transportation Officials (AASHTO), which was the American Association of State Highway Officials at the time, has been working with the Federal Highway Administration, formerly the Bureau of Public Roads, in the development of uniform, minimum standards for the design of highways.

An important part of developing specifications is incorporating changes in technology and reflecting those changes in the specifications. Just as bridge construction technologies have developed, the size of vehicles traveling on the highway system has increased. Although new bridges can be designed to accommodate the increased loads, older bridges must be evaluated to determine if they can resist loads higher than originally intended. The Interim 2003 AASHTO Manual for Condition Evaluation of Bridges (MCEB) is currently used for this purpose. The MCEB provides serviceability and strength criteria that are used to calculate the permissible loads that existing bridges can safely resist.

Two load rating levels are given in the MCEB: inventory and operating. The inventory level rating provides the safe load that may be applied to the bridge for an indefinite period of time. The operating level provides the maximum permissible live load that a bridge may sustain. The consequences associated with a bridge that fails to meet the minimum load rating may be costly, and include posting of maximum permissible loads, increased frequency of inspections, structural upgrades, or replacement. While the direct costs of these scenarios are obvious, the indirect costs are more difficult to quantify. Indirect costs include the increase in the cost of trucking and distribution of good and services due to bridge closures and construction and the costs associated with increased congestion due to remedial measures. Therefore, it is critical that the evaluation of existing bridges be accurate while maintaining an acceptable level of safety.

1.2 OVERVIEW, OBJECTIVES, AND SCOPE

1.2.1 Overview

Throughout the State of Texas, a significant number of prestressed concrete highway bridges were designed and constructed during the 1950s and 1960s. Many of these bridges have load ratings that fall below the current minimum design vehicle specified in the MCEB. Specifically, the load ratings for these bridges are being controlled by the criterion in the MCEB that limits the concrete tensile stress in prestressed concrete beams. As a result of the low load ratings, TxDOT personnel are required to increase the frequency of inspection for these bridges from once every two years to annually.

A low load rating would seem to indicate that these existing bridges would show signs of deterioration due to daily vehicular traffic. However, observations made by TxDOT during inspections indicate that the condition of these bridges is good, and that there are generally no signs of deterioration. The discrepancy between the conditions expected based on the load ratings and those observed in the field was noted by TxDOT. In an effort to increase the load rating of these bridges and reduce the required rate of inspection, TxDOT increased the concrete tensile stress limit used to establish the inventory level load rating. The limit specified in the MCEB is $6\sqrt{f_c'}$, where f_c' is taken as the specified compressive strength of the concrete in the prestressed beams and the tensile stress is calculated using the transformed, composite section assuming the section is uncracked. TxDOT is currently using a value of $12\sqrt{f_c'}$ to load rate prestressed concrete bridges and has justified this increase in stress using the provisions in the 1995 Building Code Requirements for Structural Concrete (ACI 318-95) developed by the American Concrete Institute.

However, ACI 318-95 is intended to be applied to buildings where the fatigue limit state generally does not govern. Unlike buildings, bridges see repeated cycles of the design load which makes the fatigue limit state more significant. TxDOT realized that the provisions used to justify the elevated tensile stress limit were in question. Therefore, TxDOT deemed it necessary to investigate the applicability and effects of using the elevated tensile stress for the load rating of prestressed concrete bridges in Texas and sponsored this investigation.

1.2.2 Objectives

TxDOT established two primary objectives for this investigation. The first objective is to evaluate the applicability of the elevated tensile stress limit for the load rating of prestressed concrete bridges. The second objective, which is dependent on conclusions to the first objective, is to evaluate the effect on the fatigue life of prestressed concrete bridges where an elevated tensile stress limit was used for load rating.

The objectives of this dissertation are complimentary to the primary objectives set by TxDOT for this investigation. The criteria for the evaluation of prestressed concrete bridges prescribed in the MCEB are based on serviceability and strength. However, bridges are subjected to cyclic loading and, therefore, the fatigue limit state should also be considered. Therefore, the primary objective of this dissertation is to investigate the use of the stress range in the strand as a criterion for the load rating of prestressed concrete bridges. The second objective is to evaluate the current load rating procedures and determine if the tensile stress in the concrete can be used to estimate stress range in the strand.

1.2.3 Scope

TxDOT provided the research team with a list of thirty-three bridges for which at lease one span failed to meet the tensile stress load rating criterion in the MCEB. Five bridges from this list were selected for detailed investigation. The bridges studied were two-lane, simply-supported, highway bridges composed of prestressed concrete beams and a composite, cast-in-place deck. A total of eight spans on the five bridges were inspected, instrumented, and load tested. Five of the eight spans tested had load ratings controlled by the concrete tensile stress criterion prescribed in the MCEB.

The measured data collected during the diagnostic load tests were used to evaluate the live load distribution characteristics of each bridge and provide insight into the condition of the bridges. The data collected were compared with the results from finite element analyses.

In addition to the diagnostic load tests, laboratory fatigue tests were performed on six, quarter-scale specimens. The specimens were designed based on a prototype beam that was typical of the bridges studied in this investigation. The philosophy behind the design of the test specimens was to achieve similar strand stress ranges and median stresses at similar values of calculated concrete extreme fiber stresses as that of the prototype bridge beam. The extreme fiber stresses were calculated assuming uncracked sections, which is consistent with the method of calculating stresses in the MCEB for the tensile stress criterion.

The stress levels considered were: $6\sqrt{f'_{ce}}$, $7.5\sqrt{f'_{ce}}$, and $12\sqrt{f'_{ce}}$, where f'_{ce} is the estimated in situ compressive strength of the concrete in the prestressed beams. These index stress levels correspond to nominal strand stress ranges of approximately 10, 20, and 40 ksi based on cracked section analyses.

Based on the results of the diagnostic load tests and laboratory fatigue tests, conclusions are made regarding the use of stress range in the strand as a criterion for the load rating of prestressed concrete bridges. In addition, recommendations are made for improving the current load rating procedures for bridges where the load rating is controlled by the concrete tensile stress criterion.

1.3 FATIGUE OF PRESTRESSED CONCRETE BEAMS

Previous research on the fatigue of prestressed concrete beams has focused on the fatigue behavior of the prestressing strand. The primary reason for this is that engineers generally produce designs where the fatigue strength of the concrete does not govern. Per ACI Committee 215, the fatigue strength of concrete is approximately 55% of the static strength for compression, tension and flexure (1997). In addition, ACI Committee 215 (1997) states that concrete does not exhibit an endurance limit, meaning that regardless of the magnitude of the stress range, concrete will exhibit a finite fatigue life. Therefore, the committee adopted a fatigue life of 10,000,000 cycles as the basis for their recommendations. Recommendations related to prestressed concrete are summarized below.

- For concrete in compression, the stress range in concrete should not exceed 40% of its compressive strength when the minimum stress is zero. The recommended stress range decreases linearly as the minimum stress is increased and is zero when the minimum stress is 75% of the compressive strength. This relationship is shown in Figure 1.1.

- If the nominal tensile stress in the concrete in the precompressed zone calculated using transformed composite section properties exceeds $3\sqrt{f_c'}$ under service loads and the minimum stress in the strand is less than 60% of the tensile strength of the strand, the stress range in the strand should not exceed 6% of the tensile strength of the strand based on a cracked section analysis. This corresponds to stress ranges of 15.0 ksi and 16.2 ksi for strand with tensile strengths of 250 ksi and 270 ksi, respectively.

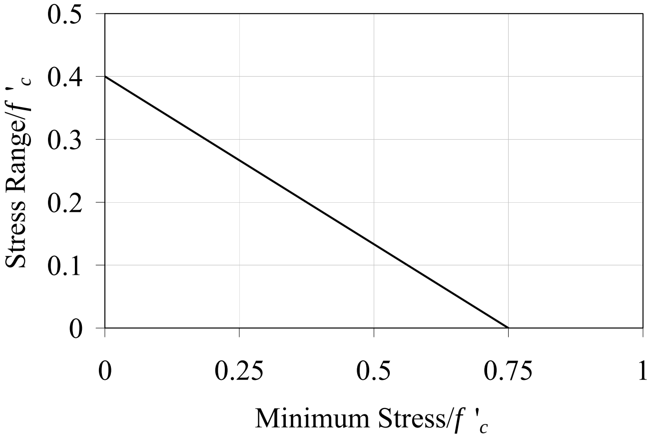

Figure 1.1 ACI 215-74 (1997) Recommended Compressive Stress Range in the Concrete for Design of Prestressed Concrete Beams Subjected to Fatigue Loading

As reported by Shahawi and Batchelor (1996), the compressive stresses produced in the concrete by the design fatigue loads are typically small when compared with the fatigue strength of concrete. Therefore, fatigue of the concrete is not considered in this investigation. However, the net tensile stresses in the precompressed zone being investigated in this study are above the limit of $3\sqrt{f_c'}$. Therefore, the stress range in the strand is considered to be critical to the fatigue life of the beams, and the balance of this section will focus the fatigue characteristics of the prestressing strand and prestressed concrete beams.

1.3.1 Fatigue Response of Prestressing Strand In-Air

Paulson, et al. (1983) studied of the fatigue characteristics of prestressing strand. The study included a comprehensive literature review and fatigue tests on prestressing strands. The results from over 700 fatigue tests were reported. Two fatigue models were proposed based on the data. The first model, given in Equation 1-1, represents the mean number of cycles that a strand should experience prior to failure when subjected to cyclic loading for a given stress range.

$$\log N = 11.45 - 3.5 \log S_r \tag{1-1}$$

where N is the number of load cycles at failure and S_r is the strand stress range, in ksi. Due to the variability of the data, Paulson, et al. (1983) proposed a second model for design purposes. A one-sided tolerance limit corresponding to a 95% probability that 97.5% of the data would be above the limit was proposed. This design model is given in Equation 1-2. Figure 1.2 shows the plots of both models and the data that were the basis for their development.

$$\log N = 11 - 3.5 \log S_r \tag{1-2}$$

More recently, data were compiled and reported by Heller (2003). Industry data that were provided to the University of Texas at Austin by VSL Corporation and the results of fatigue tests on the strand used to construct the fatigue specimens tested in this investigation are included. The industry data are shown in Figure 1.3, and the results of the tests performed by Heller (2003) are shown in Figure 1.4. These additional data support the models proposed by Paulson, et al. (1983).

1.3.2 Fatigue of Prestressed Concrete Beams with Straight Tendons

The research discussed in this section focuses on the fatigue studies performed on fully prestressed concrete beams with straight tendon profiles. The primary objective of a majority of the research presented focused on determining the fatigue performance of the prestressing strands.

In a study by Overman (1984), fatigue tests were performed on seven full-scale, prestressed concrete beams with straight strands. The specimens tested were TxDOT Type C and AASHTO-PCI Type II prestressed beams with composite 7.75-in. thick by 6 ft-3 in. wide cast-in-place slabs. The overall length of the specimens tested was 48 ft. The results of the fatigue tests are summarized in Table 1.1.

In addition to the fatigue tests, Overman conducted an exhaustive literature review. Data from 41 prestressed concrete beams that were tested in the 1950s through the late 1970s were reported. The results of these tests are summarized in Table 1.3.

A more recent study on the fatigue of prestressed concrete beams with straight tendons was performed by Muller and Dux (1994). The results of the tests on seven specimens with straight strands are summarized in Table 1.2.

The data from Overman (1984) and Muller and Dux (1994) are shown in Figure 1.5. The fatigue models developed by Paulson, et al. (1983) are also shown for comparison. The data shown in Figure 1.5 indicate that the in-air fatigue model is a reasonably good estimate of the fatigue life of prestressed concrete beams with straight tendons.

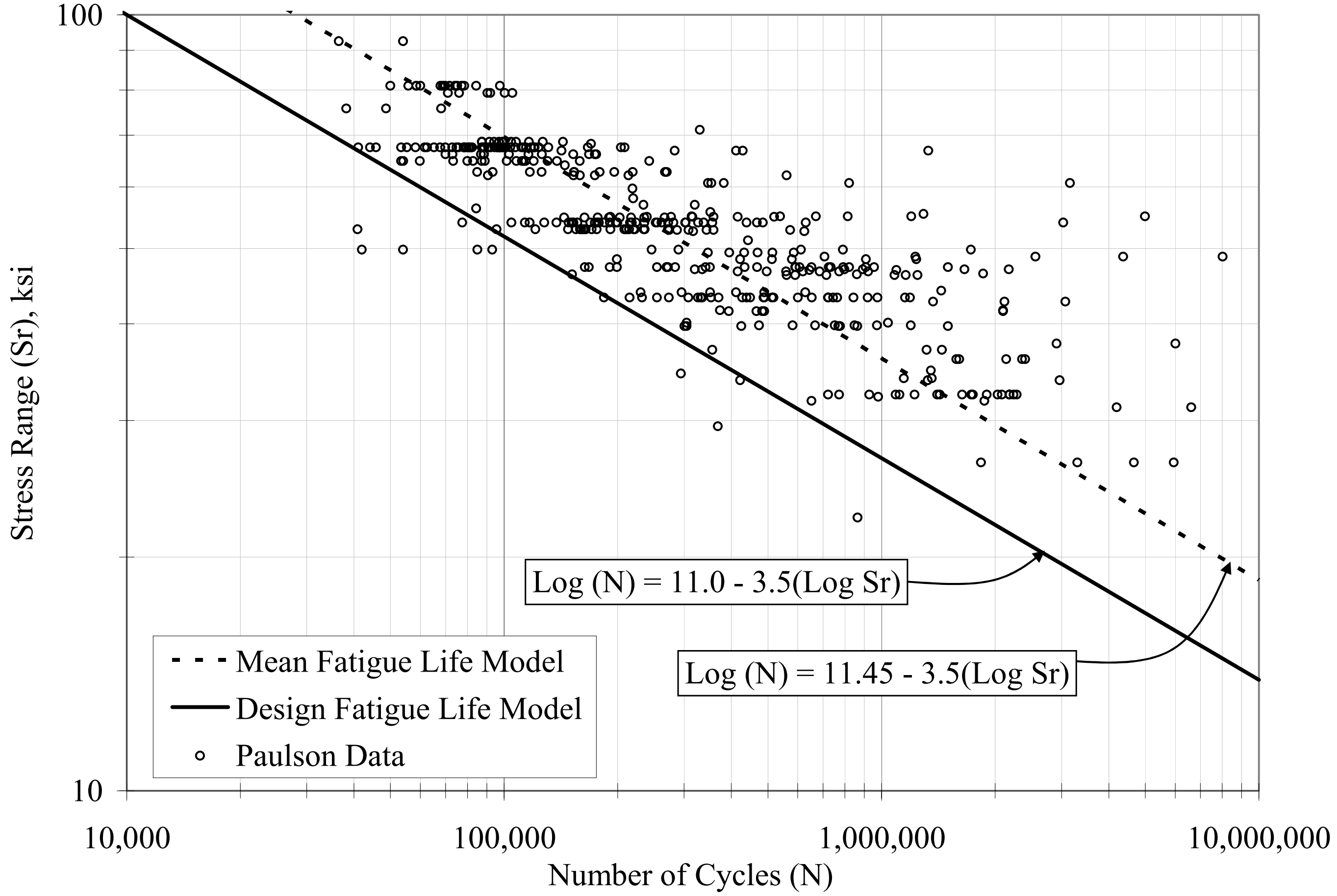

Figure 1.2 In-Air Strand Fatigue Data and Strand Fatigue Models, Paulson, et al. (1983)

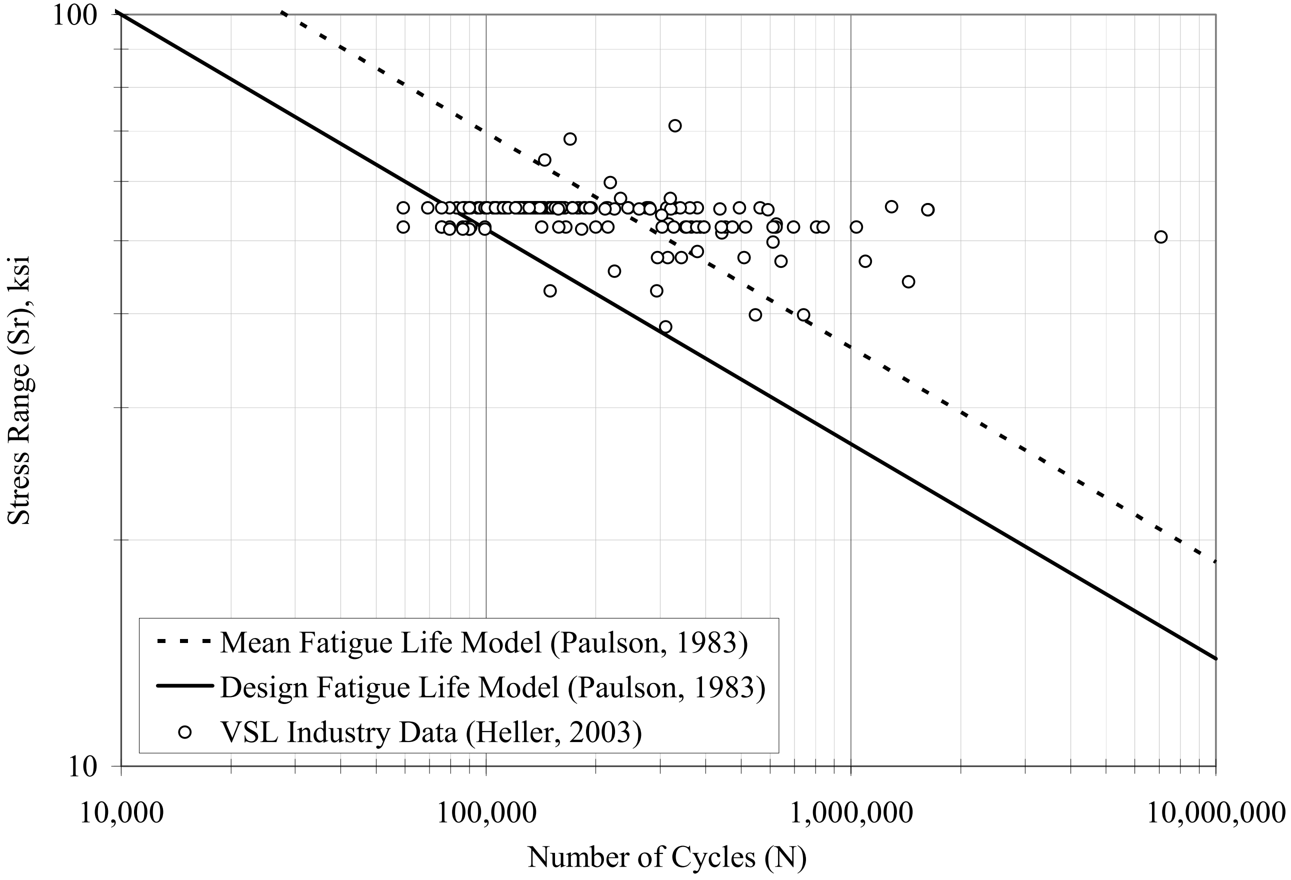

Figure 1.3 In-Air Strand Fatigue Data Compiled by Heller (2003)

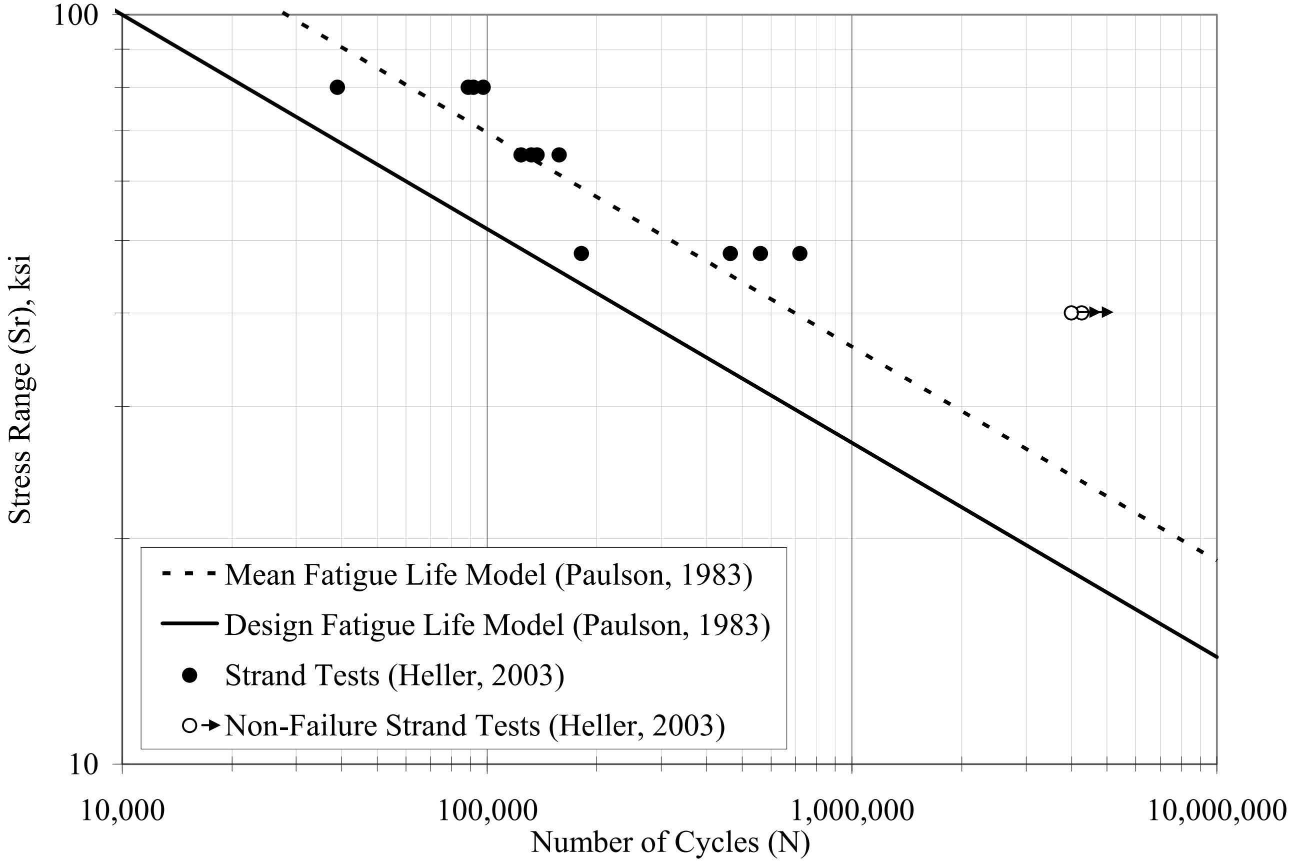

Figure 1.4 In-Air Strand Fatigue Tests Performed by Heller (2003)

Table 1.1 Summary of Fatigue Tests on Prestressed Concrete Beams with Straight Strands Performed by Overman (1984)

Beam ID	Extreme Fiber Stress Level*	Strand Stress Range** (ksi)	Number of Fatigue Cycles (million)
C-16-NP-10.5-NO-0.58	$3.5\sqrt{f'_{cm}}$	43.7	0.58
C-16-NP-7.2-OL-1.48	$7.2\sqrt{f'_{cm}}$	24.0	1.48
C-16-NP-10.1-NO-0.91	$10.1\sqrt{f'_{cm}}$	49.1	0.91
C-16-NP-6.0-NO-1.91	$6.0\sqrt{f'_{cm}}$	27.8	1.91
C-16-UP-8.0-NO-1.73	$8.0\sqrt{f'_{cm}}$	20.7	1.73
C-16-CP-7.2-NO-2.54	$7.2\sqrt{f'_{cm}}$	22.5	2.54
C-16-CP-5.5-OL-9.43	$5.5\sqrt{f'_{cm}}$	11.7	9.43

* Extreme fiber stress was calculated using uncracked, transformed, composite section properties and the measured compressive strength of the concrete.

** Strand stress range was calculated using cracked, transformed, composite section properties and the measured strength of the concrete.

Table 1.2 Summary of Fatigue Tests on Prestressed Concrete Beams with Straight Strands Performed by Muller and Dux (1994)

Beam ID	Strand Stress Range* (ksi)	Number of Fatigue Cycles (million)
PS2	27.6	7.06
PS3	27.6	2.07
PS4	27.6	4.17
PT2	31.2	1.23
VP2	36.3	1.51
VP3	27.6	2.93
VP4	27.6	2.89

* Strand stress range was calculated using cracked, transformed, composite section properties and the measured strength of the concrete.

Table 1.3 Summary of Fatigue Tests on Prestressed Concrete Beams with Straight Strands Reported by Overman (1984)

Beam ID	Strand Stress Range* (ksi)	Number of Fatigue Cycles (million)	Beam ID	Strand Stress Range* (ksi)	Number of Fatigue Cycles (million)
Ozell and Ardaman (1956)			Abeles, Brown and Hu (1974)		
L-2	41	0.46	A3	58.3	0.11
M-1	60	0.28	A5	89.9	0.02
M-2	47	0.33	A6	94.2	0.02
M-3	18	0.94	A7	114.5	0.01
M-4	80	0.13	B1	13	2.52
Nordby and Venuti (1957)			B3	79.7	0.06
6A	23.9	0.14	B4	54.3	0.17
6B	23.9	0.19	B5	84	0.05
S6	29.4	0.84	B6	58.1	0.14
Ozell and Diniz (1958)			C1	62.2	0.16
S-2	49	0.78	C3	60.8	0.17
S-3	76	0.19	C4	46.4	0.39
S-4	68	0.51	D4	53.7	0.21
S-5	43.5	0.87	D5	86.7	0.05
S-6	32.5	2.27	D6	89.1	0.04
Warner and Hulsbos ((1966)			D7	51.3	0.22
F1	44.5	0.14	E1	46.2	0.31
F2	43.5	0.16	E2	27.5	2.05
F4	43.3	0.23	E3	27.3	0.76
Rabbat et al. (1978)			E4	42.4	0.29
G11	18.2	3.78	E5	28.9	0.96
G13	20.1	3.20	F2	132.3	0.02
			F4	132.8	0.02

* Strand stress range was calculated using cracked, transformed, composite section properties.

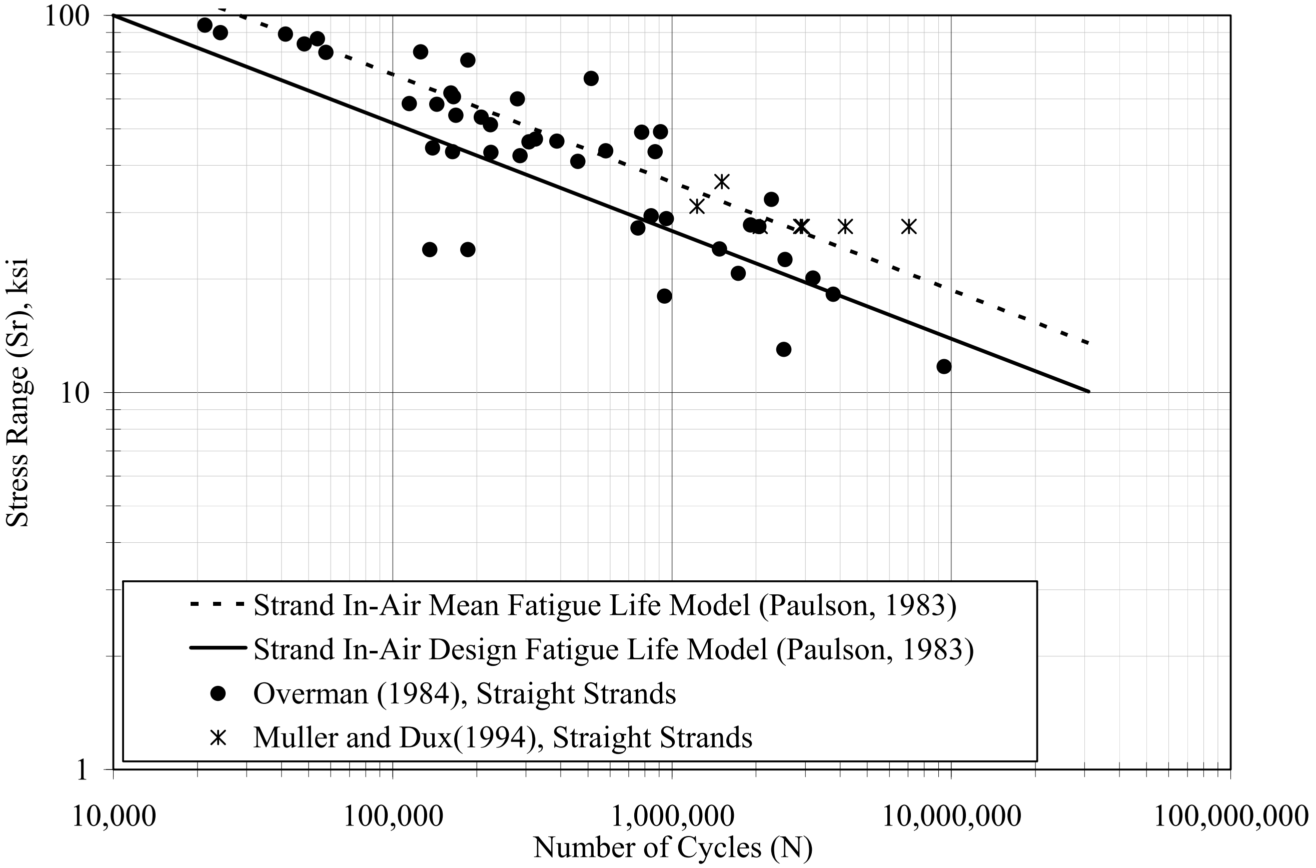

Figure 1.5 Comparison of Prestressed Concrete Beam Data with Paulson (1983) Strand In-Air Fatigue Models

1.3.3 Fatigue of Prestressed Concrete Beams with Depressed Strands

In this section, research related to the fatigue properties of prestressed concrete beams with depressed strands is presented. The research discussed includes fatigue tests on prestressed concrete beams with segmental strand profiles created with either one or two hold-downs. In this dissertation, strand profiles with one and two hold-downs are defined as draped and inclined, respectively. These strand profiles are shown in Figure 1.6.

Muller and Dux (1994) report results on the fatigue tests of both draped and inclined strands. The results from five specimens with draped strand profiles and eleven specimens with inclined profiles are summarized in Table 1.4. The researchers investigated the effects of three parameters related to the hold-down location. The parameters included the diameter of the pin, the change in angle of the strand, and the bundling of strands at the hold-down locations. Based on their data, and data from Hsu (1979), Rigon and Thürlimann (1985) and Koch (1988) the fatigue model given in Equation 1-3 was proposed.

$$\frac{S_r}{f_{pu}} = -0.12 \times \log(N) + 0.75 \tag{1-3}$$

where S_r is the stress range in the strand, f_{pu} is the tensile strength of the strand, and N is the number of load cycles at failure. The proposed fatigue model and data are shown in Figure 1.7.

Based on the limited amount of data, Muller and Dux concluded that fatigue life of prestressed concrete beams with depressed strands is decreased when the ratio of the hold-down pin diameter to strand diameter is greater than the conventional 2 to 1 ratio and when strands are bundled at the hold-down.

Overman (1984) also tested four prestressed concrete beams with draped strands. The specimens tested were identical in size to the specimens tested with straight strands. Overman also reported data from six additional prestressed concrete beams (Ozell, 1962 and Rabbat, et al., 1978). These data are summarized in Table 1.5 and shown in Figure 1.8.

The data from fatigue tests on prestressed concrete beams with depressed tendons are compared with data from fatigue tests on prestressed concrete beams with straight strands in Figure 1.9. Data reported by Muller and Dux (1994) for tests with ratios of hold-down pin diameter to strand diameter greater than 2 to 1 ratio and with bundled strands are not shown. The variability in the data for tests on prestressed concrete beams with both depressed strands and straight strands appears comparable.

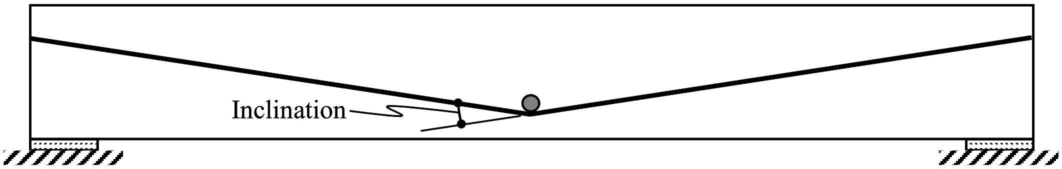

a) Inclined Strand Profile

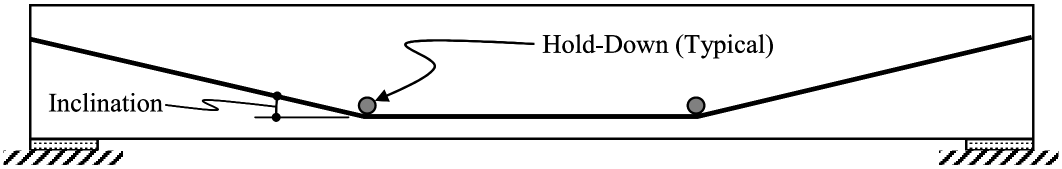

b) Draped Strand Profile

Figure 1.6 Strand Profiles of Beams Previously Tested

Table 1.4 Summary of Fatigue Tests on Prestressed Concrete Beams with Depressed Strands Performed by Muller and Dux (1994)

Beam ID	Strand Profile††	Diameter of Pin at Hold-Down (mm)	Inclination of Strand at Hold-Down (degree)	Strand Stress Range* (ksi)	Number of Fatigue Cycles (million)
HD1025-1	Inclined	25	10	32.6	0.89
HD1025-2	Inclined	25	10	56.6	0.19
HD1025-3	Inclined	25	10	14.5	5.00†
HD525-2	Inclined	25	5	15.2	7.74
HD525-3	Inclined	25	5	15.2	8.10
HD550-2	Inclined	50	5	15.2	3.80
HD550-3	Inclined	50	5	15.2	1.00
HD51400-1	Inclined	1400	5	15.2	0.84
HD51400-2	Inclined	1400	5	15.2	0.64
HD5B-2**	Inclined	25	5	15.2	1.79
HD5B-3**	Inclined	25	5	15.2	1.61
HD516-3	Draped	16	5	27.6	0.34
HD516-4	Draped	16	5	27.6	0.35
HD516-5	Draped	16	5	14.5	1.04
HD516-6	Draped	16	5	6.5	10.35†
HD516-7	Draped	16	5	6.5	10.00†

† Fatigue test stopped prior to failure.

†† Strand profiles shown in Figure 1.6.

* Strand stress range was calculated using cracked, transformed, composite section properties and the measured strength of the concrete.

** Strands were bundled at the hold-down location.

Table 1.5 Summary of Fatigue Tests on Prestressed Concrete Beams With Depressed Strands Reported by Overman (1984)

Beam ID	Strand Profile	Inclination of Strand at Hold-Down (degree)	Extreme Fiber Stress Level*	Strand Stress Range** (ksi)	Number of Fatigue Cycles (million)
C-14-NP-5.5-OL-2.29	Draped	3.3	$5.5\sqrt{f'_{cm}}$	24.7	2.98
A-22-NP-6.2-OL-2.84	Draped	3.3	$6.2\sqrt{f'_{cm}}$	20.9	2.84
A-22-NP-6.2-NO-5.0	Draped	3.3	$6.2\sqrt{f'_{cm}}$	20.5	5.00
A-22-NP-3.5-OL-5.95 (NF)	Draped	3.3	$3.5\sqrt{f'_{cm}}$	7.5	5.95†
G-10 (Rabbat, et al. 1978)	Draped	2.9	$6.0\sqrt{f'_{cm}}$	19.5	3.63
I2 (Ozell 1962)	Draped	3.6	Varied†† ($8.7\sqrt{f'_{cm}}$ to $13.0\sqrt{f'_{cm}}$)	15.3	2.50
I3 (Ozell 1962)	Draped	3.6		28.3	1.50
I4 (Ozell 1962)	Draped	3.6		24.4	0.76
I5 (Ozell 1962)	Draped	3.6		25.0	0.64
I6 (Ozell 1962)	Draped	3.6		30.5	0.21

† Fatigue test stopped prior to failure.

†† Values were not reported by Overman for individual beams.

* Extreme fiber stress was calculated using uncracked, transformed, composite section properties and the measured compressive strength of the concrete.

** Strand stress range was calculated using cracked, transformed, composite section properties and the measured strength of the concrete.

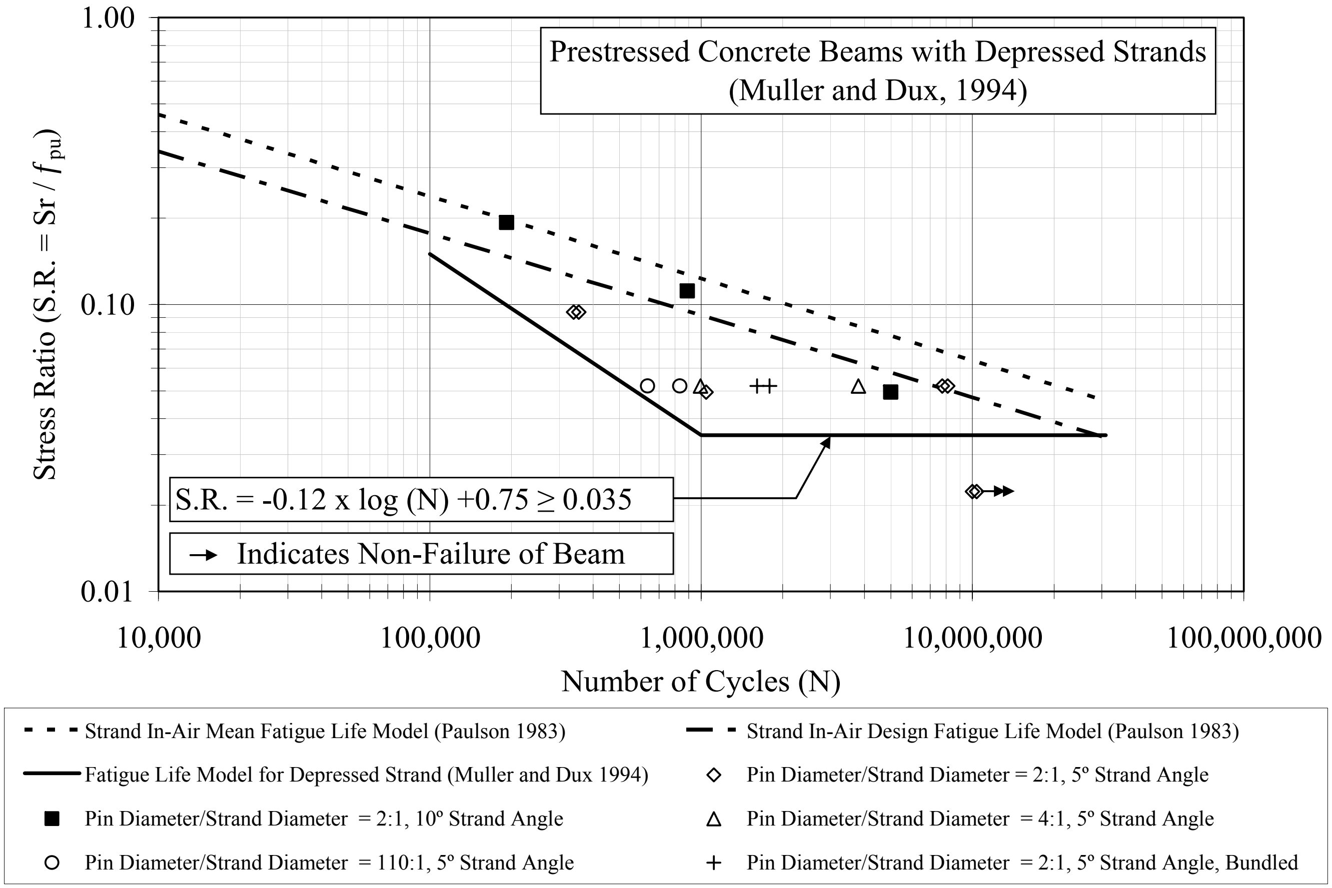

Figure 1.7 Fatigue Model for Depressed Strands Proposed by Muller and Dux (1994)

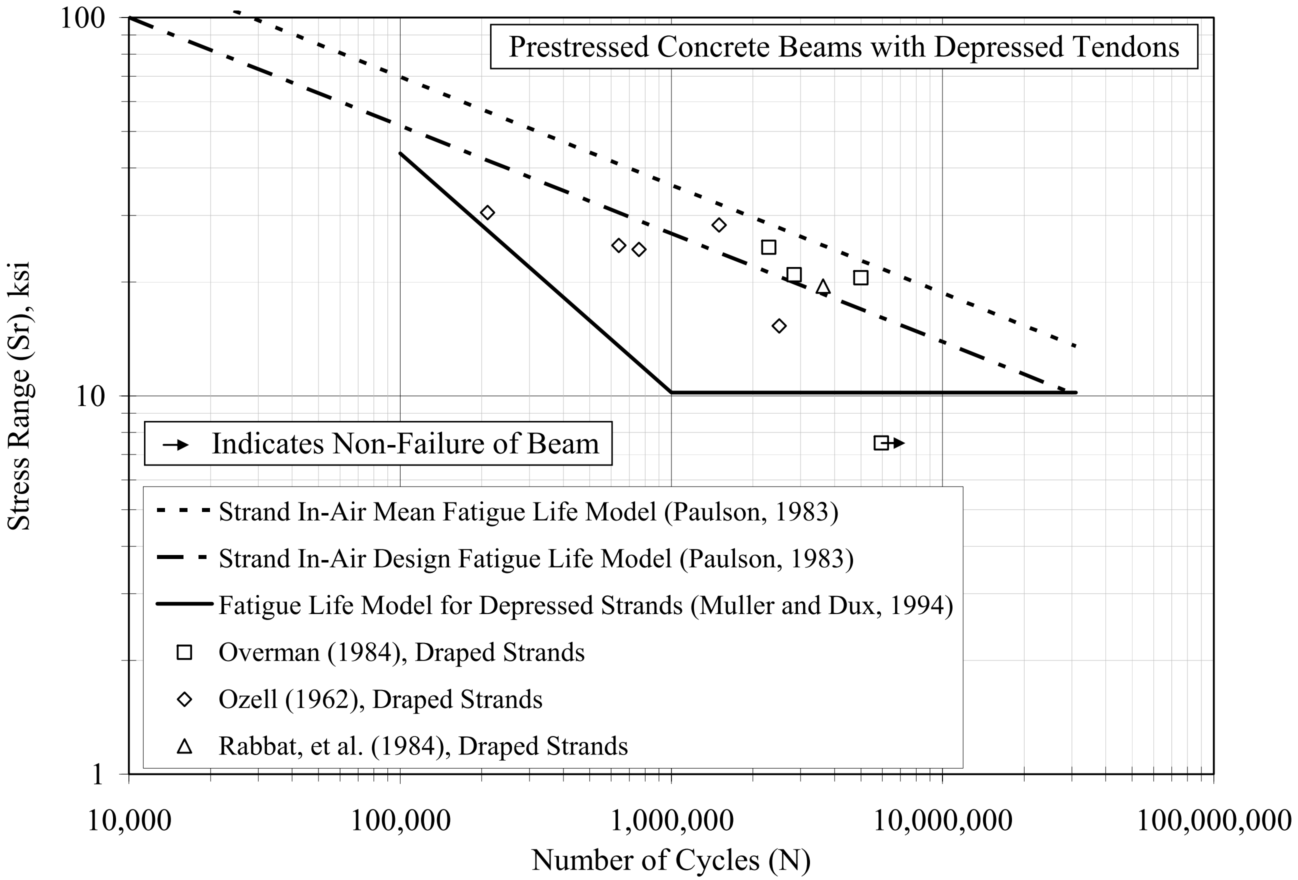

Figure 1.8 Data from Fatigue Tests of Prestressed Concrete Beams Reported by Overman (1984)

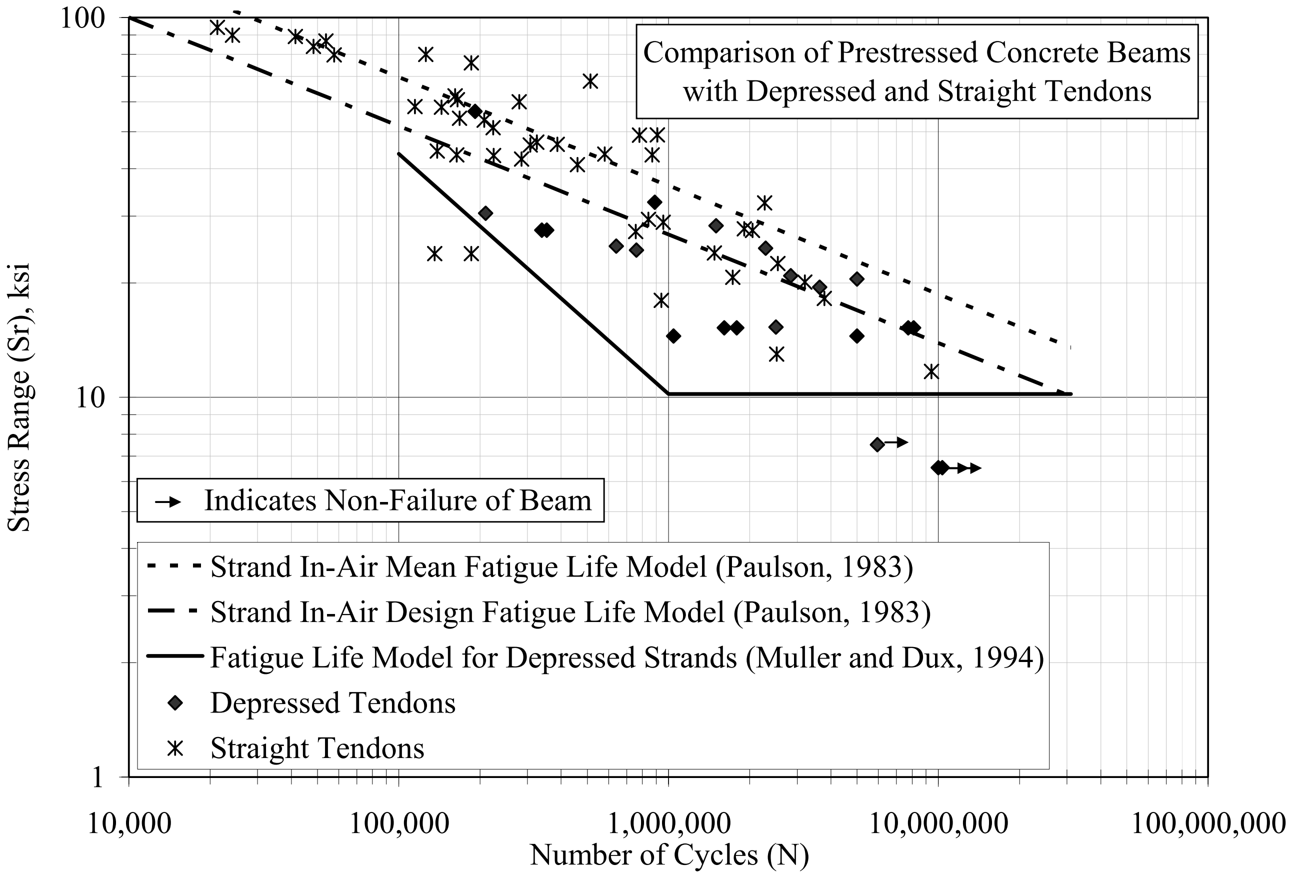

Figure 1.9 Comparison of Data from Fatigue Tests of Prestressed Concrete Beams with Depressed and Straight Tendons

1.3.4 Additional Studies on the Fatigue of Prestressed Concrete Beams

Rao and Frantz (1996) conducted fatigue tests on actual bridge girders that were taken out of service. The bridge girders were precast, prestressed concrete box beams, 36 in. wide by 27 in. deep, with a span of 56 ft. One beam was tested at a nominal bottom fiber stress of $6\sqrt{f_c'}$ and a measured strand stress range of approximately 15 ksi. The beam survived 1.5 million cycles without a significant change in behavior or increase in measured strand stress range. The other beam was tested at a nominal bottom fiber stress of $9\sqrt{f_c'}$ and an initial measured strand stress range of 27.5 ksi. After 20,000 cycles, the measured strand stress had increased approximately 5 ksi and wire failures in the strand were observed after 150,000 cycles. The concrete compressive strength (f_c') used to determine the nominal bottom fiber stress was based on cores extracted from the girders.

1.3.5 Summary

Previously reported data from fatigue tests performed on strand in-air were presented in this section. The in-air tests on strand were conducted at stress ranges between 30 and 75 ksi. The results from these tests confirm the fatigue models presented by Paulson (1983) for the stress ranges tested.

Results from fatigue tests on prestressed concrete beams with both straight and depressed tendons were also presented. A majority of the tests were performed at stress ranges above 10 ksi. There is significant scatter in the data, particularly at stress ranges between 10 and 30 ksi. In addition, as shown in Figure 1.9, the in-air design fatigue model proposed by Paulson (1983) appears to overestimate the fatigue life of prestressed concrete beams with both straight and depressed tendons.

1.4 CURRENT AASHTO PROVISIONS FOR THE DESIGN AND EVALUATION OF PRESTRESSED CONCRETE BEAMS IN FATIGUE

The Interim 2002 AASHTO Standard Specification for Highway Bridges (AASHTO Standard) does not include specific provisions for the design of prestressed concrete beams based on fatigue of the prestressing strand. Similarly, the MCEB does not provide evaluation criteria based on fatigue of the prestressing strand for prestressed concrete beams. Rather, both the AASHTO Standard and MCEB limit the extreme fiber tensile stress to $6\sqrt{f_c'}$. This limit is reduced to $3\sqrt{f_c'}$ when the member is located in a severe corrosive environment and to zero when there are unbonded tendons.

Unlike the AASHTO Standard, the Interim 2003 AASHTO LRFD Bridge Design Specifications (AASHTO LRFD) provides fatigue requirements for prestressing strand in prestressed concrete beams. Per the AASHTO LRFD, if the tensile stress in the extreme fiber exceeds $3\sqrt{f_c'}$ at a prescribed service load state, the stress range in the strand is limited to between 10 ksi and 18 ksi for bonded tendons with radii of curvature between 12 ft and 30 ft, respectively. In addition, these limits assume fretting due to tendons rubbing on hold-downs or deviators is not a concern. Where fretting is a concern, the AASHTO LRFD states that it is necessary to consult the literature for determination of appropriate stress ranges.

1.5 DEVELOPMENT AND EVALUATION OF LIVE LOAD DISTRIBUTION FACTORS

Live load distribution factors are a critical part of the load rating process. The method of calculating live load distribution factors (LLDF's) in the AASHTO Standard has remained unchanged since it was introduced based on the work by Newmark (1948). The method of calculating live load distribution factors in the AASHTO LRFD was first introduced in 1994 based on the work by

Zokaie et al. (1991). The following discussions are based on the results of investigations that discuss the accuracy of the AASHTO Standard and AASHTO LRFD methods of calculating LLDF's. In addition, the AASHTO LRFD permits the calculation of LLDF's based on finite element analyses. Therefore, some of the discussions compare LLDF's based on the AASHTO LRFD and finite element analyses.

Chen and Aswad (1996)

The main objective in Chen and Aswad (1996) was to review the accuracy of the approximate methods of analysis for determining LLDF's in the AASHTO LRFD using the results of finite element analyses. Analyses were performed on simple-span, prestressed concrete bridges, comprising prestressed I-girders and a cast-in-place concrete deck. The girders and deck were assumed to act in a composite manner. The researchers investigated bridges with spans that ranged between 90 and 140 ft, had overall widths of 48 to 60 ft, and had 5 to 7 girders spaced at 8 to 10 ft on center. A comparison of the LLDF's based on the finite element analyses and those based on the AASHTO LRFD procedures indicated that LLDF's were reduced by 18 to 23% for interior beams, and reduced 4 to 12% for exterior beams when finite element analyses were used.

Schwarz and Laman (2001)

The results of field tests on three prestressed I-girder bridges are presented, and live load distribution factors were determined from measured service load stresses due to normal truck traffic. The three bridges investigated were similar in cross section and comprised prestressed I-girders and cast-in-place decks. Girder depths ranged from 2.5 to 5 ft, spans ranged from 34 to 102 ft, roadway widths were approximately 46 ft, and all bridges had 6 girders, which were spaced between 6.75 and 7.6 ft on center. Based on measured strains at the midspan of each girder, it was concluded that both one-lane and two-lane LLDF's based on the AASHTO LRFD and AASHTO Standard were conservative. For one-lane loading, the inferred LLDF's were at least 17% lower than those predicted by the AASHTO LRFD and AASHTO Standard. The AASHTO Standard LLDF's were 17 to 41% higher than those measured for two-lane loading, with the highest difference occurring on the longest span. The AASHTO LRFD LLDF'S were 23 to 33% higher than the measured LLDF's for two-lanes.

Shahawy and Huang (2001)

The accuracy of the AASHTO LRFD procedures for calculating LLDF's were investigated in this study. The study compared LLDF's based on AASHTO LRFD with the results for the analyses of 645 bridge models analyzed using a three-dimensional finite element model. The bridge configurations analyzed consisted of spans ranging from 50 to 120 ft in length, with 4 or 5 girders spaced 4 to 10 ft on center, deck overhangs of -0.5 to 5.5 ft, and AASHTO Type II, III, IV and V girders. The girders were modeled and were assumed to act compositely with concrete decks ranging in thickness from 6 to 9 in. Shahawy and Huang concluded that LLDF's calculated using the AASHTO LRFD were generally too conservative for strength evaluation and load rating purposes. However, it was noted that for bridges with beam spacing less than 6 ft, and deck overhangs of 3 ft and greater, the LLDF's calculated using the AASHTO LRFD were lower than those calculated using finite element analyses.

In addition, seven bridges were tested in the field to verify the finite element models. The results of the finite element analyses were within 12% of the values measured in the field.

Barr, Eberhard and Stanton (2001)

A three-span, skewed prestressed concrete bridge was tested in this study and the measured response was compared to results from finite element analyses. A total of twenty-four bridge configurations were analyzed to investigate the effects due to diaphragms, continuity, and skew angle. It was concluded that finite element analyses reproduced the moments calculated using measured strains from the load tests within 6%. In addition, the LLDF's calculated using the AASHTO LRFD were up to 28% greater than those calculated using finite element analyses. The effect of end diaphragms was reported to significantly reduce the LLDF's; however, intermediate diaphragms had almost no effect. LLDF's were also found to decrease with increasing skew angles, an effect that the AASHTO LRFD reasonably approximated.

1.6 OVERVIEW OF DISSERTATION

This dissertation contains nine chapters and fourteen appendices. Chapter 2 is a description of the five bridges that were studied in detail during this investigation. Chapter 3 provides information about the diagnostic load testing program and a description of the measured data collected during the load tests. Chapter 4 provides the analysis and evaluation of the data collected during the load tests. Chapter 5 discusses the design of the fatigue test specimens and provides an overview of fatigue tests that were performed. Chapter 6 discusses the results of the fatigue tests. Chapter 7 includes an overview of the load rating procedures and discusses the results of the load rating analyses. Chapter 8 discussed the sensitivity of load ratings to the tensile stress criterion and evaluates the use of strand stress range for load rating. The conclusions of this investigation are reported in Chapter 9.

The appendices provide information to support the discussions in the chapters. Information included in Appendices A and B corresponds to Chapter 2 and describes the bridges in more detail. Appendix C corresponds to Chapter 3 and includes additional information on the diagnostic load testing program. Appendix D corresponds to Chapter 4 and includes measured data from the load tests. The results of calculations using these data are included in Appendices E and F. Specifically, Appendix E and Appendix F include moments and live load distribution factors inferred from the measured data. Appendix G includes a discussion of the finite element program used and analyses performed on the bridges in this investigation. The results of these analyses are provided in Appendix H. Appendix I corresponds to Chapter 7 and provides information on the load rating procedures used. The information included in Appendix I has been previously reported by Wagener (2002), however, it is included for the convenience of the readers of this dissertation. Appendices J through N correspond to Chapter 5 and include analyses and material property information used in the fatigue study. Appendix J is a discussion of the analysis of an interior beam for one bridge that was used as the prototype for the development of the fatigue specimens. Appendix K is a discussion of the material properties for materials used in the fabrication of the fatigue specimens. Appendices L and M describe analyses performed on the fatigue specimens and include the analysis of measured data used for evaluating the effective prestress force in the specimens, and the analyses of the fatigue specimens used for determining the loads applied to the specimens during the fatigue tests. Appendix N corresponds to Chapter 6 and includes additional data and results from the fatigue tests.

1.7 NOTATION AND DEFINITIONS

1.7.1 Abbreviation of Specifications

Throughout this dissertation, reference will be made to several specifications that are currently used for the design or evaluation of highway bridges. Because the investigation and recommendations are closely tied to these specifications, the edition of each specification used is identified here for clarity. The abbreviations that will be used for these specifications are as follows.

- MCEB – AASTHO Manual for the Condition Evaluation of Bridges (Interim 2003)
- AASHTO Standard – AASHTO Standard Specifications for Highway Bridges, 17th Edition (Interim 2002)
- AASTHO LRFD – AASHTO LRFD Bridge Design Specifications (Interim 2003)

1.7.2 Notation for Concrete Compressive Strength

Two parameters that are central to this dissertation, the limiting concrete tensile stress and the elastic modulus of concrete, are reported as a function of the compressive strength of concrete. Although the concrete compressive strength used for the evaluation of prestressed concrete bridges is typically taken to be the value specified on the design documents, the MCEB permits the use of in situ properties of the bridge for evaluation purposes. As a result, several values of compressive strength are used throughout this investigation. For clarity, the notation that is used to distinguish among the different values of concrete compressive strength is presented here.

- f'_{cs} – Specified compressive strength based on design documents
- f'_{cq} – Compressive strength determined from quality control test records
- f'_{ce} – Estimated in situ compressive strength
- f'_{cm} – Measured compressive strength of laboratory specimens

When the term f'_c is used, any of the four values of compressive strength may be appropriate. Care will be taken to discuss which value is most appropriate for each specific application.

1.7.3 Definition of Index Stress

The tensile stress limit used in the AASHTO load rating and design procedures is calculated using uncracked, transformed composite section properties. For simplicity, the maximum tensile stress calculated at the extreme fiber of the transformed cross section is defined as the index stress.

CHAPTER 2

Description of the Prestressed Concrete Bridges Tested in this Investigation

This chapter presents an overview of the five bridges tested in the diagnostic load testing portion of the project. In addition to general bridge information, the material properties and cross-sectional properties are discussed. The material properties and cross-sectional properties presented are used throughout the analyses presented in other chapters, such as analyses of measured data from diagnostic load tests, analyses used to evaluate the strand stress ranges used in the fatigue testing portion of the investigation, load rating analyses, and finite element analyses. More information regarding the bridges can be found in Appendices A and B and in Wagener (2002).

2.1 OVERVIEW OF BRIDGE STRUCTURES

The five bridges investigated were selected from a list of thirty-three bridges provided by TxDOT. A summary of the thirty-three bridges is presented in Appendix A. All of the bridges on the TxDOT list included spans that had load ratings controlled by the concrete tensile stress criterion presented in the AASHTO MCEB (2003). A visual survey of these bridges was conducted and spans were selected based on ease of access for instrumentation and load testing. A total of eight spans on five bridges were selected and tested. Five of these spans had load ratings controlled by the concrete tensile stress criterion. Table 2.1 summarizes general information about each bridge. The names assigned to each bridge in Table 2.1 are throughout this dissertation.

Table 2.1 General Bridge Information (Wagener 2002)

Bridge Name	Year Completed	Location	Daily Traffic Volume*	% Truck Traffic*
Chandler Creek	1965	IH 35 @ Chandler Creek	7,951	25%
Lake LBJ	1964	FM 1431 @ Lake LBJ	8,300	5%
Lampasas River	1970	FM 2657 @ Lampasas River	2,100	12%
Willis Creek	1961	FM 972 @ Willis Creek	800	16%
Wimberley	1959	RM 12 @ Blanco River	10,200	5%

*Recorded by TxDOT between 1999 and 2000.

All the bridges selected for load testing were two-lane highway bridges comprising prestressed concrete beams and a composite cast-in-place deck. All spans were simply-supported. Although the bridges were similar in layout and construction, their overall dimensions did vary, as shown in Table 2.2. The spans varied between 40 ft and 75 ft in length, roadway widths varied between 24 ft and 28 ft-8 in., beam spacing varied between 6 ft-8 in. and 8 ft and skew angles varied between 0° and 30°. Detailed information about each bridge, including plan dimensions, cross sections, beam details, curb details and diaphragm configurations, are summarized in Appendix A.

Table 2.2 Overall Dimensions of Bridges

Bridge Name	Bridge Length	Roadway Width	Beam Length	No. of Spans	No. of Spans Tested	No. of Beams	Spacing of Beams	Skew Angle	Slab Thickness	Curb**	Deck Overhang[†]
Chandler Creek	140′	28′-0″	40′-0″	2	1	4	8′-0″	30°	7.25″	No	3′-2″
			60′-0″	1	1						
Lake LBJ	780′	28′-0″	65′-0″	12	1	4	8′-0″	0°	7.25″	Yes	3′-7″
Lampasas River	600′	26′-0″	75′-0″	8	2	4	7′-4″	0°	6.5″	No	3′-1½″
Willis Creek	130′	24′-0″	65′-0″	2	1	4	6′-8″	0°	6″	Yes	2′-10″
Wimberley	440′	30′-0″	40′-0″	5	2	5	6′-11″	22°	6.25″	Yes	2′-2¾″*
			60′-0″	4	0						

* Overhang reported is an average dimension. Overhang varies because bridge deck is curved in plan.

** Curb dimensions vary. Curb details are included in Appendix A.

[†] Deck overhang as measured from centerline of exterior girder to exterior face of curb or slab.

2.2 COMPRESSIVE STRENGTH OF CONCRETE

As discussed in Chapter 1, the load rating for many older prestressed concrete bridges in Texas is controlled by the concrete tensile stress criterion in the MCEB (2003). TxDOT currently uses the specified concrete compressive strength in all calculations to establish the load rating. The actual concrete compressive strength is likely to be considerably higher than the specified value; therefore, available data were used to estimate the in situ strength of the concrete. Various estimates of the in situ compressive strength are discussed in this section. Additional information on the measured concrete material properties for the five bridges is summarized in Appendix B.

2.2.1 Specified Compressive Strength

Design calculations are based on the specified compressive strength of the concrete; however, the average measured strength of the concrete must exceed this value. Most ready-mix suppliers design concrete mixtures such that the average measured strength at 28 days exceeds the specified compressive strength and thereby avoid the costly penalties associated with supplying under-strength concrete. Additionally, there are significant economic advantages associated with early form removal in the precast, prestressed concrete industry. Through a combination of concrete mixture design and curing, the concrete achieves the specified strength at an early age to maximize throughput at the plant. For these reasons, load rating calculations based on the specified compressive strength of the concrete are considered to be conservative. The specified concrete compressive strengths, f'_{cs}, for the bridges considered in this study are summarized in Table 2.3. The specified compressive strengths for the prestressed beams in the bridges in this study were 4000 psi at release, f'_{csi}, and 5000 psi at 28 days, f'_{cs}, except for the Lampasas River Bridge which had a specified compressive strength of 5100 psi. The slabs and curbs for bridges in this study had a specified compressive strength of 3000 psi.

Table 2.3 Specified Compressive Strength of Concrete (Wagener 2002)

	Beam		Slab	Curb
Bridge Name	f'_{csi} (psi)	f'_{cs} (psi)	f'_{cs} (psi)	f'_{cs} (psi)
Chandler Creek	4000	5000	3000	-
Lake LBJ	4000	5000	3000	3000
Lampasas River	4000	5100	3000	-
Willis Creek	4000	5000	3000	3000
Wimberley	4000	5000	3000	3000

2.2.2 Construction Quality Control Records

The compressive strength of the concrete was measured during construction as part of the quality control process. These data were available in the TxDOT archives for the prestressed beams used to construct four of the five bridges and for the cast-in-place concrete used in the slab for the Chandler Creek bridge. All results correspond to compressive strength of 6x12-in. cylinders. Throughout this dissertation the maximum compressive strength measured during the quality control tests will be called the quality control compressive strengths, f'_{cq}.

Data from compressive strength tests on concrete from the prestressed beams were available at ages between 1 and 21 days. The average compressive strength at each age for spans where test records were available is shown in Figure 2.1. The average compressive strength for each span at release of the prestressing and for the latest available record is summarized in Table 2.4 and have been designated f'_{cqi} and f'_{cq}, respectively. As reported in Table 2.4, the compressive strengths based on the latest available record were between 48% and 74% higher than the specified compressive strengths.

Data from compressive strength tests on concrete from the Chandler Creek cast-in-place slab were available at ages between 3 and 28 days. The average compressive strength at each age is shown in Figure 2.2. The average compressive strength at 28 days is reported in Table 2.5, and was 76% higher than the specified compressive strength.

Table 2.4 Maximum Concrete Compressive Strength Reported in Quality Control Records for Prestressed Beams

		Release		Latest Available Reports			
Bridge Name		No. of Tests	f'_{cqi} (psi)	Age* (days)	No. of Tests	f'_{cq} (psi)	f'_{cq}/f'_{cs}
Chandler Creek	40-ft Span	19	5100	18	2	7400	148%
	60-ft Span	2	5500	14	6	8700	174%
Lake LBJ		30	5100	14	26	8000	160%
Lampasas River		8	6000	10	2	8300	163%
Willis Creek		4	5400	21	4	8600	172%

* Age after placement of concrete.

Table 2.5 Maximum Concrete Compressive Strength Reported in Quality Control Records for Cast-in-place Slab in Chandler Creek Bridge

Bridge Name	Latest Available Reports			
	Age (days)	Number of Tests	f'_{cq} (psi)	f'_{cq}/f'_{cs}
Chandler Creek	28	6	5300	176%

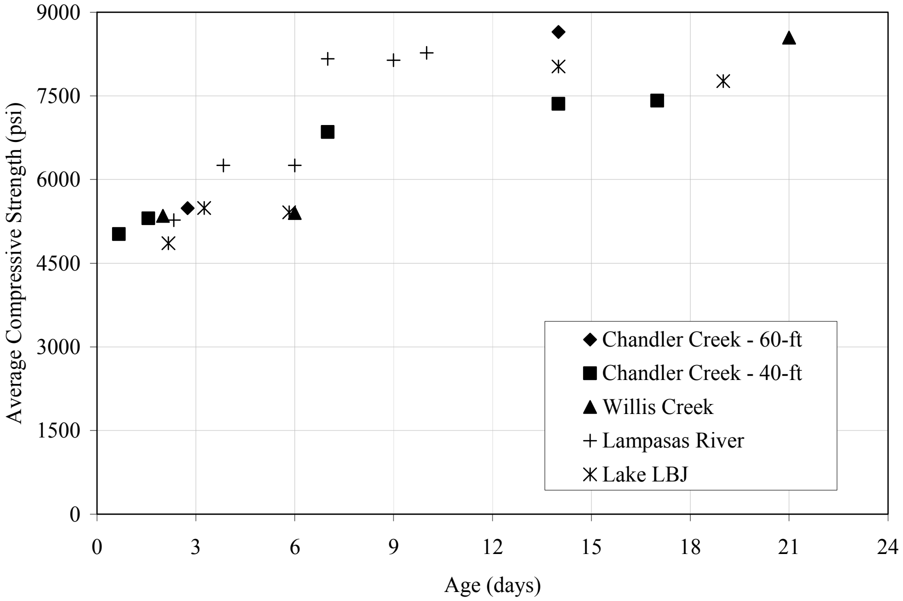

Figure 2.1 Measured Concrete Compressive Strength Obtained from Construction Quality Control Records for Prestressed Beams

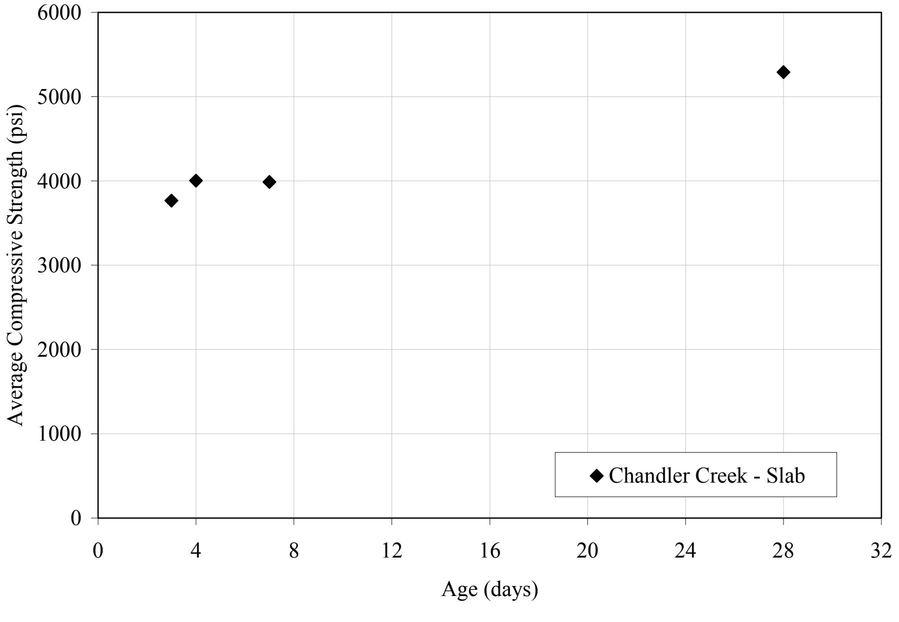

Figure 2.2 Measured Concrete Compressive Strength Obtained from Construction Quality Control Records for Slabs

The values of concrete compressive reported in Table 2.4 based on the latest available quality control test record, are considered to be lower bound estimates of the in situ compressive strength of the concrete in the prestressed beams. Quality control test records were not available for the prestressed beams in the Wimberley bridge. Therefore, quality control compressive strengths were assumed to be the average of the quality control compressive strengths of all other beams in this investigation. Additionally, quality control test records for concrete in the cast-in-place slabs and curbs were only available for the Chandler Creek bridge. Therefore, the quality control compressive strength for all other cast-in-place slabs and curbs was assumed to be the same as for the Chandler Creek slab. The quality control compressive strengths that will be used for analyses throughout this dissertation have been summarized in Table 2.6.

Table 2.6 Summary of Quality Control Compressive Strengths

Bridge Name		Beam		Slab	Curb
		f'_{cqi} (psi)	f'_{cq} (psi)	f'_{cq} (psi)	f'_{cq} (psi)
Chandler Creek	40-ft Span	5100	7400	5300	-
	60-ft Span	5500	8700	5300	-
Lake LBJ		5100	8000	5300	5300
Lampasas River		6000	8300	5300	-
Willis Creek		5400	8600	5300	5300
Wimberley		5400	8200	5300	5300

2.2.3 Estimated In Situ Compressive Strength

Concrete continues to gain strength with time; therefore, it is reasonable to expect that the in situ compressive strength is greater than the compressive strength reported in the quality control test records. The relationship between compressive strength and age given in ACI 209R-92, *Prediction of Creep,* *Shrinkage, and Temperature Effects in Concrete Structures*, was used to estimate the in situ compressive strengths using data from the quality control tests. Compressive strengths estimated based on this model will be called the estimated in situ compressive strengths, f'_{ce}, throughout this dissertation.

The ACI 209 model uses the 28-day compressive strength and two constants, α and β, to estimate the variation of the compressive strength with time. The constants α and β are functions of the type of cement used, Type I or Type III, and curing method used, moist or steam curing. Equation 2.1 is the ACI 209 relationship between the compressive strength of concrete at 28-days, $f'_c(28)$, and compressive strength at all other times, $f'_c(t)$. The constants, α and β, fall in the range of 0.05 to 9.25 and 0.67 to 0.98, respectively.

$$f'_c(t) = \frac{t}{\alpha + \beta t} f'_c(28) \tag{2.1}$$

For the prestressed beams, the values of α and β were taken as 2.3 and 0.92, respectively. These values correspond to Type III cement and moist curing. For the slabs, the values of α and β were taken as 4.0 and 0.85, respectively, which correspond to Type I cement and moist curing.

The data from the quality control tests (Table 2.4) were used in Eq. 2.1 to estimate the 28-day strength. These estimates are summarized in Table 2.7 and Table 2.8 for the prestressed beams and cast-in-place slabs, respectively. The estimated 28-day compressive strength was between 56% and 88% higher than the specified compressive strength of the prestressed beams.

The estimated 28-day compressive strength was then used to forecast the in situ compressive strength at the time of field testing. These estimates are also summarized in Table 2.7 and Table 2.8. The estimated in situ compressive strength was between 74% and 106% higher than the specified compressive strength of the prestressed beams and 107% higher than the specified strength of the Chandler Creek cast-in-place slab. The estimated in situ compressive strengths of the prestressed beams and cast-in-place slabs used for the analyses of bridges studied in this investigation are summarized in Table 2.9. The values reported for the Wimberley bridge are the average of the estimated compressive strengths of bridges for which quality control test records were available.

Table 2.7 Estimated 28-Day and In Situ Compressive Strengths of the Prestressed Beams

Bridge Name	Quality Control Records		Estimated 28-Day Strength (psi)	Estimated In Situ		Percent of Specified Strength (f'_{ce}/f'_{cs})
	Time, t (days)	f'_{cq} (psi)		Time, t (days)	f'_{ce} (psi)	
Chandler Creek (40-ft Span)	14	7400	7800	12,500	8700	174%
Chandler Creek (60-ft Span)	14	8700	9400	12,500	10,300	206%
Lake LBJ	14	8000	8700	13,500	9500	190%
Lampasas River	10	8300	9500	11,300	10,300	202%
Willis Creek	21	8600	8900	14,000	9600	192%

Table 2.8 Estimated In Situ Compressive Strength of Cast-in-Place Slabs and Curbs

Bridge Name	Quality Control Records		Estimated In Situ		Percent of Specified Strength (f'_{ce}/f'_{cs})
	Time, t (days)	f'_{cq} (psi)	Time, t (days)	f'_{ce} (psi)	
Chandler Creek	28	5300	12,500	6200	207%

Table 2.9 Summary of Estimated In Situ Compressive Strengths

Bridge Name		Beam		Slab	Curb
		f'_{cei} (psi)	f'_{ce} (psi)	f'_{ce} (psi)	f'_{ce} (psi)
Chandler Creek	40-ft Span	5100	8700	6200	-
	60-ft Span	5500	10,300	6200	-
Lake LBJ		5100	9500	6200	6200
Lampasas River		6000	10,300	6200	-
Willis Creek		5400	9600	6200	6200
Wimberley		5100	9700	6200	6200

2.2.4 Measured Strength of Cores Extracted From Chandler Creek Bridge

In addition to the estimates described in Section 2.2.3, the in situ concrete strength was evaluated from compression tests of concrete cores. TxDOT permitted a small number of concrete cores to be extracted from one bridge span. The span selected was the 60-ft span of the Chandler Creek bridge. The cores were obtained and tested in accordance with the *Standard Test Method for Obtaining and Testing Drilled Cores and Sawed Beams of Concrete* (ASTM C42).

Figure 3.2 shows the location and orientation of the cores that were extracted from the structure. Two, 3-in. diameter horizontal cores were taken from the web of each beam near midspan. The cores from the prestressed beams were extracted cleanly, did not contain any reinforcing steel and had an average diameter and length of 2.72 in. and 7.00 in., respectively. In addition, three vertical cores were extracted from the concrete slab near the eastern edge and spaced equally along the length. In an attempt to avoid coring through reinforcement in the slab, a HILTI Ferroscan FS-10 reinforcement detection system was used to locate the reinforcement. However, all three cores extracted from the deck contained reinforcing steel. As a result, in accordance with ASTM C42, these cores were not tested.

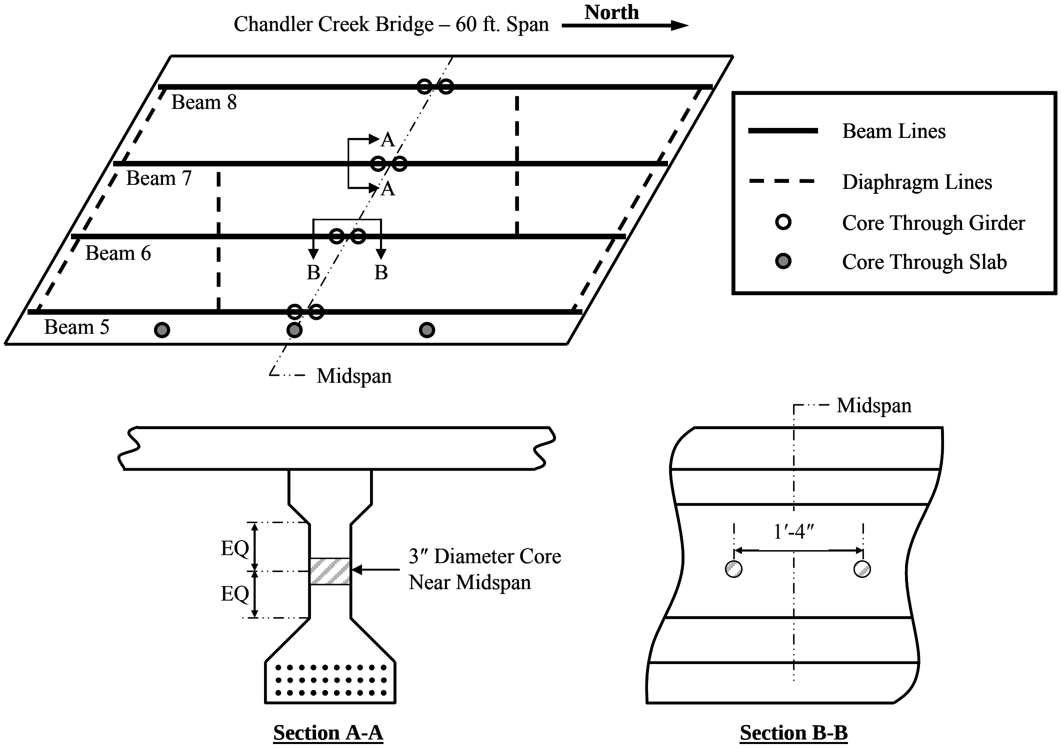

Figure 2.3 Chandler Creek Coring Plan

Prior to testing, the cores from the beams were cut to an average length of 5.09 in. and capped with sulfur. The average overall length was 6.03 in., resulting in an average length to diameter ratio of 2.22. The compression test results from these cores are summarized in Table 2.10. The mean core strength was 7400 psi, with a coefficient of variation of 12%. This is a 48% increase in strength over the minimum specified design compressive strength.

As reported by Bartlett and MacGregor (1994), the strength of concrete cores can be affected by several factors. These include, but are not limited to, specimen diameter, specimen length to diameter ratio, moisture condition, core damage, and the location and orientation of the core.

These effects have been recognized in ACI 318-02, which states that the average strength of cores extracted from a structure is likely to be less than the in situ compressive strength. In addition, ACI 318-02 permits acceptance of concrete where core strengths exceed 85% of the specified strength, provided the strength of no single core is less than 75% of the specified strength. Assuming the lowest core strength, 7000 psi, is 75% of the actual compressive strength, the compressive strength of the concrete in the Chandler Creek bridge beams may be conservatively estimated to be between 7400 and 9300 psi. Therefore, using the available material test records for load rating prestressed concrete bridges appears appropriate.

Table 2.10 Average Compressive Strength of Cores from the Prestressed Beams of the Chandler Creek Bridge

Location	Average Core Strength, f'_{cm} (psi)	Percent of Specified Compressive Strength (f'_{cm}/ f'_{cs})
East Exterior (Beam 5)	7100	142%
East Interior (Beam 6)	7300	146%
West Interior (Beam 7)	7000	140%
West Exterior (Beam 8)	8300	166%
Mean	7400	148%
Coefficient of Variation	12%	

2.3 CALCULATED SECTION PROPERTIES

The procedures used to calculate the uncracked, transformed, composite section properties for the interior and exterior sections of each bridge are described in this section. The plans, sections and details given in Appendix A were used to establish the dimensions of the cross sections. Prestressing strand configurations were based on the details provided on the design drawings. The effective flange widths were calculated using the provisions in the AASHTO LRFD Specifications, which are summarized in Figure 2.4 and Table 2.11. It should be noted that the width of the exterior overhangs were not increased when curbs were present as permitted by the AASHTO LRFD. However, the curbs were included in the calculation of the transformed, composite section properties for the exterior beams based on their transformed area and relative position.

Transformed, composite section properties were calculated for three different levels of concrete compressive strength: f'_{cs}, f'_{cq}, and f'_{ce}. The corresponding section properties are shown in Table 2.12, Table 2.13 and Table

2.14, respectively. The modulus of elasticity (E_c) for concrete was calculated using Eq. 2.2 from ACI 318-02.

$$E_c = 57{,}000\sqrt{f'_c} \tag{2.2}$$

where f'_c was the corresponding compressive strength in psi, and E_c is the modulus of elasticity in psi. The modulus of elasticity of the prestressing strand was assumed to be 28,500 ksi.

The values reported include the transformed composite area (A_{comp}), the transformed composite moment of inertia, (I_{comp}), the distance from the calculated neutral axis to the bottom fiber of the section ($y_{b\text{-}comp}$), and the distance from the calculated neutral axis to the top fiber of the slab ($y_{t\text{-}comp}$). Throughout this dissertation the transformed, composite section properties calculated based on the three levels of compressive strength will be called the specified section properties, quality control section properties and estimated in situ section properties, respectively.

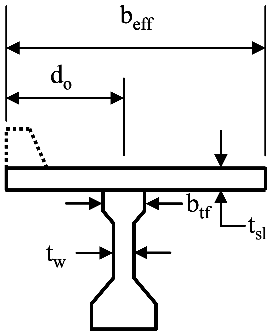

(a) Exterior Beam

b_{eff} = Effective Flange Width.

For exterior beams, the effective flange width is the minimum of the following:

1. Minimum of $L_{eff}/8 + d_o$ or $L_{eff}/4$ where L_{eff} is the effective span length taken as the center-to-center distance between the bearing pads
2. Maximum of $6t_{sl} + t_w/2 + d_o$ or $6t_{sl} + b_{tf}/2 + d_o$
3. Maximum of $12t_{sl} + t_w$ or $12t_{sl} + b_{tf}/2$
4. Minimum of $S/2 + d_o$ or S, where S is center-to-center distance to the adjacent interior beam

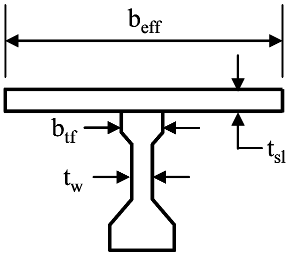

(b) Interior Beam

For interior beams, the effective flange width is the minimum of the following:

1. $L_{eff}/4$, where L_{eff} is the effective span length taken as the center to center distance between the bearing pads
2. Maximum of $12t_{sl} + t_w$ or $12t_{sl} + b_{tf}/2$
3. S, where S is center-to-center distance to the adjacent beams (This assumes the spacing to the adjacent beam is the same on both sides)

Figure 2.4 Effective Flange Width Used for Calculating Composite Section Properties

Table 2.11 Summary of Effective Flange Widths Used for Calculating Transformed Composite Section Properties

Bridge Name	Interior Beam		Exterior Beam	
	b_{eff} (in.)	Governing Criterion*	b_{eff} (in.)	Governing Criterion*
Chandler Creek – 40′ Span	93.5	2	84.8	2
Chandler Creek – 60′ Span	94.0	2	85.0	2
Lake LBJ	94.0	2	80.0	2
Lampasas River	85.0	2	80.0	2
Willis Creek	79.0	2	73.5	2
Wimberley	81.5	2	55.8	2

* Criteria are given in Figure 2.4.

Table 2.12 Specified Section Properties

Bridge Name	Interior Beam				Exterior Beam			
	A_{comp} (in.^{2})	I_{comp} (in.^{4})	$y_{b\text{-}comp}$ (in.)	$y_{t\text{-}comp}$ (in.)	A_{comp} (in.^{2})	I_{comp} (in.^{4})	$y_{b\text{-}comp}$ (in.)	$y_{t\text{-}comp}$ (in.)
Chandler Creek – 40′ Span	896	163000	28.1	13.2	847	158000	27.5	13.8
Chandler Creek – 60′ Span	1043	279000	30.3	16.9	992	269000	29.6	17.7
Lake LBJ	1058	283000	30.3	17.0	1090	331000	31.8	15.4
Lampasas River	942	254000	28.5	18.0	917	249000	28.1	18.4
Willis Creek	884	233000	27.7	18.4	935	269000	29.2	16.8
Wimberley	772	144000	26.1	14.2	753	168000	27.0	13.2

Table 2.13 Quality Control Section Properties

Bridge Name	Interior Beam				Exterior Beam			
	A_{comp} (in.^{2})	I_{comp} (in.^{4})	$y_{b\text{-}comp}$ (in.)	$y_{t\text{-}comp}$ (in.)	A_{comp} (in.^{2})	I_{comp} (in.^{4})	$y_{b\text{-}comp}$ (in.)	$y_{t\text{-}comp}$ (in.)
Chandler Creek – 40′ Span	943	166000	28.6	12.6	889	161000	28.1	13.2
Chandler Creek – 60′ Span	1041	276000	30.5	16.8	990	266000	29.8	17.5
Lake LBJ	1068	282000	30.7	16.6	1113	333000	32.3	14.9
Lampasas River	954	255000	29.0	17.5	928	249000	28.6	17.9
Willis Creek	883	232000	27.9	18.1	935	268000	29.4	16.6
Wimberley	783	144000	26.4	13.8	763	169000	27.4	12.9

Table 2.14 Estimated In Situ Section Properties

Bridge Name	Interior Beam				Exterior Beam			
	A_{comp} (in.^{2})	I_{comp} (in.^{4})	$y_{b\text{-}comp}$ (in.)	$y_{t\text{-}comp}$ (in.)	A_{comp} (in.^{2})	I_{comp} (in.^{4})	$y_{b\text{-}comp}$ (in.)	$y_{t\text{-}comp}$ (in.)
Chandler Creek – 40′ Span	941	165000	28.6	12.6	887	160000	28.1	13.2
Chandler Creek – 60′ Span	1037	274000	30.5	16.8	986	265000	29.8	17.5
Lake LBJ	1062	280000	30.7	16.6	1107	331000	32.3	14.9
Lampasas River	939	251000	28.8	17.7	914	245000	28.4	18.1
Willis Creek	891	234000	28.0	18.0	944	270000	29.6	16.4
Wimberley	779	143000	26.4	13.8	760	168000	27.4	12.9

2.4 SUMMARY

An overview of the bridges being studied was presented in this chapter. Three different estimates of compressive strength were discussed: f'_{cs}, f'_{cq}, and f'_{ce}. For each estimate of compressive strength, transformed, composite section properties were calculated for the interior and exterior beams of each bridge, and have been called specified section properties, quality control section properties and estimated in situ section properties. The notation is important because these section properties will be used in the analyses discussed in other chapters.

The quality control and estimated in situ section properties vary between 95% and 105% of the specified section properties. The difference is attributable to the varying modular ratios, which were different for each estimate of concrete compressive strength. The small variation indicates that the different estimates for concrete compressive strength had little influence on the calculation of transformed, composite areas and moment of inertias. However, both the modulus of elasticity of concrete and the tensile stress used for load rating are functions of the compressive strength of concrete. Therefore, the different levels of concrete compressive strengths will have a significant influence on the calculated values of modulus of elasticity of the concrete and the limiting tensile. The influence of these parameters will be discussed in Chapter 7.

CHAPTER 3

Description of Bridge Load Test Procedures and Measured Data

This chapter presents an overview of the test procedures used in the diagnostic load testing portion of this investigation. In addition to discussing the instrumentation and equipment used for data collection, the load paths and loading vehicles are also addressed. More information regarding the load test procedures can be found in Appendices C and D and in Wagener (2002), where this information has been previously reported.

3.1 INSTRUMENTATION

Figure 3.1 is a schematic of the components that comprised the data acquisition system used for data collection and shows the connectivity of the various components and the instrumentation used. Figure 3.2 shows several of these components and Figure 3.3 shows the typical arrangement of these components installed in the field.

The system included a Campbell Scientific CR9000 data logger, which allowed fifty-five channels of input and was powered by a 12-volt DC source. The CR9000 sampled instrumentation output voltages at a rate of 10 Hz during each load test, and then averaged those data using a five-point average before storing the value in a data file. Data files stored in the CR9000 were then downloaded to a laptop computer. The "clicker" is a device used to manually interrupt the excitation voltage sent out to the instrumentation. The interruption of the excitation voltage created a distinct record in the CR9000 data file that was used to locate the longitudinal position of the loading vehicles on the bridge.

Strain gages were connected to the CR9000 through a series of cables, junction boxes and completion boxes. To avoid electrical instability and interference, the data acquisition system was grounded, the primary and secondary cables were shielded, and the junction boxes and completion boxes were designed to minimize fluctuations in output voltage.

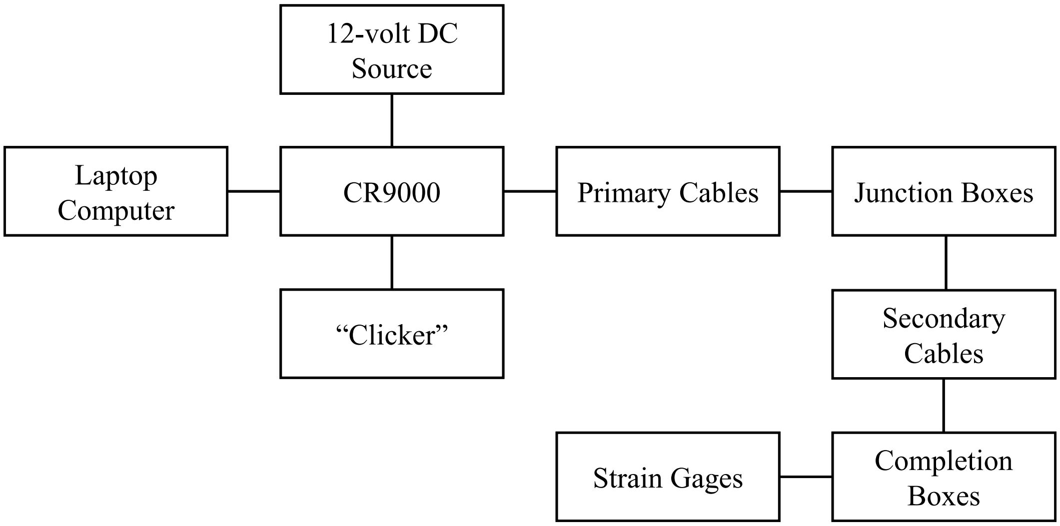

Figure 3.1 Components of the Data Acquisition System (Wagener 2002)

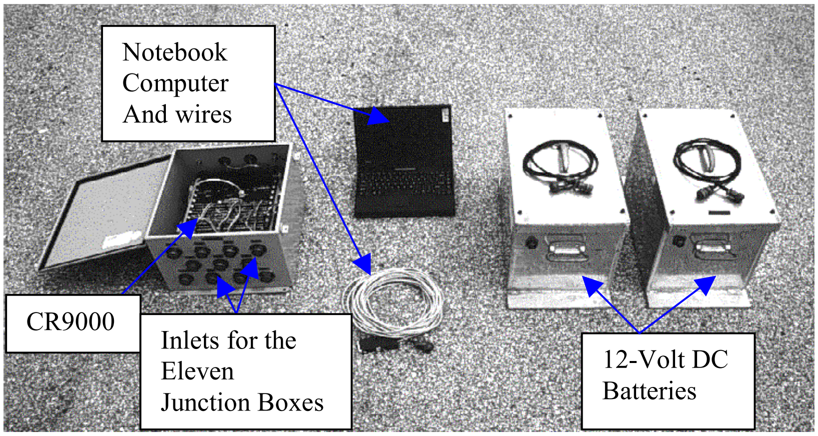

Figure 3.2 Data Acquisition System Hardware (Matsis 1999)

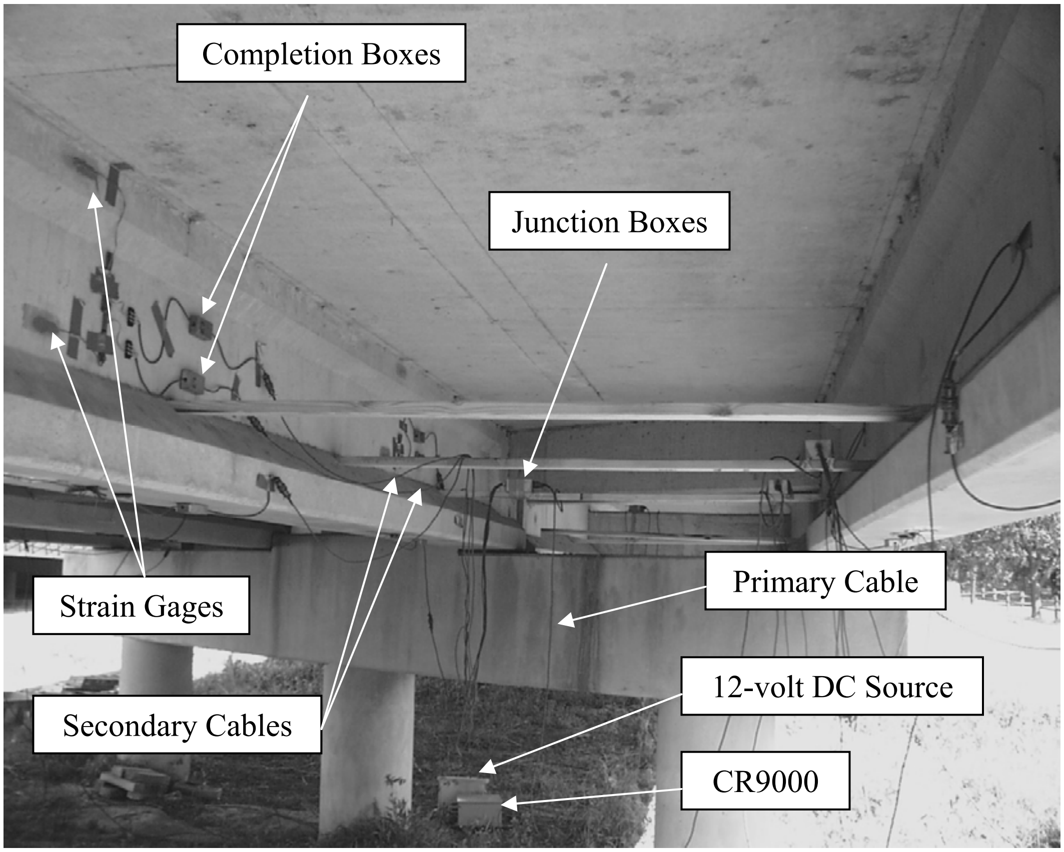

Figure 3.3 Arrangement of CR 9000, Primary Cables, Junction Boxes, Secondary Cables, Completion Boxes, and Strain Gages (Wagener 2002)

Figure 3.4 shows the instrumentation plan for the Chandler Creek bridge. Similar plans are included in Appendix C for the other four. The plan indicates the locations where strain gages were placed on the bridge. As noted, gages were installed at multiple locations along each beam within the instrumented span. At each location, strain gages were installed at several depths on the section. Gages were typically installed on the bottom fiber, web, and top flange of the beam and were designated “bottom”, “web” and “top” gages. Figure 3.5 shows the approximate position of and nomenclature for the gages installed. Where multiple spans were tested, the limitations of the data acquisition system required that the top gages away from midspan be eliminated. Temperature compensating, 120-ohm, electrical resistance strain gages with a 2-in. gage length were used for all tests. Figure 3.6 and Figure 3.7 are photographs of the strain gages as installed in the field.

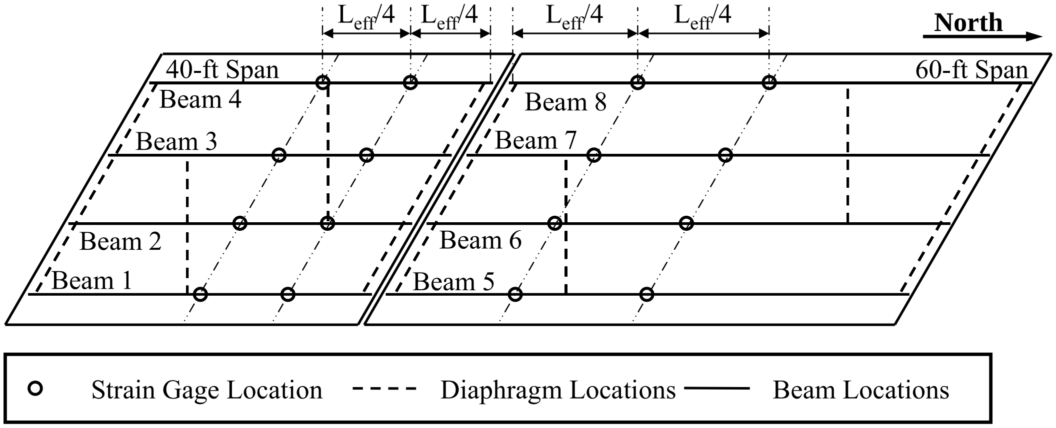

Figure 3.4 Instrumentation Plan for Chandler Creek Diagnostic Load Testing

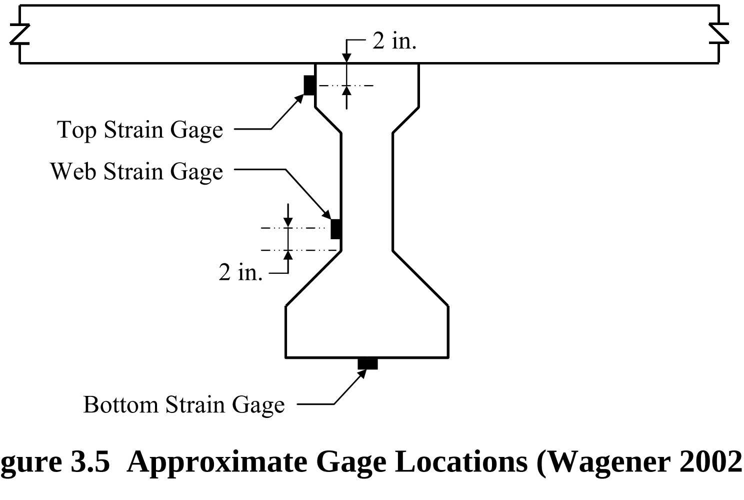

Figure 3.5 Approximate Gage Locations (Wagener 2002)

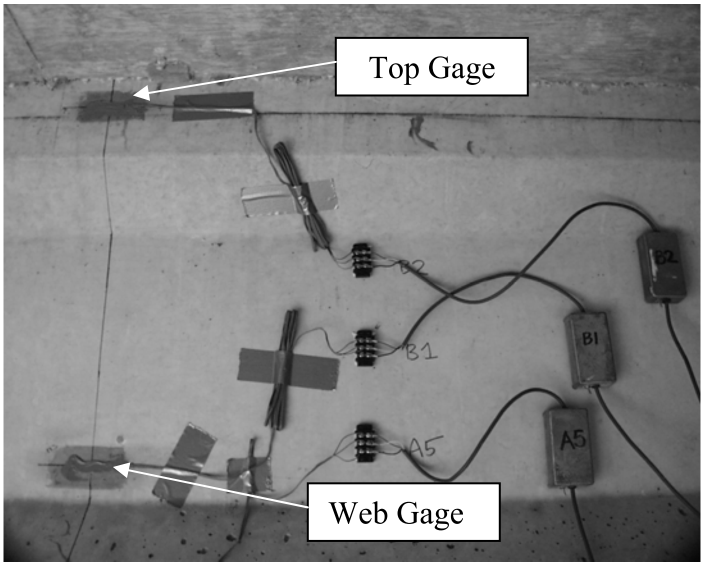

Figure 3.6 Placement of Web and Top Strain Gages (Wagener 2002)

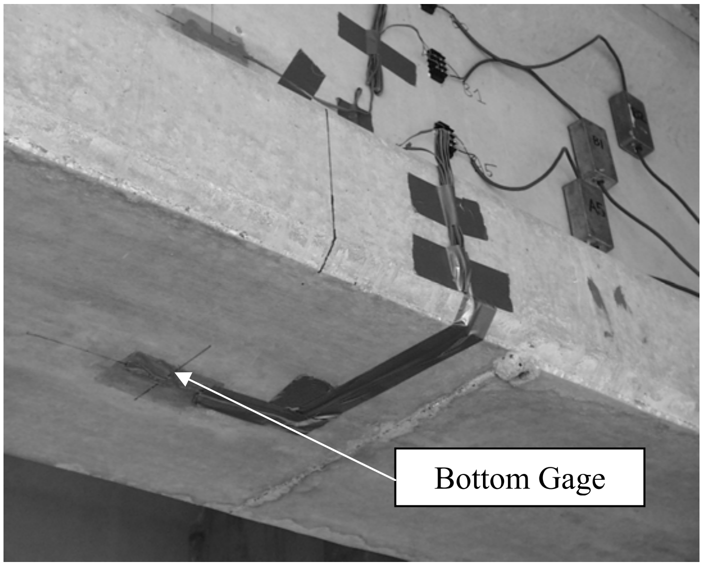

Figure 3.7 Placement of Bottom Strain Gage (Wagener 2002)

3.2 TEST VEHICLES

The vehicles used to provide live load were standard ten cubic-yard dump trucks provided by TxDOT. Figure 3.8 is a photograph of the type of vehicle used and Figure 3.9 shows the dimensions. The vehicles were loaded with various construction materials and axle weights were measured at a weigh station before the trucks arrived at the bridge site. At the Chandler Creek and Willis Creek bridges, individual wheel group loads were measured using a portable scale, provided by the Travis County Sheriff's Department, that was accurate to the nearest fifty pounds. Table 3.1 summarizes the axle weights of the trucks used for the diagnostic load tests.

Figure 3.8 Typical Vehicle Used for Diagnostic Load Testing

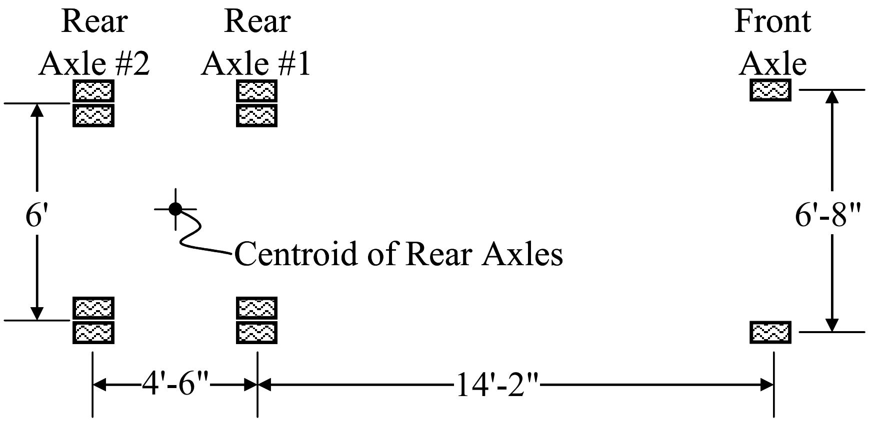

Figure 3.9 Dimensions of Loading Vehicles

Table 3.1 Axle Weights of the Loading Vehicles

Bridge Name	Truck Number	Axle Weights (kip)			Total Weight (kip)
		Front	Rear #1	Rear #2	
Chandler Creek	1	10.7	15.5	14.3	40.5
	2	11.1	15.0	14.0	40.1
Lake LBJ	1	12.7	18.0	18.0	48.7
	2	10.8	17.6	17.6	46.0
Lampasas River	1	10.9	17.2	17.2	45.3
	2	10.7	16.7	16.7	44.1
Willis Creek	1	12.6	18.6	17.9	49.1
	2	10.6	18.2	17.8	46.6
Wimberley	1	13.3	18.6	18.6	50.5
	2	9.9	18.0	18.0	45.9

3.3 LOAD PATHS, VEHICLE CONFIGURATIONS AND TEST RUNS

Several load paths and vehicle configurations were used at each bridge site to obtain a comprehensive view of the distribution of live load and bridge response. Three different vehicle configurations were used during the diagnostic load testing: “single-truck,” “side-by-side,” and “back-to-back.” Diagrams and photographs of these configurations are shown in Figure 3.10 through Figure

3.15. The lines on each diagram indicate the reference line that was used to locate the truck(s) on the bridge, and the arrow indicates the direction of truck movement.

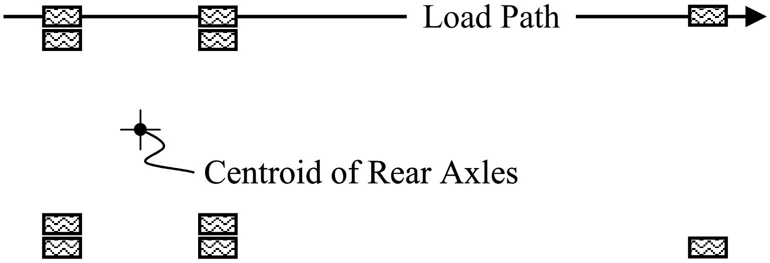

Figure 3.10 Configuration of Single Truck Run

Figure 3.11 Photograph of Single Truck Run at Willis Creek

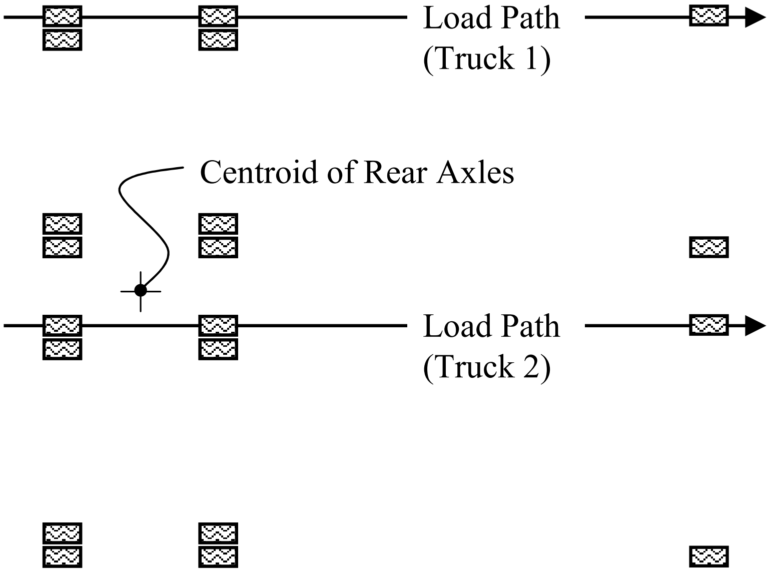

Figure 3.12 Configuration of Side-by-Side Truck Run

Figure 3.13 Photograph of Side-by-Side Truck Run at Willis Creek

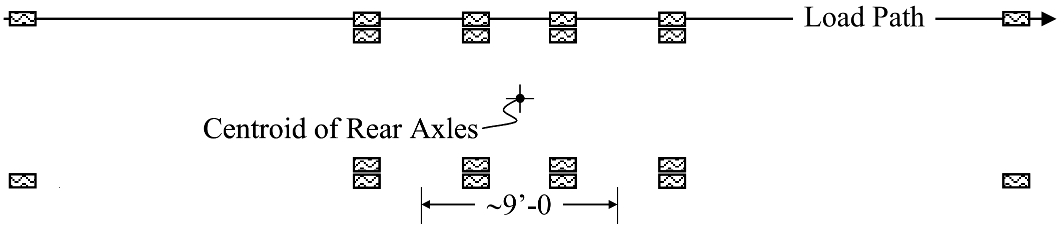

Figure 3.14 Configuration of Back-to-Back Truck Runs

Figure 3.15 Photograph of Back-to-Back Truck Run at Lampasas River

Figure 3.16 shows the load path plan for the Chandler Creek bridge. As noted, the load paths are shown as lines with an arrow indicating the direction of truck movement, and beam and diaphragm locations are shown as broken lines. These load path lines correspond to the paths indicated in the truck configuration figures previously discussed. The load paths were arranged such that the centerline of the truck axles were either centered on an interior bridge beam or between two adjacent bridge beams. This is shown more clearly in Figure 3.17 which indicates the location of the truck wheel lines for each path shown in Figure 3.16. Similar figures for the other four bridges are included in Appendix C. Figure 3.18 illustrates how these load paths were marked in the field.

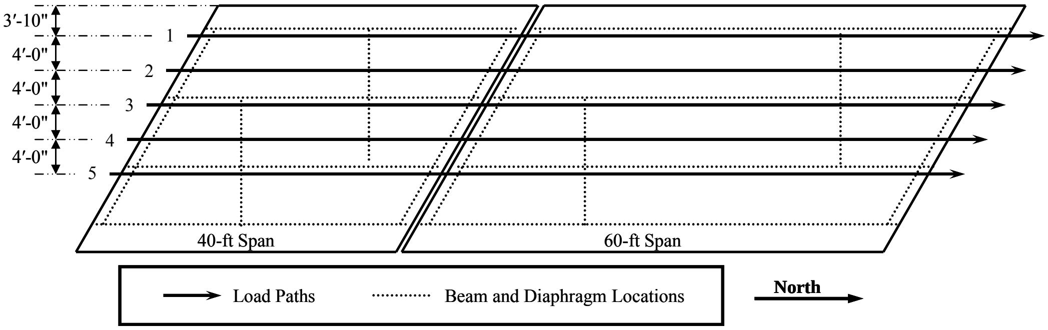

Figure 3.16 Plan of Chandler Creek Loading Paths

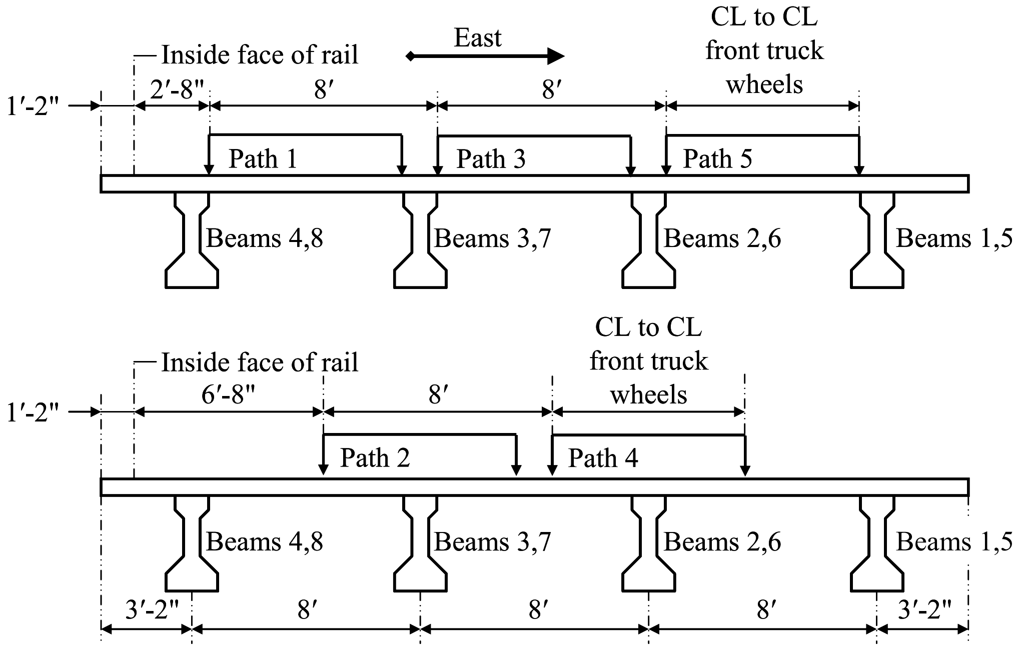

Figure 3.17 Load Paths for Chandler Creek Bridge Diagnostic Load Testing

Figure 3.18 Photograph of Load Paths at Willis Creek Looking East

At each bridge, multiple load tests were conducted and each test was designated with a “run number”. The number of load tests conducted at each bridge varied between fifteen and twenty. Table 3.2 summarizes the run number, loading configuration and path that each truck traveled on for the load tests conducted at the Chandler Creek bridge. Similar tables for the other bridges are included in Appendix C. To establish the repeatability of data, two runs were conducted for each combination of truck configuration and load paths. This also provided a level of redundancy in case unusable data were collected for any particular run.

Table 3.2 Test Runs at the Chandler Creek Bridge

Run Number	Loading Configuration	Truck 1 Path Number	Truck 2 Path Number
1	Side-by-Side	1	4
2	Side-by-Side	1	4
3	Side-by-Side	1	5
4	Side-by-Side	1	5
5	Side-by-Side	2	5
6	Side-by-Side	2	5
7	Back-to-Back	1	1
8	Back-to-Back	1	1
9	Back-to-Back	3	3
10	Back-to-Back	3	3
11	Back-to-Back	5	5
12	Back-to-Back	5	5
13	Single-Truck	1	—
14	Single-Truck	3	—
15	Single-Truck	5	—

3.4 CALCULATION OF CONCRETE STRAIN FROM MEASURED DATA

Detailed information on the measured strains has been previously reported by Wagener (2002). This section includes a discussion of the calculations that were performed to determine strains from the data collected, and a brief discussion of the general trends in the measured strains. Sample strain histories and the maximum measured strains for the gages located at the midspan of the bridges are summarized in Appendix D.

As previously discussed, the CR9000 data logger measured and recorded output voltages from the strain gages installed on the bridge. Using these measured voltages, concrete strains were calculated using Eq. 3.1.

$$\mu\varepsilon = \frac{4(V_{out})}{GF(V_{excite})} \cdot 10^6 \qquad (3.1)$$

In Eq. 3.1, V_{out} is the output voltage from the strain gages recorded by the CR9000, V_{excite} is the excitation voltage, which was supplied by the CR9000 and was approximately 5000 mV, GF is the strain gage factor, which was 2.09 for the strain gages used on this project, and $\mu\varepsilon$ is the resulting microstrain. As previously discussed, the output voltage (V_{out}) value recorded by the CR9000 and used for these calculations was the result of a five-point average with a sampling rate of 10 Hz.

Because the strain profiles were to be the basis of all subsequent analyses and evaluation of the bridges, it was important to review the measured strain histories for any problems commonly associated with electrical systems. Two common problems are noise, which is the fluctuation of output voltages due to an electrical disturbance, and drift in data during the load tests. Figure 3.19 and Figure 3.20 are sample strain plots that exhibit noise and drift, respectively. The data shown in Figure 3.19 would be deemed unusable because no clear line can be distinguished with any level of accuracy. In Figure 3.20, the data that exhibit drift are designated “before” and may be corrected. The correction would be accomplished by subtracting the initial strain reading from all subsequent strain readings, which leads to the data designated “after” in the figure. Figure 3.21 is a sample strain history from Willis Creek and is typical of the strain histories recorded during this investigation. As reported by Wagener (2002), it was concluded that noise and drift were not significant problems in the data collected during load tests on the bridges studied in this investigation.

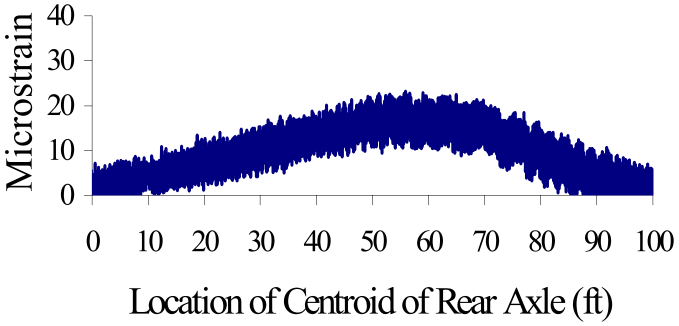

Figure 3.19 Example Strain History that Exhibits Excessive Noise

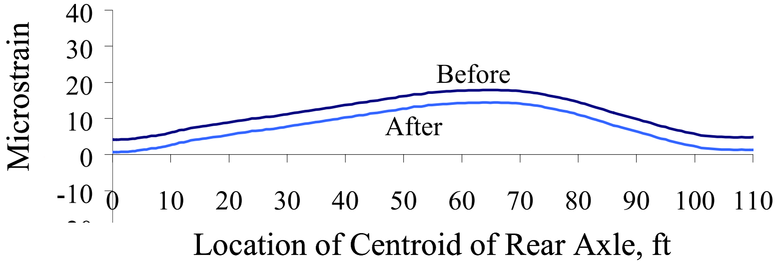

Figure 3.20 Example Strain History that Drifted During Testing

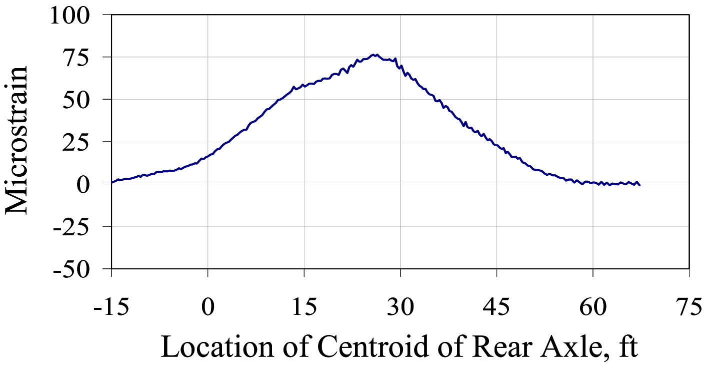

Figure 3.21 Sample Strain History for Beam 4, Midspan Bottom Gage of Willis Creek Bridge during Run 1 (Side-by-Side Configuration)

CHAPTER 4

Analysis and Evaluation of Measured Data from Bridge Load Tests

Evaluating the condition of bridges and their response to live loads is an important part of the load rating process. The 2003 MCEB provides guidelines for the inspection, testing, and rating of steel and prestressed concrete highway bridges. Although the MCEB provides simple methods for determining the live load response of structures, it also permits the use of more advanced methods for the load rating of bridges, such as finite element analyses and diagnostic load testing. Both have been used in this investigation to evaluate the five bridges discussed in Chapter 2. The analysis of measured data from load tests performed on the bridges will be discussed in this chapter. In addition, results from the analyses of the measured data will be compared with the results from finite element analyses, as well as the simple analysis methods outlined in the MCEB. The details of the finite element analyses are discussed in Appendix G.

The measured strains from the load tests were used to calculate neutral axis depths, live load moments, and live load distribution factors, which are discussed in Sections 4.2, 4.3 and 4.4, respectively. In Section 4.2, inferred neutral axis depths are compared with values calculated using the specified and estimated in situ concrete compressive strengths discussed in Chapter 2. The comparison of inferred and calculated neutral axis depths provides some insight into the condition of the bridges in the field, including in situ concrete compressive strengths and the possibility that the beams experienced flexural cracking during their service life. In addition, it will be shown that inferred estimates of neutral axis depth allowed for a more accurate calculation of live load moments from the measured data.

In Section 4.3, inferred live load moments are compared with the results of finite element analyses. Similarly to the inferred neutral axis depths, inferred live load moments provide a means of evaluating the estimated concrete compressive strengths discussed in Chapter 2. In addition, inferred live load moments were used to determine live load distribution factors (LLDF), which are a measure of the response of the structure. These inferred live load distribution factors are discussed in Section 4.4. Live load distribution factors based on finite element analyses and AASHTO specifications are also presented for comparison.

4.1 DESCRIPTION OF FINITE ELEMENT ANALYSIS SOFTWARE

As discussed in the introduction to this chapter, the results of finite element analyses were compared with the measured data and the AASHTO specifications. The software used to perform the finite element analyses is called BRUFEM (Bridge Rating Using Finite Element Modeling) and was developed at the University of Florida for the Florida Department of Transportation. The software was developed specifically for load rating bridges. Therefore, modeling of the bridges and vehicle loading configurations are easy to establish. Additional information about the software and modeling of the bridges is included in Appendix G.

4.2 NEUTRAL AXIS DEPTHS

Determination of neutral axis depths from the measured data provides insight into the condition of the bridges in the field and allows for more accurate calculation of live load moments, which will be discussed in Section 4.3. Neutral axis depths were inferred from the measured strains, and will be compared with neutral axis depths calculated using the material and section properties discussed in Chapter 2. In addition, the sensitivity of calculated neutral axis depths to several key assumptions was evaluated.

4.2.1 Inferred Neutral Axis Depth using Measured Strains

The depth of the neutral axis was calculated using the measured strains by assuming that the live-load response was in the linear range of the moment-curvature response. Therefore, as reported by Hurst (1998), it is reasonable to assume that the strain profile due to the applied live load varies linearly with depth of the composite section. This assumed strain profile is shown in Figure 4.1.

As discussed in Chapter 3, a minimum of two strain gages were installed on each beam for each longitudinal location studied. With multiple gages at each location and the assumption of a linear strain profile, it was possible to calculate the neutral axis depth from each pair of strain gages. The corresponding equations are given in Figure 4.1, where the neutral axis depth is denoted as *c*.

These calculations were performed for all possible pairs of gages for each diagnostic load test. The calculated neutral axis depths were plotted as a function of the location of the centroid of the rear axles along the span. Figure 4.2 corresponds to Run 1 on the 60-ft span of the Chandler Creek bridge using the bottom and top gages located at the midspan of Beam 5. These data are typical of the results of these calculations.

The scatter in the data at the beginning and end of the test run (Figure 4.2) is typical, and results from calculations being performed on relatively small measured strains. To eliminate the effect of this scatter on the calculation of the average inferred neutral axis depths, only the data between the vertical lines indicated in the figure were considered. The vertical lines were centered on the location corresponding to the maximum total midspan moment for the bridge and the distance between the lines is approximately one-third of the span length of the bridge. The average inferred neutral axis depth for the interior and exterior beams of each bridge is summarized in Table 4.1 and Table 4.2. The data used to determine the average inferred neutral axis depths were reported by Wagener (2002).

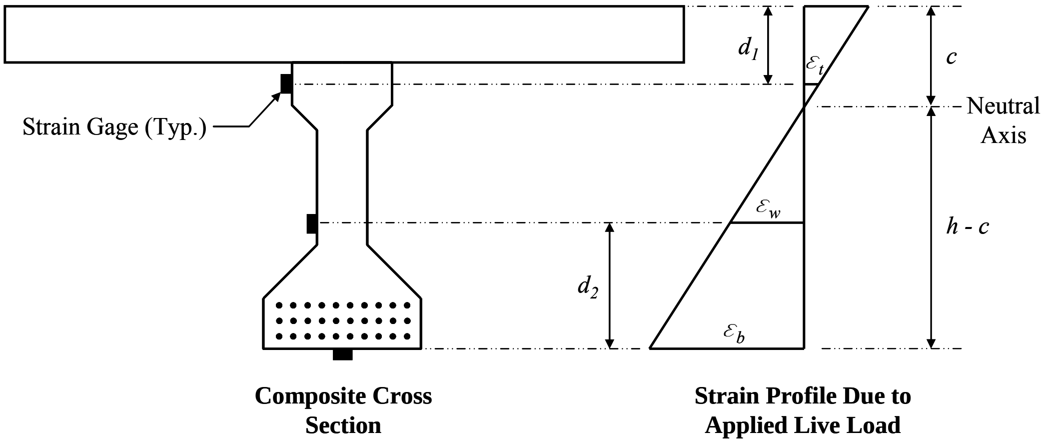

Top and Bottom Gages: $c = \dfrac{\varepsilon_t h + \varepsilon_b d_1}{\varepsilon_t + \varepsilon_b}$

Web and Bottom Gages: $c = \dfrac{(\varepsilon_w - \varepsilon_b)h + \varepsilon_b d_2}{\varepsilon_w - \varepsilon_b}$

Top and Web Gages: $c = \dfrac{\varepsilon_t (h - d_2) + \varepsilon_w d_1}{\varepsilon_t + \varepsilon_w}$

Figure 4.1 Neutral Axis Depth Inferred From Measured Data

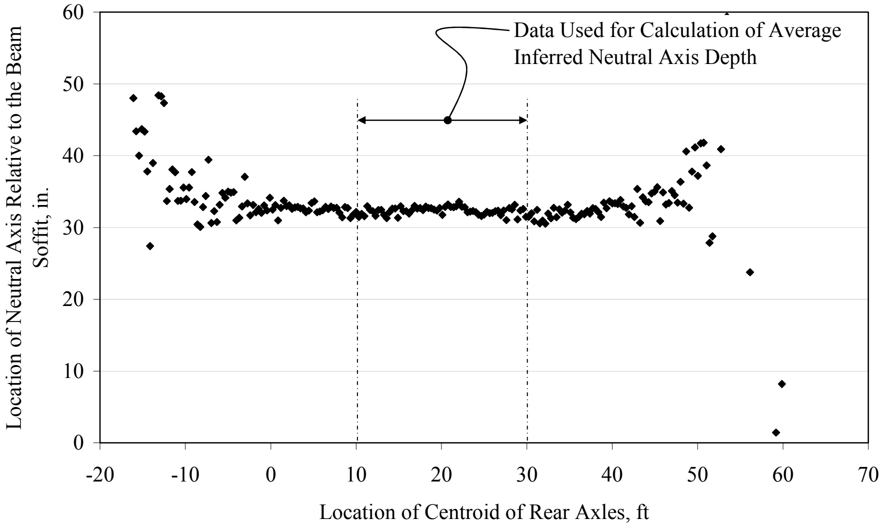

Figure 4.2 Typical Plot of Neutral Axis Location Inferred from Measured Data as a Function of Truck Location

4.2.2 Comparison of Calculated and Inferred Neutral Axis Location

The neutral axis depths inferred from the measured strains are compared with the calculated neutral axis depths corresponding to uncracked, transformed, composite section properties in Tables 4.1 and 4.2. The specified concrete compressive strengths were used to calculate the values reported in Table 4.1, and the estimated in situ compressive strength was used to calculate the values reported in Table 4.2. In all cases, the depth of the neutral axis inferred from the measured strains was less than the neutral axis depth calculated using specified section properties. The differences varied from 2.1 to 21.7%.

When the neutral axis depths calculated using the estimated in situ compressive strengths were used as the basis of comparison, the trend was similar. The neutral axis depths inferred from the measured strains for most of the beams were 1.8 to 16.0% less than the calculated values. However, using these material properties, the depth of the neutral axis inferred from the measured strains were larger than the calculated values for the exterior beams of the 40-ft span of the Chandler Creek bridge and the interior beams of the Wimberley bridge. These differences were approximately 1.5%. The slight reduction in the differences between calculated and inferred neutral axis depths when the calculations are based on estimated in situ material properties implies that these estimated values provide a better representation of the actual stiffness of the beams.

The more pronounced trend in the data indicates that the neutral axis is located closer to the top of the section than calculated using the transformed, composite section properties. This is most likely a result of flexural cracking in the beam which would shift the neutral axis closer to the top of the section. Cracking may have occurred due to significant overloads or repeated loading cycles that create a net tension at the bottom fiber of the section. Based on fatigue tests of prestressed concrete beams, Overman (1984) reported that repeated cycles that create a tensile stress at the bottom fiber greater than $3\sqrt{f_c'}$ will produce flexural cracks in the section even though the maximum tensile stress is below the modulus of rupture, which is typically taken to be $7.5\sqrt{f_c'}$. Similar results from tests on prestressed concrete beams were reported by Heller (2003). Therefore, it is within reason that the bridge girders are cracked, and the actual neutral axis location is above the neutral axis depth calculated using gross, transformed cross sectional properties.

The neutral axis depths previously discussed were calculated assuming uncracked section properties and an elastic modulus that was calculated using Eq. 2.2, which is from ACI 318-02. The influence of both of these assumptions on the calculation of neutral axis depths is discussed below.

Table 4.1 Comparison of Neutral Axis Depths Calculated Using Specified Concrete Compressive Strengths with Values Inferred from Measured Strains

Bridge	Beams	Neutral Axis Depth (in.)		
		Calculated†† (NA_c)	Average Inferred (NA_i)	% Difference†
Chandler Creek	1,4	13.8	13.4	-2.9%
	2,3	13.2	12.3	-7.5%
	5,8	17.7	15.9	-11.9%
	6,7	16.9	15.9	-7.5%
Lake LBJ	1,4	15.4	12.9	-16.8%
	2,3	17.0	14.0	-21.4%
Lampasas River	1,4,5,8	18.4	15.2	-21.7%
	2,3,6,7	18.0	15.2	-21.7%
Willis Creek	1,4	16.8	16.1	-4.7%
	2,3	18.4	17.0	-7.6%
Wimberley	1,5,6,10	13.2	12.1	-7.4%
	2-4, 7-9	14.2	14.0	-2.1%

† Percent Difference $= \dfrac{NA_i - NA_c}{NA_c} \times 100$

†† Values Reported in Table 2.12

Average % Difference
-11.1%

Table 4.2 Comparison of Neutral Axis Depths Calculated Using Estimated In Situ Concrete Compressive Strengths with Values Inferred from Measured Strains

Bridge	Beams	Neutral Axis Depth (in.)		
		Calculated†† (NA_c)	Average Inferred (NA_i)	% Difference†
Chandler Creek	1,4	13.2	13.4	1.5%
	2,3	12.6	12.3	-2.4%
	5,8	17.5	15.9	-9.1%
	6,7	16.8	15.9	-5.4%
Lake LBJ	1,4	14.9	12.9	-13.4%
	2,3	16.6	14.0	-15.7%
Lampasas River	1,4,5,8	18.1	15.2	-16.0%
	2,3,6,7	17.7	15.2	-14.1%
Willis Creek	1,4	16.4	16.1	-1.8%
	2,3	18.0	17.0	-5.6%
Wimberley	1,5,6,10	12.9	12.1	-6.2%
	2-4, 7-9	13.8	14.0	1.4%

† Percent Difference $= \dfrac{NA_i - NA_c}{NA_c} \times 100$

†† Values Reported in Table 2.14

Average % Difference
-7.7%

Table 4.3 summarizes the height of flexural cracks corresponding to a 15% reduction in the calculated neutral axis depth based on estimated in situ concrete compressive strengths for the interior and exterior beams of each bridge. The reduced neutral axis depths were calculated assuming a transformed composite section, where the concrete below the height of the crack was neglected. For the bridges considered, the presence of flexural cracks that extended an average of 3.6 in. above the bottom fiber (7.9% of the overall depth of the composite section) lead to a 15% reduction in the calculated neutral axis depth. The crack heights that resulted in the reduced neutral axis depth are relatively small and would not be visible unless a significant live load was present on the bridge. Therefore, it is reasonable to assume that these cracks would not have been visible during the visual inspections on the bridges in this study.

As discussed in Chapter 2, the modulus of elasticity was calculated using the relationship given in ACI 318-02 (Eq. 2.2), which is a function of the compressive strength of the concrete. In ACI 363R-92, *State-of-the-Art Report on High Strength Concrete* (ACI 363), the committee provides an alternate relationship between compressive strength and modulus of elasticity for concrete with compressive strengths between 6,000 and 12,000 psi. This relationship is given in Eq. 4.1.

$$\mathrm{E}_c = 40{,}000\sqrt{f'_c} + 1{,}000{,}000 \tag{4.1}$$

where f'_c is the compressive strength of the concrete in psi and E_c is the modulus of elasticity of the concrete in psi. As discussed in Chapter 2, the estimated in situ compressive strength of the concrete in the prestressed beams for the bridges in this investigation ranges from 8,700 to 10,300 psi. For this range of compressive strength, Eq. 4.1 yields values of modulus of elasticity approximately 88% of the value calculated using Eq. 2.2.

Table 4.4 summarizes the effect of using a reduced modulus of elasticity to calculate the neutral axis depth using gross, transformed section properties for both the interior and exterior beams of each bridge. The reduced modulus of elasticity of the concrete in the prestressed beam reduces the depth of the neutral axis by an average of 5.3%.

The effects of flexural cracking and variations in the elastic modulus on the calculated neutral axis depths were investigated. Although it is not possible to determine which phenomena affected the beams in the field, considering the presence of relatively small cracks and using a better approximation of the elastic modulus of the concrete both lead to closer agreement between the calculated neutral axis depths and those inferred from the measured strains.

Table 4.3 Height of Flexural Crack Corresponding to a 15% Decrease in Depth of Calculated Neutral Axis Using Estimated In Situ Section Properties

Bridge	Beams	Height of Flexural Crack (in.)	Height of Crack as a Percent of Depth of Composite Section
Chandler Creek	1,4	3.4	8.3%
	2,3	3.4	8.3%
	5,8	3.9	8.2%
	6,7	3.8	8.1%
Lake LBJ	1,4	3.4	7.3%
	2,3	3.9	8.2%
Lampasas River	1,4,5,8	3.9	8.3%
	2,3,6,7	3.8	8.2%
Willis Creek	1,4	3.5	7.6%
	2,3	3.8	8.2%
Wimberley	1,5,6,10	2.9	6.0%
	2-4, 7-9	3.4	8.3%
Average		3.6	7.9%

Table 4.4 Neutral Axis Depths Calculated Using Estimated In Situ Concrete Compressive Strengths and Different Values of Modulus of Elasticity

Bridge	Beams	Neutral Axis Depth (in.)		% Difference
		E_c†	E_c††	
Chandler Creek	1,4	13.2	12.5	-5.3%
	2,3	12.6	12.0	-4.8%
	5,8	17.5	16.6	-5.1%
	6,7	16.8	15.9	-5.4%
Lake LBJ	1,4	14.9	14.0	-6.0%
	2,3	16.6	15.8	-4.8%
Lampasas River	1,4,5,8	18.1	17.2	-5.0%
	2,3,6,7	17.7	16.8	-5.1%
Willis Creek	1,4	16.4	15.5	-5.5%
	2,3	18.0	17.1	-5.0%
Wimberley	1,5,6,10	12.9	12.1	-6.2%
	2-4, 7-9	13.8	13.1	-5.1%
			Average	-5.3%

† $E_c = 57{,}000\sqrt{f'_{ce}}$ (Eq. 2.2)

†† $E_c = 40{,}000\sqrt{f'_{ce}} + 1{,}000{,}000$ (Eq. 4.1)

4.3 LIVE LOAD MOMENTS

The calculation of live load moments from the measured data will be used to evaluate the response of the bridges to the applied live loads. In addition, comparing inferred live load moments with the results of finite element analyses provides a means of evaluating the assumed concrete compressive strengths discussed in Chapter 2. The calculated live load moments are discussed in this section.

4.3.1 Calculation of Live Load Moments using Measured Strains

Live load moments were calculated from the measured strains by assuming a linear relationship between moment and curvature and a linear variation of strain with depth:

$$M = EI\phi \tag{4.2}$$

$$\phi = \frac{\varepsilon_{gage}}{d_{gage}} \cdot 10^6 \tag{4.3}$$

where M is the live load moment in a composite bridge beam in kip-in., E is the modulus of elasticity of the prestressed beam in ksi, I is the moment of inertia for the gross, transformed, composite section in in.^{4}, ε_{gage} is the measured strain in microstrain, and d_{gage} is the distance from the strain gage to the assumed neutral axis of the composite transformed section in in.

Because the in situ properties of the concrete were not known, the live load moments were calculated using section properties corresponding to the three concrete compressive strengths discussed in Chapter 2: f'_{cs}, f'_{cq}, and f'_{ce}. In addition, each set of section properties was combined with two estimates of the neutral axis depth: calculated using the gross, transformed, composite cross sections and inferred from the measured strains.

As discussed in Chapter 2, the variation of the compressive strength of the concrete had little influence on the calculation of the moment of inertia; therefore, the differences in moment of inertia had little impact on the calculation of the live load moments. However, the modulus of elasticity is a function of the compressive strength. The values of E_c calculated and using Eq. 2.2 increased by a range of 22 to 32% for the quality control concrete compressive strengths and

32 to 44% for the estimated in situ concrete compressive strengths when compared with the modulus of elasticity based on specified concrete compressive strengths. Similarly, the modulus of elasticity calculated using Eq. 4.1 increased by a range of 16 to 24% for the quality control compressive strengths and 24 to 32% for the estimated in situ compressive strengths. The modulus of elasticity calculated using Eq. 4.1 yields a modulus of elasticity 5 to 13% lower than the value calculated using Eq. 2.2; however, both relationships result in an increase in the modulus of elasticity when the quality control and estimated in situ concrete compressive strengths are used in lieu of the specified concrete compressive strength. The relationship in ACI 318, Eq. 2.2, was used to calculate the modulus of elasticity used in the analyses presented throughout this dissertation. The increase in the modulus of elasticity results in a directly proportional increase in the calculation of live load moments.

Each of the three strain gages (bottom, web and top) were used to calculate the moment at midspan for each beam for each truck location where data were collected. The total moment in the bridge for each truck location was then calculated by summing the corresponding moments in the beams at midspan. A total moment was calculated using all the bottom gages, all the web gages and all the top gages independently. Figure 4.3 shows an example of how beam moments were calculated for a particular gage location. Figure 4.4 shows how total midspan moments were calculated for bridges with and without a skew. The maximum total midspan moment was then determined and reported. All calculated maximum midspan moments are reported in Appendix E.

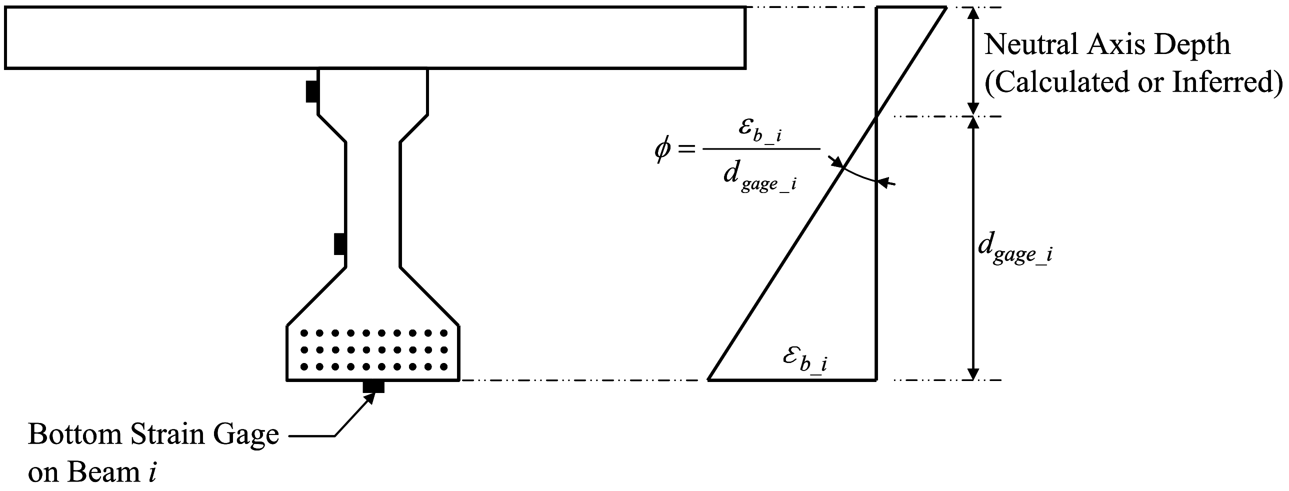

Calculation of Moment Based on
Measured Strain from Bottom Gage for Beam *i*: $M_i = EI_i \frac{\varepsilon_{b\_i}}{d_{gage\_i}}$

Notes: 1. E depends on the level of compressive strength of concrete, (f'_{cs}, f'_{cq}, or f'_{ce}), and the same value was used for all beams in a given span.
2. I_i is the gross, transformed, composite moment of inertia of beam *i* calculated using the same value of concrete compressive strength assumed for the calculation of *E*.
3. d_{gage_i} is distance between the assumed neutral axis depth for beam *i* (inferred or calculated) and the known location of the strain gage.

Figure 4.3 Calculation of Beam Moment at Midspan Based on Measured Strains and Assumed Depth of the Neutral Axis

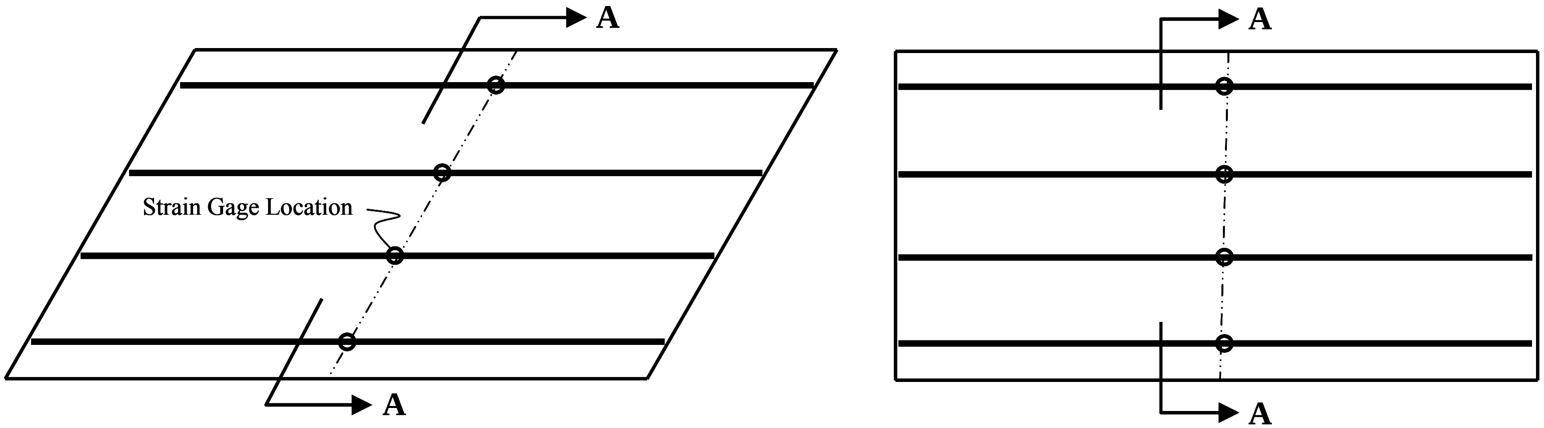

(b) Plan of Bridge with a Skew

(a) Plan of Bridge without a Skew

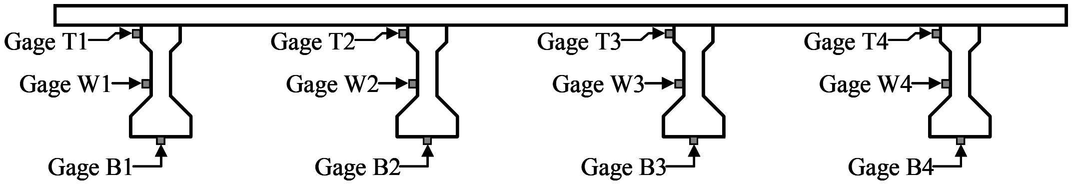

(c) Cross Section of Bridge (A-A)

Total Moment using Bottom Gages:

$$M_{Total} = M_{B1} + M_{B2} + M_{B3} + M_{B4}$$

Total Moment using Web Gages:

$$M_{Total} = M_{W1} + M_{W2} + M_{W3} + M_{W4}$$

Total Moment using Top Gages:

$$M_{Total} = M_{T1} + M_{T2} + M_{T3} + M_{T4}$$

Figure 4.4 Calculation of Total Moment at Midspan Based on Measured Strains

4.3.2 Effect of Neutral Axis Location on Inferred Live Load Moments

The moment calculated using Eq. 4.2 is sensitive to the assumed depth of the neutral axis. Ideally, the moments within a given beam calculated using the measured strains from each gage would be the same for each longitudinal position of the loading vehicle. However, the actual location of the neutral axis is not known, and it may vary along the span. In addition, the strain data include noise, which can not be eliminated. The consequences of assuming a single neutral axis depth is investigated in this section.

Figure 4.5 is a plot of total inferred live load moment at midspan for a side-by-side run performed on the 60-ft span of the Chandler Creek bridge as a function of truck location. The calculations are based on measured strains at all three locations, estimated in situ concrete compressive strengths and section properties, and the neutral axis depths corresponding to the transformed section properties. The total midspan moment obtained from the finite element analysis is also plotted for comparison. The total moment from the finite element analysis was also calculated by summing the moments at the midspan node for each beam at each truck location analyzed.

The calculated moments based on the bottom and web gages and the results of the finite element analysis gave similar results. The moment based on the top gages, however, significantly underestimates the total moment.

Figure 4.6 is a plot of total inferred midspan live load moment using the same measured data, estimated in situ concrete compressive strengths and section properties, and the neutral axis depth inferred from the measured strains. The difference between the total moments from all gage locations (top, web and bottom) is now less than 5% of the total moment calculated from the results of the finite element analysis. It is also important to note that the change in the assumed neutral axis locations did not significantly change the moments calculated from the bottom and web gages. However, the change in the moment calculated using the top gages was significant compared with the calculated neutral axis depth. This result is expected, because the distance between the top gage and the neutral axis depth is small. Therefore, the strain readings from the top gage are smaller in magnitude and more sensitive to noise.

Table 4.5 and Table 4.6 summarize the average percent difference in inferred moments calculated based on measured strains from the bottom, web and top gages at midspan for each bridge in this investigation using calculated and inferred neutral axis depths, respectively. Typically, the percent difference decreases when inferred neutral axis depths are used to calculate the live load moments in lieu of calculated neutral axis depths. In particular, the average difference between moments calculated using the bottom and web gages reduced from 8% to 5%. When moments calculated using the bottom or web gage data are compared to moments calculated using the top gage, the percent difference is significant. As previously mentioned, this is expected due to the proximity of the top gage to the neutral axis depth. Based on these trends, the average live load moment based on the bottom and web gages calculated using the inferred neutral axis depths will be used for comparative purposes in this dissertation.

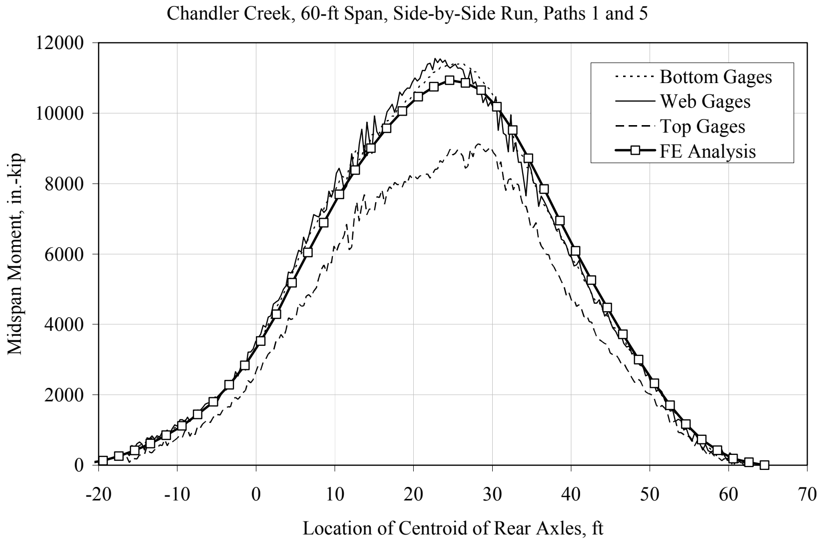

Figure 4.5 Total Inferred Midspan Live Load Moment Plotted as a Function of Truck Location using Calculated Neutral Axis Depths

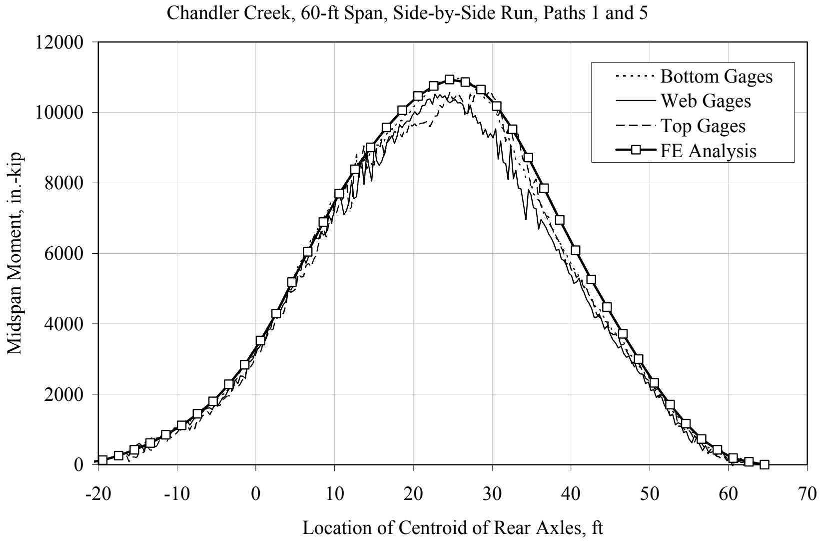

Figure 4.6 Total Inferred Midspan Live Load Moment Plotted as a Function of Truck Location using Inferred Neutral Axis Depths

Table 4.5 Comparison of Inferred Live Load Moments from Bottom, Web and Top Strain Gages using Calculated Neutral Axis Depths

Bridge Name	Average Percent Difference Between Inferred Live Load Moments at Midspan		
	Bottom and Web Gages*	Bottom and Top Gages*	Web and Top Gages**
Chandler Creek 40-ft Span	6%	16%	21%
Chandler Creek 60-ft Span	7%	22%	27%
Lake LBJ	5%	35%	36%
Lampasas River Span 1	10%	33%	39%
Lampasas River Span 2	13%	33%	41%
Willis Creek	5%	9%	9%
Wimberley Span 1	9%	NA†	NA†
Wimberley Span 2	NA†	NA†	NA†

† Not available due to gage malfunction during testing.

* Bottom gage used as basis for comparison.

** Web gage used as basis for comparison.

Table 4.6 Comparison of Inferred Live Load Moments from Bottom, Web and Top Strain Gages using Inferred Neutral Axis Depths

Bridge Name	Average Percent Difference Between Inferred Live Load Moments at Midspan		
	Bottom and Web Gages*	Bottom and Top Gages*	Web and Top Gages**
Chandler Creek 40-ft Span	5%	19%	24%
Chandler Creek 60-ft Span	4%	8%	11%
Lake LBJ	6%	11%	16%
Lampasas River Span 1	3%	6%	9%
Lampasas River Span 2	2%	3%	4%
Willis Creek	5%	21%	23%
Wimberley Span 1	8%	NA†	NA†
Wimberley Span 2	NA†	NA†	NA†

† Not available due to gage malfunction during testing.

* Bottom gage used as basis for comparison.

** Web gage used as basis for comparison.

4.3.3 Effect of Concrete Compressive Strength Assumptions

Live load moments were calculated based on each set of section properties as discussed in Section 4.3.1. Figure 4.7 is a plot of total live load moment as a function of truck location for a side-by-side run performed on the Chandler Creek 60-ft span and was calculated using specified concrete compressive strengths, design section properties and inferred neutral axis depths. The total moment based on a finite element analysis using the same truck positions and section properties at Chandler Creek is also plotted. The maximum inferred moment is approximately 70% of the total moment calculated from the finite element analysis.

Figure 4.7 and Figure 4.8 are plots of live load moment calculated using quality control and estimated in situ section properties, respectively. The total moments are approximately 85% and 95% of the live load moment calculated from the finite element analyses using the corresponding section properties, respectively. This trend is typical for bridges in this investigation. The differences between the maximum inferred live load moments and those obtained from the finite element analyses are summarized in Table 4.7 for all spans tested. The inferred live load moment reported is the average moment inferred from the bottom and web gages at midspan for each bridge. Similar information for each run performed on each bridge is presented in Appendix E. The average percent difference decreases from -44% to -12% when the estimated in situ material and section properties are used in lieu of the specified material and section properties. It is also important to note that using the estimated in situ material and section properties underestimates the live load moment from the results of the finite element analyses by 1% to 17%. The range of variation was larger for the other combinations of material and section properties. Therefore, for the bridges studied in this investigation, the estimated in situ material properties appear to be reasonable.

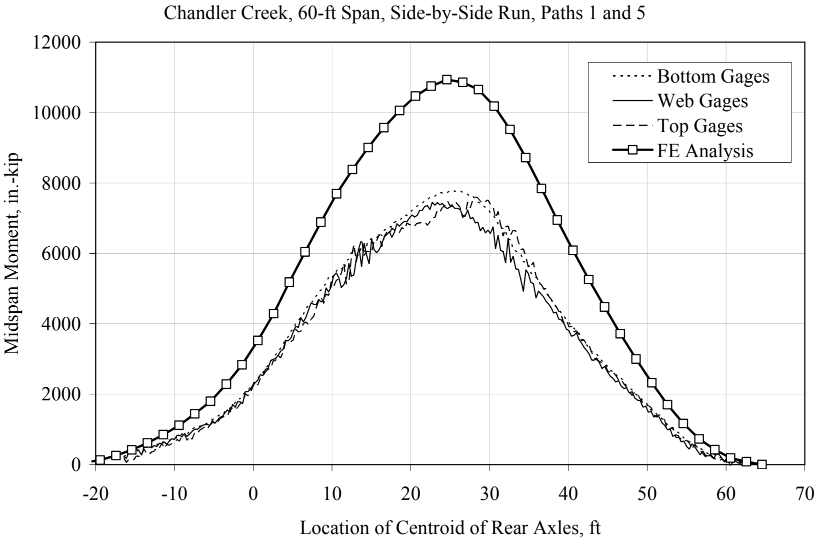

Figure 4.7 Comparison of Live Load Moments Calculated using Design Section Properties

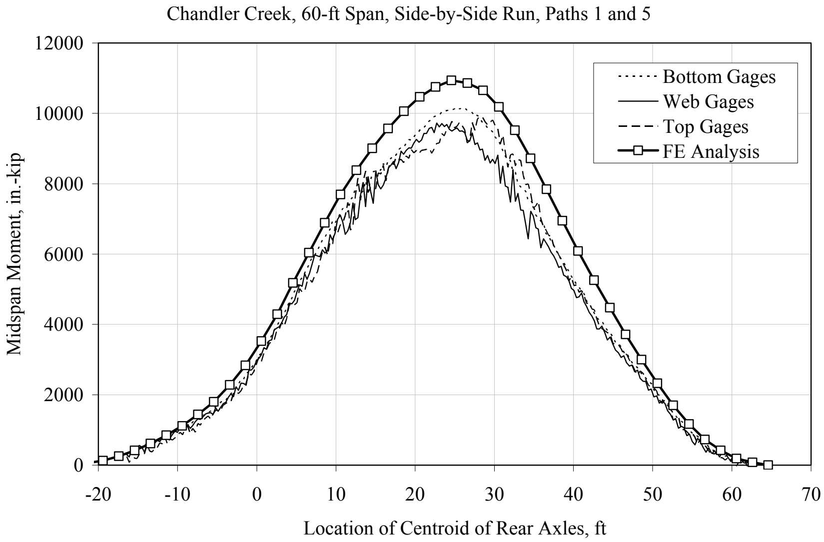

Figure 4.8 Comparison of Live Load Moments Calculated using Quality Control Section Properties

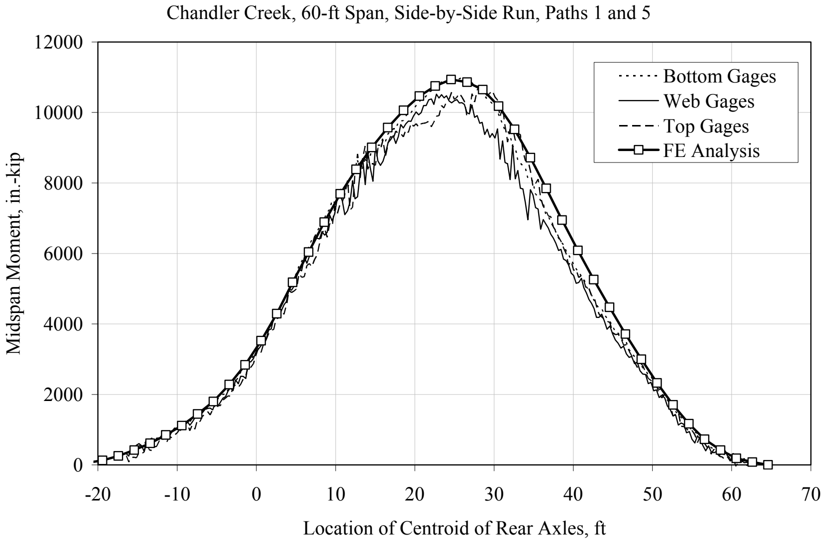

Figure 4.9 Comparison of Live Load Moments Calculated using Estimated In Situ Section Properties

Table 4.7 Comparison of Total Midspan Live Load Moments from Finite Element Analysis and Inferred from Measured Data

Bridge Name	Average Percent Difference Between Inferred[†] and Finite Element Live Load Moment For All Test Runs		
	Specified	Quality Control	Estimated In Situ
Chandler Creek 40-ft Span	-38%	-23%	-17%
Chandler Creek 60-ft Span	-30%	-9%	-1%
Lake LBJ	-34%	-17%	-11%
Lampasas River Span 1	-55%	-23%	-13%
Lampasas River Span 2	-67%	-30%	-19%
Willis Creek	-63%	-25%	-17%
Wimberley Span 1	-34%	-15%	-9%
Wimberley Span 2	-33%	-15%	-11%
Average	-44%	-20%	-12%

† Inferred live load moments calculated using inferred neutral axis depths.

4.4 LIVE LOAD DISTRIBUTION FACTORS

Accurately estimating the lateral distribution of live load moments in prestressed concrete bridges is an important aspect in the load rating process. Live load distribution factors (LLDF) are used to calculate the maximum live load resisted by individual beams in a bridge and are a percentage of the total live load moment applied to the bridge. An overly conservative estimate of LLDF's results in decreased load ratings; therefore, an important aspect of this investigation is to evaluate the LLDF's calculated per the AASHTO specifications by comparing these values with values inferred from measured data. Diagnostic load testing generally provides the best estimate of LLDF's; however, it is an unrealistic expectation to load test all bridges to determine the live load response of each bridge. Therefore, the use of finite element analyses is also investigated as a method of determining LLDF values. In this section, LLDF's based on the

AASHTO specifications, inferred from measured data, and calculated from the results of finite element analyses will be compared.

4.4.1 Inferred Live Load Distribution Factors using Measured Strains

Live load distribution factors were calculated for each beam and test run performed during diagnostic load testing. LLDF's for each beam ($LLDF_i$) were calculated from measured data using Eq. 4.4. In this equation, M_i is the maximum live load moment for each individual bridge beam. In addition, for each truck location, the total midspan moment was calculated as the sum of the calculated midspan moments in each beam. The moment in each beam was then divided by the maximum total midspan moment calculated for the same test run. Figure 4.10 is a sample plot showing the ratio of the midspan moment in a beam for a given truck location to the maximum bridge moment, $M_i / (\sum M_i)_{\max}$, plotted as a function of truck location. LLDF's were calculated based on data from the bottom and web strain gages at the midspan location. Two maximum LLDF's were calculated; one based on the bottom gages only and the other based on the web gages only. These two values were then averaged and reported as the average maximum LLDF. A summary of inferred LLDF's for each beam and test run are summarized in Appendix F.

$$LLDF_i = \frac{(M_i)_{\max}}{(\sum M_i)_{\max}} \tag{4.4}$$

Table 4.8 is a summary of the maximum inferred LLDF's for interior and exterior beams, for both one design lane and two design lane loading configurations for each bridge. The single truck and back-to-back truck runs were used to develop the LLDF's for one design lane loaded. Two design lane values are based on the side-by-side truck runs performed; however, they have been expressed in terms of a single design lane. This was accomplished by multiplying the live load distribution factor calculated using Eq. 4.4 by a factor of 2.0 as shown in Eq. 4.5. This was done to be consistent with the two-lane LLDF's calculated per the AASHTO Specifications, which are used in conjunction with the live load based on a single lane loading.

$$LLDF_i = 2\left[\frac{(M_i)_{\max}}{(\sum M_i)_{\max}}\right] \tag{4.5}$$

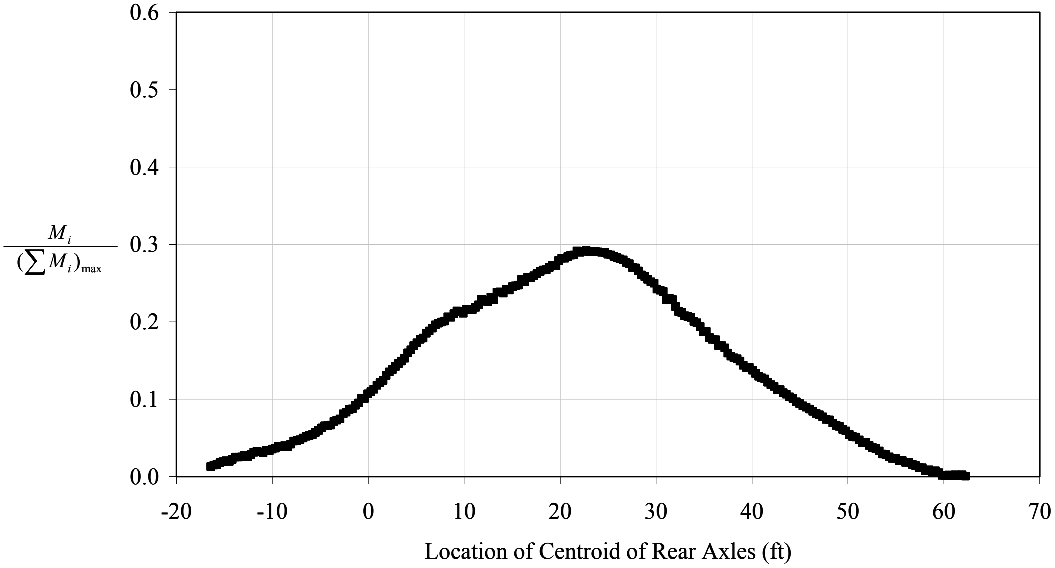

Figure 4.10 $M_i/(\sum M_i)_{\max}$ **Plotted as a Function of Truck Location**

Table 4.8 Maximum Inferred Live Load Distribution Factors Determined from Diagnostic Load Tests

Bridge Name	Interior Beams		Exterior Beams	
	One Lane†	Two Lanes††	One Lane†	Two Lanes††
Chandler Creek, 40 ft Span	0.51	0.64	0.58	0.62
Chandler Creek, 60 ft Span	0.40	0.63	0.52	0.60
Lake LBJ	0.38	0.51	0.52	0.53
Lampasas River, Span 1	0.37	0.54	0.48	0.50
Lampasas River, Span 2	0.35	0.50	0.50	0.51
Willis Creek	0.38	0.50	0.51	0.55
Wimberley, Span 1	0.47	0.55	0.51	0.55
Wimberley, Span 2	0.46	0.59	0.48	0.55

† Single truck runs and back-to-back truck runs used to determine LLDF for one design lane.

†† Side-by-side truck runs used to determine LLDF for two design lanes.

4.4.2 Live Load Distribution Factors Based on Finite Element Analyses

The results from the finite element analyses discussed in Section 4.1 and Appendix G were used to calculate LLDF's. For each bridge, an analysis was performed for each truck configuration tested in the field. Midspan moments were determined for each beam in the bridge as a function of truck location on the span. Using these values and Eq. 4.4, the live load distribution factor for each beam, $LLDF_i$, was calculated. Summaries of the maximum LLDF's calculated for each bridge and truck configuration analyzed are presented in Appendix F.

Table 4.9 is a summary of the maximum LLDF's for the interior and exterior beams based on the results in Appendix F. As with the inferred LLDF's from the measured strains, the one design lane LLDF's were based on the single truck runs and back-to-back runs, and the two design lane LLDF's were based on the side-by-side truck runs. Additionally, the two design lane LLDF's were calculated using Eq. 4.5, and therefore, are expressed in terms of a single lane load to be consistent with the values from the AASHTO Specifications.

In addition to analyses of truck configurations from the diagnostic load tests, analyses were performed using the standard HS-20 loading and truck configurations based on the provisions in AASHTO. The truck configurations considered included one and two design lanes, and the trucks were positioned on the bridge to obtain the maximum response for both the interior and exterior beams on each bridge. Figure 4.11 compares the truck configurations used for the analyses based on the AASHTO provisions for transverse truck location with trucks centered in the traffic lanes. As shown in Figure 4.11, the transverse positioning of trucks specified by AASHTO concentrate the trucks closer to the edge or centerline resulting in larger, more conservative LLDF's. Similar figures for the other bridges in this investigation are included in Appendix G. Table 4.10 is a summary of the results of these analyses and includes the maximum LLDF's for the interior and exterior beams for one and two design lanes.

Table 4.9 Maximum Live Load Distribution Factors from Finite Element Analysis Using Field Runs

Bridge Name	Interior Beams		Exterior Beams	
	One Lane†	Two Lanes††	One Lane†	Two Lanes††
Chandler Creek, 40 ft Span	0.38	0.64*	0.49	0.69*
Chandler Creek, 60 ft Span	0.35	0.60**	0.46	0.59**
Lake LBJ	0.34	0.50	0.45	0.51
Lampasas River	0.33	0.51	0.42	0.51
Willis Creek	0.34	0.50	0.44	0.50
Wimberley	0.39	0.49	0.49	0.52

† Single truck runs and back-to-back truck runs used to determine LLDF for one design lane.

†† Side-by-side truck runs used to determine LLDF for two design lanes.

* LLDF's for interior and exterior beams reduce to 0.55 and 0.57, respectively when truck path is in the actual lanes.

** LLDF.s for interior and exterior beams reduce to 0.53 and 0.54, respectively when truck path is in the actual lanes.

Table 4.10 Summary of Maximum Live Load Distribution Factors from Finite Element Analyses Using AASHTO Truck Configurations

Bridge Name	Interior Beams		Exterior Beams	
	One Lane†	Two Lanes††	One Lane†	Two Lanes††
Chandler Creek, 40 ft Span	0.39	0.65	0.53	0.57
Chandler Creek, 60 ft Span	0.35	0.62	0.48	0.66
Lake LBJ	0.34	0.61	0.48	0.55
Lampasas River	0.32	0.58	0.43	0.61
Willis Creek	0.32	0.56	0.44	0.57
Wimberley	0.37	0.58	0.47	0.55

† LLDF for typical HS-20 truck configuration producing maximum live load response.

†† LLDF for typical two design lane HS-20 truck configuration producing maximum live load response.

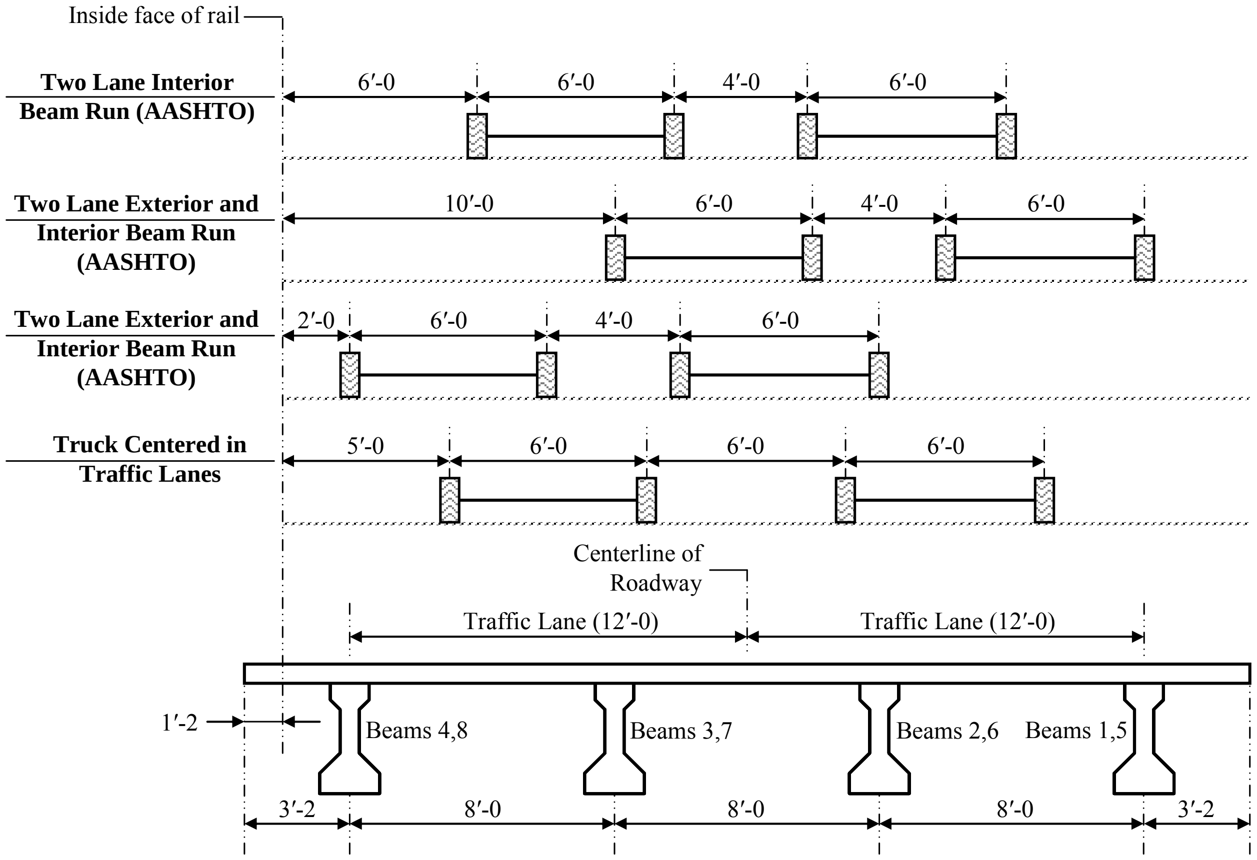

Figure 4.11 Comparison of Transverse Positioning of Trucks Specified in AASHTO and Centered in Traffic Lanes For Chandler Creek

4.4.3 Live Load Distribution Factors Based on AASHTO Specifications

The MCEB currently references the AASHTO Standard for the calculation of LLDF's to be used in the load rating process. However, as reported in Shahawy (2001) significant improvements in the calculation of LLDF's were incorporated in AASHTO LRFD. Similarly, Zokaie, et al. (1991) reported that LLDF's based on the AASHTO Standard overestimated the response for bridges with small beam spacing and overestimated the response for bridges with large beam spacing. Therefore, LLDF's based on both the AASHTO Standard and the AASHTO LRFD, will be compared with those inferred from the measured data and from the results of the finite element analyses.

4.4.3.1 Provisions in the AASHTO Standard for Calculating LLDF's

The AASHTO Standard equations for calculating the LLDF's for the interior beam of a bridge with a concrete deck and prestressed concrete beams for one and two traffic lanes are given in Eq. 4.6 and 4.7, respectively.

AASHTO Standard for Interior Beams:

$$LLDF_{One-Lane} = \frac{S}{7.0} \text{ for } S < 10 \text{ ft} \tag{4.6}$$

$$LLDF_{Two-Lane} = \frac{S}{5.5} \text{ for } S < 14 \text{ ft} \tag{4.7}$$

where S is the average center-to-center spacing to the adjacent beams.

The AASHTO Standard provisions for calculating the LLDF's for the exterior beam of a bridge with a concrete deck and prestressed concrete beams is as follows:

AASHTO Standard for Exterior Beams:

> *The LLDF shall be determined by applying to the beam the reaction of the wheel load obtained by assuming the flooring to act as a simple span between beams*

A schematic showing how to calculate the LLDF for an exterior beam is shown in Figure 4.12. Based on the provisions in the AASHTO Standard, it is required that the exterior beam have a capacity greater than or equal to the capacity of the interior beams. Therefore, this provision requires that the LLDF for the exterior beam be greater than or equal to the LLDF for the interior beam.

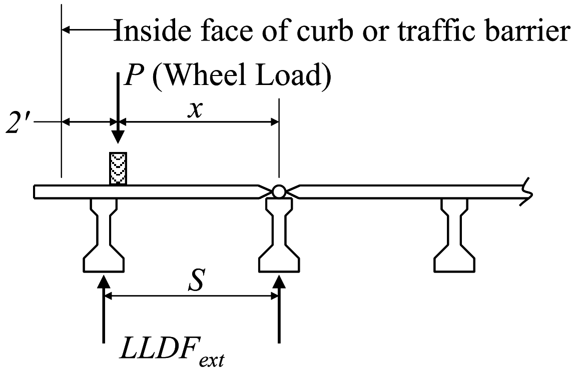

$$LLDF_{ext} = \frac{Px}{S} \geq LLDF \text{ for Interior Beam}$$

Figure 4.12 Method of Calculating LLDF in Exterior Beams per AASHTO Standard

Table 4.11 Summary of Live Load Distribution Factors Calculated Based on AASHTO Standard

Bridge Name	Interior Beams		Exterior Beams*	
	One Lane	Two Lanes	One Lane	Two Lanes
Chandler Creek (60-ft Span)	0.57	0.73	0.50	0.50
Chandler Creek (40-ft Span)	0.57	0.73	0.50	0.50
Lake LBJ	0.57	0.73	0.50	0.50
Lampasas River	0.52	0.67	0.50	0.50
Willis Creek	0.48	0.61	0.50	0.50
Wimberley	0.49	0.63	0.39	0.39

* LLDF's for exterior beams were not increased to match the capacity of the interior beams.

The provisions for calculating LLDF's based on the AASHTO Standard are based on a single wheel line. However, LLDF's calculated using the AASHTO LRFD, calculated from the results of finite element analyses, and those inferred from measured data are based on a single vehicle, or two wheel lines. Therefore, the LLDF's based on the AASHTO Standard reported in Table 4.11 have been divided by two to allow a direct comparison with the other values. In addition, where the LLDF for the exterior beam was less than the interior beam, the calculated value was retained, rather than replacing it with the LLDF for the interior beam. This allows for a more direct comparison of the LLDF's with other methods.

4.4.3.2 Provisions in the AASHTO LRFD for Calculating LLDF's

The AASHTO LRFD equations for calculating the LLDF's for the interior beam of a bridge with a concrete deck and prestressed concrete beams for one traffic lane and two traffic lanes are given in Eq. 4.8 and 4.9, respectively. These equations are applicable for bridges where the beam spacing is between 3.5 and 16 ft, the slab thickness is between 4.5 and 12 in., the span length is between 20 and 240 ft and the number of beams is 4 or greater. All the bridges in this investigation fall within these ranges.

AASHTO LRFD for Interior Beams:

$$LLDF_{One-Lane} = 0.06 + \left(\frac{S}{14}\right)^{0.4}\left(\frac{S}{L}\right)^{0.3}\left(\frac{K_g}{12.0Lt_s^3}\right)^{0.1} \tag{4.8}$$

$$LLDF_{Two-Lane} = 0.075 + \left(\frac{S}{9.5}\right)^{0.6}\left(\frac{S}{L}\right)^{0.2}\left(\frac{K_g}{12.0Lt_s^3}\right)^{0.1} \tag{4.9}$$

where S is the beam spacing in ft, L is the effective span length in ft, K_g is the longitudinal stiffness parameter and is calculated using Equation 4.10, and t_s is the thickness of the slab in in.

$$K_g = n\left(I + Ae_g^2\right) \tag{4.10}$$

where A is the area of the noncomposite beam in in.^{2}, L is the effective span length in ft, e_g is the distance between the centers of gravity of the noncomposite beam and the slab in in., I is the moment of inertia of the noncomposite beam in in.^{4}, and n is the modulus of elasticity of the concrete in the prestressed beam divided by the modulus of elasticity of the concrete in the slab.

The AASHTO LRFD equations for calculating the LLDF's for the exterior beam of a bridge with a concrete deck and prestressed concrete beams for one and two traffic lanes are given in Eq. 4.11 and 4.12, respectively. These equations are applicable for bridges where distance between the web of the exterior beam and the interior edge of the curb or traffic barrier is between -1.0 ft and 5.5 ft All the bridges in this investigation fall within these ranges.

AASHTO LRFD for Exterior Beams:

$$LLDF_{One-Lane} = \text{Use Lever Rule (See Figure 4.12)} \qquad (4.11)$$

$$LLDF_{Two-Lane} = eg_{\text{interior}} \qquad (4.12)$$

where e is calculated using Equation 4.13 and g_{interior} is the two-lane LLDF for the interior beam.

$$e = 0.77 + \left(\frac{d_e}{9.1} \right) \qquad (4.13)$$

where d_e is the distance between the web of the exterior beam and the interior edge of the curb or traffic barrier and is taken positive if the exterior web is inboard of the interior face of the traffic barrier or curb.

The lever rule is similar to the analysis performed for the exterior beams in the AASHTO Standard. A schematic showing an analysis using the lever rule is given in Figure 4.13.

Similarly to the AASHTO Standard, the provisions in the AASHTO LRFD require the exterior beam to have a capacity greater than or equal to the capacity of the interior beams. Therefore, this provision requires that the LLDF for the exterior beam be greater than or equal to the LLDF for the interior beam. However, the AASHTO LRFD permits the exterior beam to have less capacity, if the potential for future widening of the bridge is inconceivable. For the determination of LLDF's based on the AASHTO LRFD for the bridges in this investigation it has been assumed that future widening is not a consideration; therefore, it was not required that the exterior beam have a LLDF greater than or equal to the interior beam.

The AASHTO LRFD also contains a provision for the reduction of LLDF's for skewed bridges. The reduction factor (RF_{skew}) is calculated using the equation given in Equation 4.14.

$$RF_{skew} = 1 - c_1(\tan\theta)^{1.5} \tag{4.14}$$

where c_1 is calculated using Equation 4.15 and θ is the skew angle in degrees.

$$c_1 = 0.25\left(\frac{K_g}{12Lt_s^3}\right)^{0.25}\left(\frac{S}{L}\right)^{0.5} \tag{4.15}$$

where S, L, K_g, and t_s are the same as those used in Eq. 4.8 and 4.9. The skew reduction factor is applicable to any number of lanes loaded provided the beam spacing is between 3.5 and 16 ft, the slab thickness is between 4.5 and 12 in., the span length is between 20 and 240 ft, the number of beams is 4 or greater and the skew angle is between 30º and 60º. Based on these limits, the skew correction factor was only applicable to the Chandler Creek bridge.

In addition to the provisions just discussed, the AASHTO LRFD requires an additional analysis be performed for the exterior beams of beam-slab bridges with diaphragms. AASHTO LRFD states that this additional analysis is required because the effects of diaphragms were not considered in the development of the equations for determining LLDF's. The analysis assumes that the cross section of the bridge deflects and rotates as a rigid body and may be calculated using Equation 4.16.

$$LLDF_{ext} = \frac{N_L}{N_b} + \frac{x_{ext}\sum^{N_L} e}{\sum^{N_b} x^2} \tag{4.16}$$

where N_L is the number of lanes being considered, N_b is the number of beams in the cross section, x_{ext} is the horizontal distance between the center of gravity of the pattern of girders and center of gravity of the exterior beam in ft, x is the horizontal distance between the center of gravity of the pattern of girders to the center of gravity of each girder in ft, and e is the eccentricity of the design load from the center of gravity of the pattern of girders in ft. Figure 4.14 illustrates how the LLDF is determined using the rigid body analysis for the case with one design lane.

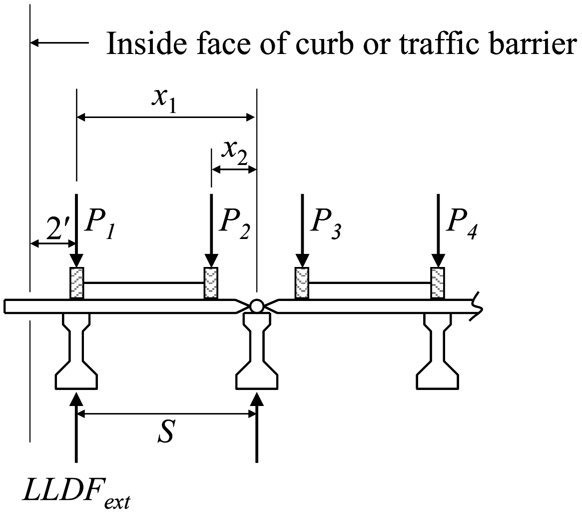

$$LLDF_{ext} = \frac{P_1 x_1 + P_2 x_2}{S}$$

Figure 4.13 Example of Lever Rule in AASHTO LRFD for Determining LLDF for Exterior Beams

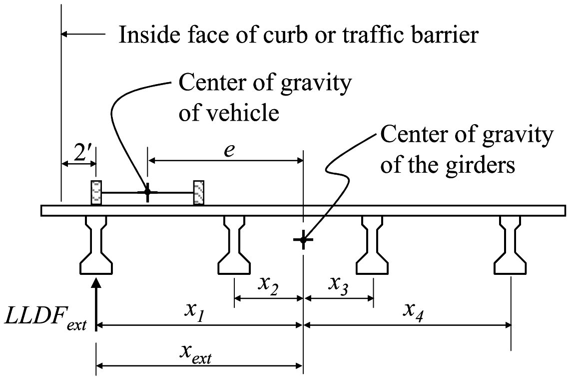

$$LLDF_{ext} = \frac{N_L}{N_b} + \frac{x_{ext}\sum^{N_L} e}{\sum^{N_b} x^2}$$

Figure 4.14 Rigid Body Analysis for Determining LLDF for Exterior Beam of Beam-Slab Bridge with Diaphragms

The multiple presence factor prescribed by the AASHTO Standard specification is 1.0 for both one and two design lanes loaded. However, in the AASHTO LRFD the multiple presence factor is 1.2 for one design lane loaded and 1.0 for two design lanes loaded. The multiple presence factors were included in the development of the equations for LLDF’s given in Eq. 4.7, 4.8 and 4.11. Therefore, when LLDF’s based on the provisions in the AASHTO LRFD are compared with the other methods of determining LLDF’s, the AASHTO LRFD values for the interior girder and one design lane have been divided by a factor of 1.2. It should also be noted that when the lever rule or rigid body analysis is used, the multiple presence factor has not been included. Therefore, these values may be compared without any modifications.

A summary of the LLDF’s calculated using the AASHTO LRFD is given in Table 4.12. For the two-lane loading case, the analysis using the rigid body assumption governs for all the bridges in this investigation. As stated previously, the provision is for bridges with diaphragms. However, in a study by Barr, et al. (2001), it was concluded that intermediate diaphragms had almost no effect on distribution factors calculated using the results of finite element analyses. In addition, the diaphragms in the bridges in this investigation are not rigidly connected to the prestressed beams, and in some cases are not connected to the cast-in-place slab. Therefore, the AASHTO LRFD provision appears overly conservative and it will be assumed the LLDF's based on the rigid body analysis do not apply.

Table 4.12 Live Load Distribution Factors Calculated using AASHTO LRFD Provisions

Bridge Name	Interior Beams		Exterior Beams*			
					Rigid Body Analysis	
	One Lane**	Two Lanes	One Lane†	Two Lanes	One Lane†	Two Lanes
Chandler Creek 60 ft Span	0.44	0.72	0.62	0.72	0.59	0.80
Chandler Creek 40 ft Span	0.49	0.76	0.62	0.76	0.59	0.80
Lake LBJ	0.43	0.71	0.63	0.70	0.59	0.80
Lampasas River	0.40	0.66	0.59	0.65	0.58	0.75
Willis Creek	0.40	0.66	0.55	0.65	0.57	0.68
Wimberley	0.46	0.72	0.35	0.59	0.47	0.65

* LLDF's for exterior beams were not increased to match the capacity of the interior beams. This was done to allow a direct comparison with the other methods of calculating LLDF's.

** One lane interior beam LLDF's were divided the multiple presence factor, 1.2, to allow comparison with other methods of calculating LLDF's.

† LLDF's based on lever rule and rigid body analysis for one lane were not modified by the multiple presence factor.

4.4.4 Comparison of AASHTO LRFD and AASTHO Standard LLDF's

Table 4.13 shows the comparison of the LLDF's calculated using the AASHTO Standard provisions with the LLDF's calculated using the AASHTO LRFD provisions. The LLDF's calculated based on the AASHTO LRFD for the interior beams and one traffic lane are average of 18% lower than the corresponding value calculated using the AASHTO Standard. For the interior beams with two traffic lanes the values based on the AASHTO LRFD are generally equivalent or slightly higher than the values calculated using the AASHTO Standard. For the exterior beams, the AASHTO LRFD LLDF's are higher than the values calculated using the AASHTO Standard. For one traffic lane, the AASHTO LRFD values are an average of 15% higher, and for two traffic lanes, the LRFD values are 40% higher.

Table 4.13 Comparison of LLDF's Calculated Using AASHTO LRFD and AASHTO Standard Provisions

Bridge Name	$LLDF_{LRFD}/LLDF_{Standard}$			
	Interior Beams		Exterior Beams	
	One Lane	Two Lanes	One Lane	Two Lanes
Chandler Creek, 60 ft Span	0.77	0.99	1.24	1.44
Chandler Creek, 40 ft Span	0.86	1.04	1.24	1.52
Lake LBJ	0.75	0.97	1.26	1.40
Lampasas River	0.77	0.99	1.18	1.30
Willis Creek	0.83	1.08	1.10	1.30
Wimberley	0.94	1.14	0.90	1.51

4.4.5 Comparisons of Inferred and Calculated Live Load Distribution Factors

The LLDF's inferred from measured data were compared with values from the results of the finite element analyses using vehicle loads and truck configurations from the diagnostic load tests. Table 4.14 summarizes the difference in maximum inferred LLDF's and maximum LLDF's based on finite element analyses. The finite element analyses reproduced the live load response within an average of 5% of the measured values. Similar results from the comparison of measured LLDF's and those calculated using the results of finite element analysis were reported by Barr, et al (2001).

Table 4.14 Comparison of Maximum Inferred Live Load Distribution Factors With Maximum LLDF from Finite Element Analysis

Bridge Name	Percent Difference*			
	Interior Beams		Exterior Beams	
	One Lane	Two Lanes	One Lane	Two Lanes
Chandler Creek, 40 ft Span	-13%	0%	-9%	7%
Chandler Creek, 60 ft Span	-5%	-3%	-6%	-1%
Lake LBJ	-4%	-1%	-7%	-2%
Lampasas River, Span 1	-4%	-3%	-6%	1%
Lampasas River, Span 2	-2%	1%	-8%	0%
Willis Creek	-4%	0%	-7%	-5%
Wimberley, Span 1	-8%	-6%	-2%	-3%
Wimberley, Span 2	-7%	-9%	-1%	-3%

* Percent difference is presented as a function of the total live load moment.

† Single truck runs and back-to-back truck runs used to determine LLDF for one-lane loading.

†† Side-by-side truck runs used to determine LLDF for two-lane loading. LLDF is based on one-lane loading.

Inferred LLDF's were compared with the LLDF's calculated using the provisions in the AASHTO Standard. The comparison is summarized in Table 4.15. For the interior beams, the inferred LLDF's were and average of 81% of the LLDF's based on the AASTHO Standard. The trend in the values shows that the AASHTO Standard approximated the actual LLDF within approximately 10% for the 40-ft spans, but the differences increased as the span length increased. The trends in the exterior beams are opposite the trends in the interior beams. For the exterior beams, the inferred LLDF's were an average of 114% of the value based on the AASHTO Standard. The AASHTO Standard provisions approximated the actual LLDF's within 5% for the longest span, Lampasas; however, the differences increased as the span length decreased.

Inferred LLDF's were also compared with those calculated using the AASHTO LRFD Specifications. These comparisons are summarized in Table 4.16. With the exception of the Wimberley one-lane exterior beam LLDF and the Chandler Creek 40-ft span one-lane interior beam, the measured LLDF's ranged from 72% to 102% of the calculated values. The one design lane, exterior beam, inferred LLDF's for the Wimberley bridge were 46% and 37% larger than the calculated value. Similar results were reported by Shahawy, et al (2001) based on extensive analyses of bridges with similar span lengths, beam spacing and deck overhangs as the Wimberley Bridge. The Wimberley bridge is a 40-ft span, with a beam spacing of 7 ft and a deck overhang of approximately 6 in. Shahawy reported a 32% error for a 50-ft span bridge, with a beam spacing of 6 ft and a deck overhang of 3 in.

LLDF's based on the AASHTO Standard and AASHTO LRFD are compared with the LLDF's calculated using the results of finite element analyses in Table 4.17 and Table 4.18, respectively. The trends are similar to the comparisons with the inferred values.

Table 4.15 Comparison of Inferred Live Load Distribution Factors and Live Load Distribution Factors Based on AASHTO Standard Specifications

Bridge Name	Inferred LLDF as a percent of AASHTO Standard Calculated LLDF			
	Interior Beams		Exterior Beams	
	One Lane	Two Lanes	One Lane	Two Lanes
Chandler Creek, 40 ft Span	89%	88%	116%	124%
Chandler Creek, 60 ft Span	70%	86%	104%	120%
Lake LBJ	67%	70%	104%	106%
Lampasas River, Span 1	71%	81%	96%	100%
Lampasas River, Span 2	67%	75%	100%	102%
Willis Creek	79%	82%	102%	110%
Wimberley, Span 1	96%	87%	131%	141%
Wimberley, Span 2	94%	94%	123%	141%

Table 4.16 Comparison of Inferred Live Load Distribution Factors and Live Load Distribution Factors Based on AASHTO LRFD Specifications

Bridge Name	Inferred LLDF as a percent of AASHTO LRFD Calculated LLDF			
	Interior Beams		Exterior Beams	
	One Lane	Two Lanes	One Lane	Two Lanes
Chandler Creek, 40 ft Span	116%	89%	94%	86%
Chandler Creek, 60 ft Span	82%	83%	84%	79%
Lake LBJ	88%	72%	83%	76%
Lampasas River, Span 1	93%	82%	81%	77%
Lampasas River, Span 2	88%	76%	85%	78%
Willis Creek	95%	76%	93%	85%
Wimberley, Span 1	102%	76%	146%	93%
Wimberley, Span 2	100%	82%	137%	93%

Table 4.17 Comparison of Live Load Distribution Factors Calculated from the Results of Finite Element Analyses and Live Load Distribution Factors Based on AASHTO Standard Specifications

Bridge Name	Finite Element Analysis LLDF as a percent of AASHTO Standard Calculated LLDF			
	Interior Beams		Exterior Beams	
	One Lane	Two Lanes	One Lane	Two Lanes
Chandler Creek, 40 ft Span	67%	73%	98%	114%
Chandler Creek, 60 ft Span	61%	73%	92%	108%
Lake LBJ	60%	68%	90%	102%
Lampasas River	63%	76%	84%	102%
Willis Creek	71%	82%	88%	100%
Wimberley	80%	78%	126%	133%

Table 4.18 Comparison of Live Load Distribution Factors Calculated from the Results of Finite Element Analyses and Live Load Distribution Factors Based on AASHTO LRFD Specifications

Bridge Name	Finite Element Analysis LLDF as a percent of AASHTO LRFD Calculated LLDF			
	Interior Beams		Exterior Beams	
	One Lane	Two Lanes	One Lane	Two Lanes
Chandler Creek, 40 ft Span	86%	74%	79%	79%
Chandler Creek, 60 ft Span	71%	70%	74%	71%
Lake LBJ	79%	70%	71%	73%
Lampasas River	83%	77%	71%	78%
Willis Creek	85%	76%	80%	77%
Wimberley	85%	68%	140%	88%

Figure 4.15, Figure 4.16 and Figure 4.17 are diagrams comparing the LLDF’s for the 60-ft span of the Chandler Creek Bridge that were inferred from measured data, calculated based on the AASHTO LRFD Specification, and from the results of finite element analyses of diagnostic load test runs. These diagrams show the generally good agreement between the inferred values and those from the results of finite element analyses, and indicate that the AASHTO values are typically conservative. In addition, the LLDF’s based on the AASHTO LRFD estimate the actual LLDF’s more accurately than the AASHTO Standard. Although the AASHTO LRFD is conservative, the profile of LLDF’s are similar in shape to the profiles based on the results of finite element analyses and diagnostic load tests. These are typical results and corresponding data for the other bridges are included in Appendix F.

Figure 4.18 and Figure 4.19 compare the LLDF’s for the 60-ft span of the Chandler Creek Bridge for one design lane and two design lanes based on the AASHTO LRFD and from the results of finite element analyses performed using the HS-20 loading vehicle and truck configurations. The trends are similar to those based on the field runs. These are typical results and corresponding data for the other bridges are included in Appendix F.

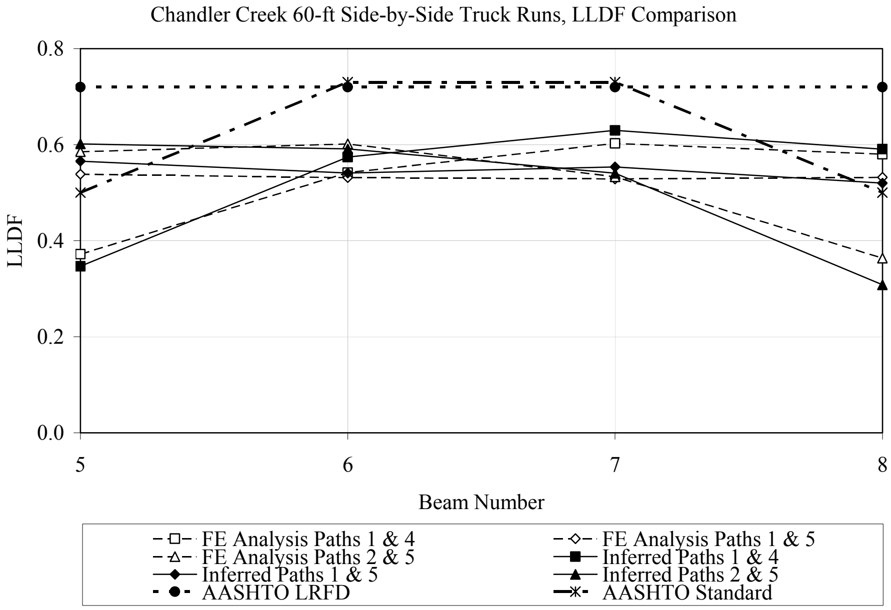

Figure 4.15 Comparison of Inferred and Calculated LLDF'S for Side-by-Side Truck Runs Performed at Chandler Creek Bridge, 60-ft Span

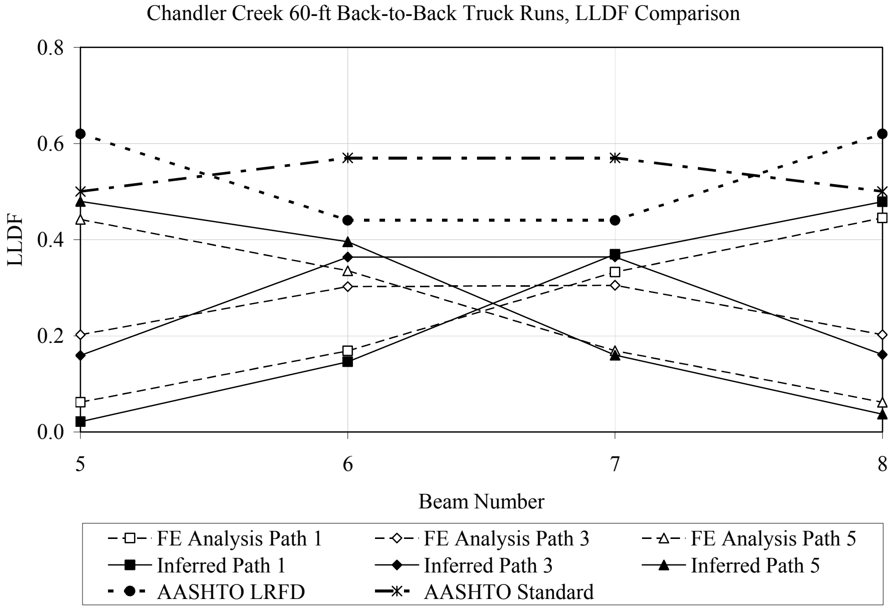

Figure 4.16 Comparison of Inferred and Calculated LLDF'S for Back-to-Back Truck Runs Performed at Chandler Creek Bridge, 60-ft Span

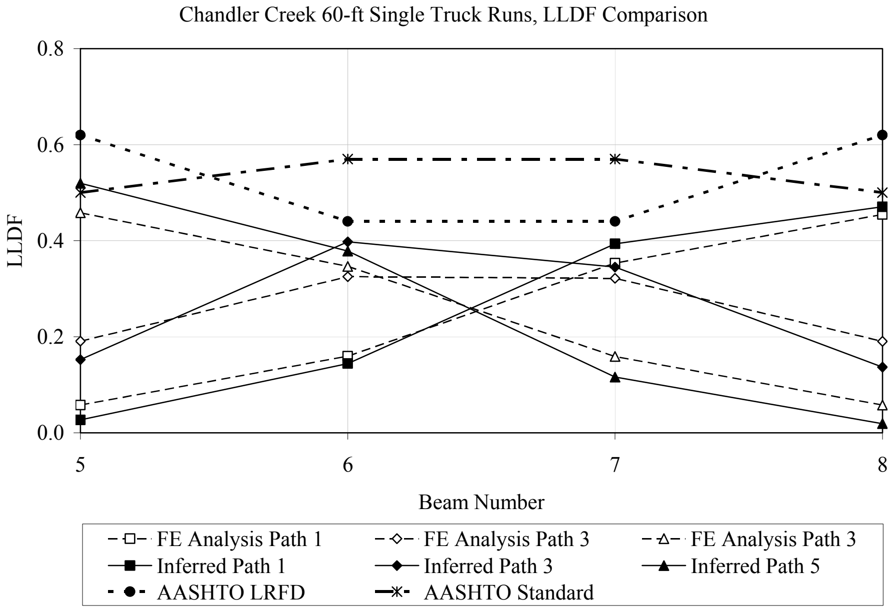
Chandler Creek 60-ft Single Truck Runs, LLDF Comparison

Figure 4.17 Comparison of Inferred and Calculated LLDF'S for Single Truck Runs Performed at Chandler Creek Bridge, 60-ft Span

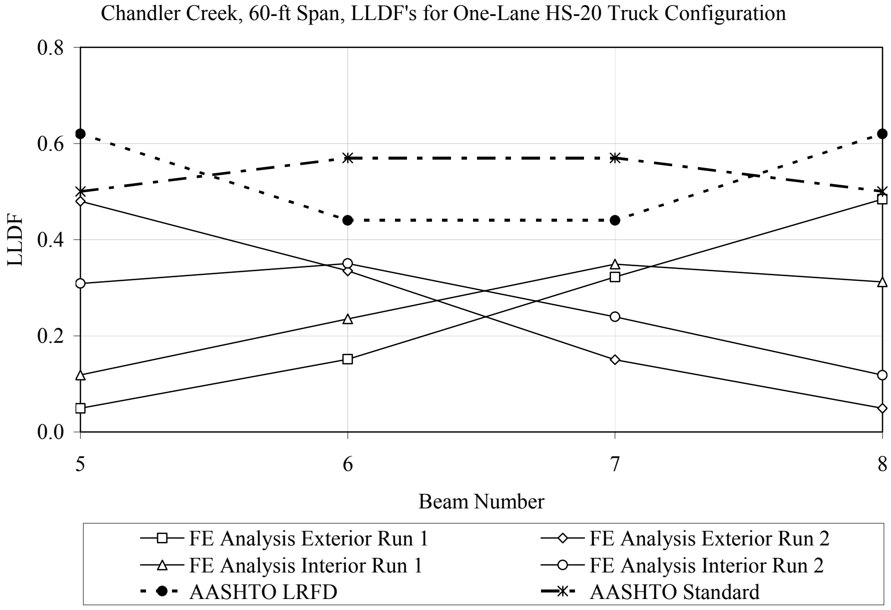
Chandler Creek, 60-ft Span, LLDF's for One-Lane HS-20 Truck Configuration

Figure 4.18 Comparison of AASHTO and FE Analysis One-Lane LLDF'S for Chandler Creek Bridge, 60-ft Span

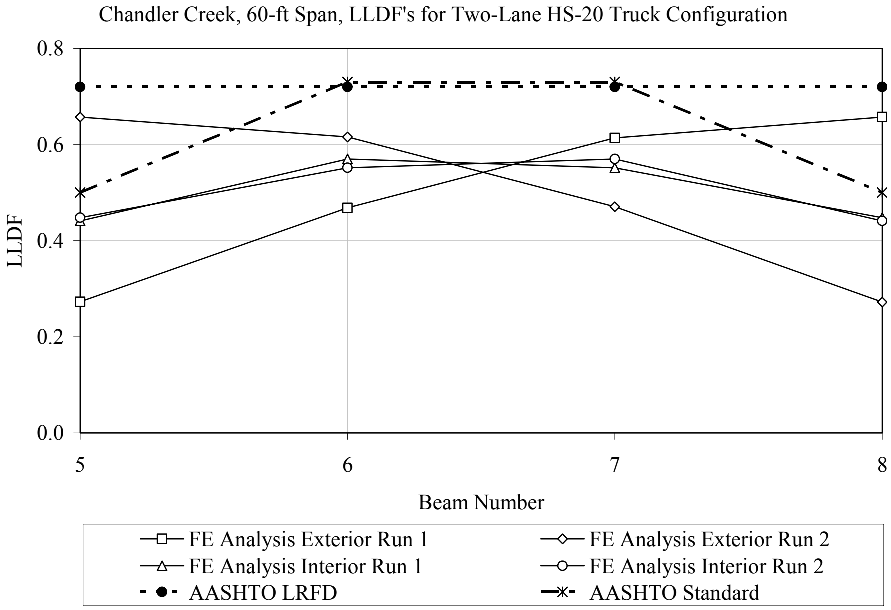

Figure 4.19 Comparison of AASHTO and FE Analysis Two-Lane LLDF'S for Chandler Creek Bridge, 60-ft Span

4.5 SUMMARY

In this chapter, the measured strain data were used to calculate the depth of the neutral axis. The inferred neutral axis depths were then compared with calculated values. The inferred depth of the neutral axis was then used to calculate live load moments and LLDF's using estimated in situ material and section properties.

The inferred neutral axis depths were typically closer to the top of the section than calculated using the gross, transformed section properties and estimated in situ material properties. It is likely that the difference between calculated and inferred neutral axis depth is caused by flexural cracking and that the value of the modulus of elasticity of the concrete in the prestressed beas was overestimated.

Live load moments calculated using the inferred neutral axis depths, estimated in situ material properties, and estimated in situ section properties were 1 to 19% lower than the live load moment estimated using the results of finite element analyses. This indicated that the estimated in situ concrete compressive strength was reasonable.

LLDF's were also investigated in this chapter. LLDF's based on the provisions in the AASTHO LRFD and AASHTO Standard, the results of finite element analyses and inferred from measured data were compared. The inferred LLDF's were estimated reasonably well using finite element analyses. In addition, the provisions in the AASHTO LRFD, although conservative, were generally more accurate than the provisions in the AASHTO Standard in predicting the live load response of the bridges.

CHAPTER 5

Description of Laboratory Fatigue Tests

This chapter presents a detailed discussion of the design, fabrication, instrumentation, and testing of six prestressed concrete beams constructed and tested as part of this investigation. The one-quarter-scale specimens were designed and fabricated to represent key features of the prototype beam, which was typical of the bridges tested in the diagnostic load-testing portion of the project. The 60-ft span of the Chandler Creek bridge was selected as being representative of the five bridges studied in the field. Properties of the interior beam from the Chandler Creek bridge are presented in Table 5.1.

The initial thrust behind the fatigue tests was to evaluate the relationship between the index stress level and the fatigue life of prestressed concrete beams. The index stress is defined as the calculated tensile stress at the extreme fiber of the cross section under the maximum applied load and is calculated using uncracked transformed section properties. However, as discussed in Chapter 1, the fatigue life of prestressed concrete beams is controlled by the fatigue of the prestressing strands. Therefore, both the index stress levels and strand stress ranges were investigated in this study.

The procedure for evaluating prestressed concrete bridges in the MCEB includes a serviceability limit for the calculated tensile stress at the extreme fiber of the cross section. This limit often controls the load rating. Although the specified concrete compressive strength is typically used for load rating prestressed concrete bridges, the index stress used in this investigation is calculated using the measured concrete compressive strength at the time of testing. The impact of using the measured compressive strength of the concrete in lieu of the specified compressive strength in the load rating calculations for beams tested in this investigation will be addressed in Chapter 7.

The stress range in the strand can only be determined reliably if the effective prestress level is known. Therefore, the instrumentation for the fatigue test specimens included a significant number of strain gages, which were used to monitor the prestress losses with time. As discussed in Chapter 1, the fatigue life of a prestressed concrete beam is directly related to the stress range in the strand; however, the calculation of the stress range is significantly more complex than the calculation of the index stress. As a result, designers and evaluators prefer to use the index stress as the criterion for evaluating the fatigue life of prestressed concrete bridges to simplify the calculations.

Three index stress levels in the prototype beam were selected for study in this investigation: $6\sqrt{f'_{ce}}$, $7.5\sqrt{f'_{ce}}$ and $12\sqrt{f'_{ce}}$. These index stress levels correspond to strand stress ranges in the prototype beam of 14, 20, and 40 ksi, respectively. In addition, test specimens were designed such that at each index stress level, the median strand stress and the range of stress in the strand would be similar to the calculated values in the prototype bridge at the same index stress level. However, due to the sensitivity of the index stress to the effective prestress and because the compressive strength of the concrete could only be estimated during the design stage, preference was given to achieving similar strand stress ranges and median stresses rather than achieving a particular index stress.

The design of the fatigue test specimens is discussed in Section 5.1. The analysis of the prototype beam is discussed in Section 5.2. The fabrication of the fatigue test specimens is discussed in Section 5.3. The test set-up used for the fatigue tests is discussed in Section 5.4. The instrumentation used to evaluate the effective prestress force is discussed in Section 5.5. The analysis of the fatigue test specimens is discussed in Section 5.6. The test procedures for the fatigue tests are discussed in Section 5.7. A summary is provided in Section 5.8.

5.1 DESIGN OF FATIGUE TEST SPECIMENS

The objective for the design of the test specimens was to achieve similar strand stress ranges at similar levels of index stress as that of the prototype bridge beam. A key requirement was to maintain comparable relationships between section properties. The test specimen elevation and cross-section are shown in Figure 5.1 and Figure 5.2, respectively. The beam properties are summarized in Table 5.1. The shape of the test specimen cross section was modified to simplify the construction process; however, other parameters are similar. The section properties for both the prototype beam and test specimens are compared in Table 5.2. The section properties for the prototype bridge beam are based on estimated in situ compressive strengths of the concrete, which are discussed in Chapter 3.

The differences in these geometrical parameters summarized in Table 5.2 vary from 0 to 17%, with an average difference of 6%. Based on these comparisons and a preliminary analysis using assumed material properties representative of the concrete compressive strengths at the age of testing, it was concluded that the behavior of the test specimens would be similar to the behavior of the prototype bridge beam.

The compressive strengths of the concrete used for design were 6000 psi for the web concrete at release, 10,000 psi for the web concrete in situ at the start of the fatigue tests, and 6000 psi for the slab concrete in situ at start of the fatigue tests. The measured compressive strengths of the web concrete at release, the web concrete at the start of the fatigue tests, and the slab concrete at the start of the fatigue tests were approximately 2, 25, and 10% greater than the compressive strengths used for design, respectively. The differences between the specified and measured material properties of the concrete are discussed further in Section 5.3.2.

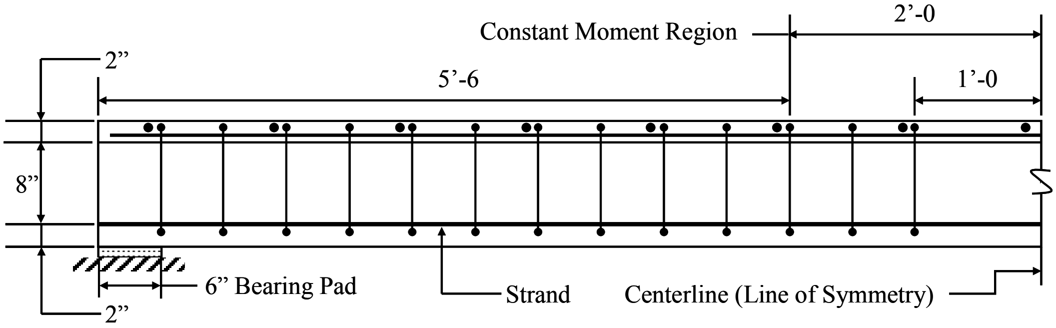

Figure 5.1 Elevation of Test Specimens

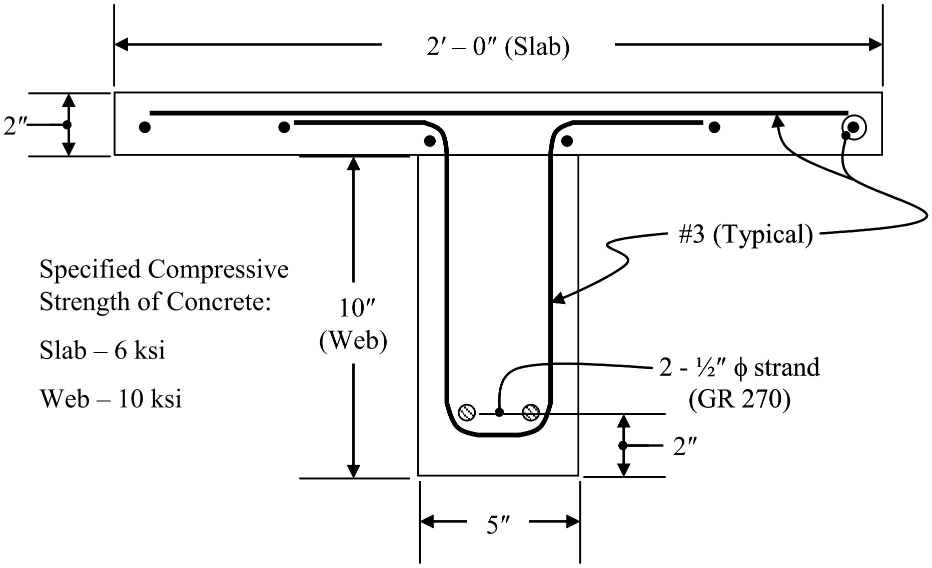

Figure 5.2 Cross Section of Test Specimens

Table 5.1 Properties of Prototype Bridge Beam and Fatigue Test Specimens

Beam Property		Prototype Bridge*	Test Specimen[†]
Beam Length	L	60 ft	15 ft
Composite Beam Depth	H	47.25 in.	12 in.
Effective Slab Width	b_e	94 in.	24 in.
Beam Moment of Inertia	I_g	82,800 in.^{4}	417 in.^{4}
Composite Beam Moment of Inertia	I_{comp}	274,000 in.^{4}	1200 in.^{4}
Area of Beam	A_g	496 in.^{2}	50 in.^{2}
Transformed Area of Composite Beam	$A_{g,tr}$	1040 in.^{2}	90 in.^{2}
Area of Prestressing Steel	A_{ps}	3.24 in.^{2}	0.306 in.^{2}
Neutral Axis of Composite Beam	y_{comp}	30.45 in.	7.48 in.

* Properties based on estimated in situ compressive strength of concrete for the Chandler Creek 60-ft span, f'_{ce}.

[†] Properties based on specified compressive strength of concrete for test specimens, f'_{cs}.

Table 5.2 Parameters from Prototype Bridge Beam and Fatigue Test Specimens

Parameter	Prototype Bridge	Test Specimen	Difference
L/H	15	15	0 %
b_e/H	2	2	0 %
I_{comp}/ I_g	3.3	2.9	12 %
A_g/ A_{ps}	153	163	6 %
$A_{g,tr}/ A_g$	2.1	1.8	17 %
$A_{g,tr}/ A_{ps}$	321	294	8 %
H/ y_{comp}	1.56	1.63	2 %

5.2 ANALYSIS OF PROTOTYPE BRIDGE BEAM

A separate analysis was performed of the prototype beam using each of three sets of section properties, which were calculated using the three values of concrete compressive strength described in Chapter 3: f'_{cs}, f'_{cq}, and f'_{ce}. For each analysis, the relationship between live load moment and stress range in the strand was calculated. The stress range in the strand corresponds to the change in strand stress induced by live load. Five live load conditions were used to generate each relationship, and are defined in Table 5.3. The resulting relationship between live load moment and strand stress range for estimated in situ material and section properties is shown in Figure 5.3.

Data point 1 represents the condition of zero live load. The effects of the effective prestress force and dead loads, which includes dead loads on the non-composite beam and the composite beam, are considered. Dead loads include the weights of the beam, deck, diaphragms, overlay, and an allowance for miscellaneous dead load. In addition, it was assumed that the prestressed beams were unshored during the placement of the deck. Data point 2 corresponds to the live load that results in zero net stress at the bottom fiber of the cross section, and is called the decompression point. Data points 3 and 4 were determined by specifying the neutral axis of the composite section and calculating the moment corresponding to equilibrium.

Data points denoted 1, 2, and 3 were calculated using compatibility and equilibrium. Stress and strain were assumed to be linearly related in both the concrete and the prestressing steel. Data point 4 was calculated using stress-block factors to estimate the nonlinear stress-strain relationship in the concrete. Data point 5 was calculated using the equation for flexural capacity given in the AASHTO Specifications. A detailed discussion of the methods used to analyze the cross section at each state of stress is presented in Appendix J.

The stress range in the strand for each level of index stress being investigated was then determined graphically using the six data points from each analysis and assuming that the live load moment varied linearly between each data point. Data points A, B, and C denoted in Figure 5.3 correspond to the live load moment and strand stress range at index stress levels of $6\sqrt{f'_{ce}}$, $7.5\sqrt{f'_{ce}}$, and $12\sqrt{f'_{ce}}$, respectively. The moments for each index stress were calculated using gross, transformed section properties. However, the strand stresses were calculated assuming a cracked section.

Table 5.4 summarizes the results of each analysis of the prototype beam. The table provides the strand stress range, median strand stress, live load moment and HS vehicle weight corresponding to each index stress level. The HS vehicle weight was calculated as shown in Figure 5.4. The bridge was modeled as a simply-supported beam and loaded with a vehicle that had the HS-20 axle spacing required by the AASHTO Standard. The AASHTO Standard live load distribution factor and dynamic impact factor were also included in the calculation.

Table 5.3 Description of Analysis Points for Prototype Beam

Point	Description
1	Full dead load state
2	Decompression of bottom fiber
3	Neutral axis at bottom of web
4	Neutral axis at top of web
5	Flexural Capacity
A	Live load moment at index stress of $6\sqrt{f'_{ce}}$
B	Live load moment at index stress of $7.5\sqrt{f'_{ce}}$
C	Live load moment at index stress of $12\sqrt{f'_{ce}}$

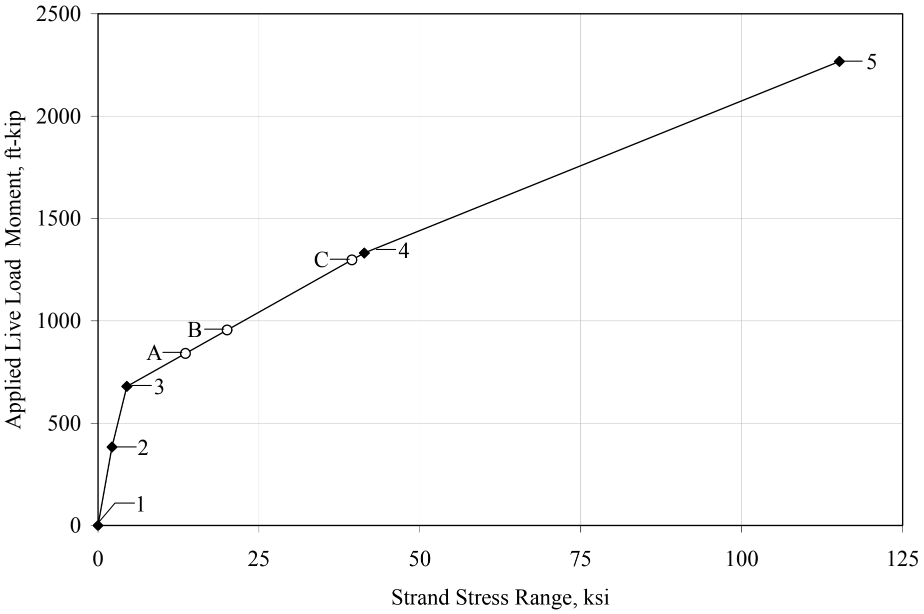

Figure 5.3 Plot of Live Load Moment as a Function of Stress Range in the Strand for Prototype Beam

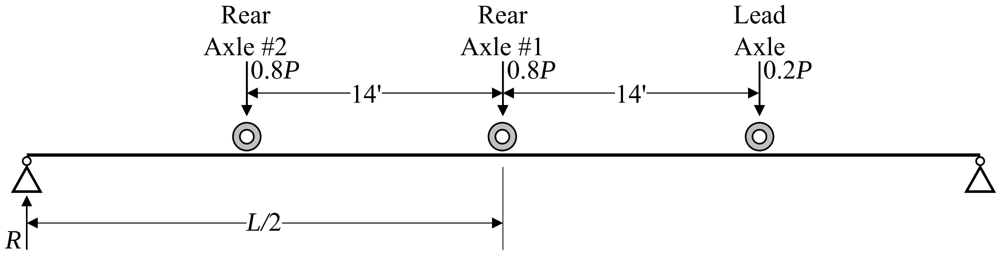

$$P = \frac{R(L/2) - M_{LL}}{11.2}$$

$$LLDF = \frac{S}{5.5}$$

$$I = 1 + \frac{50}{125 + L}$$

$$HS_{Eq} = \frac{P}{LLDF \cdot I}$$

where:

P = live load in kip

M_{LL} = the live load moment in ft-kip

L = the effective span length of the bridge and taken as the centerline-to-centerline of the bearing pads in ft

$LLDF$ = the live load distribution factor for an individual wheel line per the AASHTO Standard specification

S = the centerline-to-centerline spacing of the girders in ft

I = the impact factor per the AASHTO Standard specification

HS_{Ea} = the equivalent HS vehicle weight in ton

Figure 5.4 Calculation of Equivalent HS Loading

Tables 5.5 to 5.7 provide comparisons of the analyses for each index stress being investigated. As shown in Table 5.5, there is an 89% increase in strand stress range and a 15% increase in the loading required to produce that stress range at the index stress of $6\sqrt{f'_c}$ for the quality control analysis as compared with the design analysis. As the index stress increases, the difference in strand stress range decreases and difference in loading increases. Similar trends are exhibited in the comparison of the estimated in situ analysis with the design analysis and are shown in Table 5.6. In Table 5.7 the results from the estimated in situ analysis are compared with the results from the quality control analysis. The calculated strand stress range increases by 6% to 14% for the estimated in situ analysis as compared with the quality control analysis. This corresponds to an increase of 4% to 6% in the loading required to produce that strand stress range.

The results from the analyses of the other bridges being studied in this investigation using estimated in situ material and section properties are provided in Table 5.8. The strand stress range varies from 4 to 20 ksi, 10 to 31 ksi, and 29 to 65 ksi at index stresses of $6\sqrt{f'_{ce}}$, $7.5\sqrt{f'_{ce}}$, and $12\sqrt{f'_{ce}}$, respectively. Similarly, the median stress in the strand ranges from 137 to 146 ksi, 140 to 151 ksi and 148 to 168 ksi at index stresses of $6\sqrt{f'_{ce}}$, $7.5\sqrt{f'_{ce}}$, and $12\sqrt{f'_{ce}}$, respectively. These data indicate that as the index stress increases, the strand stress range and median strand stress increase; however, these data also indicate that for a given index stress there is no direct relationship to the range in strand stress. Rather, as shown in Figure 5.5, the trends in the data indicate that for a given value of index stress, the range in strand stress decreases with the increase in span length of the bridges. In addition, Figure 5.5 shows that the sensitivity of the calculated strand stress range increases as the index stress increases. Similar trends are found for the median strand stress; however, the median stress is less sensitive to changes in span length and index stress.

As discussed in the introduction to this chapter, it was desirable to conduct the fatigue tests on the specimens at the same index stresses as the prototype beam. However, based on the analyses of the interior beams from the other bridges, it is clear that there is no direct link between a particular index stress and stress range in the strand. In addition, as discussed in Chapter 1, the fatigue life of prestressed beams is directly related to the strand stress range and not index stress. Therefore, although it was originally planned to test the beams in the laboratory at the same index stresses as the prototype beam, the criterion that the beams be tested at similar strand stress ranges controlled for the test specimens.

Table 5.4 Results of Analysis of Prototype Bridge

Index Stress (psi)	Calculated Strand Stress Range (ksi)	Calculated Median Strand Stress (ksi)	M_{LL} (ft-kip)	HS_{Eq} (kip)
Specified Concrete Compressive Strengths				
$6\sqrt{f'_{cs}}$	6.3	139	706	19.7
$7.5\sqrt{f'_{cs}}$	11.7	142	788	22.0
$12\sqrt{f'_{cs}}$	28.6	150	1032	28.8
Quality Control Concrete Compressive Strengths				
$6\sqrt{f'_{cq}}$	11.9	141	805	22.6
$7.5\sqrt{f'_{cq}}$	18.2	144	911	25.5
$12\sqrt{f'_{cq}}$	37.1	154	1227	34.3
Estimated In Situ Concrete Compressive Strengths				
$6\sqrt{f'_{ce}}$	13.6	142	841	23.5
$7.5\sqrt{f'_{ce}}$	20.1	145	955	26.7
$12\sqrt{f'_{ce}}$	39.5	155	1298	36.2

Table 5.5 Comparison of Results of Analyses of Prototype Bridge Beam Using Quality Control and Specified Material Properties

Index Stress	Percent Difference in Strand Stress Range	Percent Difference in Median Strand Stress	Percent Difference in Equivalent HS Loading
$6\sqrt{f'_c}$	89%	1%	15%
$7.5\sqrt{f'_c}$	56%	1%	16%
$12\sqrt{f'_c}$	30%	3%	19%

Table 5.6 Comparison of Results of Analyses of Prototype Bridge Beam Using Estimated In Situ and Specified Material Properties

Index Stress	Percent Difference in Strand Stress Range	Percent Difference in Median Strand Stress	Percent Difference in Equivalent HS Loading
$6\sqrt{f'_c}$	116%	2%	19%
$7.5\sqrt{f'_c}$	72%	2%	21%
$12\sqrt{f'_c}$	38%	3%	26%

Table 5.7 Comparison of Results of Analysis of Prototype Bridge Beam Using Estimated In Situ and Quality Control Material Properties

Index Stress	Percent Difference in Strand Stress Range	Percent Difference in Median Strand Stress	Percent Difference in Equivalent HS Loading
$6\sqrt{f'_c}$	14%	1%	4%
$7.5\sqrt{f'_c}$	10%	1%	5%
$12\sqrt{f'_c}$	6%	1%	6%

Table 5.8 Results of Analysis of the Bridges in this Investigation using Estimated In Situ Material and Section Properties

Bridge	Calculated Strand Stress Range (ksi)	Calculated Median Strand Stress (ksi)	M_{LL} (ft-kip)	HS_{Eq} (kip)
Index Stress of $6\sqrt{f'_{ce}}$				
Chandler Creek (40-ft Span)	19.5	146	564	28.6
Chandler Creek (60-ft Span)	13.6	142	841	23.5
Lake LBJ	8.5	137	842	21.2
Lampasas River	4.2	139	584	13.4
Willis Creek	8.9	141	600	18.1
Wimberley	19.8	139	772	45.7
Index Stress of $7.5\sqrt{f'_{ce}}$				
Chandler Creek (40-ft Span)	30.8	151	631	32.1
Chandler Creek (60-ft Span)	20.1	145	955	26.7
Lake LBJ	14.2	140	953	24.0
Lampasas River	10.3	142	694	15.9
Willis Creek	15.9	145	702	21.2
Wimberley	26.0	142	839	49.6
Index Stress of $12\sqrt{f'_{ce}}$				
Chandler Creek (40-ft Span)	64.7	168	832	42.3
Chandler Creek (60-ft Span)	39.5	155	1298	36.2
Lake LBJ	31.4	148	1287	32.4
Lampasas River	28.8	151	1025	23.5
Willis Creek	37.0	155	1008	30.4
Wimberley	45.3	152	1039	61.5

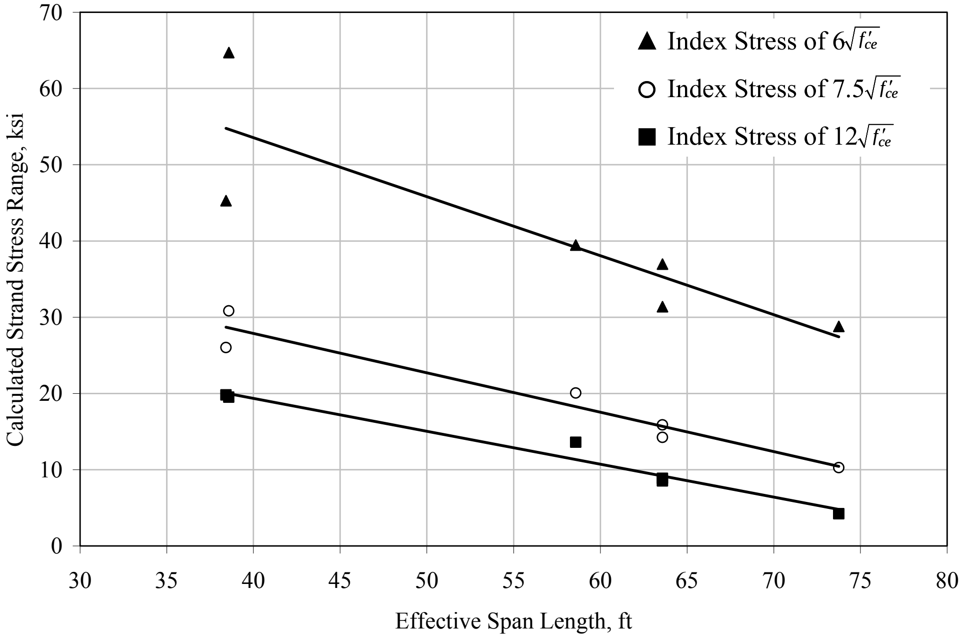

Figure 5.5 Calculated Range of Strand Stress using Estimated In Situ Section Properties Plotted as a Function of Effective Span Length

5.3 FABRICATION OF FATIGUE TEST SPECIMENS

This section presents information about the construction of the test specimens and the properties of the materials used to fabricate them. The six fatigue test specimens were constructed simultaneously, using the same construction sequence and materials. By fabricating all the specimens at one time, the impact of variation in concrete material properties and differences due to variation in the construction process were limited.

5.3.1 Phases of Fabrication of Fatigue Test Specimens

The fatigue test specimens were fabricated in the Ferguson Structural Engineering Laboratory at the University of Texas at Austin. The six beams were built in the prestressing bed pictured in Figure 5.6. The prestressing bed consisted of three beam lines and two beams were constructed along each line.

After the formwork, shear reinforcement and strain gages on the strand were in place, the strands were stressed. Each strand was stressed individually. In order to verify the initial prestress force, load tests were performed on each strand. These load tests are discussed in detail in Section 5.5.2.

After the initial prestress force was determined, concrete was placed in the web portion of the beam. Approximately twenty-four hours after placement of the web concrete, the stress in the strands was released. The slab portion of the beam was placed approximately twenty-four hours after release of the prestressing strands.

5.3.2 Fatigue Test Specimen Material Properties

The materials for the fatigue test specimens were evaluated during both the fabrication and testing phases. Material tests conducted included compression tests on the concrete, elastic modulus tests on the concrete and in-air tension and fatigue tests of the prestressing strand.

One set of compression and elastic modulus tests were conducted on the concrete used for the web portion of the beam prior to releasing the stress in the strands. To have a more accurate estimate of the compressive strength and elastic modulus of the concrete at release, Sure-Cure® cylinders were used. The Sure-Cure® cylinder system uses thermocouples to monitor the temperature of the in situ concrete and utilizes temperature-controlled, 4x8-in., steel cylinders such that the temperature of the concrete in the cylinders is the same as the concrete in the test specimen. In addition, standard 4x8-in. cylinders were cast from the concrete used in the web and concrete used in the slab. These cylinders were used to determine the compressive strength and modulus of elasticity of the web and slab concrete at the age of testing. A summary of the concrete compressive strength and elastic modulus data at various times during fabrication and testing process are presented in. Data from all tests conducted can be found in Appendix K and key results are summarized in Table 5.9.

Tensile strength tests, elastic modulus tests and in-air fatigue tests were conducted on the prestressing strand. The results of the in-air fatigue tests on the prestressing strand were discussed in Chapter 1. As a result of the tests, it was concluded that the strand used in the construction of the test specimens conformed to ASTM A 416.

A summary of the results of the static tests conducted on the strand is shown in Table 5.9. The results include yield strength, breaking strength and modulus of elasticity. Two values for the modulus of elasticity are reported. The modulus of elasticity, denoted E_s in Table 5.9, was determined using measured data from an external extensometer collected during tension tests performed on the strand. The apparent modulus of elasticity, denoted E_{sa} in Table 5.9, was determined using data collected from strain gages located on the outer wires of the prestressing strand and oriented along the local axis of the wire, which is oriented at a pitch to the longitudinal axis of the strand. As a result of the orientation of the strain gages, measured strains will be smaller than the actual longitudinal strain of the strand. Obtaining the relationship between data from the strain gages and longitudinal strain of the strain was necessary because the measured strains were used for the analyses and evaluation of the beams. A more detailed discussion of the tests conducted on the prestressing strand can be found in the thesis by Heller (2003). Additional data on both the static and fatigue tests on the prestressing strand can be found in Appendix K.

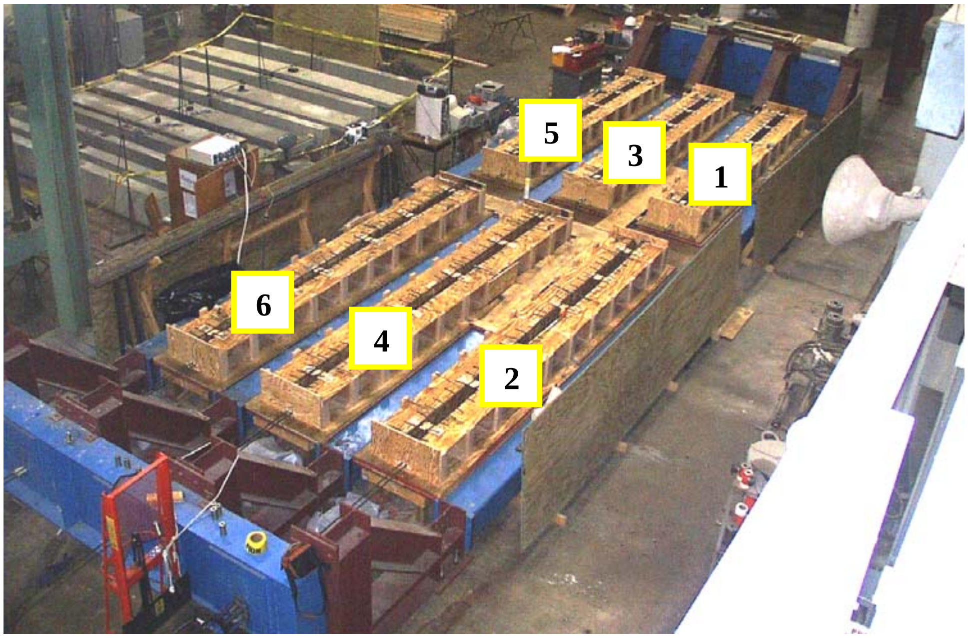

Figure 5.6 Prestressing Bed with Formwork at Ferguson Structural Engineering Laboratory Prior to Placement of Concrete

Table 5.9 Measured Concrete and Prestressing Strand Material Properties

Material Property		Measured Value
Compressive Strength of Web Concrete at Release*	f'_{ci_w}	6100 psi
Modulus of Elasticity of Web Concrete at Release*	E_{ci_w}	5200 ksi
Compressive Strength of Web Concrete at Testing**	f'_{c_w}	12,000-12,800 psi
Modulus of Elasticity of Web Concrete at Testing**	E_{c_w}	6100-6200 ksi
Compressive Strength of Slab Concrete at Testing**	f'_{c_s}	6300-6800 psi
Modulus of Elasticity of Slab Concrete at Testing**	E_{c_s}	4900-5100 ksi
Yield Stress of Prestressing Strand	f_y	245 ksi
Breaking Strength of Prestressing Strand	f_{pu}	275 ksi
Modulus of Elasticity of Prestressing Strand	E_s	29,400 ksi
Apparent Modulus of Elasticity of Prestressing Strand	E_{sa}	31,200 ksi

* Release occurred approximately 24 hours after placement of the web concrete.

** Age of concrete varied due to time between the start of the fatigue tests on the beams.

A comparison of the measured and specified material properties of the concrete for the beams is given in Table 5.10. The specified material properties were used in the design of the fatigue specimens and the measured values were used for the analyses of the beams prior to testing. The most significant difference observed was in the compressive strength of the concrete in the web. The measured compressive strength of the concrete at the time of testing was 20 to 28% higher than the specified value. The effect of this difference is discussed in Section 5.6.

Table 5.10 Comparison of Measured and Specified Concrete Material Properties

Material Property	Specified Value	Percent Difference with Measured Value
f'_{ci_w}	6000 psi	2%
$E_{ci\_w}*$	4500 ksi	16%
f'_{c_w}	10,000 psi	20-28%
$E_{c\_w}*$	5800 ksi	5-17%
f'_{c_s}	6000 psi	5-13%
$E_{c\_s}*$	4500 ksi	9-13%

* $E = 57{,}000\sqrt{f'_c}$

5.4 TEST SET-UP AND INSTRUMENTATION

5.4.1 General Geometry

Figure 5.7 is a photograph of the test setup for the beams. The setup was simple with the beam supported on elastomeric bearing pads on top of concrete piers. Each beam was loaded symmetrically with point loads located 2 ft from the beam centerline. The total length of the beam was 15 ft, with an effective span length of 14.5 ft. The effective span length was determined based on the centerline-to-centerline distance between the bearing pads. A schematic view of the test setup is shown in Figure 5.8.

As shown in Figure 5.7 and Figure 5.8, a single hydraulic ram was used to apply the load to the beam. This load was divided into two equal loads through a spreader beam. The load was transferred from the spreader beam to the beam through two, 1-in. thick elastomeric bearing pads. This loading configuration created a 4-ft constant moment region that provided a finite length of prestressing strand where material flaws may be present and ultimately result in the fatigue failure of the strand. The length of the constant moment region was the same as the length of the specimens used to evaluate the fatigue characteristics of the prestressing strand, in air.

Figure 5.7 Photograph of Fatigue Test Setup (Heller 2003)

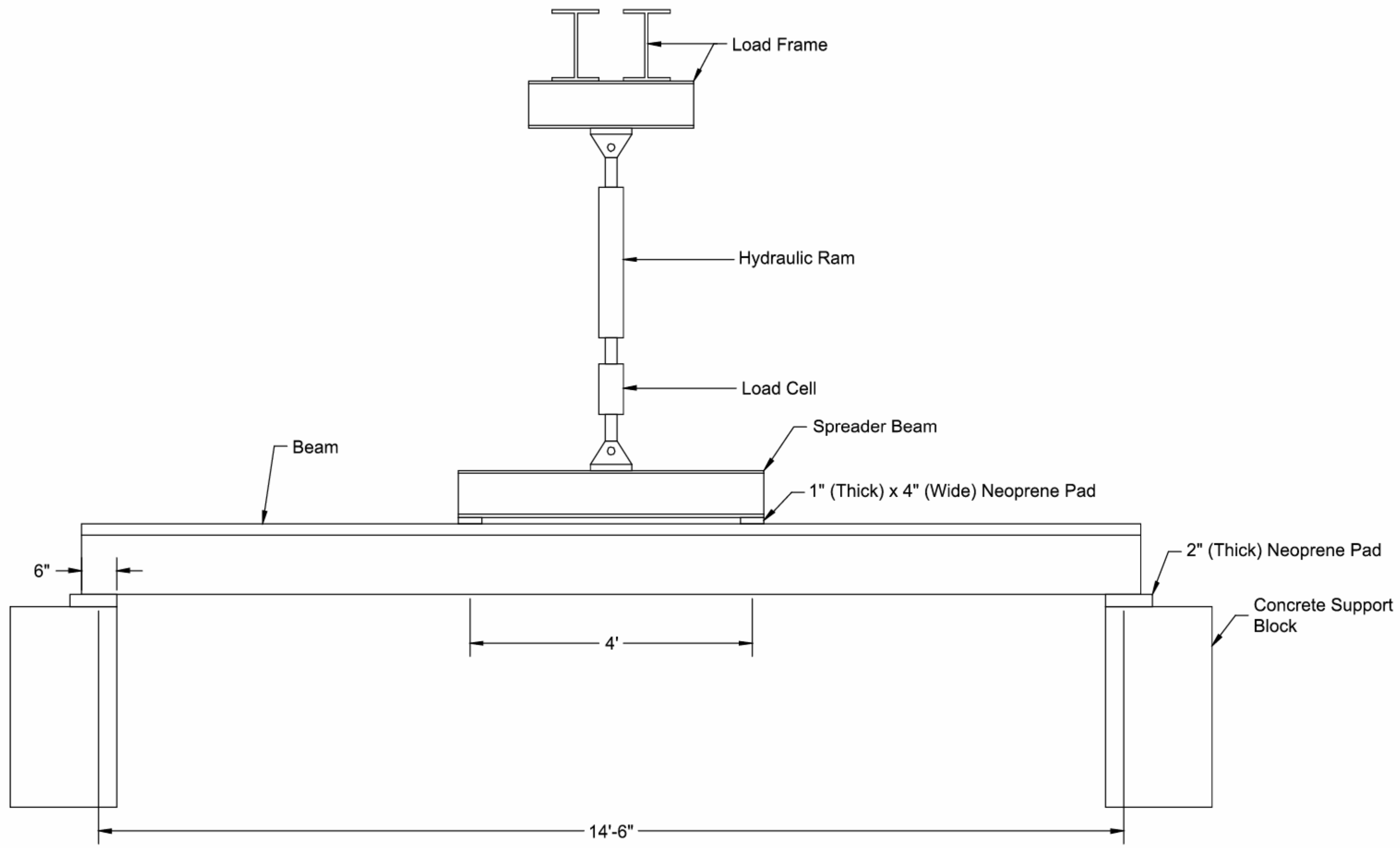

Figure 5.8 Schematic Diagram of Beam Test Setup (Heller 2003)

5.5 EFFECTIVE PRESTRESS FORCE

5.5.1 Instrumentation Used to Evaluate Effective Prestress Force

Two types of strain gages were used to evaluate the effective prestress force. These included strain gages attached to the surface of the prestressing strand, and strain gages embedded in the concrete.

Ten, 5-mm strain gages were attached to individual wires on the prestressing strand within 12-in. of the midspan of each beam. Six of the gages were installed on the strand prior to the stressing of the strand. The remaining four gages were installed after the strands were stressed and prior to the placement of the concrete. The gages installed prior to stressing had experienced a relatively large strain due to the stressing process. As a result, the additional four gages were installed as a precaution in case the original gages experienced failures due to the large strain.

In addition to the strain gages on the strand, one, 60-mm embedded concrete gage was located at the centroid of the prestressing strand and within 12-in. of midspan of each beam. Data from the gages on the strand and embedded in the concrete were used throughout the construction and testing phases of the investigation.

5.5.2 Determination of Initial Prestress Force

The initial prestress force in each strand was determined by conducting a load test, commonly called a lift-off test, after final prestressing and prior to placing the concrete. A schematic of the load test setup is shown in Figure 5.9. During each load test, data were collected from the strain gages attached to the prestressing strand and from the load cell.

The data collected during the load test included the increases in strand strain and the applied axial load. The measured strand strain was averaged to provide one reading from the strain gages installed on each prestressing strand. The corresponding strand stress was calculated by dividing the applied load as measured by the load cell, by the nominal area of the prestressing strand. It should be noted that prior to starting the load test, all strain gages were zeroed, therefore the strain readings reported represent the increase in strain from the initial prestressed condition. The idealized response and measured behavior of strands within Beams 1 and 2 are shown in Figure 5.10.

The idealized response is shown as two lines in Figure 5.10. For stress less than the initial prestress of 150 ksi, no change in strain is expected. Above the initial prestress, the change in strain is expected to vary linearly with the change in stress. As shown in Figure 5.10, a small increase in strain was observed at prestress levels between 100 and 150 ksi. However, the strand strain did not increase appreciably until after the applied stress exceeded 150 ksi. As a result, the initial stress in the strand was determined by projecting the linearly varying portion of to data to the point of zero strain and assuming this point to be the initial prestress. These points are noted in Figure 5.10. The most likely cause for the deviation of the measured response from the idealized behavior is the twisting of the strand as the applied force increases. The idealized response and measured response for all strands differed by a range of 57 to $132\mu\varepsilon$, which corresponds to a difference in strand stress of 2 to 4 ksi. Load test data from the other strands are summarized in Appendix L.

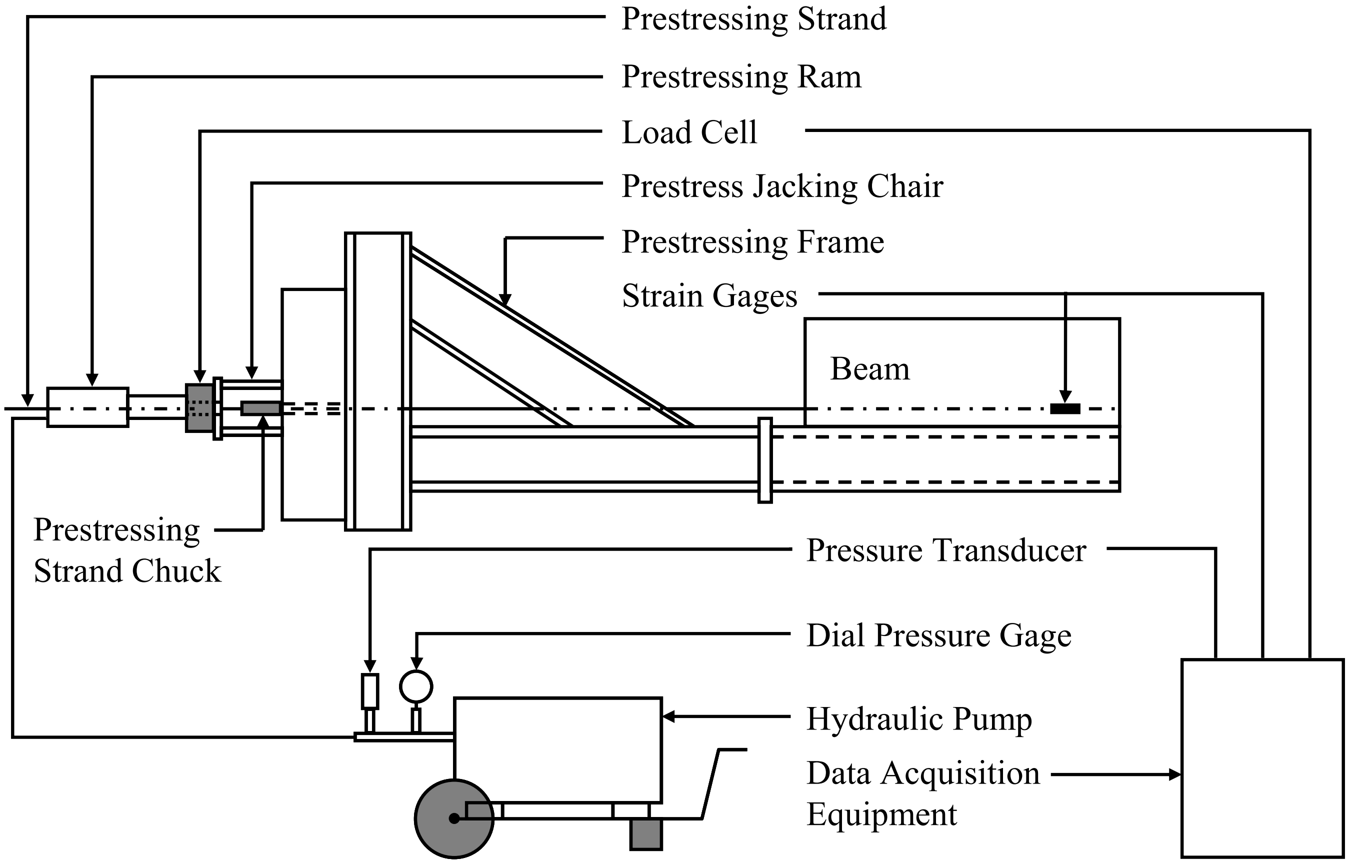

Figure 5.9 Prestressing Strand Load Test Setup

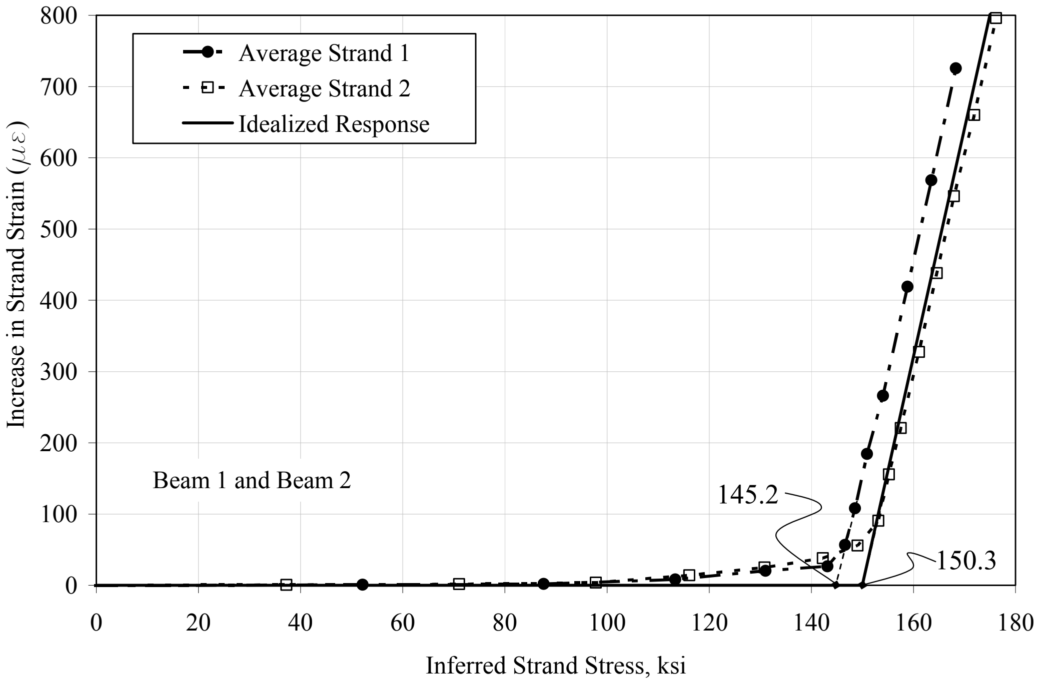

Figure 5.10 Typical Variation of Strand Strain and Inferred Strand Stress During Load Test

5.5.3 Determination of Effective Prestress Force

Knowing the effective prestress force is critical in the analysis of prestressed concrete beams and in particular for performing a load rating analysis. Therefore, the strain gages on the prestressing strand and embedded in the concrete were monitored from release up to the time of testing. A sample of the data collected is shown in Figure 5.11. The changes in strain indicated in Figure 5.11 are the immediate change in strain at release and the total change in strain up to the time of testing. The estimated change in strain is also shown in Figure 5.11, which was calculated using the time-dependent method in the PCI Design Handbook (1992). Calculations of the estimated prestress losses are presented in

Appendix L. The measured change in strain for the six beams ranged from 76% to 89% of the predicted change in strain. This corresponds to a difference of 105 to 201$\mu\varepsilon$, or approximately 3 to 6 ksi in the strand.

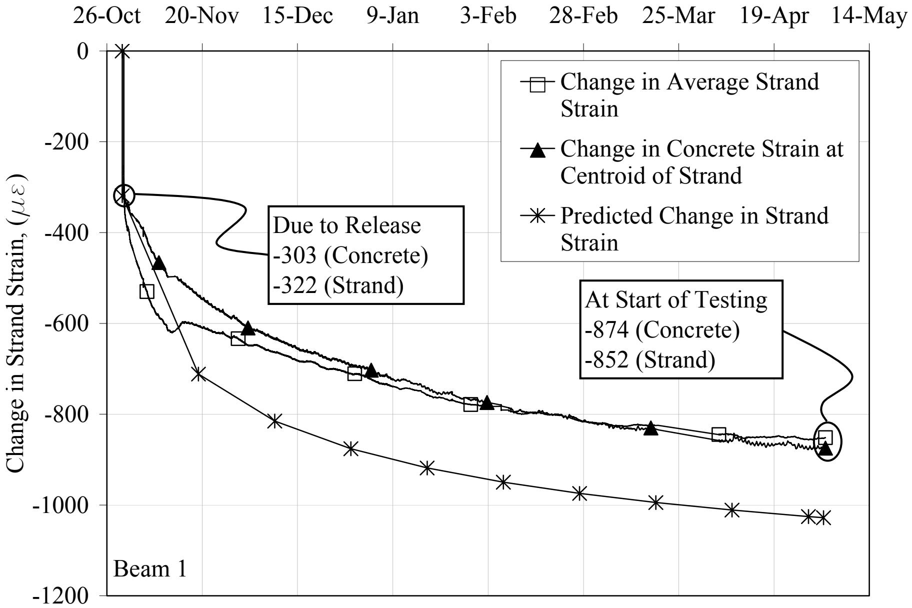

Figure 5.11 Typical Variation in Strand and Concrete Strain with Time

5.6 ANALYSIS OF THE FATIGUE TEST SPECIMENS

Prior to the start of fatigue testing, each specimen was analyzed to determine the required load range that would produce the desired index stress, strand stress range, and median strand stress. The measured concrete compressive strength and modulus of elasticity used for the analysis of each beam are summarized in Table 5.11. The properties of the prestressing strand used in the analyses were previously reported in Table 5.9. The effective prestress force used for the analyses were based on measured strains. Table 5.12 summarizes the effective prestress at release, prestress losses, and effective prestress at the start of testing. The effective prestress force at release was determined using the lift-off tests discussed in Section 5.5.1. Prestress losses were calculated based on the measured change in strain discussed in Section 5.5.2.

The analyses of the fatigue specimens were similar to the analyses used to idealize the response of the prototype beam. The applied load and stress range in the strand corresponding to the five states of stress summarized in Table 5.13 were calculated for each beam. The full dead load state, point 1, included the weight of the web, slab, and spreader beam and accounted for all prestress losses at the start of testing. The other points were similar to the points used in the analysis of the prototype beam. Using the results of the analyses, a plot of applied load as a function of stress range in the strand was generated for each beam. Figure 5.12 is a plot of applied load as a function of the range of stress in the strand for Beam 4. A detailed discussion of the methods used to analyze the cross section at each state of stress is presented in Appendix M.

The stress range in the strand being investigated was then determined graphically using the five data points from the analysis and assuming the applied load varied linearly between each data point. Data points A and B denoted in Figure 5.12 correspond to the minimum and maximum applied load used for fatigue testing, respectively. The loads were determined graphically using the median stress and strand stress range given in Table 5.14.

Table 5.11 Summary of Measured Concrete Material Properties Used in Analyses of Fatigue Test Specimens

Beam ID	Compressive Strength (psi)			Modulus of Elasticity (ksi)		
	Release	Start of Fatigue Test		Release	Start of Fatigue Test	
	Web	Web	Slab	Web	Web	Slab
1	6100	12,700	6900	5200	6200	5200
2	6100	12,600	6800	5200	6200	5200
3	6100	12,600	6800	5200	6200	5200
4	6100	12,000	6300	5200	6100	4900
5	6100	12,000	6700	5200	6100	5200
6	6100	12,700	6900	5200	6200	5300

Table 5.12 Summary of Prestressing Data Used in Analyses of Beams

Beam ID	Number of Days Between Release and Testing	Measured Prestress Prior to Release* (ksi)	Average Measured Change in Strain of Strand at Release** ($\mu\varepsilon$)	Average Total Measured Change in Strain of Strand† ($\mu\varepsilon$)	Total Prestress Losses†† (ksi)	Effective Prestress at Testing (ksi)
1	202	148	322	852	27	121
2	162	148	323	789	25	123
3	144	147	290	699	22	125
4	105	147	287	683	21	126
5	128	151	294	760	24	127
6	252	151	279	759	24	127

* Average stress for the strands in the beam line based on lift-off tests.

** Average of the change in strain from data recorded by all 10 gages on the prestressing strand at release. (See Figure 5.11 and corresponding figures for the other beams in Appendix L.)

† Average of the change in strain from data recorded by all 10 gages on the prestressing strand from release to the start of the fatigue tests. (See Figure 5.11 and corresponding figures for the other beams in Appendix L.)

†† Calculated using average measured change in strain of the strand and the apparent modulus of the prestressing strand.

Table 5.13 Description of Analysis Points for Fatigue Specimens

Point	Description
1	Full dead load state
2	Decompression of bottom fiber
3	Neutral axis at center of gravity of strand
4	Neutral axis at top of web
5	Flexural Capacity
A	Minimum applied load for fatigue test
B	Maximum applied load for fatigue test

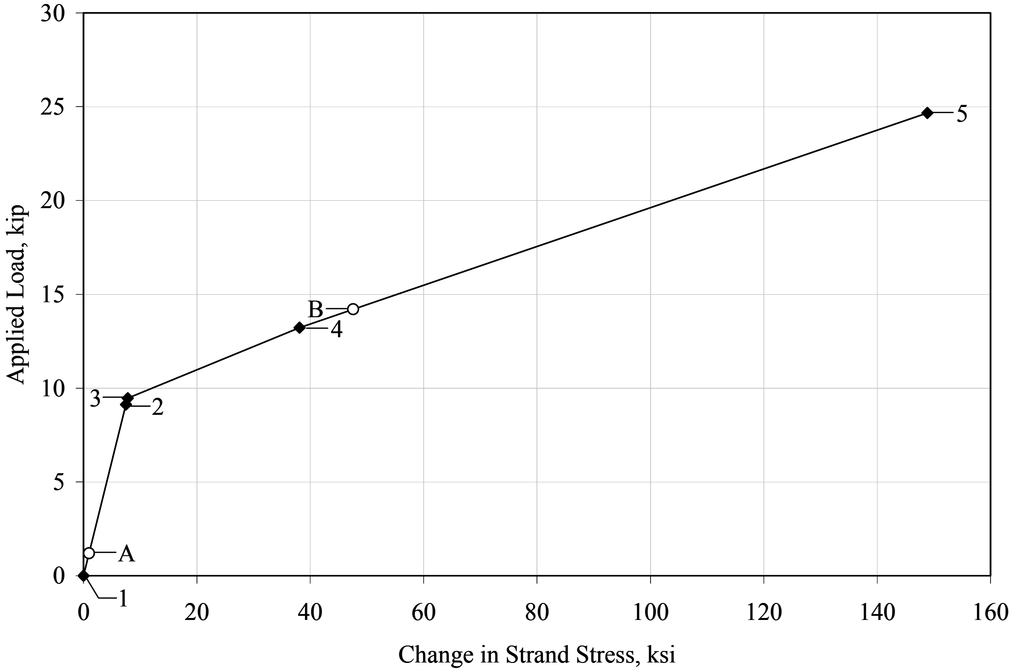

Figure 5.12 Plot of Applied Load as a Function of Stress Range in the Strand for Beam 4

The results of the analysis of each beam are summarized in Table 5.14. Although it was intended that the beams be tested at index stresses of $6\sqrt{f'_{cm}}$, $7.5\sqrt{f'_{cm}}$, and $12\sqrt{f'_{cm}}$, all the beams were tested at stress levels below the desired index stress. Differences in the compressive strength of the concrete and prestress losses between the preliminary design and actual beams required that either the median stress level in the strand or the index stress vary from the prototype beam. As discussed in Chapter 1, the strand is the key element in the fatigue life of prestressed concrete beams. Therefore, reduced index stresses were selected so that the median strand stress would be similar to the median strand stress in the prototype beam.

Beams 1 and 6 were tested at a similar strand stress range and median stress as the prototype beam at the index stress level of $6\sqrt{f'_{ce}}$, which are given in Table 5.4. Similarly, Beams 2 and 3 were tested at a similar strand stress range and median stress as the prototype beam at the index stress level of $7.5\sqrt{f'_{ce}}$, and Beams 4 and 5 were tested at a similar strand stress range and median stress as the prototype beam at the index stress level of $12\sqrt{f'_{ce}}$. Although the strand stress ranges and median stresses for the test beams did not match the calculated the prototype beam, all of the strand stress ranges and median stresses for the beams fall within the ranges calculated for the five bridges studied in this investigation.

Table 5.14 Summary of Analyses on Fatigue Test Specimens

Beam ID	Index Stress* (psi)	Min. Load (kip)	Max. Load (kip)	Strand Stress at Minimum Load (ksi)	Strand Stress Range** (ksi)	Median Strand Stress** (ksi)
1	$2.4\sqrt{f'_{cm}}$	10.5	11.4	138	7	145
2	$2.7\sqrt{f'_{cm}}$	2.8	11.7	126	22	137
3	$4.6\sqrt{f'_{cm}}$	1.9	11.9	127	25	140
4	$9.0\sqrt{f'_{cm}}$	1.0	14.2	127	47	150
5	$9.1\sqrt{f'_{cm}}$	0.6	14.3	124	47	148
6	$3.1\sqrt{f'_{cm}}$	5.5	10.8	132	14	139

* Index stress was calculated using uncracked, transformed, composite section properties and measured compressive strength of the concrete.

** Strand stress range and median strand stress were calculated based on equilibrium and compatibility using the measured properties of the materials and assuming cracked section properties.

It was also intended that Beam 2 be tested at a similar index stress to Beam 3 and that Beams 1 and 6 also be tested at a similar index stress. However, based on observations during release of the prestressing forces in the strands and the measured change in strain in the strands, it was determined that the compressive stress at the bottom fiber of Beam 2 was larger than the compressive stress at the bottom fiber of Beam 3 at the dead load state. The compressive stress at the bottom fiber has a direct impact on the calculation of the index stress and preference was given to loading the beam at a similar strand stress range and median stress over attaining a particular index stress. The observations and measured data on which this determination was made are discussed below.

The forces in the prestressing strands were released in sequential order, starting with strand 1 and finishing with strand 6. During the release of strand 1 and strand 2, which are the strands in Beams 1 and 2, significant movement of the prestressing bed and formwork for Beams 1 and 2 was observed. In contrast, when the remaining strands were released, no appreciable movement was observed. Based on this observation and the measured change in strain at the time of release, which are summarized in Table 5.15, it was reasonable to assume that the formwork was restraining Beams 3 through 6, while Beams 1 and 2 were fully released from the formwork when the prestressing strands were cut.

The possibility of the formwork restraining the beams was investigated by analyzing the non-composite beam using the measured change in strain of the strand due to the release of the prestress forces. Assuming a linear strain profile and the measured strains, an equilibrium analysis was performed and the stress at the bottom fiber of the cross section at release of the strands was determined. The compatibility and equilibrium equations used to perform this analysis are given in Figure 5.13 and addition details are given in Appendix M. The results of this analysis are shown in Table 5.15 and are compared with the bottom fiber stress calculated assuming the formwork did not restrain the beams. The general equation used to calculate the bottom fiber stress assuming the formwork did not restrain the beams is as follows:

$$f_b = \frac{P}{A} + \frac{Pec}{I} - \frac{M_{sw}c}{I} \tag{5.1}$$

where f_b is the bottom fiber stress, P is the measured effective prestress force, A is the gross area of the web, I is the gross moment inertia of the web, e is the eccentricity between the prestressing strand and the center of gravity of the web, c

is the distance from the center of gravity of the web to the bottom fiber, and M_{sw} is the self-weight moment of the web. The difference between the calculated and inferred bottom fiber stresses given in Table 5.15 are nominally the same for Beams 1 and 2, however, the calculated stress is significantly higher than the inferred stress for Beams 3 through 6.

Based on the results in summarized in Table 5.15, it is reasonable to assume that Beams 1 and 2 were not restrained by the formwork and were subjected to the full force of initial prestressing when the strands were released. However, Beams 3 through 6 were restrained by the formwork immediately after the strands were released and the compressive stresses along the bottom fiber of the web were less than anticipated. As a result, Beam 3 had a lower net compressive stress than Beam 2. Even though Beams 2 and 3 were nominally the same, the differences in behavior at release resulted in Beam 3 being tested at a lower index stress than Beam 2. A similar comparison can be made between Beams 1 and 6, which also were nominally the same, however, were tested at different index stresses due to the effects of the restraint provided by the formwork.

Table 5.15 Summary of Bottom Fiber Compressive Stresses

Beam ID	Calculated Bottom Fiber Stress At Release Assuming No Restraint* (psi)	Measured Change in Strain in the Strand at Release ($\mu\varepsilon$)	Bottom Fiber Stress at Release Inferred From Measured Change in Strain at Release** (psi)	Difference Between Calculated and Inferred Bottom Fiber Stress at Release (psi)
1	2330	322	2410	-80
2	2330	323	2420	-90
3	2320	290	2120	200
4	2320	287	2090	230
5	2390	284	2040	350
6	2390	279	2000	390

* Based on gross section properties of the web, measured concrete material properties, and measured prestress prior to release given in Table 5.12.

** Calculated using gross section properties of the web, and compatibility and equilibrium based on measured strains.

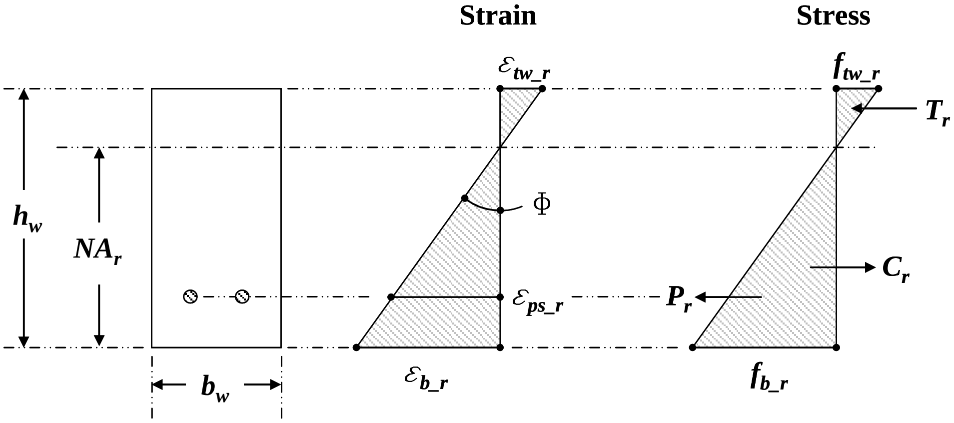

Compatibility Equations

$$\Phi = \frac{\varepsilon_{ps\_r}}{NA_r - y_{ps}}$$

$$\Phi = \frac{\varepsilon_{tw\_r}}{10 - NA_r}$$

$$\Phi = \frac{\varepsilon_{b\_r}}{NA_r}$$

Equilibrium Equations

$$C_r = f_{tw\_r}\frac{b_w(h_w - NA_r)}{2}$$

$$T_r = f_{b\_r}\frac{b_w NA_r}{2}$$

$$C_r = T_r$$

Where ε_{ps_r} is the measured change in strain in the prestressing strand. (Table 5.15)

Figure 5.13 Equations Used to Calculate the Bottom Fiber Stress Inferred from the Measured Strains

5.7 TEST PROCEDURES

Each beam was subjected to a series of static tests throughout the fatigue tests. Both the static and fatigue test procedures are discussed in the following sections.

In addition to the instrumentation previously discussed, five instruments were used to measure displacements of the beam. Three of the instruments were direct current linear variable differential transformers (LVDTs) and were used to measure the vertical displacement of each beam at midspan and at the center of each bearing pad. In addition, a linear motion transducer was used to measure midspan displacement. It should be noted that all midspan displacements reported in this document have been corrected for the average compression of the bearing pads, and represent the deformation of the test specimens. The locations of these instruments are shown in Figure 5.14.

The fifth displacement instrument was installed after a crack formed in the beam. This LVDT was installed horizontally with its axis aligned with the bottom surface of the beam, and measured displacements across the most prominent crack. Figure 5.15 is a photograph of this displacement transducer after installation. Data collected from this LVDT were used to approximate when the crack opened and closed due to the applied load.

The applied load was measured using a load cell. The location of the load cell is shown in Figure 5.7 and Figure 5.8.

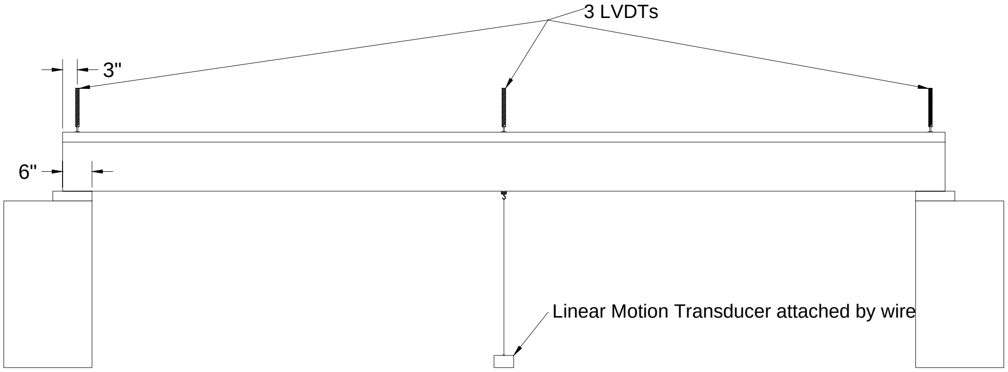

Figure 5.14 Schematic of Vertical Displacement Instruments (Heller 2003)

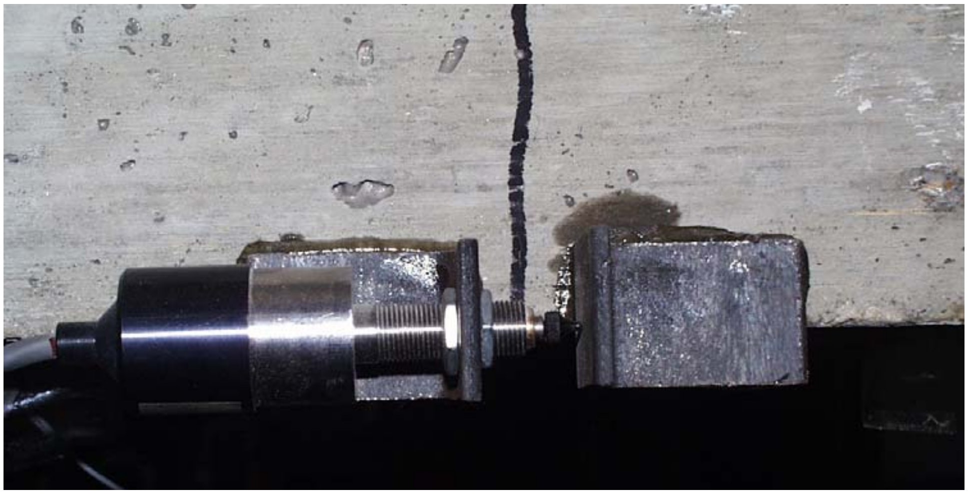

Figure 5.15 Photograph of LVDT Across Flexural Crack (Crack Displacement Gage) (Heller 2003)

5.7.1 Static Tests

5.7.1.1 Initial Static Tests

The purpose of the initial static tests was to define the baseline behavior of the beams for comparison with data collected during the fatigue tests. Data were collected from four displacement transducers (two located at the midspan of the beam and one located at the centerline of each bearing), strain gages on the prestressing strand, and an embedded concrete strain gage located at the center of gravity of the prestressing strand. Data were collected during the loading and unloading phases of the static test. In addition, cracks were marked at the maximum applied load during each test.

Beams 1, 2, 4, and 5 cracked during the initial static test. After each of these tests, a horizontal displacement transducer was installed across the most prominent crack, and two surface concrete strain gages, one on each side of the prominent crack, were installed. After this instrumentation was installed, another static test was conducted.

Beams 3 and 6 did not crack during the initial static test. As a result, a small number of fatigue cycles were performed until the first crack formed. After the crack appeared, the additional instrumentation was placed on these beams and an additional static test was performed.

The load during the initial static test was typically applied in 1-kip increments. In the vicinity of the decompression load, the load increment was reduced to approximately 0.25 to 0.5 kip to capture the nonlinear beam behavior.

5.7.1.2 Periodic Static Tests

Periodically during the fatigue tests on each beam, additional static tests were performed. In some cases the fatigue loading was interrupted because the beam had sustained a predetermined number of cycles. In other cases the displacement of the beam increased suddenly, typically due to the fracture of a wire. Each time the fatigue tests were interrupted for a static test, data were collected from all the instruments.

Similar to the initial static test, data were collected during the loading and unloading portion of the tests and cracks were marked at the maximum applied load. The load increments for these tests were the same as described for the initial static tests.

5.7.2 Fatigue Tests

Cyclic loads were applied to each beam with the maximum and minimum loads determined from the analyses presented in Appendix M. The maximum and minimum loads were selected to produce the desired range of stress in the strand and median stress. Two beams were tested at each strand stress range. Beams 1 and 6 were tested at a strand stress of approximately 10 ksi, Beams 2 and 3 were tested at a strand stress of approximately 23 ksi and Beams 4 and 5 were tested at a strand stress of approximately 47 ksi.

Detailed descriptions of the procedures for establishing the load settings and cycle frequency on the load controller used to drive the hydraulic ram are provided in Heller (2003).

5.7.3 Post Mortem Investigation

The fatigue tests were run until a prescribed number of cycles had been reached or a significant decrease in the stiffness of the beam had been achieved, which indicated that several wires had fractured. In either case, further testing of the specimens was determined to be unnecessary and the beams were removed from the test setup. The concrete around the prestressing strands was removed within the region defined by the cracks furthest from the centerline of the beam to expose the strand and determine the number of wire failures.

5.8 SUMMARY

For the prototype beam the relationship between the index stress level and strand stress range was similar at all three levels of concrete compressive strength investigated. An increase in the strand stress range of 46 to 76% was calculated when the index stress was increased from $6\sqrt{f_c'}$ to $7.5\sqrt{f_c'}$. An increase in the strand stress range of 180 to 340% was calculated when the index stress was increased from $6\sqrt{f_c'}$ to $12\sqrt{f_c'}$.

Based on the analysis of the prototype beam and interior beams from the other bridges in this investigation, it was shown that no particular strand stress range corresponds uniquely to an index stress level. However, the trends in the data indicated that strand stress range increases as span length decreases. In addition, the variation of strand stress range for a particular span length and index stress level indicates that the sensitivity of the calculation of the strand stress range increases as the index stress increases.

Six prestressed concrete beams were designed, constructed, and subjected to fatigue loads. The calculated strand stress ranges and median stresses in the specimens were similar to those in the prototype beam for three different index stress levels. When determining the load range for the fatigue tests, preference was given to achieving the strand stress range and median stress over the index stress. As a result, Beam 2 was tested at a strand stress range and median stress that was similar to the levels in the prototype beam at an index stress of $7.5\sqrt{f'_{ce}}$; however, the calculated index stress in Beam 2 was lower than the index stress level in the prototype beam.

CHAPTER 6

Results of Laboratory Fatigue Tests

As previously discussed, six prestressed concrete beams were subjected to fatigue loads as part of this investigation. Typical results at each range in nominal strand stress are presented in this chapter. Additional results can be found in Appendix N. Results for Beams 2, 3, 4 and 5 have been previously reported by Heller (2003). Table 6.1 and Table 6.2 summarize the beam tests conducted as part of this project. The tests reported in Table 6.2 were performed on two beams that had no significant fatigue damage after ten million cycles.

As discussed in Chapter 5, the nominal strand stress ranges selected for testing correspond to strand stress ranges based on analyses of the prototype beam. The prototype beam was analyzed at three load levels that correspond to index stresses of $6\sqrt{f'_{ce}}$, $7.5\sqrt{f'_{ce}}$, and $12\sqrt{f'_{ce}}$.

A minimum of two beams were tested at each range of nominal strand stress determined from the analyses of the prototype beam. The ranges of strand stress in the beams were determined based on cracked section properties, measured prestress losses, and measured material properties of the concrete and prestressing strand. Although it was desirable that the index stress in the fatigue specimens correspond to the index stress in the prototype beam, preference was given to achieving the same median stresses and range of stresses in the strand from the analyses of the prototype beam, rather than the index stress.

This chapter is divided into five sections. The fatigue response of the beams at each of the ranges of nominal strand stress is summarized in Sections 6.1, 6.2, and 6.3. Beams 1 and 6 both survived 10,000,000 cycles at a strand stress range of approximately 10 ksi, and were subsequently subjected to additional fatigue cycles at higher ranges of strand stress. Data from these tests are described in Sections 6.4 and 6.5.

6.1 BEHAVIOR OF BEAMS 1 AND 6

Beams 1 and 6 were subjected to fatigue loads corresponding to a stress range in the strand of approximately 7 ksi and 14 ksi, respectively. Based on the data presented in Chapter 1, the strand stress range for Beam 1 appears to be below the endurance limit for prestressing strand in prestressed concrete beams. However, the strand stress range for Beam 6 appears to be slightly above the endurance limit. Data from these tests are summarized in this section.

6.1.1 Initial Static Tests

During the initial static test, Beam 1 was loaded until flexural cracking occurred. As summarized in Table 6.3, the calculated cracking load was 14.4 kip, which corresponds to a modulus of rupture of $7.5\sqrt{f'_{cm}}$, and the first crack was observed at an applied load of 12 kip.

Unlike Beam 1, Beam 6 did not crack during the initial static test. Beam 6 was loaded to the maximum fatigue load during the initial static test, which was less than the calculated cracking load. Then Beam 6 was subjected to 1000 loading cycles between a minimum load of 5.5 kip and a maximum load of 10.8 kip and then was subjected to another static test. Flexural cracks were first observed during this static test at an applied load of approximately 10.5 kip.

Table 6.1 Overview of Fatigue Tests

Beam ID	f'_{cm}	Date Fatigue Test Started	Applied Load		Calculated Strand Stress Range	Calculated Median Strand Stress
			Min.	Max.		
	psi		kip	kip	ksi	ksi
1	12800	5/19/03	10.5	11.4	7	142
2	12600	4/9/03	3.4	11.7	22	137
3	12600	3/22/03	2.3	11.9	25	140
4	12000	2/11/03	1.2	14.2	47	150
5	12000	3/6/03	0.6	14.3	47	148
6	12800	7/8/03	5.5	10.8	14	139

Table 6.2 Overview of Additional Fatigue Tests of Beams 1 and 6

Beam ID	Date Fatigue Test Started	Applied Load		Calculated Strand Stress Range	Calculated Median Strand Stress
		Min.	Max.		
		kip	kip	ksi	ksi
1A	6/7/03	10.0	14.5	41	155
1B	8/13/03	0.7	13.5	44	144
6A	8/5/03	2.7	14.3	45	152

The average measured strand strain during the initial static test for Beam 1 is shown in Figure 6.1. Based on the observed change in stiffness, cracking appears to have initiated at an applied load of approximately 11.5 kip. Similar data for Beam 6 (Figure 6.2) indicate a somewhat more linear relationship between applied load and average strand strain. Data were not collected during the fatigue tests; therefore, it is not possible to estimate the cracking load from the strain data for Beam 6. The initial crack patterns for Beams 1 and 6 are shown in Figure 6.3 and Figure 6.4, respectively.

Table 6.3 Summary of Results from Initial Static Tests

Beam ID	Calculated Cracking Load*	Applied Load at First Observed Crack	Cracking Load Inferred from Strand Data	Maximum Load during Initial Static Test
	(kip)	(kip)	(kip)	(kip)
1	14.4	12.0**	11.5	12.0
2	14.5	11.0**	11.0	11.7
3	13.6	9.5††	—†	11.9
4	13.4	13.0**	11.0	18.0
5	13.4	11.3**	10.5	14.5
6	13.4	10.5†††	—†	10.8

* Calculated cracking load corresponds to a tensile stress at the extreme tension fiber of $7.5\sqrt{f'_{cm}}$ using gross section properties.

** First crack observed during initial static test.

† Cracking occurred during fatigue loading; therefore, the cracking load could not be inferred from the measured data.

††Beam did not crack during initial static test. Beam was subjected to 25 fatigue cycles, and cracking was observed in the subsequent static test.

††† Beam did not crack during initial static test. Beam was subjected to 1000 fatigue cycles, and cracking was observed in the subsequent static test.

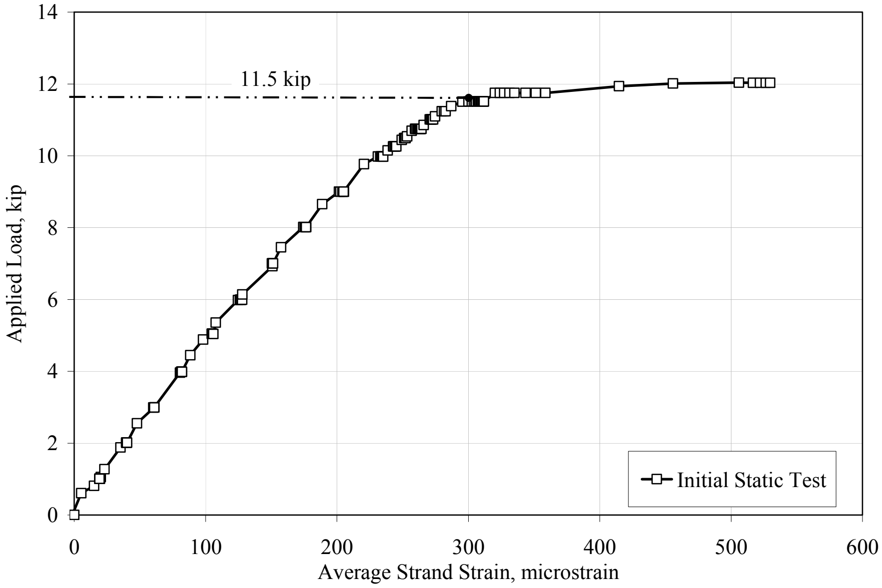

Figure 6.1 Applied Load versus Average Strand Strain during Initial Static Test for Beam 1

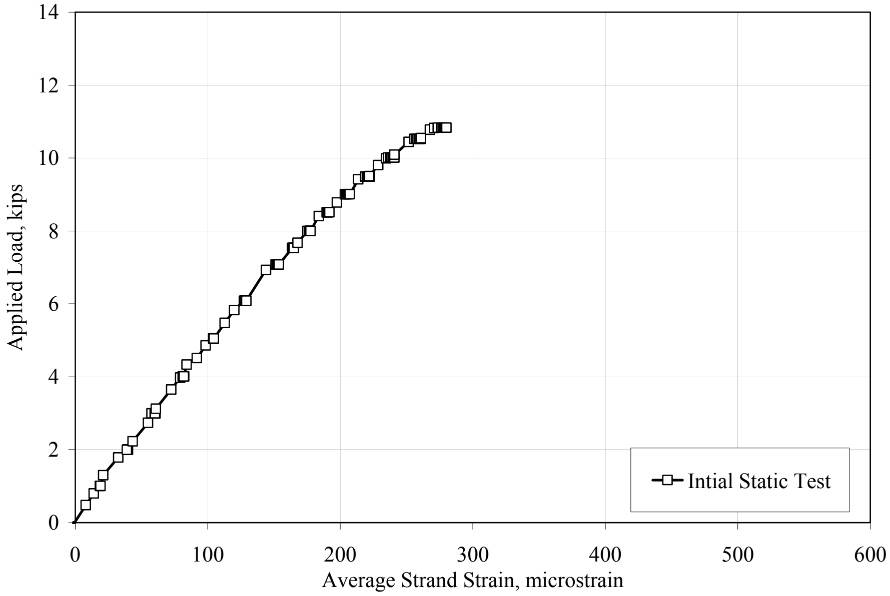

Figure 6.2 Applied Load versus Average Strand Strain during Initial Static Test for Beam 6

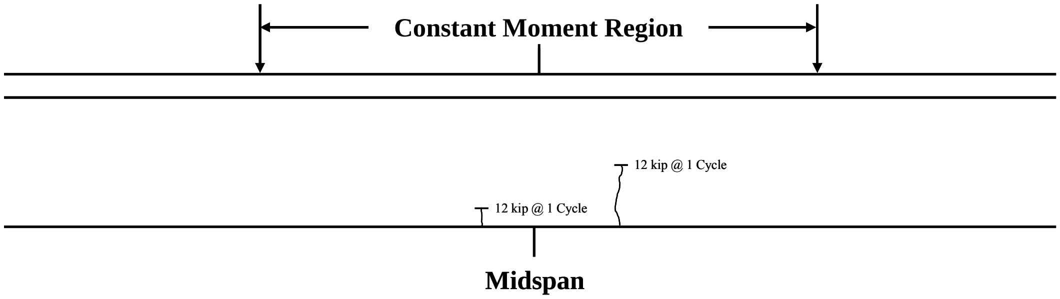

Figure 6.3 Crack Pattern for Beam 1 after Initial Static Test

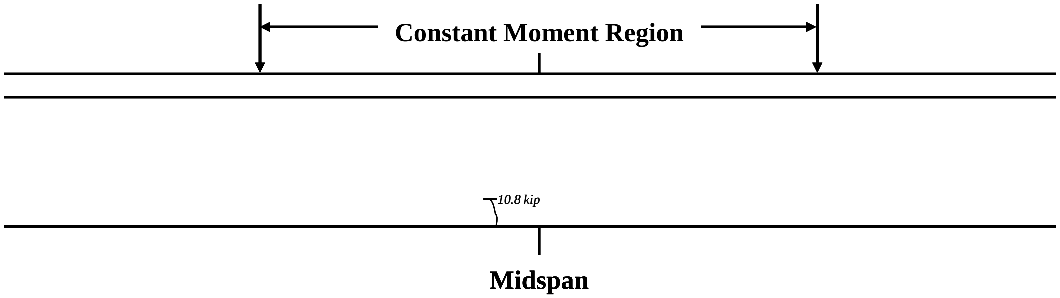

Figure 6.4 Crack Pattern for Beam 6 after 1,000 Cycles

6.1.2 Decompression Load

The decompression load is the applied load at which the flexural tensile stress at the bottom fiber overcomes the net compressive stress due to combined prestressing and dead load. The calculated decompression loads for Beams 1 and 6 were 9.2 and 9.4 kip, respectively. These calculations were performed using cracked section properties and the prestress losses inferred from the measured strains and are documented in Appendix M.

The decompression load could also be inferred from the measured response of the beams. After the initial cracks formed, the strain data from the prestressing strand, the midspan deflection data, and the data from the displacement gage across the most prominent crack were repeatable in successive static tests. Near the decompression load, the effective stiffness of the cross section changes from uncracked to cracked properties. This change in stiffness occurs gradually, and a distinct decompression load can not be clearly identified from the data. However, the decompression load was approximated as the intersection of the best-fit lines at loads above and below the nonlinear transition. A typical example using strain data from Beam 1 is shown in Figure 6.5. Additional plots are shown in Appendix N.

Decompression load results are summarized in Table 6.4. In general the decompression loads inferred from the measured data are 0 to 13% lower than the calculated values.

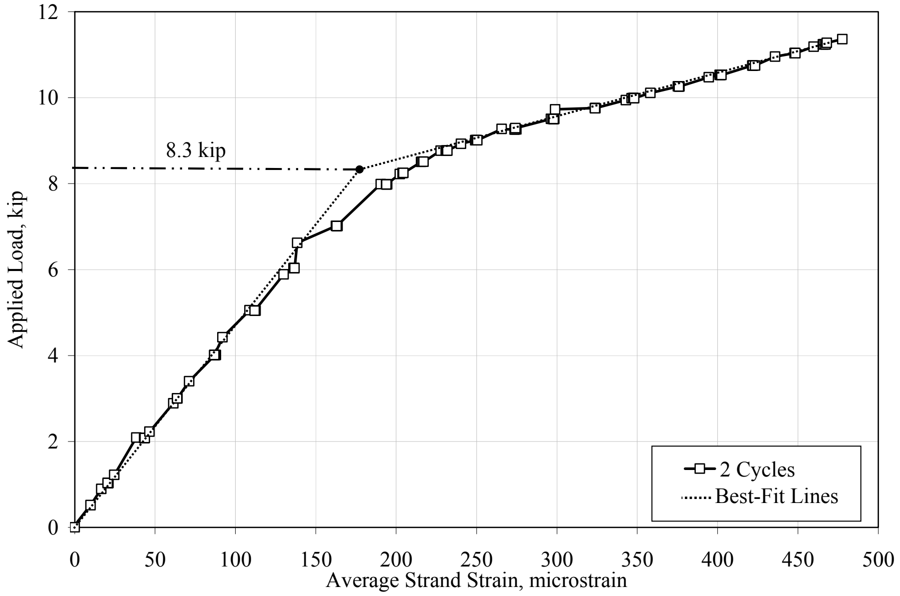

Figure 6.5 Estimated Decompression Load for Beam 1 Using Average Strand Strain

Table 6.4 Summary of Decompression Loads

Beam ID	Calculated Decompression Load* (kip)	Decompression Load Inferred from Strand Strain (kip)	Decompression Load Inferred from Midspan Displacement (kip)	Decompression Load Inferred from Crack Opening (kip)
1	9.2	8.3	8.2	8.3
2	9.4	9.3	8.9	9.1
3	9.2	8.2	7.8	8.1
4	9.1	9.1	9.5	9.6
5	9.1	9.1	9.1	9.1
6	9.0	8.2	7.8	8.1

* Calculated using cracked section properties and prestress losses inferred from the measured data.

6.1.3 Fatigue Response

The maximum and minimum loads applied to the test specimens during the fatigue tests are summarized in Table 6.1. The calculated stress range and median stress in the strand are also listed.

As noted previously, the fatigue tests were stopped periodically and the beams were subjected to additional static tests. The data collected during these tests provide a mechanism for quantifying changes in the beam response.

Applied load is plotted in Figure 6.6 as a function of the midspan displacement for the eleven static tests performed on Beam 1. A significant change in stiffness was observed between the first two static tests. The beam was initially uncracked, so this change was expected. The stiffness continued to decrease as the number of fatigue cycles increased. After ten million cycles, the maximum midspan displacement under the maximum applied fatigue load was approximately 23% larger than the maximum displacement during the initial static test and approximately 14% larger than the maximum displacement after one loading cycle.

The corresponding data from Beam 6 are shown in Figure 6.7. As previously discussed, Beam 6 did not crack during the initial static test; therefore, the significant change in stiffness did not occur until later in the loading sequence. Rather, the cracks that were observed after the initial static test for Beam 1 were not observed until Beam 6 had experienced approximately 1,000 fatigue cycles. Similarly to Beam 1, the stiffness of Beam 6 continued to decrease as the number of fatigue cycles increased. After ten million cycles, the maximum midspan displacement under the maximum applied fatigue load was approximately 27% larger than the maximum displacement during the initial static test and 23% larger than the maximum displacement after 1,000 loading cycles.

The applied load is plotted as a function of the average strain in the strand in Figure 6.8 and Figure 6.9 for Beams 1 and 6, respectively. The variation of strain is more sensitive to the number of fatigue cycles than the midspan displacement for both beams. This difference is likely due to the locations of strain gages relative to the cracks.

The applied load is plotted as a function of the width of the most prominent initial crack in Figure 6.10 and Figure 6.11 for Beams 1 and 6, respectively. The trends are not significantly different from those exhibited by the other instruments.

The variations of the midspan displacement and crack width at the maximum applied load during each static test are shown in Figure 6.12 and Figure 6.13 for Beams 1 and 6, respectively. The gradual decrease in stiffness with the number of loading cycles is observed for both beams.

The crack patterns observed in Beams 1 and 6 after ten million cycles at a strand stress range of approximately 8 ksi are shown in Figure 6.14 and Figure 6.15, respectively. The length of the initial cracks increased during the fatigue loads and several new cracks formed.

The behavior of Beams 1 and 6 did not change appreciably during the initial series of fatigue tests. As described in Sections 6.4 and 6.5, these beams were subjected to additional fatigue loading corresponding to higher ranges of strand stress.

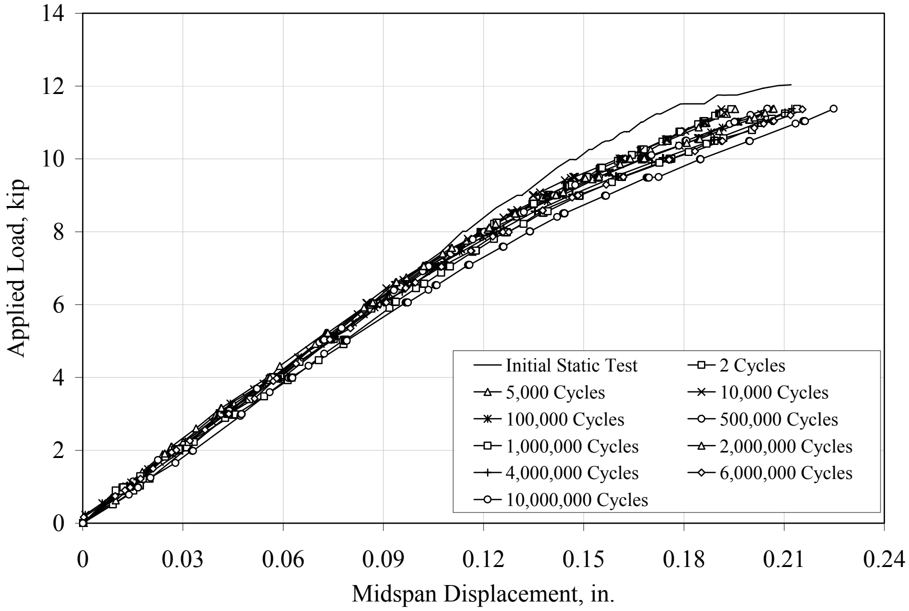

Figure 6.6 Variation of Midspan Displacement during Fatigue Tests of Beam 1 at a Strand Stress Range of 7 ksi

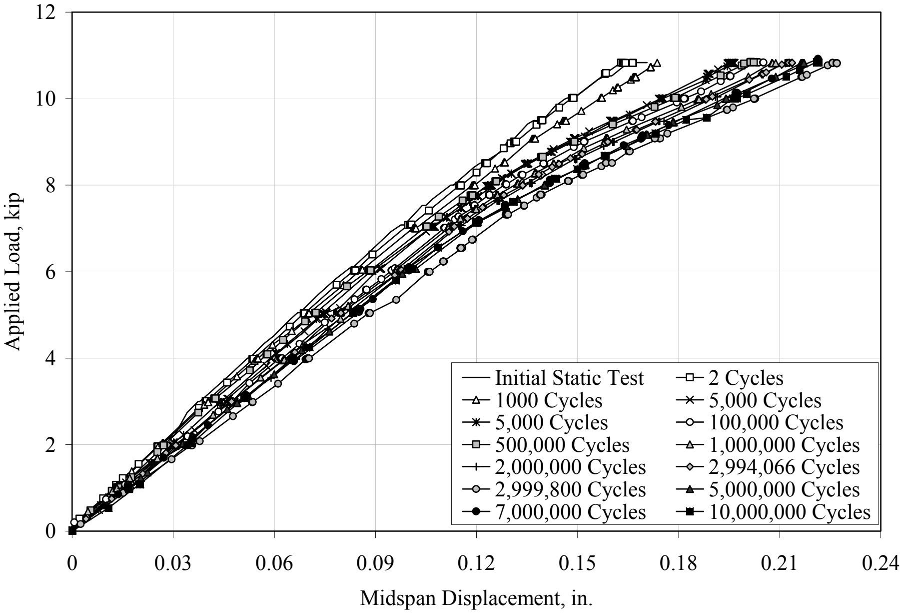

Figure 6.7 Variation of Midspan Displacement during Fatigue Tests of Beam 6 at a Strand Stress Range of 14 ksi

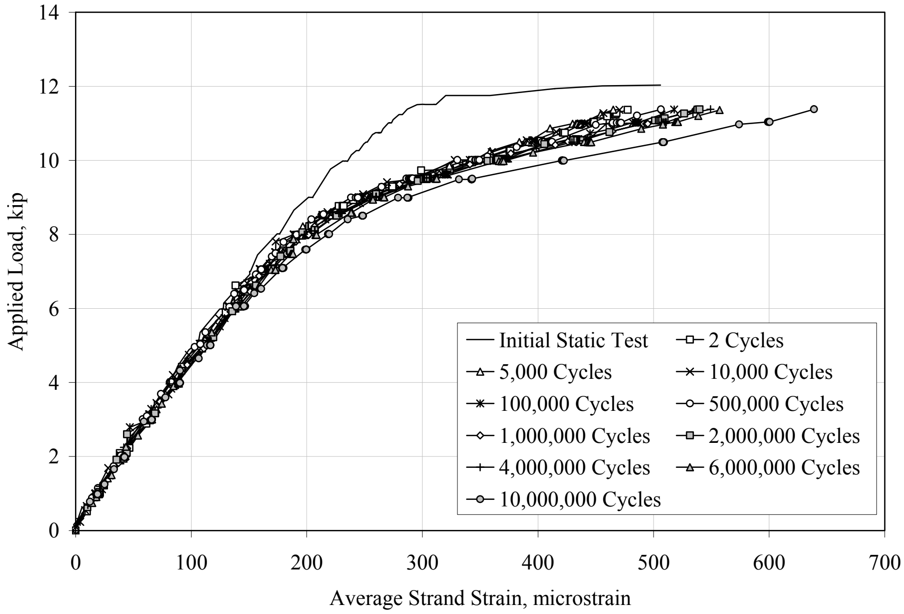

Figure 6.8 Variation of Average Strand Strain during Fatigue Tests of Beam 1 at a Strand Stress Range of 7 ksi

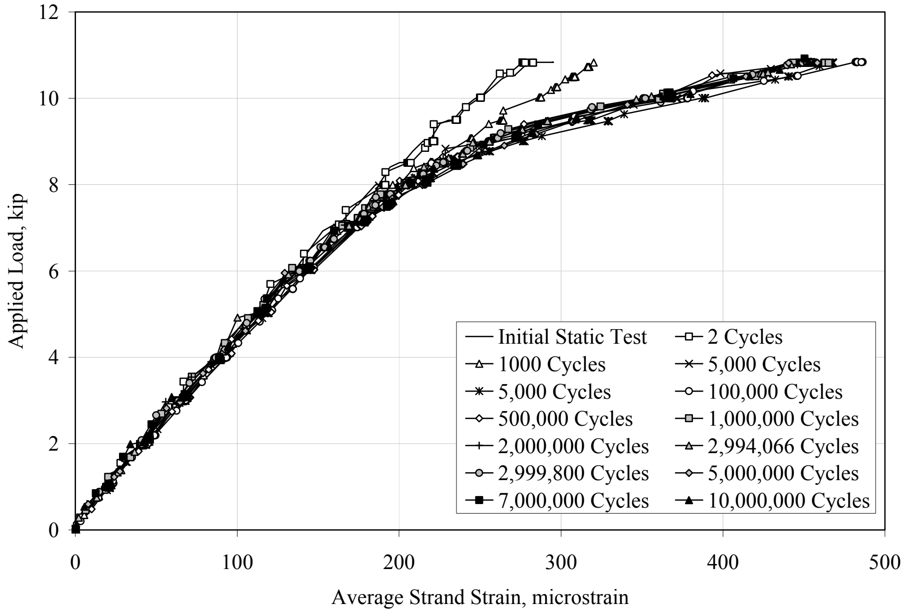

Figure 6.9 Variation of Average Strand Strain during Fatigue Tests of Beam 6 at a Strand Stress Range of 14 ksi

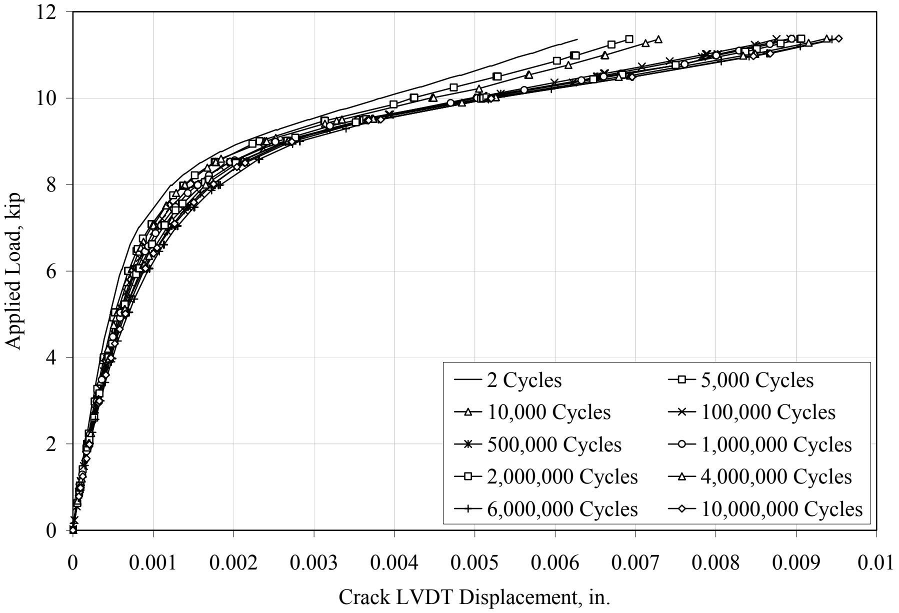

Figure 6.10 Variation of Crack LVDT Displacement during Fatigue Tests of Beam 1 at a Strand Stress Range of 7 ksi

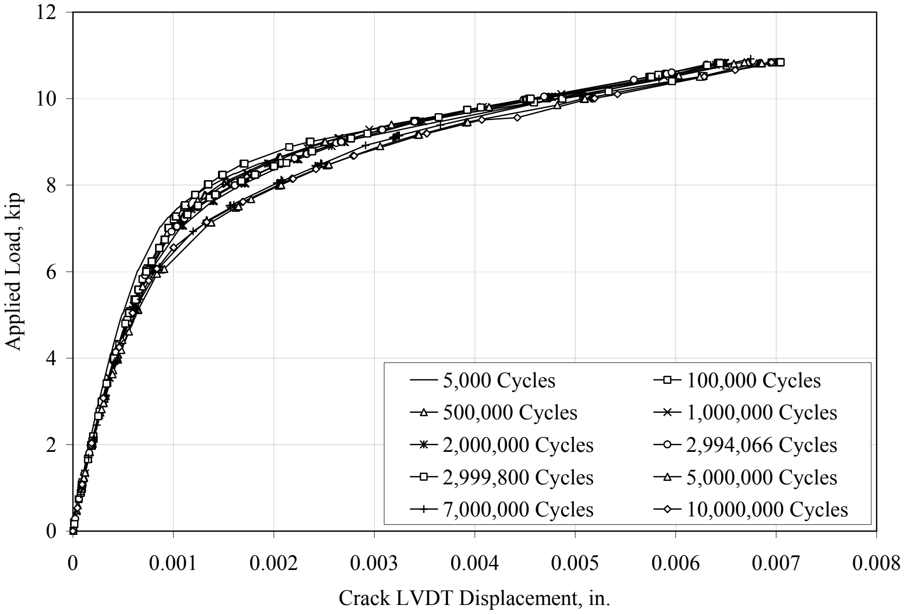

Figure 6.11 Variation of Crack Gage Displacement during Fatigue Tests of Beam 6 at a Strand Stress Range of 14 ksi

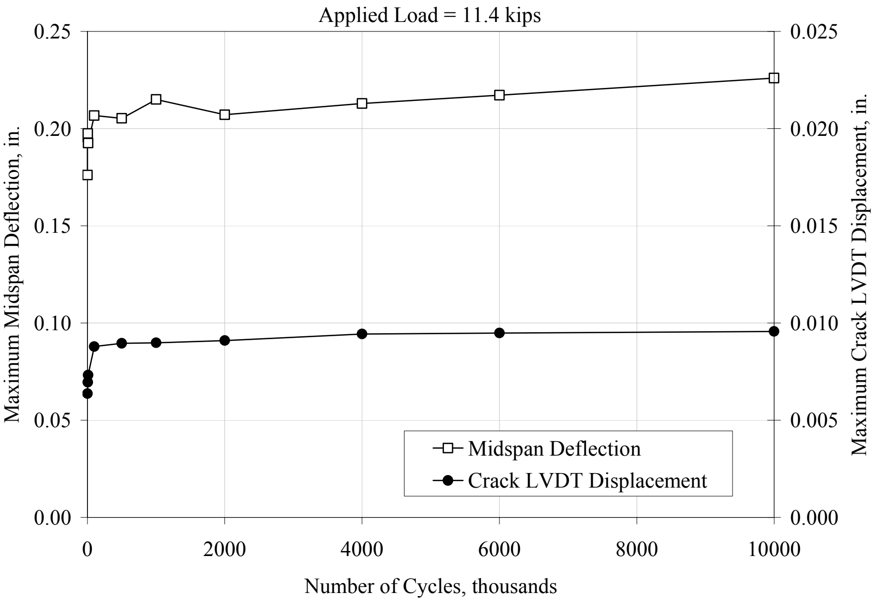

Figure 6.12 Variation of Midspan Deflection and Crack LVDT Displacement with Number of Cycles for Beam 1 at a Strand Stress Range of 7 ksi

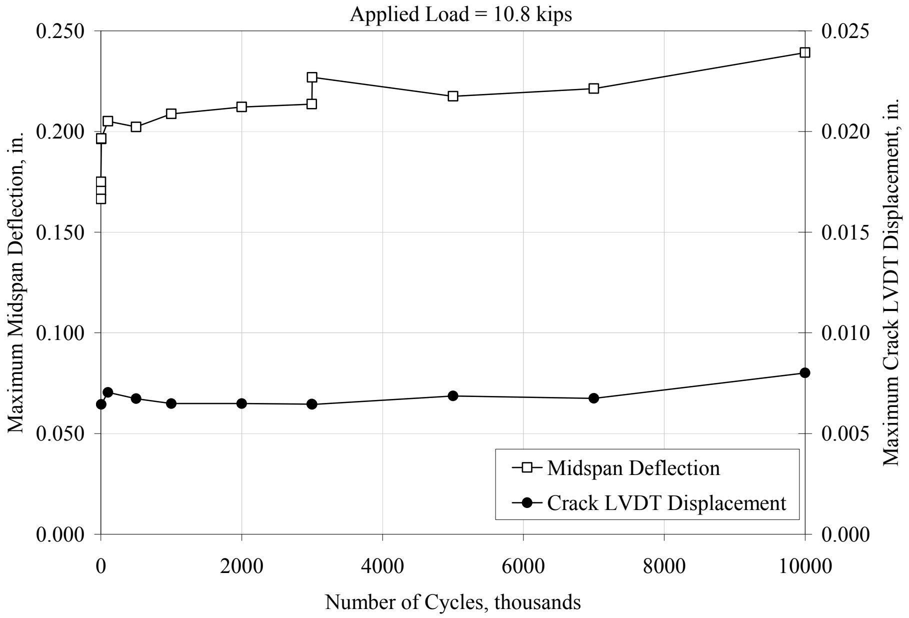

Figure 6.13 Variation of Midspan Deflection and Crack LVDT Displacement with Number of Cycles for Beam 6 at a Strand Stress Range of 14 ksi

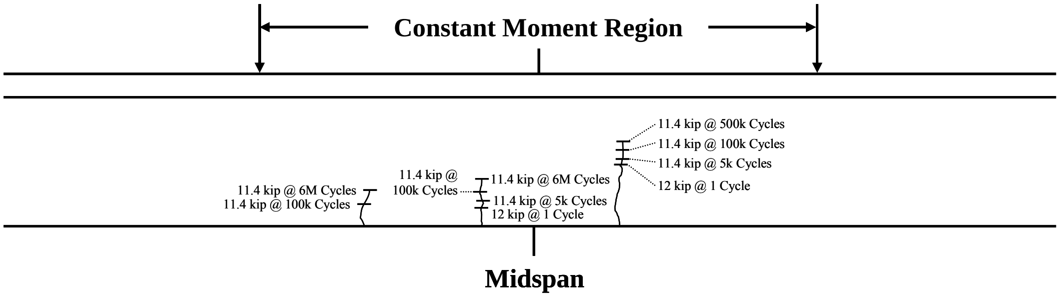

Figure 6.14 Crack Pattern for Beam 1 after 10,000,000 cycles at a Strand Stress Range of 7 ksi

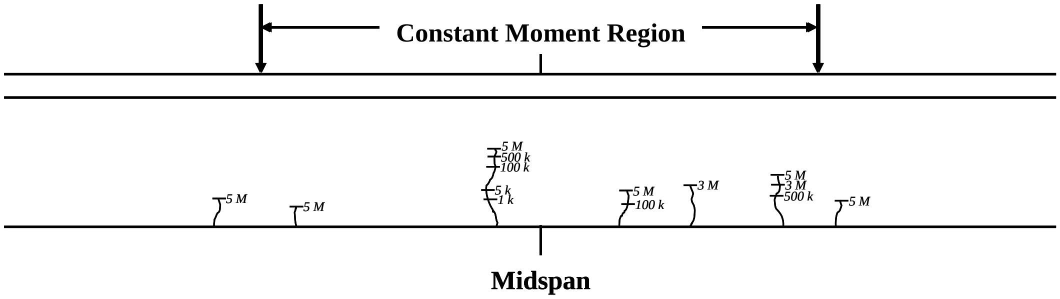

Figure 6.15 Crack Pattern for Beam 6 after 10,000,000 cycles at a Strand Stress Range of 14 ksi

6.1.4 Post Mortem Investigation

No post mortem investigation was conducted after the fatigue tests of Beams 1 and 6 described in this section. After 10 million cycles, no significant change in beam behavior was observed for either beam and therefore, the structural integrity of the beams was maintained so that further tests could be conducted.

6.2 BEHAVIOR OF BEAMS 2 AND 3

Beams 2 and 3 were subjected to fatigue loads corresponding to stress ranges in the strand of approximately 22 and 25 ksi, respectively. Data from these tests are summarized in this section.

6.2.1 Initial Static Tests

During the initial static test, Beam 2 was loaded until flexural cracking occurred. As summarized in Table 6.3, the calculated cracking load was 14.5 kip, which corresponds to a modulus of rupture of $7.5\sqrt{f'_{cm}}$, and the first crack was observed at an applied load of approximately 11 kip.

Unlike Beam 2, Beam 3 did not crack during the initial static test. Therefore, Beam 3 was subjected to 25 loading cycles between a minimum load of 2.3 kip and a maximum load of 11.9 kip. The beam was then subjected to another static test, and flexural cracking was observed at an applied load of approximately 9.5 kip.

The average strand strain during the initial static test for Beam 2 is shown in Figure 6.16. Based on the observed change in stiffness, cracking appears to have initiated at an applied load of approximately 11.0 kip. Similar data for Beam 3 (Figure 6.17) indicate a near linear relationship between applied load and average strand strain. Data were not collected during the fatigue tests; therefore it is not possible to estimate the cracking load from the strain data for Beam 3. The initial crack patterns for Beams 2 and 3 are shown in Figure 6.18 and Figure 6.19, respectively.

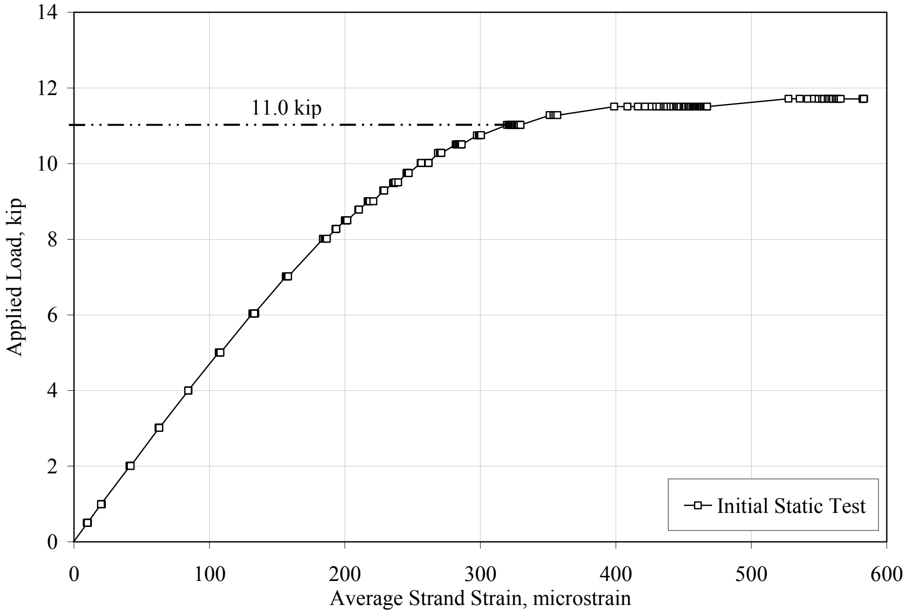

Figure 6.16 Applied Load versus Average Strand Strain during Initial Static Test for Beam 2

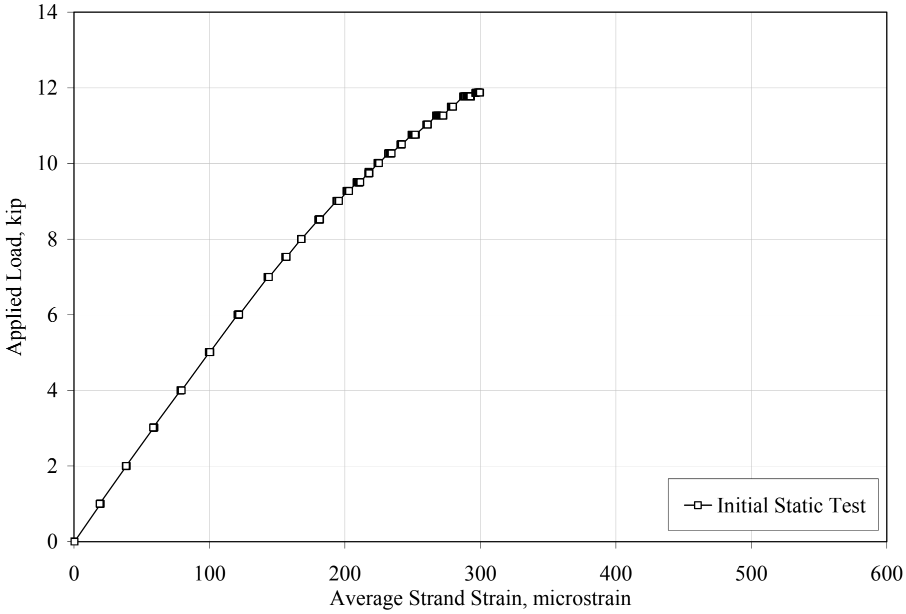

Figure 6.17 Applied Load versus Average Strand Strain during Initial Static Test for Beam 3

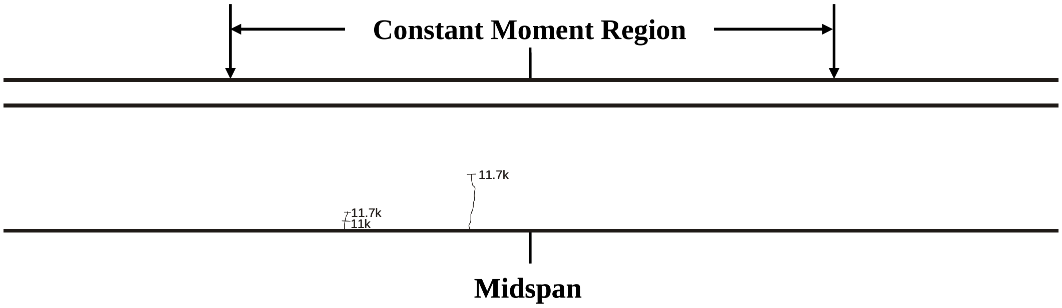

Figure 6.18 Crack Pattern for Beam 2 after Initial Static Test (Heller 2003)

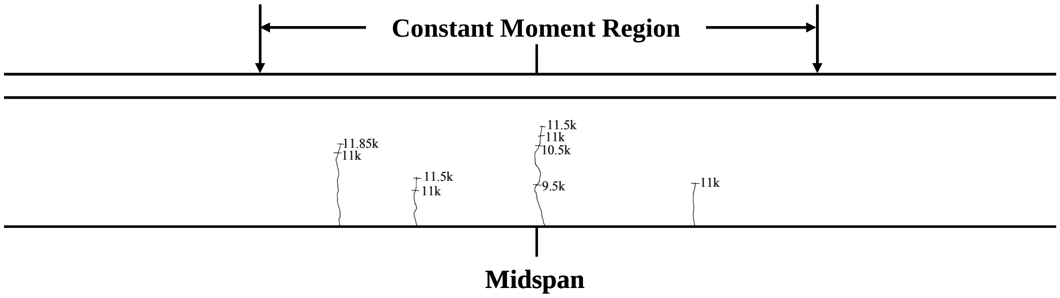

Figure 6.19 Crack Pattern for Beam 3 after 25 Cycles (Heller 2003)

6.2.2 Decompression Load

The calculated decompression loads for Beams 2 and 3 were 9.4 and 9.2 kip, respectively, and the calculations are documented in Appendix M. As with Beams 1 and 6, the decompression load could also be inferred from the measured response of the beams. Results for Beams 2 and 3 are summarized in Table 6.4, and decompression load plots for Beams 2 and 3 are shown in Appendix N.

6.2.3 Fatigue Response

The maximum and minimum applied loads, and calculated stress range and median stress in the strand for Beams 2 and 3 during the fatigue tests are summarized in Table 6.1.

In Figure 6.20, applied load is plotted as a function of the midspan displacement for the seventeen static tests performed on Beam 2. A change in stiffness was observed between the first two static tests as a result of flexural cracking of the concrete. During subsequent static tests, up to and including the test conducted at 5,000,000 cycles, new cracks and the propagation of existing cracks were observed resulting in small changes in stiffness. After 5,000,000 cycles, the maximum midspan displacement was approximately 34% larger than the maximum displacement during the initial static test and 31% larger than the maximum displacement after one fatigue cycle. With each test beyond 5,000,000 cycles, a significant increase in midspan displacement was observed after relatively few fatigue cycles. These changes in stiffness are likely due to the fatigue failure of individual wires in the strand. After approximately 5.8 million cycles, the final static test was performed and the maximum midspan displacement was approximately 200% larger than the maximum displacement during the initial static test and 190% larger than the maximum displacement after one load cycle.

The corresponding midspan displacement data from Beam 3 are shown in Figure 6.21. Similarly to Beam 6, Beam 3 did not crack during the initial static test; therefore, the significant change in stiffness did not occur until later in the loading sequence. Cracks were observed after Beam 3 had experienced approximately 25 fatigue cycles. Similarly to Beam 2, the stiffness of Beam 3 continued to decrease as the number of fatigue cycles increased. After 2,000,000 cycles, the maximum midspan displacement was approximately 36% larger than the maximum displacement during the initial static test and 14% larger than the maximum displacement after 25 fatigue cycles. The response of Beam 3 beyond 2,000,000 cycles was similar to the response of Beam 2 after 5,000,000 cycles. With each static test a significant increase in midspan displacement was observed after relatively few load cycles. After approximately 3.1 million cycles, the final static test was performed and the maximum midspan displacement was approximately 185% larger than the maximum displacement during the initial static test and 140% larger than the maximum displacement after 25 fatigue cycles.

The applied load is plotted as a function of the average strain in the strand in Figure 6.22 and Figure 6.23 for Beams 2 and 3, respectively. For both Beams 2 and 3, the maximum average measured strain in the strand after 100 fatigue cycles was approximately 35% larger than the average measured strain during the initial static test. This increase in strain is a result of flexural cracking. After 5,000 fatigue cycles on Beam 2 and 500 fatigue cycles on Beam 3, a significant number of strain gages on the strand failed. As a result, no reliable strain data were available beyond these static tests.

The applied load is plotted as a function of the width of the most prominent initial crack in Figure 6.24 and Figure 6.25 for Beams 2 and 3, respectively. Similarly to Beams 1 and 6, the trends are not significantly different from those exhibited by the other instruments.

The variations of the midspan deflection and crack width at the maximum applied load during each static test are shown in Figure 6.26 and Figure 6.27 for Beams 2 and 3, respectively. A gradual decrease in stiffness with the number of loading cycles is observed for the first 5,000,000 and 2,000,000 cycles for Beams 2 and 3, respectively. Beyond this point, both beams exhibit significant increases in displacement with relatively few additional fatigue cycles. As mentioned previously, this rapid degradation of the stiffness of the beam is likely due individual wire failures in the strand.

The crack patterns observed in Beams 2 and 3 after 5.8 and 3.1 million cycles at a stress range of approximately 22 ksi are shown in Figure 6.28 and Figure 6.30, respectively. The length of the initial cracks and total number of cracks increased significantly during the fatigue loads for both beams.

The behavior of Beams 2 and 3 did not change appreciably during the first five million cycles in Beam 2 and two million cycles in Beam 3. Beyond this point, a rapid decrease in stiffness with relatively few additional fatigue cycles occurred in both beams.

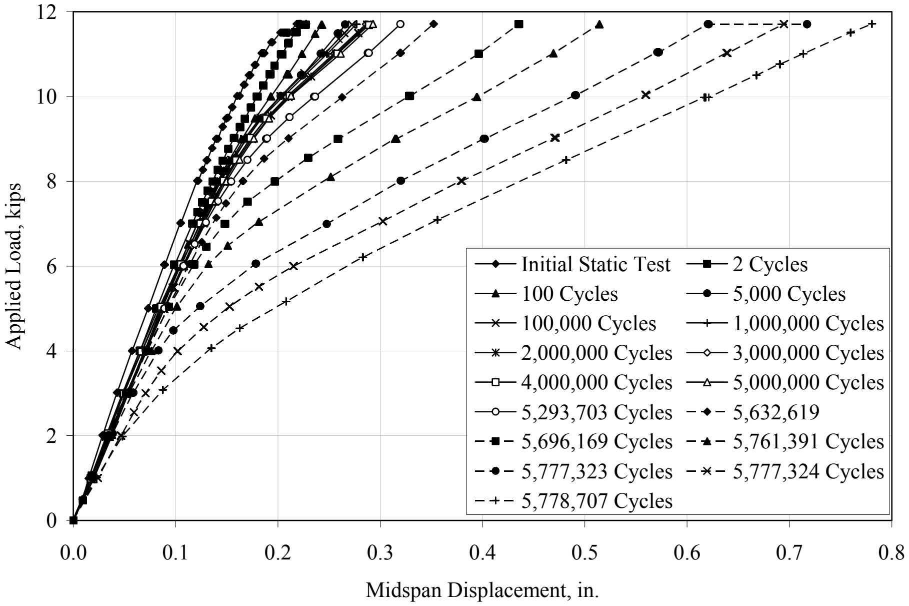

Figure 6.20 Variation of Midspan Deflection during Fatigue Tests of Beam 2 at a Strand Stress Range of 22 ksi (Heller 2003)

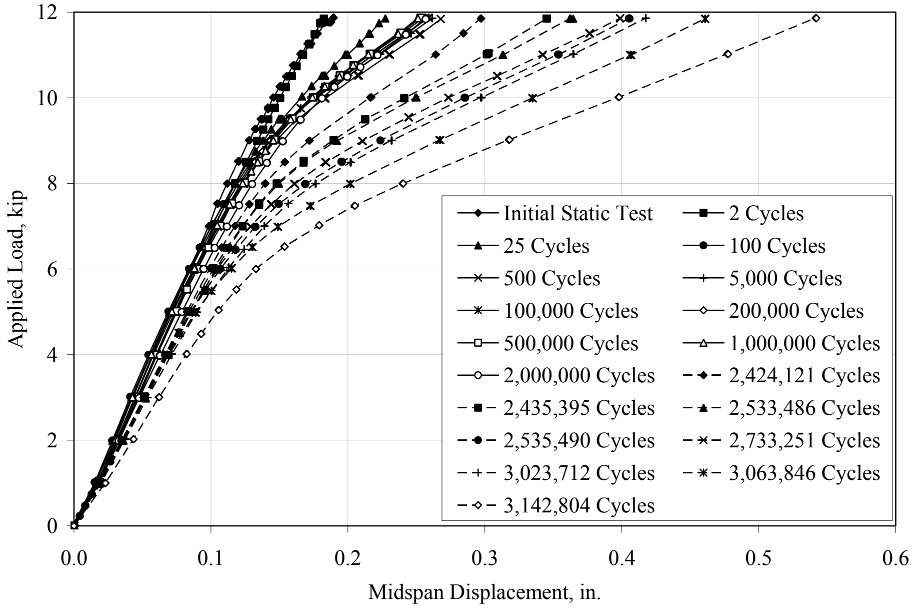

Figure 6.21 Variation of Midspan Deflection during Fatigue Tests of Beam 3 at a Strand Stress Range of 25 ksi (Heller 2003)

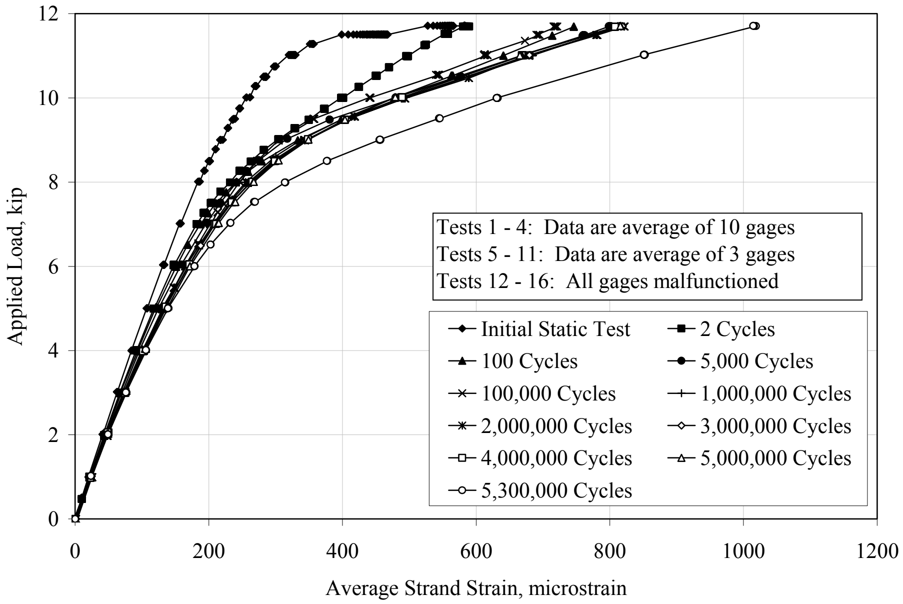

Figure 6.22 Variation of Average Strand Strain during Fatigue Tests of Beam 2 at a Strand Stress Range of 22 ksi (Heller 2003)

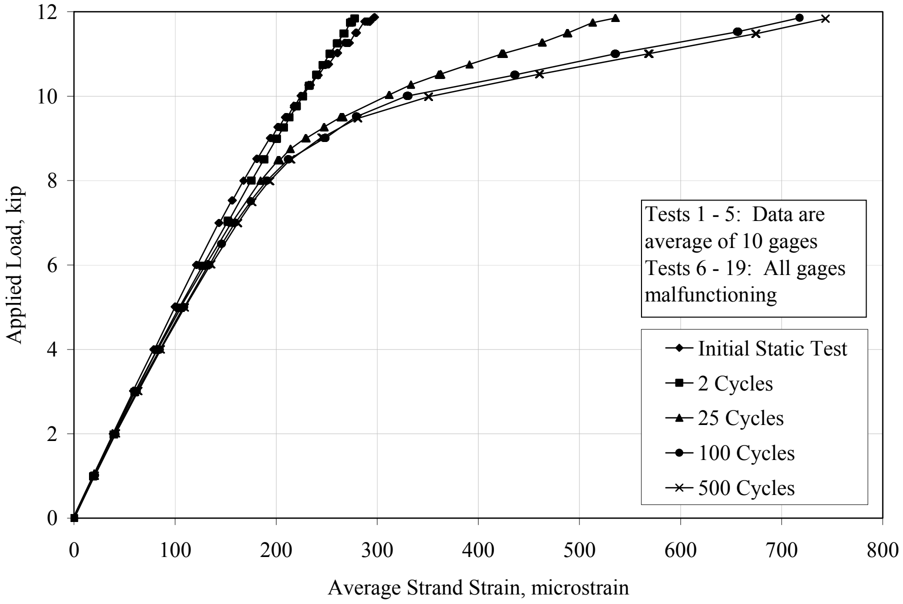

Figure 6.23 Variation of Average Strand Strain during Fatigue Tests of Beam 3 at a Strand Stress Range of 25 ksi (Heller 2003)

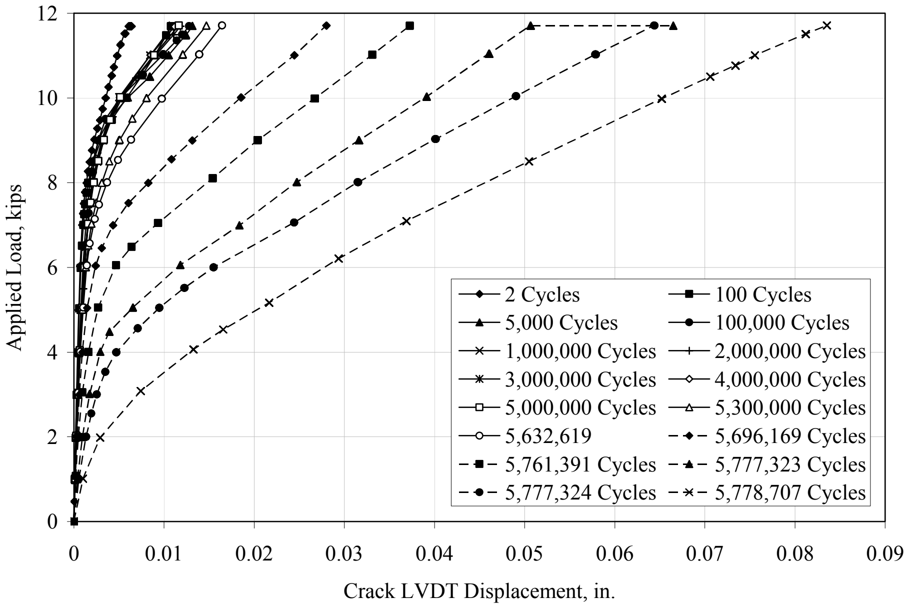

Figure 6.24 Variation of Crack LVDT Displacement during Fatigue Tests of Beam 2 at a Strand Stress Range of 22 ksi (Heller 2003)

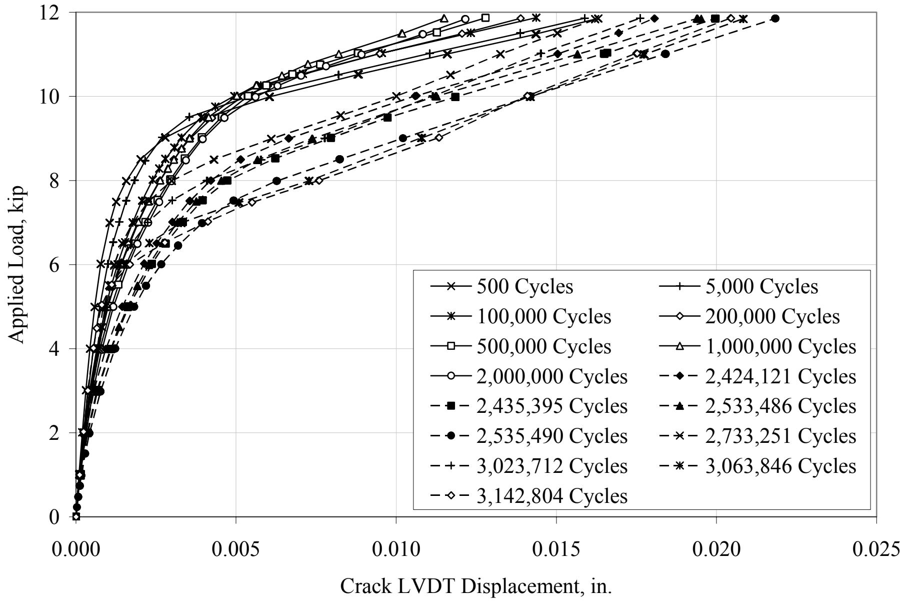

Figure 6.25 Variation of Crack LVDT Displacement during Fatigue Tests of Beam 3 at a Strand Stress Range of 25 ksi (Heller 2003)

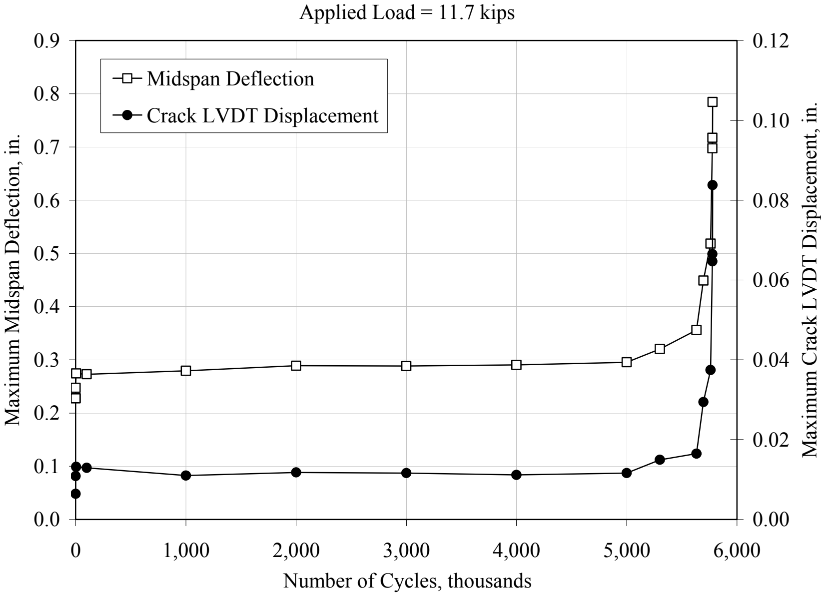

Figure 6.26 Variation of Midspan Deflection and Crack LVDT Displacement with Number of Cycles for Beam 2 at a Strand Stress Range of 22 ksi (Heller 2003)

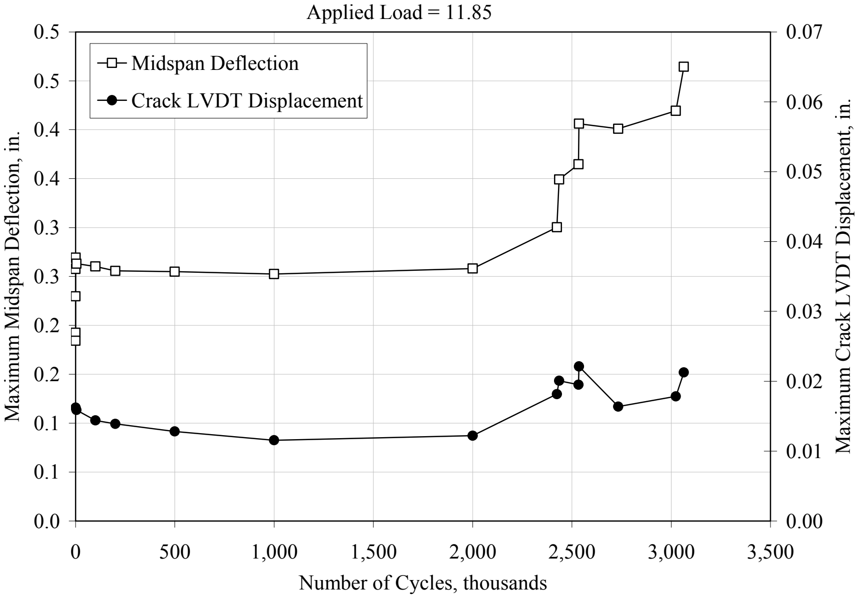

Figure 6.27 Variation of Midspan Deflection and Crack LVDT Displacement with Number of Cycles for Beam 3 at a Strand Stress Range of 25 ksi (Heller 2003)

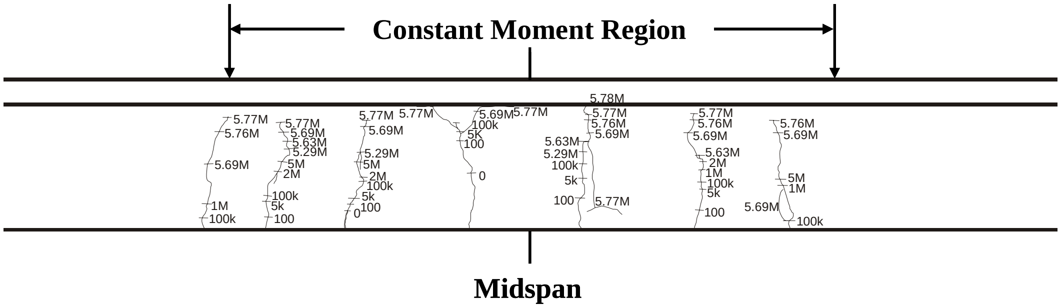

Figure 6.28 Crack Pattern for Beam 2 at End of Fatigue Tests at a Strand Stress Range of 22 ksi (Heller 2003)

Figure 6.29 Composite Photograph of Beam 2 at End of Fatigue Tests at a Strand Stress Range of 22 ksi (Heller 2003)

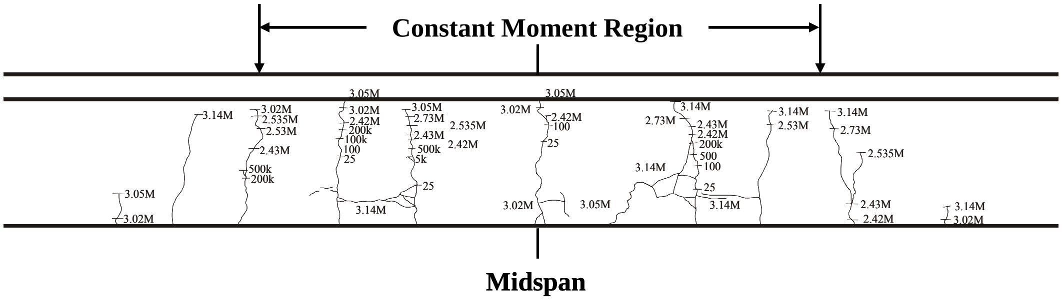

Figure 6.30 Crack Pattern for Beam 3 at End of Fatigue Tests at a Strand Stress Range of 25 ksi (Heller 2003)

Figure 6.31 Composite Photograph of Beam 3 at End of Fatigue Tests at a Strand Stress Range of 25 ksi (Heller 2003)

6.2.4 Post-Mortem Investigation

Upon completion of the fatigue testing, post mortem investigations of Beams 2 and 3 were conducted. For each beam the prestressing strand was exposed between the cracks shown in Figure 6.33 and Figure 6.35. After carefully removing the concrete seven wire breaks were noted in Beam 2 and six wire breaks in Beam 3. The wire failures, which were deemed fatigue failures due to their appearance, were located near cracks within the constant moment region of the beam. Figure 6.32 and Figure 6.34 are photographs of the beams after the concrete was removed and indicate the location of the wire failures. Figure 6.33 and Figure 6.35 illustrate the final crack patterns after the conclusion of fatigue testing and indicate the location of the wire breaks.

It is important to note that the wire failures uncovered in the post-mortem investigations can be correlated to the changes in midspan deflection and crack LVDT displacement noted in Figure 6.26 and Figure 6.27. It can be seen that six significant changes in displacement occurred during the fatigue loading on each beam. Therefore, it is assumed that these changes in displacement are due to the wire failures.

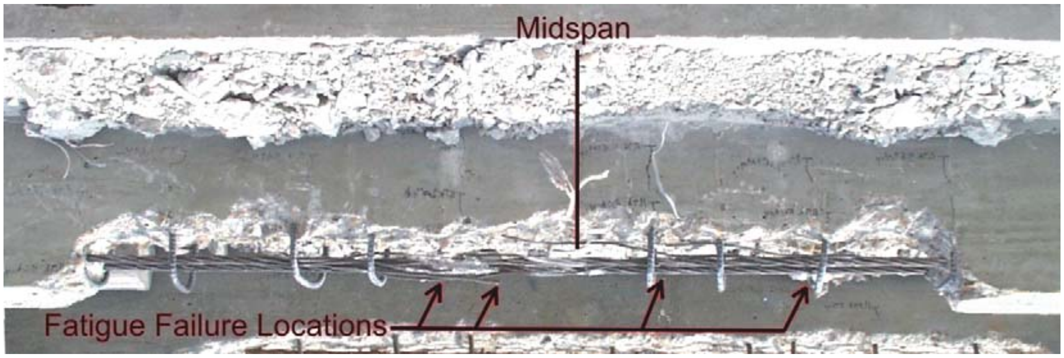

Figure 6.32 Photograph of Beam 2 after Removal of Concrete to Expose Strand (Heller 2003)

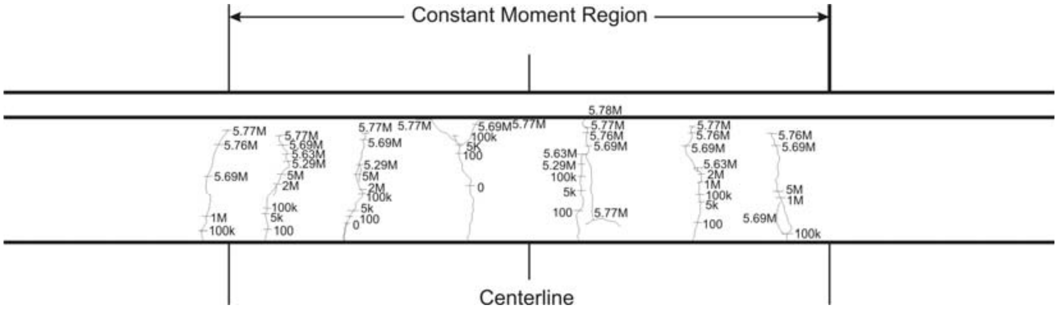

Figure 6.33 Location of Wire Failures in Beam 2 (Heller 2003)

Figure 6.34 Photograph of Beam 3 after Removal of Concrete to Expose Strand (Heller 2003)

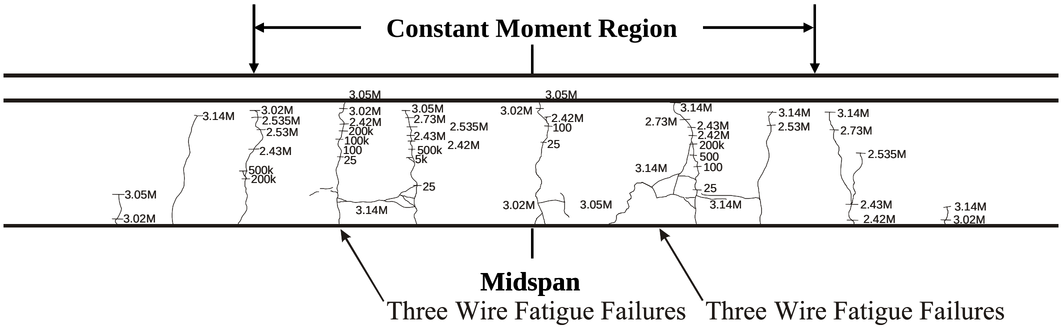

Figure 6.35 Locations of Wire Failures in Beam 3 (Heller 2003)

6.3 BEHAVIOR OF BEAMS 4 AND 5

Beams 4 and 5 were subjected to fatigue loads corresponding to a stress range in the strand of approximately 47 ksi. Data from these tests are summarized in this section.

6.3.1 Initial Static Tests

During the initial static tests, Beams 4 and 5 were loaded until flexural cracking occurred. As summarized in Table 6.3, the calculated cracking load was 13.4 kip for both beams. As noted, these loads correspond to a modulus of rupture of $7.5\sqrt{f'_{cm}}$. The first cracks were observed at an applied load of 13.0 and 11.3 kip for Beams 4 and 5, respectively.

The average strand strain during the initial static test for Beam 4 is shown in Figure 6.36. Based on the observed change in stiffness, cracking appears to have initiated at an applied load of approximately 11.0 kip. Similar data for Beam 5 (Figure 6.37) indicates cracking initiated at an applied load of approximately 10.5 kip. The initial crack patterns for Beams 4 and 5 are shown in Figure 6.38 and Figure 6.39, respectively.

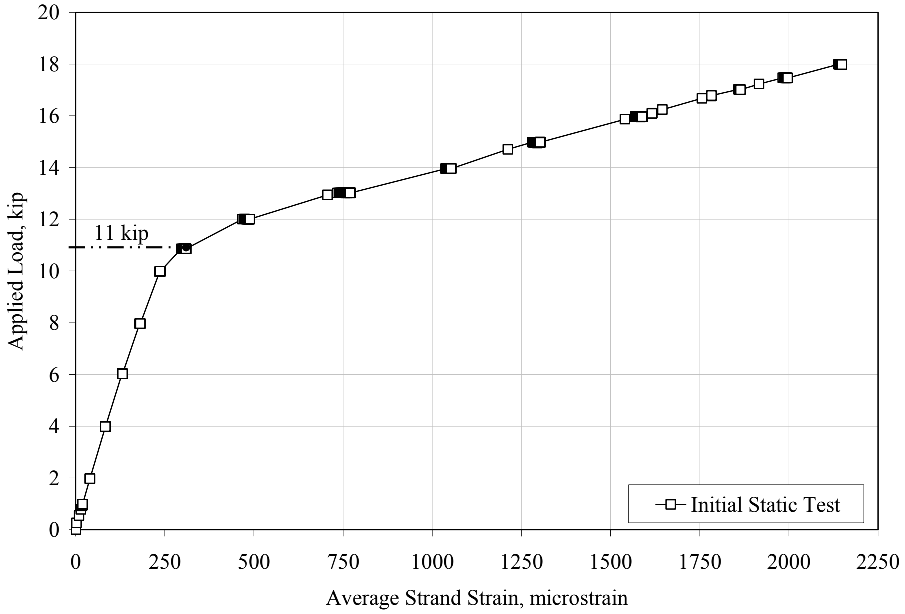

Figure 6.36 Applied Load versus Average Strand Strain during Initial Static Test for Beam 4

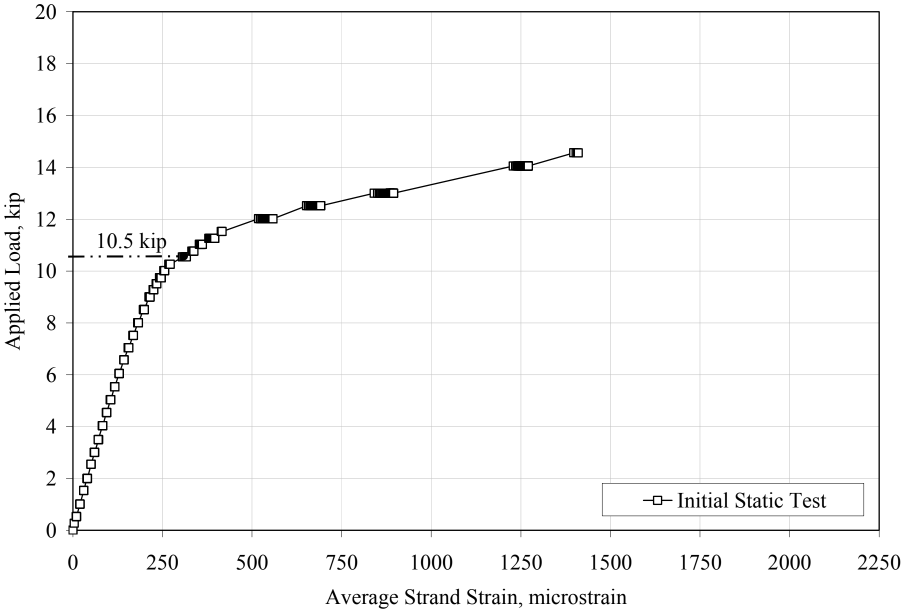

Figure 6.37 Applied Load versus Average Strand Strain during Initial Static Test for Beam 5

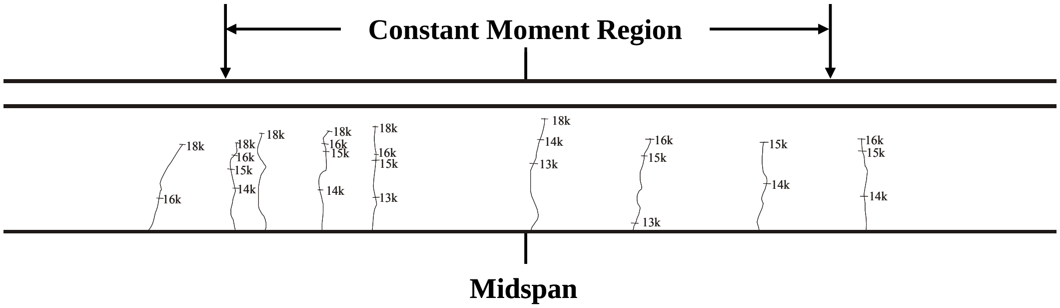

Figure 6.38 Crack Pattern for Beam 4 after Initial Static Test (Heller 2003)

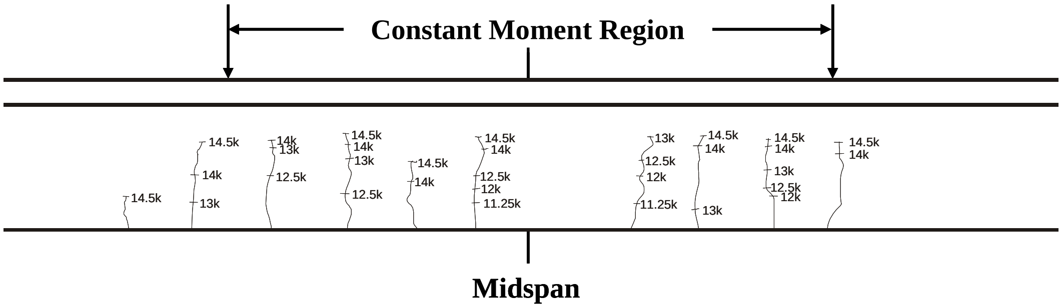

Figure 6.39 Crack Pattern for Beam 5 after Initial Static Test (Heller 2003)

6.3.2 Decompression Load

The calculated decompression load for Beams 4 and 5 was 9.1 kip, and the calculations are documented in Appendix M. As with previous beams, the decompression load could also be inferred from the measured response of the beams. Results for Beams 4 and 5 were similar to the results for all previous beams and are summarized in Table 6.4. Decompression load plots for Beams 4 and 5 are shown in Appendix N.

6.3.3 Fatigue Response

The maximum and minimum applied loads, and calculated stress range and median stress in the strand for Beams 4 and 5 during the fatigue tests are summarized in Table 6.1.

In Figure 6.40, applied load is plotted as a function of the midspan displacement for the ten static tests performed on Beam 4. A change in stiffness was observed between the first two static tests as a result of flexural cracking of the concrete. During subsequent static tests, up to and including the test conducted at 500,000 cycles, results were repeatable and no significant change in beam response was observed. After 500,000 cycles, the maximum midspan displacement was approximately 37% larger than the maximum displacement during the initial static test and 4% larger than the maximum displacement after one fatigue cycle. With each test beyond 500,000 cycles, a significant increase in midspan displacement was observed after relatively few fatigue cycles. These changes in stiffness are likely due to the fatigue failure of individual wires in the strand. After approximately 543,000 cycles, the final static test was performed and the maximum midspan displacement was approximately 95% larger than the maximum displacement during the initial static test and 45% larger than the maximum displacement after one load cycle.

The corresponding data from Beam 5 are shown in Figure 6.41. The observed trends for Beam 5 are similar to those for Beam 4. After 320,000 cycles, the maximum midspan displacement was approximately 14% larger than the maximum displacement during the initial static test and 4% larger than the maximum displacement after one fatigue cycle. After approximately 366,000 cycles, the final static test was performed and the maximum midspan displacement was approximately 70% larger than the maximum displacement during the initial static test and 60% larger than the maximum displacement after one load cycle.

The applied load is plotted as a function of the average strain in the strand in Figure 6.42 and Figure 6.43 for Beams 4 and 5, respectively. For Beam 4, the maximum average measured strain in the strand after one fatigue cycle was approximately 26% larger than the average measured strain during the initial static test. This increase in strain is a result of flexural cracking. After 100,000 fatigue cycles on Beam 4 a significant number of strain gages on the strand failed. As a result, no reliable strain data were available beyond that static test.

For Beam 5, the maximum average measured strain in the strand after one fatigue cycle was approximately 5% larger than the average measured strain during the initial static test. Like Beam 4 this increase in strain is a result of flexural cracking; however, the increase in Beam 5 was significantly less than the increase in Beam 4. This discrepancy is likely due to location of the strain gages relative to the cracks, and length of debonding of the strand adjacent to cracks after the initial static test. Similar to Beam 4, after 100,000 fatigue cycles on Beam 5 a significant number of strain gages on the strand failed. As a result, no reliable strain data was available beyond that static test.

The applied load is plotted as a function of the width of the most prominent initial crack for Beams 4 and 5 in Figure 6.44 and Figure 6.45, respectively. As with beams previously discussed, the trends are not significantly different from those exhibited by the other instruments.

The variations of the midspan deflection and crack width at the maximum applied load during each static test are shown in Figure 6.46 and Figure 6.47 for Beams 4 and 5, respectively. A relatively constant stiffness with the number of loading cycles is observed for the first 500,000 and 300,000 cycles for Beams 4 and 5, respectively. Beyond this point, both beams exhibit significant increases in displacement with relatively few additional fatigue cycles. As mentioned previously, this rapid degradation of the stiffness of the beam is likely due to individual wire failures in the strand.

The crack patterns observed in Beams 2 and 3 after 643,000 and 362,000 cycles with at a strand stress range of approximately 43 ksi are shown in Figure 6.48 and Figure 6.50, respectively. The length of the initial cracks and total number of cracks increased significantly during the fatigue loads for both beams.

The behavior of Beams 4 and 5 did not change appreciably during the first 500,000 cycles in Beam 4 and 320,000 cycles in Beam 5. Beyond this point, a rapid decrease in stiffness with relatively few additional fatigue cycles occurred in both beams.

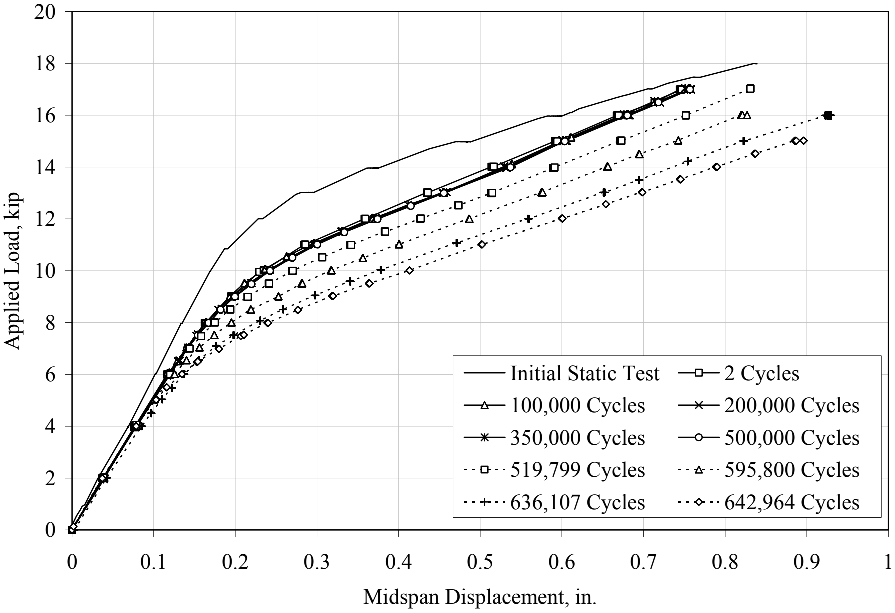

Figure 6.40 Variation of Midspan Deflection during Fatigue Tests of Beam 4 at Strand Stress Range of 47 ksi (Heller 2003)

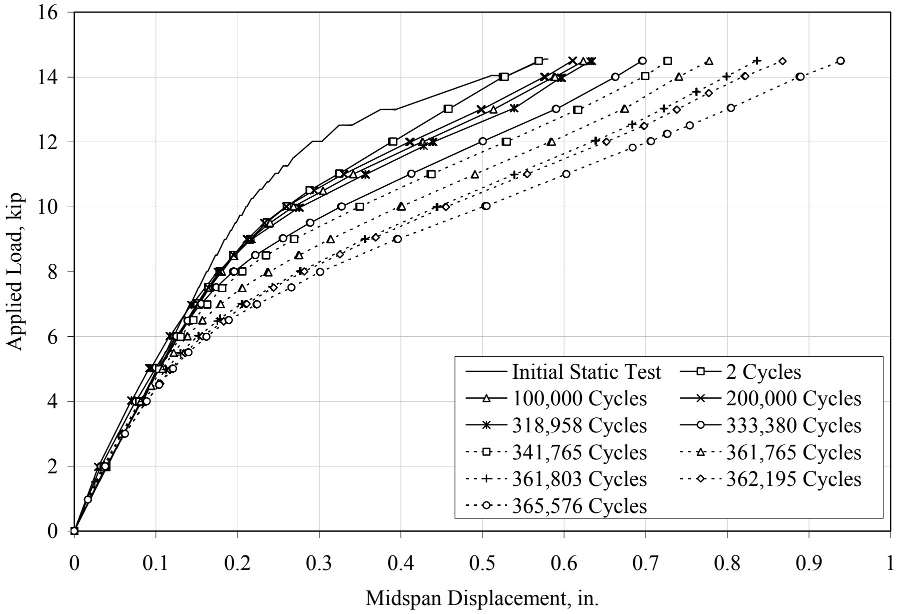

Figure 6.41 Variation of Midspan Displacement during Fatigue Tests of Beam 5 at Strand Stress Range of 47 ksi (Heller 2003)

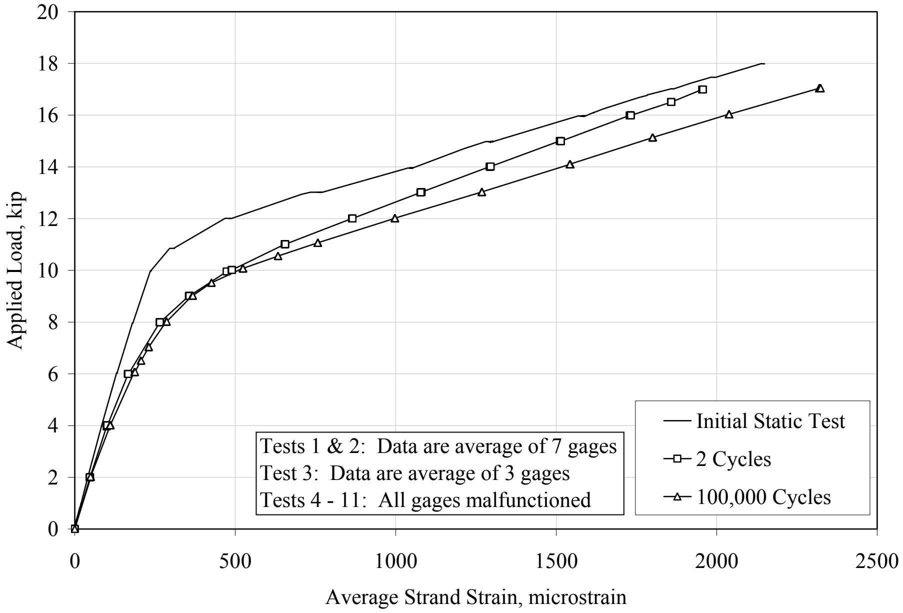

Figure 6.42 Variation of Average Strand Strain during Fatigue Tests of Beam 4 at Strand Stress Range of 47 ksi (Heller 2003)

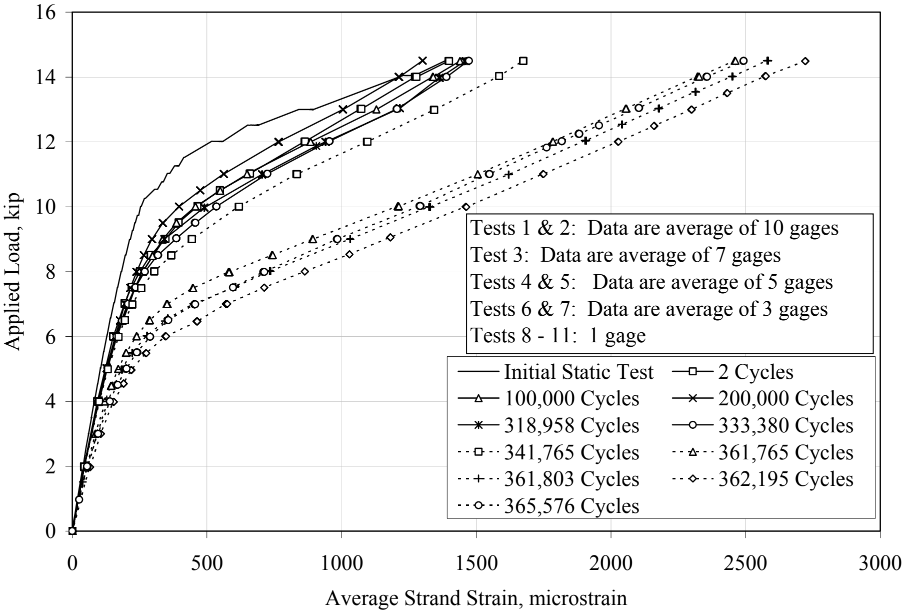

Figure 6.43 Variation of Average Strand Strain during Fatigue Tests of Beam 5 at Strand Stress Range of 47 ksi (Heller 2003)

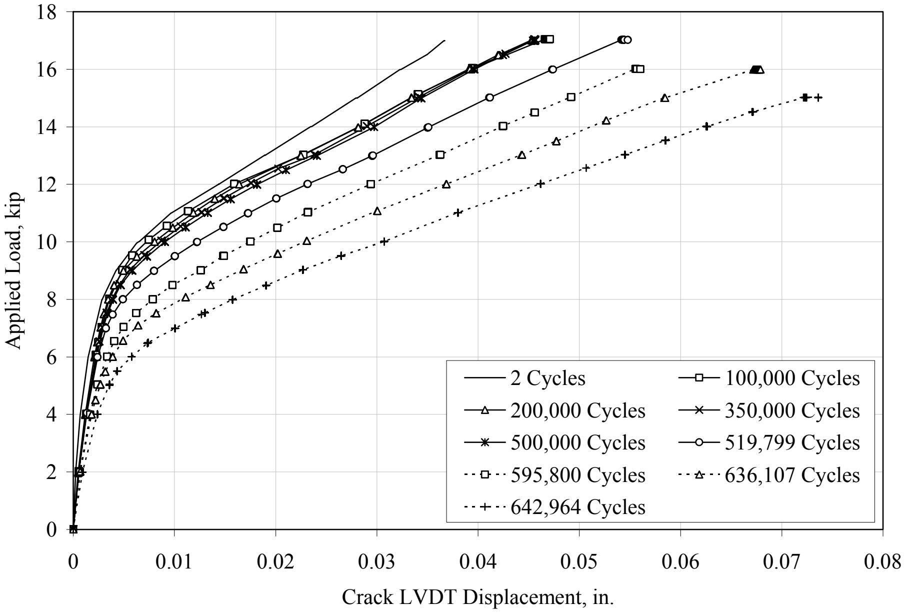

Figure 6.44 Variation of Crack Gage Displacement during Fatigue Tests of Beam 4 at Strand Stress Range of 47 ksi (Heller 2003)

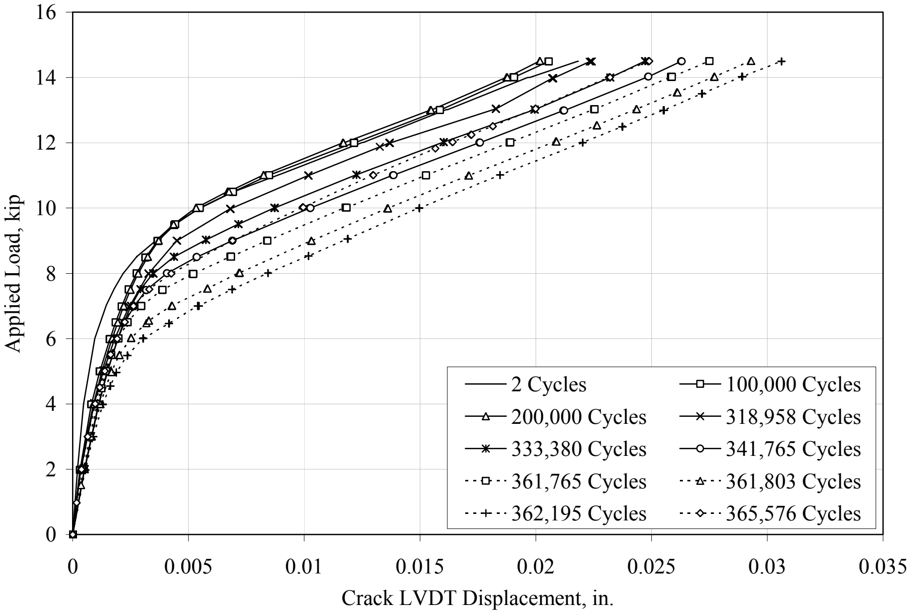

Figure 6.45 Variation of Crack Gage Displacement during Fatigue Tests of Beam 5 at Strand Stress Range of 47 ksi (Heller 2003)

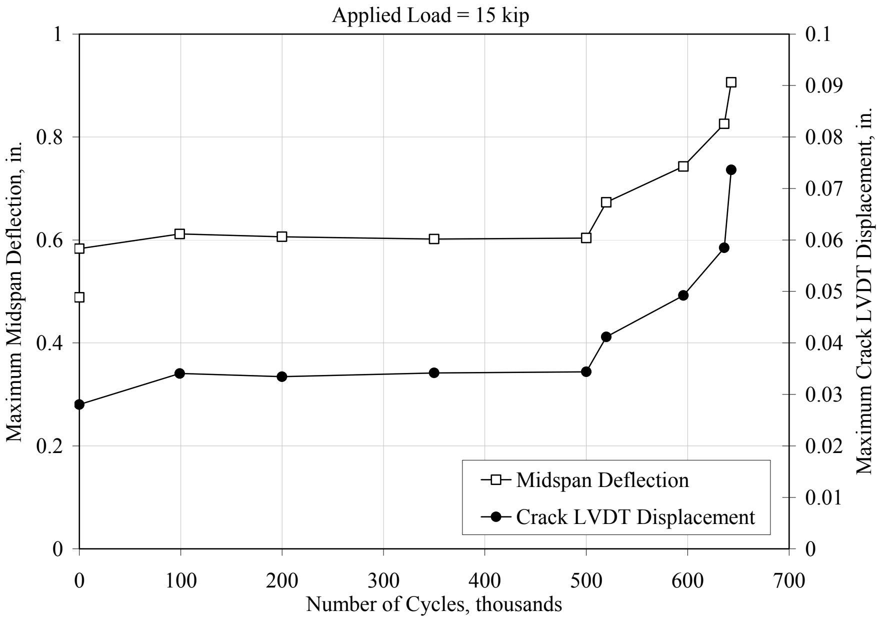

Figure 6.46 Variation of Midspan Deflection and Crack LVDT Displacement with Number of Cycles for Beam 4 at an Strand Stress Range of 47 ksi (Heller 2003)

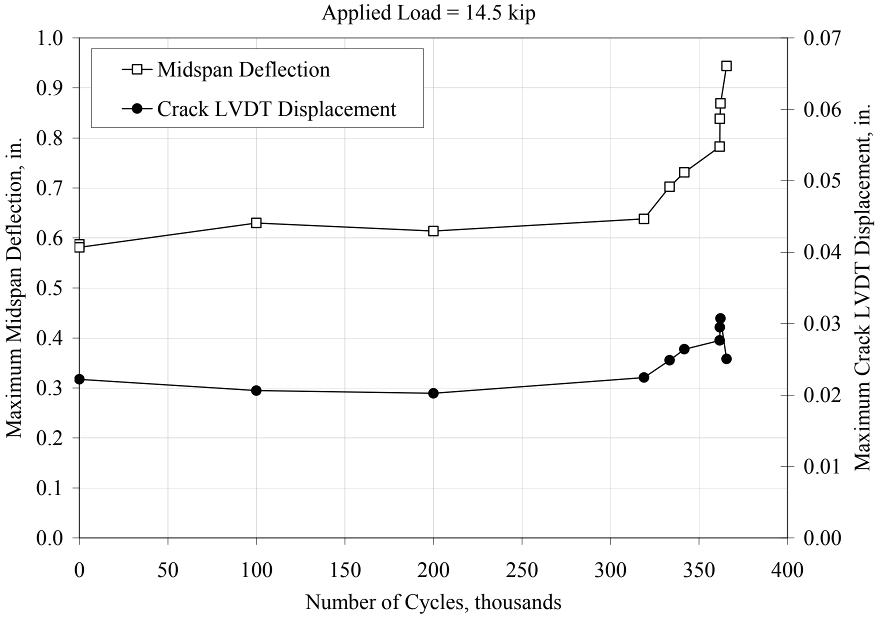

Figure 6.47 Variation of Midspan Deflection and Crack LVDT Displacement with Number of Cycles for Beam 5 Strand Stress Range of 47 ksi (Heller 2003)

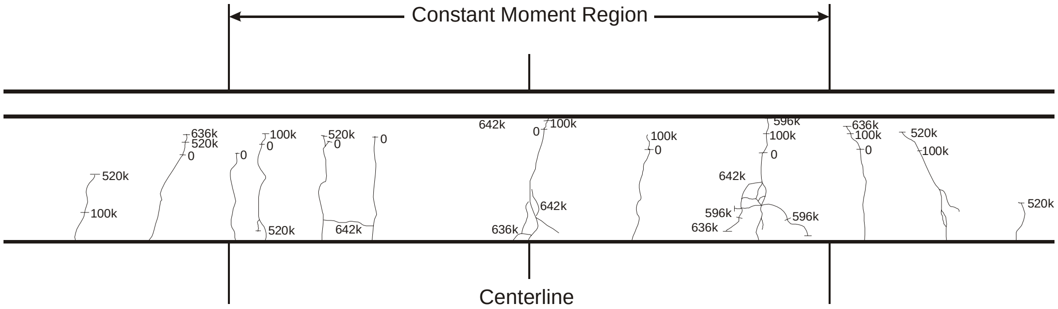

Figure 6.48 Crack Pattern for Beam 4 at End of Fatigue Tests at a Strand Stress Range of 47 ksi (Heller 2003)

Figure 6.49 Composite Photograph of Beam 4 at End of Fatigue Tests at a Strand Stress Range of 47 ksi (Heller 2003)

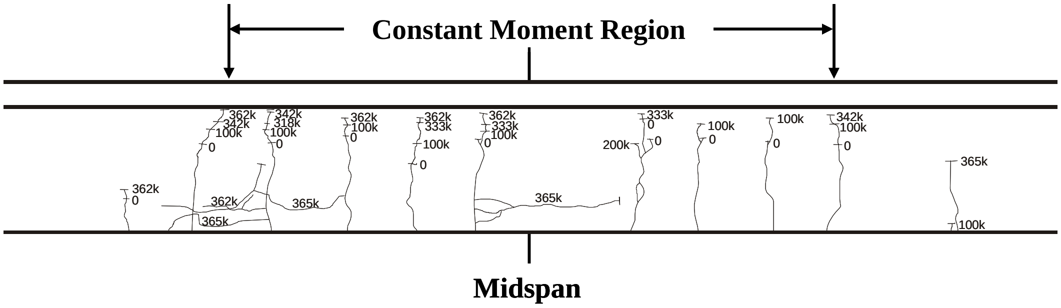

Figure 6.50 Crack Pattern for Beam 5 at End of Fatigue Tests at a Strand Stress Range of 47 ksi (Heller 2003)

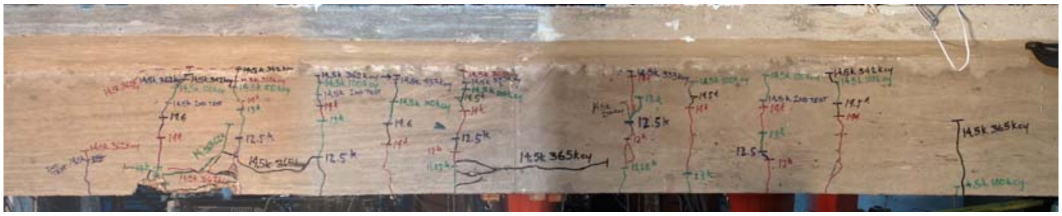

Figure 6.51 Composite Photograph of Beam 5 at End of Fatigue Tests at a Strand Stress Range of 47 ksi (Heller 2003)

6.3.4 Post-Mortem Investigation

Upon completion of the fatigue testing, post mortem investigations of Beams 4 and 5 were conducted. The prestressing strand in each beam was exposed between the cracks shown in Figure 6.53 and Figure 6.55. After carefully removing the concrete, four wire breaks were noted in Beam 4 and seven wire breaks were noted in Beam 5. The wire failures, which were deemed fatigue failures due to their appearance, were located near cracks within the constant moment region of the beam. Figure 6.52 and Figure 6.54 are photographs of the beams after the concrete was removed and indicate the location of the wire failures. Figure 6.53 and Figure 6.55 illustrate the final crack patterns after the conclusion of fatigue testing and indicate the location of the wire breaks.

Similar to Beams 2 and 3, the wire failures uncovered in the post-mortem investigations of Beam 4 can be correlated to the changes in midspan deflection and crack LVDT displacement noted in Figure 6.46. It can be seen that four significant changes in displacement occurred during the fatigue loading; therefore, it is assumed that these changes in displacement are due to the wire failures. For Beam 5, based on Figure 6.47, only six significant changes in displacement occurred, however seven wire failures were observed. This discrepancy is likely due to the failure of two wires during one series of fatigue cycles. Therefore, similar to previous beams, it is assumed that the changes in displacement do correspond to wire failures.

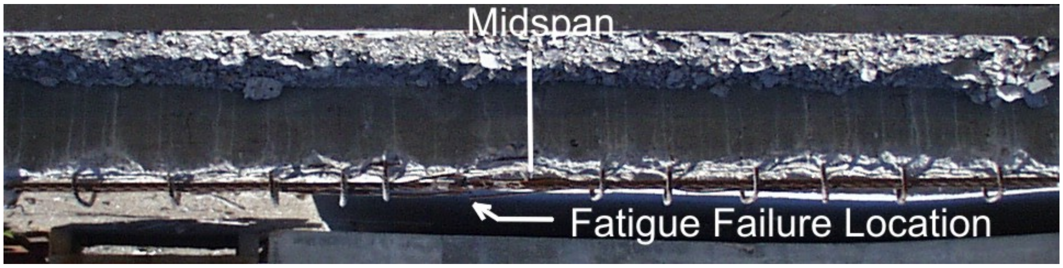

Figure 6.52 Photograph of Beam 4 after Removal of Concrete to Expose Strand (Heller 2003)

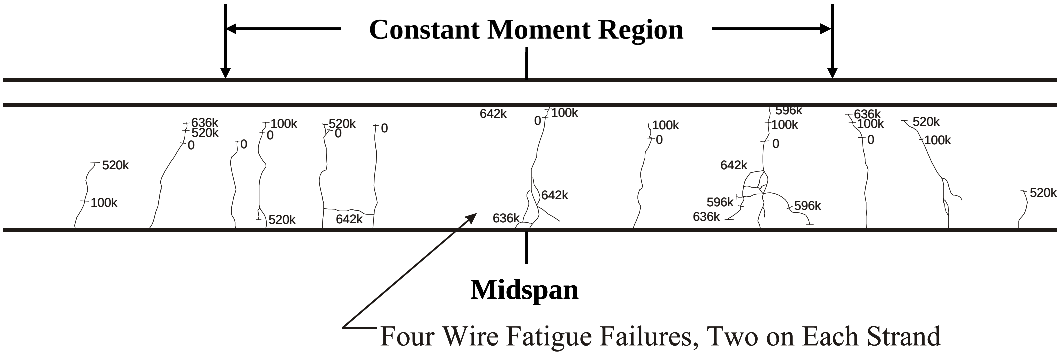

Figure 6.53 Location of Wire Failures in Beam 4 (Heller 2003)

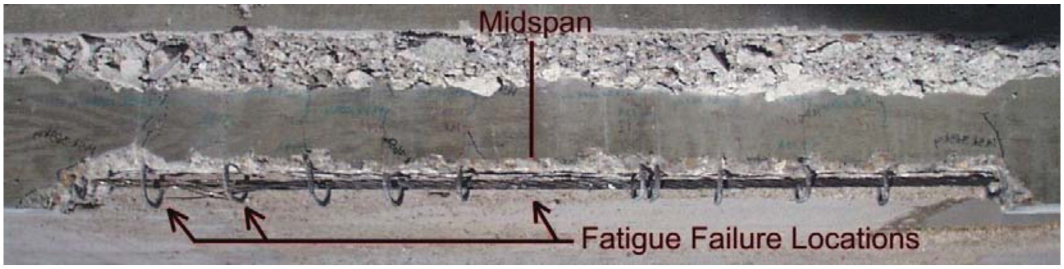

Figure 6.54 Photograph of Beam 5 After Removal of Concrete to Expose Strand (Heller 2003)

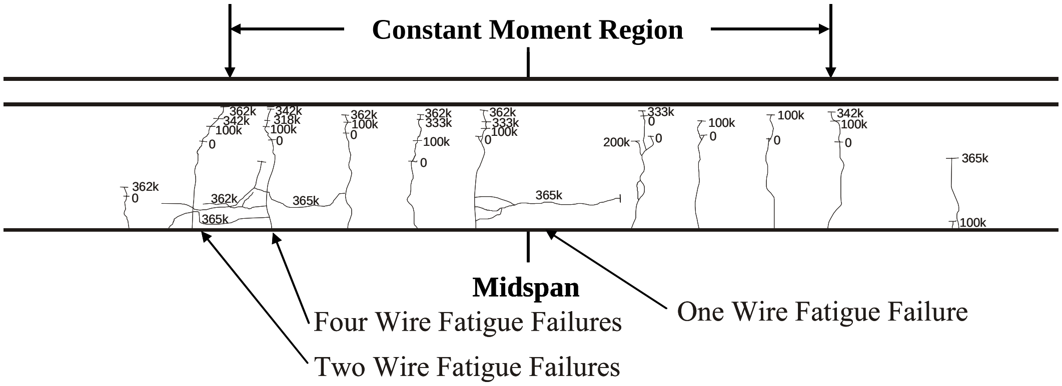

Figure 6.55 Location of Wire Failures in Beam 5 (Heller 2003)

6.4 BEHAVIOR OF BEAMS 1A AND 6A

After surviving 10 million fatigue cycles at a stress range of approximately 7 and 14 ksi, respectively, Beams 1 and 6 were subjected to additional fatigue cycles at loads corresponding to a stress range in the strand of approximately 43 ksi. Beams 1 and 6 will be designated as Beams 1A and 6A for this series of fatigue tests. Data from these tests are summarized in this section.

6.4.1 Baseline Static Tests

In order to evaluate the change in beam response during this series of fatigue cycles, a baseline static test was performed for both Beams 1A and 6A.

Beam 1A was loaded from zero to 14.5 and Beam 6A was loaded from zero to 14.3 kip. The crack patterns for Beams 1 and 6 after the baseline static test are shown in Figure 6.56 and Figure 6.57, respectively.

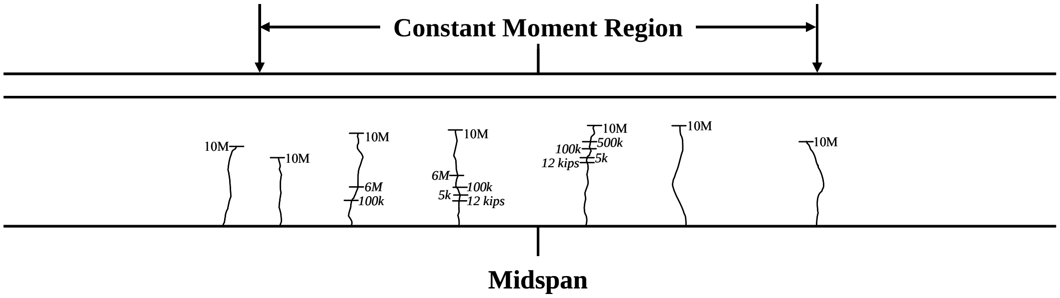

Figure 6.56 Crack Pattern for Beam 1A after Baseline Static Test

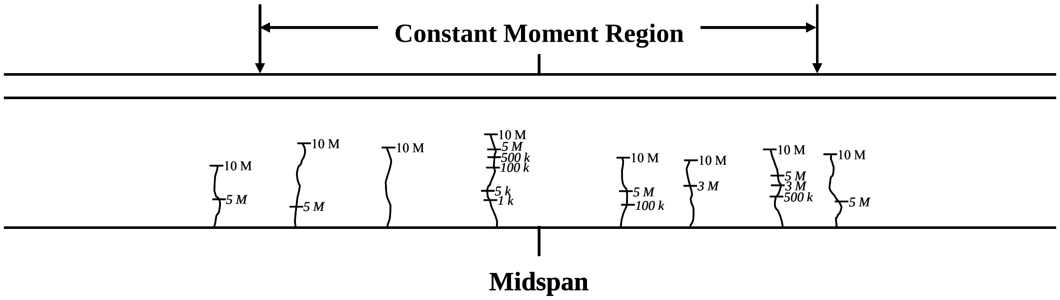

Figure 6.57 Crack Pattern for Beam 6A after Baseline Static Test

6.4.2 Fatigue Response

The maximum and minimum loads applied to Beams 1A and 6A during this series of fatigue cycles are summarized in Table 6.1. The calculated stress range and median stress in the strand are also listed.

Applied load is plotted as a function of the midspan displacement for all the static tests performed in this series of fatigue cycles in Figure 6.58 and Figure 6.59 for Beams 1A and 6A, respectively. A change in stiffness was observed between the first two static tests. Although the beams were initially cracked, additional flexural cracking occurred due to the higher loads applied during this series of tests, so this change was expected. The stiffness of Beam 1A remained relatively constant as the number of fatigue cycles increased. Unlike Beam 1A, the stiffness of Beam 6A decreased as the number of fatigue cycles increased. After 110,000 cycles, the maximum midspan displacement under the maximum applied fatigue load was approximately 64% larger than the maximum displacement during the initial static test.

Applied load is plotted as a function of the average strain in the strand in Figure 6.60 and Figure 6.61 for Beams 1 and 6, respectively. Applied load is plotted as a function of the width of the most prominent initial crack in Figure 6.62 and Figure 6.63 for Beams 1A and 6A, respectively. The trends observed in the strand strain and crack width data for each beam were similar to the trends observed from the corresponding midspan displacement data.

The variations of the midspan displacement and crack width at the maximum applied load during each static test are shown in Figure 6.64 and Figure 6.65 for Beams 1A and 6A, respectively. A relatively constant stiffness is observed in Beam 1A, while a steady decrease in stiffness is observed for Beam 6A.

The crack pattern observed in Beam 1A after 3.4 million cycles at the increased range of strand stress is shown in Figure 6.66. For Beam 1, small crack extensions were observed beyond the baseline static test. The crack pattern observed in Beam 6A after 110,000 cycles at the increased range of strand stress is shown in Figure 6.67. Unlike Beam 1A, several new cracks formed during the fatigue loading of Beam 6A. In addition to the new cracks, extensions of the cracks present after the baseline static test were observed.

The behavior of Beam 6A at a range of strand stress of 44 ksi changed significantly during the fatigue cycles. After only 20,000 cycles a significant change in stiffness was observed during each static test. Unlike Beam 6A, the behavior of Beam 1A did not change appreciably during this series of fatigue cycles.

Beam 6A was subjected to additional fatigue cycles after 10.11 million cycles; however, no additional static tests were conducted. A mechanical failure of the displacement limit switch used to terminate the fatigue loading when a significant change in midspan displacement occurred, allowed the beam to be subjected to approximately 50,000 additional cycles even though significant changes in stiffness had occurred. During these loading cycles, numerous fatigue wire failures occurred and the beam ultimately failed in flexure under the applied load. Figure 6.68 is a photograph of Beam 6A after failure and indicates the location of all the wire fatigue failures.

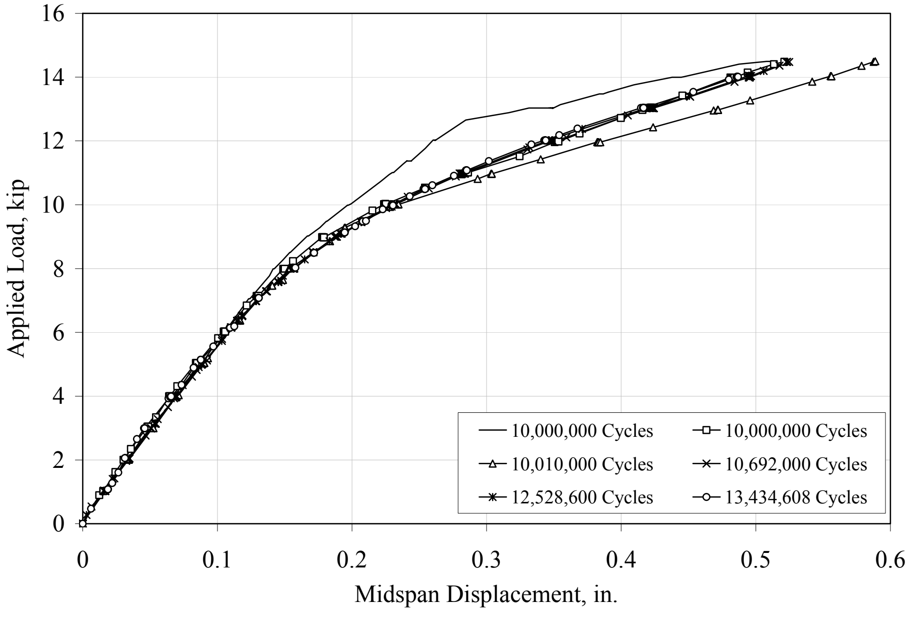

Figure 6.58 Variation of Midspan Displacement during Fatigue Tests of Beam 1A at a Strand Stress Range of 41 ksi

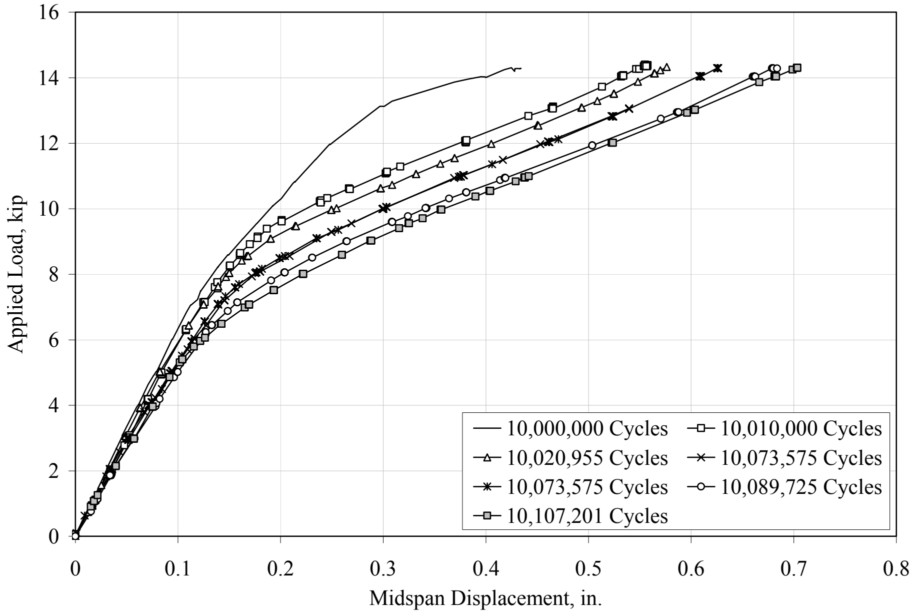

Figure 6.59 Variation of Midspan Displacement during Fatigue Tests of Beam 6A at a Strand Stress Range of 45 ksi

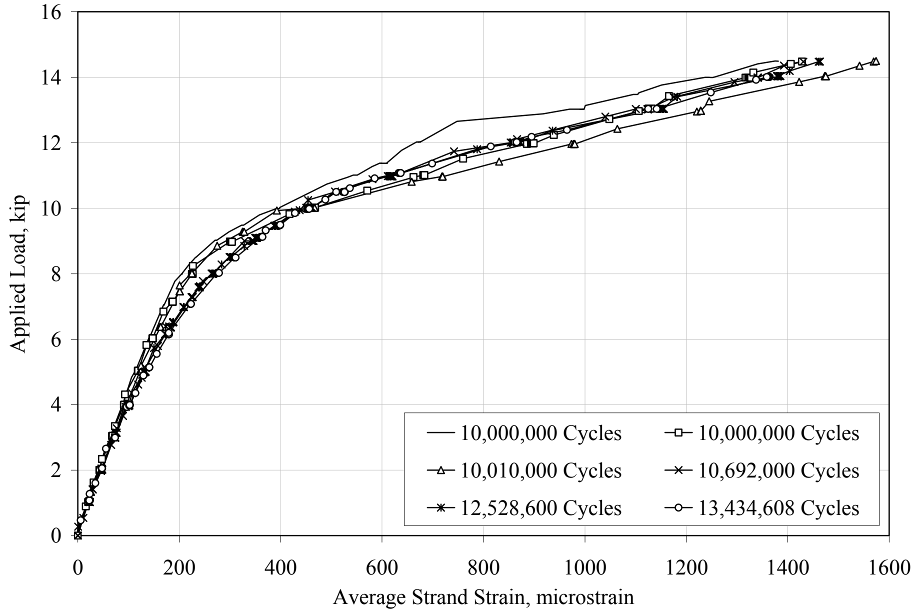

Figure 6.60 Variation of Average Strand Strain during Fatigue Tests of Beam 1A at a Strand Stress Range of 41 ksi

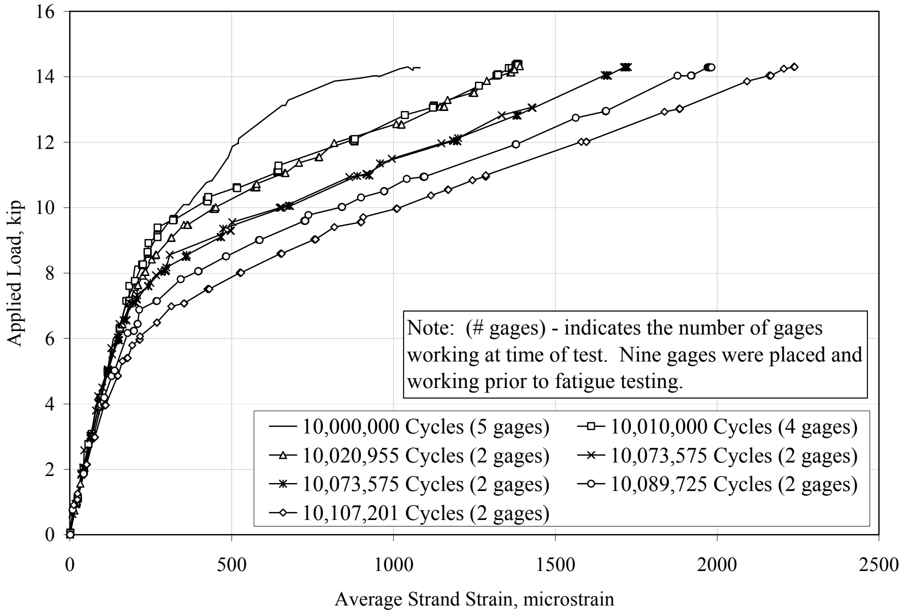

Figure 6.61 Variation of Average Strand Strain during Fatigue Tests of Beam 6A at a Strand Stress Range of 45 ksi

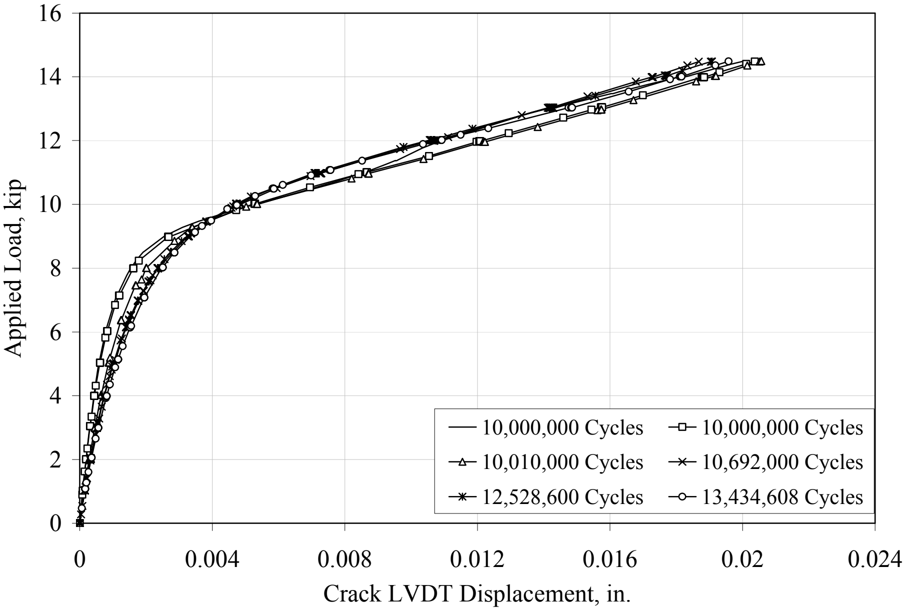

Figure 6.62 Variation of Crack LVDT Displacement during Fatigue Tests of Beam 1A at a Strand Stress Range of 41 ksi

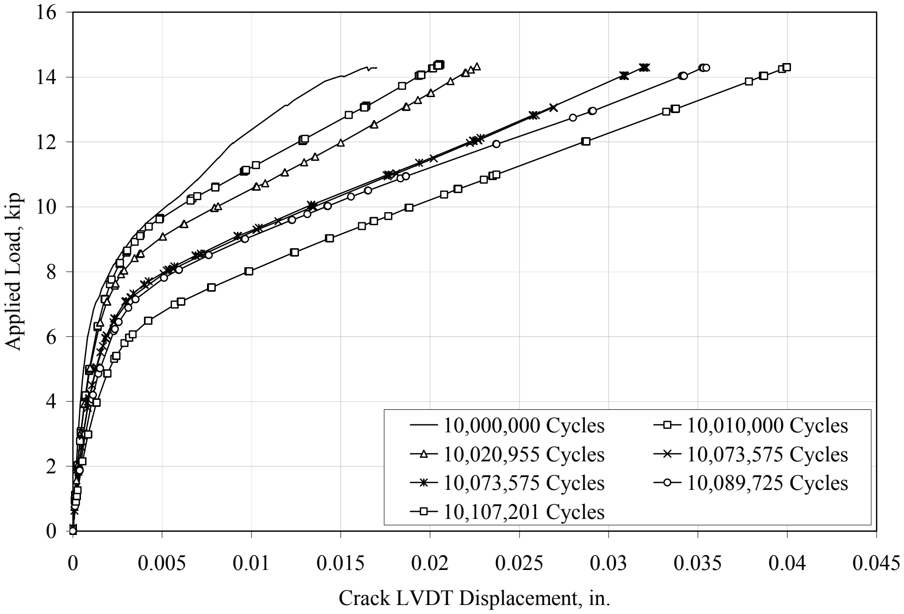

Figure 6.63 Variation of Crack LVDT Displacement during Fatigue Tests of Beam 6A at a Strand Stress Range of 45 ksi

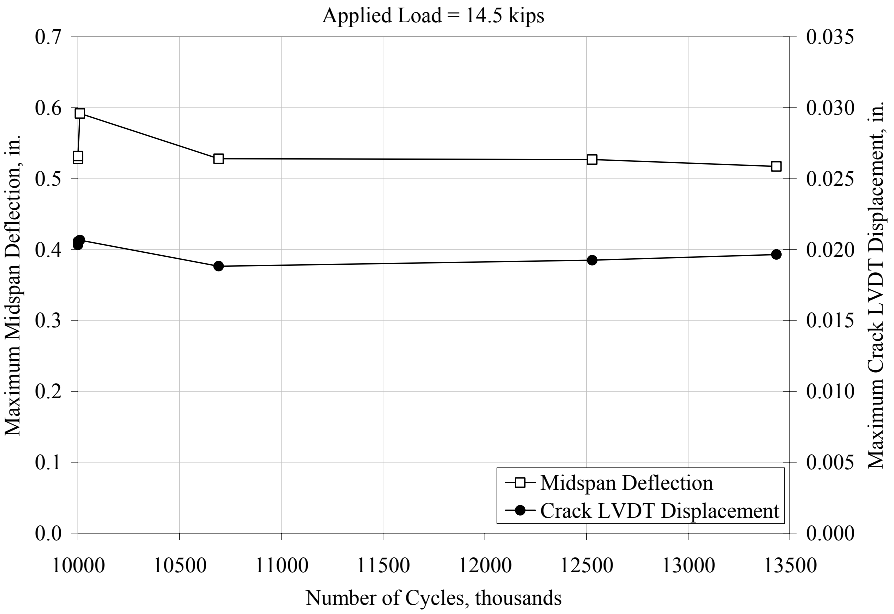

Figure 6.64 Variation of Midspan Deflection and Crack LVDT Displacement with Number of Cycles for Beam 1A at a Strand Stress Range of 41 ksi

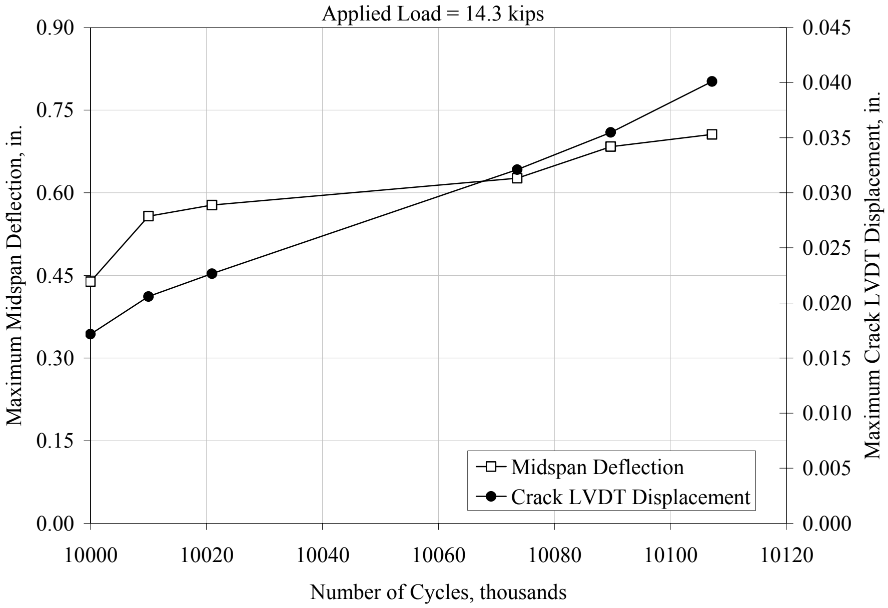

Figure 6.65 Variation of Midspan Deflection and Crack LVDT Displacement with Number of Cycles for Beam 6A at a Strand Stress Range of 45 ksi

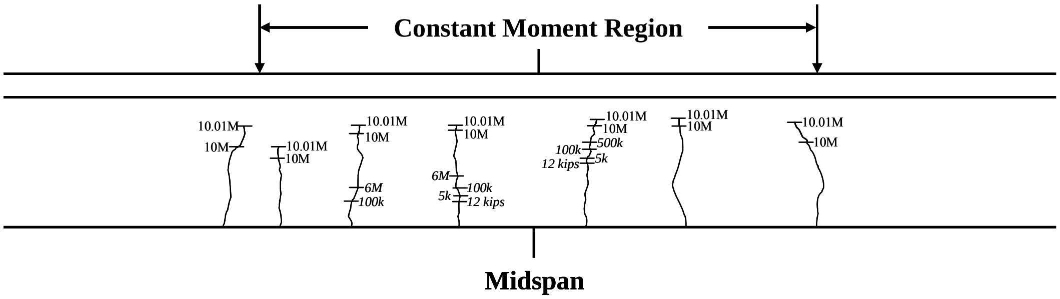

Figure 6.66 Crack Pattern for Beam 1A at End of Fatigue Tests at a Strand Stress Range of 41 ksi

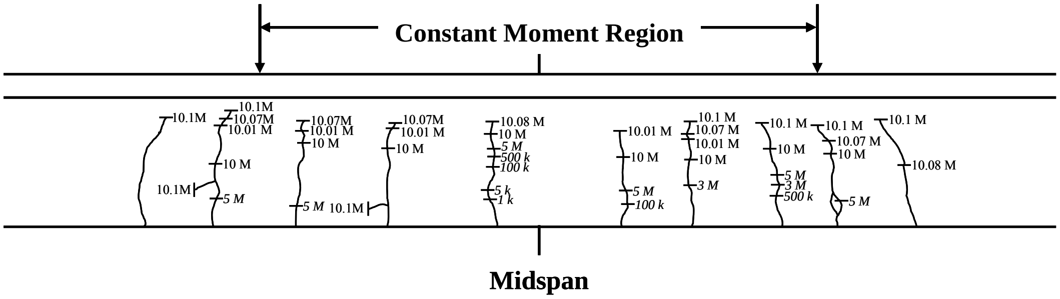

Figure 6.67 Crack Pattern for Beam 6A after Final Static Test at a Strand Stress Range of 45 ksi

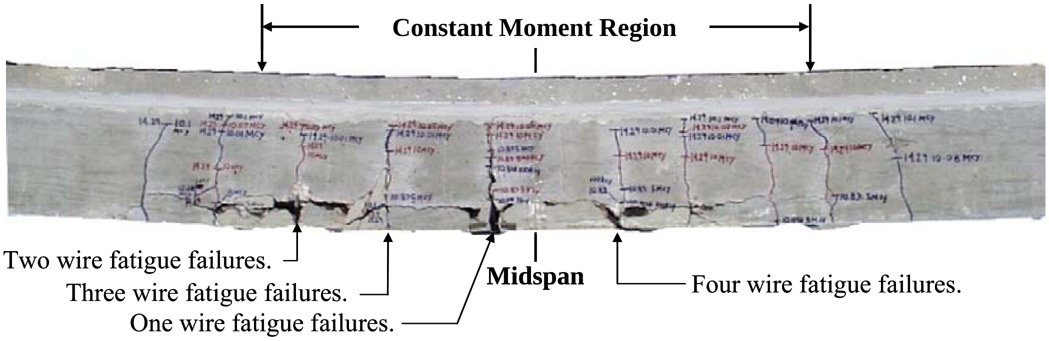

Figure 6.68 Photograph of Beam 6A after Failure

6.4.3 Post Mortem Investigation

No post mortem investigation was conducted on Beam 1A after the fatigue tests at a stress range in the strand of 41 ksi. At the end of 3.5 million cycles at a stress range in the strand of 41 ksi, no significant change in beam behavior was realized, and therefore, the structural integrity of the beam was maintained so that further testing could be conducted.

A post mortem investigation was conducted on Beam 6A after the fatigue tests at a stress range in the strand of 45 ksi. Figure 6.69 illustrates the final crack pattern for Beam 6A prior to failure and indicates the location and number of the wire fatigue failures. Each location, designated as A, B, C and D in Figure 6.69, correspond to the photographs of the wire failures shown in Figure 6.70 and in additional photos included in Appendix N. Figure 6.70 is a photograph of location D and is typical of wire fatigue failures in Beam 6A.

Figure 6.71 is a photo of Beam 6A that shows a wire that failed due to tension rather than fatigue. Two wires failed due to tension; therefore, it was concluded that the ultimate failure of the beam was a flexural failure.

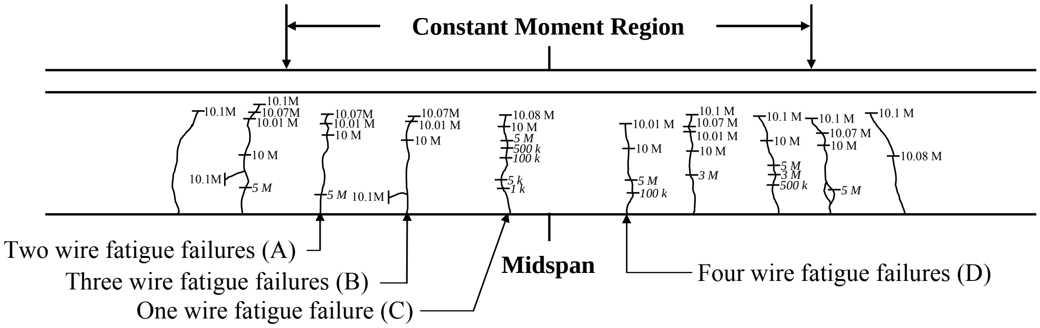

Figure 6.69 Location of Wire Failures – Beam 6A

Figure 6.70 Typical Wire Fatigue Failure in Beam 6A – Location D

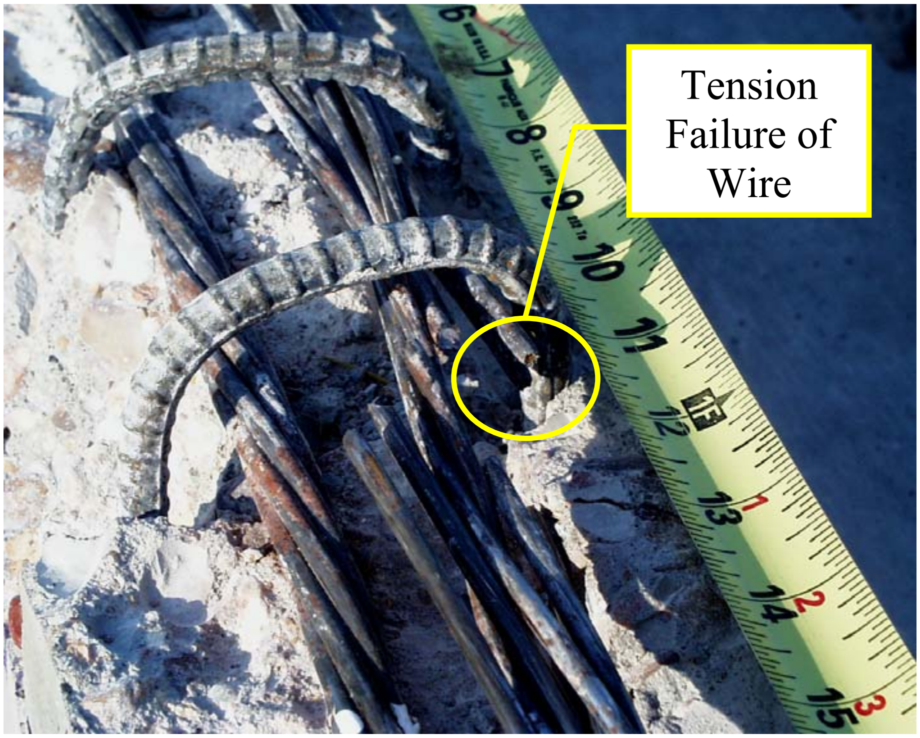

Figure 6.71 Picture of Wire Tension Failure in Beam 6A

6.5 BEHAVIOR OF BEAM 1B

After surviving 10 million fatigue cycles at an a stress range in the strand of 7 ksi, and 3.5 million fatigue cycles at a stress range in the strand of 41 ksi corresponding to a median stress in the strand of 155 ksi, Beam 1 was subjected to additional fatigue cycles at loads corresponding to stress range in the strand approximately 44 ksi and at a median stress in the strand of 146 ksi. For this series of fatigue cycles Beam 1 will be designated as Beam 1B.

This test was performed due to an observed discrepancy between the test on Beam 1A at a stress range in the strand and all other tests performed on beams at a stress range in the strand of approximately 45 ksi. Average measured strand strain as a function of applied load is plotted in Figure 6.72 for Beams 4, 5 and

6A for static tests performed during the fatigue tests at a strand stress range of approximately 45 ksi. In addition, the applied load ranges for the fatigue testing are shown. During each static test at this load level, three distinct regions of beam behavior are observed. These include the linear region below the decompression load, where the beam behavior corresponds to an uncracked section, the nonlinear decompression region, and the linear region above the decompression load, where the beam behavior corresponds to a cracked section. The load ranges for Beams 4, 5 and 6 corresponding to a range in strand stress of 42 ksi include all three regions of beam behavior.

Maximum measured strand strain as a function of applied load is plotted in Figure 6.73 for Beams 1A and 1B. The applied load ranges for each series of fatigue cycles are shown. As shown, the load range for the fatigue loading of Beam 1A at a range of strand stress of 41 ksi included only the linear portion above the decompression load, which varied from all previous tests conducted at this index stress. As a result, an additional series of fatigue cycles at a stress range in the strand of 41 ksi was performed on Beam 1 with a load range that included all three regions and applied the same stress range in the strand. Data from this test are summarized in this section.

6.5.1 Baseline Static Test

In order to evaluate the change in beam response to this series of fatigue cycles, a baseline static test was performed on Beam 1B. The beam was loaded from zero to 13.5 kip during the baseline static test. The maximum fatigue load for this series of cycles was lower than previous tests conducted on Beam 1B; therefore, there was no change in the crack pattern from the end of the previous series shown in Figure 6.66.

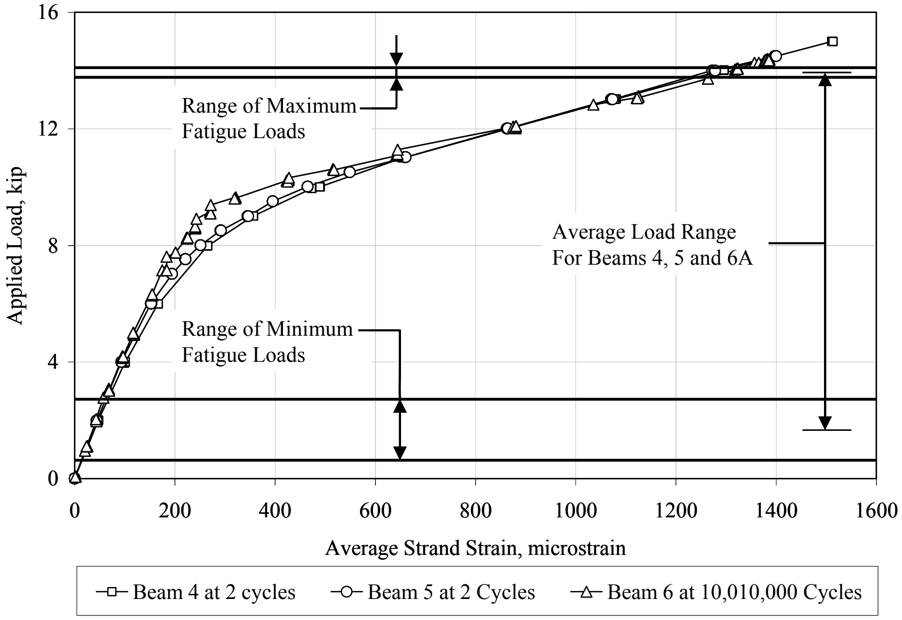

Figure 6.72 Comparison of Applied Load Ranges for Beams 4, 5 and 6A

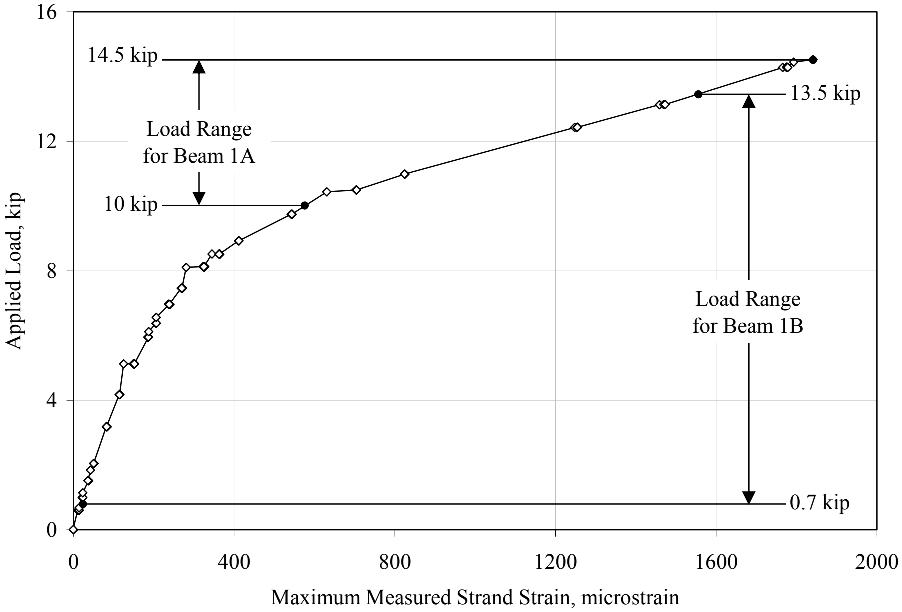

Figure 6.73 Comparison of Applied Load Ranges for Beam 1A and Beam 1B

6.5.2 Fatigue Response

The maximum and minimum load applied to Beam 1B during this series of fatigue cycles are summarized in Table 6.1. The calculated stress range and median stress in the strand are also listed.

During static tests on Beam 1B during this series of fatigue cycles similar data were collected as for previous fatigue tests. These data are shown in Figure 6.74 through Figure 6.77. The behavior of Beam 1B did not change appreciably during this series of fatigue tests. This was similar to the trends observed from data collected during static tests of Beam 1A at a stress range in the strand of 41 ksi.

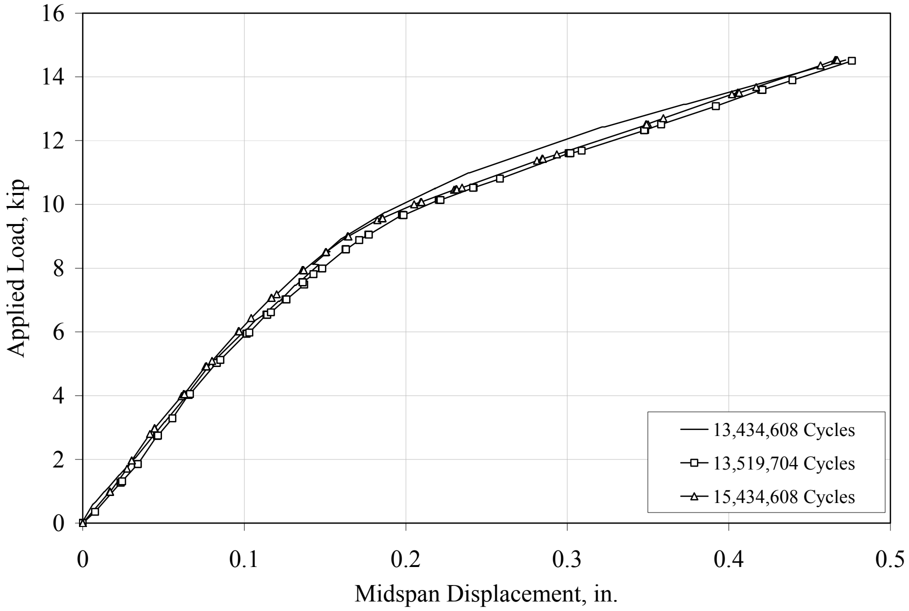

Figure 6.74 Variation of Midspan Displacement during Fatigue Tests of Beam 1B at a Strand Stress Range of 44 ksi

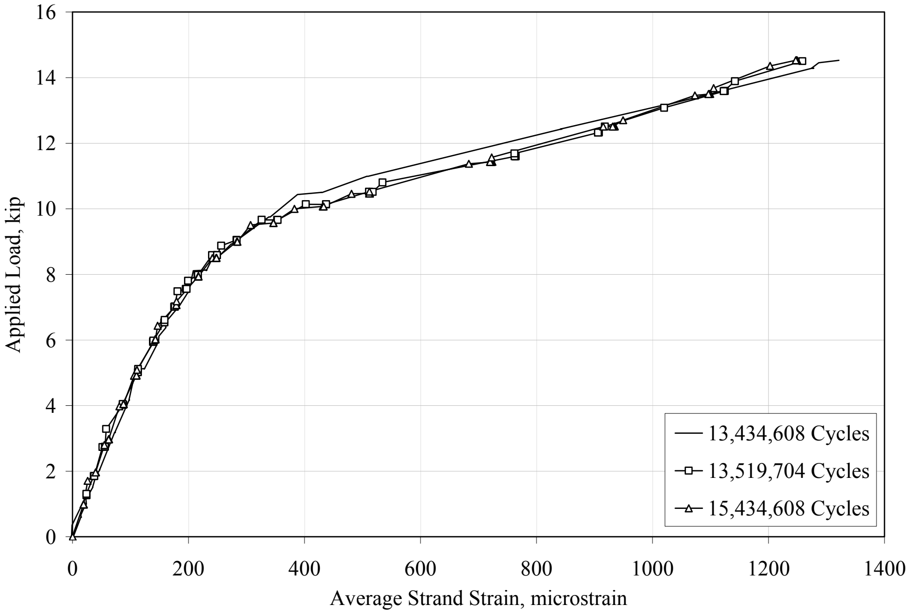

Figure 6.75 Variation of Average Strand Strain during Fatigue Tests of Beam 1B at a Strand Stress Range of 44 ksi

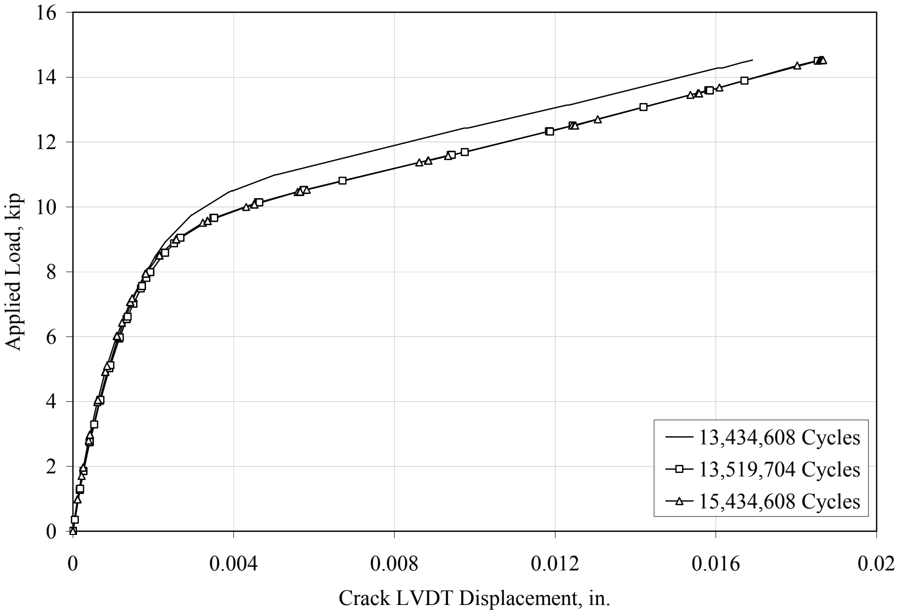

Figure 6.76 Variation of Crack LVDT Displacement during Fatigue Tests of Beam 1B at a Strand Stress Range of 44 ksi

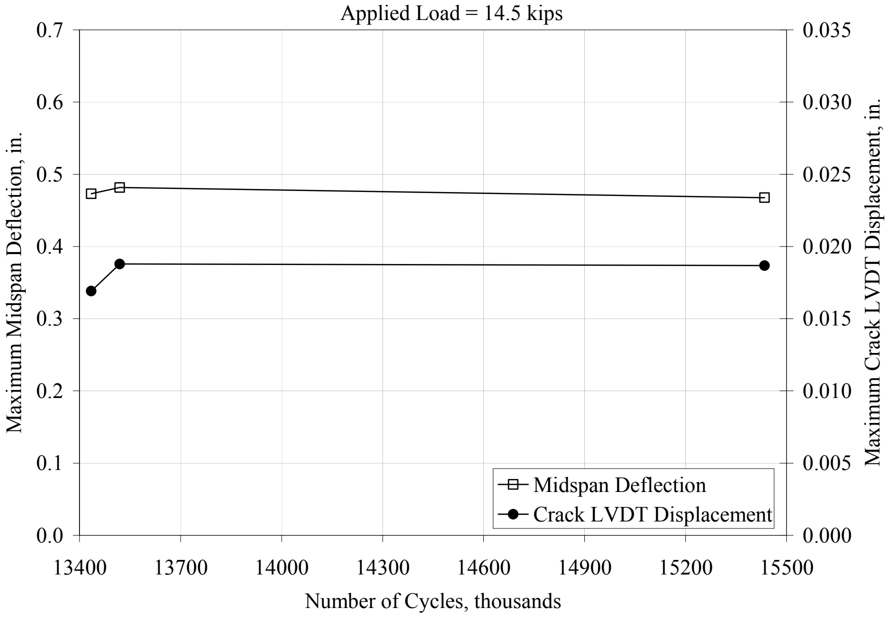

Figure 6.77 Variation of Midspan Deflection and Crack LVDT Displacement with Number of Cycles for Beam 1B at a Strand Stress Range of 44 ksi

6.5.3 Post Mortem Investigation

No post mortem investigation was conducted at the conclusion of the fatigue tests. After approximately 15.5 million cycles, no significant change in beam behavior was realized, and therefore, no post mortem investigation was conducted.

6.6 SUMMARY OF FATIGUE TESTS

Table 6.5 summarizes the total number of fatigue cycles performed on each beam. Generally the trends in the data were as expected. As the stress range in the strand increased, the fatigue life decreased significantly. Beams 1 and 6, tested at the lowest strand stress range, survived 10,000,000 cycles with no signs of significant deterioration. Beams 2 and 3 survived an average of 3,900,000 cycles at a stress range of approximately 24 ksi after which significant deterioration began. Beams 4 and 5 survived an average of 420,000 cycles at a stress range of approximately 47 ksi after which significant deterioration began. The results from these six fatigues tests are compared with data from previous studies in Figure 6.78. The maximum measured range in stress of the strand was used to plot these data for comparison with previous studies. These data correlate well with previous studies and the in-air fatigue life model proposed by Paulson (1983).

As previously discussed, Beams 1 and 6 were tested at a stress range in the strand of approximately 43 ksi after surviving 10,000,000 cycles at the previously a stress range in the strand of less than 15 ksi. Two series of fatigue cycles were performed on Beam 1 and one series of fatigue cycles were performed on Beam 6. These series of fatigue cycles were designated as Beam 1A, Beam 1B and Beam 6A. The results for these fatigue tests are summarized in Table 6.5. Beam 1 survived 5,400,000 additional fatigue cycles without signs of deterioration; however, Beam 6 began deteriorating after only 21,000 cycles at a stress range in the strand of approximately 43 ksi. The results from Beam 1 are most likely due to a lack of material defects in the strand in the highly stressed region of the test specimen resulting in a significantly longer fatigue life. Similar results were obtained during in-air fatigue tests on samples of the same strand that was used in the test specimens. These results are discussed in Chapter 1 and have been previously discussed by Heller (2003). The results from Beam 6 indicate that the fatigue cycles at the strand stress range of 14 ksi produced some fatigue damage resulting in the significantly reduced fatigue life when tested at the higher range of strand stress.

Table 6.5 Summary of Fatigue Tests

Beam ID	Calculated Stress Range in the Strand* (ksi)	Measured Maximum Stress Range in the Strand† (ksi)	Number of Cycles at First Sign of Deterioration	Total Number of Fatigue cycles
1	7	4	NA	10,000,000††
2	22	19	5,300,000	5,800,000
3	25	26	2,400,000	3,100,000
4	47	44	520,000	640,000
5	47	47	320,000	370,000
6	14	14	NA	10,000,000††
1A	41	38	NA	3,400,000††§
1B	44	48	NA	2,000,000††§§
6A	45	42	21,000*	110,000§

† Maximum strand stress range calculated using measured strain data collected during static tests.

†† Testing stopped at predetermined number of cycles.

* Range of stress in the strand calculated using cracked section properties.

§ Number of cycles in addition to 10,000,000 cycles at a stress range in the strand of approximately 7 ksi.

§§ Number of cycles in addition to 10,000,000 cycles at a stress range in the strand of approximately 7 ksi and 3,400,000 cycles at a stress range in the strand of approximately 38 ksi.

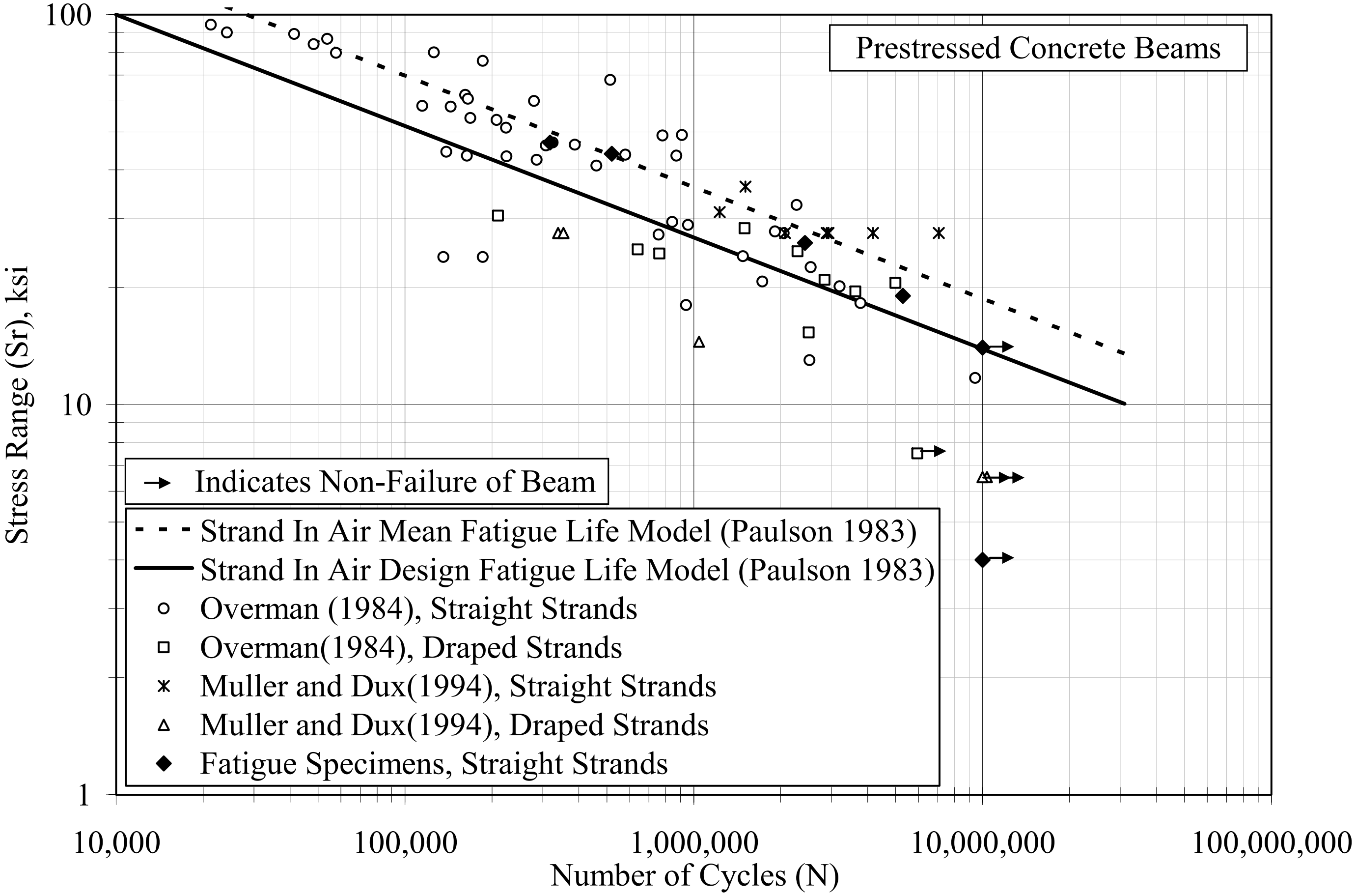

Figure 6.78 Comparison of Fatigue Specimens with Data Reported in Previous Studies

The maximum, minimum, and average measured strains at the maximum and minimum applied fatigue loads test have been summarized and are presented in Appendix N. The resulting maximum and minimum inferred strand stress ranges are shown in Table 6.6. These data were taken from static tests where results were repeatable and before any significant fatigue damage had occurred. These measured ranges of stress in the strand are compared with the Paulson (1983) fatigue life models in Figure 6.79. There is relatively good agreement between the Paulson model for strain in-air and these tests on prestressed beams with straight strand.

Typically, the maximum measured ranges of stress are within 12% of the calculated strand stress range. This indicates that the analyses discussed in Chapter 5 were in relatively good agreement with the measured results. The measured range of strand stress for Beam 1 is approximately 45% lower than the calculated strand stress range. This is most likely due to the location of the strain gages relative to the locations of the flexural cracks in the beam. In addition, Beam 1 experienced a limited amount of cracking, which increased the likelihood that the strain gages were located near a crack. Therefore, it is reasonable to assume that the discrepancy between the calculated and measured results was caused by the location of strain gages relative to the flexural cracks.

Table 6.6 Summary of Strand Stress Ranges Inferred from Measured Strains due to Static Loads at the Fatigue Load Range for Beams 1 to 6

Beam ID	Calculated Strand Stress Range* (ksi)	Inferred Strand Stress Range			
		Reference Figure†	Maximum (ksi)	Minimum (ksi)	Average (ksi)
1	7	Figure 6.8	4	3	4
2	22	Figure 6.22	19	10	16
3	25	Figure 6.23	26	16	21
4	47	Figure 6.42	44	30	40
5	47	Figure 6.43	47	35	42
6	14	Figure 6.9	14	7	11

† The maximum, minimum and average strand stress range reported are from data collected during the static test performed when results were repeatable. See the reference figure for plots of applied load as a function of average measured strain. See Appendix N for corresponding strain data.

* Calculated stress range in the strand based on cracked section properties and measured material properties.

Table 6.7 Summary of Strand Stress Ranges Inferred from Measured Strains due to Static Loads at the Fatigue Load Range for Beams 1A, 1B and 6A

Beam ID	Calculated Strand Stress Range* (ksi)	Inferred Strand Stress Range			
		Reference Figure†	Maximum (ksi)	Minimum (ksi)	Average (ksi)
1A	41	Figure 6.60	38	37	38
1B	44	Figure 6.75	48	30	36
6A	45	Figure 6.61	42	39	41

† The maximum, minimum and average strand stress range reported are from data collected during the static test performed when results were repeatable. See the reference figure for plots of applied load as a function of average measured strain. See Appendix N for corresponding strain data.

* Calculated stress range in the strand based on cracked section properties and measured material properties.

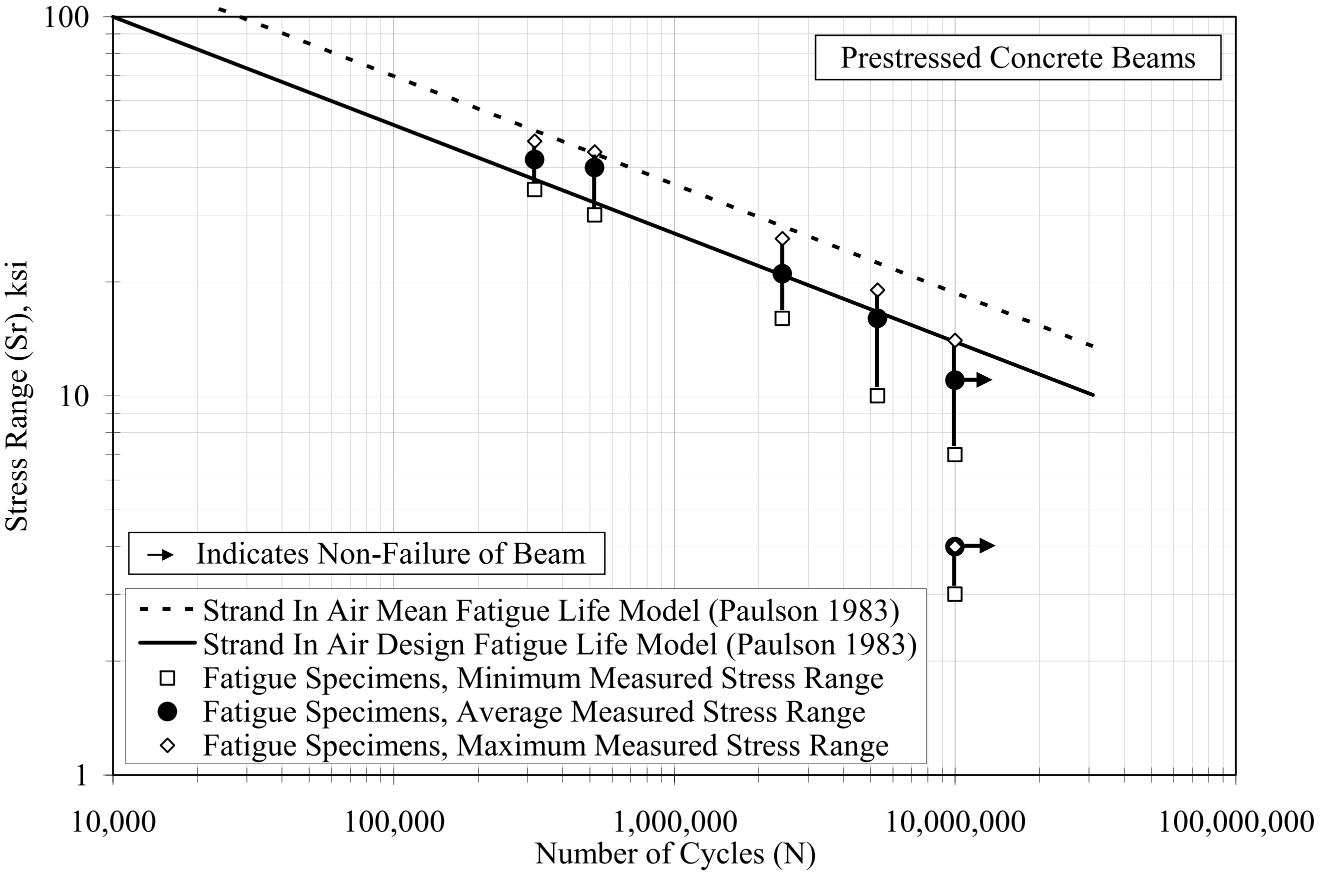

Figure 6.79 Measured Range of Strand Stress in Fatigue Specimens Compared with Paulson (1983) Strand In-Air Fatigue Life Models

In previous sections, the average measured strain in the strand plotted as a function of applied load was used as an indicator of the change in beam response to the applied loads. As discussed in Chapter 4, ten strain gages were attached to individual wires on the prestressing strand in a staggered pattern and within 12 in. of the midspan of each beam. As a result of the staggered pattern, the location of each gage relative to flexural cracks in the beam varied. In the vicinity of a flexural crack, the strand will experience an increase in strain due to the discontinuity caused by the crack. In addition, as the number of loading cycles increases, the debonded length of strand from the crack will increase. Therefore, strains will be highest at gages located at a crack and will decrease as the distance between the crack and gage increases and at locations where the strand has debonded near a crack.

For comparison with the analyses of the beams discussed in Chapter 5, plots of applied load as a function of change of stress in the strand are given in Figures 6.80 through 6.87. Data from two static tests and the corresponding analysis are provided on each plot. The first set of measured data was selected from the static test where the results were repeatable. This generally corresponds to the static test where no additional, significant concrete cracking occurred. The second set of measured data was taken from the latest static test where the gages were functioning and no wire breaks had occurred.

The calculated stress range in the strand based on the analyses discussed in Chapter 5 and inferred stress range in the strand based on measured strains at the maximum and minimum loads for fatigue testing summarized in Table 6.7. The change in stress in the strand at the minimum fatigue load is the change in stress from zero load to the minimum fatigue load. Similarly, the change in stress in the strand at the maximum fatigue load is the change in stress from zero load to the maximum fatigue load. Where the stress changed significantly between the static tests shown, the measured value from both static tests is included. On average, the difference between the calculated strand stress range and measured strand stress range at both the minimum and maximum fatigue load was 10%. Again, this indicates that the analyses of the beams discussed in Chapter 5 are in relatively good agreement with the measured results.

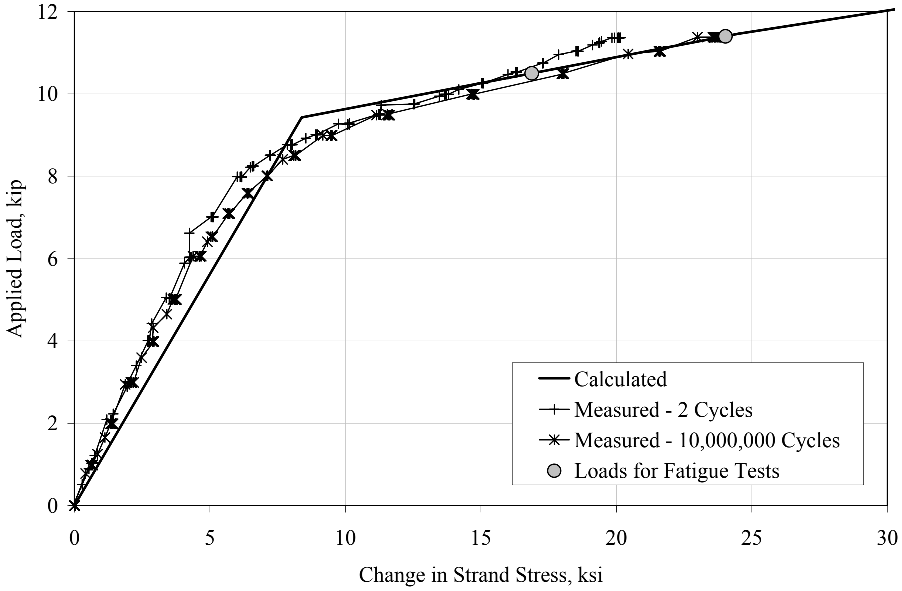

Figure 6.80 Comparison of Calculated and Measured Load Plotted as a Function of Change in Strand Stress for Beam 1

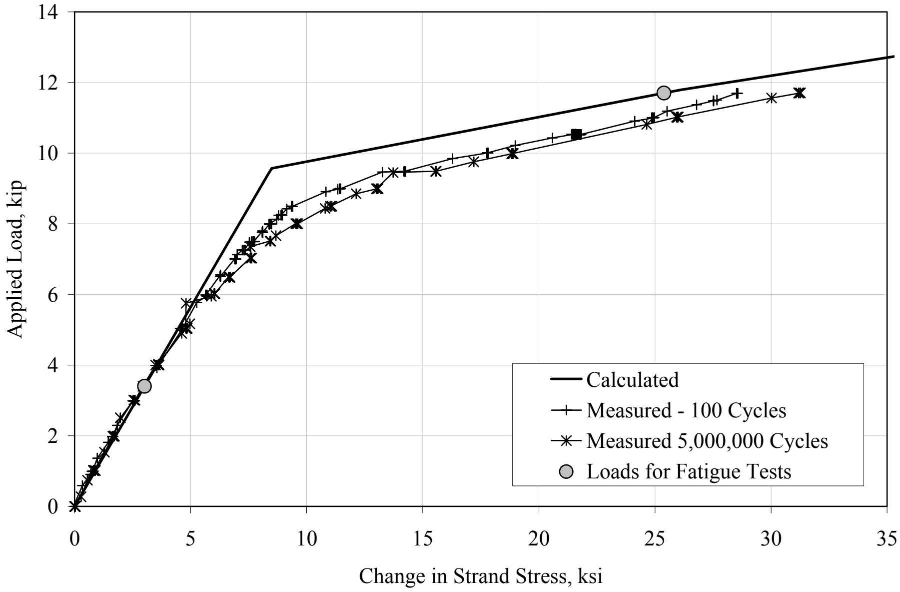

Figure 6.81 Comparison of Calculated and Measured Load Plotted as a Function of Change in Strand Stress for Beam 2

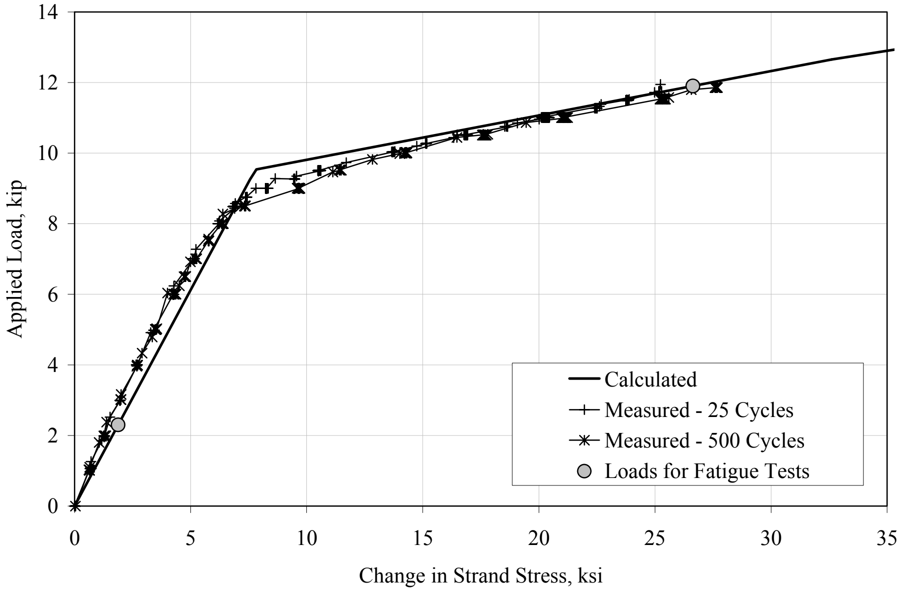

Figure 6.82 Comparison of Calculated and Measured Load Plotted as a Function of Change in Strand Stress for Beam 3

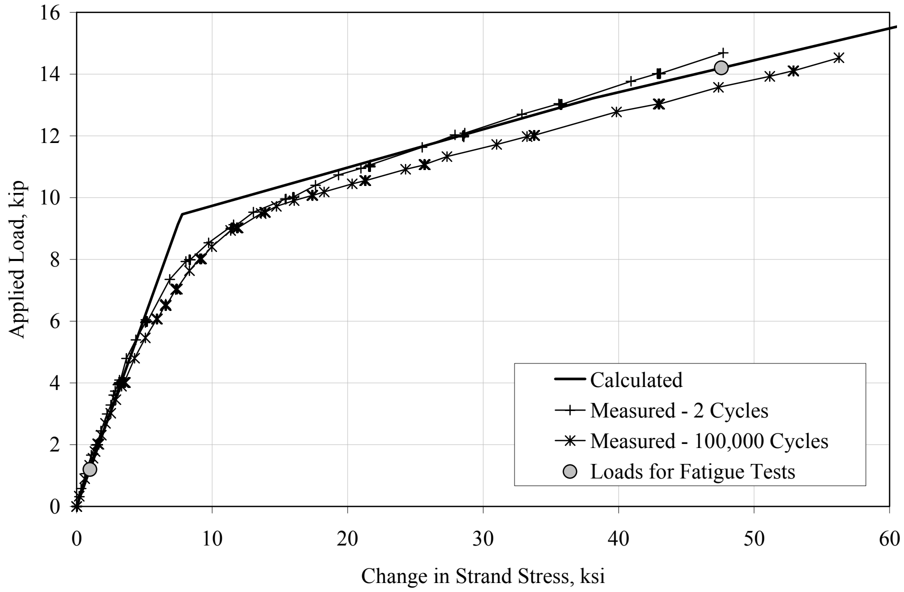

Figure 6.83 Comparison of Calculated and Measured Load Plotted as a Function of Change in Strand Stress for Beam 4

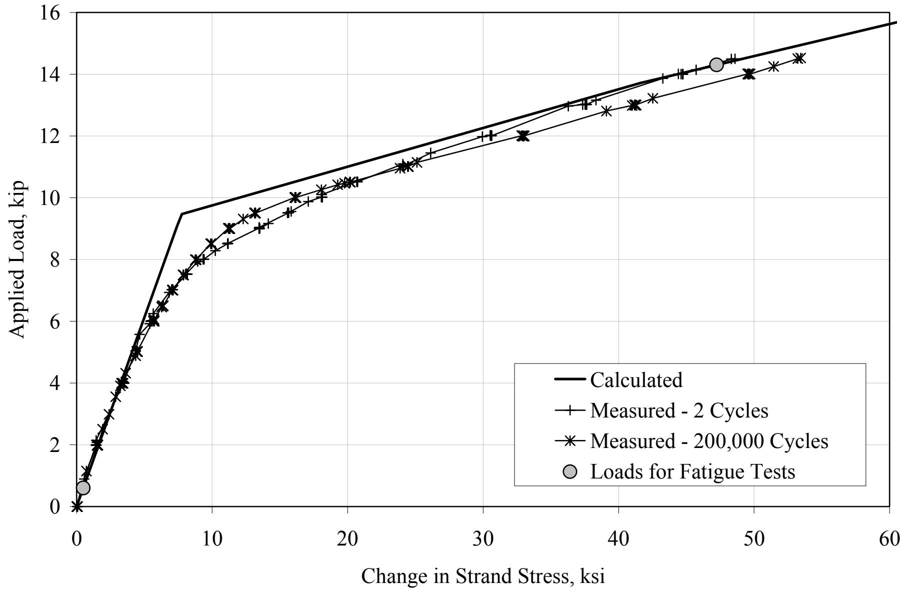

Figure 6.84 Comparison of Calculated and Measured Load Plotted as a Function of Change in Strand Stress for Beam 5

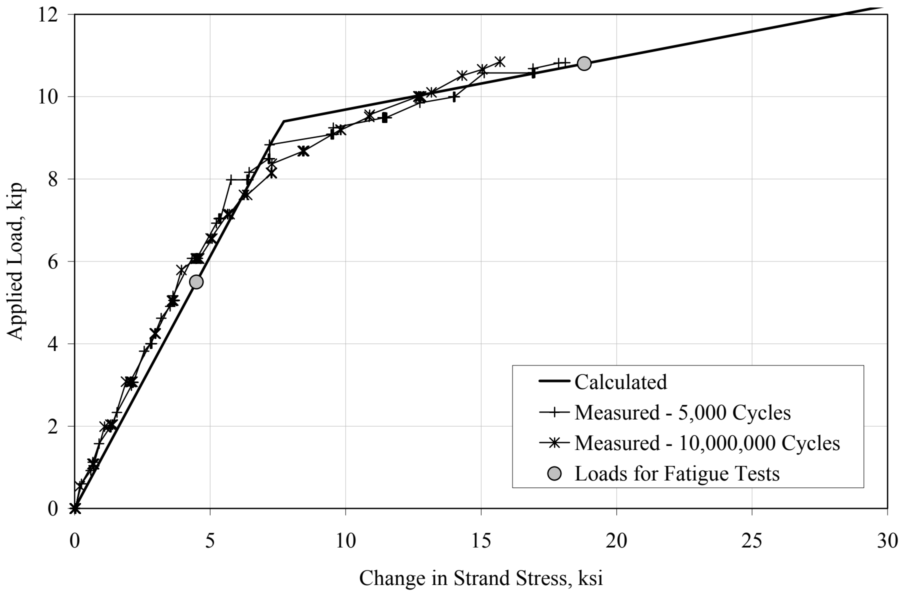

Figure 6.85 Comparison of Calculated and Measured Load Plotted as a Function of Change in Strand Stress for Beam 6

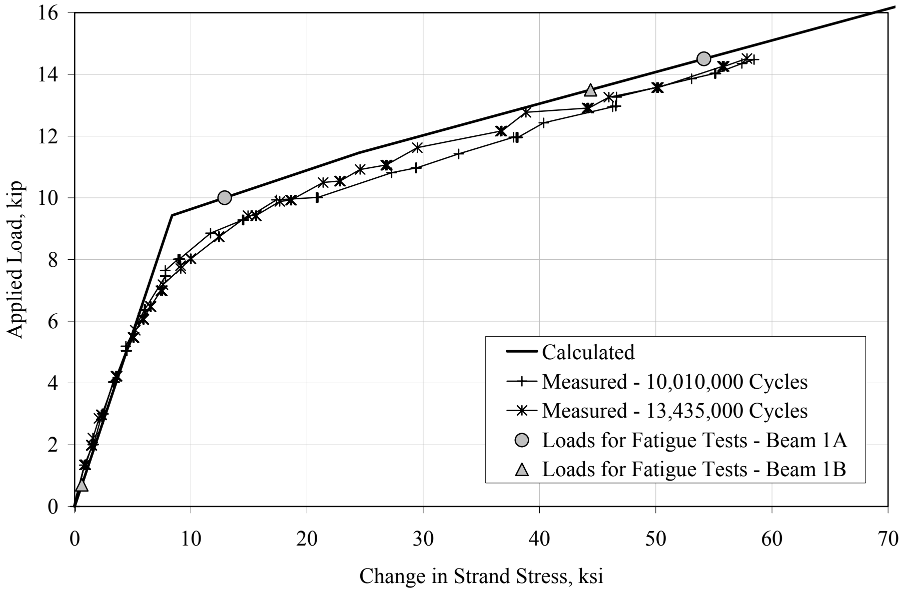

Figure 6.86 Comparison of Calculated and Measured Load Plotted as a Function of Change in Strand Stress for Beams 1A and 1B

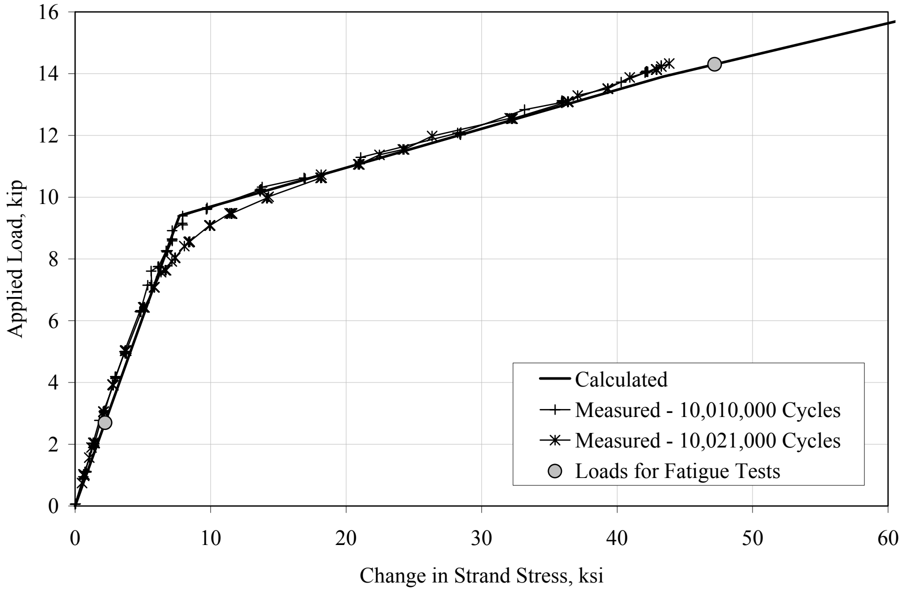

Figure 6.87 Comparison of Calculated and Measured Load Plotted as a Function of Change in Strand Stress for Beam 6A

Table 6.8 Comparison of Results of Beam Analyses with Maximum Measured Change in Strand Stress

Beam ID	Change in Strand Stress*, ksi			
	At Minimum Fatigue Load		At Maximum Fatigue Load	
	Analysis	Inferred**†	Analysis	Inferred**†
1	17	18	24	20, 24
2	3	3	25	29, 31
3	2	1	27	25, 28
4	1	1	48	44, 54
5	0.5	0.5	47	47, 51
6	4	4	19	16, 18
Additional Fatigue Tests Performed on Beams 1 and 6				
1A	13	17, 18	54	59, 58
1B	1	1	44	46, 47
6A	2	2	47	43, 44

* Change in strand stress is calculated

** Inferred strand stress from corresponding Figures 6.80 through 6.87.

† Where the stress changed significantly between the static tests shown in the figures, values from both tests are shown.

CHAPTER 7

Load Rating of Prestressed Concrete Bridges

The Interim 2003 AASHTO Manual for Condition Evaluation of Bridges (MCEB) is currently used for the load rating of prestressed concrete bridges in the United States. The MCEB provides several criteria that are used to determine the load rating for a bridge. These criteria include concrete compressive and tensile stress limits, maximum levels of tensile stress in the prestressing strand, and the flexural strength of the prestressed beams. Although the load rating process requires that each criterion be considered, the thrust of this investigation is to evaluate the appropriateness of using the concrete tensile stress criterion as an indicator of fatigue life. Therefore, this chapter focuses on the load ratings based on the tensile stress criterion. Load rating results for the other criteria are summarized in Appendix I, and Wagener (2002) provides additional details on the criteria not discussed in this dissertation.

Section 7.1 provides an overview of the load rating process. The calculated load ratings for the bridges in this investigation are discussed in Section 7.2. Several load ratings are presented, including the load rating based exclusively on the provisions in the MCEB and load ratings that take advantage of the finite element analyses, diagnostic load tests, and updated design provisions in the AASHTO LRFD specifications. The possibility that the bridges experienced flexural cracks is discussed in Section 7.3. The use of strand stress range for load rating prestressed concrete bridges is given in Section 7.4. Recommended criteria for load rating prestressed concrete bridges are given in Section 7.5.

7.1 OVERVIEW OF THE LOAD RATING PROCEDURE

Load rating is a method of determining the safe live load capacity of a bridge. Bridges are rated at two levels: inventory and operating. The inventory level rating provides the safe live load that a particular structure can resist for an indefinite period of time. The operating level provides the maximum safe live load that a bridge may resist; however, unlimited loadings at this level may shorten the expected life of the bridge. The load rating procedure in the MCEB is similar to the load factor design method. The load rating is determined by multiplying the design vehicle load by a calculated rating factor. The rating factor (RF) defined in the MCEB is:

$$RF = \frac{C - A_1 D}{A_2 L(1 + I)} \tag{7.1}$$

where C is the capacity of the member, D is the dead load effect, L is the live load effect, I is the impact factor, A_1 is the dead load factor, and A_2 is the live load factor.

Typically, the values of A_1, A_2, and I used in Eq. 7.1 are taken from the MCEB, which are based on the AASHTO Standard specifications. Two limit states are defined: serviceability and capacity. The appropriate values of the three parameters are given in Table 7.1 for each limit state. As discussed in Sections 7.2, 7.4, and 7.5, some of the design provisions in the AASHTO LRFD specification were also considered for load rating in this investigation. The values of A_1, A_2, and I corresponding to serviceability and fatigue limit states from the AASHTO LRFD specifications are also given in Table 7.1.

Using the rating factor calculated using Equation 7.1, the bridge load rating (RT) is determined using the rating equation:

$$RT = RF(W) \qquad (7.2)$$

where W is the weight of the design loading vehicle in tons and RF is the rating factor calculated in Eq. 7.1. For the bridges in this investigation the design loading vehicle is the HS-20 truck, which is the current AASHTO design vehicle and comprises an 8-kip lead axle and two, 32-kip rear axles. The design weight of the vehicle is 20 ton, which is taken as the sum of the weights of the lead axle and the first rear axle. The design vehicle is shown schematically in Figure 7.1. It should be noted that for the bridges in this investigation, a rear axle spacing of 14 ft always produced the maximum response in the members being investigated at the serviceability and capacity limit states. The AASHTO LFRD specifications stipulate a rear axle spacing of 30 ft for the fatigue limit state.

Table 7.1 Summary of Load Factors for Various Limit States

Specification	Limit State	A_1	A_2	I**
MCEB*	Serviceability	1.0	1.0	$\frac{50}{L+125}$
	Capacity	1.3	2.17	
AASHTO LRFD	Serviceability	1.0	0.8	0.33
	Fatigue	1.0	0.75	0.15

* Values are based on AASHTO Standard specifications.
** L is the effective span length of the member being considered (ft).

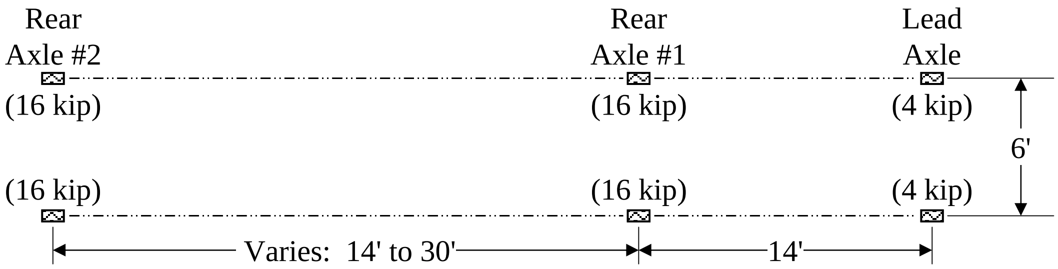

Figure 7.1 Schematic Representation of HS-20 Design Vehicle

7.1.1 Overview of the Tensile Stress Criterion for Load Rating

As discussed previously, the load rating criterion for prestressed concrete bridges being investigated in this chapter is the tensile stress criterion. This criterion is an inventory level rating factor and represents a serviceability limit that is intended to control cracking in prestressed members. Because the rating criterion represents a serviceability condition, the load factors A_1 and A_2 are taken equal to 1.0 (Table 7.1). The limiting tensile stress at the extreme fiber of the member is defined as $6\sqrt{f_c'}$ (psi), where f_c' is the typically taken equal to the specified concrete compressive strength of the beam being investigated. Because the MCEB permits the use of measured material properties of an existing structure, load ratings based on f_c' being equal to the estimated in situ compressive strength of the concrete, f_{ce}', are also presented in this chapter.

Based on the general form of the equation for rating factors given in Eq. 7.1, the rating factor for the concrete tensile stress criterion (RF_{CT}) for prestressed concrete beams is:

$$RF_{CT} = \frac{6\sqrt{f'_c} - A_1(F_d + F_p + F_s)}{A_2 F_l} \tag{7.3}$$

where F_d is the unfactored dead load stress, F_p is the unfactored stress due to the prestress force after all losses, F_s is the unfactored stress due to secondary prestress forces, and F_l is the unfactored live load stress. The values of the load factors A_1 and A_2 are given in Table 7.1. The stresses in Eq. 7.3, F_d, F_p, and F_s, are evaluated at the bottom fiber of the cross section for the bridges in this investigation. As discussed, two values of f_c' will be used in the load rating calculations: the specified compressive strength, f'_{cs}, and the estimated in situ compressive strength, f'_{ce}.

7.1.2 Overview of the Inventory Level Flexural Strength Criterion

Although the inventory level flexural strength criterion is not the focus of this dissertation, as will be shown in the following section, this criterion does govern the load rating for some of the bridges considered in this investigation. The rating factor for the inventory level flexural strength criterion given in Eq. 7.4:

$$RF_{FSINV} = \frac{\phi M_n - A_1(D)}{A_2 L(I+1)} \tag{7.4}$$

where ϕM_n is the nominal flexural capacity of the composite section, D is the unfactored dead load moment, and L is the unfactored live load moment. Load factor provisions in the AASHTO LRFD related to strength were not considered in this investigation; therefore, values of A_1 and A_2 specified in the MCEB were used for all analyses related to the strength limit state (Table 7.1). However, it should be noted that an impact factor of 0.33 was used for evaluating all limit states when the AASHTO LRFD provisions were used to evaluate the corresponding serviceability limit state.

7.2 LOAD RATINGS FOR BRIDGES IN THIS INVESTIGATION

A number of other parameters influence the calculated load rating. The sensitivity of the assumed material properties, live load distribution factors (LLDF), transverse position of live loads, and load factors used in the equation for the rating factor are addressed in this section. Although load ratings are typically based on design drawings and the procedures in the AASHTO Standard specification, the MCEB permits properties of the existing structure to be used in the load rating process. In addition, the MCEB allows advanced methods of evaluating the live load response of a bridge, including load tests and advanced structural analyses. The flexibility of the MCEB with regard to using field conditions and advanced methods to determine live load response provides for the possibility of significantly improved load ratings.

Several load ratings based on the tensile stress criterion for the bridges in this investigation will be presented in this section. The first load rating discussed uses the basic provisions of the MCEB and the AASHTO Standard, which is referenced in the MCEB. Subsequent load ratings take advantage of the flexibility of the MCEB and utilize the results from field tests, finite element analyses, and provisions in the AASHTO LRFD. The assumptions made for each analysis performed are summarized in Table 7.2. The specifics of each assumption are included in the discussions that follow in Sections 7.2.1 through 7.2.5.

7.2.1 Load Rating Analyses A and B

The load ratings summarized in this section are based on specified compressive strengths of the concrete and corresponding section properties. In addition, the MCEB live load factor A_2 was taken equal to 1.0 for the tensile stress rating factor, and LLDF's calculated using the provisions in the AASHTO Standard specification. The current MCEB references the AASHTO Standard specification for matters it does not cover, such as determining LLDF's. As discussed in Chapter 4, the LLDF's are easily calculated using the AASHTO Standard, but they are conservative.

In Analysis A, the tensile stress limit of $6\sqrt{f'_{cs}}$ was used. This value was selected because it is specified in the MCEB and most load ratings are performed using the specified compressive strength of the concrete. In Analysis B, a tensile stress limit of $12\sqrt{f'_{cs}}$ was used. This elevated corresponds to the largest value currently used by TxDOT for the load rating of prestressed concrete bridges. Analyses A and B represent baselines for comparison with the other analyses.

Table 7.3 summarizes the rating factors and load ratings from Analysis A based on the tensile stress and flexural strength criteria for the bridges. The tensile stress rating factors range from 0.50 to 2.04, which correspond to load ratings of 10.1 to 40.7 ton. Four of the six bridges have a tensile stress rating factor below 1.0, which indicates that the bridges fail to satisfy the criterion, and as a result, have a load rating less than the design vehicle load. The rating factors for the flexural strength criterion for Analysis A are also summarized in Table 7.2. The rating factors range from 1.04 to 2.00 and this criterion controls the load rating for the two bridges with spans of 40 ft.

Table 7.3 summarizes the tensile stress and flexural strength rating factors and load ratings from Analysis B. The use of the elevated tensile stress limit resulted in three of the four bridges that failed to satisfy the tensile stress criterion in Analysis A to have load ratings controlled by the flexural strength criterion. Based on Analysis B, five of the six bridges have load ratings above HS-20. The increase in the tensile stress criterion rating factor ranged between 25 and 70%, with an average increase of 50%. Because the tensile stress criterion did not control the load ratings for all bridges, the increase in the controlling load rating ranged between 0 and 70%, with an average increase of 35%.

Table 7.2 Summary of Assumptions Used for Load Rating Analyses

Load Rating Analysis	Live Loads			Material and Section Properties	Tensile Stress Limit
	Load Factor for Live Load*	LLDF's	Transverse Truck Position		
A	MCEB	AASHTO Standard	NA	Specified	$6\sqrt{f'_{cs}}$
B	MCEB	AASHTO Standard	NA	Specified	$12\sqrt{f'_{cs}}$
C	LRFD	AASHTO LRFD	NA	Specified	$6\sqrt{f'_{cs}}$
D	LRFD	Finite Element Analyses	Located to Produce Maximum Response	Specified	$6\sqrt{f'_{cs}}$
E	MCEB	Finite Element Analyses	Located to Produce Maximum Response	Estimated In Situ	$6\sqrt{f'_{ce}}$
F	MCEB	Finite Element Analyses	Centered in Traffic Lanes	Estimated In Situ	$6\sqrt{f'_{ce}}$

* Live load factors for serviceability and capacity limit states are given in Table 7.1, and discussed in Sections 7.1.1 and 7.1.2.

Table 7.3 Summary of Load Rating Load Rating Analysis A

Bridge		Load Rating Criterion†			
		Tensile Stress		Flexural Strength	
		RF_{CT}	*RT* (ton)	RF_{FSINV}	*RT* (ton)
Chandler Creek	40-ft Span	1.23	24.7	1.17*	23.3
	60-ft Span	0.97*	19.5	1.25	24.9
Lake LBJ		0.90*	17.9	1.31	26.1
Lampasas River		0.50*	10.1	1.04	20.8
Willis Creek		0.72*	14.5	1.16	23.3
Wimberley		2.04	40.7	2.00*	40.1

* Controls load rating at inventory level.

Table 7.4 Summary of Load Rating Load Rating Analysis B

Bridge		Load Rating Criterion†			
		Tensile Stress		Tensile Stress	
		RF_{CT}	*RT* (ton)	RF_{FSINV}	*RT* (ton)
Chandler Creek	40-ft Span	1.74	34.8	1.17*	23.3
	60-ft Span	1.42	28.4	1.25*	24.9
Lake LBJ		1.31*	26.1	1.31*	26.1
Lampasas River		0.86*	17.3	1.04	20.8
Willis Creek		1.17	23.3	1.16*	23.3
Wimberley		2.60	52.0	2.00*	40.1

* Controls load rating at inventory level.

7.2.2 Load Rating Analysis C

The load ratings summarized in this section are based on specified compressive strengths of the concrete, corresponding section properties, load factors from the AASHTO LRFD specification and LLDF's based on the AASHTO LRFD. Analysis C differs from Analysis A in the choice of live load factors and method of calculating LLDF's.

In Analysis A, the dead load and live load factors were based on the MCEB and were taken to be 1.0. However, when checking for tension in prestressed concrete members where the objective is crack control, the specified AASHTO LRFD load combination is dead load plus live load, with load factors of 1.0 and 0.8, respectively (Table 7.1). This objective of the tensile stress criterion load rating factor is the same as the provision in the design AASHTO LRFD. The commentary in the AASHTO LRFD attributes the reduced load factor to field observations that indicate no significant signs of detrimental cracking have occurred in bridges that have been in service since before 1993 and subjected to the current design loads in the specification. The commentary also states that the statistical significance of this load factor is based on the assumption that the live load event is expected to occur about once a year for bridges with two lanes and less frequently for bridges with more than two lanes. Therefore, the design load for the tensile stress criterion may be effectively reduced by 20% if the AASHTO LRFD load factors are used.

It should be noted that the strength reduction factor for prestressed concrete beams in flexure and shear is given as 1.0 in the AASHTO LRFD. In the MCEB there is no strength reduction factor applied to the tensile stress criterion. Therefore, the load factors in the AASHTO LRFD may be directly compared with the load factors in the MCEB.

In addition to the load factor, the LLDF’s used for Analysis C are also based on the AASHTO LRFD. As discussed in Chapter 4, the provisions in the AASHTO LRFD provide a more accurate estimate of the live-load response of a bridge than the provisions in the AASHTO Standard.

Table 7.4 summarizes the rating factors and load ratings from Analysis C based on the tensile stress and flexural strength criteria for the bridges. The tensile stress rating factors range from 0.59 to 2.17, which correspond to load ratings of 11.9 to 43.4 ton. The increase in the tensile stress rating factor from Analysis C compared with Analysis A ranged from 10 to 20%, with an average of

15%. Two of the six bridges have a tensile stress rating factor below 1.0, as compared to four bridges based on Analysis A. The rating factors for the flexural strength criterion for Analysis C are also summarized in Table 7.4. The rating factors range from 0.93 to 1.71. When compared with the results from Analysis A, the flexural strength criterion decreased by an average of 10%. This is the result of using the LLDF's based on the AASHTO LRFD, which generally resulted in higher LLDF's for the exterior beams for the bridges being studied. On average, the controlling load rating factor increased by 8% using the provisions in the AASHTO LRFD.

Table 7.5 Summary of Load Rating Load Rating Analysis C

Bridge		Inventory Level Load Rating†			
		Tensile Stress Criterion		Flexural Strength Criterion	
		RF_{CT}	RT (ton)	RF_{FSINV}	RT (ton)
Chandler Creek	40-ft Span	1.44	28.9	1.09*	21.9
	60-ft Span	1.17	23.4	1.18*	23.5
Lake LBJ		1.06*	21.2	1.17	23.4
Lampasas River		0.59*	11.9	0.93	18.7
Willis Creek		0.76*	15.3	0.99	19.8
Wimberley		2.17	43.4	1.71*	34.3

* Controls load rating at inventory level.

7.2.3 Load Rating Analysis D

The load ratings summarized in this section are based on specified compressive strengths of the concrete, corresponding section properties, the reduced load factor in the AASHTO LRFD specification, and LLDF's determined from the results of finite element analyses. Analysis D differs from Analysis C only in the method of calculating LLDF's. The LLDF's used for Analysis C were calculated using the equations in the AASHTO LRFD; however, Analysis D takes advantage of the provisions in the MCEB that permits the use of finite element analyses for determining LLDF's. The LLDF's used in the analysis are summarized in Appendix I, and are based on truck configurations that produce the maximum response in each component. Figure 7.2 and Figure 7.3 show the transverse truck locations used for determining the maximum response in each beam at the Chandler Creek bridge. Similar figures for the other bridges in this investigation are shown in Appendix G. The transverse position of the trucks shown in Figure 7.2 and Figure 7.3 are based on the AASHTO Standard and AASHTO LRFD design requirements.

Table 7.5 summarizes the rating factors and load ratings from Analysis D based on the tensile stress and flexural strength criteria for the bridges. The tensile stress rating factors range from 0.68 to 2.69, which correspond to load ratings of 13.5 to 53.8 ton. The increase in the tensile stress rating factor from Analysis D compared with Analysis A ranged from 25 to 40%, with an average of 35%. Two of the six bridges have a tensile stress rating factor below 1.0, as compared to four bridges based on Analysis A. The rating factors for the flexural strength criterion for Analysis D are also summarized in Table 7.5. The rating factors range from 1.09 to 2.13. When compared with the results from Analysis A, the flexural strength criterion increased an average of 7%. In Analysis D, the controlling rating factor for the bridges increased between 6 and 41%, which is an average increase of 26% when compared with Analysis A.

Both the tensile stress and flexural strength rating factors increased by approximately 18% when the results from Analysis D are compared with the results from Analysis C. This increase is directly attributable to the decrease in LLDF's based on the results of finite element analyses as compared with the LLDF's based on the provisions in the AASHTO LRFD.

Table 7.6 Summary of Load Rating Load Rating Analysis D

Bridge		Inventory Level Load Rating†			
		Tensile Stress Criterion		Flexural Strength Criterion	
		RF_{CT}	*RT* (ton)	RF_{FSINV}	*RT* (ton)
Chandler Creek	40-ft Span	1.69	33.7	1.28*	25.6
	60-ft Span	1.36	27.2	1.34*	26.7
Lake LBJ		1.26*	25.3	1.49	29.8
Lampasas River		0.68*	13.5	1.09	21.8
Willis Creek		0.89*	17.7	1.14	22.9
Wimberley		2.69	53.8	2.13*	42.6

* Controls load rating at inventory level.

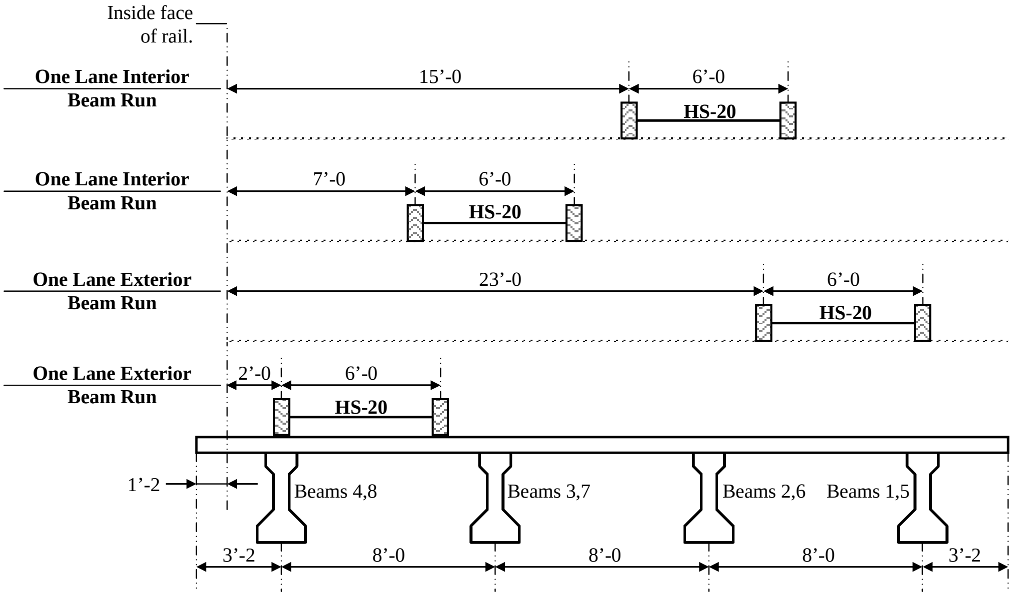

Figure 7.2 One-Design Lane Truck Configurations based on AASHTO Specifications Used for Finite Element Analyses of Chandler Creek Bridge

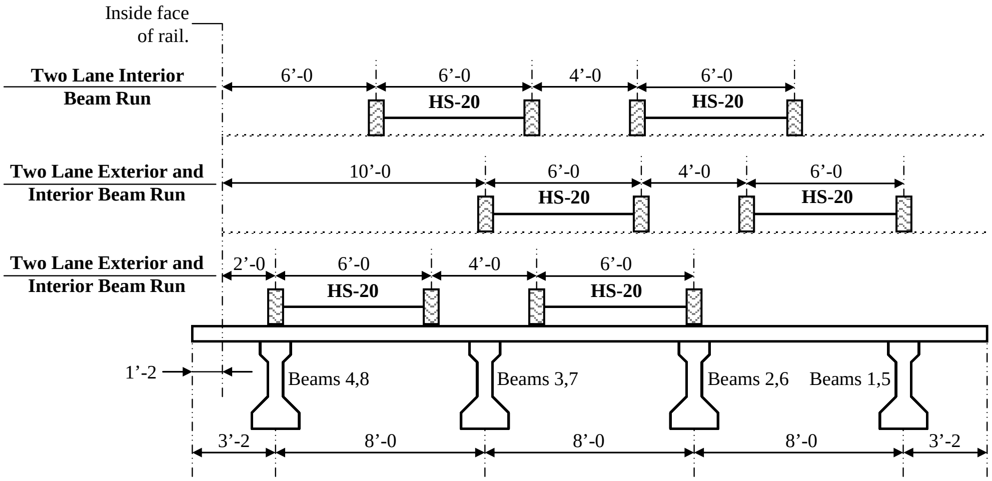

Figure 7.3 Two-Design Lane Truck Configurations based on AASHTO Specifications Used for Finite Element Analyses of Chandler Creek Bridge

7.2.4 Load Rating Analysis E

The load ratings summarized in this section are based on estimated in situ compressive strengths of the concrete, corresponding section properties and LLDF's based on finite element analyses with truck positioned in the transverse direction as specified by the AASHTO LRFD and AASHTO Standard. However, because refined estimates of compressive strength and advanced analyses are being used, the load factor from the MCEB is being used rather than the load factor from the AASHTO LRFD. It is believed that the 0.8 load factor in the AASHTO LRFD for the serviceability limit state is an attempt to account for the conservative design assumptions. These may include material strengths, live load distribution factors, and transverse position of the trucks. Based on this, it is considered inappropriate to use reduced load factors when more accurate estimates of material strengths and live load distribution factors are used simultaneously. Therefore, Analysis E differs from Analysis D in the choice to use estimated in situ material and section properties in lieu of the specified material and section properties and as a result of this choice the live load factor given in the MCEB is used in lieu of the reduced live load factor given in the AASHTO LRFD.

Table 7.7 summarizes the rating factors and load ratings from Analysis E based on the tensile stress and flexural strength criteria for the bridges. The tensile stress rating factors range from 0.71 to 2.37, which correspond to load ratings of 14.2 to 47.4 ton. The increase in the tensile stress rating factor from Analysis E compared with Analysis A ranged from 20 to 45%, with an average of 30%. Two of the six bridges have a tensile stress rating factor below 1.0, as compared to four bridges based on Analysis A. The rating factors for the flexural strength criterion for Analysis E are also summarized in Table 7.6. The rating factors range from 1.15 to 2.21. When compared with the results from Analysis A, the flexural strength criterion increased by an average of 10%. In Analysis E, the controlling rating factor for the bridges increased between 10 and 45%, which is an average increase of 26% when compared with Analysis A.

When the results for Analysis E are compared with the results from Analysis D, the change in the controlling rating factor for the bridges ranged between -6 and 6%, with an average increase of 1%. The average changes in the tensile stress rating factor and flexural strength rating were -4% and 4%, respectively. These results indicate that the use of the live load factor prescribed in the AASHTO LRFD for the serviceability limit state appears appropriate when load ratings are based on specified compressive strengths.

Table 7.7 Summary of Load Rating Load Rating Analysis E

Bridge		Inventory Level Load Rating†			
		Tensile Stress Criterion		Flexural Strength Criterion	
		RF_{CT}	*RT* (ton)	RF_{FSINV}	*RT* (ton)
Chandler Creek	40-ft Span	1.53	30.6	1.30*	26.1
	60-ft Span	1.29*	25.7	1.39	27.8
Lake LBJ		1.18*	23.6	1.55	31.1
Lampasas River		0.71*	14.2	1.15	23.1
Willis Creek		0.90*	18.0	1.22	24.3
Wimberley		2.37	47.4	2.21*	44.2

* Controls load rating at inventory level.

7.2.5 Load Rating Analysis F

The load ratings summarized in this section are based on estimated in situ compressive strengths, estimated in situ section properties and LLDF's based on finite element analyses with truck positioned in the center of the traffic lanes. Similarly to Analysis E, because refined estimates of compressive strength and advanced analyses are being used, the load factor from the MCEB is being used rather than the load factor from the AASHTO LRFD. Analysis F differs from Analysis E only in the choice of the transverse positioning of the vehicles.

While the transverse truck positions in the AASHTO LRFD and AASHTO Standard are appropriate for design, this assumption appears overly conservative for the evaluation of existing bridges at the inventory level. Therefore, the effect of locating the trucks in the center of the traffic lanes is investigated.

Table 7.7 summarizes the rating factors and load ratings from Analysis F based on the tensile stress and flexural strength criteria for the bridges. The tensile stress rating factors range from 0.81 to 2.67, which correspond to load ratings of 16.2 to 53.5 ton. The increase in the tensile stress rating factor from Analysis F compared with Analysis A ranged from 30 to 65%, with an average of

40%. As a result of the increased tensile stress rating factor, two of the six bridges have a tensile stress rating factor below 1.0, as compared to four bridges based on Analysis A. The rating factors for the flexural strength criterion for Analysis E are also summarized in Table 7.7. The rating factors range from 1.31 to 2.14. When compared with the results from Analysis A, the flexural strength criterion increased an average of 25%. In Analysis E, the controlling rating factor for the bridges increased between 10 and 65%, which is an average increase of 40% compared with Analysis A.

When the results for Analysis F are compared with the results from Analysis E, the controlling rating factor for the bridges increased by an average of 10%. The average increases in the tensile stress rating factor and flexural strength rating was 15% and 10%, respectively.

Table 7.8 Summary of Load Rating Load Rating Analysis F

Bridge		Inventory Level Load Rating[†]			
		Tensile Stress Criterion		Flexural Strength Criterion	
		RF_{CT}	RT (ton)	RF_{FSINV}	RT (ton)
Chandler Creek	40-ft Span	1.75	35.0	1.46*	29.2
	60-ft Span	1.52*	30.4	1.67	33.4
Lake LBJ		1.40*	28.1	1.71	34.3
Lampasas River		0.81*	16.2	1.36	27.2
Willis Creek		0.97*	19.4	1.31	26.2
Wimberley		2.67	53.5	2.14*	42.7

* Controls load rating at inventory level.

7.2.6 Summary of Load Ratings Analyses

Figure 7.4 summarizes the controlling load rating factors discussed in the previous sections for each bridge in this investigation. Figure 7.5 and Figure 7.6 summarize the tensile stress criterion and flexural strength criterion rating factors, respectively. The analyses identified in the figures correspond to the parameters given in Table 7.2.

Based on a comparison of Analysis C and Analysis D, the use of LLDF's from finite element analyses resulted in an average increase of 18% in the load ratings for the bridges. Therefore, taking advantage of the provisions in the MCEB that allow the use of refined analyses for determining LLDF's is recommended.

Based on a comparison of Analysis D and Analysis E, the use of estimated in situ compressive strengths in conjunction with the live load factor given in the MCEB resulted in load ratings that were similar when the reduced live load factor prescribed in the AASHTO LRFD was used in conjunction with specified compressive strengths. This suggests that the reduced live load factor given in the AASHTO LRFD approximates the effects of having in situ compressive strengths that are higher than specified. Therefore, it appears appropriate that the reduced load factor in the AASHTO LRFD be used when the load ratings are performed in a manner that is consistent with the provisions in the AASHTO LRFD; however, when assumptions beyond those anticipated by the AASHTO LRFD specification, such as estimating the in situ compressive strength of the concrete, or using the combination of trucks located in the center of the traffic lanes and finite element analyses, the use of the reduced live load factor is not recommended.

Based on a comparison of Analysis E and Analysis F, locating the design vehicles in the center of the traffic lanes in lieu of the transverse position that generate the maximum effects as prescribed in the AASTHO Standard and AASTHO LRFD, increased the load ratings an average of 10%.

For bridges that were controlled by the tensile stress criterion, the load ratings from Analysis F compared with Analysis A increased by 35 to 65%, with an average increase of 55%. Two of the four bridges that were controlled by the tensile stress criterion based on Analysis A have load ratings above the minimum specified in the MCEB based on Analysis F. The Willis Creek bridge has a load rating of 19.4 ton, which is 97% of the minimum load rating. Although the Lampasas river bridge does not have a load rating at or above the HS-20, the load rating was increased by 64%.

As previously discussed, Analysis B represents the upper limit of the load ratings being performed by TxDOT based on an arbitrary elevated tensile stress limit of $12\sqrt{f'_{cs}}$. The increase in the tensile stress limit resulted in an average increase in the load ratings of 35% over the provisions in the MCEB, which is represented by Analysis A. In lieu of using an arbitrary increase in the tensile stress limit to improve load ratings, a rational approach of using refined analyses and estimates of the in situ concrete compressive strengths is recommended. The results of these analyses are in Analysis F and yielded an average increase in the load ratings of 40% over the provisions in the MCEB for all the bridges considered in this investigation.

Although it appears that the simple approach to improving load ratings used in Analysis B yields similar results to the load ratings from Analysis F, which requires significantly more effort, a critical difference does exist. Analysis B represents an arbitrary increase in the limiting tensile stress and does not always provide conservative results. The increases in load ratings using Analysis B were largest for the Lampasas and Willis Creek bridges. As indicated in Figure 7.4, the increased load ratings are not supported by detailed analyses of these bridges. Therefore, the elevated tensile stress limit is not recommended for load rating prestressed concrete bridges. The fatigue limit state should be considered explicitly. Suggested procedures for incorporating fatigue into the load rating procedures for prestressed concrete bridges are given in Section 7.5.

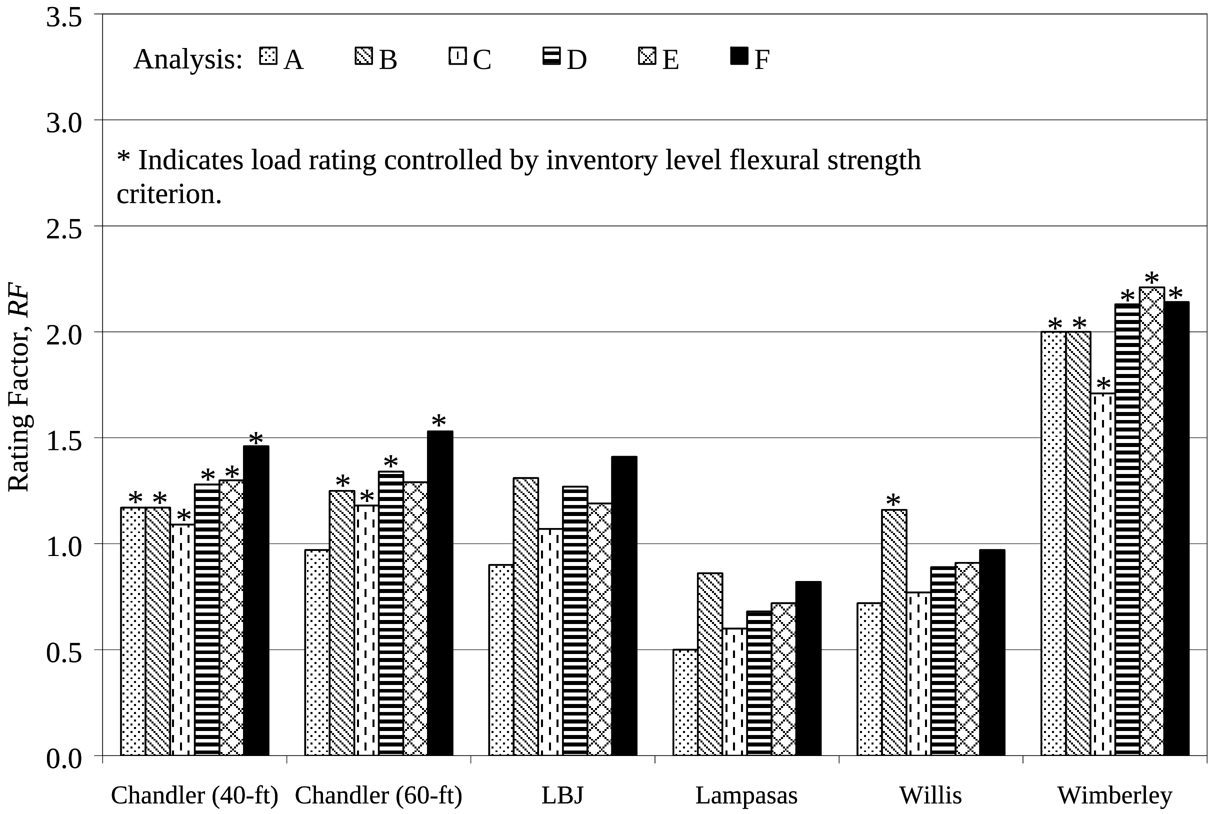

Figure 7.4 Summary of Controlling Load Rating Factors

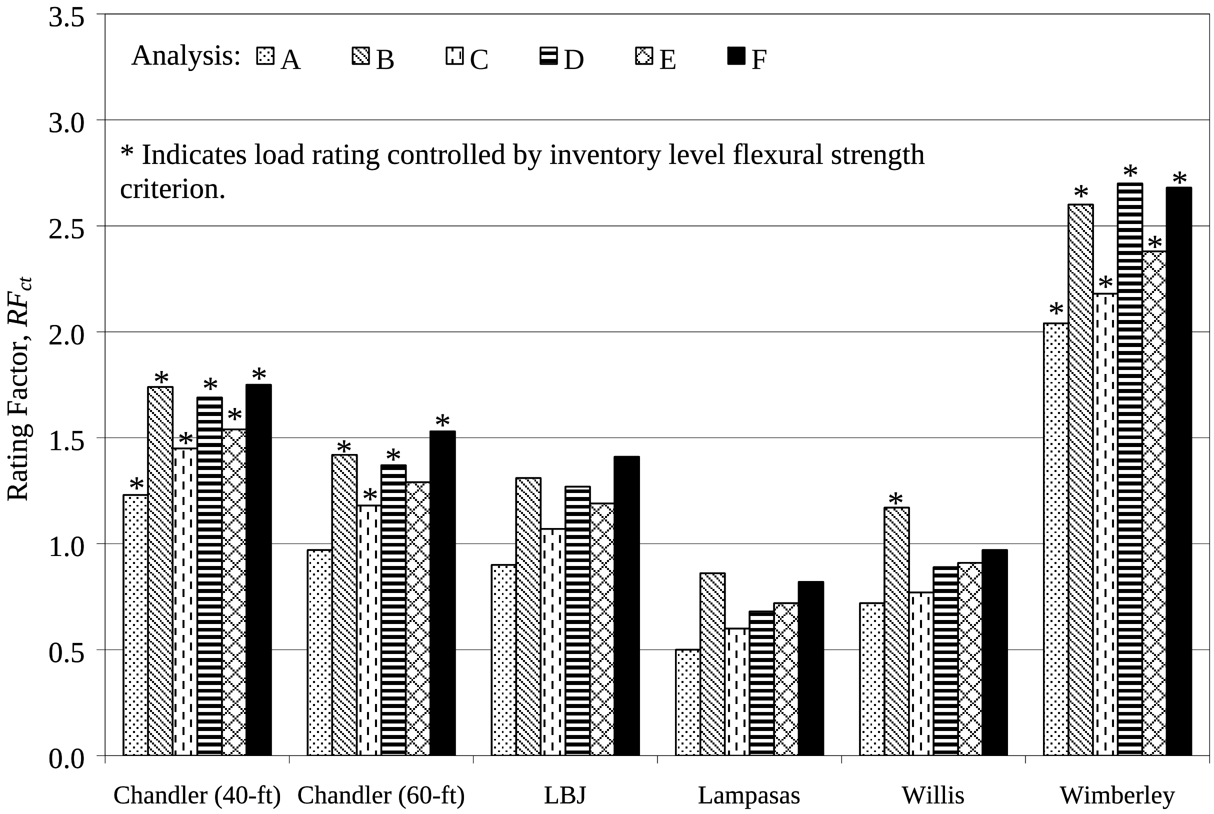

* Indicates load rating controlled by inventory level flexural strength criterion.

Figure 7.5 Summary of Tensile Stress Criterion Rating Factors

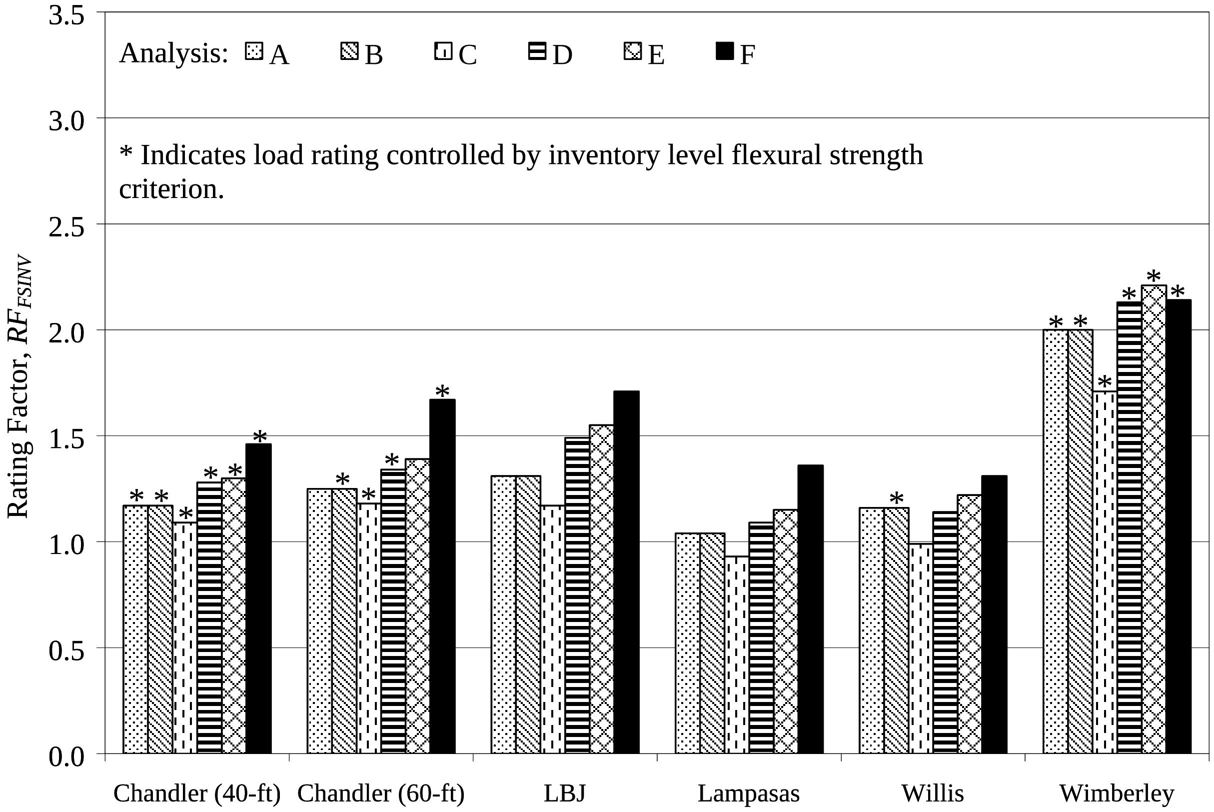

Figure 7.6 Summary of Inventory Level Flexural Strength Rating Factors

7.3 EVALUATION OF POSSIBILITY OF CRACKING UNDER SERVICE LOADS

Table 7.8 summarizes the moments required to produce an index stress of $3\sqrt{f'_{ce}}$ and $6\sqrt{f'_{ce}}$ in the interior beam of each bridge. The moment due to an HS-20 vehicle is calculated based on the load factors, LLDF's, vehicle positions, and material properties used in Analysis F. These moments are used to investigate the possibility that flexural cracks developed in the bridges under service loads. However, it is important to note that many factors, such as material strengths and traffic history, influence the extent of cracking. Therefore, these calculations alone may not be sufficient to determine whether cracks are present.

The HS-20 moment for both the Chandler Creek 40-ft span and Wimberley bridge are approximately 65% below the moment required to produce a tensile stress of $3\sqrt{f'_{ce}}$. Therefore, even with repeated cycles at, or slightly above, the HS-20 moment, it is unlikely that flexural cracks developed in these bridges. This conclusion is supported by the comparison of calculated and inferred neutral axis depths reported in Section 4.2, which shows the inferred neutral axis depths are within approximately 5% of the calculated values.

In contrast, the HS-20 moment for the Lampasas bridge is significantly above the moment required to produce a tensile stress of $3\sqrt{f'_{ce}}$. Therefore, loading cycles at, or slightly below, the HS-20 moment are likely to crack the prestressed concrete beams.. This conclusion is also supported by the comparison of the inferred neutral axis depths with the calculated neutral axis depths reported in Section 4.2, which shows the inferred neutral axis depths were significantly closer to the top of the section than calculated using gross composite section properties.

The comparison of the inferred and calculated neutral axis depths for Chandler Creek 60-ft span and Lake LBJ bridge indicate that flexural cracks are likely present. However, the moments summarized in Table 7.8 indicate that either a significant overload or a significant number of cycles above the HS-20 moment would be required to produce cracking. This discrepancy may be a result of the loading history of each bridge. The Chandler Creek bridge is located on the frontage road of a major highway and as reported in Table 2.1, has an a daily traffic volume of approximately 2,000 trucks. Therefore, it is also possible that a significant overload has occurred on this bridge in the 40 years it has been in service. The Lake LBJ bridge has a daily traffic volume of approximately 400 trucks, but is located less than five miles from a stone quarry. Therefore, it is possible that a significant overload has occurred during its 40 years in service. Without knowing the complete load history, it is impossible to determine if cracks formed in these beams. However, the measured strains and inferred neutral axis depths provide convincing evidence that the beams were cracked under service loads.

It is difficult to draw conclusions regarding flexural cracking for the Willis Creek bridge. The comparison of inferred and calculated neutral axis depths indicates that the bridge may not be cracked. The comparison of moments summarized in Table 7.8 indicates that a relatively small overload or a repeated number of cycles slightly below the HS-20 moment could produce flexural cracks. The Willis Creek bridge is located on a rural road and is subjected to approximately 130 trucks daily. Therefore, it is possible that the bridge has not seen a sufficient number of cycles that would produce a tensile stress of $3\sqrt{f'_{ce}}$ or an overload that would produce flexural cracking.

Based on the discussion in this section, it is clear that the presence of flexural cracks can not be determined solely from the load rating calculations. As discussed, the traffic history for a particular bridge is also important in evaluating the potential for the existence of flexural cracks. For the bridges in this investigation, the condition could be established using the results of the diagnostic load tests; however, performing diagnostic load tests to determine the condition of bridges is neither practical, nor economical. Determining the presence of flexural cracks is important for the bridges considered in this investigation because the possibility of fatigue problems increases dramatically in prestressed concrete beams with flexural cracks.

Table 7.9 Comparison of Live-Load Moments for Bridges

Bridge Name	Live Load Moments*, ft-kip		
	Moment Corresponding to an Index Stress of $3\sqrt{f'_{ce}}$ ††	Moment Corresponding to an Index Stress of $6\sqrt{f'_{ce}}$ ††	Moment Due to HS-20 Vehicle†
Chandler Creek (40-ft Span)	490	630	310
Chandler Creek (60-ft Span)	740	980	550
Lake LBJ	780	1000	580
Lampasas River	570	790	710
Willis Creek	460	670	580
Wimberley	410	540	280

* Moments calculated for typical interior beam.

† Moments were calculated using load rating parameters from Analysis F, assuming two design lanes and the impact factor based on AASHTO LRFD, rather than the AASHTO Standard (Table 7.1).

†† Moment calculated using gross, transformed composite section properties.

7.4 CONSIDERATION OF STRESS RANGE IN THE STRAND

The load ratings discussed in Section 7.2 do not explicitly consider the fatigue limit state. In this section, the stress range in the strand is considered as a criterion for load rating. In addition, the tensile stress criterion in the MCEB is evaluated to determine if it is adequate for estimating the fatigue life of prestressed concrete bridges.

7.4.1 Fatigue Design Provisions in the AASHTO LRFD

The AASHTO LRFD provides loading criteria and maximum ranges of stress in the strand for the design of prestressed concrete beams for the fatigue limit state. No specific provisions are included in the AASHTO LRFD that relate to the fatigue of concrete. However, as discussed in Chapter 1, the stress levels in the concrete for typical prestressed concrete beams at fatigue load levels are generally significantly lower that the fatigue strength of the concrete.

The loading prescribed in the AASHTO LRFD for the fatigue limit state corresponds to one design vehicle, the HS-20 truck, which is shown in Figure 7.1. However, the spacing of the rear axles is fixed at 30 ft for the fatigue limit state. A dynamic load allowance of 15% is also specified for the fatigue limit state, which results in a dynamic impact factor of 1.15. For the fatigue live load, a load factor of 0.75 is prescribed. The distribution of the fatigue live load to individual members in the bridge may be calculated using the AASHTO LRFD provisions for one design lane, which are discussed in Chapter 4, or using refined methods of analysis. Although the AASHTO LRFD specifies a multiple presence factor of 1.2 for one design lane, which is intended to account for the worst case scenario, the AASHTO LRFD does not require that the multiple presence factor be used when designing for fatigue. Where refined methods of analysis are used, the AASHTO LRFD requires that vehicles be positioned transversely and longitudinally to produce the maximum stress range in the detail or member being considered, regardless of the position of the traffic lanes or design lanes.

The provisions in the AASHTO LRFD require that fatigue for prestressed concrete beams be considered only if the compressive stress in the precompressed zone is less than twice the tensile stress caused by the prescribed fatigue loading based on uncracked section properties.

When fatigue must be considered, the AASHTO LRFD provides the following limits on the stress range in the strand:

1. For prestressed concrete beams that have a tendon profile with a radius of curvature in excess of 30 ft, the range of stress in the strand shall not exceed 18 ksi.
2. For prestressed concrete beams that have a tendon profile with a radius of curvature in not exceeding 12 ft, the range of stress in the strand shall not exceed 10 ksi.
3. A linear interpolation may be used for prestressed concrete beams that have a tendon profile between 12 and 18 ft.

The AASHTO LRFD does not limit the number of cycles that the bridge may experience at the above stress ranges, and it is therefore assumed that the above stress limits are based on an infinite fatigue life. However, the AASHTO LRFD provides guidelines for the expected frequency of fatigue loads:

$$ADTT_{SL} = p \times ADTT \tag{7.5}$$

where $ADTT_{SL}$ is single lane average daily truck traffic, $ADTT$ is the number of trucks per day in one direction averaged over the design life, and p is the fraction of trucks in a single lane and is taken as 1.00, 0.85 and 0.80 for 1, 2 and 3 or more traffic lanes, respectively.

Where traffic data are not available for a bridge, the AASHTO LRFD provides the values in Table 7.9 which are based on research that indicates the number of vehicles per lane is physically limited to approximately 20,000 vehicles per lane per day under normal conditions and that trucks make up 10 to 20% of those vehicles depending on the class of highway being considered. Based on a 75-year design life, these values correspond to between 54 and 110 million cycles of the fatigue loading. Table 7.10 shows the average daily truck traffic and number of fatigue cycles expected for a 75-year design life for the bridges in this investigation based on the traffic data provided by TxDOT, which is given in Table 2.1.

Table 7.10 Average Daily Truck Traffic Provided by AASHTO LRFD for Bridges Where Site Specific Data are Not Available

Class of Highway Being Considered	*ADTT*	Cycles for 75-year Design Life (million)
Rural Interstate	4,000	109.5
Urban Interstate	3,000	82.1
Other Rural	3,000	82.1
Other Urban	2,000	54.8

Table 7.11 Average Daily Truck Traffic for Bridges in this Investigation

Bridge	*ADTT**	Cycles for 75-year Design Life (million)
Chandler Creek	2,000	54.8
Lake LBJ	420	11.5
Lampasas River	250	6.8
Willis Creek	130	3.6
Wimberley	510	14.0

* Based on data recorded by TxDOT between 1999 and 2000.

Based on the design fatigue life model proposed by Paulson (1983), which appears appropriate for prestressed concrete beams with straight strand, the stress ranges of 18 ksi and 10 ksi correspond to approximately 4 and 32 million fatigue cycles, respectively. Based on the fatigue life model for prestressed concrete beams with depressed strands proposed by Muller and Dux (1994), the stress ranges of 18 ksi and 10 ksi correspond to approximately 0.5 and 0.8 million cycles, respectively. Therefore, the limits on stress range in the strand prescribed by the AASHTO LRFD appear to be inappropriate as an infinite fatigue life criterion and provisions relating the range of stress in the strand to the number of fatigue cycles are discussed in Section 7.5.

7.4.2 AASHTO LRFD Fatigue Requirements for the Bridges in this Investigation

As discussed in Section 7.4.1, the AASHTO LRFD only requires that fatigue be considered if the sustained compressive stress at the bottom fiber of a section is less than twice the tensile stress caused by the fatigue design vehicle. Table 7.11 summarizes the fatigue moments and corresponding tensile stresses for the interior beams of the bridges considered in this investigation. The corresponding fatigue moment in the member is calculated using the fatigue moment for the bridge (Table 7.12) and live load distribution factors based on the AASHTO LRFD specification (Table 4.12). The corresponding tensile stress was calculated assuming uncracked cross-sectional properties, and estimated in situ material properties.

Table 7.12 summarizes the in situ compressive stress for the interior beams of the bridges. The calculated stress accounts for all prestress losses and dead loads applied to the member. The in situ compressive stress is compared with the tensile stress from Table 7.11, and the AASHTO LRFD requirement to design for fatigue is evaluated. As shown in Table 7.12, five of the six bridges would be required to be designed for fatigue based on the current provisions in the

AASHTO LRFD specification. The Wimberley bridge is the only bridge that would not be required to be designed for fatigue. It is also reasonable to conclude that older bridges that would be required to be designed for fatigue based on the current design provisions should be load rated using fatigue as a criterion.

Table 7.12 Calculated Tensile Stress at Bottom Fiber of Interior Beams Corresponding to Fatigue Design Vehicle and Live Load Distribution Factors from AASHTO LRFD Specification

Bridge	Fatigue Moment for Bridge* (ft-kip)	Fatigue Moment for Member** (ft-kip)	Corresponding Tensile Stress† (psi)
Chandler Creek 40-ft Span	282	139	288
Chandler Creek 60-ft Span	455	200	266
Lake LBJ	524	225	295
Lampasas River	680	272	375
Willis Creek	524	209	301
Wimberley	281	129	284

* Calculated using parameters for fatigue limit state (Table 7.1).

** Calculated using live load distribution factors for interior beams based on AASHTO LRFD specification. (Table 4.12)

† Calculated gross, transformed, composite section properties and estimated in situ material properties.

Table 7.13 Evaluation of AASHTO Fatigue Design Criterion Using AASHTO LRFD Live Load Distribution Factors

Bridge	Bottom Fiber Compressive Stress* (psi)	2 x Tensile Stress from Table 7.11	Fatigue Check Required**
Chandler Creek 40-ft Span	580	577	No
Chandler Creek 60-ft Span	469	532	Yes
Lake LBJ	468	590	Yes
Lampasas River	129	750	Yes
Willis Creek	227	602	Yes
Wimberley	1084	569	No

* Net compressive stress assuming all prestress losses and all dead load, and based on analyses of members using estimated in situ material and section properties.

** Based on AASHTO LRFD design requirement that fatigue be checked if compressive stress is less than twice the tensile stress due to the design vehicle.

The results summarized in Tables 7.11 and 7.12 were repeated using live load distribution factors based on the results of finite element analyses corresponding to transverse truck positions that produce the maximum effect in the member (Table 4.10). The results of this analysis are summarized in Tables 7.13 and 7.14.

As shown in Table 7.14, the number of bridges that would be required to be designed for fatigue is reduced from five to two. The observation that the use of advanced analyses did not eliminate the need to design for fatigue supports the previous conclusion that a criterion for load rating based the fatigue limit state is appropriate.

Table 7.14 Calculated Tensile Stress at Bottom Fiber of Interior Beams Corresponding to Fatigue Design Vehicle and Live Load Distribution Factors from Finite Element Analyses

Bridge	Fatigue Moment for Bridge* (ft-kip)	Fatigue Moment for Member** (ft-kip)	Corresponding Tensile Stress[†] (psi)
Chandler Creek 40-ft Span	282	110	230
Chandler Creek 60-ft Span	455	159	212
Lake LBJ	524	178	233
Lampasas River	680	218	300
Willis Creek	524	167	241
Wimberley	281	104	229

* Calculated using parameters for fatigue limit state (Table 7.1).

** Calculated using live load distribution factors for interior beams based on the results of finite element analyses. (Table 4.10)

[†] Calculated gross, transformed, composite section properties and estimated in situ material properties.

Table 7.15 Evaluation of AASHTO Fatigue Design Criterion Using Live Load Distribution Factors from Finite Element Analyses

Bridge	Bottom Fiber Compressive Stress* (psi)	2 x Tensile Stress from Table 7.13	Fatigue Check Required**
Chandler Creek 40-ft Span	580	560	No
Chandler Creek 60-ft Span	469	424	No
Lake LBJ	468	466	No
Lampasas River	129	600	Yes
Willis Creek	227	482	Yes
Wimberley	1084	458	No

* Net compressive stress assuming all prestress losses and all dead load, and based on analyses of members using estimated in situ material and section properties.

** Based on AASHTO LRFD design requirement that fatigue be checked if compressive stress is less than twice the tensile stress due to the design vehicle.

7.5 RECOMMENDED CRITERIA FOR INCORPORATING FATIGUE CONSIDERATIONS INTO LOAD RATING PROCEDURES

As discussed in Section 7.3, the results of this investigation do not support increasing the tensile stress limit given in the MCEB for load rating prestressed concrete bridges. The index stress does not provide an adequate representation of the tensile stresses in the prestressing strand. Rather, the stress range in the strand should be considered explicitly in any refined load rating procedure. Three fatigue criteria are presented in this section.

It should be noted that unlike the serviceability and strength criteria given in the MCEB for loading rating, the proposed fatigue criteria are not used to quantify the maximum vehicle weight corresponding to inventory or operating levels. The proposed fatigue criteria are used only to check that the selected fatigue vehicle will not generate stresses that will cause premature fatigue damage to the bridge. Because the relationship between applied live load and strand stress range is nonlinear for prestressed concrete beams, separate analyses must be conducted for each fatigue vehicle considered. In developing the fatigue criteria, the AASHTO LRFD design vehicle and load factors for fatigue (Table 7.1) were used.

7.5.1 Overview of Proposed Fatigue Criteria

Three fatigue criteria were developed for load rating prestressed concrete bridges. The first criterion is based on the existing design procedures in the AASHTO LRFD specifications and is intended to provide a simple check of the susceptibility of the bridge to fatigue damage. As discussed in Section 7.4.1, the LRFD design procedures indicate that fatigue can be ignored if the calculated tensile stress in the concrete at the bottom fiber of the cross section, with a live load equal to two times the fatigue design vehicle, is less than the calculated compressive stress at the extreme fiber under the full dead load.

Although the stress range in the strand is not calculated directly using this procedure, this approach offers two distinct advantages over the other two proposed criteria: (1) the criterion is simple to apply because all calculations are based on gross cross-sectional properties, and (2) the criterion is conservative because the moment due to the prescribed live load are less than the decompression moment for the beam.

The influence of flexural cracking is considered in the second and third criteria, where the stress range in the strand must be calculated using the cracked, composite cross-sectional properties. The calculated strand stress range is then compared with a fatigue life model for prestressed concrete beams. The maximum stress range corresponding to an infinite fatigue life is used in the second criterion, while the calculated stress range and the expected number of loading cycles during the 75-year design life of the bridge are compared with the finite fatigue model in the third criterion.

The fatigue model proposed for prestressed concrete beams is presented in Section 7.5.2. The three fatigue criteria are described in Sections 7.5.3 through 7.5.5. The six spans studied in this investigation are evaluated using the three criteria in Section 7.6. The choice of the fatigue vehicle will be discussed in Section 7.7.

7.5.2 Proposed Fatigue Life Model for Prestressed Concrete Beams

The proposed strand stress ranges for load rating prestressed concrete bridges are based on the results of laboratory fatigue tests. Figure 7.7 is a plot of the measured strand stress range, S_r, as a function of the number of number of cycles to failure, N. The individual points plotted in Figure 7.7 correspond to the prestressed concrete beams tested in this investigation and the investigations summarized in Chapter 1. Beams with both depressed and straight tendon profiles are included. It should be noted that the beams tested by Muller and Dux (1994) with depressed tendons that were bundled and/or had large hold downs were not considered, because these beams are not considered to be representative of current practice.

Equation 7.6 was developed using the data shown in Figure 7.7 to relate the stress range in the strand to the expected fatigue life. A total of eighty-four prestressed concrete beams were considered. Sixty-four beams had straight strands, and twenty beams had depressed strands.

$$Log(N) = 8.8 - 2.3Log(S_r) \tag{7.6}$$

where S_r is greater than 5 ksi.

As shown in Figure 7.7, Eq. 7.6 is more conservative than the fatigue life model proposed by Paulson (1983) for stress ranges below 70 ksi. Sixty-two of the of the sixty-four of the beams with straight strands and eighteen of the twenty beams with depressed strands survived more loading cycles at a given stress range than estimated using Eq. 7.6. Therefore, Eq. 7.6 is conservative for 93% of the available data.

Only four beams were subjected to fatigue loads with a strand stress range below 10 ksi. All four tests were terminated before fatigue failures were observed; therefore, no experimental data are available to support the development of the fatigue life model in this critical range of response. The decision to establish the boundary between the finite and infinite fatigue life at a stress range of 5 ksi was arbitrary and is considered to be conservative. A stress range of 5 ksi corresponds to a fatigue life of approximately 15,000,000 loading cycles using Eq. 7.6.

Based on the fatigue life model given in Figure 7.7, two ranges of response are defined for prestressed concrete beams:

(1) <u>Infinite Fatigue Life:</u> If the calculated stress range in the strand due to the fatigue vehicle is less than 5 ksi, the prestressed concrete beam is assumed to have an infinite fatigue life.

(2) <u>Finite Fatigue Life:</u> If the calculated stress range in the strand due to the fatigue vehicle exceeds 5 ksi, the fatigue life of the prestressed concrete beam should be estimated using Eq. 7.6.

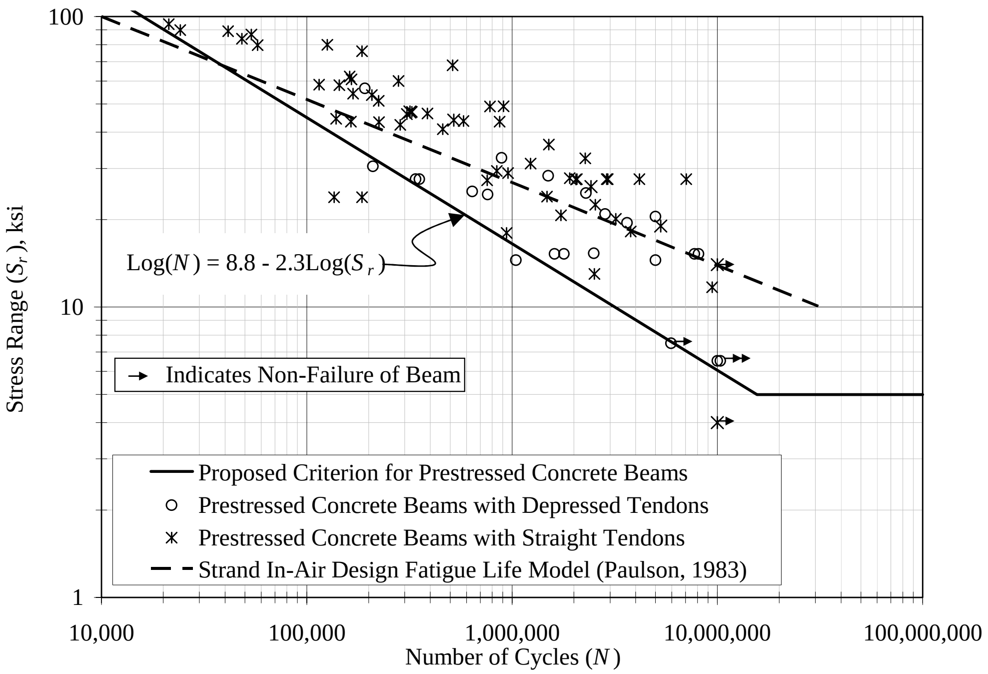

Figure 7.7 Recommended Finite Fatigue Model for Load Rating Prestressed Concrete Bridges Using Strand Stress Range

7.5.3 Fatigue Criterion Based on the Decompression Load

The first fatigue criterion is based on the current AASHTO LRFD design requirements for fatigue (Section 7.4.2). The fatigue criterion factor, $F1$, is given in Eq. 7.7.

$$F1 = \frac{F_p - A_1 F_d}{2A_2 F_{lf}(1+I)} \tag{7.7}$$

where F_p is the unfactored compressive stress at the bottom fiber due to prestressing after all losses, F_d is the unfactored tensile stress at the bottom fiber due to dead loads, and F_{lf} is the unfactored tensile stress at the bottom fiber due to the AASHTO LRFD fatigue design vehicle. The values of A_1, A_2, and I are given in Table 7.1 for the fatigue limit state. All stresses used in Eq. 7.7 are calculated assuming gross section properties.

A bridge is considered to have an infinite fatigue life if the fatigue criterion factor, $F1$, is greater than 1.0 based on Eq. 7.7. Bridges that satisfy this requirement do not need to be checked using the second or third fatigue criteria. . However, if $F1$ is less than 1.0, the fatigue life of the bridge must be evaluated using the calculated stress range in the strand.

7.5.4 Fatigue Criterion Based on Infinite Fatigue Life

The calculated stress range in the strand is compared directly with the stress range corresponding to an infinite fatigue life using the second criterion. It is important to note that a cracked-section analysis must be used to evaluate the stress range in the strand. The cracked-section analysis may be performed using simple analyses, as discussed in Appendix J for the bridges considered in this investigation, or using commercially available software.

The fatigue criterion factor, $F2$, is given in Eq. 7.8.

$$F2 = \frac{5}{\Delta F_f} \tag{7.8}$$

where ΔF_f is the calculated strand stress range due to the fatigue design vehicle in ksi and 5 ksi is the maximum stress range corresponding to an infinite fatigue life (Figure 7.7). The value of ΔF_f is calculated using the load and impact factors given in Table 7.1 for the fatigue limit state.

Based on Eq. 7.8, a bridge is considered to have an infinite fatigue life if the fatigue criterion factor, $F2$, is greater than 1.0. It should be noted that the fatigue criterion factors $F1$ and $F2$ are not related. The gross cross-sectional properties are used in the analyses that form the basis for $F1$, while cracked cross-sectional properties are used in the analyses that form the basis for $F2$. In addition, the fatigue design vehicle is used to calculate stress range in Eq. 7.8, while the design vehicle is multiplied by a factor of two in Eq. 7.7 to determine if the tensile stresses due to live load at the extreme fiber exceed the decompression load. Therefore, the live load used to evaluate the second fatigue criterion is half the live load used to evaluate the first fatigue criterion. As a result of the different assumptions used to calculate the first and second fatigue criterion factors, a bridge that does not satisfy the fatigue criterion based on the decompression load may still be considered to have an infinite fatigue life if it satisfies the second fatigue criterion.

Bridges that satisfy the infinite life fatigue criterion requirement do not need to be checked using the third fatigue criterion. However, if $F2$ is less than

1.0, the fatigue life of the bridge must be evaluated by considering the expected number of loading cycles.

7.5.5 Fatigue Criterion Based on Finite Fatigue Life

The calculated stress range in the strand is compared directly with the stress range corresponding to a finite fatigue life using the third criterion. The fatigue criterion factor, $F3$, is given in Eq. 7.9.

$$F3 = \frac{S_r}{\Delta F_f} \tag{7.9}$$

where S_r is calculated from Eq. 7.6 using the number of loading cycles expected based on the average daily truck traffic and a 75-year design life and ΔF_f is calculated using the same procedures described in Section 7.5.4.

Based on Eq. 7.9, the fatigue life of a bridge exceeds the 75-year design life if the fatigue criterion factor, $F3$, is greater than 1.0. It is important to note that if the traffic volumes on the bridge change significantly, this fatigue criterion must be re-evaluated.

7.6 LOAD RATING FOR INTERIOR BEAMS INCLUDING FATIGUE CRITERIA

The bridges considered in this investigation were evaluated using the three fatigue criteria proposed in Section 7.5. Two sets of analyses were performed, and the input parameters are summarized in Table 7.20. Both analyses used estimated in situ material and cross-sectional properties, the MCEB live load factors for rating criteria other than fatigue, and the LRFD live load factor of 0.75 for fatigue. Because fatigue was considered explicitly in these analyses, the tensile stress load rating criterion described in Section 7.1.1 was not considered. The difference between the two analyses is that Analysis G uses LLDF’s calculated using the equations in the AASHTO LRFD and Analysis H uses LLDF's calculated using the results of finite element analyses.

Table 7.16 Summary of Load Rating Analyses Including Fatigue

Load Rating Analysis	Live Loads			Material Properties
	Load Factor for Live Load	LLDF's	Transverse Truck Position	
G	MCEB/ LRFD*	AASHTO LRFD	NA	Estimated In Situ
H	MCEB/ LRFD*	Finite Element Analyses	Located to Produce Maximum Response	Estimated In Situ

* Live load factors for serviceability and capacity limit states are taken from the MCEB. Live load factors for fatigue limit state are taken from the LRFD. Values of all parameters are given in Table 7.1.

7.6.1 Load Rating Analysis G

The calculated values of $F1$ for the six spans considered in this investigation are reported in Table 7.17. The live loads do not exceed the decompression load for two of the six spans. Therefore, the 40-ft span of the Chandler Creek bridge and the Wimberley bridge are assumed to have infinite fatigue lives based on the first fatigue criterion. This result is expected because these were the only two spans that were assumed not to have cracked under service loads (Section 7.3).

The values of $F1$ for the remaining four spans were less than 1.0; therefore, the strand stress range must be calculated to evaluate the other two fatigue criteria. Values of ΔF_f are reported in Table 7.18 and vary from 2.1 to 3.9 ksi. Because the calculated stresses do not exceed 5 ksi, all spans satisfy the second fatigue criterion and all six spans are assumed to have an infinite fatigue life. It was, therefore, not necessary to check the third fatigue criterion.

The load ratings calculated using the other criteria in the MCEB are reported in Appendix I and the controlling ratings are summarized in Table 7.19. For all bridges considered in this investigation, the flexural strength criterion controlled the load ratings based on the parameters for Analysis G. The rating factors ranged from 0.99 to 1.78 which corresponds to ratings of 19.8 to 25.6 ton. Five of the six bridges have load ratings that satisfy the minimum requirements of the MCEB and all of the bridges are expected to have an infinite fatigue life. It is important to note that the standard fatigue vehicle was used to evaluate the fatigue life of the bridges, and not the vehicle corresponding to the controlling load rating.

Table 7.17 Summary of First Fatigue Criterion – Analysis G

Bridge	F_{lf}^{*}, psi	$F_p - A_1F_d$, psi	$F1$
Chandler Creek 40-ft Span	334	580	1.01
Chandler Creek 60-ft Span	308	469	0.88
Lake LBJ	342	468	0.79
Lampasas River	435	129	0.17
Willis Creek	349	227	0.38
Wimberley	329	1084	1.91

* If the values of F_{lf} are multiplied by $A_2(1+I)$, the resulting tensile stresses equal the values reported in Table 7.11.

Table 7.18 Summary of Second Fatigue Criterion – Analysis G

Bridge	ΔF_f, ksi	$F2$
Chandler Creek 40-ft Span*	2.8	1.8
Chandler Creek 60-ft Span	2.3	2.2
Lake LBJ	2.7	1.9
Lampasas River	3.9	1.3
Willis Creek	2.9	1.7
Wimberley*	2.1	2.4
* Bridge satisfies fatigue criterion $F1$, and does not need to be evaluated using fatigue criterion $F2$. Results are reported for completeness.		

Table 7.19 Summary of Controlling Load Ratings for Analysis G

Bridge	Controlling Criterion	Controlling Rating Factor	Controlling Load Rating
Chandler Creek 40-ft Span	Flexural Strength	1.12	22.3
Chandler Creek 60-ft Span	Flexural Strength	1.22	25.4
Lake LBJ	Flexural Strength	1.23	24.7
Lampasas River	Flexural Strength	0.99	19.8
Willis Creek	Flexural Strength	1.05	21.0
Wimberley	Flexural Strength	1.78	25.6

7.6.2 Load Rating Analysis H

The results from Analysis H are essentially the same as those from Analysis G. Four of the six spans satisfied the first fatigue criterion (Table 7.20) and all spans satisfied the second fatigue criterion (Table 7.21). The only significant difference between the two analyses is that the Lampasas River bridge now satisfies the load rating criterion for flexural strength (Table 7.22), with a rating factor of 1.15.

Using the parameters defined in Analysis H, all six spans have load ratings that satisfy the minimum requirements in the MCEB and all are considered to have infinite fatigue lives.

Table 7.20 Summary of First Fatigue Criterion – Analysis H

Bridge	F_{lf}*, psi	$F_p - A_1F_d$, psi	FC_I
Chandler Creek 40-ft Span	267	580	1.26
Chandler Creek 60-ft Span	246	469	1.11
Lake LBJ	270	468	1.00
Lampasas River	348	129	0.22
Willis Creek	279	227	0.47
Wimberley	266	1084	2.37

* If the values of F_{lf} are multiplied by $A_2(1+I)$, the resulting tensile stresses equal the values reported in Table 7.13.

Table 7.21 Summary of Second Fatigue Criterion – Analysis H

Bridge	ΔF_f, ksi	$F2$
Chandler Creek 40-ft Span*	2.2	2.3
Chandler Creek 60-ft Span*	1.8	2.8
Lake LBJ*	2.0	2.6
Lampasas River	3.1	1.6
Willis Creek	2.2	2.3
Wimberley*	1.7	2.9
* Bridge satisfies fatigue criterion $F1$, and does not need to be evaluated using fatigue criterion $F2$. Results are reported for completeness.		

Table 7.22 Summary of Controlling Load Ratings for Analysis H

Bridge	Controlling Criterion	Controlling Rating Factor	Controlling Load Rating
Chandler Creek 40-ft Span	Flexural Strength	1.30	26.1
Chandler Creek 60-ft Span	Flexural Strength	1.39	27.8
Lake LBJ	Flexural Strength	1.55	31.1
Lampasas River	Flexural Strength	1.15	23.1
Willis Creek	Flexural Strength	1.22	24.3
Wimberley	Flexural Strength	2.21	44.2

7.7 SELECTION OF FATIGUE RATING VEHICLE

As discussed in Section 7.5, the decision was made to use the design fatigue vehicle from the AASHTO LRFD specifications to evaluate the fatigue characteristics of the prestressed concrete bridges considered in this investigation. One of the consequences of this decision is that the unfactored live load moments corresponding to an HS-20 vehicle with a rear axle spacing of 30 ft are considerably less than those corresponding to an HS-20 vehicle with a rear axle spacing of 14 ft, which was used to evaluate the other load rating criteria. As shown in Table 7.23, the unfactored live load moments with a rear axle spacing of 30 ft are 67 to 77% of the live load moments with a rear axle spacing of 14 ft. Given that the spans of the bridges considered varied from 40 to 75 ft, the rear axle spacing of 30 ft seems to be too long, as the specified rear axle spacing represented 40 to 75% of the spans.

For the class of prestressed concrete bridge considered in this investigation, trucks with shorter axle spacings, such as gravel or concrete trucks, will likely generate the highest moments under service loads. It is therefore recommended that a vehicle representative of the actual traffic loads be used to evaluate the fatigue life of the prestressed concrete brides. Selection of that vehicle, however, is beyond the scope of this investigation.

Table 7.23 Comparison of Live Load Moments for HS-20 Vehicle with Rear Axle Spacings of 14 and 30-ft

Bridge	Unfactored Live Load Moment, ft-kip		M_{30}/M_{14}
	14-ft Rear Axle Spacing, M_{14}	30-ft Rear Axle Spacing, M_{30}	
Chandler Creek 40-ft Span	425	327	0.77
Chandler Creek 60-ft Span	781	527	0.67
Lake LBJ	871	607	0.70
Lampasas River	1053	788	0.75
Willis Creek	871	607	0.70
Wimberley	422	325	0.77

7.8 SUMMARY

The load rating criteria given in the MCEB were used in Section 7.2 to evaluate six prestressed concrete bridges. Because the MCEB provides the engineer with the flexibility to use advanced analyses and measured characteristics of the bridge, a series of six analyses were conducted to evaluate the sensitivity of the load rating to the choice of input parameters. Using a rational approach that combined finite element analyses and the estimated in situ comrpessive strength of the concrete, the load ratings increased approximately 40% compared with the simple provisions in the MCEB.

Because flexural cracks significantly increase the potential for fatigue problems in prestressed concrete bridges, the possiblity that flexural cracks developed during the service life of the bridges was evaluated. The load rating criteria were found to be insufficient to assess the presence of flexural cracks. Therefore, it was considered appropriate to assume that cracks were present and evaluate the fatigue life of the bridges directly.

A conservative relationship was developed between the strand stress range and the expected fatigue life of prestressed concrete beams. In addition, three rating criteria for fatigue were proposed as an alternative to the current tensile stress criterion for load rating. All the bridges considered in this investigation had an infinite fatigue life based on the proposed criteria and exceeded the minimum load rating of HS-20. This result is consistent with the conclusions of TxDOT personnel following periodic inspections of the bridges: no evidence of deterioration was observed.

CHAPTER 8

Recommendations and Conclusions

8.1 SUMMARY OF INVESTIGATION

Five prestressed concrete bridges constructed in the 1950s and 1960s were studied in this investigation. Using the current procedures in the AASHTO Manual for Condition Evaluation of Bridges (1994, Interim 2003) the load rating for each bridge was limited by the serviceability criterion related to the calculated tensile stress at the extreme fiber of the cross section. In addition, the inventory rating for four of the five bridges was less than the current design vehicle. The results of the load rating calculations did not agree with the results of visual inspections of the bridges, as no evidence of structural deterioration was observed. The primary objective of this investigation was to develop appropriate methods for improving the load ratings of existing prestressed concrete bridges.

All five bridges were two-lane, simply-supported, highway bridges composed of prestressed concrete beams and a composite cast-in-place deck. Although the bridges were similar in layout and construction, their overall dimensions varied. The spans varied between 40 and 75 ft, roadway widths varied between 24 ft and 28 ft-8 in., beam spacing varied between 6 ft-8 in. and 8 ft, and skew angles varied between 0° and 30°. Design documents and available quality control test reports were collected for each of the bridges.

A total of eight spans on the five bridges were visually inspected, instrumented and load tested. Five of the eight spans tested had load ratings controlled by the concrete tensile stress criterion prescribed by the MCEB and the resulting load ratings were less than HS-20 for these spans. The three spans that did not have a load rating controlled by the tensile stress criterion were the shortest considered with overall spans of 40 ft.

No signs of flexural cracking in the concrete or corrosion of the prestressing strand were observed during the visual inspections. Based on these observations, it was concluded that all the spans selected for testing were in good condition.

Each span was load tested using standard dump trucks weighing between 20 and 25 ton. Several load paths and vehicle configurations were used at each bridge site to obtain a comprehensive view of the live load distribution characteristics of the spans being investigated.

Measured data collected during the load tests were used to determine live load distribution factors (LLDF) for each bridge. The inferred LLDF's were compared with LLDF's calculated using the design provisions in the AASHTO Standard (2002) and LRFD (2003) specifications, and using the results of finite element analyses.

As a percent of total live load moment, the average difference between LLDF's based on the results of finite element analyses and those inferred from the measured strains was less than 5%. These results are similar to results reported by Barr, et al. (2001), confirming that finite element analyses provide a relatively simple means of determining the live load response of bridges.

LLDF's based on the AASHTO LRFD were calculated to be between 91% and 114% of the LLDF's based on the AASHTO Standard for the bridges in this investigation. In addition, for trucks centered in the traffic lanes, both the AASHTO LRFD and AASHTO Standard LLDF's were approximately 25% higher than those calculated using finite element analyses. Similarly, for trucks positioned transversely to induce the maximum response in each bridge beam, the AASHTO LRFD and AASHTO Standard LLDF's were approximately 20%

higher than LLDF's calculated using finite element analyses. Therefore, using LLDF's calculated from finite element analyses will lead to higher load ratings for the class of prestressed concrete bridge considered.

The in situ compressive strengths of the concrete in the prestressed beams and cast-in-place slabs were estimated using quality control test records and the ACI-209 (1992) model for the increase of concrete compressive strength as a function of time.

Measured strains from the diagnostic load tests were used to calculate live load moments using gross cross-sectional properties corresponding to the specified and estimated in situ compressive strengths. The inferred live load moments were then compared with live load moments calculated using finite element analyses. On average, the inferred live load moments calculated using the specified compressive strengths were 40% lower than the values from finite element analyses. In contrast, the inferred live load moments calculated using the estimated in situ compressive strengths were on average 15% lower than the values from the finite element analyses. Therefore, it was concluded that the estimated in situ compressive strengths were a reasonable approximation of the actual concrete compressive strengths in the field.

An interior beam from the 60-ft span of the Chandler Creek bridge was selected as the prototype for the laboratory fatigue tests. Three levels of index stress (the tensile stress at the extreme fiber calculated using gross cross-sectional properties) were used to establish live-load levels in the prototype: $6\sqrt{f'_{ce}}$, $7.5\sqrt{f'_{ce}}$, and $12\sqrt{f'_{ce}}$. The strand stress ranges corresponding to these levels of live load (14, 20, and 40 ksi) were then used as the targets for the laboratory specimens.

It was also concluded that for a particular member, the strand stress range increases as the index stress increases. However, a particular index stress does not correspond to a unique strand stress range when multiple bridges are considered. Therefore, it was concluded that the index stress should not be used as an indicator of the fatigue life of prestressed concrete beams.

The two laboratory specimens tested with calculated strand stress ranges of 7 and 14 ksi survived 10 million loading cycles and exhibited no appreciable degradation beam behavior. The two specimens tested with calculated strand stress ranges of 22 and 25 ksi had fatigue lives of 5.4 and 2.4 million cycles, respectively. The two specimens tested with a calculated strand stress range of 47 ksi had fatigue lives of 0.3 and 0.5 million cycles, respectively. These results are comparable with those from previous experimental investigations.

Measured data could not be collected during the actual fatigue tests; therefore, static tests were performed periodically. The data collected during the static tests include measured strains and displacements and were used to evaluate changes in behavior of the specimens throughout the fatigue tests. In particular, distinct changes in beam stiffness were directly correlated to the number of wire failures observed in the beams.

Analyses of the bridges considered in this investigation, evaluation of the measured data, and the results of the laboratory fatigue tests confirmed the assumption that prestressed concrete bridges are likely to crack under service loads. Even at repeated cycles that cause tensile stresses in the concrete as low as $3\sqrt{f_c'}$, cracking of the concrete will occur. As discussed in Chapter 1, fatigue related problems increase significantly in prestressed concrete beams after flexural cracks develop. In particular, fatigue of the prestressing strands may occur more rapidly due to the stress concentrations at the cracks caused by the discontinuity in the concrete.

Because flexural cracks are expected, calculations based on the gross cross-sectional properties are not considered to be representative of the response of prestressed concrete bridges. The current tensile stress criterion in the MCEB is not sufficient to ensure the fatigue does not limit the life of these bridges. Therefore, fatigue criteria were proposed as an alternative to the tensile stress criterion for load rating.

The recommendations related to of this investigation are divided into two groups. The first set of recommendations address methods for improving the load ratings of existing prestressed concrete bridges using the current provisions in the MCEB and are summarized in Section 8.2. The second set of recommendations address methods for considering the fatigue response of prestressed concrete bridges explicitly in the load rating process and are summarized in Section 8.3.

8.2 SUMMARY FOR IMPROVED LOAD RATING USING THE CURRENT MCEB PROVISIONS

Several aspects of the load rating procedure were investigated in this dissertation with the intent of improving the load rating process for the prestressed concrete bridges in Texas. The bridges investigated are limited to a class of bridges for which the load rating is controlled by the concrete tensile stress criterion and the bridges display no visual indications of deterioration. Specifically, the bridges in this investigation were designed in the 1950s and 1960s, have prestressed concrete beams with a specified compressive strength of approximately 5,000 psi, two design lanes, and spans between 40 ft and 75 ft. The applicability of these recommendations to modern structures, in particular those with overall spans significantly greater than 75 ft and with specified concrete compressive strengths significantly higher than 5,000 psi, has not been investigated.

The recommendations discussed in this section are intended to be used with the current provisions of the MCEB. Specific issues addressed include the choice of concrete compressive strength, the transverse position of loading vehicles, and the calculation of the live load distribution factors.

8.2.1 Material Properties

The MCEB currently permits properties representative of the existing structure to be used in load rating. Techniques recommended for determining the concrete compressive strength include nondestructive methods, such as the Schmidt hammer and Windsor probe, and destructive methods, such as drilling cores.

As an alternative to the field tests mentioned in the MCEB, it has been proposed to use the results of quality control test records to estimate the in situ concrete compressive strength. Quality control test records were obtained from TxDOT for four of the five bridges considered in this investigation. The in situ concrete compressive strengths were estimated using the oldest available measured concrete compressive strengths and the ACI 209 (1992) model for relating concrete compressive strength to age. The 28-day compressive strengths of the concrete in the prestressed beams were estimated to be 48 to 72% higher than the specified compressive strengths, while the in situ strengths were estimated to be 74 to 106 % higher than the specified strengths. Based on the data collected during the load tests and the results of the analyses discussed in Chapter 4, the estimates of in situ compressive strength appear to be conservative. Therefore, the method of estimating the in situ compressive strength of the concrete presented in Section 2.2.3 is recommended for load rating procedure prestressed concrete bridges.

8.2.2 Live Loads

The MCEB (2003) uses the design truck, number of lanes, transverse position of vehicle loads, and live load factors given in the 1989 AASHTO Standard Specification for Highway Bridges (AASHTO Standard) for the load rating calculations. The design truck is defined as the standard HS-20 vehicle.

Two issues were considered in the parametric study described in Section 7.2: the choice of load and impact factors and the transverse position of the loading vehicle. When the other recommendations described in this section are adopted, the live load factor of 1.0 given in the MCEB for serviceability limit states appears to be appropriate. The impact factor of 0.33 given in the AASHTO LRFD specifications also appears to be appropriate.

The MCEB requires that trucks be positioned transversely on the bridge to produce the maximum response in each member when advanced analysis or properties of the existing bridge are being used for load rating. While the commentary to the MCEB does not discuss this requirement, the commentary to the AASHTO LRFD addresses a similar requirement for fatigue loads. The provision is included in the LRFD design requirements to account for possible changes in the lane configurations during the life of the bridge.

This requirement appears to be conservative for load rating, and it is recommended that trucks be positioned in the center of the lanes regardless of the level of sophistication of analyses or bridge properties being used in the analysis. However, the load ratings should be updated if the lane configurations change.

8.2.3 Live Load Distribution Factors

The MCEB currently uses the provisions in the 1989 AASHTO Standard specification to calculate the live load distribution factors (LLDF). The results from this investigation, as well as studies by Mabsout et al. (1997) and Barr et al. (2001), indicate that these LLDF's are extremely conservative.

As discussed in Chapter 7, the LLFD's calculated based on the Interim 2003 AASHTO LRFD Design Specifications for Bridges have been found to be a more accurate representation of the actual live load response of existing bridges. This increase in accuracy comes as a result of an increase in the complexity of the calculations, as compared with the AASHTO Standard provisions. The increase in complexity allows for the modeling of behavior that the simple calculations in the AASTHO Standard do not. The difference between LLDF's calculated using the AASHTO Standard and the AASTHO LRFD ranges between -9% and 14% for the bridges in this investigation. As a result, simply updating to the AASHTO LRFD LLDF's will not significantly improve load ratings, and in some instances it may reduce them.

The LLDF's calculated based on the finite element analyses performed as part of this investigation correlate well with the measured data from the load tests. Similar results were found in the previous studies discussed in Chapter 1. When using LLDF's based on loads positioned in the center of the traffic lanes, finite element analyses resulted in an average decrease of 26% in LLDF's from the AASHTO Standard and AASHTO LRFD. Similarly, when using LLDF's based on loads positioned to produce the maximum response in each member, finite element analyses resulted in an average decrease of 20% in LLDF's from the AASHTO Standard and AASHTO LRFD. Therefore, it is recommended that for the purpose of improving load ratings, finite element analyses be used to determine LLDF's.

8.2.4 Tensile Stress Criterion

The tensile stress criterion in the MCEB represents a serviceability criterion used to load rate prestressed concrete bridges. The purpose of the criterion is to limit cracking in prestressed concrete beams that could lead to deterioration of strength. In addition, the criterion is for load rating at the inventory level. The inventory level load rating defines the load that the member can resist for an indefinite period of time.

The current limit for prestressed beams in the MCEB is $6\sqrt{f'_c}$ (psi), where f'_c is typically taken as the specified concrete compressive strength. Because of the discrepancy between their field inspections and the low load ratings that result from the current criterion, TxDOT increased the limit to $12\sqrt{f'_c}$, based on the limit for concrete building structures in ACI 318 (1995).

Based on the results of the fatigue tests described in Chapter 5, it is recommended that the limit of $6\sqrt{f'_c}$ for load rating based on the tensile stress criterion be maintained. When considering the set of bridges included in this investigation, no unique relationship between the index stress and strand stress range was identified. In addition, beams subjected to fatigue loads in the laboratory experienced flexural cracks at index stress levels less than $3\sqrt{f'_{cm}}$. Loads exceeding the $6\sqrt{f'_c}$ level may not cause damage, but it is not possible to assess the likelihood of fatigue damage without considering the strand stress range explicitly.

Therefore, in lieu of using an arbitrary increase in the tensile stress limit to improve load ratings, a rational approach of using refined analyses and estimates of the in situ concrete compressive strengths is recommended.

8.2.5 Impact of Revised Load Rating Procedures

The rating factors for the bridges considered in this investigation ranged from 0.5 to 2.0 when the provisions of the MCEB were applied with all the default assumptions. The load ratings for four of the six spans were controlled by the tensile stress criterion, and the inventory ratings for all four spans were less than the standard HS-20 vehicle.

When the recommendations described in this section were used, the range of rating factors increased to 0.8 to 2.1. Although the load ratings for four of the six spans were still controlled by the tensile stress criterion, only two of the spans had inventory ratings less than the standard HS-20 vehicle.

The improved load ratings were accomplished with slight modifications to the provisions in the MCEB and without changing the tensile stress limit, other than using the estimated in situ compressive strength of the concrete rather than the specified compressive strength.

8.3 RECOMMENDED FATIGUE CRITERIA FOR LOAD RATING PRESTRESSED CONCRETE BRIDGES

The recommendations presented in Section 8.2 address methods for improving the load ratings of prestressed concrete bridges using the current criteria in the MCEB. However, the results of this investigation have shown that fatigue should be considered explicitly for load rating prestressed concrete bridges. The existing tensile stress criterion provides only an indirect representation of the fatigue response of these bridges. Because existing prestressed concrete beams are likely to experience cracks under service loads, the stress range in the strand should be considered to determine if fatigue loads will limit the life of prestressed concrete beams. A fatigue life model and three fatigue criteria were proposed for load rating prestressed concrete bridges.

8.3.1 Proposed Fatigue-Life Model

A total of eighty-four prestressed concrete beams, with both straight and depressed strand profiles, were used to develop the fatigue life relationship shown in Fig. 8.1. Two ranges of response are defined for prestressed concrete beams:

(1) Infinite Fatigue Life: If the calculated stress range in the strand due to the fatigue vehicle is less than 5 ksi, the prestressed concrete beam is assumed to have an infinite fatigue life.

(2) Finite Fatigue Life: If the calculated stress range in the strand due to the fatigue vehicle exceeds 5 ksi, the fatigue life of the prestressed concrete beam should be estimated using Eq. 7.6.

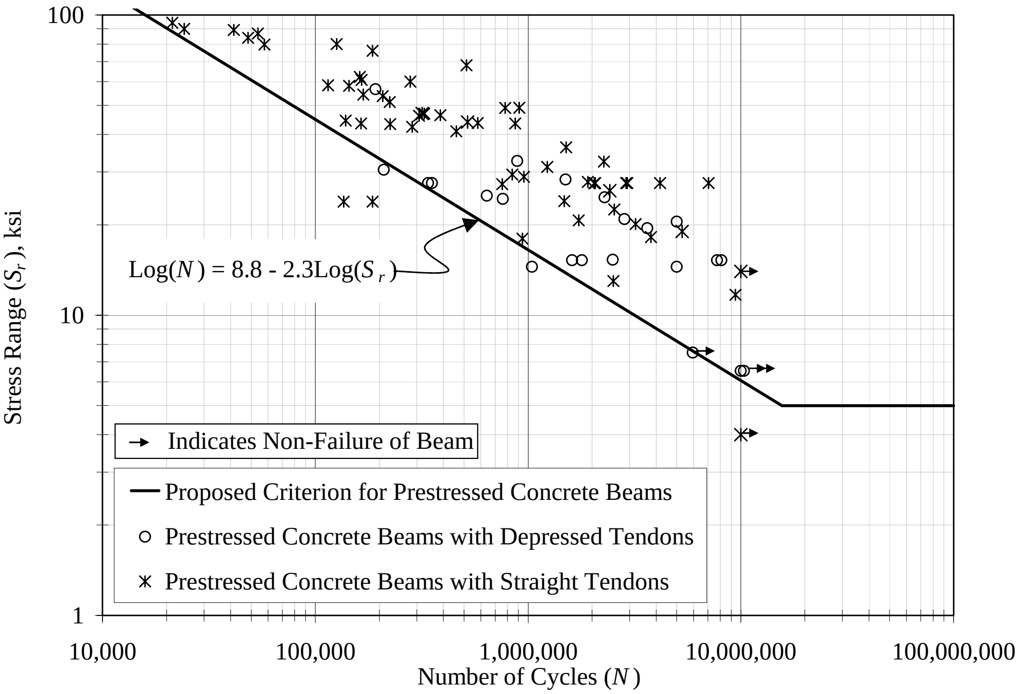

Figure 8.1 Recommended Finite Fatigue Model for Load Rating Prestressed Concrete Bridges Using Strand Stress Range

8.3.2 Proposed Fatigue Criteria for Load Rating

Three criteria were proposed to incorporate fatigue considerations into the load rating procedures for prestressed concrete bridges. These fatigue criteria replace the tensile stress criterion given in the MCEB.

The first fatigue criterion is based on the current AASHTO LRFD design requirements for fatigue and compares the tensile stresses due to live loads at the extreme fiber with the compressive stresses at the extreme fiber due to dead loads (Eq. 7.7). If the live-load response of the beam remains below the decompression load, the beam is considered to have an infinite fatigue life. If the beam does not satisfy this criterion, the stress range in the strand due to live loads must be evaluated.

The first fatigue criterion is easily checked because gross cross-sectional properties are used for all calculations. This criterion is also considered to be conservative. Beams that do not satisfy this criterion may have an infinite fatigue life, but additional calculations are required to reach this conclusion.

The second criterion (Eq. 7.8) compares the calculated stress range in the strand with a stress range of 5 ksi, which is assumed to correspond to an infinite fatigue life.

Although both the first and second fatigue criteria are used to identify beams with infinite fatigue lives, two important differences must be noted. Gross cross-sectional properties are used to evaluate the first fatigue criterion, while cracked cross-sectional properties are used to evaluate the second. The fatigue design vehicle used to evaluate the first fatigue criterion is twice as heavy as the fatigue vehicle used to evaluate the second. As a result of these differences, a bridge that does not satisfy the fatigue criterion based on the decompression load may still be considered to have an infinite fatigue life if the calculated stress range in the strand is less than 5 ksi.

When considering the third fatigue criterion, the stress range in the strand and the expected number of loading cycles must be considered. The number of loading cycles is estimated using the average daily truck traffic and a 75-year design life. The calculated stress range in the strand is then compared with the stress range corresponding to the required fatigue life (Eq. 7.9).

If the stress range corresponding to the required fatigue life exceeds the stress range in the strand due to fatigue loads, fatigue is not expected to limit the design life of the bridge. However, if the stress range in the strand due to the fatigue loads exceeds the stress range corresponding to the required fatigue life, the Department of Transportation must either reduce the allowable loads on the bridge or plan to replace the bridge earlier than anticipated during design. Because traffic volume is expected to increase with time, the third fatigue criterion should be re-evaluated periodically for all bridges with finite fatigue lives.

8.3.3 Impact of Proposed Load Rating Procedures

All the bridges considered in this investigation satisfied the criteria for infinite fatigue life. This result is expected, because the bridges have been in service for more than 30 years and no indication of structural deterioration has been observed.

The proposed fatigue criteria do not, however, provide an inventory-level load rating for the bridges. Rather, the fatigue criteria simply indicate if the selected fatigue vehicle is likely to generate sufficient loads to limit the fatigue life of the bridge. The remaining criteria in the MCEB must still be used to establish an inventory-level load rating.

When considering the recommendations given in Section 8.2 and the fatigue criteria described in this section, all five bridges had inventory ratings that exceeded the standard HS-20 vehicle. The revised load ratings were between 20 and 100% higher than the original ratings calculated using the MCEB with all the default assumptions.

The advantages of the recommended procedures are clear: the inventory-level load ratings for prestressed concrete bridges constructed in the 1950s and 1960s are higher, yet the susceptibility to fatigue damage has been considered directly. While the revised procedures will require more engineering calculations, the economic savings in terms of fewer bridges with posted loads should be significant.

8.4 ADDITIONAL RESEARCH NEEDS

In the development of the proposed recommendations, two issues were identified that require additional research.

As discussed in Section 7.7, the choice of fatigue vehicle does not appear to be appropriate for the class of bridges considered. The fatigue vehicle used in the AASHTO LRFD design specifications may be appropriate for long-span bridges, but trucks with a rear axle spacing less than 30 ft are likely to generate higher live-load moments in bridges with spans less than 75 ft. Selection of the appropriate fatigue vehicle for load rating will depend on the traffic patterns for the bridge and was considered to be beyond the scope of this investigation.

The choice of the stress range corresponding to the infinite fatigue life (Section 7.5.2) was also arbitrary. Only four of the eighty-four beams considered were subjected to fatigue loads with a strand stress range below 10 ksi, and none of these beams actually failed in fatigue. Additional testing is required to determine if the 5 ksi level is appropriate.

APPENDIX A

Bridges in This Investigation

Information about each of the five bridges tested in this investigation is summarized in this appendix. Each section includes a photograph, plan, cross section details and diaphragm details for one bridge. Tables of section dimensions and beam properties are presented in Section A.6. A summary of all the bridges considered for detailed investigation in this study is presented in Section A.7.

A.1 CHANDLER CREEK BRIDGE

Figure A.1 Photograph of Chandler Creek Bridge

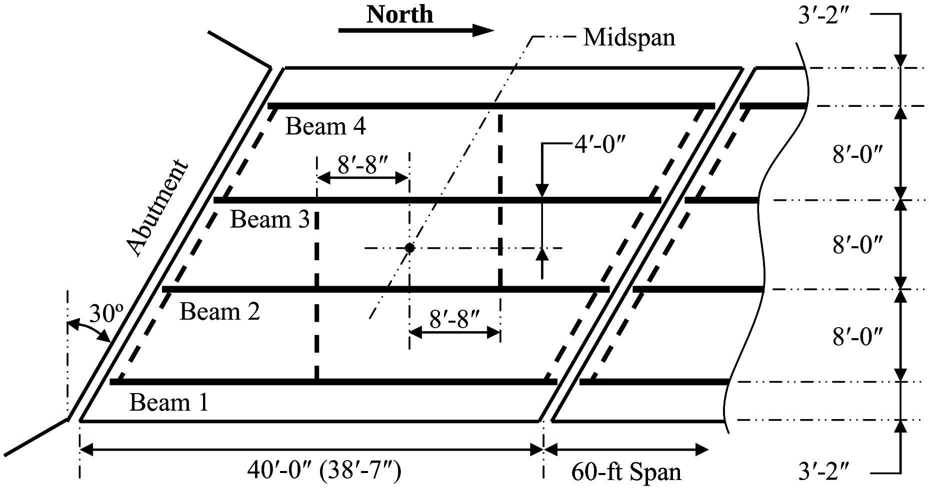

(a) 40-ft Span

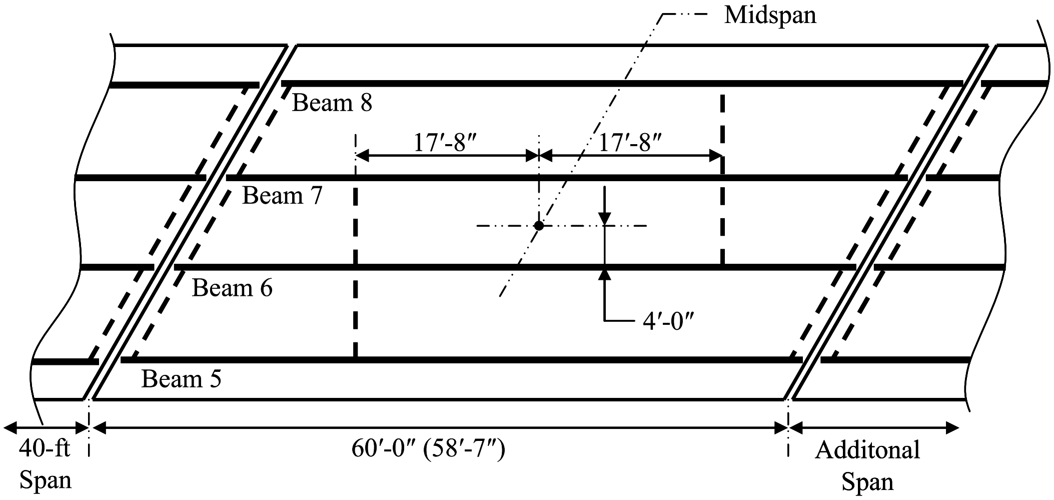

(b) 60-ft Span

━━ Beam Locations

- - - Diaphragm Locations

#′-#″(#′-#″) Overall Length (Effective Span Length, L_{eff})

Figure A.2 Plan of Chandler Creek Bridge

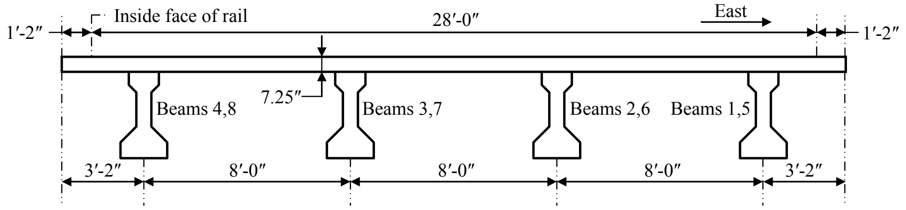

(a) Cross Section

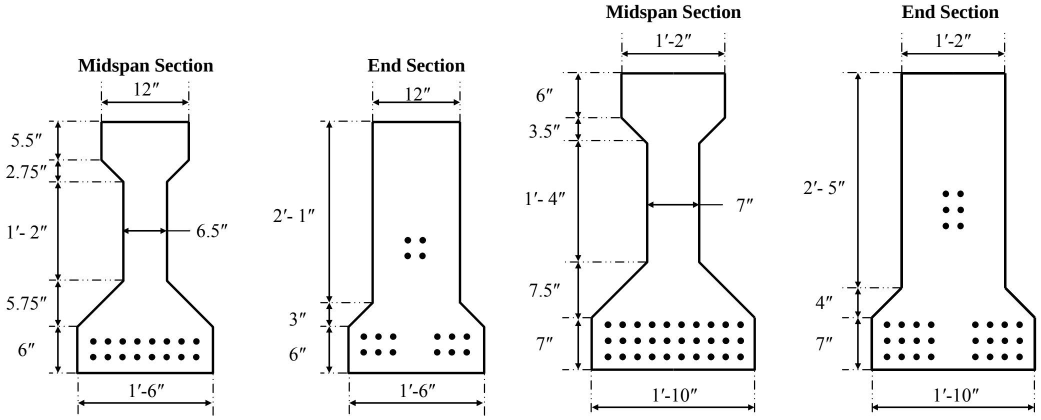

(b) Type B Beams (40-ft Span)

(c) Type C Beams (60-ft Span)

Figure A.3 Cross Section and Beam Details for Chandler Creek Bridge

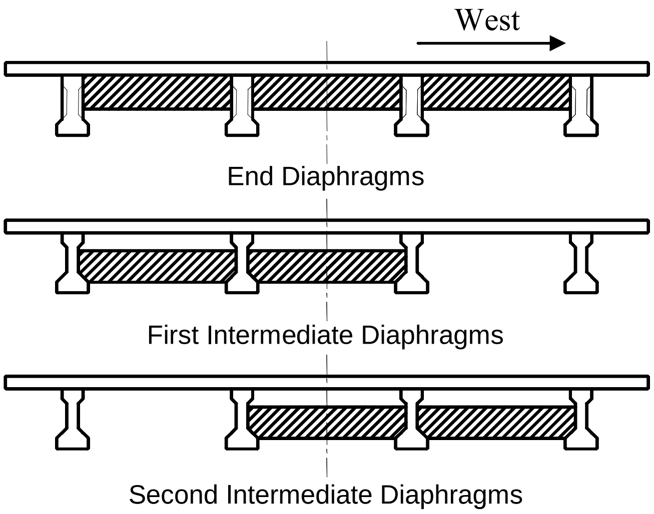

(a) 40-ft Span

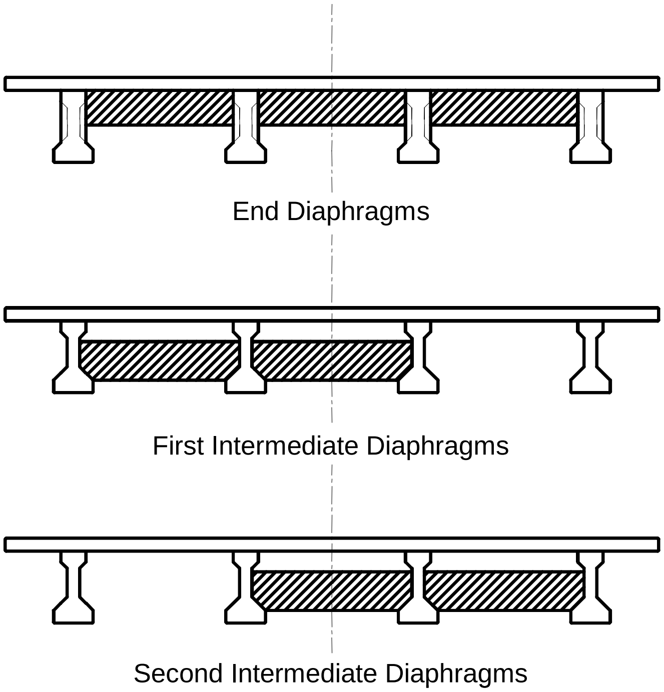

(b) 60-ft Span

Figure A.4 Diaphragm Details for Chandler Creek Bridge (Wagener 2002)

A.2 LAKE LBJ BRIDGE

Figure A.5 Photograph of Lake LBJ Bridge

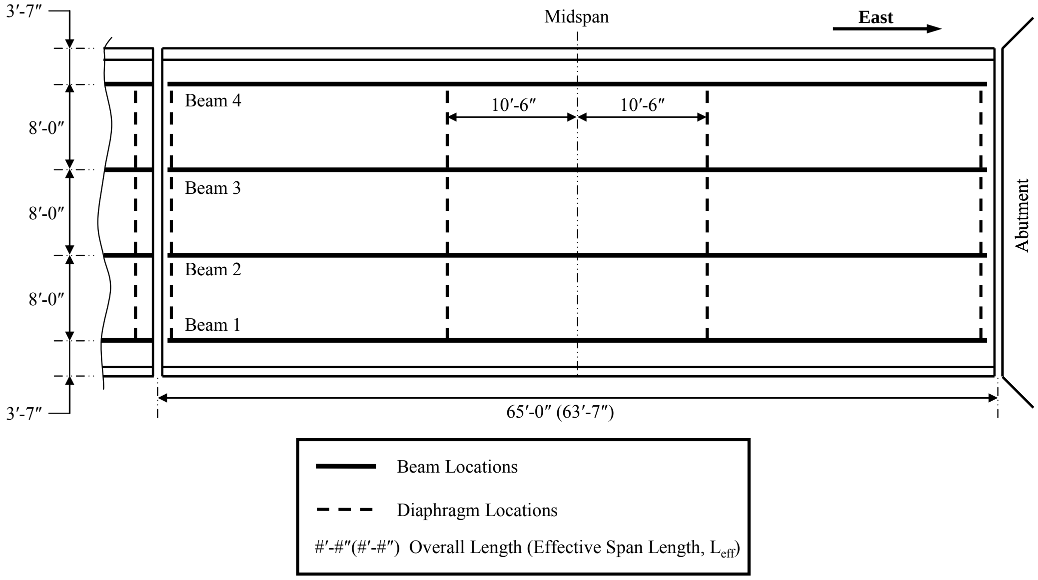

Figure A.6 Plan of Lake LBJ Bridge

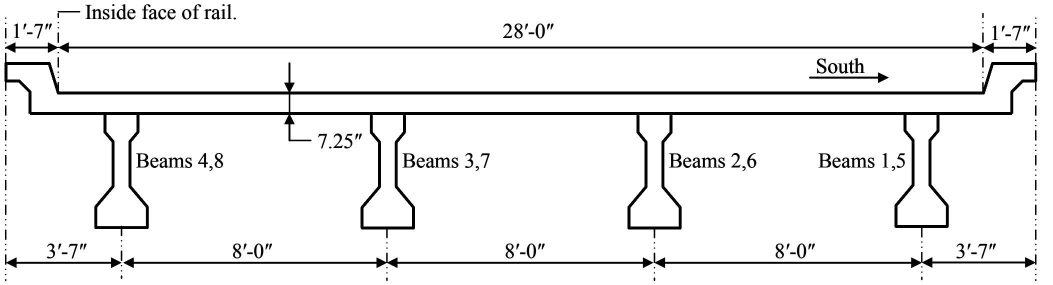

(a) Cross Section

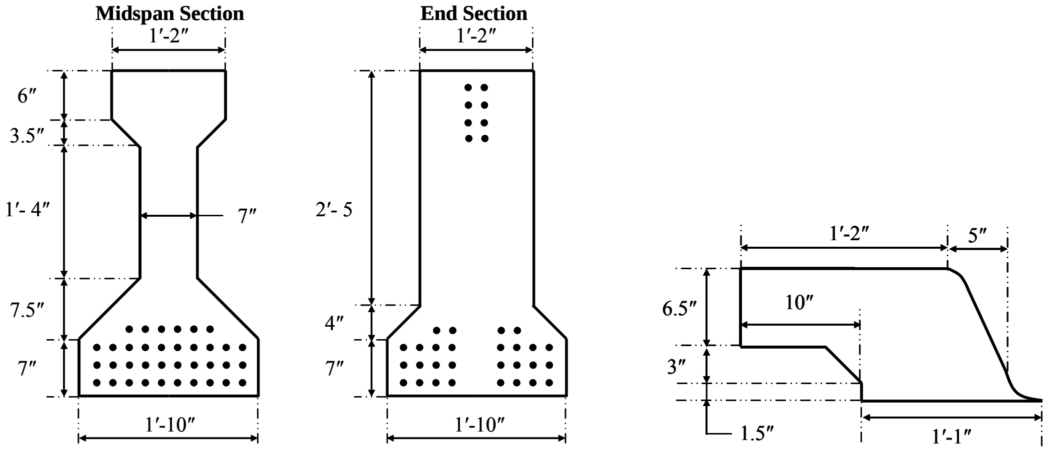

(b) Type C Beams **(c) Curb Detail**

Figure A.7 Cross Section, Beam, and Curb Detail for Lake LBJ Bridge

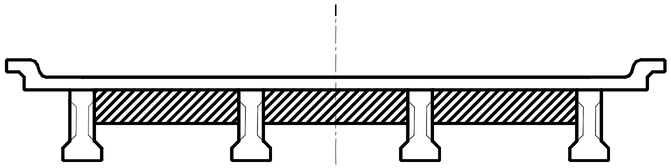

End Diaphragms

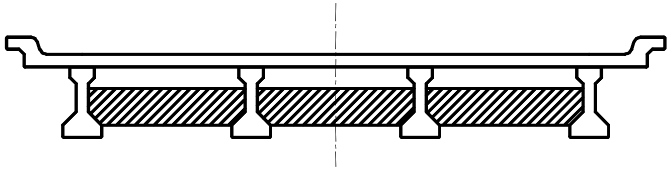

Intermediate Diaphragms

Figure A.8 Diaphragm Details for Lake LBJ Bridge (Wagener 2002)

A.3 LAMPASAS RIVER BRIDGE

Figure A.9 Photograph of Lampasas River Bridge

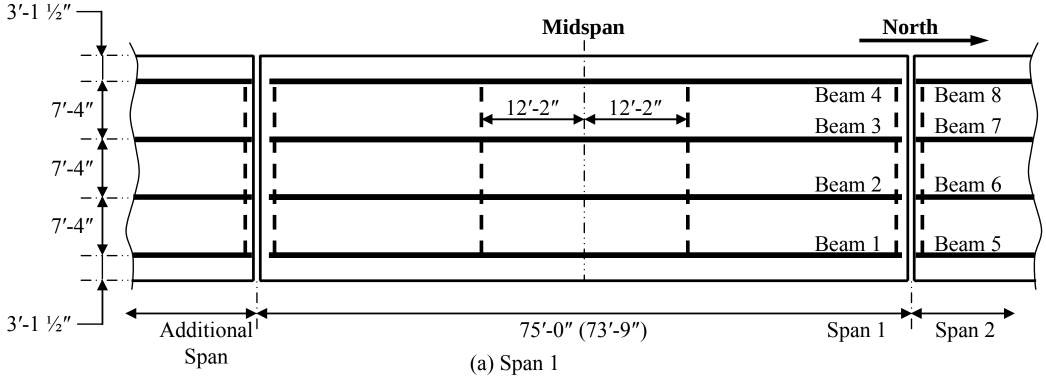

(a) Span 1

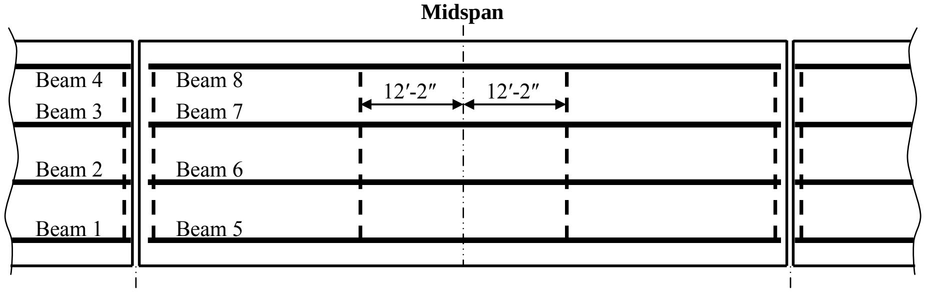

(b) Span 2

━━ Beam Locations

– – – Diaphragm Locations

#′-#″(#′-#″) Overall Length (Effective Span Length, L_{eff})

Figure A.10 Plan of Lampasas River Bridge

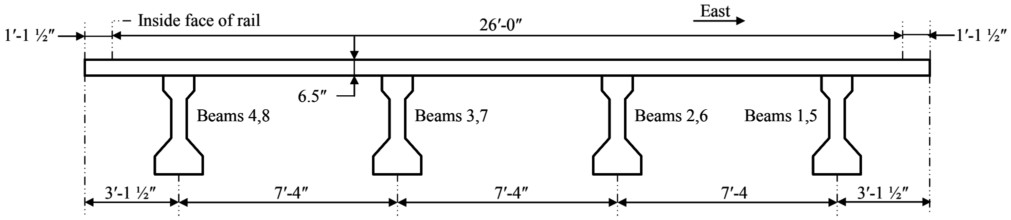

(a) Cross Section

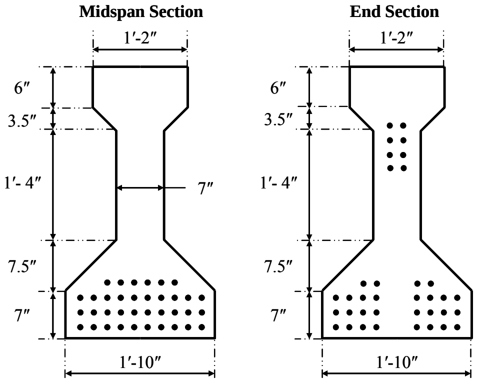

(b) Type C Beams

Figure A.11 Cross Section and Beam Details for Lampasas River

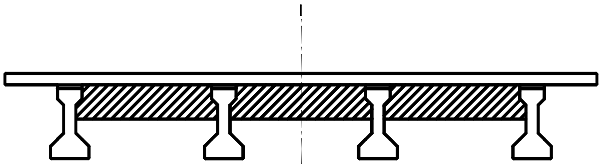

End Diaphragms

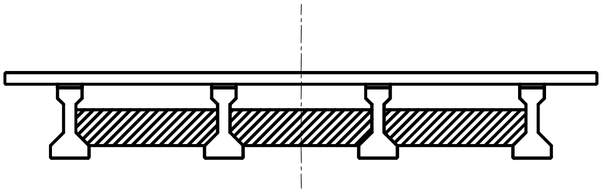

Intermediate Diaphragms

Figure A.12 Diaphragm Details for Lampasas River (Wagener 2002)

A.4 WILLIS CREEK BRIDGE

Figure A.13 Photograph of Willis Creek Bridge

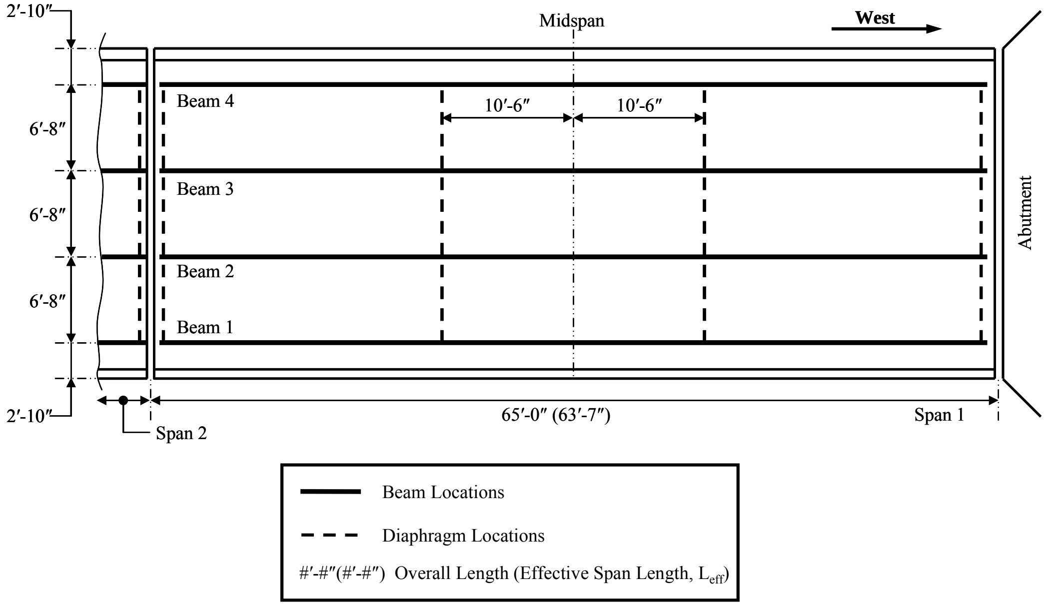

Figure A.14 Plan of Willis Creek Bridge

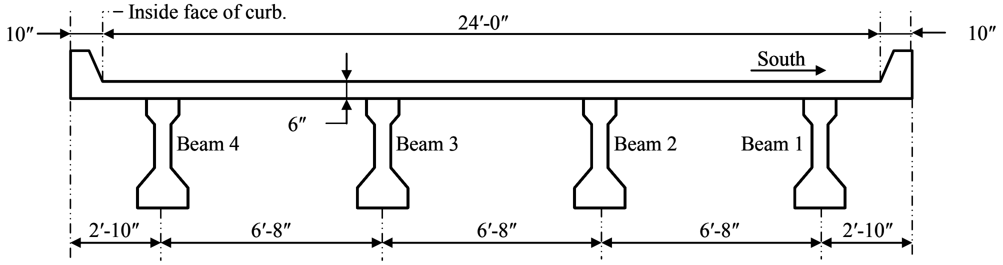

(a) Cross Section

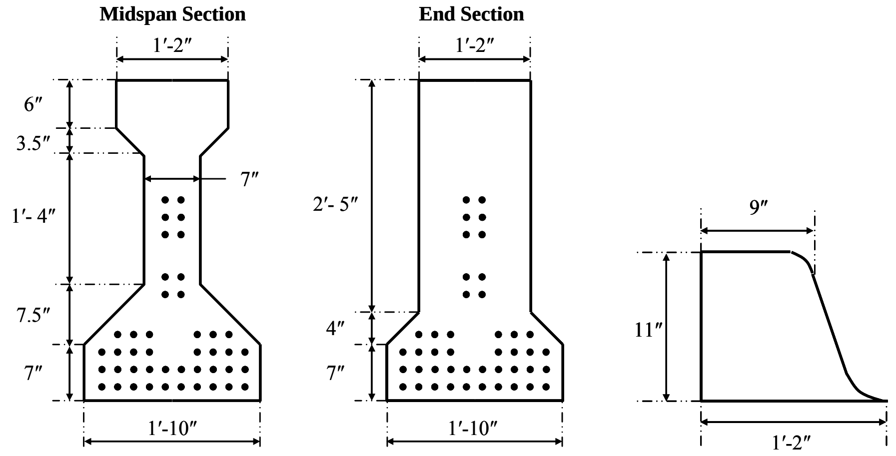

(b) Type C Beams **(c) Curb Detail**

Figure A.15 Cross Section, Beam, and Curb Detail for Willis Creek Bridge

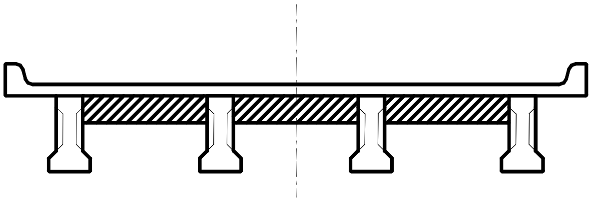

End Diaphragms

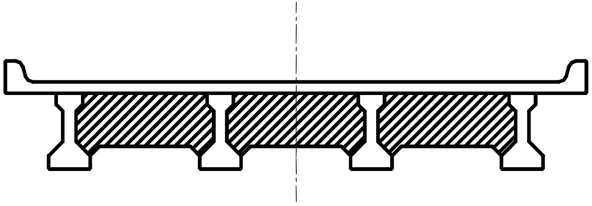

Intermediate Diaphragms

Figure A.16 Diaphragm Details for Wills Creek Bridge (Wagener 2002)

A.5 WIMBERLEY BRIDGE

Figure A.17 Photograph of Wimberley Bridge

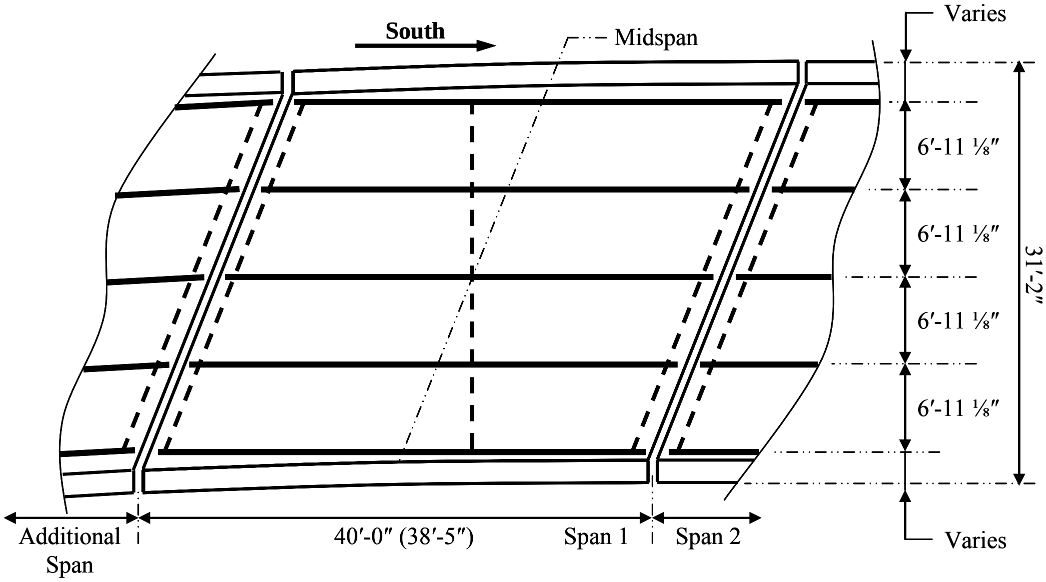

(a) Span 1

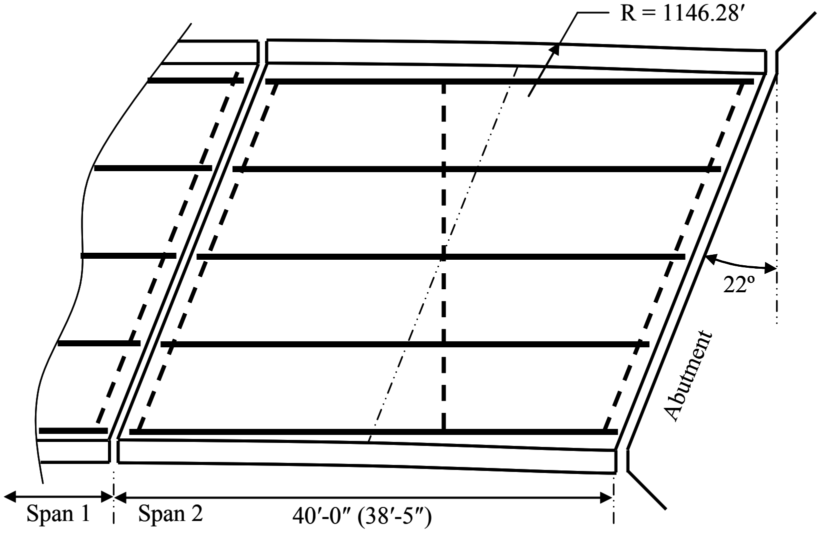

(b) Span 2

▬ Beam Locations

– – – Diaphragm Locations

#′-#″(#′-#″) Overall Length (Effective Span Length, L_{eff})

Figure A.18 Plan of Wimberley Bridge

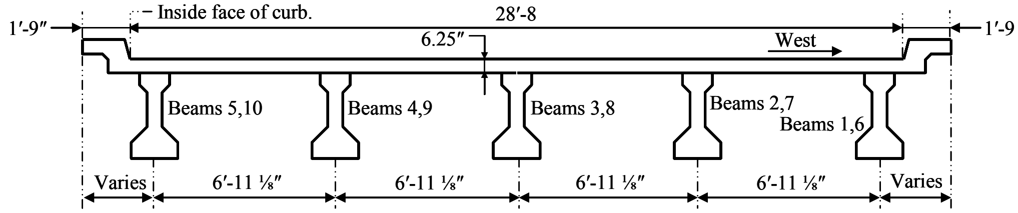

(a) Cross Section

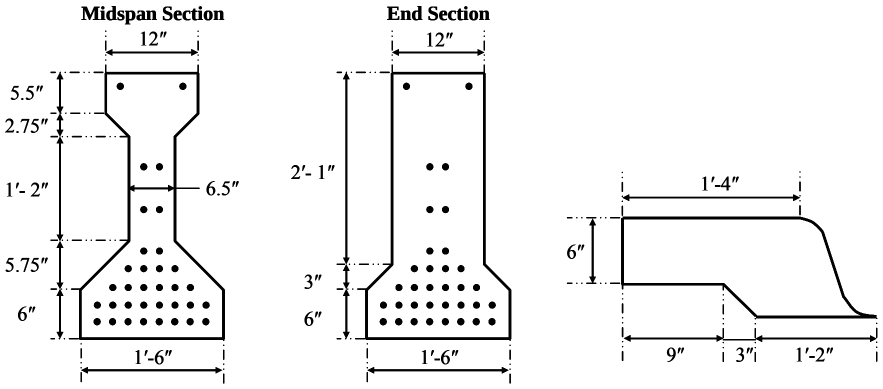

(b) Type B Beams

(c) Curb Detail

Figure A.19 Cross Section and Beam and Curb Details for Wimberley Bridge

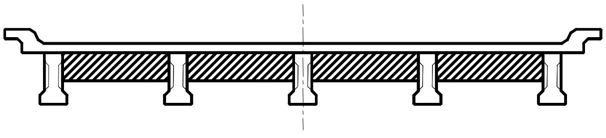

End Diaphragms

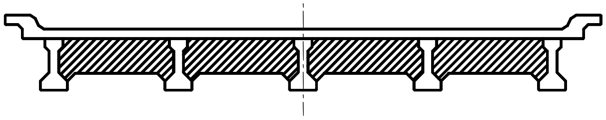

Intermediate Diaphragms

Figure A.20 Diaphragm Details for Wimberley Bridge (Wagener 2002)

A.6 DIMENSIONS AND BEAM PROPERTIES

Table A.1 Diaphragm Dimensions (Wagener 2002)

Bridge Name	$h_{diaphragm}$ (in.)	h_{clear} (in.)	$h_{diagonal}$ (in.)	$t_{diaphragm}$ (in.) End	$t_{diaphragm}$ (in.) Intermediate
Chandler Creek – 40’ Span	14.75	10.25	—	8.5	8.25
Chandler Creek – 60’ Span	20.75	11.5	—	8.25	8.25
Lake LBJ	21	12	—	8.5	8
Lampasas River	22.5	14.5	—	8.5	8.5
Willis Creek	25.75	12	5	8	8.5
Wimberley	15.5	11	5	8.5	8.5

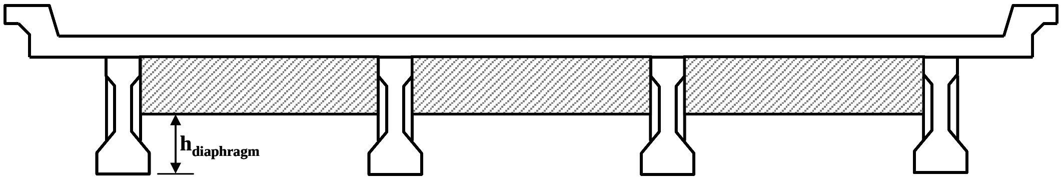

(a) Typical End Diaphragms

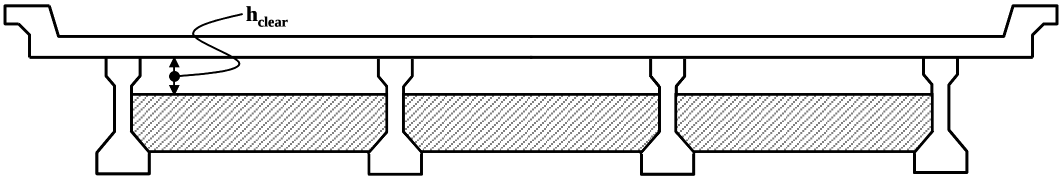

(b) Typical Non-composite Intermediate Diaphragm

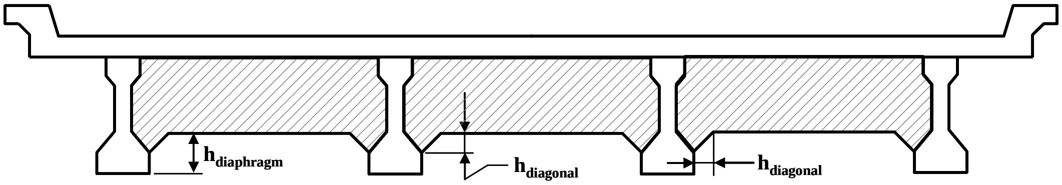

(c) Typical Composite Intermediate Diaphragm

Figure A.21 Diaphragm Measurements

Table A.2 Prestressing Strand Properties (Wagener 2002)

Bridge Name	f_{pu} / f_{pi} (ksi)	Type	D_{strand} (in.)	A_{strand} (in.)	N_{strand} Interior	N_{strand} Exterior	A_{total} (in.^{2})
Chandler Creek - 40' Span	250/175	Stress-relieved	7/16	0.108	16	16	1.73
Chandler Creek - 60' Span	250/175	Stress-relieved	7/16	0.108	30	30	3.24
Lake LBJ	250/175	Stress-relieved	7/16	0.108	36	36	3.89
Lampasas River	250/175	Stress-relieved	7/16	0.108	36	36	3.89
Willis Creek	250/175	Stress-relieved	3/8	0.080	44	44	3.52
Wimberley	250/175	Stress-relieved	3/8	0.080	34	34	2.72

Table A.3 Eccentricity of Prestressing Strand In Beams (Wagener 2002)

Bridge Name	Interior Beams		Exterior Beams		Number of Depressed Strands
	e_{end} (in.)	e_{mid} (in.)	e_{end} (in.)	e_{mid} (in.)	
Chandler Creek – 40' Span	8.40	11.90	8.40	11.90	4
Chandler Creek – 60' Span	9.07	13.07	9.07	13.07	6
Lake LBJ	5.74	12.40	5.74	12.40	8
Lampasas River	7.09	12.42	7.09	12.42	8
Willis Creek	8.02	8.02	8.02	8.02	0
Wimberley	8.14	8.14	8.14	8.14	0

Table A.4 General Cross Section Properties (Wagener 2002)

Bridge Name	Beam Type	Beam Height (in.)	Slab Thickness (in.)	Concrete Curb
Chandler Creek – 40’ Span	B	34	7.25	No
Chandler Creek – 60’ Span	C	40	7.25	No
Lake LBJ	C	40	7.25	Yes
Lampasas River	C	40	6.50	No
Willis Creek	C	40	6.00	Yes
Wimberley	B	34	6.25	Yes

Table A.5 Prestressed Beam Properties (Wagener 2002)

Bridge Name	A_{beam} (in.^{2})	I_{beam} (in.^{4})	$y_{b\text{-}beam}$ (in.)	$y_{t\text{-}beam}$ (in.)
Chandler Creek – 40’ Span	360	43300	14.9	19.1
Chandler Creek – 60’ Span	496	82800	17.1	22.9
Lake LBJ	496	82800	17.1	22.9
Lampasas River	496	82800	17.1	22.9
Willis Creek	496	82800	17.1	22.9
Wimberley	360	43300	14.9	19.1

Table A.6 Deck Dimensions (Wagener 2002)

Bridge Name	**$b_{effective}$ (in.) Interior**	**$b_{effective}$ (in.) Exterior**	**A_{curb} (in.^{2})**	**y_{curb} (in.)**	**I_{curb} (in.^{4})**
Chandler Creek – 40’ Span	93.5	84.8	—	—	—
Chandler Creek – 60’ Span	94.0	85.0	—	—	—
Lake LBJ	94.0	80.0	158	6.3	1500
Lampasas River	85.0	80.0	—	—	—
Willis Creek	79.0	73.5	99	5.3	1000
Wimberley	81.5	61.8	137	5.3	700

A.7 SUMMARY OF BRIDGES CONSIDERED FOR DETAILED STUDY IN THIS INVESTIGATION

A total of 33 bridges were considered for detailed study in this investigation. Table A.7 is a summary of the bridges and includes several key parameters for each bridge. The load ratings provided in Table A.7 are as reported by TxDOT. Where the symbol (**) is given in the table, the information was not available.

Table A.7 Summary of Bridges Considered for Detail Study in this Investigation

Bridge \ Characteristic	Span	No. of Girders	Beam Spacing	Slab Thickness	Diaphragms	Skew	f'_{cs} (ksi)		TxDOT Load Rating			Girder type	Year Built (19XX)
							Prestressed Beam	Slab	Tensile Stress Limit	Tensile Stress Criterion	Flexural Strength Criterion		
FM2657 @ Lampasas River	75	4	7.33	6.50	Yes	No	5.1	3	7.5	HS-14.0	HS-21.0	C	‘70
FM1431 @ LBJ Lake	65	4	8.00	7.25	Yes	No	5	3	7.5	HS-13.0	HS-19.8	C	‘64
FM972 @ Willis Creek	65	4	6.67	6.00	Yes	No	5	3	7.5	HS-19.7	HS-23.9	C	‘61
IH-35 EFR @ Chandler Creek	40	4	8.00	7.25	Yes	Yes	5	3	**	**	**	B	‘65
IH-35 EFR @ Chandler Creek	60	4	8.00	7.25	Yes	Yes	5	3	7.5	HS-21.5	HS-24.1	C	‘65
FM12 @ Blanco River	40	5	7.00	6.25	Yes	Yes	5	3	**	**	**	B	‘59
FM12 @ Blanco River	60	**	7.42	6.25	Yes	Yes	5	3	7.5	HS-23.3	HS-26.1	B	‘59
IH-35 WFR @ Chandler Creek	65	4	8.00	7.25	Yes	Yes	5	3	7.5	HS-20.9	HS-25.8	C	‘65
US-290 @ Yeager Creek	50	**	7.67	7.25	**	**	4.7	3	7.5	HS-19.7	HS-23.5	B	‘64

Bridge \ Characteristic	Span	No. of Girders	Beam Spacing	Slab Thickness	Diaphragms	Skew	f'_{cs} (ksi)		TxDOT Load Rating			Girder type	Year Built (19XX)
							Prestressed Beam	Slab	Tensile Stress Limit	Tensile Stress Criterion	Flexural Strength Criterion		
US-290 @ Middle Creek	50	**	7.67	7.25	**	**	4.7	3	7.5	HS-19.7	HS-23.5	B	‘64
US-281 @ Miller Creek (NB)	50	**	6.00	6.00	**	**	5	3	7.5	HS-27.1	HS27.2	B	‘64
US-281 @ Miller Creek (SB)	50	**	6.00	6.00	**	**	5	3	7.5	HS-27.1	HS27.2	B	‘64
I-35 @ Westinghouse Road	65	**	8.00	7.25	**	**	5	3	7.5	HS-21.1	HS-25.7	C	‘65
I-35 @ FM2001	65	**	6.67	6.25	**	**	5	3	7.5	HS-20.0	HS-24.6	C	‘61
I-35 @ Bunton Road	65	**	6.67	6.25	**	**	5	3	7.5	HS-18.5	HS-24.5	B	‘61
I-35 @ Loop 150	65	**	6.00	6.00	**	**	5	3	7.5	HS-23.8	HS-27.4	C	‘61
I-35 @ Plum Creek	50	**	7.33	6.50	**	**	5	3	7.5	HS-37.7	HS-21.4	C	‘61
I-35 @ Yarrington Road	70	**	6.67	6.50	**	**	5	3	7.5	HS-22.4	HS-26.8	C	‘62
I-35 @ Redwood Road	65	**	6.00	6.00	**	**	5	3	7.5	HS-24.2	HS-27.6	C	‘58

Bridge \ Characteristic	Span	No. of Girders	Beam Spacing	Slab Thickness	Diaphragms	Skew	f'_{cs} (ksi)		TxDOT Load Rating			Girder type	Year Built (19XX)
							Prestressed Beam	Slab	Tensile Stress Limit	Tensile Stress Criterion	Flexural Strength Criterion		
I-35 @ McCarty Lane	65	**	6.00	6.67	**	**	5	3	7.5	HS-20.7	HS-24.7	C	‘58
I-35 @ Center Point Road	65	**	6.67	6.00	**	**	5	3	7.5	HS-20.7	HS-24.7	C	‘58
I-35 @ Posey Road	65	**	6.67	6.00	**	**	5	3	7.5	HS-20.7	HS-24.7	C	‘58
I-35 @ Loop 418	75	**	8.67	7.75	**	**	5	3	12	HS-21.6	HS-24.8	C	‘65
MoPac RR Opass @ US-290	60	**	8.56	6.75	**	**	5	3	7.5	HS21.8	HS-24.6	C	‘61
US-290 @ Loop 360 (EB)	61	**	7.50	7.00	**	**	5	3	7.5	HS-17.2	HS-19.1	C	‘69
US-290 @ Loop 360 (WB)	59	**	7.50	7.00	**	**	5	3	7.5	HS19.7	HS-20.5	C	‘69
US-290 @ Loop 275	45	**	7.25	6.25	**	**	5	3	7.5	HS-27.7	HS-27.9	B	‘61
Loop 343 @ IH-35 (NB&SB)	70	**	7.17	6.50	**	**	5	3	7.5	HS-25.7	HS-30.9	C	‘62
US-183 @ FM969	70	**	7.00	7.00	**	**	5	3	7.5	HS-23.1	HS-28.2	C	‘66
US-183 @ IH-35 (NB)	70	**	7.17	6.50	**	**	5	3	7.5	HS-25.5	HS-30.9	C	‘62

Bridge \ Characteristic	Span	No. of Girders	Beam Spacing	Slab Thickness	Diaphragms	Skew	f'_{cs} (ksi)		TxDOT Load Rating			Girder type	Year Built (19XX)
							Prestressed Beam	Slab	Tensile Stress Limit	Tensile Stress Criterion	Flexural Strength Criterion		
US-183 @ IH-35 (SB)	70	**	7.17	6.50	**	**	5	3	7.5	HS-25.5	HS-30.9	C	‘62
Bergrstrom Main @ SH71	60	**	8.33	7.50	**	**	5	3	7.5	HS-18.6	HS-21.4	C	‘68
SH95 @ Mustang Creek	50	**	8.00	7.25	**	**	5	3	7.5	HS-15.8	HS-17.8	B	‘46

APPENDIX B

Bridge Concrete Material Properties

Information about the cores extracted from the Chandler Creek Bridge is summarized in this appendix. Table B.1 summarizes the dimensions of the cores as extracted from the bridge. Table B.2 summarizes the dimensions of the cores as tested and the results of the compressive strength tests. A complete discussion of the test results is presented in Chapter 3.

In addition, a summary of the quality control test records available for each bridge studied in this investigation is reported in Table B.3 through Table B.7. This information was previously reported in Wagener (2002).

B.1 COMPRESSIVE STRENGTH OF CORES EXTRACTED FROM CHANDLER CREEK BRIDGE

Table B.1 Dimensions of Cores Extracted from Chandler Creek Bridge

Measured Dimension	West Exterior (Beam 8)		West Interior (Beam 7)		East Interior (Beam 6)		East Exterior (Beam 5)	
	Core 8-1	Core 8-2	Core 7-1	Core 7-2	Core 6-1	Core 6-2	Core 5-1	Core 5-2
Diameter 1a (in.)	2.720	2.727	2.719	2.719	2.718	2.723	2.721	2.720
Diameter 1b (in.)	2.725	2.718	2.718	2.718	2.725	2.718	2.722	2.721
Diameter 2a (in.)	2.726	2.718	2.720	2.724	2.721	2.723	2.718	2.719
Diameter 2b (in.)	2.725	2.723	2.719	2.718	2.723	2.724	2.719	2.721
Diameter 3a (in.)	2.718	2.712	2.719	2.715	2.723	2.722	2.718	2.716
Diameter 3b (in.)	2.718	2.719	2.718	2.719	2.725	2.717	2.723	2.723
Mean Diameter (in.)	2.724	2.721	2.719	2.720	2.721	2.721	2.720	2.720
Area of Core (in.^{2})	5.826	5.815	5.806	5.812	5.816	5.816	5.812	5.811
Drilled Length (in.)	7.040	7.038	6.977	6.962	6.958	6.934	7.045	7.045
Note: Two diameter measurements were taken at 90 degrees to each other at three points along the length of each specimen.								

Table B.2 Test Dimensions and Compression Test Results from Cores Extracted From Chandler Creek Bridge

Test Property	West Exterior (Beam 8)		West Interior (Beam 7)		East Interior (Beam 6)		East Exterior (Beam 5)	
	Core 8-1	Core 8-2	Core 7-1	Core 7-2	Core 6-1	Core 6-2	Core 5-1	Core 5-2
Capped Test Length (in.)	6.25	6.19	6.19	6.20	6.19	5.56	6.13	5.56
Capped Test Length to Diameter Ratio	2.29	2.27	2.28	2.28	2.27	2.04	2.25	2.05
Uncapped Test Length (in.)	5.25	5.00	5.13	5.20	5.00	5.00	5.13	5.00
Uncapped Test Length to Diameter Ratio	1.93	1.84	1.88	1.91	1.84	1.84	1.88	1.84
Force (lb)	34178	47886	40175	44873	43780	38167	45759	50167
Stress (psi)	5866	8235	6919	7721	7527	6562	7873	8634
Mean Core Strength for Each Girder (psi)	7051		7320		7044		8253	
Mean Core Strength of All Specimens (psi)							7417	
Coefficient of Variation of Core Strength of All Specimens							12%	

B.2 QUALITY CONTROL COMPRESSIVE STRENGTH TEST RECORDS

Table B.3 Concrete Test Data from the Prestressed Girders – Chandler Creek Bridge (Wagener 2002)

Sample Identification	Beam Type	Length (ft)	Compressive Strength at Initial Prestress (psi)	Age at Initial Prestress (hr)	Average Compressive Strength (psi)	Age (day)
B2 (B-13)	B	40	5082	16	6357	7
B3 (B-110	B	40	5135	17	6375	7
B3 (B-14)	B	40	5082	16	6357	7
B5 (B-10)	B	40	5135	17	6375	7
B5 (B-16)	B	40	4752	14.25	6928	7
B2 (B-09)	B	40	5717	37.5	7916	8
B2 (B-15)	B	40	4700	17.5	6678	8
B3 (B-17)	B	40	4700	17.5	6678	8
A-1 (B-01)	B	40	4069	42	7119	14
A-2 (B-02)	B	40	4069	42	7119	14
A-3 (B-01)	B	40	5547	48	8245	14
A-4 (B-03)	B	40	5547	48	8245	14
B3 (B-07)	B	40	5440	19.5	6889	14
B3 (B-08)	B	40	5440	19.5	6889	14
B5 (B-12)	B	40	4700	14.5	7182	14
A-7 (B-04)	B	40	5476	66	7237	17
A-8 (B-03)	B	40	5476	66	7237	17
A-5 (B-02)	B	40	5511	43	7591	18
A-6 (B-04)	B	40	5511	43	7591	18
B1 (C-05)	C	60	5515	48	—	—
B3 (C-07)	C	60	5498	67.5	—	—
B2 (C-06)	C	60	—	—	8569	14
B2 (C-06)	C	60	—	—	8723	14
B2 (C-06)	C	60	—	—	8523	14
B4 (C-08)	C	60	—	—	8185	14
B4 (C-08)	C	60	—	—	9075	14
B4 (C-08)	C	60	—	—	8808	14

Table B.4 Test Data from the Slab – Chandler Creek Bridge (Wagener 2002)

Cylinder ID	Age (day)	Compressive Strength (psi)
M1	3	3771
M2	3	3796
M3	3	3733
M13	4	3929
M14	4	3880
M15	4	4200
RC-1	7	3395
RC-2	7	3913
RC-3	7	3767
RC7	7	3813
RC8	7	3796
RC9	7	3696
M4	7	4197
M5	7	4816
M6	7	4699
M10	7	4114
M11	7	4064
M12	7	3579
RC-4	28	5100
RC-5	28	5100
RC-6	28	4682
M7	28	5500
M8	28	5613
M9	28	5748

Table B.5 Concrete Test Data from the Prestressed Girders – Lake LBJ Bridge (Wagener 2002)

Identification	Beam Type	Length (ft)	Compressive Strength at Initial Prestress (psi)	Age at Initial Prestress (hr)	Average Compressive Strength (psi)	Age (day)
B 1-5	C	64.67	4500	26	7292	14
A 1-5	C	64.67	5200	27	7945	14
B 1-5	C	64.67†	5400	90	9102	14
A 1&2	C	64.67†	5400	47	7273	14
A 3-5	C	64.67†	5200	28	8816	14
B 1-5	C	64.67†	5200	28	7827	14
A 1-5	C	64.67†	4840	24	7765	19
B-1	C	64.67†	5470	70	7441	15
B-5	C	64.67†	5420	39	7760	14
B-3	C	64.67†	4945	28	7677	14
A-1	C	64.67†	5650	46	8308	14
A-4	C	64.67†	4315	27	8318	14
B-1	C	64.67†	4100	27	8420	14
B 1-3	C	64.67†	5375	90	7651	14
B 4-5	C	64.67†	5400	70	8553	14

† Length not on quality control test report; therefore, length was assumed.

Table B.6 Concrete Test Data from the Prestressed Girders – Lampasas River Bridge (Wagener 2002)

Identification	Beam Type	Length (ft)	Compressive Strength at Initial Prestress (psi)	Age at Initial Prestress (hr)	Average Compressive Strength (psi)	Age (day)
C1	C	74.67	6254	46	8036	7
C2	C	74.67				
C3	C	74.67				
C4	C	74.67				
B1	C	74.67	4616	22	8244	7
B2	C	74.67				
B3	C	74.67				
B4	C	74.67				
A1	C	74.67	6254	43	8272	7
A2	C	74.67				
A3	C	74.67				
A4	C	74.67				
B1	C	74.67	6254	47	8205	7
B2	C	74.67				
B3	C	74.67				
B4	C	74.67				
A1	C	74.67	5930	28	8256	7
A2	C	74.67				
A3	C	74.67				
A4	C	74.67				
B1	C	74.67	6254	42	7969	7
B2	C	74.67				
B3	C	74.67				
B4	C	74.67				
A1	C	74.67	6254	47	8140	9
A2	C	74.67				
A3	C	74.67				
A4	C	74.67				
C1	C	74.67	6254	72	8272	10
C2	C	74.67				
C3	C	74.67				
C4	C	74.67				

Table B.7 Concrete Test Data from the Prestressed Girders – Willis Creek Bridge (Wagener 2002)

Identification	Beam Type	Length (ft)	Compressive Strength at Initial Prestress (psi)	Age at Initial Prestress (hr)	Average Compressive Strength (psi)	Age (day)
B (1&2)	C	64.67	5300	48	7898	21
B (1&2)	C	64.67	5400	72	8862	21
None Listed	C	64.67	5400	144	9180	21
None Listed	C	64.67	5400	120	8239	21

APPENDIX C

Bridge Testing

Instrumentation plans, load test path plans, load path diagrams, test run summaries for the bridges studied in this investigation are included in this appendix. This appendix compliments the discussion in Chapter 3.

C.1 INSTRUMENTATION PLANS FOR BRIDGES IN THIS INVESTIGATION

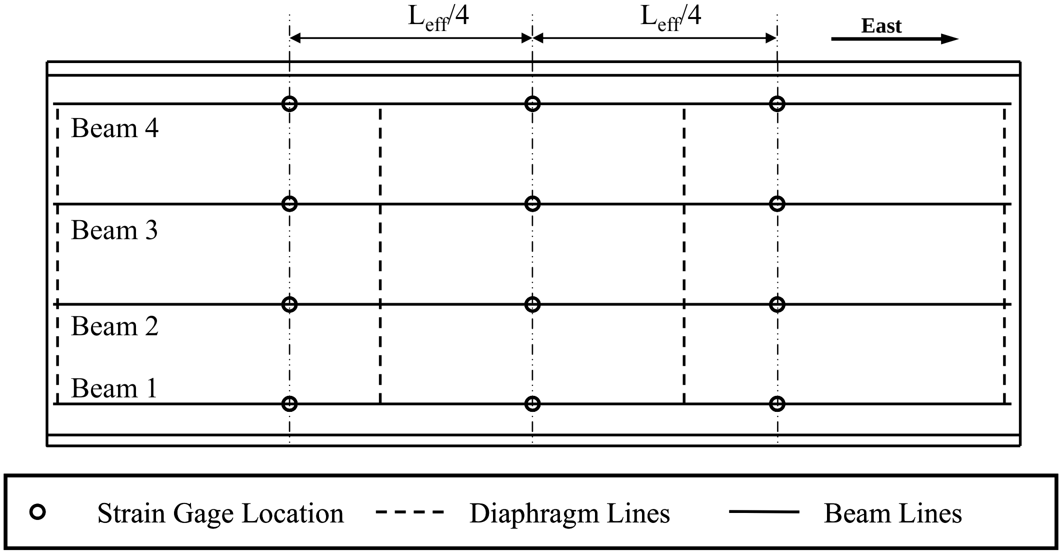

Figure C.1 Instrumentation Plan for Lake LBJ Load Tests

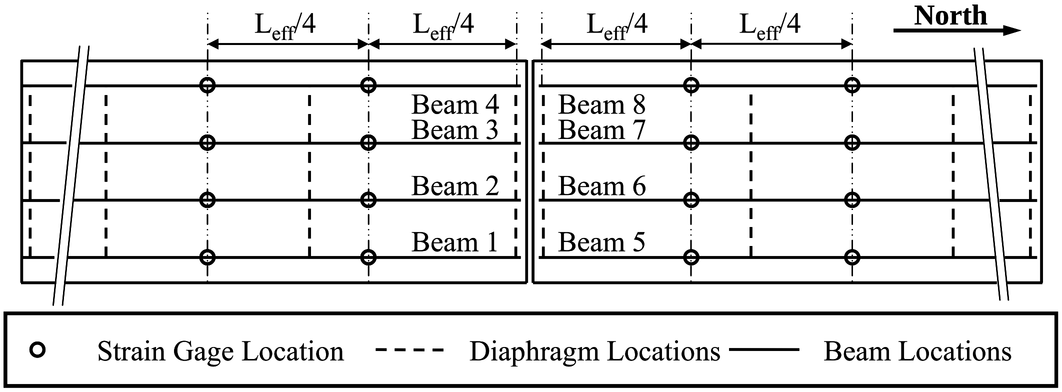

Figure C.2 Instrumentation Plan for Lampasas River Load Tests

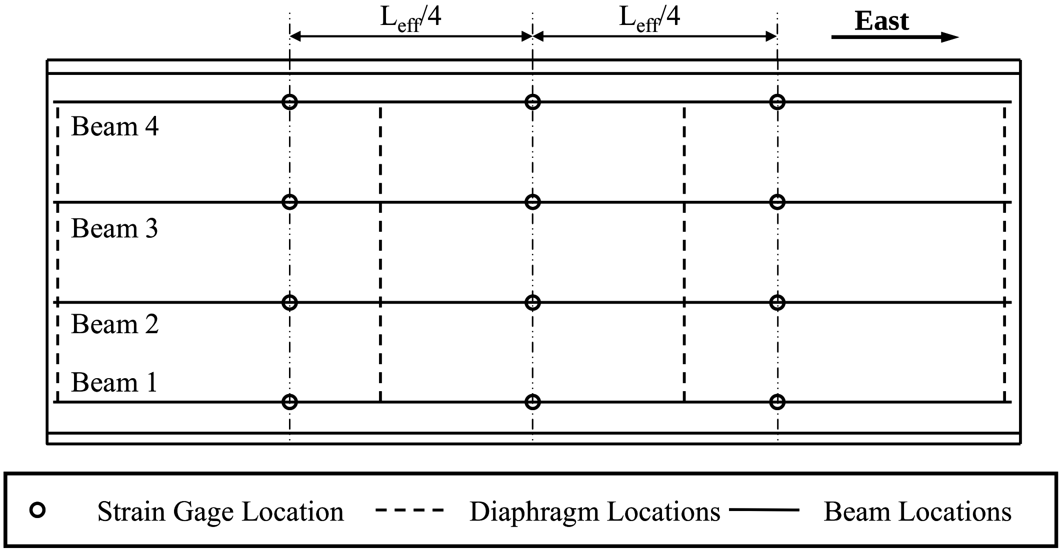

Figure C.3 Instrumentation Plan for Willis Creek Load Tests

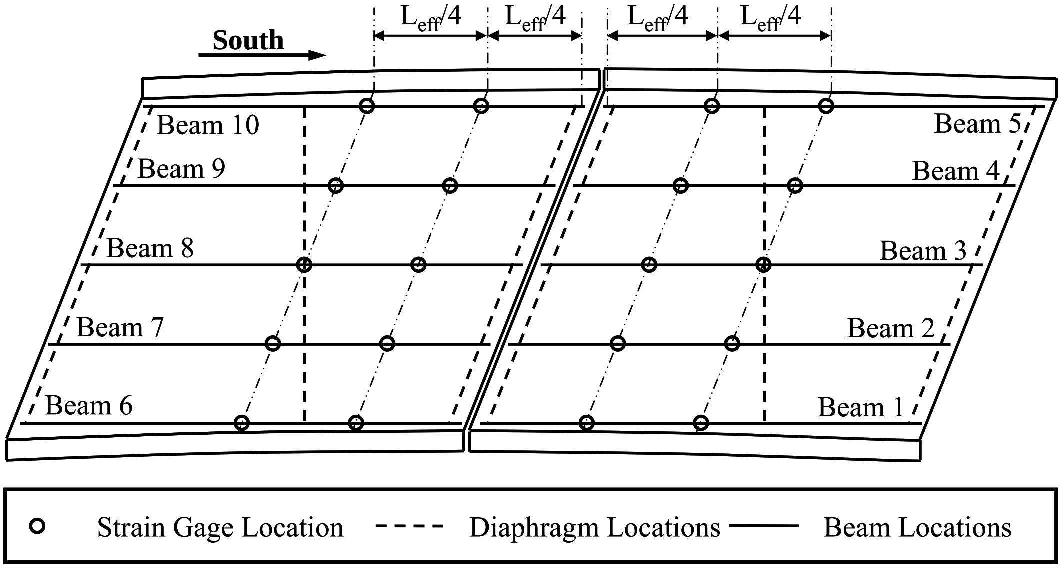

Figure C.4 Instrumentation Plan for Wimberley Load Tests

C.2 LOAD PATHS AND TEST RUNS

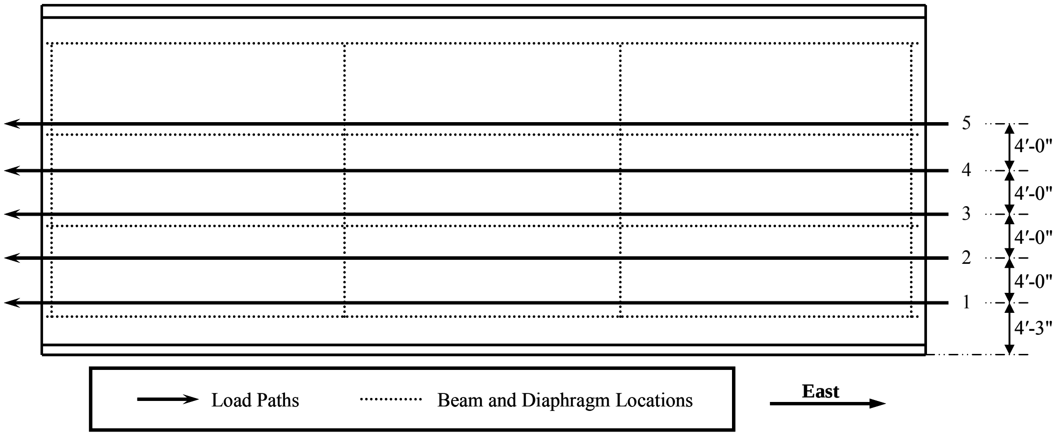

Figure C.5 Plan of Loading Paths for Lake LBJ Load Tests

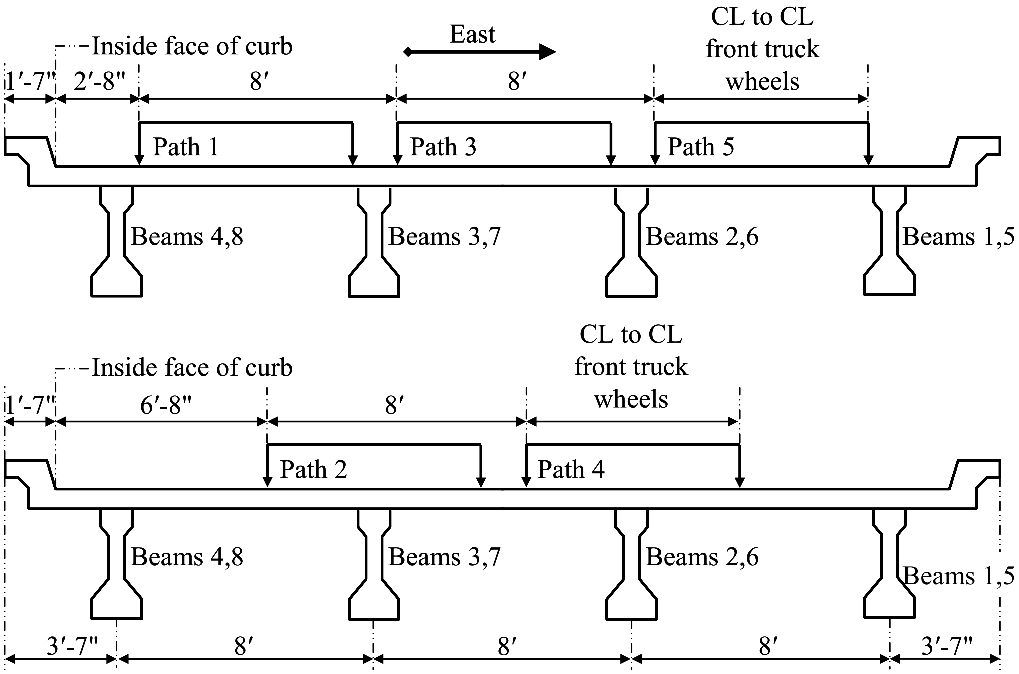

Figure C.6 Load Paths for Lake LBJ Bridge Load Tests

Table C.1 Test Runs at the Lake LBJ Bridge

Run Number	Loading Configuration	Truck 1 Path Number	Truck 2 Path Number
1	Back-to-Back	1	1
2	Back-to-Back	1	1
3	Back-to-Back	2	2
4	Back-to-Back	2	2
5	Back-to-Back	3	3
6	Back-to-Back	3	3
7	Back-to-Back	4	4
8	Side-by-Side	1	5
9	Side-by-Side	1	5
10	Single-Truck	1	—
11	Single-Truck	3	—
12	Single-Truck	5	—
13	Side-by-Side	1	5
14	Side-by-Side	1	5
15	Side-by-Side	1	5

C.3 LAMPASAS RIVER LOAD PATHS AND TEST RUNS

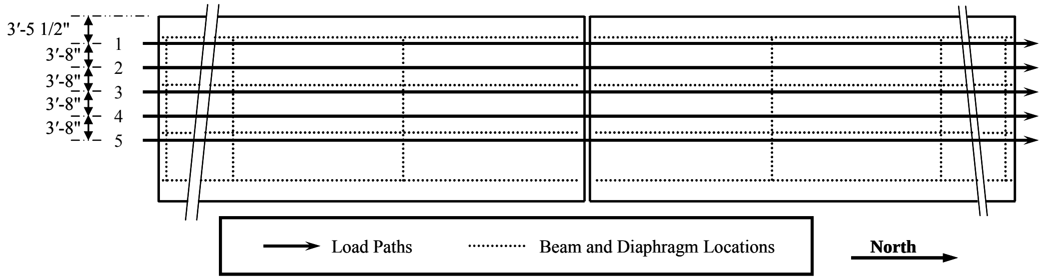

Figure C.7 Plan of Loading Paths for Lampasas River Load Tests

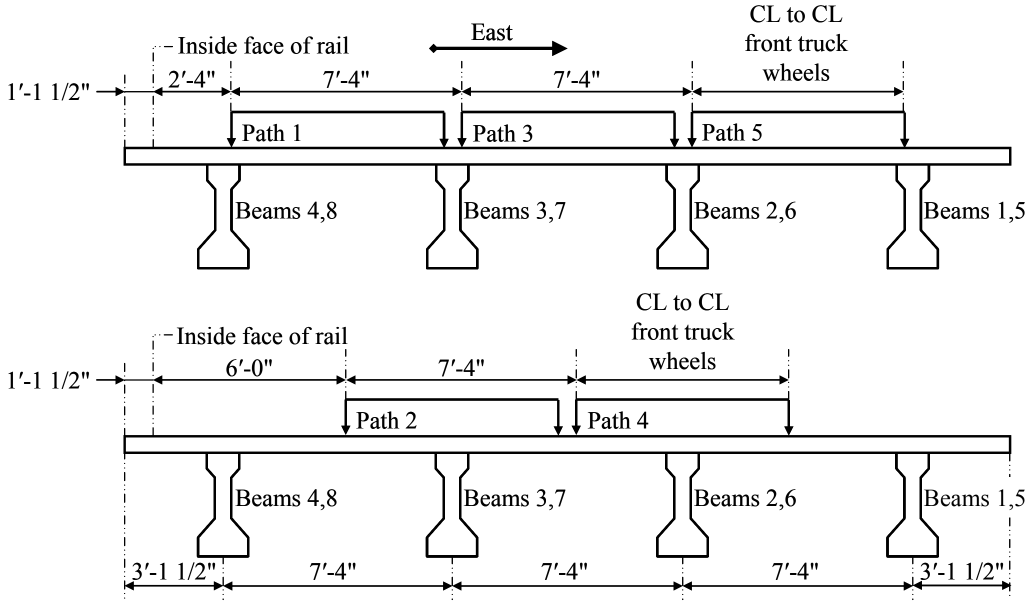

Figure C.8 Load Paths for Lampasas River Bridge Load Tests

Table C.2 Test Runs at the Lampasas River Bridge

Run Number	Loading Configuration	Truck 1 Path Number	Truck 2 Path Number
1	Back-to-Back	1	1
2	Back-to-Back	1	1
3	Back-to-Back	1	1
4	Back-to-Back	2	2
5	Back-to-Back	2	2
6	Back-to-Back	3	3
7	Back-to-Back	3	3
8	Side-by-Side	1	5
9	Side-by-Side	1	5
10	Single-Truck	1	—
11	Single-Truck	3	—
12	Single-Truck	5	—
13	Side-by-Side	1	5
14	Side-by-Side	1	5
15	Back-to-Back	1	1
16	Back-to-Back	1	1

C.4 WILLIS CREEK LOAD PATHS AND TEST RUNS

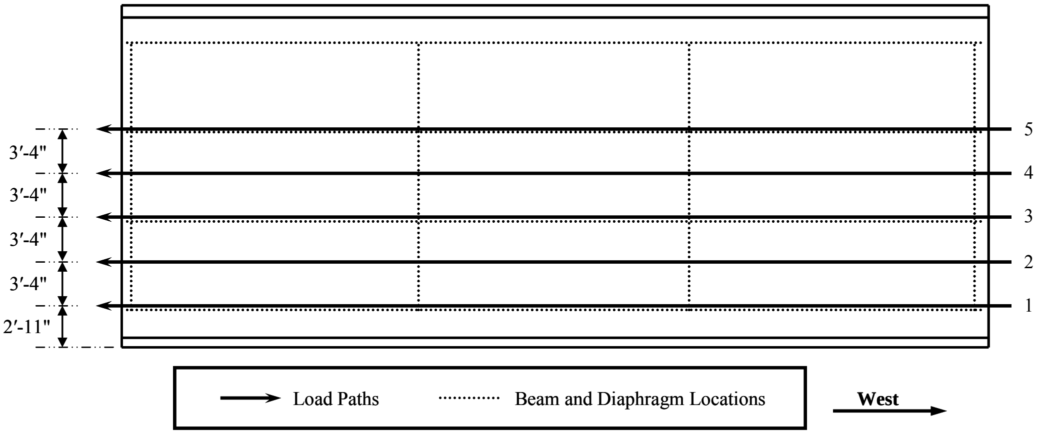

Figure C.9 Plan of Loading Paths for Willis Creek Load Tests

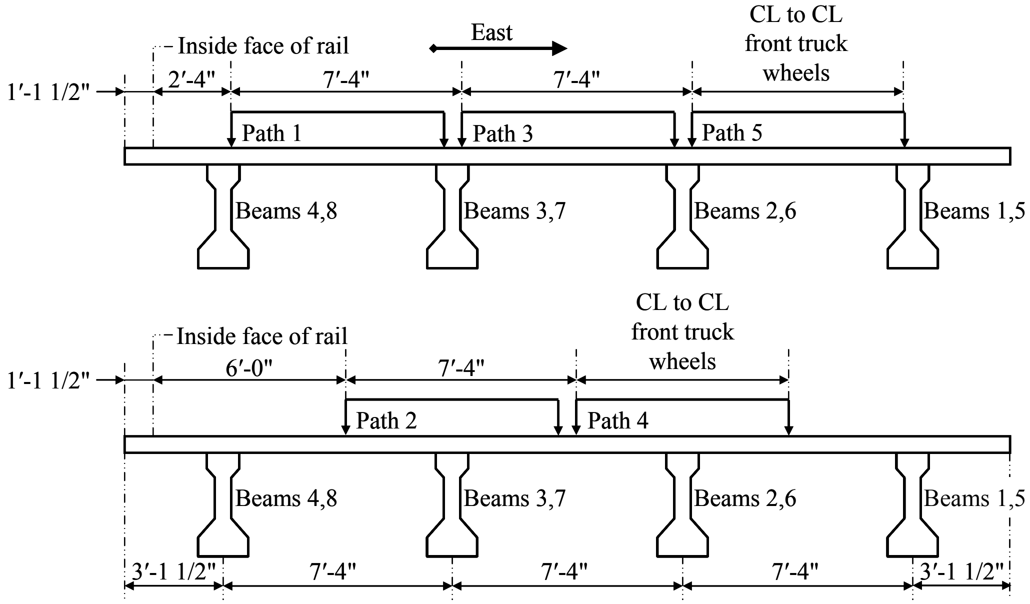

Figure C.10 Load Paths for Willis Creek Bridge Load Tests

Table C.3 Test Runs at the Willis Creek Bridge

Run Number	Loading Configuration	Truck 1 Path Number	Truck 2 Path Number
1	Side-by-Side	1	5
2	Side-by-Side	1	5
3	Back-to-Back	1	1
4	Back-to-Back	1	1
5	Back-to-Back	1	1
6	Back-to-Back	1	1
7	Back-to-Back	2	2
8	Back-to-Back	2	2
9	Back-to-Back	3	3
10	Back-to-Back	3	3
11	Back-to-Back	4	4
12	Back-to-Back	4	4
13	Back-to-Back	5	5
14	Back-to-Back	5	5
15	Single-Truck	1	—
16	Single-Truck	2	—
17	Single-Truck	3	—
18	Single-Truck	4	—
19	Single-Truck	5	—
20	Side-by-Side	1	5

C.5 WIMBERLEY LOAD PATHS AND TEST RUNS

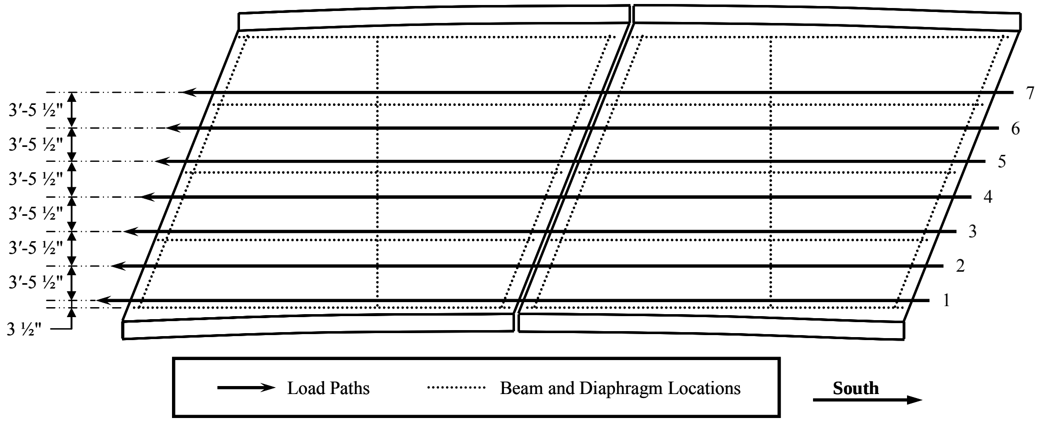

Figure C.11 Plan of Loading Paths for Wimberley Load Tests

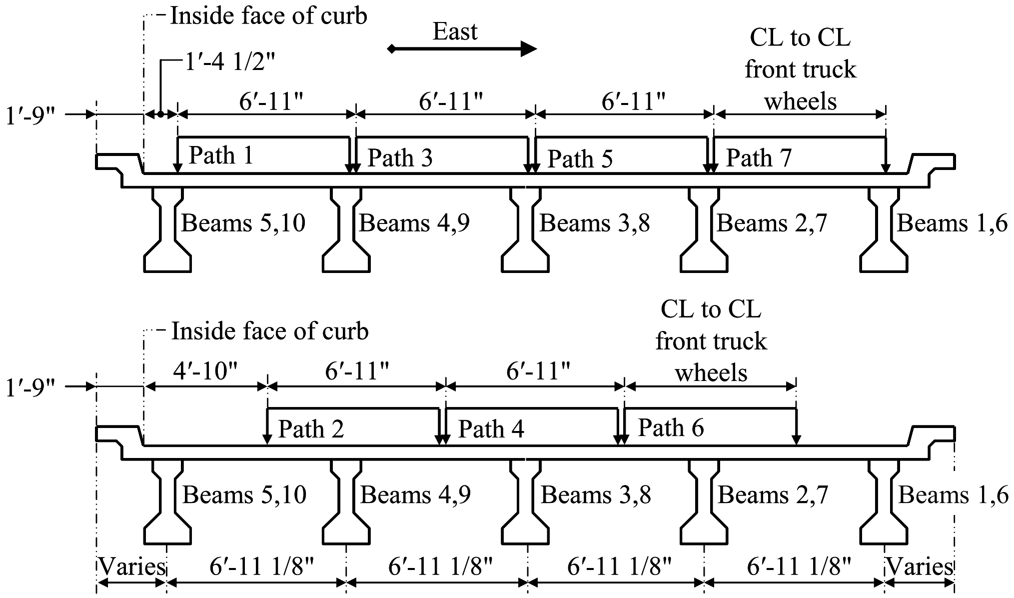

Figure C.12 Load Paths for Wimberley Bridge Load Tests

Table C.4 Test Runs at the Wimberley Bridge

Run Number	Loading Configuration	Truck 1 Path Number	Truck 2 Path Number
1	Back-to-Back	1	1
2	Back-to-Back	1	1
3	Back-to-Back	4	4
4	Back-to-Back	4	4
5	Back-to-Back	7	7
6	Back-to-Back	7	7
7	Side-by-Side	2	6
8	Side-by-Side	2	6
9	Single-Truck	1	1
10	Single-Truck	2	2
11	Single-Truck	3	3
12	Single-Truck	4	4
13	Single-Truck	5	5
14	Single-Truck	6	6
15	Single-Truck	7	7
16	Side-by-Side	1	7
17	Side-by-Side	1	7

APPENDIX D

Measured Strains from Bridge Load Tests

Sample strain histories and the maximum measured strains for the gages located at the midspan of the bridges studied in this investigation are summarized in this appendix. This information was previously reported by Wagener (2002).

D.1 SAMPLE STRAIN HISTORIES

The sample strain histories included in this section are typical of the strain histories recorded during the diagnostic load tests. As discussed in Chapter 3, the strain histories show no significant levels of noise or drift.

For simplicity, each strain gage was given a gage name. The gage name included a reference for the beam number, span location, and location on the beam. Figure D.1 is a sample gage name with an explanation for each portion of the name. The gage name is included on each strain history included in this section.

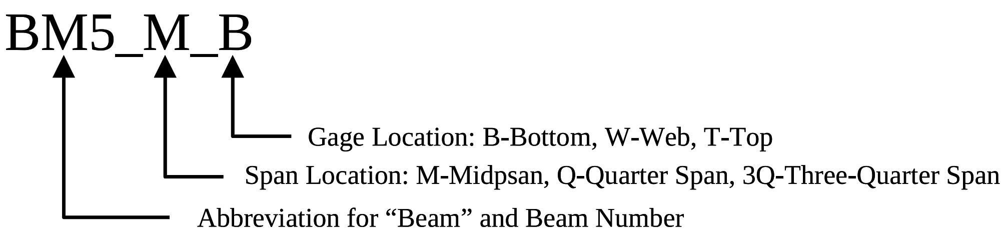

Figure D.1 Strain Gage Notation

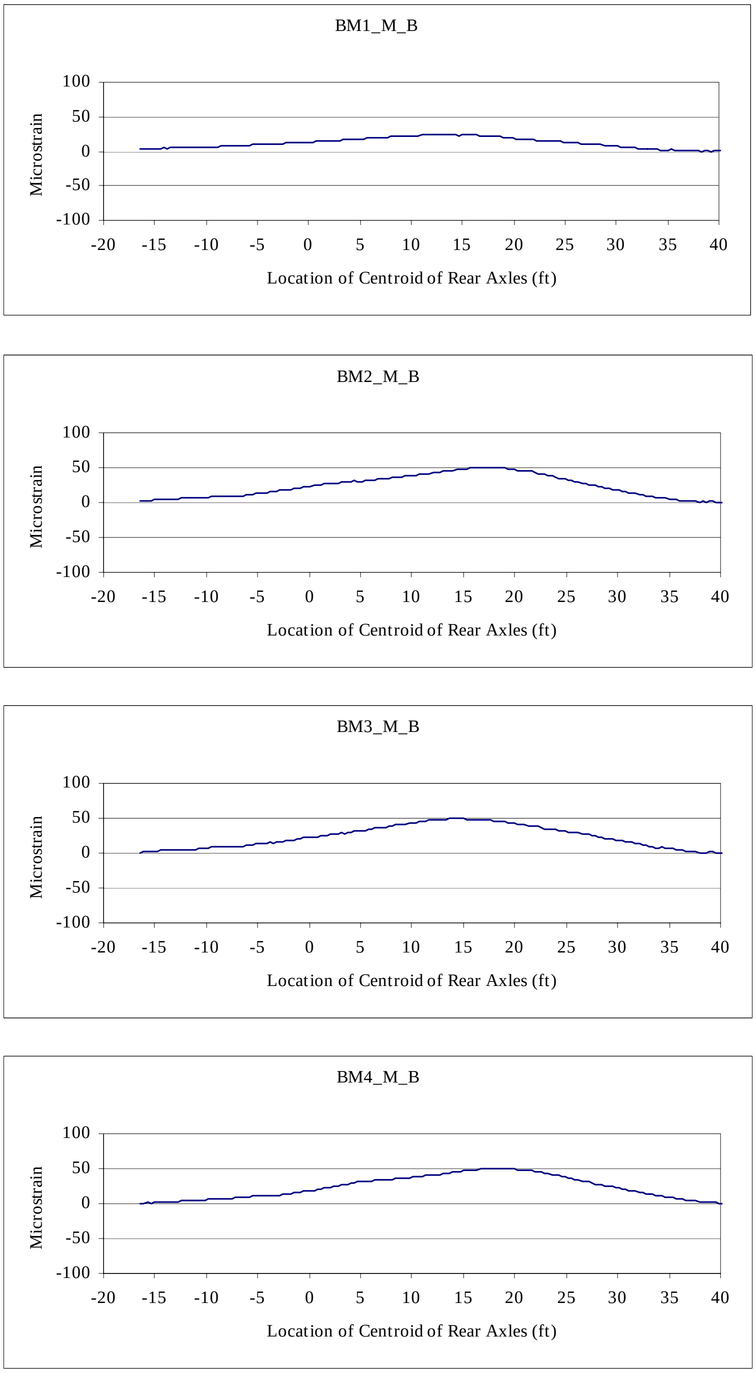

Figure D.2 Sample Strain History – Chandler Creek Bridge – 40' Span – Run 1 – Side-by-Side Configuration (Wagener 2002)

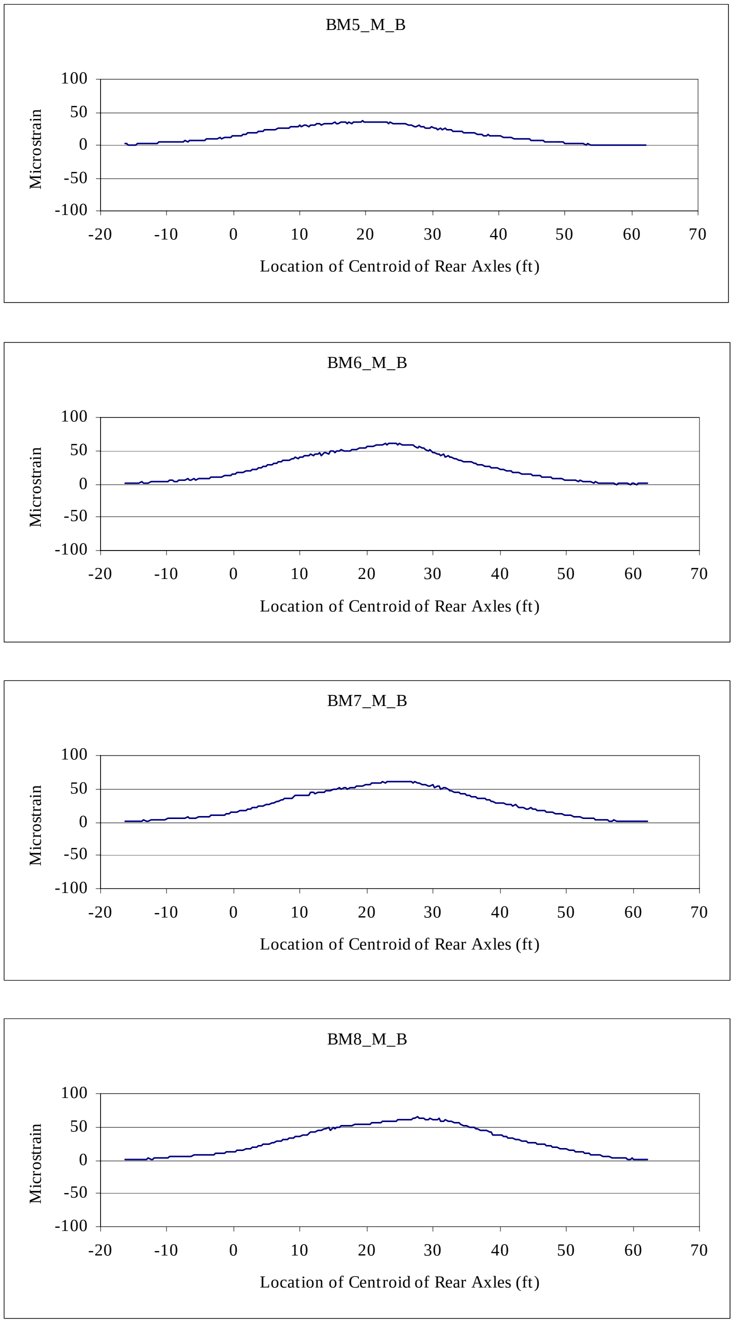

Figure D.3 Sample Strain History – Chandler Creek Bridge – 60’ Span – Run 1 – Side-by-Side Configuration (Wagener 2002)

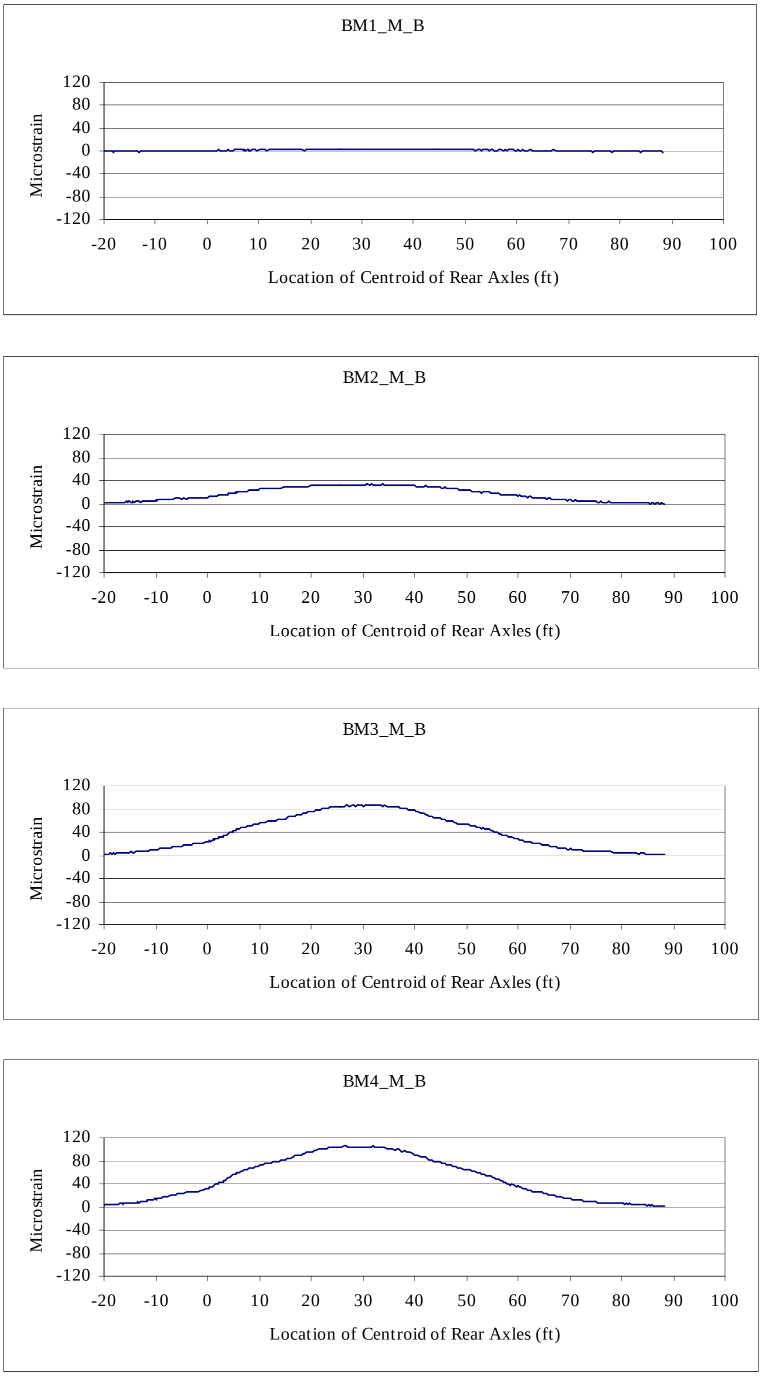

Figure D.4 Sample Strain History – Lake LBJ Bridge – Run 1 – Back-to-Back Configuration (Wagener 2002)

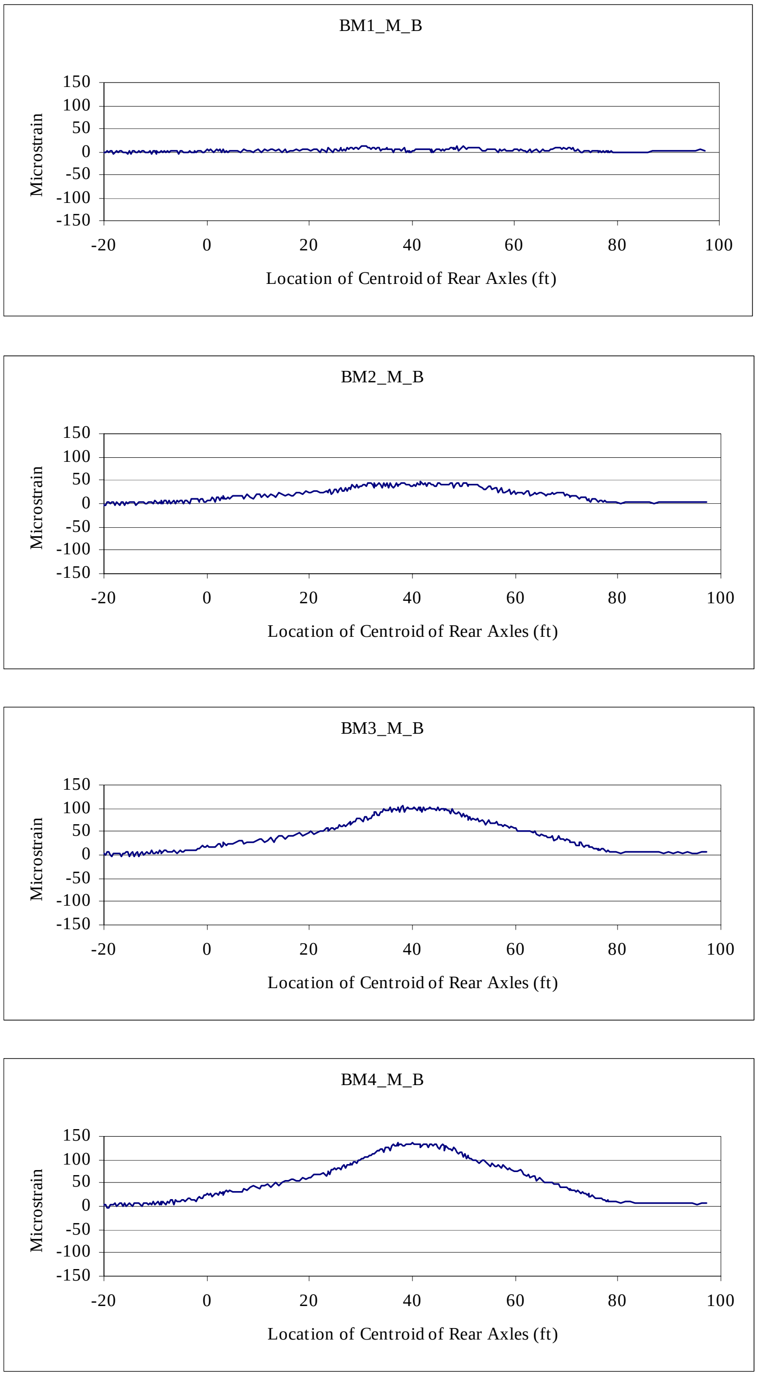

Figure D.5 Sample Strain History – Lampasas River Bridge – Span 1 – Run 1 – Back-to-Back Configuration (Wagener 2002)

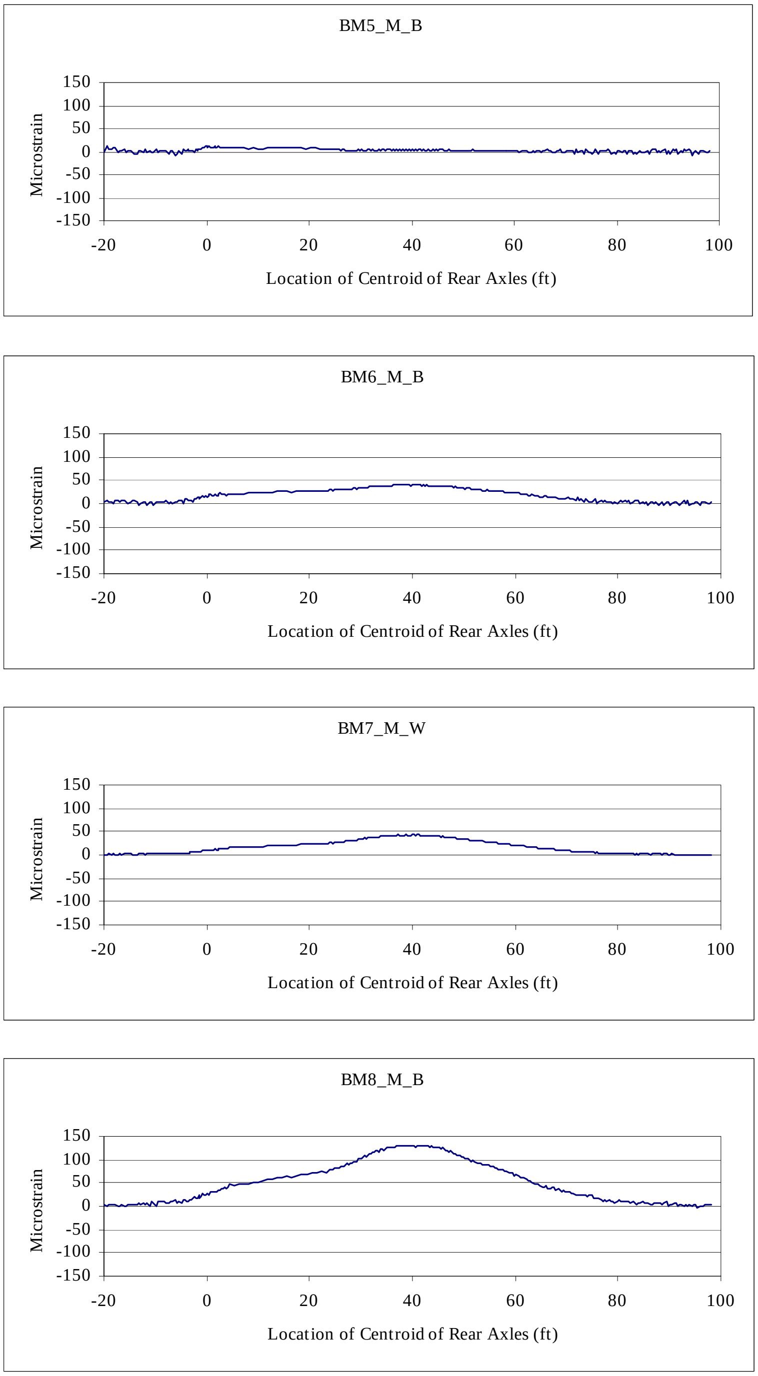

Figure 4.8 Sample Strain History – Lampasas River Bridge – Span 2 – Run 1 – Back-to-Back Configuration (Wagener 2002)

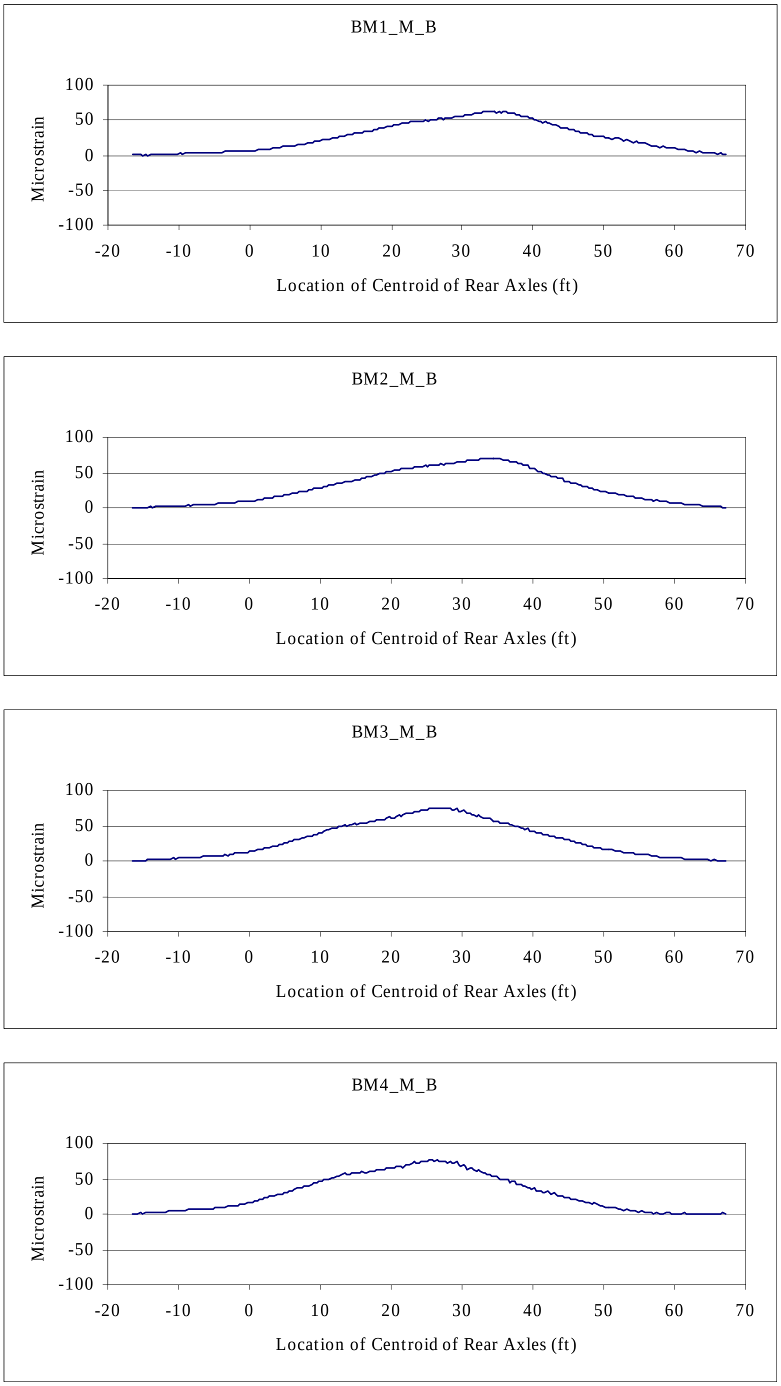

Figure D.6 Sample Strain History – Willis Creek Bridge – Run 1 – Side-by-Side Configuration (Wagener 2002)

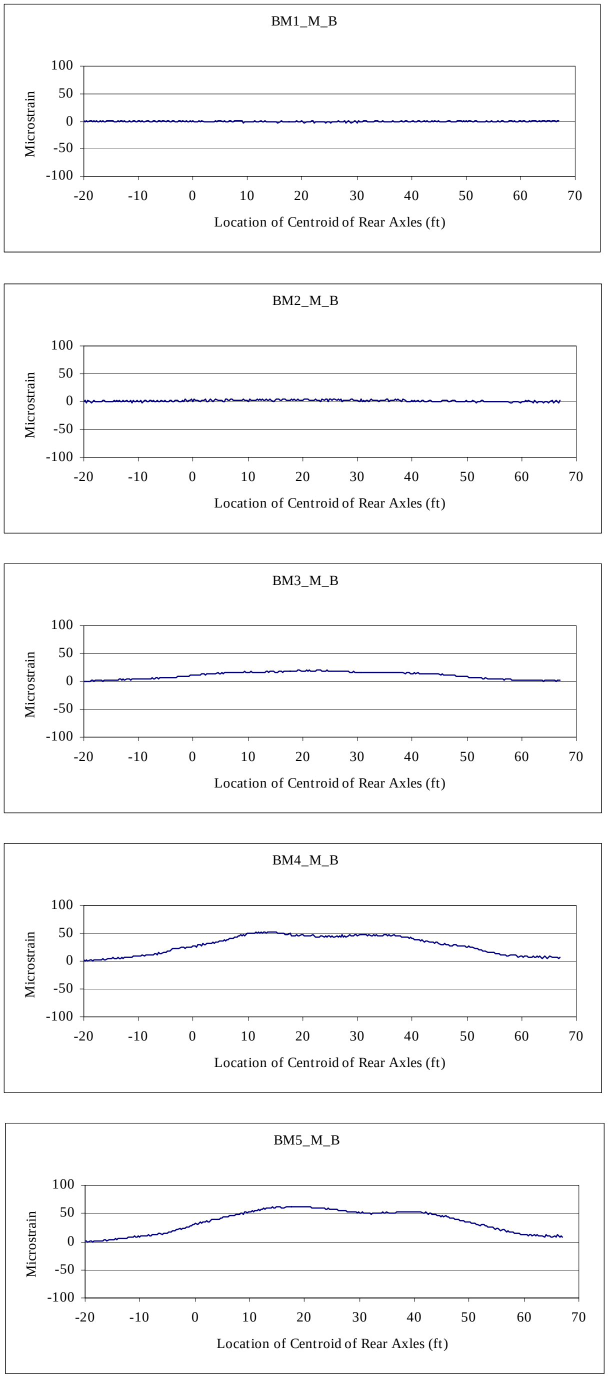

Figure D.7 Sample Strain History – Wimberley Bridge – Span 1 – Run 1 – Back-to-Back Configuration (Wagener 2002)

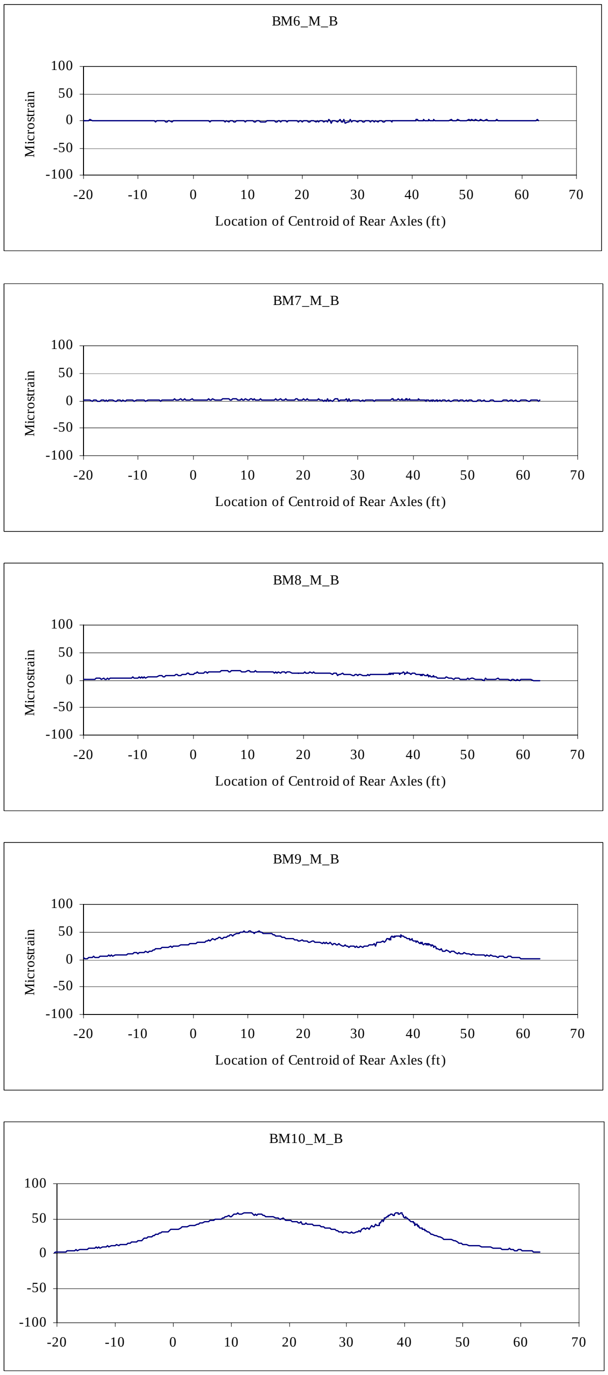

Figure 4.11 Sample Strain History – Wimberley Bridge – Span 2 – Run 1 – Back-to-Back Configuration (Wagener 2002)

D.2 MAXIMUM MEASURED STRAINS

The maximum measured strains at midspan for each bridge beam are summarized in Table D.1 through Table D.3. All values are in units of microstrain, and a positive value indicates tensile strain while a negative value indicates compressive strain.

Table D.1 Maximum Measured Concrete Tensile Strains from Midspan Bottom Gages, $\mu\varepsilon$ (Wagener 2002)

Bridge Name	Beam 1	Beam 2	Beam 3	Beam 4	Beam 5
Chandler Creek – 40’ Span	66	52	51	61	—
Chandler Creek – 60’ Span	86	68	63	84	—
Lake LBJ	71	88	104	105	—
Lampasas River – Span 1	89	92	108	139	—
Lampasas River – Span 2	83	84	97	131	—
Willis Creek	101	87	91	117	—
Wimberley – Span 1	76	68	65	61	73
Wimberley – Span 2	76	63	69	66	78

Table D.2 Maximum Measured Concrete Tensile Strains from Midspan Web Gages, $\mu\varepsilon$ (Wagener 2002)

Bridge Name	Beam 1	Beam 2	Beam 3	Beam 4	Beam 5
Chandler Creek – 40’ Span	28	26	26	28	—
Chandler Creek – 60’ Span	39	32	30	37	—
Lake LBJ	32	46	56	48	—
Lampasas River – Span 1	41	53	50	68	—
Lampasas River – Span 2	39	42	47	69	—
Willis Creek	51	41	40	50	—
Wimberley – Span 1	40	30	30	27	37
Wimberley – Span 2	40	Bad Gage	33	29	36

Table D.3 Maximum Measured Concrete Compressive Strains from Midspan Top Gages, $\mu\varepsilon$ (Wagener 2002)

Bridge Name	Beam 1	Beam 2	Beam 3	Beam 4	Beam 5
Chandler Creek – 40’ Span	-9	-9	-7	-6	—
Chandler Creek – 60’ Span	-19	-16	-13	-15	—
Lake LBJ	-8	-10	-12	-10	—
Lampasas River – Span 1	-18	-18	-25	-30	—
Lampasas River – Span 2	-17	-19	-21	-25	—
Willis Creek	-26	-32	-31	-29	—
Wimberley – Span 1	—	-11	-5	-11	—
Wimberley – Span 2	—	-14	-16	-15	—

Appendix E

Inferred Live Load Moments from Diagnostic Load Tests

This appendix contains two sections. The first section contains total midspan live load moments inferred from measured data collected during each load test for all five bridges. Moments calculated using design, quality control, and estimated in situ section properties, combined with the corresponding calculated or inferred neutral axis depths are reported for each bridge. The values reported are the maximum midspan moments and are calculated by summing the moments for each beam based on data from the bottom, web or top gages. The second section contains summaries comparing the total inferred midspan moments, based on estimated in situ section properties and inferred neutral axis depths, with moments calculated using finite element analyses.

E.1 TOTAL MIDSPAN LIVE LOAD MOMENTS INFERRED FROM MEASURED DATA

Table E.1 Maximum Total Moments based on Calculated Neutral Axis Depths for Chandler Creek Bridge, 40-ft Span

Run	Total Midspan Moment, in-kip								
	Design Section Properties			Quality Control Section Properties			Estimated In Situ Section Properties		
	Bottom Gages	Web Gages	Top Gages	Bottom Gages	Web Gages	Top Gages	Bottom Gages	Web Gages	Top Gages
1	4006	4082	3106	4889	4915	4237	5280	5429	3883
2	3831	3969	3253	4676	4778	4463	5050	5159	4824
3	3929	3923	3550	4769	4670	5032	5150	5042	5440
4	3776	3791	3550	4585	4512	5043	4951	4871	5452
5	3956	3974	3380	4805	4727	4823	5189	5103	5213
6	4006	3990	3476	4866	4747	4964	5254	5125	5366
7	2689	2937	1711	3258	3501	2365	3518	3780	2557
8	2617	2998	1635	3171	3574	2266	3424	3859	2450
9	2710	2967	2291	3292	3529	3252	3555	3811	3515
10	2690	2833	2229	3268	3370	3162	3530	3640	3418
11	2910	2731	3215	3538	3246	4608	3821	3504	4981
12	2800	2629	3099	3404	3125	4443	3675	3373	4804
13-1	2001	2210	1479	2425	2635	2044	2618	2845	2211
13-2	1944	2152	1331	2356	2564	1842	2544	2769	1991
14-1	1966	2062	1976	2389	2453	2807	2580	2649	3034
14-2	1924	1974	1782	2337	2347	2535	2524	2535	2740
15-1	2120	1947	2294	2578	2313	3281	2784	2498	3547
15-2	2068	1884	2307	2514	2238	3297	2715	2417	3565

Table E.2 Maximum Total Moments based on Inferred Neutral Axis Depths for Chandler Creek Bridge, 40-ft Span

Run	Total Midspan Moment, in-kip								
	Design Section Properties			Quality Control Section Properties			Estimated In Situ Section Properties		
	Bottom Gages	Web Gages	Top Gages	Bottom Gages	Web Gages	Top Gages	Bottom Gages	Web Gages	Top Gages
1	3933	3942	3557	4935	5074	3629	5329	5480	3920
2	3759	3826	3783	4661	4744	4690	5034	5123	5065
3	3842	3759	4217	4764	4661	5229	5145	5034	5647
4	3694	3635	4218	4581	4507	5230	4948	4868	5648
5	3865	3790	4100	4793	4699	5083	5176	5075	5489
6	3914	3806	4224	4853	4719	5236	5241	5097	5655
7	2626	2819	1979	3256	3495	2454	3516	3775	2650
8	2555	2876	1897	3168	3566	2352	3422	3851	2540
9	2636	2803	2771	3268	3474	3434	3529	3752	3709
10	2618	2674	2707	3245	3314	3356	3505	3580	3624
11	2852	2615	3858	3536	3243	4783	3819	3502	5166
12	2743	2519	3722	3401	3124	4615	3673	3374	4984
13-1	1955	2119	1696	2424	2628	2102	2618	2838	2270
13-2	1898	2061	1536	2354	2556	1905	2542	2760	2057
14-1	1912	1946	2404	2370	2412	2980	2560	2604	3219
14-2	1871	1862	2173	2319	2307	2694	2505	2492	2909
15-1	2078	1867	2761	2577	2315	3423	2783	2500	3697
15-2	2027	1807	2746	2514	2241	3405	2715	2420	3677

Table E.3 Maximum Total Moments based on Calculated Neutral Axis Depths for Chandler Creek Bridge, 60-ft Span

Run	Total Midspan Moment, in-kip								
	Design Section Properties			Quality Control Section Properties			Estimated In Situ Section Properties		
	Bottom Gages	Web Gages	Top Gages	Bottom Gages	Web Gages	Top Gages	Bottom Gages	Web Gages	Top Gages
1	8010	8678	5873	10384	11144	7848	11239	12065	8486
2	7570	8189	5916	9871	10727	7666	10684	11613	8289
3	7840	8264	6332	10165	10613	8463	11001	11489	9151
4	7885	8658	6181	10223	11119	8260	11064	12037	8932
5	8158	8311	6317	10576	10673	8442	11447	11555	9129
6	8199	8398	6240	10629	10786	8339	11504	11676	9017
7	6240	7010	4165	8090	9003	5566	8756	9746	6019
8	6295	7066	4285	8161	9075	5726	8833	9824	6192
9	6436	7241	4846	8344	9300	6477	9032	10070	7003
10	6386	7506	4786	8279	9640	6396	8961	10438	6916
11	6695	7035	5820	8680	9035	7778	9394	9781	8410
12	6407	7264	5339	8306	9330	7135	8990	10101	7715
13-1	4069	4572	2670	5276	5871	3568	5710	6356	3859
13-2	4007	4492	2609	5196	5769	3486	5623	6245	3770
14-1	4011	4201	3004	5201	5396	4015	5629	5843	4341
14-2	3993	4225	77	5177	5427	103	5604	5876	111
15-1	4183	4116	3600	5423	5286	4811	5870	5722	5202
15-2	4120	4149	3533	5342	5329	4722	5782	5768	5106

Table E.4 Maximum Total Moments based on Inferred Neutral Axis Depths for Chandler Creek Bridge, 60-ft Span

Run	Total Midspan Moment, in-kip								
	Design Section Properties			Quality Control Section Properties			Estimated In Situ Section Properties		
	Bottom Gages	Web Gages	Top Gages	Bottom Gages	Web Gages	Top Gages	Bottom Gages	Web Gages	Top Gages
1	7661	7787	7059	9996	10159	9209	10817	10994	9966
2	7286	7497	6870	9506	9782	8963	10286	10585	9700
3	7491	7396	7613	9773	9650	9932	10576	10442	10748
4	7532	7753	7421	9827	10115	9682	10634	10946	10478
5	7801	7451	7601	10177	9721	9917	11013	10519	10731
6	7839	7527	7505	10227	9820	9791	11067	10627	10596
7	5960	6272	5025	7776	8183	6557	8414	8855	7095
8	6011	6319	5162	7842	8244	6735	8486	8921	7288
9	6172	6570	5835	8052	8572	7613	8713	9276	8239
10	6122	6788	5784	7987	8856	7546	8643	9584	8166
11	6395	6287	7006	8344	8203	9141	9029	8877	9892
12	6122	6536	6407	7987	8527	8359	8643	9227	9046
13-1	3886	4085	3222	5070	5330	4204	5487	5768	4550
13-2	3828	4024	3152	4994	5250	4113	5405	5682	4451
14-1	3850	3803	3598	5022	4962	4695	5435	5370	5080
14-2	3832	3825	98	5000	4990	128	5410	5400	139
15-1	3996	3666	4324	5213	4783	5641	5642	5175	6104
15-2	3934	3699	4246	5133	4826	5539	5555	5222	5994

Table E.5 Maximum Total Moments based on Calculated Neutral Axis Depths for Lake LBJ Bridge

Run	Total Midspan Moment, in-kip								
	Design Section Properties			Quality Control Section Properties			Estimated In Situ Section Properties		
	Bottom Gages	Web Gages	Top Gages	Bottom Gages	Web Gages	Top Gages	Bottom Gages	Web Gages	Top Gages
1	9176	9528	4890	11467	11727	6601	12414	12700	7133
2	9370	9919	4996	11708	12209	6747	12675	13223	7291
3	10543	11329	5638	13169	13946	7633	14257	15104	8248
4	9020	9765	4953	11704	12295	8046	12671	13315	8694
5	8983	10033	5170	11219	12352	7007	12145	13377	7571
6	9359	10509	5328	11689	12938	7222	12655	14012	7804
7	9363	10094	4941	11696	12429	6693	12662	13460	7232
8	11151	11169	5949	14585	14127	9426	15790	15299	10186
9	11105	11291	5832	13878	13901	7872	15024	15054	8506
10-1	5630	5603	3235	7364	7084	5142	7973	7672	5557
10-2	5630	5603	3235	7364	7084	5142	7973	7672	5557
11-1	5575	6261	3851	6962	7709	5215	7537	8349	5635
11-2	5575	6261	3851	7193	7864	6290	7787	8517	6796
12-1	5808	5898	3109	7604	7470	5020	8232	8090	5425
12-2	5808	5898	3109	7604	7470	5020	8232	8090	5425
13	10236	10652	5057	13388	13475	8049	14494	14593	8697
14	11254	11342	6247	14717	14344	9918	15933	15534	10717
15	11310	11204	6279	14784	14168	9961	16005	15344	10764

Table E.6 Maximum Total Moments based on Inferred Neutral Axis Depths for Lake LBJ Bridge

Run	Total Midspan Moment, in-kip								
	Design Section Properties			Quality Control Section Properties			Estimated In Situ Section Properties		
	Bottom Gages	Web Gages	Top Gages	Bottom Gages	Web Gages	Top Gages	Bottom Gages	Web Gages	Top Gages
1	8430	7985	8095	10675	10110	10251	11553	10941	11094
2	8605	8304	8277	10894	10509	10482	11790	11373	11344
3	9671	9451	9368	12236	11950	11869	13242	12932	12846
4	8597	8336	9873	10879	10541	12518	11774	11408	13547
5	8235	8360	8608	10415	10566	10909	11272	11435	11806
6	8581	8754	8871	10853	11062	11243	11745	11972	12167
7	8590	8432	8227	10868	10661	10424	11762	11538	11282
8	10727	9632	11576	13587	12196	14668	14705	13199	15875
9	10204	9477	9667	12923	12000	12242	13986	12987	13248
10-1	5416	4827	6305	6860	6113	7990	7425	6615	8647
10-2	5416	4827	6305	6860	6113	7990	7425	6615	8647
11-1	5109	5211	6407	6460	6583	8119	6991	7124	8786
11-2	5279	5316	7727	6676	6717	9801	7225	7269	10607
12-1	5593	5101	6177	7086	6460	7831	7668	6991	8475
12-2	5593	5101	6177	7086	6460	7831	7668	6991	8475
13	9846	9188	9892	12471	11634	12537	13497	12591	13568
14	10823	9778	12182	13709	12380	15436	14836	13398	16706
15	10872	9657	12232	13770	12227	15500	14902	13233	16775

Table E.7 Maximum Total Moments based on Calculated Neutral Axis Depths for Lampasas River Bridge, Span 1

Run	Total Midspan Moment, in-kip								
	Design Section Properties			Quality Control Section Properties			Estimated In Situ Section Properties		
	Bottom Gages	Web Gages	Top Gages	Bottom Gages	Web Gages	Top Gages	Bottom Gages	Web Gages	Top Gages
1	10351	11950	7201	13034	14748	9661	14365	16361	10422
2	10770	11724	6934	13562	14468	9298	14946	16051	10033
3	10064	10952	6536	12673	13516	8766	13967	14994	9458
4	10503	11628	6621	13225	14352	8876	14575	15922	9578
5	10430	11601	6440	13134	14318	8633	14475	15884	9316
6	10707	12168	6533	13482	15019	8754	14858	16661	9448
7	9983	11515	6089	12570	14213	8158	13854	15767	8805
8	12502	13510	8198	15743	16673	10987	17350	18497	11857
9	12598	13538	8089	15863	16707	10842	17483	18535	11700
10-1	6166	6490	4235	7765	8010	5681	8557	8886	6129
10-2	6143	6532	4013	7735	8061	5382	8524	8943	5807
11-1	6261	7226	3884	7884	8919	5205	8689	9894	5618
11-2	6192	7246	3890	7797	8944	5214	8593	9922	5627
12-1	6494	7379	4315	8177	9106	5780	9012	10102	6239
12-2	6413	7096	4203	8076	8757	5630	8900	9715	6077
13	12696	13728	8122	15987	16942	10887	17619	18795	11749
14	—	13689	8294	—	16894	11117	—	18742	11997
15	—	9797	6086	—	12091	8163	—	13414	8806
16	—	12168	6533	—	13808	9051	—	15319	9765

Table E.8 Maximum Total Moments based on Inferred Neutral Axis Depths for Lampasas River Bridge, Span 1

Run	Total Midspan Moment, in-kip								
	Design Section Properties			Quality Control Section Properties			Estimated In Situ Section Properties		
	Bottom Gages	Web Gages	Top Gages	Bottom Gages	Web Gages	Top Gages	Bottom Gages	Web Gages	Top Gages
1	9365	9538	10811	11967	12189	13815	13125	13368	15152
2	9744	9364	10413	12452	11966	13307	13657	13124	14594
3	9105	8748	9811	11636	11178	12538	12761	12260	13750
4	9516	9330	9906	12159	11922	12659	13336	13076	13883
5	9450	9311	9636	12075	11898	12313	13243	13049	13504
6	9704	9780	9742	12400	12497	12450	13600	13706	13654
7	9048	9252	9079	11562	11823	11602	12680	12967	12724
8	11310	10793	12224	14453	13792	15621	15851	15126	17132
9	11397	10815	12061	14564	13821	15413	15972	15158	16904
10-1	5579	5183	6361	7129	6623	8128	7818	7264	8915
10-2	7789	7316	8447	7789	7316	8447	7789	7316	8447
11-1	5676	5813	5790	7253	7427	7399	7955	8146	8115
11-2	5614	5828	5799	7173	7446	7411	7867	8167	8128
12-1	5874	5892	6386	7507	7530	8161	8233	8258	8950
12-2	5801	5667	6219	7413	7242	7947	8131	7942	8716
13	11486	10962	12111	14677	14009	15477	16097	15363	16974
14	—	10934	12377	—	13972	15817	—	15324	17347
15	—	7824	9136	—	9999	11674	—	10966	12804
16	—	9780	9742	—	11419	12943	—	12523	14194

Table E.9 Maximum Total Moments based on Calculated Neutral Axis Depths for Lampasas River Bridge, Span 2

Run	Total Midspan Moment, in-kip								
	Design Section Properties			Quality Control Section Properties			Estimated In Situ Section Properties		
	Bottom Gages	Web Gages	Top Gages	Bottom Gages	Web Gages	Top Gages	Bottom Gages	Web Gages	Top Gages
1	9929	11800	6142	12503	14564	8207	13779	16157	8866
2	9803	11646	6038	12344	14373	8067	13604	15945	8715
3	9883	11563	6061	12445	14271	8098	13715	15831	8748
4	9811	11247	6189	12355	13883	8269	13616	15400	8934
5	9595	10950	6042	12083	13517	8073	13316	14994	8722
6	9882	11212	6319	12443	13842	8442	13713	15354	9120
7	9466	10821	6160	11920	13359	8230	13137	14818	8891
8	11726	12889	7618	14765	15908	10178	16273	17648	10996
9	11731	12907	7591	14772	15931	10143	16280	17673	10957
10-1	5956	6891	3796	7500	8505	5072	8265	9435	5480
10-2	5742	6720	3582	7231	8294	4786	7969	9201	5171
11-1	5879	6767	3778	7403	8354	5048	8158	9267	5453
11-2	5727	6549	3756	7211	8085	5019	7947	8968	5422
12-1	6052	6447	3983	7620	7958	5321	8398	8828	5749
12-2	5719	6413	4102	7202	7915	5481	7937	8781	5921
13	11868	13356	7398	14945	16486	9884	16471	18288	10678
14	11953	13413	7516	15051	16555	10042	16588	18365	10849
15	8813	10282	5553	11098	12690	7419	12231	14078	8015
16	9882	11212	6319	11862	13695	7848	13073	15193	8478

Table E.10 Maximum Total Moments based on Inferred Neutral Axis Depths for Lampasas River Bridge, Span 2

Run	Total Midspan Moment, in-kip								
	Design Section Properties			Quality Control Section Properties			Estimated In Situ Section Properties		
	Bottom Gages	Web Gages	Top Gages	Bottom Gages	Web Gages	Top Gages	Bottom Gages	Web Gages	Top Gages
1	8982	9416	8876	11478	12032	11343	12588	13196	12440
2	8868	9294	8725	11332	11876	11150	12429	13025	12228
3	8940	9228	8761	11425	11792	11196	12530	12932	12279
4	8887	9017	8949	11356	11523	11436	12455	12638	12542
5	8691	8776	8739	11105	11214	11167	12180	12299	12247
6	8954	9007	9137	11442	11510	11676	12549	12623	12806
7	8578	8693	8909	10961	11108	11384	12021	12183	12485
8	10607	10294	11007	13554	13154	14066	14865	14427	15427
9	10611	10305	10973	13559	13169	14022	14871	14443	15378
10-1	5387	5499	5489	6885	7028	7015	7550	7707	7693
10-2	5195	5365	5181	6639	6855	6621	7281	7518	7261
11-1	5329	5441	5457	6810	6953	6973	7469	7625	7648
11-2	5191	5268	5427	6634	6731	6934	7275	7383	7605
12-1	5474	5149	5756	6995	6581	7355	7672	7217	8067
12-2	5173	5121	5930	6611	6544	7577	7250	7177	8310
13	10737	10665	10695	13720	13629	13667	15047	14947	14989
14	10811	10706	10857	13815	13681	13874	15151	15004	15216
15	7973	8204	8027	10188	10484	10257	11174	11498	11249
16	8954	9007	9137	10890	11316	10852	11943	12411	11901

Table E.11 Maximum Total Moments based on Calculated Neutral Axis Depths for Willis Creek Bridge

Run	Total Midspan Moment, in-kip								
	Design Section Properties			Quality Control Section Properties			Estimated In Situ Section Properties		
	Bottom	Web Gages	Top Gages	Bottom	Web Gages	Top Gages	Bottom	Web Gages	Top Gages
1	9549	10060	9422	12432	12716	12700	13158	13348	13783
2	10324	10234	10467	13388	13134	13992	14169	13786	15185
3	7938	8016	7872	10294	10287	10524	10894	10797	11422
4	7996	8402	8072	10368	10783	10791	10974	11319	11712
5	8544	8517	8425	11079	10930	11263	11726	11473	12225
6	8647	8620	8758	11213	11062	11709	11867	11611	12708
7	8678	8850	9018	11253	11355	12056	11910	11916	13084
8	8524	8762	8846	11053	11242	11826	11698	11798	12835
9	8405	8762	8819	10899	11241	11789	11534	11796	12795
10	8343	8601	8926	10819	11034	11932	11450	11579	12950
11	8339	9049	8823	10814	11611	11794	11444	12185	12799
12	7909	8063	8548	10256	10345	11427	10855	10856	12401
13	8206	8704	8330	10641	11170	11134	11262	11724	12083
14	8156	8924	8190	10576	11453	10948	11193	12021	11882
15-1	5487	5327	5482	7116	6837	7328	7531	7176	7953
15-2	5344	5462	5336	6930	7010	7132	7335	7359	7740
16-1	5285	5489	5653	6854	7043	7557	7254	7391	8201
16-2	5241	5660	5570	6796	7263	7445	7193	7622	8080
17-1	5193	6060	5295	6733	7775	7075	7126	8159	7676
17-2	5162	6211	5285	6694	7969	7063	7084	8363	7663
18-1	5235	5626	5405	6788	7219	7224	7184	7576	7839
18-2	5125	5595	5352	6646	7179	7155	7033	7534	7764
19-1	5060	4905	5456	6562	6294	7294	6945	6607	7915
19-2	4968	4305	5730	6442	5524	7660	6818	5798	8314
20	10399	10441	10686	13484	13399	14285	14271	14064	15503

Table E.12 Maximum Total Moments based on Inferred Neutral Axis Depths for Willis Creek Bridge

Run	Total Midspan Moment, in-kip								
	Design Section Properties			Quality Control Section Properties			Estimated In Situ Section Properties		
	Bottom	Web Gages	Top Gages	Bottom	Web Gages	Top Gages	Bottom	Web Gages	Top Gages
1	9244	9097	10658	12078	11885	13925	12861	12656	14828
2	9960	9393	11739	13013	12273	15338	13857	13068	16332
3	7658	7356	8824	10005	9612	11529	10654	10235	12276
4	7713	7720	9049	10078	10086	11823	10731	10740	12589
5	8243	7817	9437	10770	10213	12330	11468	10875	13129
6	8343	7910	9812	10901	10334	12820	11607	11004	13651
7	8353	8052	10111	10914	10520	13210	11621	11201	14066
8	8205	7976	9916	10721	10421	12956	11415	11096	13795
9	8079	7936	9888	10555	10369	12919	11239	11040	13756
10	8021	7794	10007	10479	10183	13075	11158	10842	13922
11	8021	8225	9899	10480	10747	12934	11159	11443	13773
12	7610	7321	9586	9942	9565	12525	10587	10185	13337
13	7912	7977	9352	10337	10423	12219	11007	11098	13011
14	7863	8191	9187	10273	10701	12003	10939	11395	12781
15-1	5295	4892	6147	6918	6392	8031	7367	6806	8552
15-2	5157	5033	5985	6739	6575	7820	7175	7002	8327
16-1	5083	4990	6343	6642	6520	8288	7072	6943	8825
16-2	5042	5159	6253	6588	6740	8170	7015	7177	8700
17-1	4987	5503	5962	6516	7190	7789	6938	7656	8294
17-2	4958	5655	5948	6477	7388	7771	6897	7867	8274
18-1	5035	5117	6071	6579	6685	7932	7005	7118	8446
18-2	4930	5092	6005	6441	6654	7846	6859	7085	8355
19-1	4881	4501	6119	6377	5881	7995	6791	6262	8514
19-2	4792	3927	6416	6261	5131	8383	6666	5463	8926
20	10029	9580	11979	13104	12517	15651	13953	13328	16666

Table E.13 Maximum Total Moments based on Calculated Neutral Axis Depths for Wimberley Bridge, Span 1

Run	Total Midspan Moment, in-kip					
	Design Section Properties		Quality Control Section Properties		Estimated In Situ Section Properties	
	Bottom Gages	Web Gages	Bottom Gages	Web Gages	Bottom Gages	Web Gages
1	3164	2960	4056	3731	4389	4037
2	3662	3368	4694	4245	5079	4594
3	3503	3359	4453	4215	4818	4561
4	3489	3276	4437	4113	4801	4450
5	3904	3790	4952	4746	5358	5135
6	3780	3710	4796	4646	5190	5027
7	5253	6304	6686	7914	7235	8564
8	5289	5001	6731	6281	7283	6796
9-1	2950	2772	3782	3494	4092	3781
9-2	2754	2541	3530	3203	3819	3466
10-1	2911	2629	3721	3314	4026	3586
10-2	2638	2427	3371	3058	3648	3309
11-1	2941	3277	2951	3277	4004	4435
11-2	2741	3097	3450	3878	3733	4196
12-1	2874	2663	3639	3341	3938	3615
12-2	2667	2507	3378	3143	3655	3401
13-1	3050	2918	3867	3654	4184	3954
13-2	2846	2801	3608	3509	3904	3797
14-1	3130	2889	3969	3617	4294	3914
14-2	2857	2689	3622	3366	3920	3643
15-1	3231	2871	4099	3596	4435	3891
15-2	2975	2613	3775	3271	4085	3539
16	5563	4944	6875	6086	7440	6585
17	5556	5086	6869	6258	7432	6771

Table E.14 Maximum Total Moments based on Inferred Neutral Axis Depths for Wimberley Bridge, Span 1

Run	Total Midspan Moment, in-kip					
	Design Section Properties		Quality Control Section Properties		Estimated In Situ Section Properties	
	Bottom Gages	Web Gages	Bottom Gages	Web Gages	Bottom Gages	Web Gages
1	3123	2834	4011	3641	4160	3903
2	3614	3222	4642	4138	4814	4435
3	3483	3317	4468	4256	4823	4604
4	3467	3229	4448	4143	4795	4481
5	3813	3617	4897	4645	5302	5027
6	3693	3547	4744	4555	5132	4929
7	5197	6067	6671	7791	7145	8417
8	5227	4868	6710	6249	7187	6748
9-1	2910	2649	3738	3403	3867	3650
9-2	2717	2430	3490	3121	3619	3347
10-1	2889	2561	3709	3288	3925	3542
10-2	2618	2364	3361	3034	3559	3269
11-1	2891	3177	3709	4078	3982	4407
11-2	2697	3007	3460	3860	3716	4172
12-1	2849	2632	3655	3377	3947	3654
12-2	2643	2475	3392	3175	3663	3435
13-1	3018	2868	3872	3679	4187	3981
13-2	2816	2749	3614	3527	3907	3817
14-1	3081	2806	3955	3602	4278	3898
14-2	2812	2613	3609	3354	3904	3629
15-1	3159	2744	4058	3524	4391	3813
15-2	2905	2493	3731	3201	4038	3464
16	5298	4640	6805	5959	7218	6419
17	5294	4765	6800	6121	7213	6592

Table E.15 Maximum Total Moments based on Calculated Neutral Axis Depths for Wimberley Bridge, Span 2

Run	Total Midspan Moment, in-kip					
	Design Section Properties		Quality Control Section Properties		Estimated In Situ Section Properties	
	Bottom Gages	Web Gages	Bottom Gages	Web Gages	Bottom Gages	Web Gages
1	2980	—	3826	—	4139	—
2	4052	—	5201	—	5627	—
3	3782	—	4843	—	5240	—
4	3200	—	4098	—	4434	—
5	3872	—	4970	—	5377	—
6	3881	—	4981	—	5390	—
7	4994	—	6402	—	6927	—
8	5141	—	6590	—	7130	—
9-1	2957	—	3795	—	4106	—
9-2	2718	—	3489	—	3775	—
10-1	2891	—	3706	—	4010	—
10-2	2765	—	3423	—	3704	—
11-1	2887	—	3648	—	3947	—
11-2	2681	—	3383	—	3661	—
12-1	2855	—	3629	—	3927	—
12-2	2660	—	3379	—	3656	—
13-1	2914	—	3677	—	3978	—
13-2	2914	—	3676	—	3978	—
14-1	2946	—	3656	—	3956	—
14-2	2838	—	3523	—	3812	—
15-1	3205	—	3862	—	4179	—
15-2	2956	—	3559	—	3851	—
16	5324	—	6442	—	6971	—
17	5425	—	6546	—	7083	—

Table E.16 Maximum Total Moments based on Inferred Neutral Axis Depths for Wimberley Bridge, Span 2

Run	Total Midspan Moment, in-kip					
	Design Section Properties		Quality Control Section Properties		Estimated In Situ Section Properties	
	Bottom Gages	Web Gages	Bottom Gages	Web Gages	Bottom Gages	Web Gages
1	2946	—	3784	—	3926	—
2	4005	—	5144	—	5335	—
3	3787	—	4860	—	5225	—
4	3204	—	4111	—	4418	—
5	3828	—	4916	—	5105	—
6	3838	—	4929	—	5119	—
7	4975	—	6387	—	6770	—
8	5121	—	6573	—	6965	—
9-1	2924	—	3755	—	3901	—
9-2	2688	—	3452	—	3583	—
10-1	2879	—	3695	—	3912	—
10-2	2659	—	3413	—	3613	—
11-1	2850	—	3657	—	3924	—
11-2	2642	—	3391	—	3635	—
12-1	2840	—	3644	—	3925	—
12-2	2644	—	3393	—	3653	—
13-1	2871	—	3685	—	3950	—
13-2	2871	—	3684	—	3949	—
14-1	2842	—	3648	—	3867	—
14-2	2738	—	3515	—	3726	—
15-1	2975	—	3821	—	3967	—
15-2	2741	—	3520	—	3651	—
16	4969	—	6382	—	6648	—
17	5046	—	6481	—	6742	—

E.2 COMPARISON OF LIVE LOAD MOMENTS INFERRED FROM MEASURED DATA WITH RESULTS FROM FINITE ELEMENT ANALYSIS

Table E.17 Comparison of Calculated and Inferred Maximum Total Moments based on Estimated In Situ Section Properties and Inferred Neutral Axis Depths for Chandler Creek, 40-ft Span

Run	Total Inferred Midspan Moment, in-kip		Total Midspan Moment From FE Analysis, in-kip	Average Percent Difference
	Bottom Gages	Web Gages		
1	5329	5480	5976	-10%
2	5034	5123	5976	-15%
3	5145	5034	5776	-12%
4	4948	4868	5776	-15%
5	5176	5075	5988	-14%
6	5241	5097	5988	-14%
7	3516	3775	4430	-18%
8	3422	3851	4430	-18%
9	3529	3752	4335	-16%
10	3505	3580	4335	-18%
11	3819	3502	4426	-17%
12	3673	3374	4426	-20%
13-1	2618	2838	5988	-54%
13-2	2542	2760	3237	-18%
14-1	2560	2604	3176	-19%
14-2	2505	2492	3176	-21%
15-1	2783	2500	3242	-19%
15-2	2715	2420	3242	-21%

Table E.18 Comparison of Calculated and Inferred Maximum Total Moments based on Estimated In Situ Section Properties and Inferred Neutral Axis Depths for Chandler Creek, 60-ft Span

Run	Total Inferred Midspan Moment, in-kip		Total Midspan Moment From FE Analysis, in-kip	Average Percent Difference
	Bottom Gages	Web Gages		
1	10817	10994	10909	0%
2	10286	10585	10909	-4%
3	10576	10442	10735	-2%
4	10634	10946	10735	1%
5	11013	10519	10935	-2%
6	11067	10627	10935	-1%
7	8414	8855	8826	-2%
8	8486	8921	8826	-1%
9	8713	9276	8721	3%
10	8643	9584	8721	4%
11	9029	8877	8833	1%
12	8643	9227	8833	1%
13-1	5487	5768	5709	-1%
13-2	5405	5682	5709	-3%
14-1	5435	5370	5653	-4%
14-2	5410	5400	5653	-4%
15-1	5642	5175	5730	-6%
15-2	5555	5222	5730	-6%

Table E.19 Comparison of Calculated and Inferred Maximum Total Moments based on Estimated In Situ Section Properties and Inferred Neutral Axis Depths for Lake LBJ

Run	Total Inferred Midspan Moment, in-kip		Total Midspan Moment From FE Analysis, in-kip	Average Percent Difference
	Bottom Gages	Web Gages		
1	11553	10941	12616	-11%
2	11790	11373	12616	-8%
3	13242	12932	12610	4%
4	11774	11408	12610	-8%
5	11272	11435	12602	-10%
6	11745	11972	12602	-6%
7	11762	11538	12610	-8%
8	14705	13199	15872	-12%
9	13986	12987	15872	-15%
10-1	7425	6615	8116	-14%
10-2	7425	6615	8116	-14%
11-1	6991	7124	8108	-13%
11-2	7225	7269	8108	-11%
12-1	7668	6991	8116	-10%
12-2	7668	6991	8116	-10%
13	13497	12591	15872	-18%
14	14836	13398	15872	-11%
15	14902	13233	15872	-11%

Table E.20 Comparison of Calculated and Inferred Maximum Total Moments based on Estimated In Situ Section Properties and Inferred Neutral Axis Depths for Lampasas River Bridge, Span 1

Run	Total Inferred Midspan Moment, in-kip		Total Midspan Moment From FE Analysis, in-kip	Average Percent Difference
	Bottom Gages	Web Gages		
1	13125	13368	14693	-10%
2	13657	13124	14693	-9%
3	12761	12260	14693	-15%
4	13336	13076	14695	-10%
5	13243	13049	14695	-11%
6	13600	13706	14690	-7%
7	12680	12967	14690	-13%
8	15851	15126	17672	-12%
9	15972	15158	17672	-12%
10-1	7818	7264	8955	-16%
10-2	7789	7316	8955	-16%
11-1	7955	8146	8953	-10%
11-2	7867	8167	8953	-10%
12-1	8233	8258	8955	-8%
12-2	8131	7942	8955	-10%
13	16097	15363	17672	-11%
14	—	15324	17672	-13%
15	—	10966	14693	-25%
16	—	12523	14693	-15%

Table E.21 Comparison of Calculated and Inferred Maximum Total Moments based on Estimated In Situ Section Properties and Inferred Neutral Axis Depths for Lampasas River Bridge, Span 2

Run	Total Inferred Midspan Moment, in-kip		Total Midspan Moment From FE Analysis, in-kip	Average Percent Difference
	Bottom Gages	Web Gages		
1	12588	13196	14693	-12%
2	12429	13025	14693	-13%
3	12530	12932	14693	-13%
4	12455	12638	14695	-15%
5	12180	12299	14695	-17%
6	12549	12623	14690	-14%
7	12021	12183	14690	-18%
8	14865	14427	17672	-17%
9	14871	14443	17672	-17%
10-1	7550	7707	8955	-15%
10-2	7281	7518	8955	-17%
11-1	7469	7625	8953	-16%
11-2	7275	7383	8953	-18%
12-1	7672	7217	8955	-17%
12-2	7250	7177	8955	-19%
13	15047	14947	17672	-15%
14	15151	15004	17672	-15%
15	11174	11498	14693	-23%
16	11943	12411	14693	-17%

Table E.22 Comparison of Calculated and Inferred Maximum Total Moments based on Estimated In Situ Section Properties and Inferred Neutral Axis Depths for Willis Creek

Run	Total Inferred Midspan Moment, in-kip		Total Midspan Moment From FE Analysis, in-kip	Average Percent Difference
	Bottom Gages	Web Gages		
1	12861	12656	16128	-26%
2	13857	13068	16128	-20%
3	10654	10235	12789	-22%
4	10731	10740	12789	-19%
5	11468	10875	12789	-14%
6	11607	11004	12789	-13%
7	11621	11201	12763	-12%
8	11415	11096	12763	-13%
9	11239	11040	12763	-15%
10	11158	10842	12763	-16%
11	11159	11443	12763	-13%
12	10587	10185	12763	-23%
13	11007	11098	12789	-16%
14	10939	11395	12789	-15%
15-1	7367	6806	8224	-16%
15-2	7175	7002	8224	-16%
16-1	7072	6943	8169	-17%
16-2	7015	7177	8169	-15%
17-1	6938	7656	8201	-12%
17-2	6897	7867	8201	-11%
18-1	7005	7118	8170	-16%
19-2	6859	7085	8170	-17%
19-1	6791	6262	8224	-26%
19-2	6666	5463	8224	-36%
20	13953	13328	16128	-18%

Table E.23 Comparison of Calculated and Inferred Maximum Total Moments based on Estimated In Situ Section Properties and Inferred Neutral Axis Depths for Wimberley, Span 1

Run	Total Inferred Midspan Moment, in-kip		Total Midspan Moment From FE Analysis, in-kip	Average Percent Difference
	Bottom Gages	Web Gages		
1	4160	3903	5756	-30%
2	4814	4435	5756	-20%
3	4823	4604	5627	-16%
4	4795	4481	5627	-18%
5	5302	5027	5720	-10%
6	5132	4929	5720	-12%
7	7145	8417	7829	-1%
8	7187	6748	7829	-11%
9-1	3867	3650	4209	-11%
9-2	3619	3347	4209	-17%
10-1	3925	3542	4173	-11%
10-2	3559	3269	4173	-18%
11-1	3982	4407	4147	1%
11-2	3716	4172	4147	-5%
12-1	3947	3654	4147	-8%
12-2	3663	3435	4147	-14%
13-1	4187	3981	4144	-1%
13-2	3907	3817	4144	-7%
14-1	4278	3898	4172	-2%
14-2	3904	3629	4172	-10%
15-1	4391	3813	4209	-3%
15-2	4038	3464	4209	-11%
16	7218	6419	7585	-10%
17	7213	6592	7585	-9%

Table E.24 Comparison of Calculated and Inferred Maximum Total Moments based on Estimated In Situ Section Properties and Inferred Neutral Axis Depths for Wimberley, Span 2

Run	Total Inferred Midspan Moment, in-kip		Total Midspan Moment From FE Analysis, in-kip	Average Percent Difference
	Bottom Gages	Web Gages		
1	3926	—	5756	-32%
2	5335	—	5756	-7%
3	5225	—	5627	-7%
4	4418	—	5627	-21%
5	5105	—	5720	-11%
6	5119	—	5720	-11%
7	6770	—	7829	-14%
8	6965	—	7829	-11%
9-1	3901	—	4209	-7%
9-2	3583	—	4209	-15%
10-1	3912	—	4173	-6%
10-2	3613	—	4173	-13%
11-1	3924	—	4147	-5%
11-2	3635	—	4147	-12%
12-1	3925	—	4147	-5%
12-2	3653	—	4147	-12%
13-1	3950	—	4144	-5%
13-2	3949	—	4144	-5%
14-1	3867	—	4172	-7%
14-2	3726	—	4172	-11%
15-1	3967	—	4209	-6%
15-2	3651	—	4209	-13%
16	6648	—	7585	-12%
17	6742	—	7585	-11%

Appendix F

Calculated and Inferred Live Load Distribution Factors

This appendix contains six sections. Live load distribution factors (LLDF) inferred from the measured data are summarized for each bridge in Section F.1. The average maximum LLDF's are summarized in Section F.2. The average maximum live LLDF was calculated as the average live load distribution factor based on data from the bottom and web gages. The LLDF's reported in Sections F.1 and F.2 are based on the total applied load. LLDF's calculated from finite element analyses of the field runs are presented in Section F.3. Comparisons of LLDF's inferred from measured data and calculated from finite element analyses are summarized in Section F.4. The difference in LLDF's reported in Section F.4 is expressed as a percent of the total live load moment. Inferred and calculated LLDF's are plotted as a function of beam number in Section F.5. LLDF's based on AASHTO LRFD, AASHTO Standard, finite element analyses, and inferred from measured data are plotted for comparison. In Section F.6, LLDF's calculated using the AASHTO LRFD, AASHTO Standard, and finite element analyses with trucks positioned such that the maximum response is created are plotted as a function of beam number for comparison. LLDF's in Sections F.5and F.6 have been reported in terms of a single design truck, which is consistent with LLDF's calculated using AASHTO LRFD. Additional information regarding the information presented here can be found in Chapter 4.

F.1 LIVE LOAD DISTRIBUTION FACTORS INFERRED FROM MEASURED DATA

Table F.1 LLDF Based on Estimated In Situ Material Properties and Inferred Neutral Axis Depths for Chandler Creek Bridge, 40-ft Span

Run	Beam 1			Beam 2			Beam 3			Beam 4		
	Bottom Gages	Web Gages	Top Gages	Bottom Gages	Web Gages	Top Gages	Bottom Gages	Web Gages	Top Gages	Bottom Gages	Web Gages	Top Gages
1	0.15	0.14	0.16	0.30	0.30	0.39	0.29	0.31	0.31	0.29	0.27	0.28
2	0.14	0.13	0.12	0.31	0.31	0.40	0.31	0.33	0.37	0.30	0.28	0.22
3	0.29	0.28	0.23	0.26	0.24	0.41	0.25	0.27	0.26	0.28	0.27	0.19
4	0.32	0.30	0.27	0.26	0.24	0.45	0.26	0.27	0.28	0.28	0.28	0.17
5	0.31	0.31	0.24	0.31	0.32	0.44	0.29	0.30	0.33	0.14	0.12	0.11
6	0.31	0.31	0.25	0.30	0.31	0.43	0.28	0.29	0.32	0.13	0.12	0.11
7	0.00	0.03	0.02	0.10	0.11	0.29	0.39	0.41	0.42	0.53	0.49	0.41
8	0.01	0.02	0.01	0.11	0.11	0.28	0.40	0.41	0.42	0.52	0.49	0.39
9	0.09	0.09	0.13	0.41	0.44	0.40	0.41	0.40	0.41	0.10	0.08	0.16
10	0.10	0.10	0.11	0.42	0.46	0.40	0.41	0.41	0.40	0.10	0.07	0.15
11	0.53	0.54	0.37	0.41	0.41	0.48	0.09	0.08	0.21	0.01	0.02	0.02
12	0.53	0.54	0.38	0.40	0.40	0.48	0.09	0.09	0.23	0.01	0.03	0.02
13-1	0.01	0.03	0.04	0.08	0.09	0.23	0.40	0.43	0.40	0.56	0.51	0.42
13-2	0.01	0.03	0.04	0.10	0.10	0.28	0.43	0.46	0.46	0.52	0.47	0.43
14-1	0.08	0.09	0.11	0.44	0.50	0.36	0.44	0.40	0.44	0.09	0.07	0.13
14-2	0.08	0.09	0.13	0.46	0.52	0.38	0.42	0.38	0.45	0.08	0.06	0.12
15-1	0.55	0.58	0.36	0.41	0.41	0.52	0.09	0.08	0.21	0.00	0.03	0.03
15-2	0.55	0.57	0.37	0.41	0.40	0.49	0.08	0.08	0.18	0.01	0.02	0.03

Table F.2 LLDF Based on Estimated In Situ Material Properties and Inferred Neutral Axis Depths for Chandler Creek Bridge, 60-ft Span

Run	Beam 1			Beam 2			Beam 3			Beam 4		
	Bottom Gages	Web Gages	Top Gages	Bottom Gages	Web Gages	Top Gages	Bottom Gages	Web Gages	Top Gages	Bottom Gages	Web Gages	Top Gages
1	0.17	0.19	0.16	0.29	0.28	0.29	0.29	0.31	0.30	0.29	0.28	0.33
2	0.16	0.17	0.18	0.30	0.28	0.31	0.31	0.34	0.32	0.30	0.30	0.30
3	0.27	0.30	0.27	0.28	0.26	0.33	0.25	0.29	0.26	0.26	0.27	0.26
4	0.28	0.28	0.27	0.28	0.26	0.34	0.26	0.30	0.28	0.26	0.25	0.25
5	0.29	0.32	0.29	0.30	0.30	0.34	0.26	0.27	0.25	0.15	0.14	0.20
6	0.29	0.31	0.28	0.30	0.29	0.33	0.26	0.28	0.25	0.17	0.16	0.20
7	0.02	0.03	0.01	0.15	0.14	0.19	0.37	0.38	0.36	0.49	0.46	0.49
8	0.01	0.02	0.01	0.14	0.15	0.18	0.36	0.37	0.39	0.49	0.48	0.49
9	0.16	0.15	0.25	0.36	0.38	0.27	0.34	0.39	0.31	0.17	0.15	0.26
10	0.16	0.17	0.26	0.36	0.36	0.29	0.34	0.38	0.33	0.17	0.16	0.26
11	0.47	0.51	0.46	0.39	0.38	0.39	0.14	0.16	0.20	0.02	0.05	0.06
12	0.46	0.47	0.47	0.40	0.42	0.43	0.14	0.20	0.23	0.02	0.05	0.09
13-1	0.02	0.03	0.01	0.13	0.15	0.18	0.38	0.39	0.40	0.51	0.47	0.54
13-2	0.02	0.04	0.01	0.14	0.15	0.17	0.39	0.41	0.37	0.47	0.43	0.53
14-1	0.14	0.16	0.19	0.38	0.40	0.28	0.36	0.35	0.36	0.15	0.13	0.24
14-2	0.15	0.17	0.19	0.39	0.41	0.29	0.34	0.33	0.36	0.14	0.12	0.24
15-1	0.49	0.55	0.44	0.40	0.36	0.43	0.12	0.11	0.18	0.01	0.02	0.02
15-2	0.50	0.54	0.44	0.40	0.36	0.42	0.12	0.12	0.19	0.02	0.03	0.02

Table F.3 LLDF Based on Estimated In Situ Material Properties and Inferred Neutral Axis Depths for Lake LBJ Bridge

Run	Beam 1			Beam 2			Beam 3			Beam 4		
	Bottom Gages	Web Gages	Top Gages	Bottom Gages	Web Gages	Top Gages	Bottom Gages	Web Gages	Top Gages	Bottom Gages	Web Gages	Top Gages
1	0.02	0.02	0.14	0.14	0.16	0.16	0.35	0.36	0.34	0.49	0.47	0.40
2	0.04	0.03	0.15	0.15	0.18	0.15	0.37	0.39	0.34	0.47	0.43	0.39
3	0.09	0.06	0.20	0.22	0.26	0.15	0.37	0.41	0.27	0.32	0.27	0.37
4	0.09	0.07	0.24	0.21	0.25	0.13	0.36	0.40	0.23	0.35	0.29	0.43
5	0.19	0.15	0.30	0.31	0.34	0.19	0.33	0.38	0.23	0.19	0.14	0.31
6	0.18	0.14	0.29	0.31	0.34	0.18	0.33	0.39	0.23	0.19	0.14	0.32
7	0.33	0.28	0.34	0.35	0.38	0.23	0.23	0.28	0.19	0.09	0.06	0.25
8	0.27	0.26	0.28	0.23	0.25	0.20	0.24	0.26	0.23	0.27	0.25	0.32
9	0.26	0.25	0.24	0.24	0.25	0.24	0.25	0.26	0.28	0.26	0.25	0.28
10-1	0.02	0.02	0.14	0.12	0.16	0.12	0.34	0.34	0.31	0.52	0.51	0.46
10-2	0.02	0.02	0.14	0.12	0.16	0.12	0.34	0.34	0.31	0.52	0.51	0.46
11-1	0.17	0.13	0.31	0.32	0.36	0.20	0.35	0.39	0.23	0.18	0.14	0.31
11-2	0.18	0.13	0.35	0.31	0.36	0.17	0.34	0.39	0.19	0.19	0.14	0.35
12-1	0.53	0.50	0.45	0.33	0.34	0.27	0.13	0.15	0.14	0.03	0.03	0.19
12-2	0.53	0.50	0.45	0.33	0.34	0.27	0.13	0.15	0.14	0.03	0.03	0.19
13	0.30	0.28	0.33	0.24	0.25	0.22	0.24	0.26	0.24	0.28	0.25	0.37
14	0.26	0.24	0.28	0.22	0.25	0.19	0.24	0.27	0.22	0.27	0.25	0.31
15	0.27	0.26	0.27	0.23	0.26	0.19	0.25	0.28	0.23	0.29	0.27	0.33

Table F.4 LLDF Based on Estimated In Situ Material Properties and Inferred Neutral Axis Depths for Lampasas River Bridge, Span 1

Run	Beam 5			Beam 6			Beam 7			Beam 8		
	Bottom Gages	Web Gages	Top Gages	Bottom Gages	Web Gages	Top Gages	Bottom Gages	Web Gages	Top Gages	Bottom Gages	Web Gages	Top Gages
1	0.04	0.04	0.05	0.17	0.19	0.15	0.37	0.37	0.42	0.47	0.49	0.46
2	0.02	0.01	0.03	0.16	0.19	0.15	0.36	0.35	0.40	0.47	0.48	0.47
3	0.02	0.02	0.04	0.16	0.20	0.15	0.36	0.33	0.37	0.46	0.47	0.45
4	0.09	0.08	0.13	0.24	0.30	0.20	0.38	0.37	0.31	0.30	0.27	0.38
5	0.09	0.08	0.14	0.24	0.30	0.21	0.38	0.37	0.30	0.30	0.27	0.39
6	0.18	0.16	0.24	0.32	0.38	0.25	0.33	0.33	0.25	0.18	0.15	0.28
7	0.19	0.17	0.26	0.32	0.38	0.25	0.32	0.33	0.24	0.18	0.14	0.27
8	0.25	0.25	0.23	0.25	0.28	0.26	0.26	0.24	0.26	0.24	0.23	0.26
9	0.25	0.25	0.23	0.25	0.28	0.26	0.26	0.24	0.26	0.24	0.23	0.26
10-1	0.02	0.03	0.03	0.15	0.18	0.15	0.37	0.34	0.38	0.47	0.47	0.46
10-2	0.03	0.03	0.03	0.15	0.20	0.15	0.37	0.34	0.38	0.46	0.44	0.47
11-1	0.18	0.16	0.25	0.34	0.40	0.26	0.34	0.34	0.25	0.16	0.13	0.26
11-2	0.18	0.16	0.23	0.33	0.39	0.25	0.33	0.33	0.26	0.17	0.13	0.27
12-1	0.48	0.47	0.43	0.37	0.36	0.38	0.15	0.16	0.15	0.02	0.03	0.06
12-2	0.48	0.47	0.42	0.37	0.37	0.39	0.15	0.16	0.16	0.03	0.02	0.07
13	0.25	0.26	0.22	0.26	0.28	0.25	0.26	0.24	0.27	0.25	0.25	0.26
14	—	0.25	0.22	—	0.28	0.24	—	0.25	0.29	—	0.25	0.28
15	—	0.02	0.03	—	0.20	0.16	—	0.33	0.38	—	0.48	0.45
16	—	0.02	0.04	—	0.20	0.17	—	0.33	0.37	—	0.47	0.46

Table F.5 LLDF Based on Estimated In Situ Material Properties and Inferred Neutral Axis Depths for Lampasas River Bridge, Span 2

Run	Beam 1			Beam 2			Beam 3			Beam 4		
	Bottom Gages	Web Gages	Top Gages	Bottom Gages	Web Gages	Top Gages	Bottom Gages	Web Gages	Top Gages	Bottom Gages	Web Gages	Top Gages
1	0.05	0.09	0.10	0.15	0.15	0.17	0.36	0.32	0.38	0.48	0.51	0.42
2	0.02	0.06	0.06	0.16	0.16	0.17	0.35	0.32	0.37	0.47	0.51	0.43
3	0.02	0.02	0.04	0.16	0.15	0.17	0.36	0.33	0.37	0.47	0.51	0.43
4	0.10	0.08	0.15	0.23	0.25	0.23	0.37	0.37	0.31	0.31	0.32	0.35
5	0.10	0.08	0.14	0.23	0.24	0.23	0.36	0.37	0.30	0.31	0.32	0.35
6	0.19	0.18	0.25	0.32	0.32	0.28	0.31	0.34	0.25	0.18	0.18	0.25
7	0.20	0.18	0.25	0.31	0.32	0.27	0.31	0.33	0.25	0.18	0.18	0.24
8	0.25	0.25	0.23	0.25	0.24	0.28	0.26	0.25	0.27	0.25	0.27	0.24
9	0.26	0.25	0.24	0.25	0.23	0.29	0.25	0.25	0.26	0.25	0.28	0.24
10-1	0.03	0.03	0.06	0.15	0.16	0.18	0.36	0.33	0.38	0.47	0.50	0.44
10-2	0.04	0.04	0.06	0.16	0.17	0.17	0.37	0.34	0.38	0.46	0.48	0.45
11-1	0.19	0.16	0.25	0.33	0.33	0.29	0.33	0.35	0.26	0.17	0.16	0.25
11-2	0.18	0.15	0.24	0.32	0.33	0.29	0.34	0.36	0.26	0.18	0.18	0.26
12-1	0.49	0.53	0.43	0.36	0.32	0.43	0.14	0.16	0.16	0.02	0.03	0.05
12-2	0.49	0.50	0.42	0.36	0.33	0.40	0.14	0.16	0.16	0.03	0.04	0.06
13	0.25	0.25	0.25	0.25	0.23	0.29	0.26	0.25	0.26	0.25	0.27	0.24
14	0.24	0.24	0.23	0.24	0.23	0.28	0.26	0.26	0.27	0.27	0.29	0.25
15	0.02	0.02	0.05	0.16	0.15	0.18	0.35	0.33	0.37	0.48	0.52	0.44
16	0.02	0.03	0.05	0.16	0.16	0.18	0.35	0.33	0.36	0.47	0.51	0.43

Table F.6 LLDF Based on Estimated In Situ Material Properties and Inferred Neutral Axis Depths for Willis Creek Bridge

Run	Beam 1			Beam 2			Beam 3			Beam 4		
	Bottom Gages	Web Gages	Top Gages	Bottom Gages	Web Gages	Top Gages	Bottom Gages	Web Gages	Top Gages	Bottom Gages	Web Gages	Top Gages
1	0.25	0.27	0.22	0.25	0.26	0.26	0.26	0.25	0.29	0.30	0.27	0.32
2	0.25	0.27	0.22	0.24	0.25	0.26	0.24	0.25	0.26	0.28	0.25	0.26
3	0.04	0.03	0.11	0.14	0.16	0.17	0.33	0.33	0.34	0.50	0.50	0.43
4	0.04	0.06	0.07	0.14	0.15	0.17	0.33	0.32	0.34	0.50	0.48	0.43
5	0.03	0.01	0.11	0.14	0.16	0.17	0.33	0.33	0.34	0.51	0.51	0.40
6	0.03	0.01	0.13	0.14	0.17	0.17	0.33	0.33	0.34	0.51	0.52	0.39
7	0.08	0.05	0.17	0.21	0.26	0.20	0.35	0.38	0.32	0.37	0.33	0.34
8	0.08	0.07	0.15	0.22	0.26	0.20	0.35	0.37	0.31	0.36	0.32	0.34
9	0.16	0.14	0.23	0.30	0.36	0.25	0.32	0.35	0.27	0.22	0.17	0.27
10	0.18	0.15	0.24	0.30	0.37	0.26	0.32	0.35	0.26	0.21	0.16	0.25
11	0.30	0.30	0.29	0.35	0.38	0.30	0.24	0.27	0.22	0.11	0.07	0.19
12	0.31	0.28	0.36	0.35	0.40	0.30	0.24	0.28	0.22	0.12	0.06	0.16
13	0.47	0.49	0.38	0.35	0.36	0.36	0.15	0.16	0.18	0.04	0.01	0.11
14	0.46	0.50	0.34	0.35	0.34	0.36	0.15	0.16	0.18	0.04	0.02	0.14
15-1	0.04	0.05	0.08	0.13	0.15	0.16	0.34	0.33	0.37	0.51	0.51	0.43
15-2	0.04	0.15	0.08	0.13	0.14	0.16	0.34	0.32	0.38	0.52	0.50	0.47
16-1	0.09	0.09	0.15	0.23	0.28	0.21	0.37	0.38	0.34	0.33	0.28	0.36
16-2	0.08	0.12	0.13	0.21	0.25	0.20	0.38	0.37	0.36	0.35	0.28	0.36
17-1	0.17	0.22	0.17	0.32	0.33	0.29	0.33	0.33	0.30	0.19	0.15	0.31
17-2	0.18	0.25	0.16	0.33	0.32	0.29	0.34	0.32	0.29	0.18	0.15	0.32
18-1	0.31	0.31	0.29	0.36	0.38	0.34	0.23	0.26	0.21	0.10	0.07	0.19
18-2	0.32	0.32	0.32	0.37	0.39	0.34	0.22	0.25	0.20	0.09	0.07	0.17
19-1	0.49	0.50	0.42	0.35	0.36	0.37	0.14	0.15	0.16	0.04	0.02	0.09
19-2	0.47	0.43	0.51	0.35	0.43	0.36	0.14	0.18	0.15	0.06	0.02	0.02
20	0.24	0.26	0.22	0.24	0.25	0.25	0.25	0.25	0.26	0.29	0.26	0.28

Table F.7 LLDF Based on Estimated In Situ Material Properties and Inferred Neutral Axis Depths for Wimberley Bridge, Span 1

Run	Beam 1		Beam 2		Beam 3		Beam 4		Beam 5	
	Bottom Gages	Web Gages	Bottom Gages	Web Gages	Bottom Gages	Web Gages	Bottom Gages	Web Gages	Bottom Gages	Web Gages
1	0.02	0.01	0.04	0.04	0.15	0.11	0.40	0.37	0.47	0.53
2	0.01	0.01	0.03	0.04	0.15	0.10	0.39	0.37	0.48	0.55
3	0.05	0.05	0.28	0.30	0.42	0.42	0.26	0.26	0.04	0.02
4	0.06	0.06	0.27	0.30	0.41	0.40	0.26	0.26	0.04	0.03
5	0.49	0.48	0.40	0.39	0.12	0.13	0.02	0.03	0.01	0.01
6	0.49	0.47	0.40	0.40	0.13	0.13	0.02	0.03	0.01	0.02
7	0.14	0.31	0.28	0.23	0.27	0.20	0.27	0.21	0.12	0.10
8	0.16	0.14	0.28	0.29	0.26	0.24	0.26	0.27	0.12	0.13
9-1	0.02	0.05	0.03	0.04	0.12	0.08	0.39	0.37	0.49	0.52
9-2	0.03	0.07	0.04	0.04	0.13	0.09	0.40	0.39	0.46	0.51
10-1	0.03	0.05	0.08	0.09	0.26	0.21	0.45	0.46	0.24	0.26
10-2	0.03	0.05	0.08	0.10	0.27	0.22	0.45	0.45	0.24	0.26
11-1	0.02	0.21	0.16	0.13	0.40	0.30	0.40	0.36	0.09	0.07
11-2	0.02	0.21	0.16	0.13	0.39	0.30	0.39	0.35	0.09	0.08
12-1	0.05	0.04	0.28	0.32	0.45	0.43	0.26	0.28	0.03	0.02
12-2	0.05	0.03	0.29	0.32	0.45	0.42	0.24	0.27	0.03	0.02
13-1	0.12	0.10	0.43	0.43	0.37	0.40	0.11	0.12	0.02	0.01
13-2	0.12	0.10	0.41	0.42	0.37	0.39	0.11	0.11	0.02	0.02
14-1	0.28	0.25	0.47	0.48	0.22	0.24	0.05	0.05	0.01	0.01
14-2	0.29	0.25	0.46	0.48	0.22	0.23	0.05	0.06	0.01	0.01
15-1	0.46	0.47	0.41	0.41	0.11	0.13	0.03	0.03	0.01	0.01
15-2	0.50	0.50	0.40	0.38	0.11	0.11	0.02	0.03	0.01	0.02
16	0.27	0.24	0.23	0.23	0.14	0.12	0.22	0.22	0.26	0.30
17	0.27	0.27	0.23	0.23	0.14	0.11	0.22	0.21	0.26	0.29

Table F.8 LLDF Based on Estimated In Situ Material Properties and Inferred Neutral Axis Depths for Wimberley Bridge, Span 2

Run	Beam 1		Beam 2		Beam 3		Beam 4		Beam 5	
	Bottom Gages	Web Gages	Bottom Gages	Web Gages	Bottom Gages	Web Gages	Bottom Gages	Web Gages	Bottom Gages	Web Gages
1	0.02	—	0.03	—	0.14	—	0.41	—	0.47	—
2	0.01	—	0.03	—	0.16	—	0.39	—	0.46	—
3	0.04	—	0.25	—	0.41	—	0.30	—	0.04	—
4	0.05	—	0.26	—	0.42	—	0.28	—	0.04	—
5	0.47	—	0.38	—	0.16	—	0.02	—	0.01	—
6	0.45	—	0.39	—	0.16	—	0.03	—	0.01	—
7	0.12	—	0.27	—	0.28	—	0.29	—	0.13	—
8	0.13	—	0.26	—	0.27	—	0.28	—	0.13	—
9-1	0.02	—	0.03	—	0.14	—	0.40	—	0.47	—
9-2	0.02	—	0.03	—	0.16	—	0.41	—	0.46	—
10-1	0.02	—	0.06	—	0.27	—	0.47	—	0.24	—
10-2	0.02	—	0.07	—	0.28	—	0.46	—	0.24	—
11-1	0.01	—	0.13	—	0.39	—	0.43	—	0.10	—
11-2	0.02	—	0.13	—	0.39	—	0.42	—	0.10	—
12-1	0.03	—	0.25	—	0.45	—	0.27	—	0.03	—
12-2	0.04	—	0.25	—	0.44	—	0.27	—	0.04	—
13-1	0.10	—	0.40	—	0.39	—	0.14	—	0.01	—
13-2	0.10	—	0.40	—	0.39	—	0.14	—	0.01	—
14-1	0.23	—	0.46	—	0.27	—	0.07	—	0.01	—
14-2	0.23	—	0.45	—	0.27	—	0.07	—	0.01	—
15-1	0.48	—	0.40	—	0.14	—	0.02	—	0.01	—
15-2	0.48	—	0.40	—	0.14	—	0.03	—	0.01	—
16	0.25	—	0.23	—	0.16	—	0.24	—	0.28	—
17	0.25	—	0.22	—	0.16	—	0.24	—	0.28	—

F.2 AVERAGE MAXIMUM LIVE LOAD DISTRIBUTION FACTORS INFERRED FROM MEASURED DATA

Table F.9 Inferred Live Load Distribution Factors for Chandler Creek Bridge, 40-ft Span

Run			Average Maximum LLDF†			
No.	Type	Path(s)	Beam 1	Beam 2	Beam 3	Beam 4
1	Side-by-Side	1 & 4	0.15	0.30	0.31	0.29
2	Side-by-Side	1 & 4	0.14	0.31	0.33	0.30
3	Side-by-Side	1 & 5	0.29	0.26	0.27	0.28
4	Side-by-Side	1 & 5	0.32	0.26	0.27	0.28
5	Side-by-Side	2 & 5	0.31	0.32	0.30	0.14
6	Side-by-Side	2 & 5	0.31	0.31	0.29	0.13
7	Back-to-Back	1	0.03	0.11	0.41	0.53
8	Back-to-Back	1	0.02	0.11	0.41	0.52
9	Back-to-Back	3	0.09	0.44	0.41	0.10
10	Back-to-Back	3	0.10	0.46	0.41	0.10
11	Back-to-Back	5	0.54	0.41	0.09	0.02
12	Back-to-Back	5	0.54	0.40	0.09	0.03
13-1	Single Truck (1)	1	0.03	0.09	0.43	0.56
13-2	Single Truck (2)	1	0.03	0.10	0.46	0.52
14-1	Single Truck (1)	3	0.09	0.50	0.44	0.09
14-2	Single Truck (2)	3	0.09	0.52	0.42	0.08
15-1	Single Truck (1)	5	0.58	0.41	0.09	0.03
15-2	Single Truck (2)	5	0.57	0.41	0.08	0.02

† Moments inferred from bottom and web strain gages at midspan were used to calculate the average LLDF for each beam.

Table F.10 Inferred Live Load Distribution Factors for Chandler Creek Bridge, 60-ft Span

Run			Average Maximum LLDF†			
No.	Type	Path(s)	Beam 5	Beam 6	Beam 7	Beam 8
1	Side-by-Side	1 & 4	0.15	0.30	0.31	0.29
2	Side-by-Side	1 & 4	0.14	0.31	0.33	0.30
3	Side-by-Side	1 & 5	0.29	0.26	0.27	0.28
4	Side-by-Side	1 & 5	0.32	0.26	0.27	0.28
5	Side-by-Side	2 & 5	0.31	0.32	0.30	0.14
6	Side-by-Side	2 & 5	0.31	0.31	0.29	0.13
7	Back-to-Back	1	0.03	0.11	0.41	0.53
8	Back-to-Back	1	0.02	0.11	0.41	0.52
9	Back-to-Back	3	0.09	0.44	0.41	0.10
10	Back-to-Back	3	0.10	0.46	0.41	0.10
11	Back-to-Back	5	0.54	0.41	0.09	0.02
12	Back-to-Back	5	0.54	0.40	0.09	0.03
13-1	Single Truck (1)	1	0.03	0.09	0.43	0.56
13-2	Single Truck (2)	1	0.03	0.10	0.46	0.52
14-1	Single Truck (1)	3	0.09	0.50	0.44	0.09
14-2	Single Truck (2)	3	0.09	0.52	0.42	0.08
15-1	Single Truck (1)	5	0.58	0.41	0.09	0.03
15-2	Single Truck (2)	5	0.57	0.41	0.08	0.02

† Moments inferred from bottom and web strain gages at midspan were used to calculate the average LLDF for each beam.

Table F.11 Inferred Live Load Distribution Factors for Lake LBJ Bridge

Run			Average Maximum LLDF†			
No.	Type	Path(s)	Beam 1	Beam 2	Beam 3	Beam 4
1	Back-to-Back	1	0.02	0.15	0.36	0.48
2	Back-to-Back	1	0.03	0.17	0.38	0.45
3	Back-to-Back	2	0.08	0.24	0.39	0.29
4	Back-to-Back	2	0.08	0.23	0.38	0.32
5	Back-to-Back	3	0.17	0.32	0.35	0.16
6	Back-to-Back	3	0.16	0.32	0.36	0.17
7	Back-to-Back	4	0.31	0.37	0.26	0.08
8	Side-by-Side	1 & 5	0.26	0.24	0.25	0.26
9	Side-by-Side	1 & 5	0.26	0.24	0.25	0.26
10-1	Single Truck (1)	1	0.02	0.14	0.34	0.52
10-2	Single Truck (2)	1	0.02	0.14	0.34	0.52
11-1	Single Truck (1)	3	0.15	0.34	0.37	0.16
11-2	Single Truck (2)	3	0.15	0.33	0.37	0.17
12-1	Single Truck (1)	5	0.52	0.33	0.14	0.03
12-2	Single Truck (2)	5	0.52	0.33	0.14	0.03
13	Side-by-Side	1 & 5	0.29	0.25	0.25	0.27
14	Side-by-Side	1 & 5	0.25	0.24	0.25	0.26
15	Side-by-Side	1 & 5	0.27	0.24	0.26	0.28

† Moments inferred from bottom and web strain gages at midspan were used to calculate the average LLDF for each beam.

Table F.12 Inferred Live Load Distribution Factors for Lampasas River Bridge, Span 1

Run			Average Maximum LLDF†			
No.	Type	Path(s)	Beam 1	Beam 2	Beam 3	Beam 4
1	Back-to-Back	1	0.04	0.18	0.37	0.48
2	Back-to-Back	1	0.02	0.17	0.36	0.48
3	Back-to-Back	1	0.02	0.18	0.35	0.47
4	Back-to-Back	2	0.09	0.27	0.37	0.29
5	Back-to-Back	2	0.08	0.27	0.37	0.28
6	Back-to-Back	3	0.17	0.35	0.33	0.16
7	Back-to-Back	3	0.18	0.35	0.33	0.16
8	Side-by-Side	1 & 5	0.25	0.27	0.25	0.24
9	Side-by-Side	1 & 5	0.25	0.27	0.25	0.24
10-1	Single Truck (1)	1	0.03	0.17	0.36	0.47
10-2	Single Truck (2)	1	0.03	0.17	0.36	0.45
11-1	Single Truck (1)	3	0.17	0.37	0.34	0.15
11-2	Single Truck (2)	3	0.17	0.36	0.33	0.15
12-1	Single Truck (1)	5	0.47	0.36	0.15	0.02
12-2	Single Truck (2)	5	0.48	0.37	0.15	0.02
13	Side-by-Side	1 & 5	0.25	0.27	0.25	0.25
14	Side-by-Side	1 & 5	0.25	0.28	0.25	0.25
15	Back-to-Back	1	0.02	0.20	0.33	0.48
16	Back-to-Back	1	0.02	0.20	0.33	0.47

† Moments inferred from bottom and web strain gages at midspan were used to calculate the average LLDF for each beam.

Table F.13 Inferred Live Load Distribution Factors for Lampasas River Bridge, Span 2

Run			Average Maximum LLDF[†]			
No.	Type	Path(s)	Beam 5	Beam 6	Beam 7	Beam 8
1	Back-to-Back	1	0.01	0.15	0.35	0.49
2	Back-to-Back	1	0.02	0.15	0.35	0.48
3	Back-to-Back	1	0.02	0.15	0.35	0.48
4	Back-to-Back	2	0.10	0.23	0.35	0.32
5	Back-to-Back	2	0.10	0.23	0.35	0.32
6	Back-to-Back	3	0.20	0.31	0.31	0.19
7	Back-to-Back	3	0.20	0.30	0.30	0.19
8	Side-by-Side	1 & 5	0.25	0.25	0.25	0.25
9	Side-by-Side	1 & 5	0.26	0.24	0.25	0.25
10-1	Single Truck (1)	1	0.02	0.15	0.35	0.48
10-2	Single Truck (2)	1	0.03	0.15	0.35	0.47
11-1	Single Truck (1)	3	0.20	0.31	0.31	0.18
11-2	Single Truck (2)	3	0.19	0.30	0.32	0.19
12-1	Single Truck (1)	5	0.50	0.34	0.14	0.02
12-2	Single Truck (2)	5	0.50	0.34	0.14	0.01
13	Side-by-Side	1 & 5	0.25	0.24	0.25	0.26
14	Side-by-Side	1 & 5	0.25	0.24	0.25	0.26
15	Back-to-Back	1	0.02	0.15	0.34	0.49
16	Back-to-Back	1	0.02	0.15	0.35	0.48

[†] Moments inferred from bottom and web strain gages at midspan were used to calculate the average LLDF for each beam.

Table F.14 Inferred Live Load Distribution Factors for Willis Creek Bridge

Run			Average Maximum LLDF[†]			
No.	Type	Path(s)	Beam 1	Beam 2	Beam 3	Beam 4
1	Side-by-Side	1 & 5	0.26	0.26	0.26	0.29
2	Side-by-Side	1 & 5	0.26	0.24	0.25	0.27
3	Back-to-Back	1	0.04	0.15	0.33	0.50
4	Back-to-Back	1	0.05	0.15	0.33	0.49
5	Back-to-Back	1	0.02	0.15	0.33	0.51
6	Back-to-Back	1	0.02	0.15	0.33	0.51
7	Back-to-Back	2	0.06	0.24	0.37	0.35
8	Back-to-Back	2	0.08	0.24	0.36	0.34
9	Back-to-Back	3	0.15	0.33	0.34	0.19
10	Back-to-Back	3	0.16	0.34	0.33	0.18
11	Back-to-Back	4	0.30	0.37	0.26	0.09
12	Back-to-Back	4	0.29	0.37	0.26	0.09
13	Back-to-Back	5	0.48	0.35	0.16	0.03
14	Back-to-Back	5	0.48	0.34	0.15	0.03
15-1	Single Truck (1)	1	0.04	0.14	0.33	0.51
15-2	Single Truck (2)	1	0.09	0.13	0.33	0.51
16-1	Single Truck (1)	2	0.09	0.25	0.37	0.30
16-2	Single Truck (2)	2	0.10	0.23	0.37	0.32
17-1	Single Truck (1)	3	0.20	0.33	0.33	0.17
17-2	Single Truck (2)	3	0.21	0.32	0.33	0.17
18-1	Single Truck (1)	4	0.31	0.37	0.25	0.09
18-2	Single Truck (2)	4	0.32	0.38	0.24	0.08
19-1	Single Truck (1)	5	0.49	0.35	0.15	0.03
19-2	Single Truck (2)	5	0.45	0.39	0.16	0.04
20	Side-by-Side	1 & 5	0.25	0.24	0.25	0.27

† Moments inferred from bottom and web strain gages at midspan were used to calculate the average LLDF for each beam.

Table F.15 Inferred Live Load Distribution Factors for Wimberley Bridge, Span 1

Run			Average Maximum LLDF[†]				
No.	Type	Path(s)	Beam 1	Beam 2	Beam 3	Beam 4	Beam 5
1	Back-to-Back	1	0.01	0.04	0.13	0.38	0.50
2	Back-to-Back	1	0.01	0.03	0.12	0.38	0.51
3	Back-to-Back	4	0.05	0.29	0.42	0.26	0.03
4	Back-to-Back	4	0.06	0.29	0.41	0.26	0.03
5	Back-to-Back	7	0.49	0.40	0.12	0.02	0.01
6	Back-to-Back	7	0.48	0.40	0.13	0.03	0.01
7	Side-by-Side	2 & 6	0.23	0.26	0.23	0.24	0.11
8	Side-by-Side	2 & 6	0.15	0.29	0.25	0.27	0.12
9-1	Single Truck (1)	1	0.04	0.03	0.10	0.38	0.51
9-2	Single Truck (2)	1	0.05	0.04	0.11	0.40	0.49
10-1	Single Truck (1)	2	0.04	0.08	0.23	0.46	0.25
10-2	Single Truck (2)	2	0.04	0.09	0.24	0.45	0.25
11-1	Single Truck (1)	3	0.12	0.14	0.35	0.38	0.08
11-2	Single Truck (2)	3	0.12	0.14	0.34	0.37	0.08
12-1	Single Truck (1)	4	0.04	0.30	0.44	0.27	0.03
12-2	Single Truck (2)	4	0.04	0.31	0.44	0.25	0.02
13-1	Single Truck (1)	5	0.11	0.43	0.38	0.11	0.02
13-2	Single Truck (2)	5	0.11	0.42	0.38	0.11	0.02
14-1	Single Truck (1)	6	0.26	0.48	0.23	0.05	0.01
14-2	Single Truck (2)	6	0.27	0.47	0.23	0.06	0.01
15-1	Single Truck (1)	7	0.47	0.41	0.12	0.03	0.01
15-2	Single Truck (2)	7	0.50	0.39	0.11	0.03	0.01
16	Side-by-Side	1 & 7	0.26	0.23	0.13	0.22	0.28
17	Side-by-Side	1 & 7	0.27	0.23	0.12	0.22	0.27

† Moments inferred from bottom and web strain gages at midspan were used to calculate the average LLDF for each beam.

F.3 LIVE LOAD DISTRIBUTION FACTORS BASED ON FINITE ELEMENT ANALYSIS OF FIELD RUNS PERFORMED DURING DIAGNOSTIC LOAD TESTS

Table F.16 LLDF Based on Finite Element Analysis of Field Runs Performed at Chandler Creek Bridge, 40-ft Span

Field Runs Analyzed			Live Load Distribution Factor from Finite Element Analysis†			
Run Type	Run Nos.	Truck Path(s)	Beam 1	Beam 2	Beam 3	Beam 4
Side –by-Side	1, 2	1,4	0.17	0.29	0.32	0.29
Side –by-Side	3, 4	1,5	0.29	0.28	0.28	0.28
Side –by-Side	5, 6	2,5	0.30	0.32	0.28	0.17
Back-to-Back	7, 8	1	0.04	0.15	0.35	0.48
Back-to-Back	9, 10	3	0.17	0.34	0.34	0.17
Back-to-Back	11, 12	5	0.47	0.36	0.15	0.04
Single Truck*	13	1	0.03	0.14	0.38	0.48
Single Truck*	14	3	0.16	0.36	0.35	0.16
Single Truck*	15	5	0.49	0.36	0.14	0.03

† LLDF based on total applied live load.

* Truck 1, as described in Chapter 3, was used as loading vehicle for finite element analysis.

Table F.17 LLDF Based on Finite Element Analysis of Field Runs Performed at Chandler Creek Bridge, 60-ft Span

Field Runs Analyzed			Live Load Distribution Factor from Finite Element Analysis†			
Run Type	Run Nos.	Truck Path(s)	Beam 5	Beam 6	Beam 7	Beam 8
Side -by-Side	1, 2	1,4	0.19	0.27	0.30	0.29
Side -by-Side	3, 4	1,5	0.27	0.27	0.26	0.27
Side -by-Side	5, 6	2,5	0.29	0.30	0.27	0.18
Back-to-Back	7, 8	1	0.06	0.17	0.33	0.45
Back-to-Back	9, 10	3	0.20	0.30	0.31	0.20
Back-to-Back	11, 12	5	0.44	0.34	0.17	0.06
Single Truck*	13	1	0.06	0.16	0.35	0.45
Single Truck*	14	3	0.19	0.32	0.32	0.19
Single Truck*	15	5	0.46	0.35	0.16	0.06

† LLDF based on total applied live load.

* Truck 1, as described in Chapter 3, was used as loading vehicle for finite element analysis.

Table F.18 LLDF Based on Finite Element Analysis of Field Runs Performed at Lake LBJ Bridge

Field Runs Analyzed			Live Load Distribution Factor from Finite Element Analysis†			
Run Type	Run Nos.	Truck Path(s)	Beam 1	Beam 2	Beam 3	Beam 4
Side -by-Side	8, 9, 13, 14, 15	1,5	0.25	0.25	0.25	0.25
Back-to-Back	1, 2	1	0.06	0.18	0.33	0.44
Back-to-Back	3, 4, 7	2 or 4	0.13	0.23	0.33	0.32
Back-to-Back	5, 6	3	0.21	0.29	0.29	0.21
Single Truck*	10	1	0.05	0.16	0.34	0.45
Single Truck*	11	3	0.20	0.30	0.30	0.20
Single Truck*	12	5	0.45	0.34	0.16	0.05

† LLDF based on total applied live load.

* Truck 1, as described in Chapter 3, was used as loading vehicle for finite element analysis.

Table F.19 LLDF Based on Finite Element Analysis of Field Runs Performed at Lampasas River Bridge

Field Runs Analyzed			Live Load Distribution Factor from Finite Element Analysis†			
Run Type	Run Nos.	Truck Path(s)	Beams 1,5	Beams 2,6	Beams 3,7	Beams 4,8
Side -by-Side	8, 9, 13, 14	1,5	0.24	0.25	0.25	0.25
Back-to-Back	1, 2, 3, 15, 16	1	0.09	0.19	0.32	0.41
Back-to-Back	4, 5	2	0.14	0.23	0.31	0.31
Back-to-Back	6, 7	3	0.21	0.28	0.28	0.23
Single Truck*	10	1	0.08	0.18	0.33	0.42
Single Truck*	11	3	0.20	0.30	0.30	0.20
Single Truck*	12	5	0.42	0.33	0.18	0.08

† LLDF based on total applied live load.

* Truck 1, as described in Chapter 3, was used as loading vehicle for finite element analysis.

Table F.20 LLDF Based on Finite Element Analysis of Field Runs Performed at Willis Creek Bridge

Field Runs Analyzed			Live Load Distribution Factor from Finite Element Analysis†			
Run Type	Run Nos.	Truck Path(s)	Beam 1	Beam 2	Beam 3	Beam 4
Side -by-Side	1, 2, 20	1,5	0.25	0.25	0.25	0.25
Back-to-Back	3, 4, 5, 6	1	0.08	0.18	0.32	0.42
Back-to-Back	7, 8	2	0.14	0.24	0.32	0.31
Back-to-Back	9, 10	3	0.22	0.29	0.28	0.22
Back-to-Back	11, 12	4	0.31	0.32	0.24	0.14
Back-to-Back	13, 14	5	0.42	0.32	0.18	0.08
Single Truck*	15	1	0.07	0.17	0.33	0.43
Single Truck*	16	2	0.13	0.24	0.33	0.30
Single Truck*	17	3	0.20	0.30	0.30	0.20
Single Truck*	18	4	0.31	0.34	0.23	0.12
Single Truck*	19	5	0.44	0.33	0.17	0.07

† LLDF based on total applied live load.

* Truck 1, as described in Chapter 3, was used as loading vehicle for finite element analysis.

Table F.21 LLDF Based on Finite Element Analysis of Field Runs Performed at Wimberley Bridge

Field Runs Analyzed			Live Load Distribution Factor from Finite Element Analysis†				
Run Type	Run Nos.	Truck Path(s)	Beam 1	Beam 2	Beam 3	Beam 4	Beam 5
Side -by-Side	7, 8	2, 6	0.16	0.24	0.24	0.24	0.16
Side-by-Side	16, 17	1, 7	0.26	0.22	0.17	0.23	0.21
Back-to-Back	1, 2	1	0.00	0.04	0.15	0.34	0.49
Back-to-Back	3, 4	4	0.09	0.24	0.35	0.24	0.09
Back-to-Back	5, 6	7	0.48	0.35	0.15	0.04	0.00
Single Truck*	9	1	0.00	0.04	0.14	0.36	0.49
Single Truck*	10	2	0.01	0.08	0.24	0.39	0.30
Single Truck*	11	3	0.03	0.15	0.34	0.34	0.17
Single Truck*	12	4	0.08	0.24	0.37	0.23	0.08
Single Truck*	13	5	0.17	0.34	0.33	0.14	0.04
Single Truck*	14	6	0.31	0.39	0.23	0.08	0.01
Single Truck*	15	7	0.49	0.36	0.14	0.04	0.00

† LLDF based on total applied live load.

* Truck 1, as described in Chapter 3, was used as loading vehicle for finite element analysis.

F.4 COMPARISON OF LIVE LOAD DISTRIBUTION FACTORS BASED ON FINITE ELEMENT ANALYSIS OF FIELD RUNS AND INFERRED LIVE LOAD DISTRIBUTION FACTORS

Table F.22 Comparison of Inferred and Finite Element Analysis LLDF's for Field Runs Performed at Chandler Creek Bridge, 40-ft Span

Field Runs Analyzed			Difference in Inferred and FE Analysis LLDF's for Field Runs†			
Run Type	Run Nos.	Truck Path(s)	Beam 1	Beam 2	Beam 3	Beam 4
Side –by-Side	1, 2	1,4	3%	-2%	0%	0%
Side –by-Side	3, 4	1,5	-2%	2%	0%	0%
Side –by-Side	5, 6	2,5	-1%	1%	-1%	3%
Back-to-Back	7, 8	1	1%	4%	-6%	-5%
Back-to-Back	9, 10	3	8%	-11%	-7%	7%
Back-to-Back	11, 12	5	-7%	-5%	6%	1%
Single Truck*	13	1	1%	5%	-7%	-6%
Single Truck*	14	3	8%	-14%	-7%	7%
Single Truck*	15	5	-8%	-4%	5%	1%

† Difference is expressed as a percentage of the total live load moment.

* Truck 1, as described in Chapter 3, was used as loading vehicle for finite element analysis.

Table F.23 Comparison of Inferred and Finite Element Analysis LLDF's for Field Runs Performed at Chandler Creek Bridge, 60-ft Span

Field Runs Analyzed			Difference in Inferred and FE Analysis LLDF's for Field Runs†			
Run Type	Run Nos.	Truck Path(s)	Beam 5	Beam 6	Beam 7	Beam 8
Side -by-Side	1, 2	1,4	1%	-2%	-1%	-1%
Side -by-Side	3, 4	1,5	-1%	0%	-1%	1%
Side -by-Side	5, 6	2,5	-1%	1%	0%	3%
Back-to-Back	7, 8	1	4%	2%	-4%	-3%
Back-to-Back	9, 10	3	4%	-6%	-6%	4%
Back-to-Back	11, 12	5	-4%	-6%	1%	2%
Single Truck*	13	1	3%	2%	-4%	-2%
Single Truck*	14	3	4%	-7%	-2%	5%
Single Truck*	15	5	-6%	-3%	4%	4%

† Difference is expressed as a percentage of the total live load moment.

* Truck 1, as described in Chapter 3, was used as loading vehicle for finite element analysis.

Table F. Comparison of Inferred and Finite Element Analysis LLDF's for Field Runs Performed at Lake LBJ Bridge

Field Runs Analyzed			Difference in Inferred and FE Analysis LLDF's for Field Runs†			
Run Type	Run Nos.	Truck Path(s)	Beam 1	Beam 2	Beam 3	Beam 4
Side -by-Side	8, 9, 13, 14, 15	1,5	-2%	1%	0%	-1%
Back-to-Back	1, 2	1	3%	2%	-4%	-2%
Back-to-Back	3, 4, 7	2 or 4	5%	0%	-6%	1%
Back-to-Back	5, 6	3	5%	-3%	-7%	5%
Single Truck*	10	1	4%	2%	0%	-7%
Single Truck*	11	3	4%	-3%	-7%	3%
Single Truck*	12	5	-7%	0%	2%	3%

† Difference is expressed as a percentage of the total live load moment.

* Truck 1, as described in Chapter 3, was used as loading vehicle for finite element analysis.

Table F.24 Comparison of Inferred and Finite Element Analysis LLDF's for Field Runs Performed at Lampasas River Bridge, Span 1

Field Runs Analyzed			Difference in Inferred and FE Analysis LLDF's for Field Runs†			
Run Type	Run Nos.	Truck Path(s)	Beam 1	Beam 2	Beam 3	Beam 4
Side -by-Side	8, 9, 13, 14	1,5	-1%	-2%	0%	1%
Back-to-Back	1, 2, 3, 15, 16	1	7%	0%	-3%	-6%
Back-to-Back	4, 5	2	6%	-3%	-6%	3%
Back-to-Back	6, 7	3	4%	-7%	-4%	6%
Single Truck*	10	1	5%	1%	-3%	-4%
Single Truck*	11	3	4%	-7%	-4%	6%
Single Truck*	12	5	-6%	-4%	2%	6%

† Difference is expressed as a percentage of the total live load moment.

* Truck 1, as described in Chapter 3, was used as loading vehicle for finite element analysis.

Table F.25 Comparison of Inferred and Finite Element Analysis LLDF’s for Field Runs Performed at Lampasas River Bridge, Span 2

Field Runs Analyzed			Difference in Inferred and FE Analysis LLDF’s for Field Runs†			
Run Type	Run Nos.	Truck Path(s)	Beam 5	Beam 6	Beam 7	Beam 8
Side -by-Side	8, 9, 13, 14	1,5	-1%	1%	1%	0%
Back-to-Back	1, 2, 3, 15, 16	1	7%	4%	-3%	-8%
Back-to-Back	4, 5	2	5%	0%	-4%	-1%
Back-to-Back	6, 7	3	1%	-3%	-2%	4%
Single Truck*	10	1	6%	3%	-2%	-6%
Single Truck*	11	3	1%	-1%	-2%	2%
Single Truck*	12	5	-8%	-2%	3%	7%

† Difference is expressed as a percentage of the total live load moment.

* Truck 1, as described in Chapter 3, was used as loading vehicle for finite element analysis.

Table F.26 Comparison of Inferred and Finite Element Analysis LLDF's for Field Runs Performed at Willis Creek Bridge

Field Runs Analyzed			Difference in Inferred and FE Analysis LLDF's for Field Runs†			
Run Type	Run Nos.	Truck Path(s)	Beam 1	Beam 2	Beam 3	Beam 4
Side -by-Side	1, 2, 20	1,5	-1%	0%	0%	-2%
Back-to-Back	3, 4, 5, 6	1	5%	3%	-1%	-8%
Back-to-Back	7, 8	2	7%	0%	-5%	-3%
Back-to-Back	9, 10	3	6%	-5%	-5%	3%
Back-to-Back	11, 12	4	2%	-5%	-2%	5%
Back-to-Back	13, 14	5	-6%	-3%	3%	5%
Single Truck*	15	1	0%	3%	0%	-8%
Single Truck*	16	2	3%	-1%	-4%	-1%
Single Truck*	17	3	0%	-3%	-3%	3%
Single Truck*	18	4	-1%	-4%	-1%	4%
Single Truck*	19	5	-4%	-4%	1%	3%

† Difference is expressed as a percentage of the total live load moment.

* Truck 1, as described in Chapter 3, was used as loading vehicle for finite element analysis.

Table F.27 Comparison of Inferred and Finite Element Analysis LLDF's for Field Runs Performed at Wimberley Bridge

Field Runs Analyzed			Difference in Inferred and FE Analysis LLDF's for Field Runs†				
Run Type	Run Nos.	Truck Path(s)	Beam 1	Beam 2	Beam 3	Beam 4	Beam 5
Side -by-Side	7, 8	2, 6	-3%	-3%	0%	-1%	4%
Side-by-Side	16, 17	1, 7	0%	-1%	5%	1%	-6%
Back-to-Back	1, 2	1	-1%	0%	2%	-4%	-2%
Back-to-Back	3, 4	4	4%	-5%	-6%	-2%	6%
Back-to-Back	5, 6	7	0%	-5%	2%	1%	-1%
Single Truck*	9	1	-4%	0%	3%	-3%	-1%
Single Truck*	10	2	-3%	-1%	0%	-7%	5%
Single Truck*	11	3	-8%	0%	-1%	-3%	8%
Single Truck*	12	4	4%	-6%	-6%	-3%	6%
Single Truck*	13	5	5%	-8%	-5%	3%	2%
Single Truck*	14	6	5%	-9%	0%	3%	0%
Single Truck*	15	7	1%	-4%	2%	1%	-1%

† Difference is expressed as a percentage of the total live load moment.

* Truck 1, as described in Chapter 3, was used as loading vehicle for finite element analysis.

F.5 COMPARISON OF INFERRED AND CALCULATED LIVE LOAD DISTRIBUTION FACTORS

F.5.1 Comparison of Inferred and Calculated LLDF's for Chandler Creek Bridge, 40-ft Span

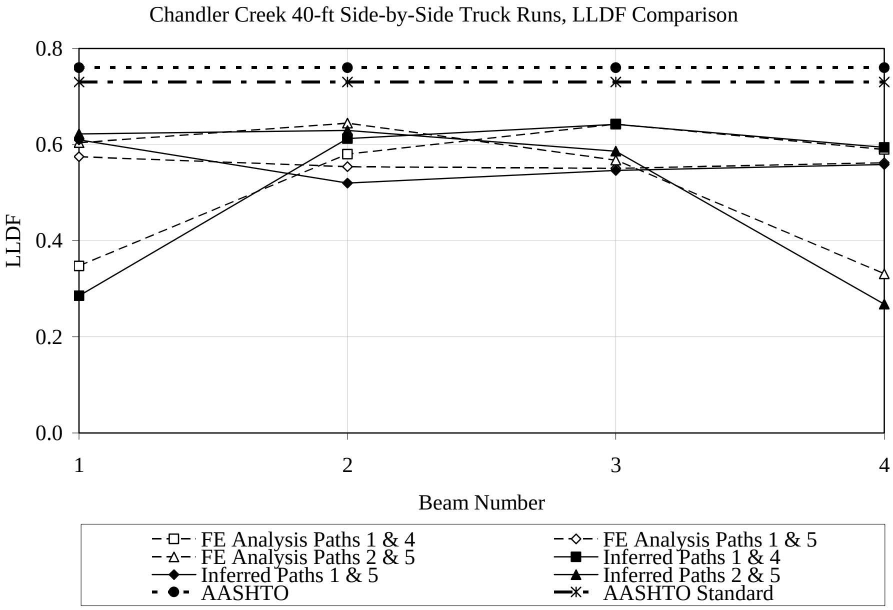

Figure F.1 Comparison of Inferred and Calculated LLDF'S for Side-by-Side Truck Runs Performed at Chandler Creek Bridge, 40-ft Span

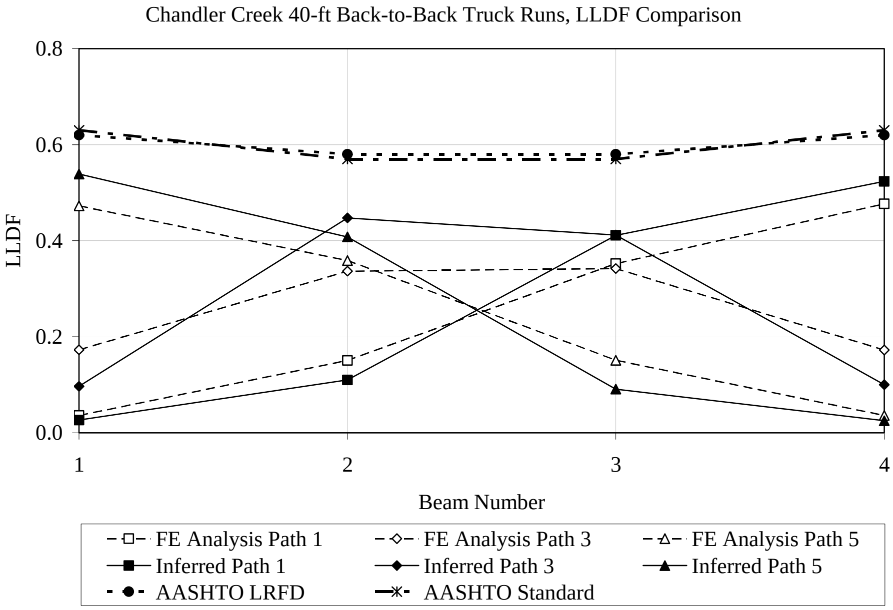

Figure F.2 Comparison of Inferred and Calculated LLDF'S for Back-to-Back Truck Runs Performed at Chandler Creek Bridge, 40-ft Span

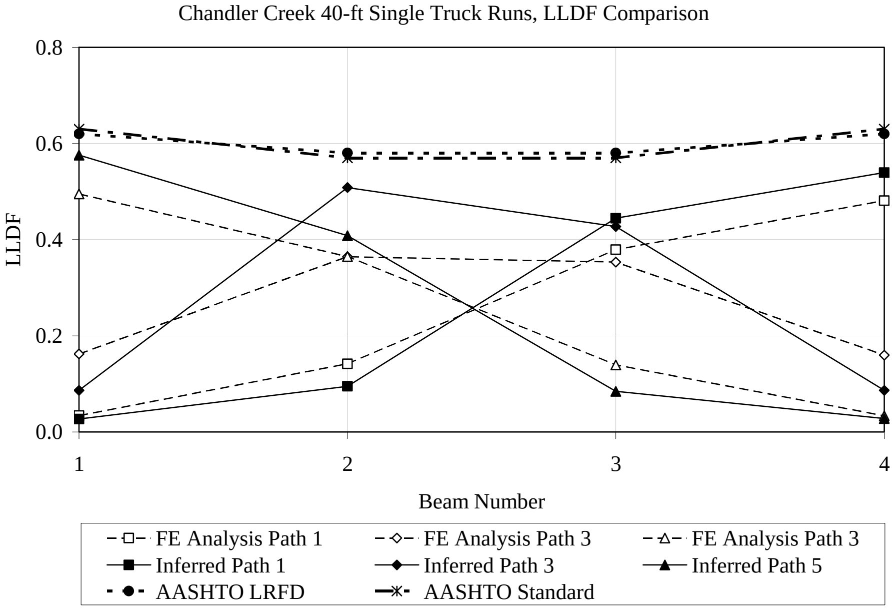

Figure F.3 Comparison of Inferred and Calculated LLDF'S for Single Truck Runs Performed at Chandler Creek Bridge, 40-ft Span

F.5.2 Comparison of Inferred and Calculated LLDF'S for Chandler Creek Bridge, 60-ft Span

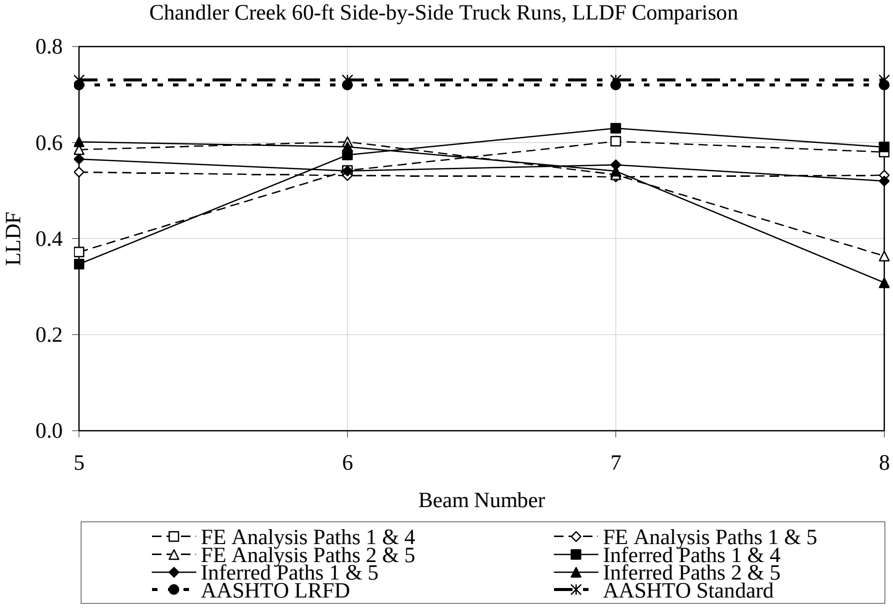

Figure F.4 Comparison of Inferred and Calculated LLDF'S for Side-by-Side Truck Runs Performed at Chandler Creek Bridge, 60-ft Span

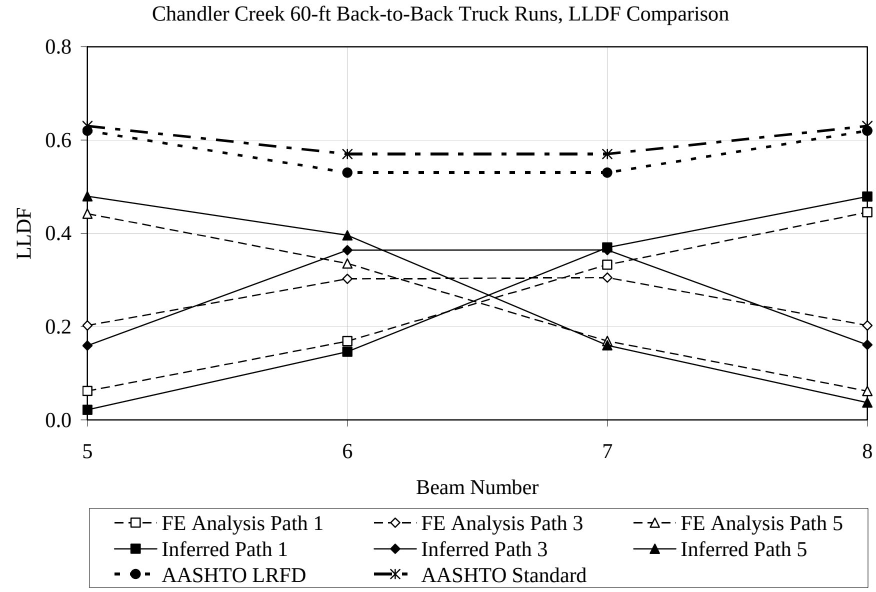

Figure F.5 Comparison of Inferred and Calculated LLDF'S for Back-to-Back Truck Runs Performed at Chandler Creek Bridge, 60-ft Span

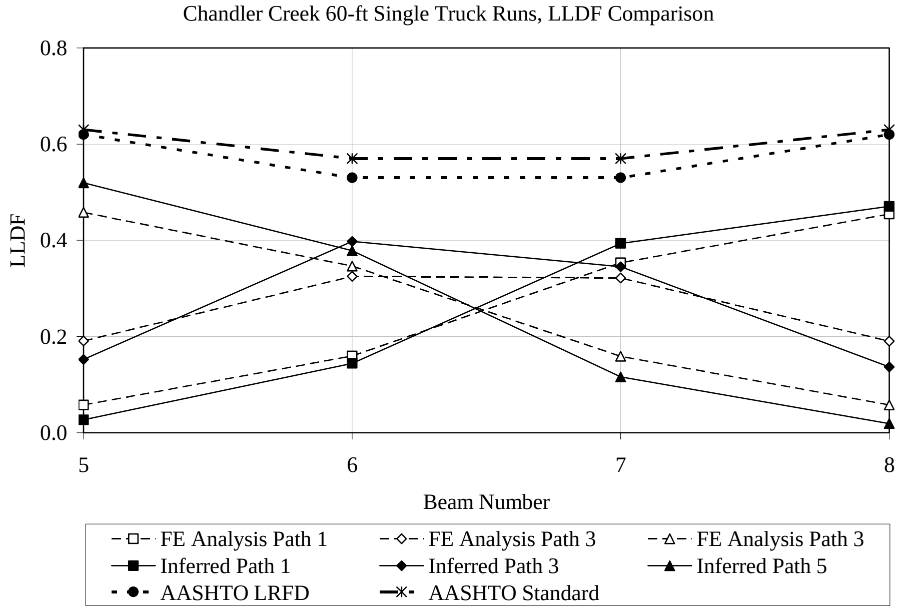

Figure F.6 Comparison of Inferred and Calculated LLDF'S for Single Truck Runs Performed at Chandler Creek Bridge, 60-ft Span

F.5.3 Comparison of Inferred and Calculated LLDF’S for Lake LBJ Bridge

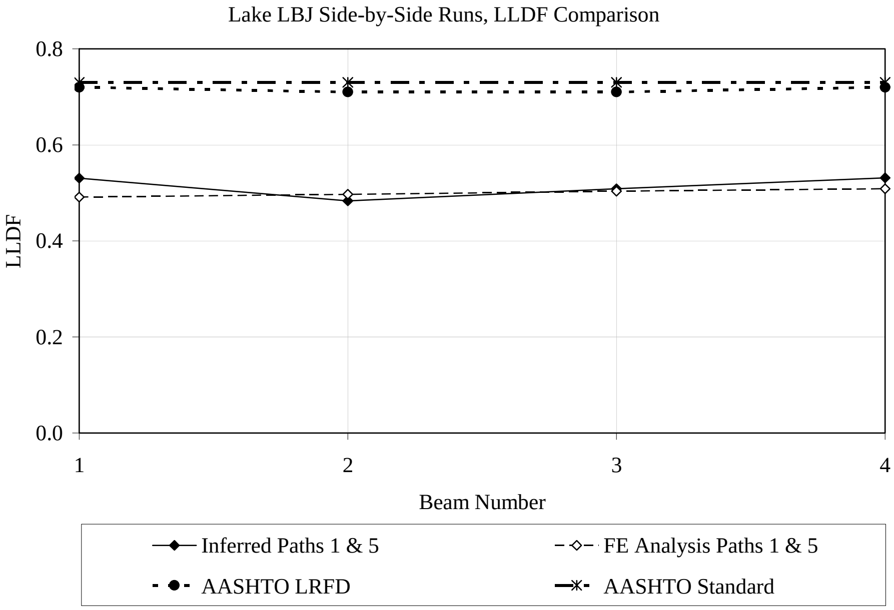

Figure F.7 Comparison of Inferred and Calculated LLDF’S for Side-by-Side Truck Runs Performed at Lake LBJ Bridge

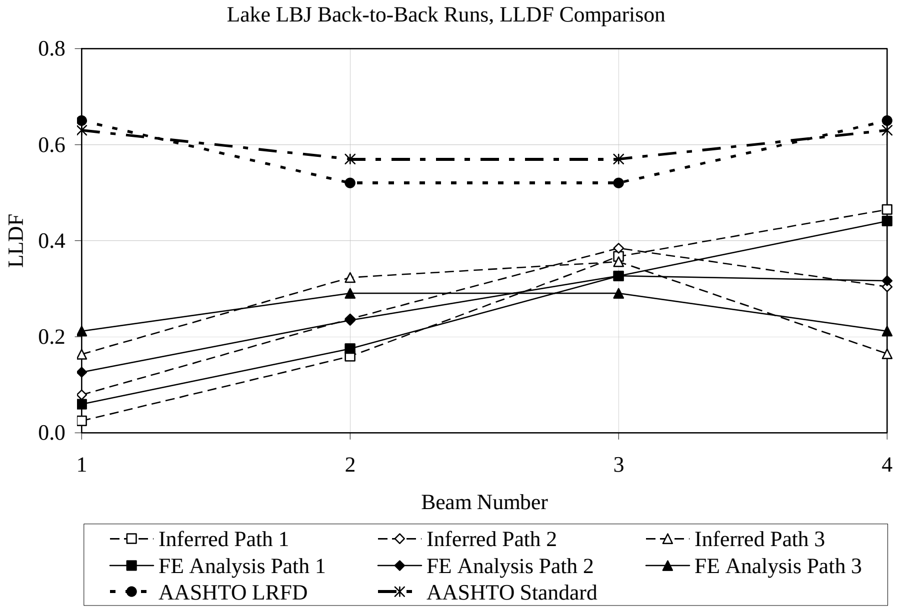

Figure F.8 Comparison of Inferred and Calculated LLDF'S for Back-to-Back Truck Runs Performed at Lake LBJ Bridge

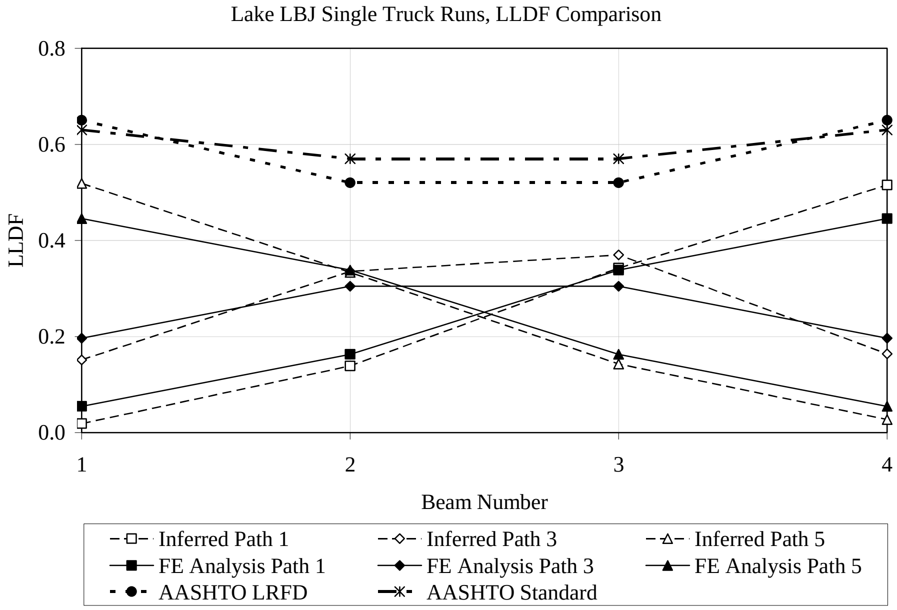

Figure F.9 Comparison of Inferred and Calculated LLDF'S for Single Truck Runs Performed at Lake LBJ Bridge

F.5.4 Comparison of Inferred and Calculated LLDF'S's for Lampasas River Bridge

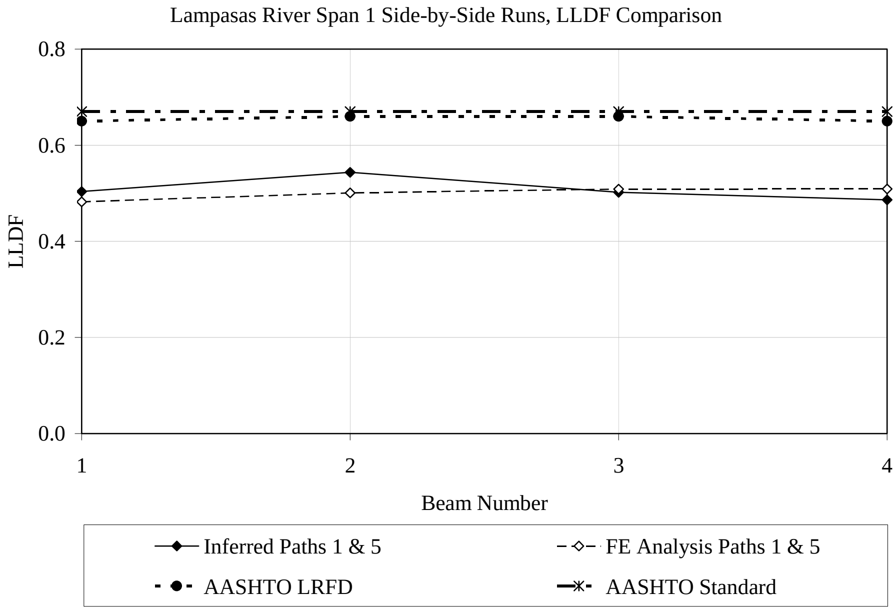

Figure F.10 Comparison of Inferred and Calculated LLDF'S for Side-by-Side Truck Runs Performed at Lampasas River Bridge, Span 1

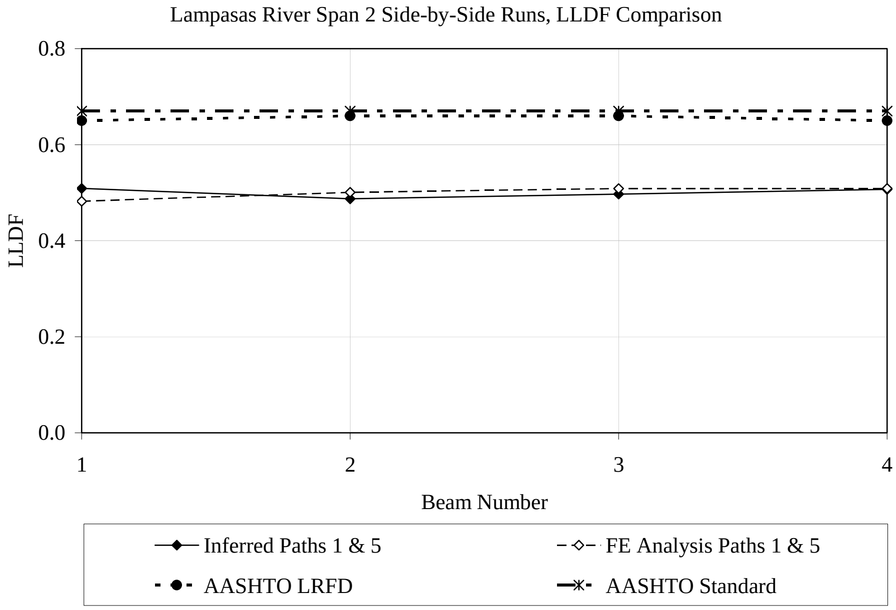

Figure F.11 Comparison of Inferred and Calculated LLDF'S for Side-by-Side Truck Runs Performed at Lampasas River Bridge, Span 2

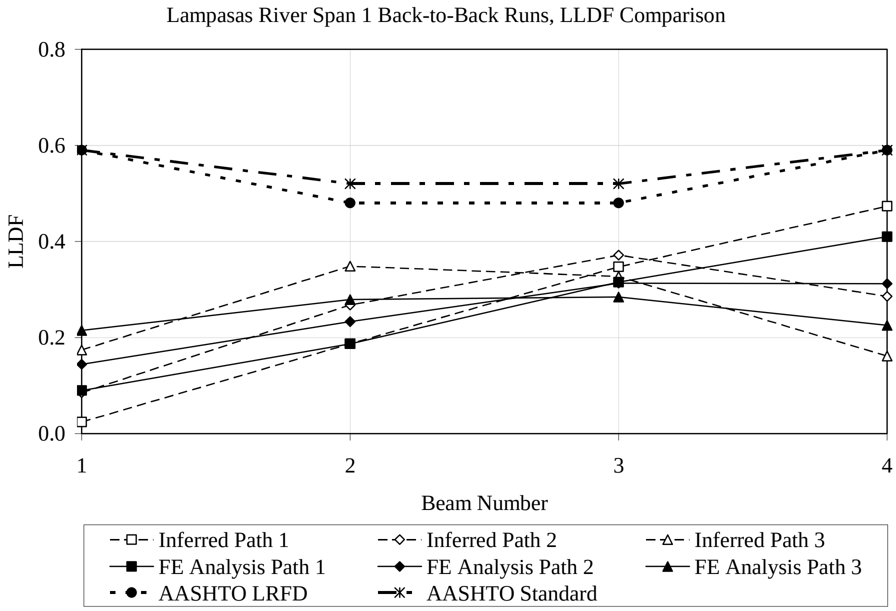

Figure F.12 Comparison of Inferred and Calculated LLDF'S for Back-to-Back Truck Runs performed at Lampasas River Bridge, Span 1

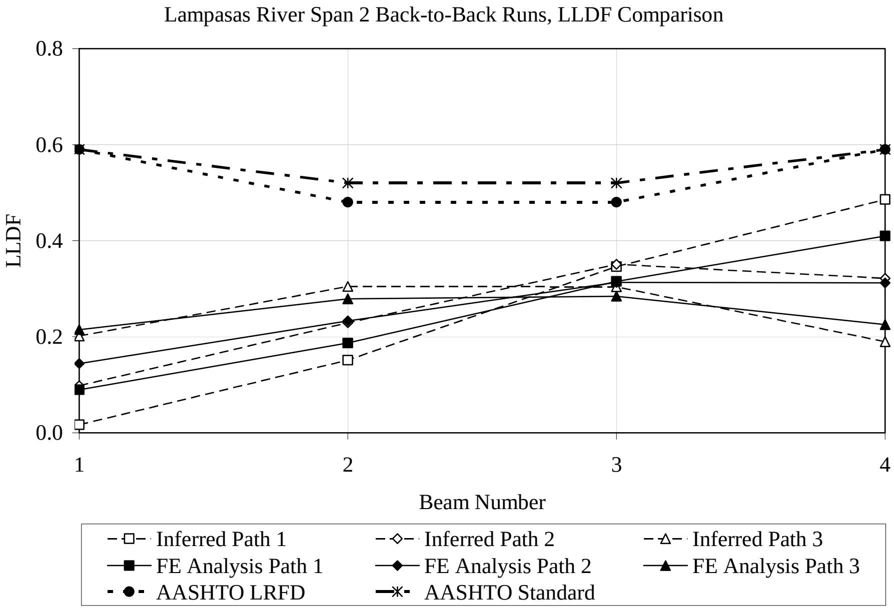

Figure F.13 Comparison of Inferred and Calculated LLDF'S for Lampasas River Bridge, Span 2, Back-to-Back Truck Runs

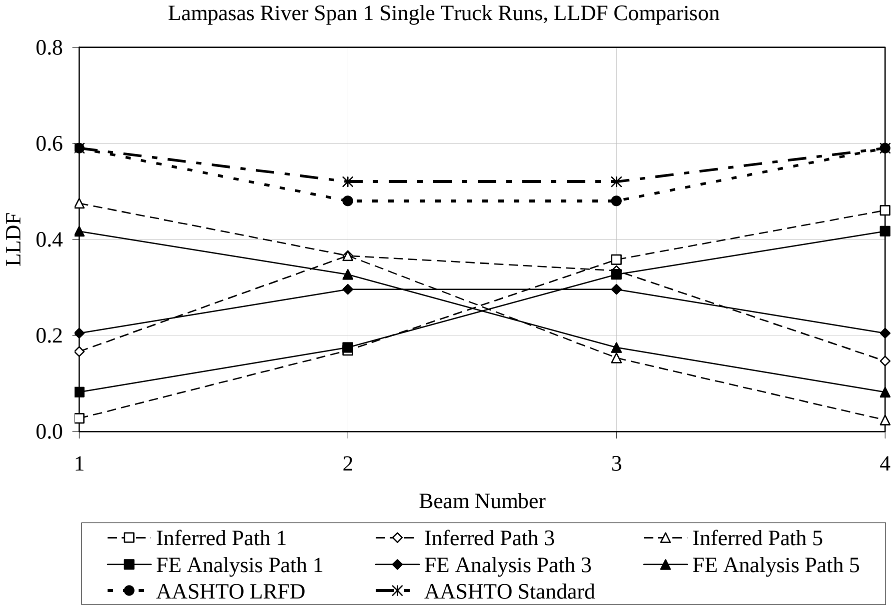

Figure F.14 Comparison of Inferred and Calculated LLDF'S for Single Truck Runs Performed at Lampasas River Bridge, Span 1

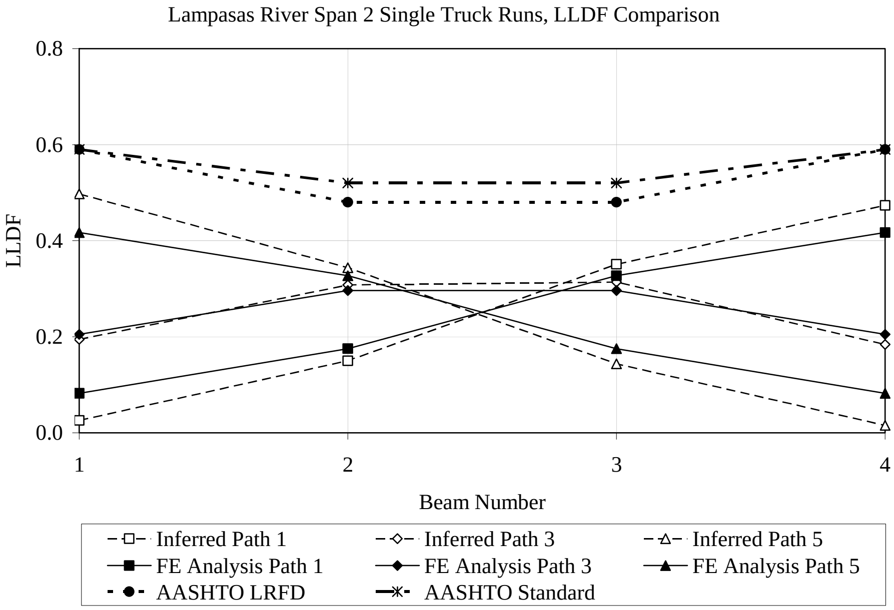

Figure F.15 Comparison of Inferred and Calculated LLDF'S for Single Truck Runs Performed at Lampasas River Bridge, Span 2

F.5.5 Comparison of Inferred and Calculated LLDF'S for Willis Creek Bridge

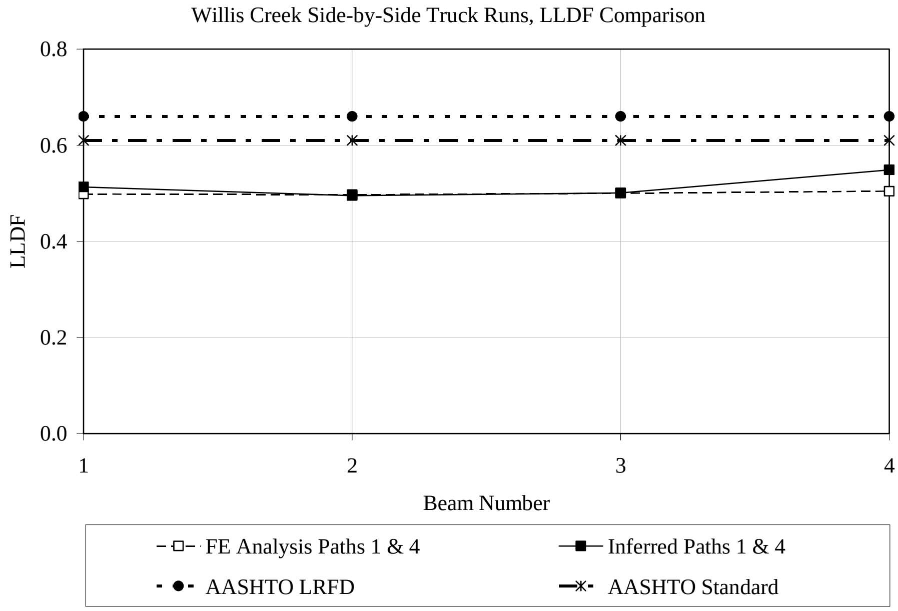

Figure F.16 Comparison of Inferred and Calculated LLDF'S for Side-by-Side Truck Runs Performed at Willis Creek Bridge

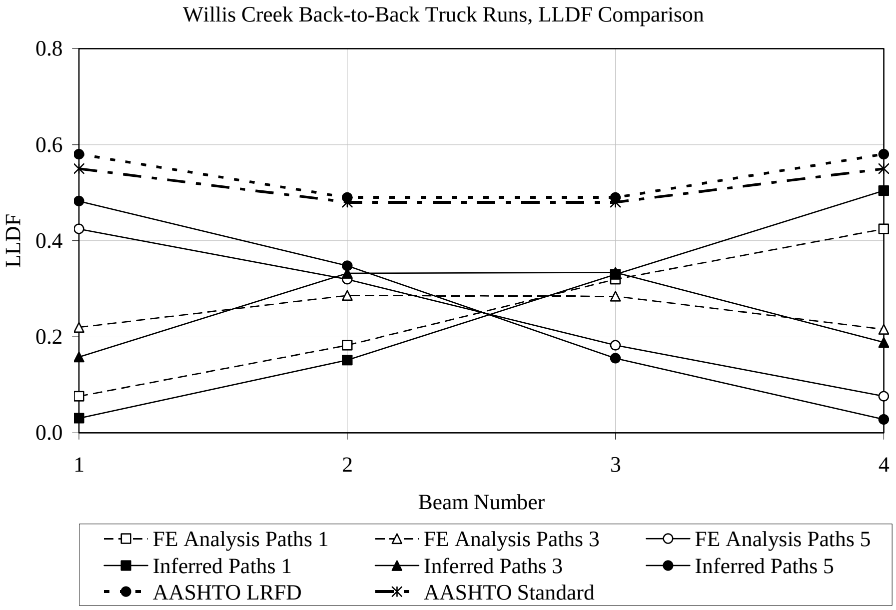

Figure F.17 Comparison of Inferred and Calculated LLDF'S for Back-to-Back Truck Runs Performed at Willis Creek Bridge

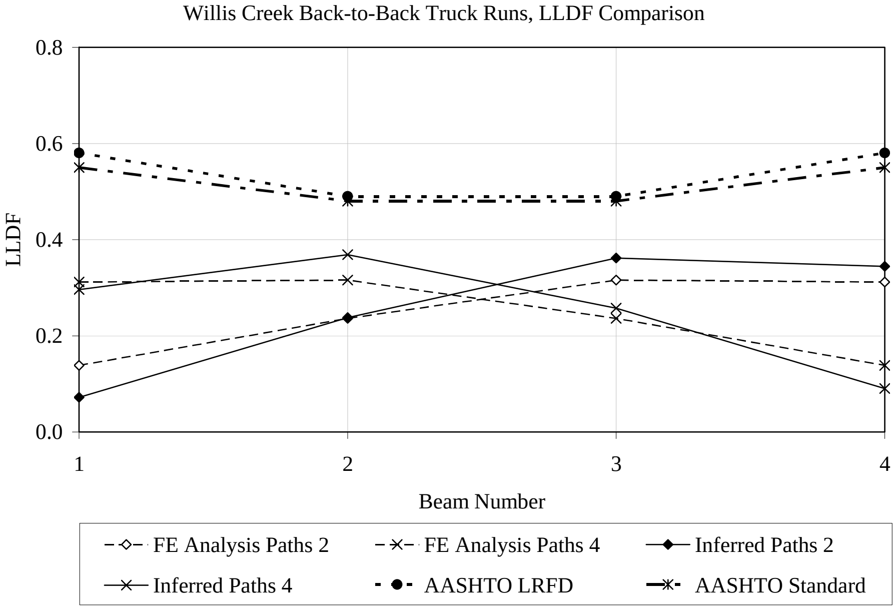

Figure F.18 Comparison of Inferred and Calculated LLDF'S for Back-to-Back Truck Runs Performed at Willis Creek Bridge

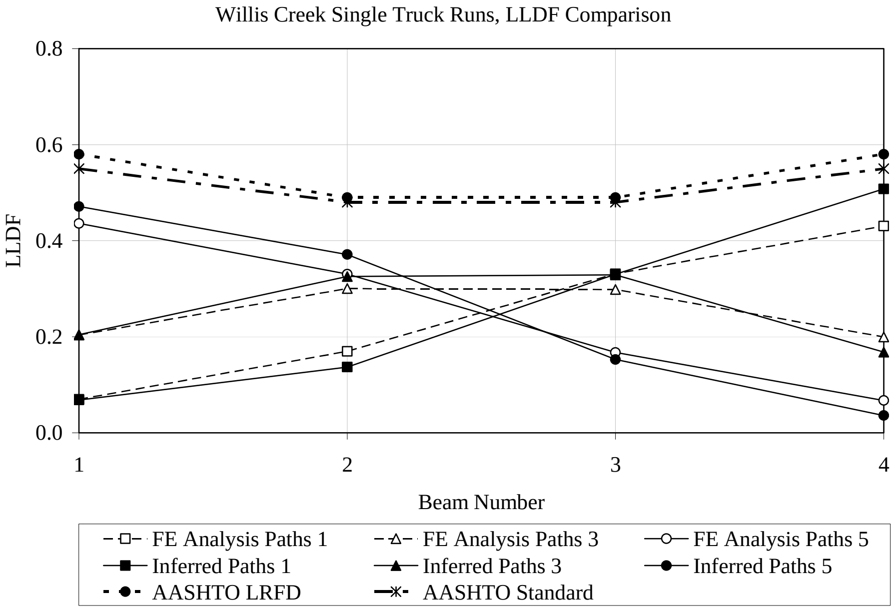

Figure F.19 Comparison of Inferred and Calculated LLDF'S for Single Truck Runs Performed at Willis Creek Bridge

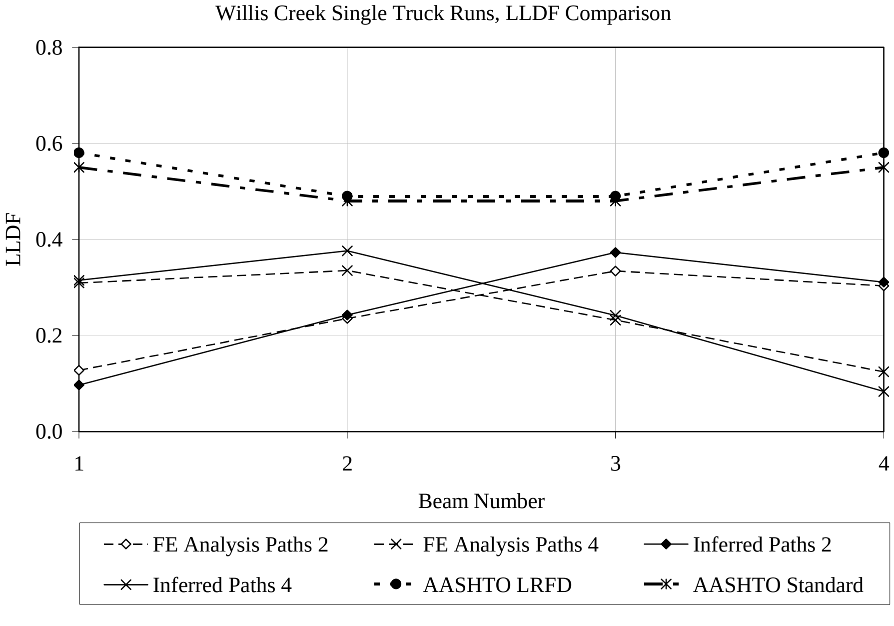

Figure F.20 Comparison of Inferred and Calculated LLDF'S for Single Truck Runs Performed at Willis Creek Bridge

F.5.6 Comparison of Inferred and Calculated LLDF'S for Wimberley Bridge, Span 1

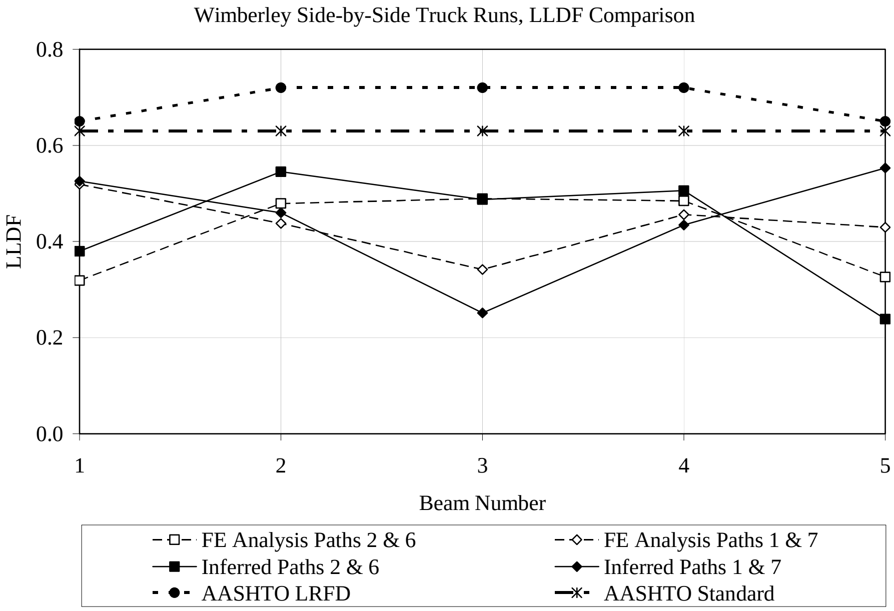

Figure F.21 Comparison of Inferred and Calculated LLDF for Wimberley Side-by-Side Truck Runs, Span 1

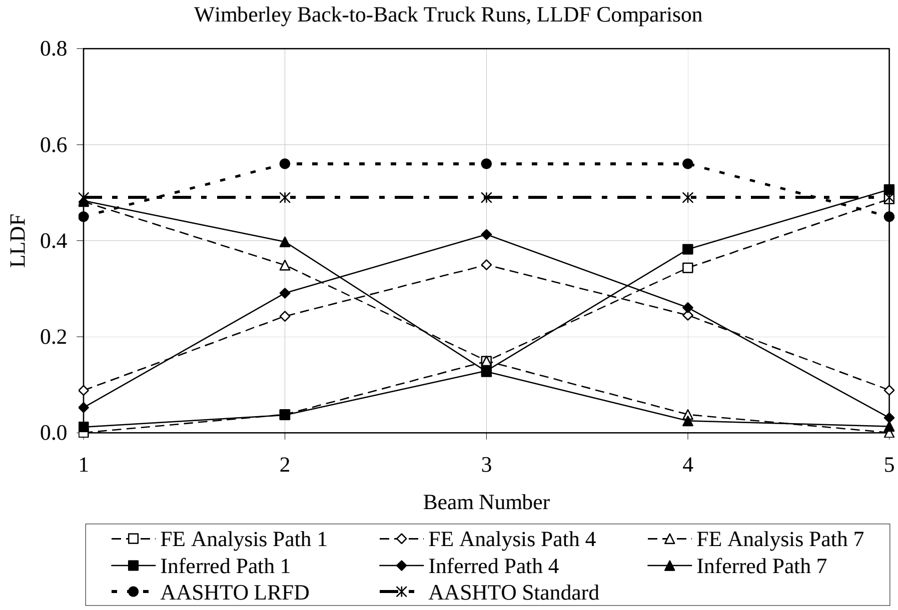

Figure F.22 Comparison of Inferred and Calculated LLDF for Wimberley Back-to-Back Truck Runs, Span 1

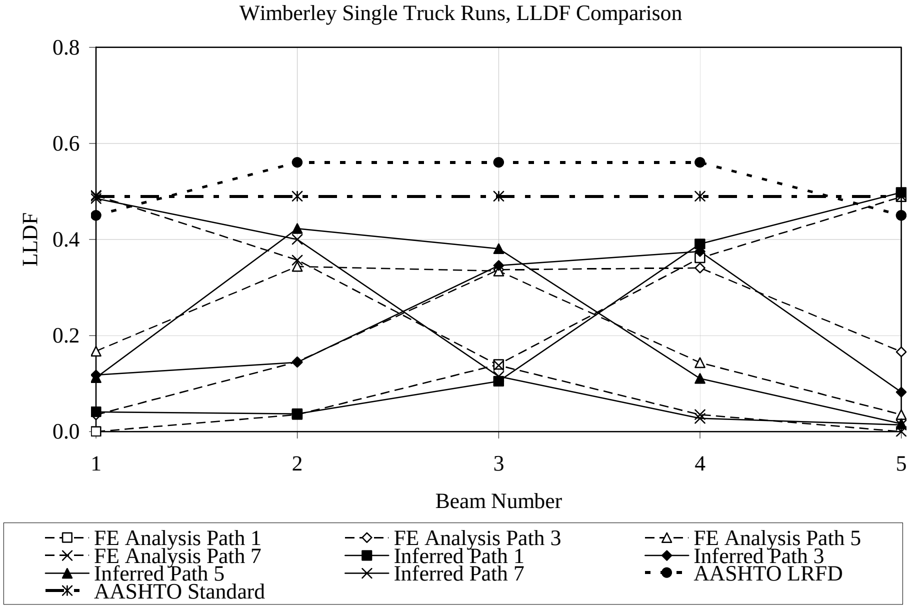

Figure F.23 Comparison of Inferred and Calculated LLDF for Wimberley Single Truck Runs, Span 1

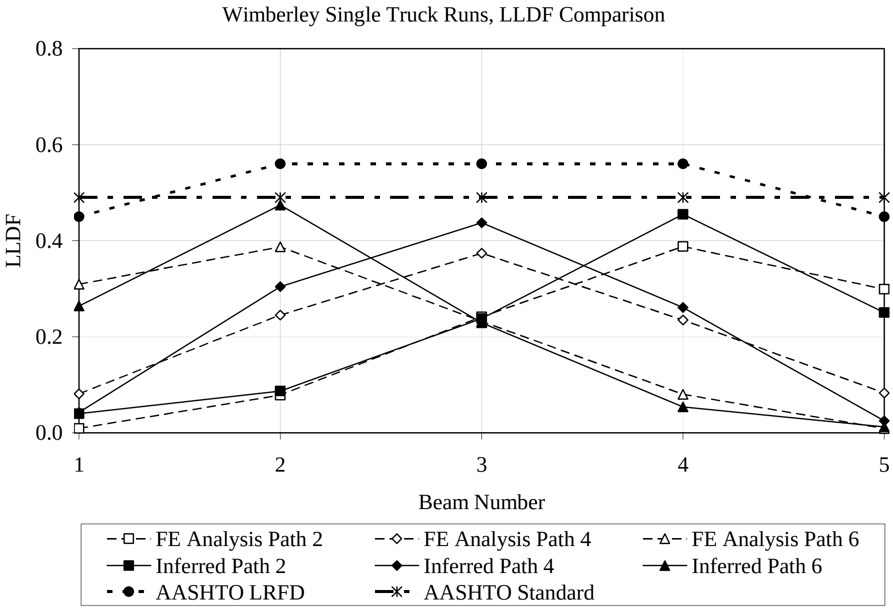

Figure F.24 Comparison of Inferred and Calculated LLDF for Wimberley Single Truck Runs, Span 1

F.5.7 Comparison of Inferred and Calculated LLDF'S for Wimberley Bridge, Span 2

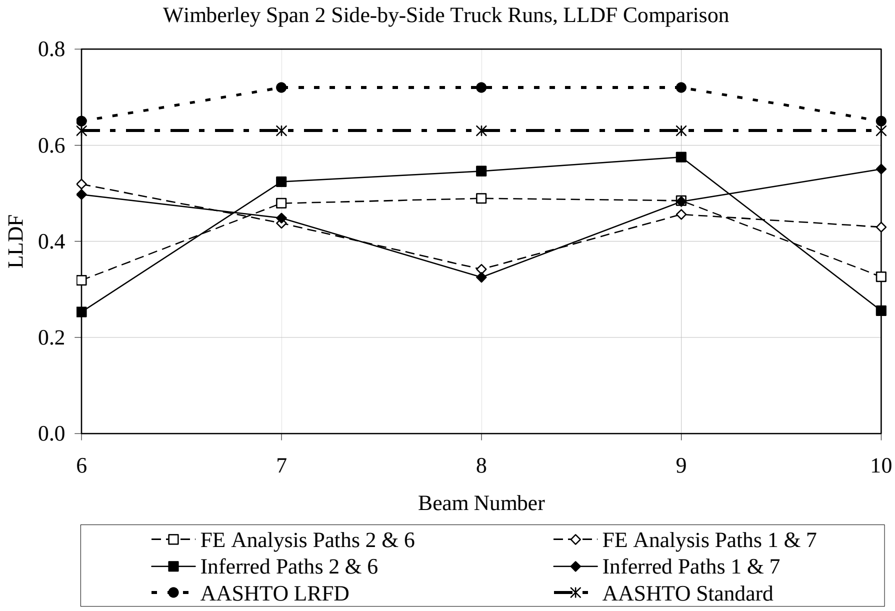

Figure F.25 Comparison of Inferred and Calculated LLDF for Wimberley Side-by-Side Truck Runs, Span 2

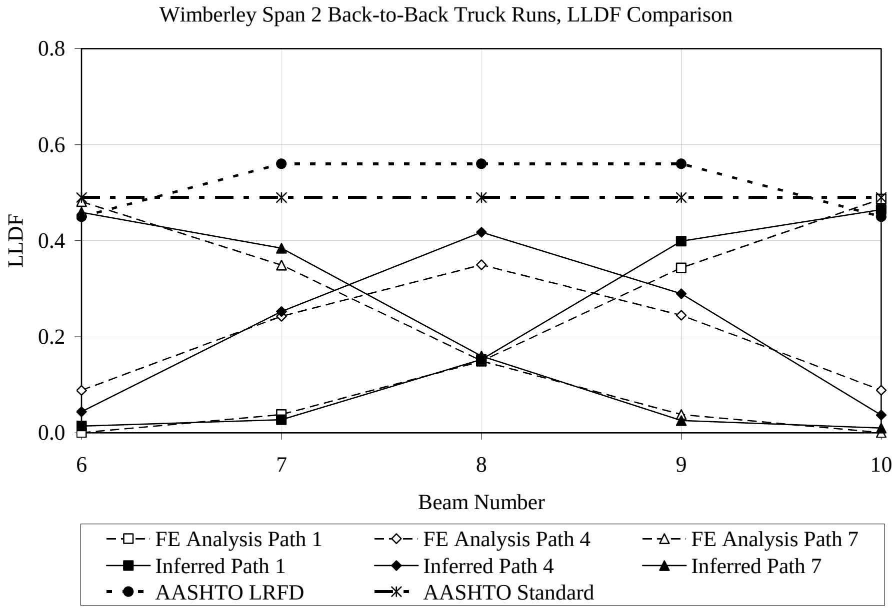

Figure F.26 Comparison of Inferred and Calculated LLDF for Wimberley Back-to-Back Truck Runs, Span 2

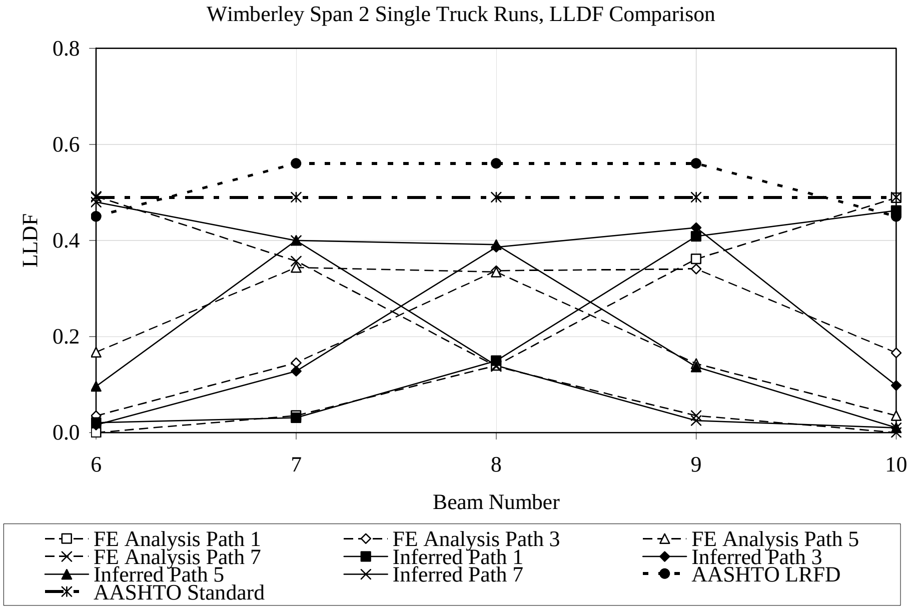

Figure F.27 Comparison of Inferred and Calculated LLDF for Wimberley Single Truck Runs, Span 2

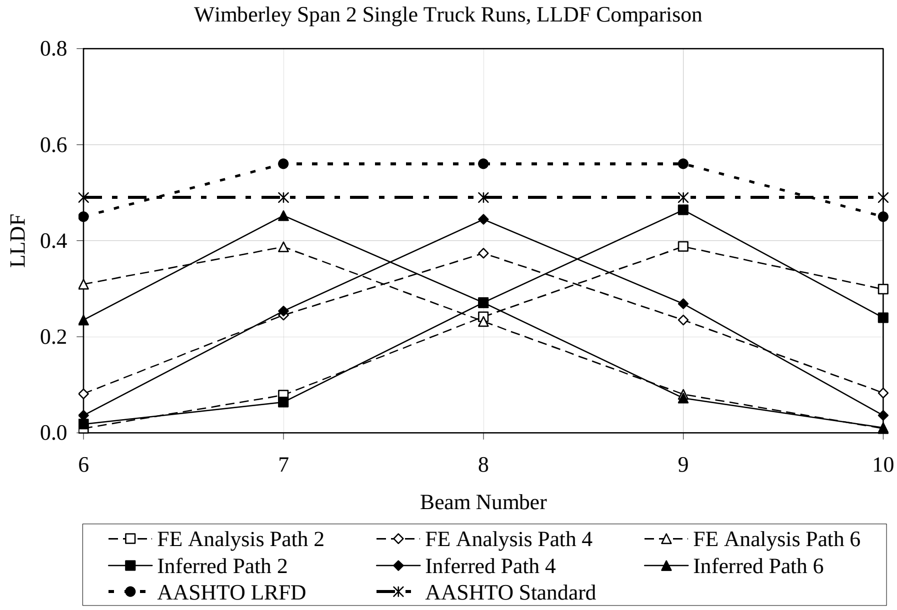

Figure F.28 Comparison of Inferred and Calculated LLDF for Wimberley Single Truck Runs, Span 2

F.6 COMPARISON OF AASHTO LLDF'S AND LIVE LOAD DISTRIBUTION FACTORS BASED ON FINITE ELEMENT ANALYSIS

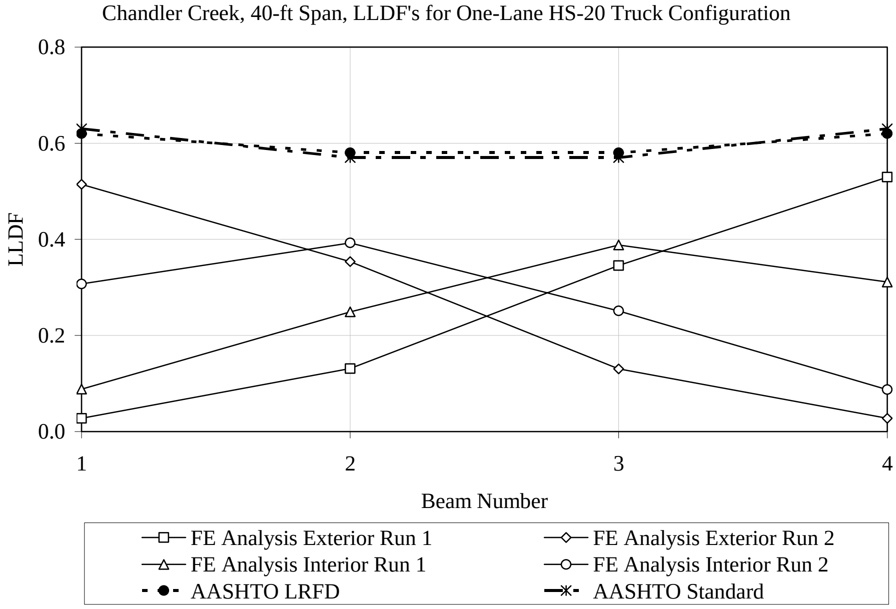

Figure F.29 Comparison of AASHTO and FE Analysis One-Lane LLDF'S for Chandler Creek Bridge, 40-ft Span

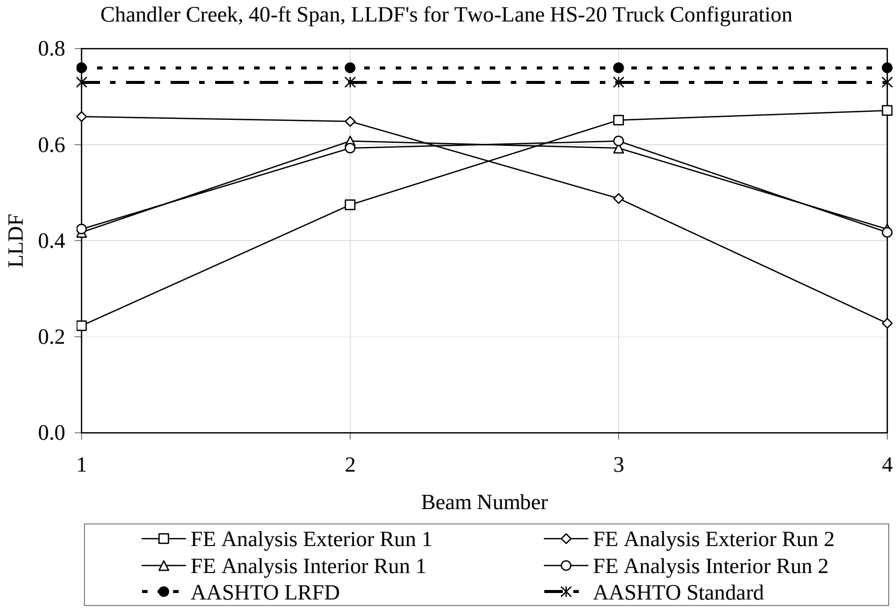

Figure F.30 Comparison of AASHTO and FE Analysis Two-Lane LLDF'S for Chandler Creek Bridge, 40-ft Span

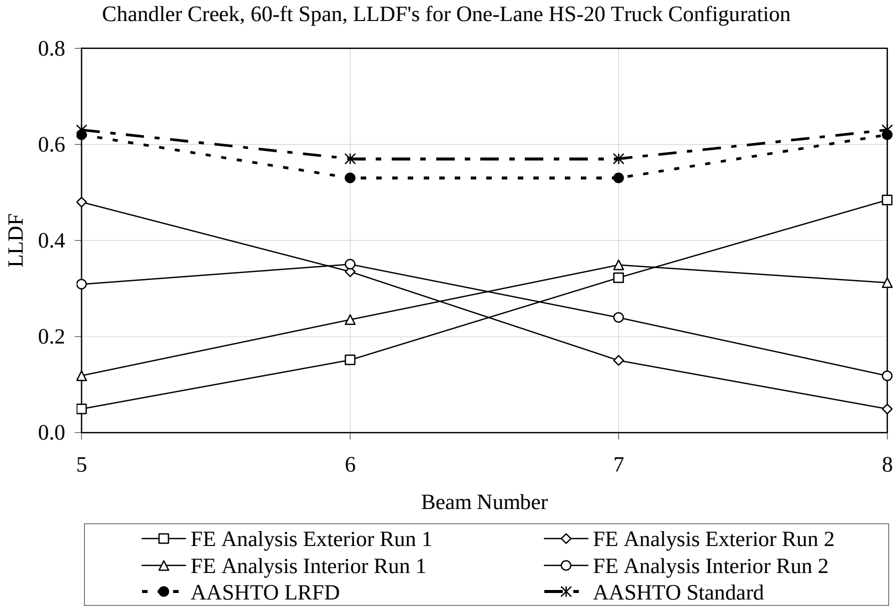

Figure F.31 Comparison of AASHTO and FE Analysis One-Lane LLDF'S for Chandler Creek Bridge, 60-ft Span

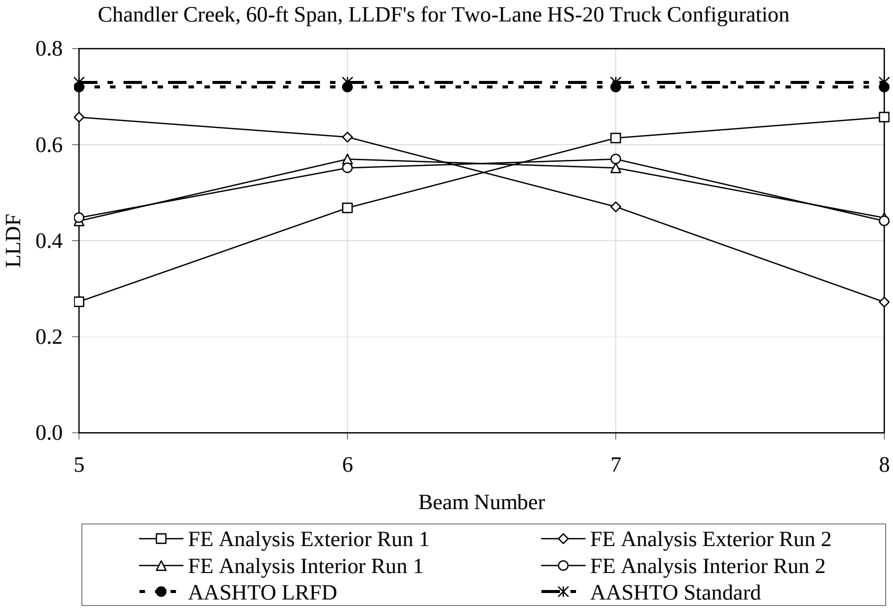

Figure F.32 Comparison of AASHTO and FE Analysis Two-Lane LLDF'S for Chandler Creek Bridge, 60-ft Span

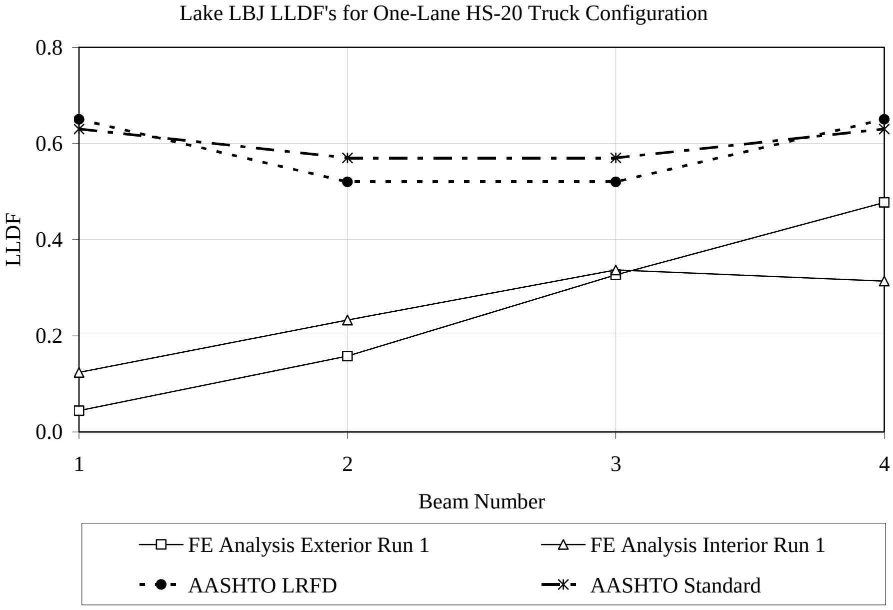

Figure F.33 Comparison of AASHTO and FE Analysis One-Lane LLDF'S for Lake LBJ Bridge

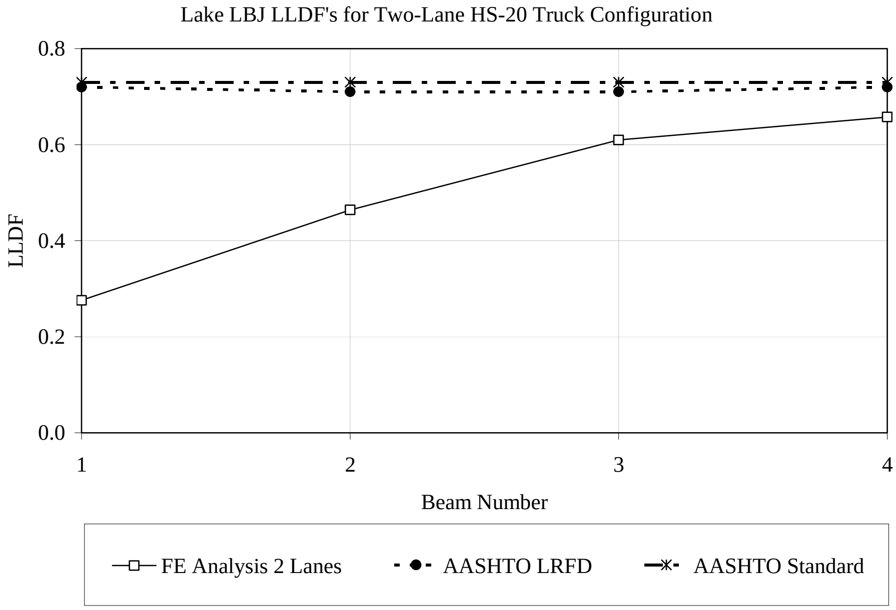

Figure F.34 Comparison of AASHTO and FE Analysis Two-Lane LLDF'S for Lake LBJ Bridge

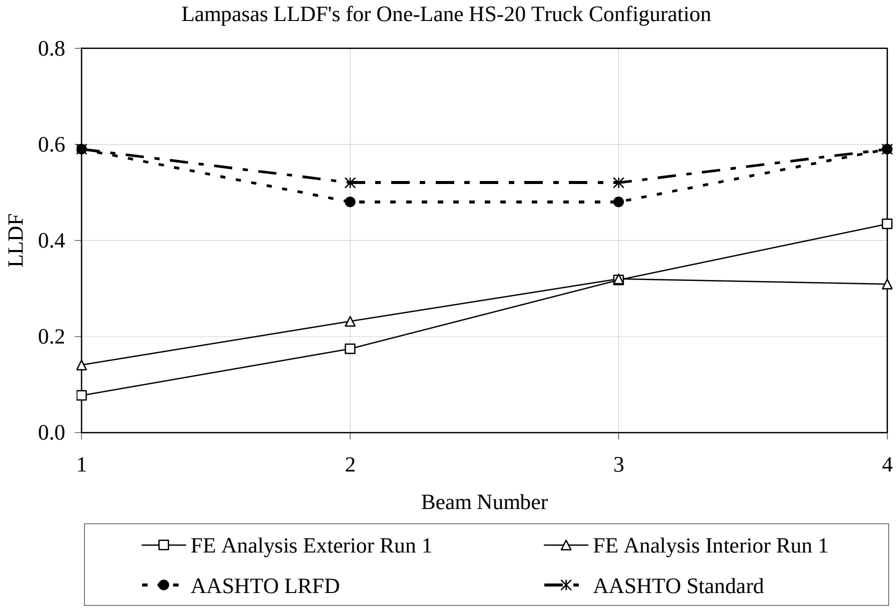

Figure F.35 Comparison of AASHTO and FE Analysis One-Lane LLDF'S for Lampasas River Bridge

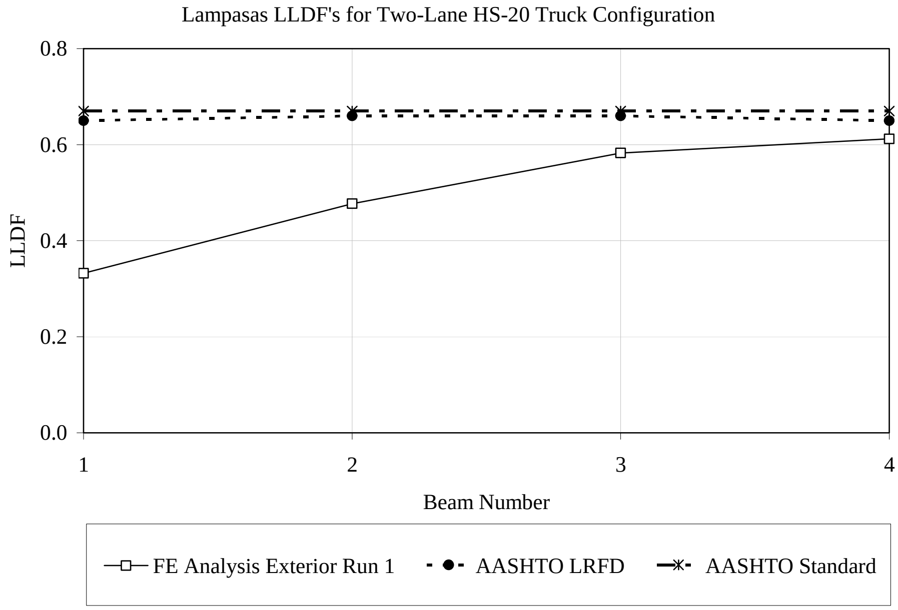

Figure F.36 Comparison of AASHTO and FE Analysis Two-Lane LLDF'S for Lampasas River Bridge

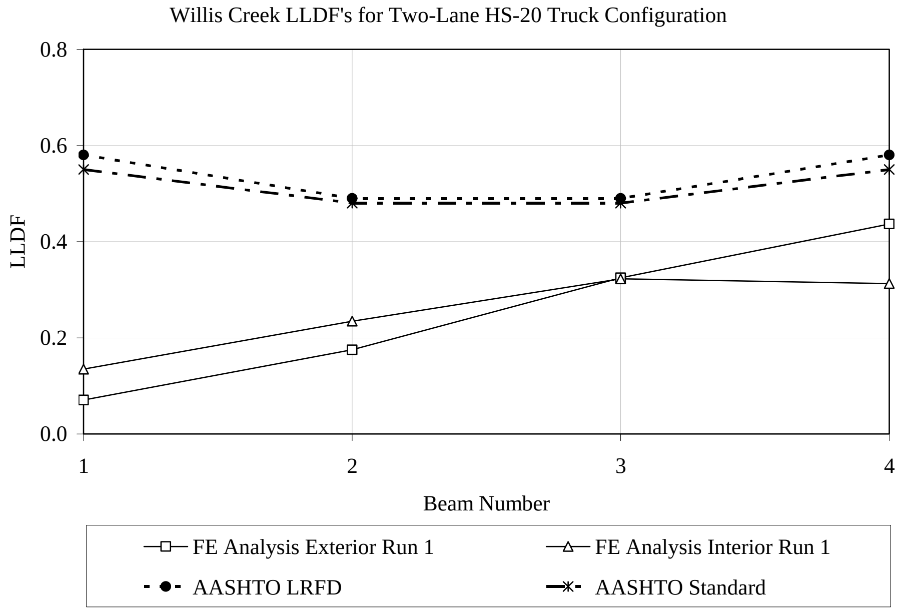

Figure F.37 Comparison of AASHTO and FE Analysis One-Lane LLDF'S for Willis Creek Bridge

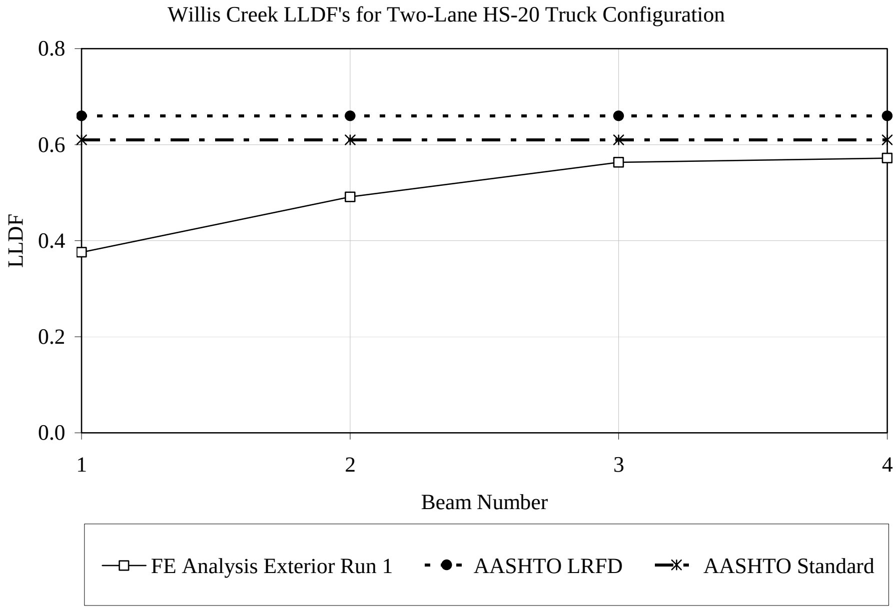

Figure F.38 Comparison of AASHTO and FE Analysis Two-Lane LLDF'S for Willis Creek Bridge

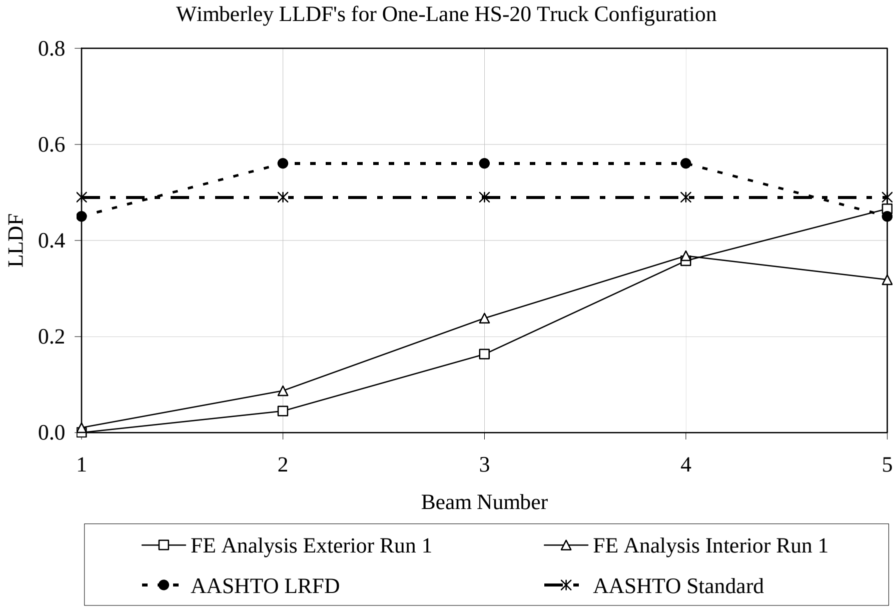

Figure F.39 Comparison of AASHTO and FE Analysis One-Lane LLDF'S for Wimberley Bridge

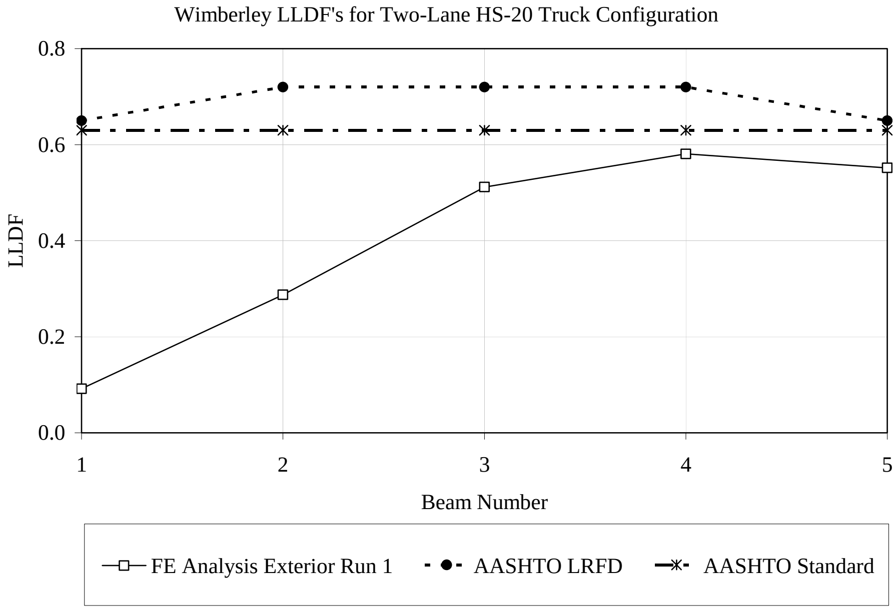

Figure F.40 Comparison of AASHTO and FE Analysis Two-Lane LLDF'S for Wimberley Bridge

CHAPTER G

Discussion of Finite Element Analyses Performed on Bridges in This Investigation

An overview of the finite element analyses performed on the bridges in this investigation is given in this appendix. Section G.1 gives the requirements outlined in the AASHTO LRFD specifications for the finite element analysis of beam-slab bridges, which is the type of bridge being studied in this dissertation. Section G.2 is an overview of the software used for the analyses, and includes a description of the finite element model, required input, and truck configurations used. More detailed information on the software used can be found in Hays, et al. (1994).

G.1 AASHTO LRFD REQUIREMENTS FOR FINITE ELEMENT ANALYSIS

The AASHTO LRFD provides several requirements and guidelines for the analysis of beam-slab bridges using finite element analysis. The requirements are given in the specification, while the guidelines are provided in the commentary and are to be used at the discretion of the engineer. The requirements and guidelines are as follows.

Requirements:

1. The aspect ratio of finite elements should not exceed 5.0.
2. Abrupt changes in size and/or shape of finite elements should be avoided.
3. Nodal loads shall be statically equivalent to the actual loads being applied.

Guidelines:

1. A minimum of five, and preferably nine, nodes per beam should be used.
2. For finite element analyses involving plate and beam elements, it is preferable to maintain the relative vertical distances between various elements.
3. For analyses of live load, the slab shall be assumed to be effective for stiffness in both positive and negative flexure.
4. In finite element analysis, an element should have membrane capability with discretization sufficient to properly account for shear lag.
5. The Saint Venant torsional inertia may be determined using Eq. G.1.

$$J \approx \frac{A^4}{40 I_p} \tag{G.1}$$

where A is the area of the cross-section in in.^{2}, and I_p is the polar moment of inertia in in.^{4}.

G.2 FINITE ELEMENT ANALYSIS SOFTWARE USED

As previously discussed in Chapter 4, the software used to perform the finite element analyses is called BRUFEM (Bridge Rating Using Finite Element Modeling) and was developed at the University of Florida for the Florida Department of Transportation. A description of the bridge model used, required user input, and transverse position of the trucks used for the finite element analyses are included in this section.

G.2.1 Description of Bridge Model

The BRUFEM software offers two methods of modeling the composite action of beam-slab bridges. The first model, called the composite girder model

(CGM), uses the composite properties of each member as input by the user. For the bridges in this investigation the composite properties would be the combination of the prestressed beams and effective slab width. In this model, the centroid of the composite section is set at the same elevation as the centroid of the slab. In the CGM model, the slab elements are modeled as plate elements, which are bending elements that are not capable of developing in plane stresses. Therefore, the sole purpose of the slab elements is to distribute the live loads to the girders, which are modeled as frame elements. Because the slab and beam elements are located at the same elevation, this does not conform to the guideline outlined by the AASHTO recommendations that state it is preferable to maintain the relative vertical distance between elements. Therefore, this model was not used for the analyses of bridges in this investigation.

The second model, called the eccentric girder model (EGM), does maintain the relative vertical distance between elements, and this model was used in this investigation. Figure G.1 is a typical plan of a bridge model developed using the eccentric girder model. Section G.2.2 includes a discussion of the input required to generate such a model. In the EGM, the properties of the non-composite prestressed beam are input by the user and are located vertically below the slab at a distance equal to the distance between the centroid of the non-composite beam and centroid of the slab elements. This is shown schematically in Figure G.2, which is a cross-section taken through the exterior beam of the typical plan in Figure G.1. As shown in Figure G.2, the slab elements and beam elements are connected with a vertical rigid link. The slab elements in the EGM are modeled using shell elements. Shell elements, unlike plate elements, are capable of developing plane stresses. Therefore, composite action is achieved by using the shell elements in the slab in conjunction with the eccentricity between the slab and beam elements.

In addition to the beams, frame elements are used to model the edge stiffeners, such as curbs and parapets, and stiffeners over the prestressed beams. Figure G.2 shows an example of an edge stiffener and the stiffener over the beams. The edge stiffener elements are also connected to the slab with a rigid link. In the field, the slab essentially spans between the edges of the flanges of adjacent beams. BRUFEM models this behavior by using frame elements that effectively stiffen the slab over the beams.

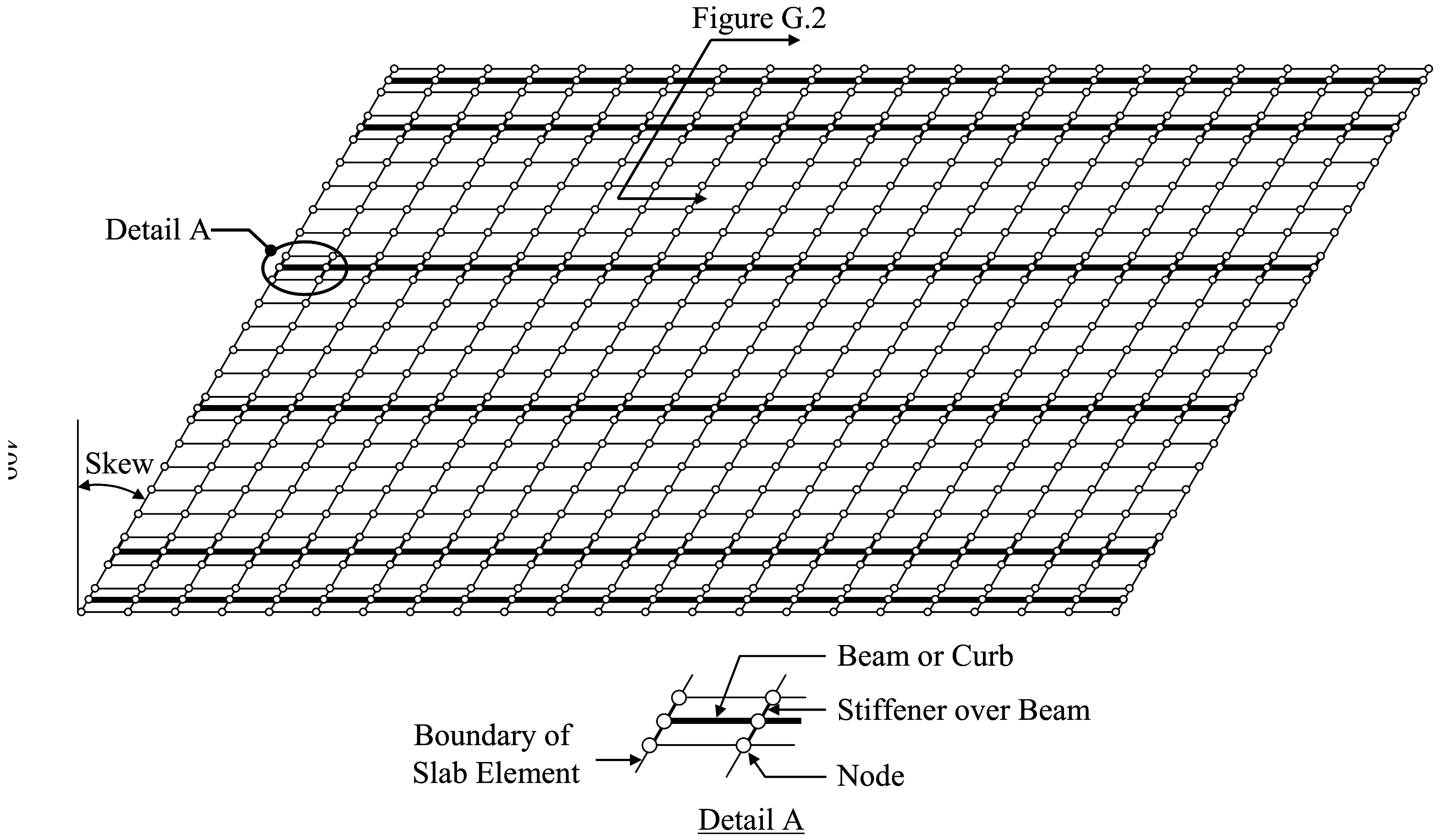

Figure G.1 Typical Plan of Bridge Model

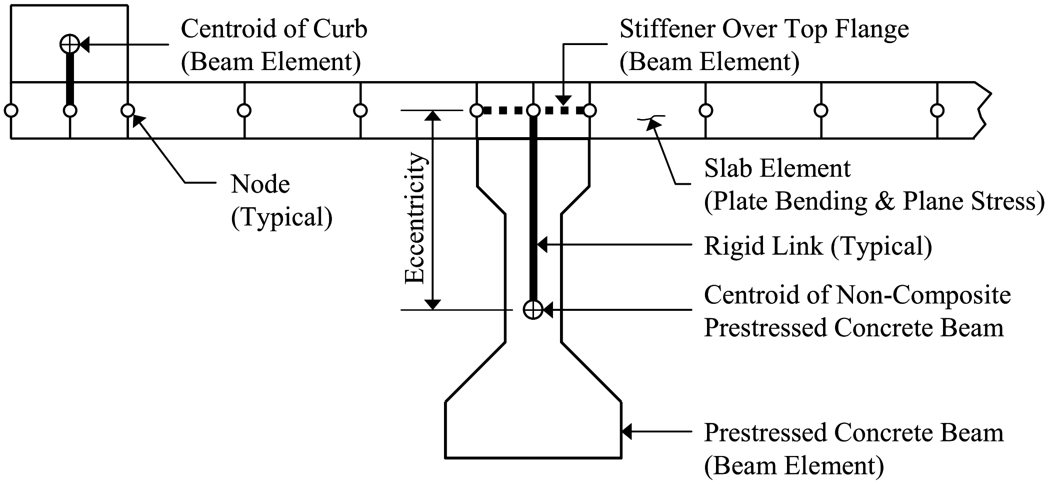

Figure G.2 Schematic of Elements in Bridge Model Used by BRUFEM

G.2.2 Discussion of the Input for Modeling the Bridges being Studied

Because BRUFEM was specifically developed for load rating bridges, the preprocessor simplified the development of the models used in the finite element program. This section discusses the parameters that were used in the development of the models. The input parameters include general bridge parameters, prestressed concrete beam parameters, slab and curb parameters, live load parameters, and material parameters. Although BRUFEM will model transverse diaphragms, this feature was not used in this study. The decision not to model the diaphragms was based on the research by Barr, et al. (2001), where the addition of intermediate diaphragms was determined to have no effect on the live load distribution factors calculated using finite element analyses.

G.2.2.1 General Bridge Parameters

The general parameters that the user must input to the preprocessor to develop of the finite element models include the following.

- Number of beams (Table 2.2)
- Beam spacing (Table 2.2)
- Skew angle (Table 2.2)
- Number of spans (always taken as 1 for the simple-span bridges)
- Effective span length (Figures A.2, A.6, A.10, A.14, and A.18)

This information has been previously discussed for the bridges considered in tis investigation and may be found in Chapter 2 and Appendix A as referenced. All of the bridges were modeled as simple spans.

In addition to the above parameters, the user is required to input the number of longitudinal elements and transverse elements used in the model. Therefore, the aspect ratio of the elements is dependent on user defined input. For the models used in this investigation, the aspect ratio of elements was approximately two or less. This is well below the AASHTO guideline of five, and is consistent with the recommendations of Chen et al. (1996).

G.2.2.2 Prestressed Concrete Beam Parameters

The preprocessor has several options for the input of prestressed concrete beams. As part of the software, standard AASTHO prestressed concrete beam sections are included, which would eliminate the need to input the general section parameters. However, the prestressed concrete beams in the bridges were not standard AASHTO beams, and therefore the general section parameters for the prestressed beams were input. The following general beam dimensions are required:

- Width of top flange

- Width of web
- Width of bottom flange
- Thickness of top flange
- Thickness of bottom flange

For the bridges considered in this investigation, the values of these parameters are given in Figures A.3, A.7, A.11, A.15, and A.19. The thickness of the top and bottom flanges was taken as the thickness of the constant width portion of the flange. For Type B beams, the thicknesses of the top and bottom flanges were 5.5 and 6 in., respectively. For Type C beams, the thicknesses for the top and bottom flanges were 6 and 7 in., respectively.

The general cross section and material properties input included the following:

- Moment of inertia of non-composite beam (Table A.5)
- Area of non-composite beam (Table A.5)
- Distance from centroid of beam to top of beam (Table A.5, $y_{t\text{-beam}}$)
- Torsional moment of inertia calculated using Eq. G.1 (Table G.1)

G.2.2.3 Slab and Curb Parameters

The curb parameters input in the model are listed below. The values are given in Table A.6, and in Figures A.2, A.3, A.6, A.7, A.10, A.11, A.14, A.15, A.18, and A.19.

- Moment of inertia of stiffener
- Depth of stiffener
- Area of member
- Slab thickness

Table G.1 Prestressed Beam Properties (Wagener 2002)

Bridge Name	$I_{y\text{-}beam}$ (in.^{4})	I_p (in.^{4})*	J (in.^{4})**
Chandler Creek – 40' Span	9700	48100	8800
Chandler Creek – 60' Span	4800	92500	16300
Lake LBJ	9700	92500	16300
Lampasas River	9700	92500	16300
Willis Creek	9700	92500	16300
Wimberley	4800	48100	8800

* $I_p = I_{y-beam} + I_{beam}$ (I_{beam} is given in Table A.5)

** J is calculated using Eq. G.1

G.2.2.4 Live Load Parameters

BRUFEM allows the input of standard vehicles, such as the HS-20, as well as general vehicles. Where standard vehicles are used, only the transverse location of the vehicle on the bridge must be input. For non-standard vehicles, the following input is also required:

- Number of axle groups
- Axle gage, which is the distance between the wheels on the axle
- Distance between the axles
- Axle weights

The preprocessor also automatically generates load cases by shifting the location of the vehicle loads relative to the start position of the vehicle. The input required for generating load cases includes the longitudinal start location of the vehicle, the number of shifts desired longitudinally and transversely, and the desired shift dimension. The transverse locations of the vehicles for the analyses performed as part of this study are discussed in Section G.2.3. The number and spacing of longitudinal shifts varied depending on the length of the bridge, and truck configuration.

G.2.2.5 Material Parameters

Estimated in situ concrete compressive strengths were used in all the finite element models. These values have been previously reported in Table 2.9.

G.2.3 Truck Configurations Analyzed Using Finite Element Analysis

Two sets of truck configurations were used in the finite element analyses of the bridges being studied. The first set of truck configurations were based on the load paths, truck configurations, and truck weights from the diagnostic load tests. This information has been reported in Chapter 3 and Appendix C.

The second set of truck configurations were based on the AASHTO specifications for one and two design lanes. The transverse positions of the vehicles were located such that the maximum effect was induced in either the interior or exterior bridge girder. The transverse positions of the trucks are shown schematically in Figures G.3 through G.8. The standard HS-20 vehicle, shown in Figure 7.1, with a fixed rear axle spacing of 14-ft was used for these analyses.

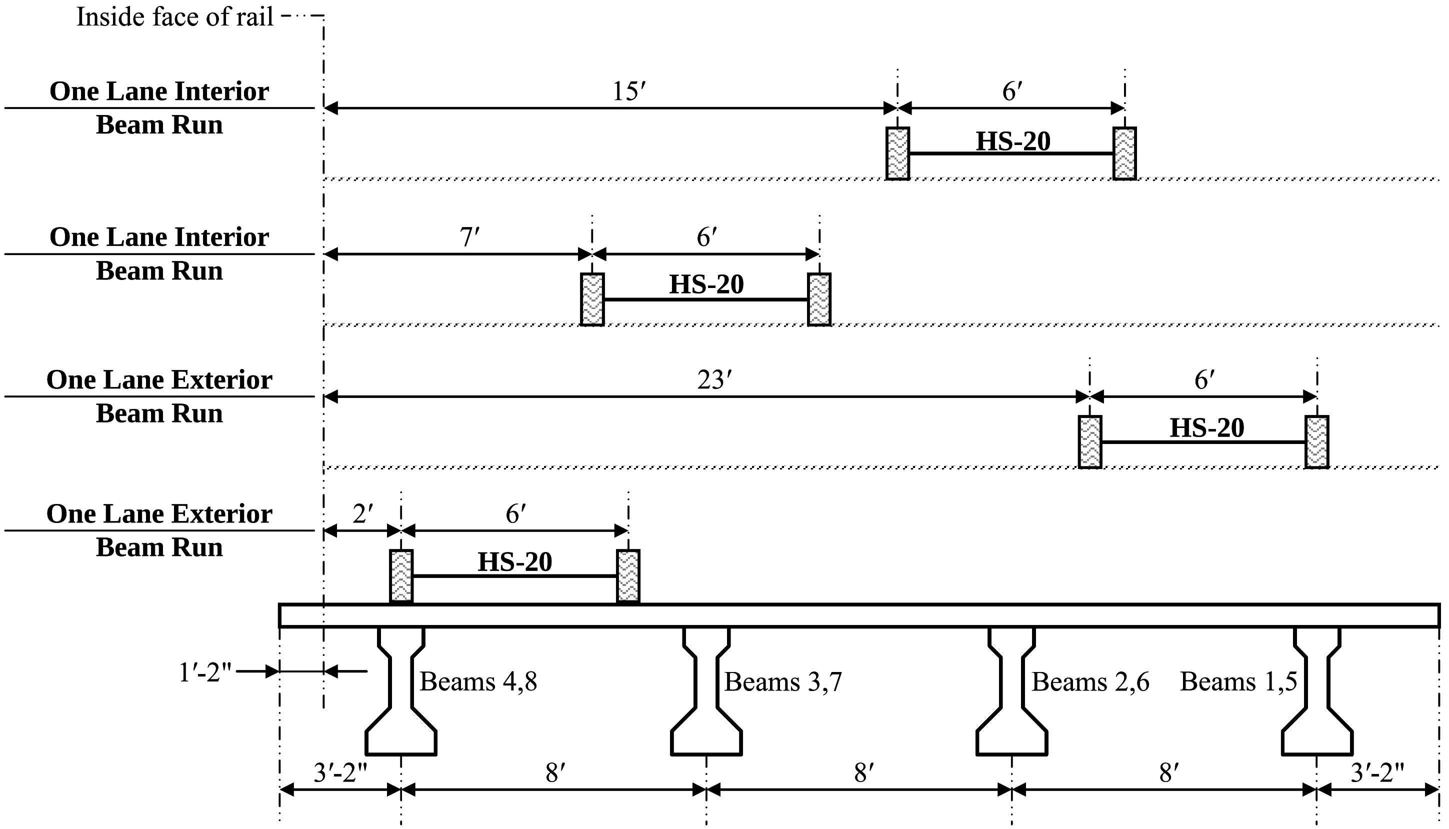

Figure G.3 Transverse Position of Trucks for One-Lane Loading Based on AASHTO Specifications Used in Finite Element Analysis of Chandler Creek Bridge

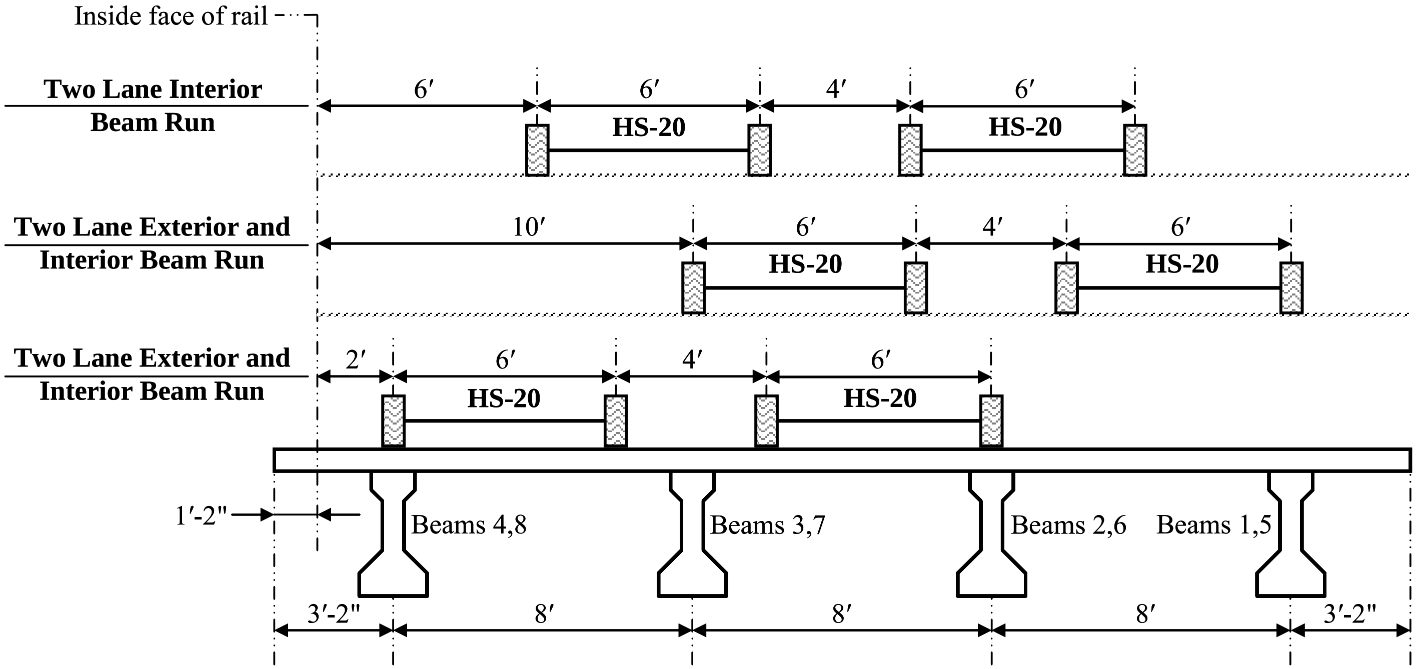

Figure G.4 Transverse Position of Trucks for Two-Lane Loading Based on AASHTO Specifications Used in Finite Element Analysis of Chandler Creek Bridge

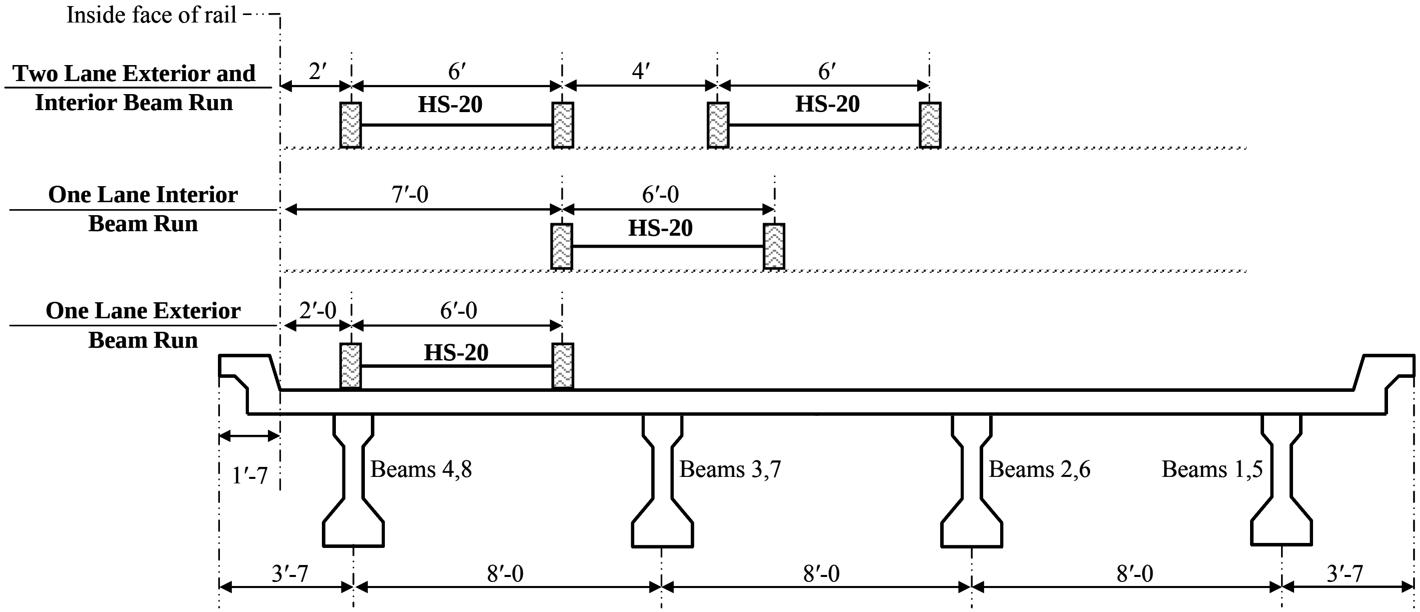

Figure G.5 Transverse Position of Trucks for One-Lane and Two-Lane Loadings Based on AASHTO Specifications Used in Finite Element Analysis of Lake LBJ Bridge

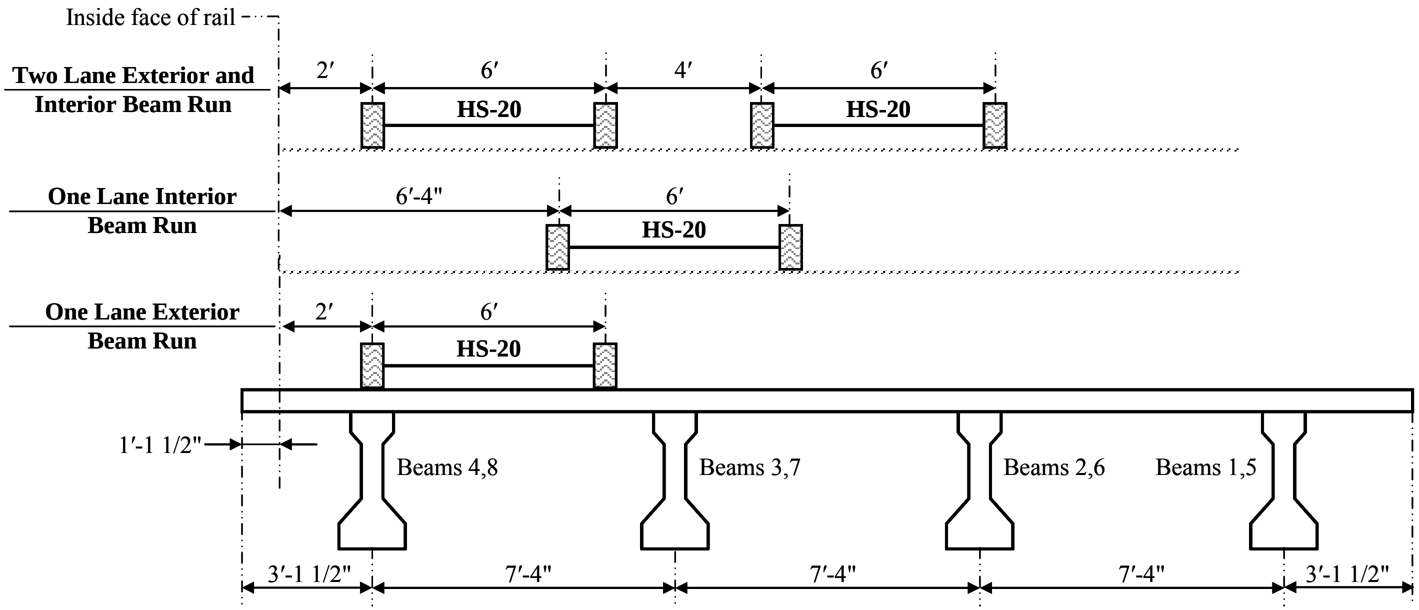

Figure G.6 Transverse Position of Trucks for One-Lane and Two-Lane Loadings Based on AASHTO Specifications Used in Finite Element Analysis of Lampasas River Bridge

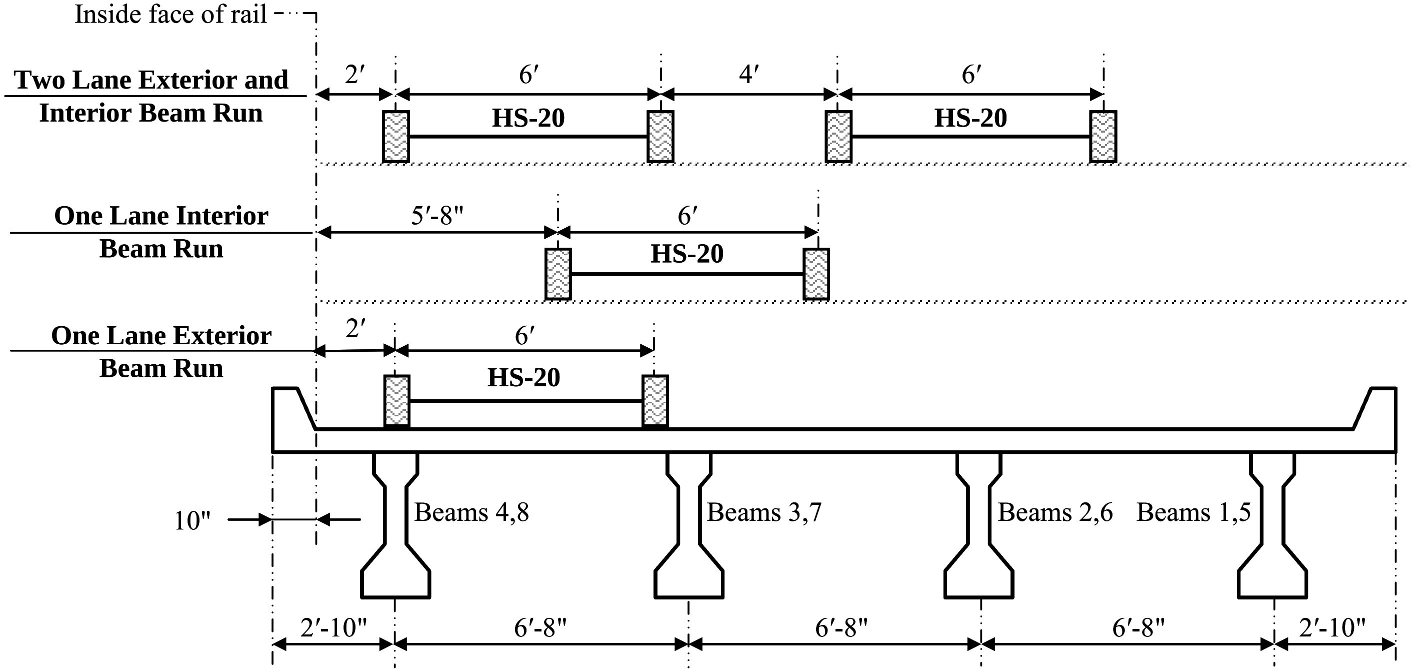

Figure G.7 Transverse Position of Trucks for One-Lane and Two-Lane Loadings Based on AASHTO Specifications Used in Finite Element Analysis of Willis Creek Bridge

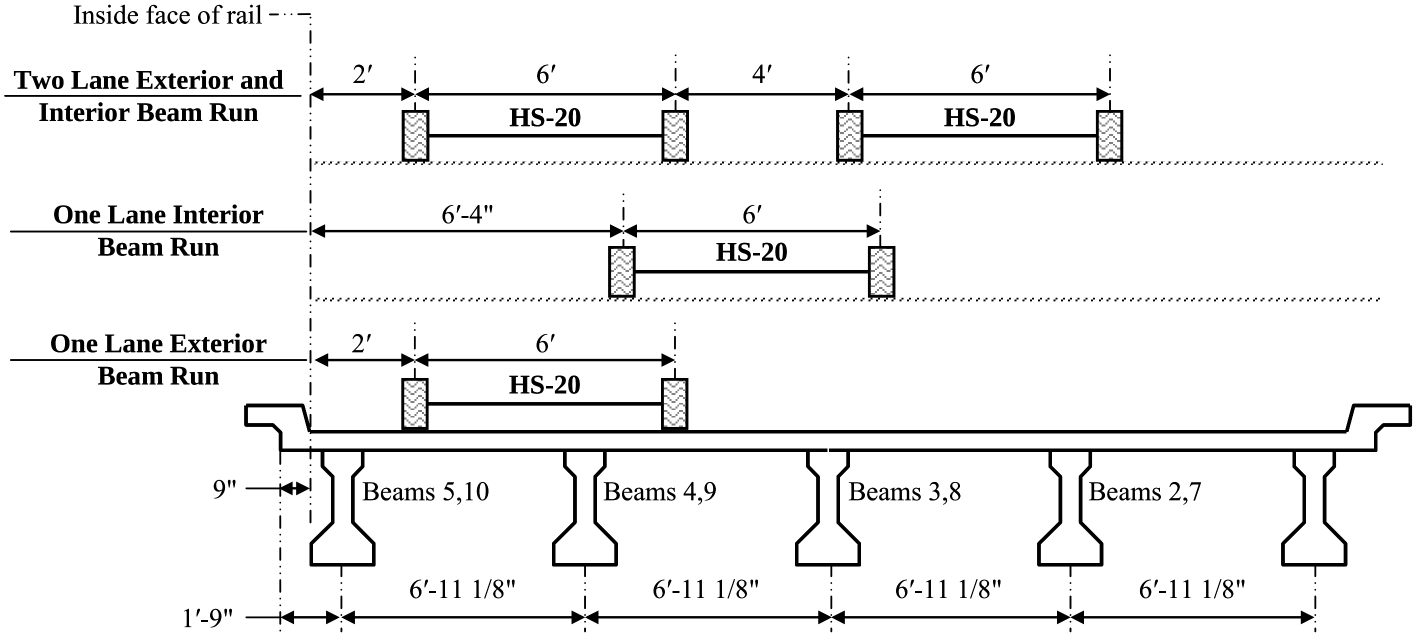

Figure G.8 Transverse Position of Trucks for One-Lane and Two-Lane Loadings Based on AASHTO Specifications Used in Finite Element Analysis of Wimberley Bridge

Appendix H

Results of Finite Element Analysis of Bridges Tested in this Investigation

Maximum, total midspan live load moments calculated from the results of the finite element analyses of the bridges tested in this investigation are summarized in this appendix. As discussed in Appendix G, each truck run was modeled as a series of load cases where each load case represented a particular transverse position of the truck or trucks, which moved longitudinally along a particular path or paths. For each load case, the total live load moment was determined by summing the moments from the midspan node for each beam. This was done regardless of the skew of the bridge, which is the same methodology used for determining total moments from the diagnostic load test data discussed in Chapter 4. The maximum moment for each truck run are reported in this appendix.

H.1 MAXIMUM, TOTAL MIDSPAN LIVE LOAD MOMENTS FROM FINITE ELEMENT ANALYSIS

Table H.1 Total Midspan Moments from Finite Element Analysis on Chandler Creek Bridge, 40-ft Span

Run Type	Corresponding Field Runs	Truck Path(s)	Moment, in-kip
Side -by-Side	1, 2	1,4	5976
Side -by-Side	3, 4	1,5	5776
Side -by-Side	5, 6	2,5	5988
Back-to-Back	7, 8	1	4430
Back-to-Back	9, 10	3	4335
Back-to-Back	11, 12	5	4426
Single Truck*	13	1	3237
Single Truck*	14	3	3176
Single Truck*	15	5	3242

*Single truck runs were completed using truck 1 weights.

Table H.2 Total Midspan Moments from Finite Element Analysis on Chandler Creek Bridge, 60-ft Span

Run Type	Corresponding Field Runs	Truck Path(s)	Moment, in-kip
Side -by-Side	1, 2	1,4	10909
Side -by-Side	3, 4	1,5	10735
Side -by-Side	5, 6	2,5	10935
Back-to-Back	7, 8	1	8826
Back-to-Back	9, 10	3	8721
Back-to-Back	11, 12	5	8833
Single Truck*	13	1	5709
Single Truck*	14	3	5653
Single Truck*	15	5	5730

*Single truck runs were completed using truck 1 weights.

Table H.3 Total Midspan Moments from Finite Element Analysis on Lake LBJ Bridge

Run Type	Corresponding Field Runs	Truck Path(s)	Moment, in-kip
Side -by-Side	8, 9, 13, 14, 15	1,5	15872
Back-to-Back	1, 2	1	12616
Back-to-Back	3, 4, 7	2 or 4	12610
Back-to-Back	5, 6	3	12602
Single Truck*	10	1	8116
Single Truck*	11	3	8108
Single Truck*	12	5	8116

*Single truck runs were completed using truck 1 weights.

Table H.4 Total Midspan Moments from Finite Element Analysis on Lampasas River Bridge

Run Type	Corresponding Field Runs	Truck Path(s)	Moment, in-kip
Side -by-Side	8, 9, 13, 14	1,5	17672
Back-to-Back	1, 2, 3, 15, 16	1	14693
Back-to-Back	4, 5	2	14695
Back-to-Back	6, 7	3	14690
Single Truck*	10	1	8955
Single Truck*	11	3	8953
Single Truck*	12	5	8955

*Single truck runs were completed using truck 1 weights.

Table H.5 Total Midspan Moments from Finite Element Analysis on Willis Creek Bridge

Run Type	Corresponding Field Runs	Truck Path(s)	Moment, in-kip
Side -by-Side	1, 2, 20	1,5	16128
Back-to-Back	3, 4, 5, 6	1	12789
Back-to-Back	7, 8	2	12763
Back-to-Back	9, 10	3	12753
Back-to-Back	11, 12	4	12763
Back-to-Back	13, 14	5	12789
Single Truck*	15	1	8224
Single Truck*	16	2	8169
Single Truck*	17	3	8201
Single Truck*	18	4	8170
Single Truck*	19	5	8224

*Single truck runs were completed using truck 1 weights.

Table H.6 Total Midspan Moments from Finite Element Analysis on Wimberley Bridge

Run Type	Corresponding Field Runs	Truck Path(s)	Moment, in-kip
Side -by-Side	7, 8	2, 6	7829
Side-by-Side	16, 17	1, 7	7585
Back-to-Back	1, 2	1	5756
Back-to-Back	3, 4	4	5627
Back-to-Back	5, 6	7	5720
Single Truck*	9	1	4209
Single Truck*	10	2	4173
Single Truck*	11	3	4147
Single Truck*	12	4	4147
Single Truck*	13	5	4144
Single Truck*	14	6	4172
Single Truck*	15	7	4209

*Single truck runs were completed using truck 1 weights.

APPENDIX I

Load Rating Analyses

Additional information is provided in this appendix to compliment the load rating analyses discussed in Chapter 7. The load rating criteria prescribed in the MCEB is discussed in Section I.1. Analysis A, as described in Chapter 7, for the Chandler Creek 60-ft span is presented in Section I.2 as an example of the load rating calculations performed. Results for Analyses A through H for each bridge in this investigation are summarized in Sections I.3 through I.99, respectively.

I.1 DISCUSSION OF LOAD RATING ANALYSES

As discussed in Chapter 7, eight load rating analyses were performed. Additional information regarding the calculation of the load ratings are presented in this section. The load rating criteria not discussed in Chapter 7 are presented in Section I.1.1. Summaries of prestress losses, impact factors, live load moments, and live load distribution factors used in the analyses are presented in Sections I.1.2 through I.1.5.

I.1.1 MCEB Load Rating Criteria

In addition to the tensile stress criterion discussed in Chapter 7, the MCEB prescribes load rating criteria for concrete in compression, tension in the prestressing strand, flexural strength, and shear strength. The rating criteria, and equations for the corresponding rating factors, are summarized in Table I.1 through Table I.3.

Table I.1 Inventory Level Rating Factors Based on MCEB

Inventory Level Load Rating Factors and Notation		
Rating Criterion	Rating Notation	Rating Factor Equation[†]
Concrete Tension	CT$_6$	$RF_{CT} = \frac{6\sqrt{f'_c} - (F_d + F_p + F_s)}{F_l}$
Concrete Compression	CC$_1$	$RF_{CC_1} = \frac{0.6 f'_c - A_1(F_d + F_p + F_s)}{A_2 F_l}$
Concrete Compression	CC$_2$	$RF_{CC_2} = \frac{0.4 f'_c - 0.5(F_d + F_p + F_s)}{F_l}$
Prestressing Steel Tension	PST$_{INV}$	$RF_{PST_{INV}} = \frac{0.8 f_y - (F_d + F_p + F_s)}{F_l}$
Flexural/Shear Strength	FS$_{INV}$	$RF_{FS_{INV}} = \frac{\phi R_n - (1.3D + S)}{2.17L(I+1)}$

[†] Variables in the rating factor equations are described in Table I.4.

Table I.2 Additional Inventory Level Rating Factors Used in this Investigation

Additional Inventory Level Load Rating Factors and Notation		
Rating Criterion	Rating Notation	Rating Factor Equation[†]
Concrete Tension	CT$_{7.5}$	$RF_{CT} = \frac{7.5\sqrt{f'_c} - (F_d + F_p + F_s)}{F_l}$
Concrete Tension	CT$_{12}$	$RF_{CT} = \frac{12\sqrt{f'_c} - (F_d + F_p + F_s)}{F_l}$

[†] Variables in the rating factor equations are described in Table I.4.

Table I.3 Operating Level Rating Factors Based on MCEB

Operating Level Load Rating Factors and Notation		
Rating Criterion	Rating Notation	Rating Factor Equation[†]
Flexural/Shear Strength	FS_{OP}	$RF_{FS_{OP}} = \dfrac{\phi R_n - (1.3D + S)}{1.3L(I+1)}$
Prestressing Steel Tension	PST_{OP}	$RF_{PS_{OP}} = \dfrac{0.9 f_y - (F_d + F_p + F_s)}{F_l}$

[†] Variables in the rating factor equations are described in Table I.4.

Table I.4 Variable Definitions for MCEB Rating Factors

Variable Symbol	Definition
D	Unfactored dead load moment or shear
f'_c	Concrete compressive strength[†]
F_d	Unfactored dead load stress
F_l	Unfactored live load stress including impact
F_p	Unfactored stress due to prestress force after all losses
F_s	Unfactored stress due to secondary prestress forces*
f_y	Prestressing steel yield stress
I	Dynamic impact factor
L	Unfactored live load moment or shear
S	Unfactored prestress secondary moment or shear*
ϕR_n	Nominal moment or shear capacity of the composite section

*The variables involving secondary prestressing effects are not used in this study because the bridges in this investigation are simply supported.
†Compressive strength may correspond to specified, measured from quality control tests, or estimated in situ strength.

I.1.2 Calculation of Prestress Losses Used in Load Rating Analyses

The provisions in the AASHTO LRFD specification were used for calculating prestress losses for all load rating analyses. For time-dependent losses, the refined methods were used. An example of these calculations can be found in Appendix J, which is an analysis of the Chandler Creek bridge.

The decision to use the AASHTO LRFD specification to model prestress losses was made for two reasons. First, as reported by Onyemelukwe (1999), the AASHTO LRDF provisions provide more conservative estimates than methods based on ACI-209 (2001) and PCI (1992). Second, it is probable that those interested in using the recommendations provided in this dissertation will use the prestress loss provisions provided by the AASHTO LRFD.

I.1.3 Calculation of Impact Factors Used in Load Rating Analyses

Impact factors based on the AASHTO Standard specification were used for Analysis A:

$$I = \frac{50}{L + 125} \tag{I.1}$$

where *I* is the impact factor and L is the effective span length in feet.

The balance of the analyses used impact factors based on the AASHTO LRFD specification. The prescribed dynamic load allowances are 15% and 33% for the fatigue limit state and all other limit states, respectively. These dynamic load allowances correspond to impact factors of 1.15 and 1.33.

I.1.4 Summary of Unfactored Live Load Moments Used in Load Rating Analyses

A summary of the unfactored live load moments used in the load rating of bridges in this investigation is provided in Table I.5. The live load moments reported are for one HS-20 design vehicle and do not include the effects of impact.

Table I.5 Unfactored Live Load Moments Used in Load Rating Analyses

Bridge		Unfactored Live Load Moment Used for Load Rating† (ft-kip)
Chandler Creek	40-ft Span	425
	60-ft Span	781
Lake LBJ		870
Lampasas River		1053
Willis Creek		871
Wimberley		422

† Live load moment reported does not include the dynamic impact factor and is based on HS-20 vehicle with a rear axle spacing of 14 ft.

I.1.5 Summary of Live Load Distribution Factors Used in Load Rating Analyses

Live load distribution factors based on the AASHTO Standard, AASHTO LRFD and finite element analyses were used for load rating the bridges in this investigation. Summaries of the live load distribution factors used are provided in this section.

Table I.6 Live Load Distribution Factors Used for Load Rating Analyses A and B

Bridge Name	Interior Beams		Exterior Beams	
	One Lane	Two Lanes	One Lane	Two Lanes
Chandler Creek, 40 ft. Span	0.57	0.73	0.50	0.50
Chandler Creek, 60 ft. Span	0.57	0.73	0.50	0.50
Lake LBJ	0.57	0.73	0.50	0.50
Lampasas River	0.52	0.67	0.50	0.50
Willis Creek	0.48	0.61	0.50	0.50
Wimberley	0.49	0.63	0.39	0.39

Note: Live load distribution factors based on AASHTO Standard Specification.

Table I.7 Live Load Distribution Factors Used for Load Rating Analysis C

Bridge Name	Interior Beams		Exterior Beams	
	One Lane	Two Lanes	One Lane	Two Lanes
Chandler Creek, 40 ft. Span	0.58	0.76	0.75	0.76
Chandler Creek, 60 ft. Span	0.53	0.72	0.75	0.72
Lake LBJ	0.52	0.71	0.75	0.70
Lampasas River	0.48	0.66	0.71	0.65
Willis Creek	0.49	0.66	0.66	0.65
Wimberley	0.56	0.72	0.47	0.59

Note: Live load distribution factors based on AASHTO LRFD Specification.

Table I.8 Live Load Distribution Factors Used for Load Rating Analysis D and E

Bridge Name	Interior Beams		Exterior Beams	
	One Lane*	Two Lanes	One Lane*	Two Lanes
Chandler Creek, 40 ft. Span	0.47	0.65	0.64	0.57
Chandler Creek, 60 ft. Span	0.42	0.62	0.58	0.66
Lake LBJ	0.41	0.61	0.58	0.55
Lampasas River	0.38	0.58	0.52	0.61
Willis Creek	0.38	0.56	0.53	0.57
Wimberley	0.44	0.58	0.56	0.55

Note: Live load distribution factors based on finite element analyses with trucks positioned transversely to produce maximum effect.

* A multiple presence factor of 1.2 was used to determine live load distribution factors for one-lane case.

Table I.9 Live Load Distribution Factors Used for Load Rating Analysis F

Bridge Name	Interior Beams		Exterior Beams	
	One Lane*	Two Lanes	One Lane*	Two Lanes
Chandler Creek, 40 ft. Span	0.46	0.53	0.59	0.57
Chandler Creek, 60 ft. Span	0.42	0.53	0.55	0.54
Lake LBJ	0.41	0.50	0.54	0.51
Lampasas River	0.40	0.51	0.50	0.51
Willis Creek	0.41	0.50	0.53	0.50
Wimberley	0.47	0.49	0.59	0.52

Note: Live load distribution factors based on finite element analyses with trucks positioned transversely in the center of the traffic lanes.

* A multiple presence factor of 1.2 was used to determine live load distribution factors for one-lane case.

I.2 SAMPLE LOAD RATING ANALYSIS

The load rating analyses discussed in Chapter 7 were performed for each bridge using the Excel spreadsheet developed by Wagener (2002). The input parameters, calculated values, and results for Analysis A for the Chandler Creek 60-ft span are provided in this section. The shear strength load rating criterion has not been considered in the analyses reported in this dissertation.

Table I.10 Input Parameters for Load Rating Analysis A For Chandler Creek, 60-ft Span (Wagener 2002)

Parameter†	Units	Interior Girder Value	Exterior Girder Value	Parameter†	Units	Interior Girder Value	Exterior Girder Value
A_{ps}	in^2	3.24	3.24	f_{pu}	ksi	250	250
A_s	in^2	0.00	0.00	$f_{y-steel}$	ksi	60	60
A_{curb}	in^2	0.00	0.00	H	%	65	65
A_{girder}	in^2	495.50	495.50	h_f	in	7.25	7.25
A_{slab}	in^2	681.50	616.25	I_{girder}	in^4	82761	82761
b_{eff}	in	94.00	85.00	I_{comp}	in^4	278969	269272
b_w	in	14.00	14.00	L	kip-ft	781.2	781.2
d_{girder}	in	40.00	40.00	$L_{bearing}$	in	8.50	8.50
$d_{overhang}$	in	48.00	38.00	L_{span}	ft	58.58	58.58
$d_{p-bottom}$	in	4.00	4.00	L_{beam}	ft	60.00	60.00
d_{p-comp}	in	43.25	43.25	S_{girder}	ft	8.00	8.00
DF_1	-	0.570	0.630	$w_{diaphragm}$	kip/ft	0.090	0.090
DF_2	-	0.730	0.730	$w_{miscellaneous}$	kip/ft	0.040	0.040
DF_{max}	-	0.730	0.730	$w_{overlay}$	kip/ft	0.048	0.048
E_{ci}	ksi	3834	3834	g_{curb}	lb/ft^3	150	150
E_c	ksi	4287	4287	g_{girder}	lb/ft^3	150	150
E_p	ksi	28500	28500	g_{slab}	lb/ft^3	150	150
E_{slab}	ksi	3321	3321	y_{b_girder}	in	17.07	17.07
$e_{midspan-girder}$	in	13.07	13.07	y_{t_girder}	in	22.93	22.93
$f'_{ci-girder}$	ksi	4.0	4.0	y_{b_comp}	in	30.27	29.59
$f'_{c-girder}$	ksi	5.0	5.0	y_{t_comp}	in	16.98	17.66
f'_{c-slab}	ksi	3.0	3.0	Strand Type*	-	1	1
f_{pi}	ksi	175	175				

*Stress relieved strands are Type 1; Low relaxation strands are Type 2

†Definitions of parameters are provided in Table I.13.

Table I.11 Specified Input Parameters and Calculated Values for Load Rating Analysis A of Chandler Creek, 60-ft Span (Wagener 2002)

Parameter[†]	Units	Interior Girder Value	Exterior Girder Value	Parameter[†]	Units	Interior Girder Value	Exterior Girder Value
Specified Values				Stresses and Moments			
W	ton	20.00	20.00	$e_{midspan\text{-}comp}$	in	26.27	25.59
k	-	0.38	0.38	E_p/E_c	-	6.65	6.65
f	-	1.00	1.00	$F_{d\text{-}b\text{-}comp}$	ksi	0.0492	0.0498
f_{py}/f_{pu}	-	0.85	0.85	$F_{d\text{-}t\text{-}comp}$	ksi	-0.028	-0.030
A_1	-	1.30	1.30	$F_{d\text{-}p\text{-}comp}$	ksi	0.284	0.286
A_2 (Inventory)	-	2.17	2.17	$F_{d\text{-}b\text{-}noncomp}$	ksi	1.413	1.333
A_2 (Operating)	-	1.30	1.30	$F_{d\text{-}t\text{-}noncomp}$	ksi	-1.899	-1.791
I	-	1.27	1.27	$F_{d\text{-}p\text{-}noncomp}$	ksi	7.195	6.787
Moment Capacity				$F_{d\text{-}b}$	ksi	1.463	1.383
b_1	-	0.800	0.800	$F_{d\text{-}t}$	ksi	-1.926	-1.821
$0.85f'_cb_1$	ksi	3.40	3.40	$F_{d\text{-}p}$	ksi	7.478	7.073
$b_{eff\text{-}modified}$	in	72.81	65.84	$F_{L\ b}$	ksi	0.945	0.957
$b\text{-}b_w$	in	58.81	51.84	$F_{L\ t}$	ksi	-0.530	-0.571
$A_{ps}{*}f_{pu}$	kips	810	810	$F_{L\ p}$	ksi	5.451	5.501
$c_{rectangular}$	in	3.18	3.51	$F_{p\ b}$	ksi	-1.96	-1.95
$c_{T\text{-}section}$	in	-11.69	-8.55	$F_{p\ t}$	ksi	0.67	0.66
c	in	3.18	3.51	$6\sqrt{f'_c}$	ksi	0.424	0.424
a	in	2.54	2.81	$7.5\sqrt{f'_c}$	ksi	0.530	0.530
f_{ps}	ksi	243.01	242.30	$12\sqrt{f'_c}$	ksi	0.849	0.849
ϕM_n	kip-ft	2754	2738	$M_{DL\text{-}curb}$	kip-ft	0.00	0.00
Prestress Losses				$M_{DL\text{-}girder}$	kip-ft	221	221
$f_{p\text{-}transfer}$	ksi	162.5	162.5	$M_{DL\text{-}slab}$	kip-ft	311	279
f_{cgp}	ksi	1.73	1.73	$P_i{*}e_{midspan\text{-}girder}$	kip-in	6881	6881
Df_{pES}	ksi	12.86	12.86	$P_{eff}{*}e_{midspan\text{-}girder}$	kip-in	5428	5414
Df_{pSH}	ksi	7.25	7.25	D_{comp}	kip-ft	38	38
Df_{pCR}	ksi	16.63	17.06	$D_{noncomp}$	kip-ft	571	539
Df_{pSR}	ksi	10.08	10.00	L(1+I)	kip-ft	994	994
Df_{pTotal}	ksi	46.82	47.16	w_{curb}	kip/ft	0.000	0.000
f_{pe}	ksi	128.18	127.84	w_{girder}	kip/ft	0.516	0.516
f^*_y	ksi	212.5	212.5	w_{slab}	kip/ft	0.725	0.649

[†] Definitions of parameters are provided in Table I.13.

Table I.12 Results of Load Rating Analysis A for Chandler Creek 60-ft Span

Inventory Level Rating Factors			Inventory Level Rating		
RF†	Interior Girder	Exterior Girder	RT† (ton)	Interior Girder	Exterior Girder
RF_{CC1}	3.28	4.71	CC_1	65.6	94.2
RF_{CC2}	2.58	3.63	CC_2	51.7	72.7
RF_{CT6}	0.97	1.52	CT_6	19.5	30.3
$RF_{CT7.5}$	1.09	1.68	$CT_{7.5}$	21.7	33.6
RF_{CT12}	1.42	2.16	CT_{12}	28.4	43.3
RF_{PSTINV}	6.30	9.31	PST_{INV}	126.0	186.3
RF_{FSINV}	1.25	1.84	FS_{INV}	24.9	36.9
Operating Level Rating Factors			Operating Level Rating		
RF	Interior Girder	Exterior Girder	RT (ton)	Interior Girder	Exterior Girder
RF_{FSOP}	2.08	3.08	FS_{OP}	41.6	61.6
RF_{PSTOP}	10.20	14.95	PST_{OP}	204.0	299.1

†Definitions of rating factors and ratings are provided in Table I.13.

Table I.13 Parameter Definitions Used by Wagener (2002) for Load Rating Calculations

Notation	Units	Definition
a	in.	Depth of compression block at nominal flexural capacity
A_1	-	Dead load factor
A_2	-	Live load factor
A_{curb}	in.^{2}	Cross-sectional area of a given curb
A_{girder}	in.^{2}	Cross-sectional area of a given girder
A_{ps}	in.^{2}	Area of prestressing steel
A_s	in.^{2}	Area of plain reinforcing steel
A_{slab}	in.^{2}	Cross-sectional area of bridge deck slab associated with a given girder
b_{eff}	in.	Effective slab width, used in calculating A_{slab}
$b_{eff\text{-}modified}$	in.	Modified effective slab width, used in calculating c and ϕM_n
β_1	-	Rectangular stress block factor
b_w	in.	Top flange width of girder
c	in.	Depth of neutral axis at nominal flexural capacity; used to calcuate ϕM_n
CC_1	ton	Load rating for concrete compression
CC_2	ton	Load rating for concrete compression

Table I.13 Parameter Definitions Used by Wagener (2002) for Load Rating Calculations (con't)

$c_{rectangular}$	in.	Calculated neutral axis based on rectangular section behavior
CT_6	ton	Load rating for concrete tension assuming $6\sqrt{f'_c}$
$CT_{7.5}$	ton	Load rating for concrete tension assuming $7.5\sqrt{f'_c}$
CT_{12}	ton	Load rating for concrete tension assuming $12\sqrt{f'_c}$
$c_{T\text{-}section}$	in.	Calculated neutral axis depth based on T-section behavior
D_{comp}	kip-ft	Dead load moment on the composite section
$D_{noncomp}$	kip-ft	Dead load moment on the girders
DF_1	-	Live load distribution factor for one design lane
DF_2	-	Live load distribution factor for two or more design lanes
DF_{max}	-	Maximum live load distribution factor
$d_{overhang}$	in.	Overhang distance, from the centerline of the girder
Δf_{pES}	ksi	Prestress loss due to elastic shortening
Δf_{pSH}	ksi	Prestress loss due to concrete shrinkage
Δf_{pCR}	ksi	Prestress loss due to concrete creep
Δf_{pSR}	ksi	Prestress loss due to steel relaxation
ΔfpTotal	ksi	Total prestress losses
d_{girder}	in.	Depth of a given girder
$d_{p\text{-}bottom}$	in.	Distance from center of gravity of prestressed steel to bottom fiber of girder
$d_{p\text{-}comp}$	in.	Depth from extreme compression fiber to the centroid of prestressing steel (composite section)
E_{ci}	ksi	Modulus of elasticity of concrete at transfer
E_c	ksi	Modulus of elasticity of concrete
$e_{midspan\text{-}comp}$	in.	Midspan strand eccentricity of the composite section
$e_{midspan\text{-}girder}$	in.	Midspan strand eccentricity of the girder
E_{ps}	ksi	Modulus of elasticity of prestressing steel (28,500 ksi)
E_{slab}	ksi	Modulus of elasticity of the slab
ϕ	-	Strength reduction factor for flexure
f^*_y	ksi	Yield stress of prestressing steel
$f'_{ci\text{-}girder}$	ksi	Design compressive strength of the girder at transfer
$f'_{c\text{-}girder}$	ksi	Design compressive strength of the girder
$f'_{c\text{-}slab}$	ksi	Design compressive strength of the slab
f_{cgp}	ksi	Assumed stress at the centroid of prestressing steel due to prestress force and self weight of the girder; used in loss calculations
$F_{d\text{-}b}$	ksi	Total unfactored dead load tensile stress on the composite section, taken at the girder soffit

Table I.13 Parameter Definitions Used by Wagener (2002) for Load Rating Calculations (con’t)

$F_{d\text{-}b\text{-}comp}$	ksi	Unfactored dead load tensile stress on the composite section, taken at the girder soffit
$F_{d\text{-}t\text{-}comp}$	ksi	Unfactored dead load compressive stress on the composite section, taken at the top of the girder
$F_{d\text{-}p\text{-}comp}$	ksi	Unfactored tensile stress on the prestressing strands due to dead load (composite section)
$F_{d\text{-}b\text{-}noncomp}$	ksi	Unfactored dead load tensile stress on the girder, taken at the girder soffit
$F_{d\text{-}t\text{-}noncomp}$	ksi	Unfactored dead load tensile stress on the girder, taken at the top of the beam
$F_{d\text{-}p\text{-}noncomp}$	ksi	Unfactored dead load tensile stress on the prestressing strands due to dead load (noncomposite)
$F_{d\text{-}p}$	ksi	Total unfactored dead load tensile stress on the prestressing steel
$F_{d\text{-}t}$	ksi	Total unfactored dead load compressive stress, taken at the top of the girder
F_{L_b}	ksi	Unfactored live load tensile stress due to HS20 loading
F_{L_p}	ksi	Unfactored live load tensile stress in the prestressing steel due to HS20 loading
F_{L_t}	ksi	Unfactored live load compressive stress due to HS20 loading
ϕM_n	kip-ft	Factored flexural capacity of a given girder
F_{p_b}	ksi	Unfactored tensile stress due to prestressing, taken at the girder soffit
F_{p_t}	ksi	Unfactored compressive stress due to prestressing, taken at the top of the girder
f_{pe}	ksi	Effective prestressing stress
f_{pi}	ksi	Initial prestressing stress
$f_{p\text{-}transfer}$	ksi	Assumed stress in the prestressing steel at transfer; used to calculate f_{cgp}
f_{ps}	ksi	Average prestressing stress at nominal capacity
f_{pu}	ksi	Ultimate specified tensile strength of prestressing strands
f_{py}/f_{pu}	-	Ratio of yield stress to ultimate stress
FS_{INV}	ton	Load rating for flexural strength, inventory level
FS_{OP}	ton	Load rating for flexural strength, operating level
$f_{y\text{-}steel}$	ksi	Yield stress of plain reinforcing steel
γ_{curb}	lb/ft^3	Unit weight of concrete in the curb
γ_{girder}	lb/ft^3	Unit weight of concrete in the girder
γ_{slab}	lb/ft^3	Unit weight of concrete in the slab
h_f	in	Height of the compression flange
H	%	Average annual relative humidity at bridge location

Table I.13 Parameter Definitions Used by Wagener (2002) for Load Rating Calculations (con't)

I_{comp}	in^4	Moment of inertia of the composite section
I	-	Dynamic load impact factor
I_{girder}	in^4	Moment of inertia of a given girder
k	-	Factor used to compute f_{ps}
L	kip-ft	Unfactored live load moment due to HS20
L (1+I)	kip-ft	HS20 live load moment with the impact factor
L_{beam}	ft	Length of prestressed beams, from end of beam to end of beam
$L_{bearing}$	in	Distance from end of beam to centerline of bearing pad
L_{span}	ft	Overall span length
$M_{DL\text{-}curb}$	kip-ft	Unfactored dead load moment on the girder due to curb weight
$M_{DL\text{-}girder}$	kip-ft	Unfactored dead load moment on the girder due to its self weight
$M_{DL\text{-}slab}$	kip-ft	Unfactored dead load moment on girder due to wet concrete
PST_{INV}	-	Inventory rating factor for prestressing steel tension
PST_{OP}	-	Operating rating factor for prestressing steel tension
PST	ton	Load rating for prestressing steel tension
RF_{CC1}	-	Load rating factor for concrete compression
RF_{CC2}	-	Load rating factor for concrete compression
RF_{CT6}	-	Load rating factor for concrete tension ($6\sqrt{f'_c}$)
$RF_{CT7.5}$	-	Load rating factor for concrete tension ($7.5\sqrt{f'_c}$)
RF_{CT12}	-	Load rating factor for concrete tension ($12\sqrt{f'_c}$)
RF_{PSTINV}	-	Load rating factor for prestressing steel at inventory level
RF_{FSINV}	-	Load rating factor for flexural strength at inventory level
RF_{PSTOP}	-	Load rating factor for prestressing steel at operating level
RF_{FSOP}	-	Load rating factor for flexural strength at operating level
RT	ton	AASHTO load rating
S_{girder}	ft	Girder spacing, from centerline to centerline of girders
W	ton	Weight of the first two axles of load rating vehicle (HS20)
w_{curb}	kip/ft	Distributed load due to curb dead weight
$w_{diaphragm}$	kip/ft	Distributed load due to weight of diaphragms
w_{girder}	kip/ft	Distributed load due to girder dead weight
$w_{miscellaneous}$	kip/ft	Miscellaneous distributed load
$w_{overlay}$	kip/ft	Distributed load due to overlay
w_{slab}	kip/ft	Distributed load due to slab dead weight
y_{b_comp}	in.	Distance from the neutral axis to girder soffit of the composite section

Table I.13 Parameter Definitions Used by Wagener (2002) for Load Rating Calculations (con't)		
y_{b_girder}	in.	Distance from the neutral axis to girder soffit (non-composite)
y_{t_comp}	in.	Distance from the neutral axis to top of the deck of the composite section
y_{t_girder}	in.	Distance from the neutral axis to top of the girder (non-composite)

I.3 RESULTS FROM LOAD RATING ANALYSES A AND B

Table I.14 Results of Load Rating Analyses A and B for Chandler Creek 40-ft Span

Inventory Level Rating Factors			Inventory Level Rating		
RF†	Interior Girder	Exterior Girder	RT† (ton)	Interior Girder	Exterior Girder
RF_{CC1}	6.06	8.48	CC_1	121.1	169.6
RF_{CC2}	4.30	5.97	CC_2	86.1	119.5
RF_{CT6}	1.23	1.88	CT_6	24.7	37.5
$RF_{CT7.5}$	1.36	2.06	$CT_{7.5}$	27.2	41.2
RF_{CT12}	1.74	2.61	CT_{12}	34.8	52.2
RF_{PSTINV}	6.83	10.05	PST_{INV}	136.6	201.1
RF_{FSINV}	1.17	1.72	FS_{INV}	23.3	34.5
Operating Level Rating Factors			Operating Level Rating		
RF	Interior Girder	Exterior Girder	RT (ton)	Interior Girder	Exterior Girder
RF_{FSOP}	1.95	2.88	FS_{OP}	38.9	57.6
RF_{PSTOP}	11.12	16.26	PST_{OP}	222.4	325.2

†Definitions of rating factors and ratings are provided in Table I.13.

Table I.15 Results of Load Rating Analysis A and B for Chandler Creek 60-ft Span

Inventory Level Rating Factors			Inventory Level Rating		
RF[†]	Interior Girder	Exterior Girder	RT[†] (ton)	Interior Girder	Exterior Girder
RF_{CC1}	3.28	4.71	CC_1	65.6	94.2
RF_{CC2}	2.58	3.63	CC_2	51.7	72.7
RF_{CT6}	0.97	1.52	CT_6	19.5	30.3
$RF_{CT7.5}$	1.09	1.68	$CT_{7.5}$	21.7	33.6
RF_{CT12}	1.42	2.16	CT_{12}	28.4	43.3
RF_{PSTINV}	6.30	9.31	PST_{INV}	126.0	186.3
RF_{FSINV}	1.25	1.84	FS_{INV}	24.9	36.9
Operating Level Rating Factors			Operating Level Rating		
RF	Interior Girder	Exterior Girder	RT (ton)	Interior Girder	Exterior Girder
RF_{FSOP}	2.08	3.08	FS_{OP}	41.6	61.6
RF_{PSTOP}	10.20	14.95	PST_{OP}	204.0	299.1

[†] Definitions of rating factors and ratings are provided in Table I.13.

Table I.16 Results of Load Rating Analysis A and B for Lake LBJ

Inventory Level Rating Factors			Inventory Level Rating		
RF[†]	Interior Girder	Exterior Girder	RT[†] (ton)	Interior Girder	Exterior Girder
RF_{CC1}	2.46	4.35	CC_1	49.22	87.0
RF_{CC2}	2.10	3.80	CC_2	41.93	76.0
RF_{CT6}	0.90	1.35	CT_6	17.91	27.0
$RF_{CT7.5}$	1.00	1.52	$CT_{7.5}$	19.96	30.4
RF_{CT12}	1.31	2.02	CT_{12}	26.11	40.4
RF_{PSTINV}	6.29	10.23	PST_{INV}	125.72	204.6
RF_{FSINV}	1.31	1.85	FS_{INV}	26.15	37.0
Operating Level Rating Factors			Operating Level Rating		
RF	Interior Girder	Exterior Girder	RT (ton)	Interior Girder	Exterior Girder
RF_{FSOP}	2.18	3.09	FS_{OP}	43.6	61.7
RF_{PSTOP}	9.94	16.12	PST_{OP}	198.7	322.5

[†] Definitions of rating factors and ratings are provided in Table I.13.

Table I.17 Results of Load Rating Analysis A and B for Lampasas River Bridge

Inventory Level Rating Factors			Inventory Level Rating		
RF†	Interior Girder	Exterior Girder	RT† (ton)	Interior Girder	Exterior Girder
RF_{CC1}	1.33	1.87	CC_1	26.7	37.5
RF_{CC2}	1.35	1.81	CC_2	27.0	36.2
RF_{CT6}	0.50	0.75	CT_6	10.1	14.9
$RF_{CT7.5}$	0.59	0.87	$CT_{7.5}$	11.9	17.3
RF_{CT12}	0.86	1.22	CT_{12}	17.3	24.5
RF_{PSTINV}	4.91	6.68	PST_{INV}	98.2	133.6
RF_{FSINV}	1.04	1.41	FS_{INV}	20.8	28.2
Operating Level Rating Factors			Operating Level Rating		
RF	Interior Girder	Exterior Girder	RT (ton)	Interior Girder	Exterior Girder
RF_{FSOP}	1.74	2.35	FS_{OP}	34.7	47.1
RF_{PSTOP}	8.16	11.00	PST_{OP}	163.1	220.0

†Definitions of rating factors and ratings are provided in Table I.13.

Table I.18 Results of Load Rating Analysis A and B for Willis Creek Bridge

Inventory Level Rating Factors			Inventory Level Rating		
RF†	Interior Girder	Exterior Girder	RT† (ton)	Interior Girder	Exterior Girder
RF_{CC1}	1.88	2.64	CC_1	37.6	52.8
RF_{CC2}	1.73	2.53	CC_2	34.6	50.5
RF_{CT6}	0.72	0.85	CT_6	14.5	17.1
$RF_{CT7.5}$	0.83	1.00	$CT_{7.5}$	16.7	20.0
RF_{CT12}	1.17	1.45	CT_{12}	23.3	28.9
RF_{PSTINV}	7.66	9.92	PST_{INV}	153.2	198.3
RF_{FSINV}	1.16	1.36	FS_{INV}	23.3	27.2
Operating Level Rating Factors			Operating Level Rating		
RF	Interior Girder	Exterior Girder	RT (ton)	Interior Girder	Exterior Girder
RF_{FSOP}	1.94	2.27	FS_{OP}	38.9	45.5
RF_{PSTOP}	12.63	16.37	PST_{OP}	252.6	327.4

†Definitions of rating factors and ratings are provided in Table I.13.

Table I.19 Results of Load Rating Analysis A and B for Wimberley Bridge

Inventory Level Rating Factors			Inventory Level Rating		
RF[†]	Interior Girder	Exterior Girder	RT[†] (ton)	Interior Girder	Exterior Girder
$\mathrm{RF}_{\mathrm{CC1}}$	5.59	11.47	CC_{1}	111.7	229.3
$\mathrm{RF}_{\mathrm{CC2}}$	4.02	8.21	CC_{2}	80.4	164.3
$\mathrm{RF}_{\mathrm{CT6}}$	2.04	3.77	CT_{6}	40.7	75.5
$\mathrm{RF}_{\mathrm{CT7.5}}$	2.18	4.03	$\mathrm{CT}_{7.5}$	43.6	80.6
$\mathrm{RF}_{\mathrm{CT12}}$	2.60	4.80	CT_{12}	52.0	96.1
$\mathrm{RF}_{\mathrm{PSTINV}}$	11.11	20.30	$\mathrm{PST}_{\mathrm{INV}}$	222.1	406.1
$\mathrm{RF}_{\mathrm{FSINV}}$	2.00	3.13	$\mathrm{FS}_{\mathrm{INV}}$	40.1	62.6
Operating Level Rating Factors			Operating Level Rating		
RF	Interior Girder	Exterior Girder	RT (ton)	Interior Girder	Exterior Girder
$\mathrm{RF}_{\mathrm{FSOP}}$	3.35	5.23	$\mathrm{FS}_{\mathrm{OP}}$	66.9	104.5
$\mathrm{RF}_{\mathrm{PSTOP}}$	16.85	30.67	$\mathrm{PST}_{\mathrm{OP}}$	336.9	613.4

[†] Definitions of rating factors and ratings are provided in Table I.13.

I.4 LOAD RATING ANALYSIS C

Table I.20 Results of Load Rating Analysis C for Chandler Creek 40-ft Span

Inventory Level Rating Factors			Inventory Level Rating		
RF[†]	Interior Girder	Exterior Girder	RT[†] (ton)	Interior Girder	Exterior Girder
$\mathrm{RF}_{\mathrm{CC1}}$	5.68	5.45	CC_{1}	113.7	109.0
$\mathrm{RF}_{\mathrm{CC2}}$	4.04	3.84	CC_{2}	80.8	76.8
$\mathrm{RF}_{\mathrm{CT6}}$	1.44	1.50	CT_{6}	28.9	30.1
$\mathrm{RF}_{\mathrm{CT7.5}}$	1.59	1.65	$\mathrm{CT}_{7.5}$	31.8	33.0
$\mathrm{RF}_{\mathrm{CT12}}$	2.04	2.09	CT_{12}	40.8	41.9
$\mathrm{RF}_{\mathrm{PSTINV}}$	6.11	6.16	$\mathrm{PST}_{\mathrm{INV}}$	122.2	123.2
$\mathrm{RF}_{\mathrm{FSINV}}$	1.09	1.11	$\mathrm{FS}_{\mathrm{INV}}$	21.9	22.2
Operating Level Rating Factors			Operating Level Rating		
RF	Interior Girder	Exterior Girder	RT (ton)	Interior Girder	Exterior Girder
$\mathrm{RF}_{\mathrm{FSOP}}$	1.83	1.85	$\mathrm{FS}_{\mathrm{OP}}$	36.5	37.0
$\mathrm{RF}_{\mathrm{PSTOP}}$	9.93	9.95	$\mathrm{PST}_{\mathrm{OP}}$	198.7	199.1

[†] Definitions of rating factors and ratings are provided in Table I.13.

Table I.21 Results of Load Rating Analysis C for Chandler Creek 60-ft Span

Inventory Level Rating Factors			Inventory Level Rating		
RF†	Interior Girder	Exterior Girder	RT† (ton)	Interior Girder	Exterior Girder
$\mathrm{RF}_{\mathrm{CC1}}$	3.18	3.00	CC_1	63.6	60.0
$\mathrm{RF}_{\mathrm{CC2}}$	2.50	2.32	CC_2	50.1	46.3
$\mathrm{RF}_{\mathrm{CT6}}$	1.17	1.20	CT_6	23.4	24.0
$\mathrm{RF}_{\mathrm{CT7.5}}$	1.31	1.33	$\mathrm{CT}_{7.5}$	26.2	26.6
$\mathrm{RF}_{\mathrm{CT12}}$	1.72	1.72	CT_{12}	34.3	34.4
$\mathrm{RF}_{\mathrm{PSTINV}}$	5.81	5.65	$\mathrm{PST}_{\mathrm{INV}}$	116.2	113.0
$\mathrm{RF}_{\mathrm{FSINV}}$	1.21	1.18	$\mathrm{FS}_{\mathrm{INV}}$	24.2	23.5
Operating Level Rating Factors			Operating Level Rating		
RF	Interior Girder	Exterior Girder	RT (ton)	Interior Girder	Exterior Girder
$\mathrm{RF}_{\mathrm{FSOP}}$	2.02	1.96	$\mathrm{FS}_{\mathrm{OP}}$	40.4	39.3
$\mathrm{RF}_{\mathrm{PSTOP}}$	9.40	9.07	$\mathrm{PST}_{\mathrm{OP}}$	188.1	181.4

[†] Definitions of rating factors and ratings are provided in Table I.13.

Table I.22 Results of Load Rating Analysis C for Lake LBJ

Inventory Level Rating Factors			Inventory Level Rating		
RF†	Interior Girder	Exterior Girder	RT† (ton)	Interior Girder	Exterior Girder
$\mathrm{RF}_{\mathrm{CC1}}$	2.40	2.75	CC_1	48.1	55.1
$\mathrm{RF}_{\mathrm{CC2}}$	2.05	2.41	CC_2	41.0	48.1
$\mathrm{RF}_{\mathrm{CT6}}$	1.09	1.06	CT_6	21.7	21.2
$\mathrm{RF}_{\mathrm{CT7.5}}$	1.21	1.19	$\mathrm{CT}_{7.5}$	24.2	23.9
$\mathrm{RF}_{\mathrm{CT12}}$	1.59	1.59	CT_{12}	31.7	31.8
$\mathrm{RF}_{\mathrm{PSTINV}}$	5.85	6.17	$\mathrm{PST}_{\mathrm{INV}}$	116.9	123.4
$\mathrm{RF}_{\mathrm{FSINV}}$	1.28	1.17	$\mathrm{FS}_{\mathrm{INV}}$	25.6	23.4
Operating Level Rating Factors			Operating Level Rating		
RF	Interior Girder	Exterior Girder	RT (ton)	Interior Girder	Exterior Girder
$\mathrm{RF}_{\mathrm{FSOP}}$	2.13	1.96	$\mathrm{FS}_{\mathrm{OP}}$	42.7	39.1
$\mathrm{RF}_{\mathrm{PSTOP}}$	9.24	9.72	$\mathrm{PST}_{\mathrm{OP}}$	184.8	194.4

[†] Definitions of rating factors and ratings are provided in Table I.13.

Table I.23 Results of Load Rating Analysis C for Lampasas River Bridge

Inventory Level Rating Factors			Inventory Level Rating		
RF[†]	Interior Girder	Exterior Girder	RT[†] (ton)	Interior Girder	Exterior Girder
RF_{CC1}	1.27	1.24	CC_1	25.4	24.8
RF_{CC2}	1.29	1.20	CC_2	25.7	24.0
RF_{CT6}	0.59	0.61	CT_6	11.9	12.2
$RF_{CT7.5}$	0.70	0.71	$CT_{7.5}$	14.0	14.2
RF_{CT12}	1.02	1.01	CT_{12}	20.5	20.1
RF_{PSTINV}	4.45	4.20	PST_{INV}	88.9	83.9
RF_{FSINV}	0.99	0.93	FS_{INV}	19.9	18.7
Operating Level Rating Factors			Operating Level Rating		
RF	Interior Girder	Exterior Girder	RT (ton)	Interior Girder	Exterior Girder
RF_{FSOP}	1.66	1.56	FS_{OP}	33.2	31.2
RF_{PSTOP}	7.39	6.92	PST_{OP}	147.8	138.4

[†] Definitions of rating factors and ratings are provided in Table I.13.

Table I.24 Results of Load Rating Analysis C for Willis Creek Bridge

Inventory Level Rating Factors			Inventory Level Rating		
RF[†]	Interior Girder	Exterior Girder	RT[†] (ton)	Interior Girder	Exterior Girder
RF_{CC1}	1.65	1.90	CC_1	33.1	38.0
RF_{CC2}	1.52	1.82	CC_2	30.4	36.4
RF_{CT6}	0.79	0.76	CT_6	15.8	15.3
$RF_{CT7.5}$	0.91	0.90	$CT_{7.5}$	18.2	18.0
RF_{CT12}	1.28	1.30	CT_{12}	25.6	25.9
RF_{PSTINV}	6.41	6.80	PST_{INV}	128.3	136.0
RF_{FSINV}	1.02	0.99	FS_{INV}	20.5	19.8
Operating Level Rating Factors			Operating Level Rating		
RF	Interior Girder	Exterior Girder	RT (ton)	Interior Girder	Exterior Girder
RF_{FSOP}	1.71	1.65	FS_{OP}	34.2	33.0
RF_{PSTOP}	10.56	11.22	PST_{OP}	211.3	224.5

[†] Definitions of rating factors and ratings are provided in Table I.13.

Table I.25 Results of Load Rating Analysis C for Wimberley Bridge

Inventory Level Rating Factors			Inventory Level Rating		
RF[†]	Interior Girder	Exterior Girder	RT[†] (ton)	Interior Girder	Exterior Girder
RF$_{CC1}$	4.78	7.41	CC$_{1}$	95.5	148.1
RF$_{CC2}$	3.44	5.31	CC$_{2}$	68.7	106.1
RF$_{CT6}$	2.17	3.03	CT$_{6}$	43.4	60.7
RF$_{CT7.5}$	2.32	3.24	CT$_{7.5}$	46.4	64.9
RF$_{CT12}$	2.77	3.87	CT$_{12}$	55.4	77.4
RF$_{PSTINV}$	9.08	12.55	PST$_{INV}$	181.6	250.9
RF$_{FSINV}$	1.71	2.02	FS$_{INV}$	34.3	40.5
Operating Level Rating Factors			Operating Level Rating		
RF	Interior Girder	Exterior Girder	RT (ton)	Interior Girder	Exterior Girder
RF$_{FSOP}$	2.86	3.38	FS$_{OP}$	57.2	67.5
RF$_{PSTOP}$	13.75	18.91	PST$_{OP}$	275.0	378.2

[†] Definitions of rating factors and ratings are provided in Table I.13.

I.5 LOAD RATING ANALYSIS D

Table I.26 Results of Load Rating Analysis D for Chandler Creek 40-ft Span

Inventory Level Rating Factors			Inventory Level Rating		
RF[†]	Interior Girder	Exterior Girder	RT[†] (ton)	Interior Girder	Exterior Girder
RF$_{CC1}$	6.64	6.47	CC$_{1}$	132.9	129.4
RF$_{CC2}$	4.72	4.56	CC$_{2}$	94.5	91.2
RF$_{CT6}$	1.69	1.78	CT$_{6}$	33.7	35.7
RF$_{CT7.5}$	1.86	1.96	CT$_{7.5}$	37.2	39.2
RF$_{CT12}$	2.38	2.48	CT$_{12}$	47.7	49.7
RF$_{PSTINV}$	7.14	7.32	PST$_{INV}$	142.9	146.3
RF$_{FSINV}$	1.28	1.32	FS$_{INV}$	25.6	26.3
Operating Level Rating Factors			Operating Level Rating		
RF	Interior Girder	Exterior Girder	RT (ton)	Interior Girder	Exterior Girder
RF$_{FSOP}$	2.14	2.14	FS$_{OP}$	42.7	44.0
RF$_{PSTOP}$	11.62	15.64	PST$_{OP}$	232.3	236.4

[†] Definitions of rating factors and ratings are provided in Table I.13.

Table I.27 Results of Load Rating Analysis D for Chandler Creek 60-ft Span

Inventory Level Rating Factors			Inventory Level Rating		
RF†	Interior Girder	Exterior Girder	RT† (ton)	Interior Girder	Exterior Girder
RF_{CC1}	3.69	3.41	CC_1	73.8	68.2
RF_{CC2}	2.91	2.63	CC_2	58.2	52.6
RF_{CT6}	1.36	1.37	CT_6	27.2	27.3
$RF_{CT7.5}$	1.52	1.51	$CT_{7.5}$	30.4	30.2
RF_{CT12}	1.99	1.95	CT_{12}	39.9	39.0
RF_{PSTINV}	6.75	6.42	PST_{INV}	134.9	128.4
RF_{FSINV}	1.40	1.34	FS_{INV}	28.1	26.7
Operating Level Rating Factors			Operating Level Rating		
RF	Interior Girder	Exterior Girder	RT (ton)	Interior Girder	Exterior Girder
RF_{FSOP}	2.34	2.23	FS_{OP}	46.9	44.6
RF_{PSTOP}	10.92	10.31	PST_{OP}	218.4	206.1

†Definitions of rating factors and ratings are provided in Table I.13.

Table I.28 Results of Load Rating Analysis D for Lake LBJ

Inventory Level Rating Factors			Inventory Level Rating		
RF†	Interior Girder	Exterior Girder	RT† (ton)	Interior Girder	Exterior Girder
RF_{CC1}	2.80	3.56	CC_1	55.9	71.2
RF_{CC2}	2.38	3.11	CC_2	47.7	62.2
RF_{CT6}	1.26	1.37	CT_6	25.3	27.4
$RF_{CT7.5}$	1.41	1.54	$CT_{7.5}$	28.2	30.9
RF_{CT12}	1.85	2.06	CT_{12}	36.9	41.1
RF_{PSTINV}	6.81	7.98	PST_{INV}	136.1	159.5
RF_{FSINV}	1.49	1.52	FS_{INV}	29.8	30.3
Operating Level Rating Factors			Operating Level Rating		
RF	Interior Girder	Exterior Girder	RT (ton)	Interior Girder	Exterior Girder
RF_{FSOP}	2.48	2.53	FS_{OP}	49.7	50.6
RF_{PSTOP}	10.76	12.57	PST_{OP}	215.1	251.4

†Definitions of rating factors and ratings are provided in Table I.13.

Table I.29 Results of Load Rating Analysis D for Lampasas River Bridge

Inventory Level Rating Factors			Inventory Level Rating		
RF[†]	Interior Girder	Exterior Girder	RT[†] (ton)	Interior Girder	Exterior Girder
RF_{CC1}	1.45	1.44	CC_1	28.9	28.9
RF_{CC2}	1.46	1.40	CC_2	29.3	27.9
RF_{CT6}	0.68	0.71	CT_6	13.5	14.2
$RF_{CT7.5}$	0.80	0.83	$CT_{7.5}$	16.0	16.5
RF_{CT12}	1.17	1.17	CT_{12}	23.3	23.4
RF_{PSTINV}	5.06	4.88	PST_{INV}	101.2	97.7
RF_{FSINV}	1.13	1.09	FS_{INV}	22.6	21.8
Operating Level Rating Factors			**Operating Level Rating**		
RF	Interior Girder	Exterior Girder	RT (ton)	Interior Girder	Exterior Girder
RF_{FSOP}	1.89	1.82	FS_{OP}	37.7	36.3
RF_{PSTOP}	8.41	8.05	PST_{OP}	168.2	161.0

[†] Definitions of rating factors and ratings are provided in Table I.13.

Table I.30 Results of Load Rating Analysis D for Willis Creek Bridge

Inventory Level Rating Factors			Inventory Level Rating		
RF[†]	Interior Girder	Exterior Girder	RT[†] (ton)	Interior Girder	Exterior Girder
RF_{CC1}	1.95	2.20	CC_1	39.0	44.0
RF_{CC2}	1.79	2.11	CC_2	35.8	42.2
RF_{CT6}	0.93	0.89	CT_6	18.6	17.7
$RF_{CT7.5}$	1.08	1.04	$CT_{7.5}$	21.5	20.8
RF_{CT12}	1.51	1.50	CT_{12}	30.1	30.0
RF_{PSTINV}	7.56	7.88	PST_{INV}	151.2	157.5
RF_{FSINV}	1.21	1.14	FS_{INV}	24.1	22.9
Operating Level Rating Factors			**Operating Level Rating**		
RF	Interior Girder	Exterior Girder	RT (ton)	Interior Girder	Exterior Girder
RF_{FSOP}	2.01	1.91	FS_{OP}	40.3	38.2
RF_{PSTOP}	12.45	12.99	PST_{OP}	249.0	259.9

[†] Definitions of rating factors and ratings are provided in Table I.13.

Table I.31 Results of Load Rating Analysis D for Wimberley Bridge

Inventory Level Rating Factors			Inventory Level Rating		
RF†	Interior Girder	Exterior Girder	RT† (ton)	Interior Girder	Exterior Girder
RF_{CC1}	5.93	7.80	CC_1	118.6	156.0
RF_{CC2}	4.27	5.59	CC_2	85.3	111.8
RF_{CT6}	2.69	3.20	CT_6	53.8	63.9
$RF_{CT7.5}$	2.88	3.42	$CT_{7.5}$	57.6	68.3
RF_{CT12}	3.44	4.07	CT_{12}	68.8	81.5
RF_{PSTINV}	11.27	13.22	PST_{INV}	225.5	264.3
RF_{FSINV}	2.13	2.13	FS_{INV}	42.6	42.6
Operating Level Rating Factors			Operating Level Rating		
RF	Interior Girder	Exterior Girder	RT (ton)	Interior Girder	Exterior Girder
RF_{FSOP}	3.55	3.56	FS_{OP}	71.0	71.2
RF_{PSTOP}	17.07	19.93	PST_{OP}	341.3	398.5

†Definitions of rating factors and ratings are provided in Table I.13.

I.6 LOAD RATING ANALYSIS E

Table I.32 Results of Load Rating Analysis E for Chandler Creek 40-ft Span

Inventory Level Rating Factors			Inventory Level Rating		
RF†	Interior Girder	Exterior Girder	RT† (ton)	Interior Girder	Exterior Girder
RF_{CC1}	13.64	13.10	CC_1	272.9	262.0
RF_{CC2}	9.40	8.99	CC_2	188.1	179.8
RF_{CT6}	1.53	1.61	CT_6	30.6	32.2
$RF_{CT7.5}$	1.71	1.79	$CT_{7.5}$	34.3	35.9
RF_{CT12}	2.26	2.35	CT_{12}	45.3	46.9
RF_{PSTINV}	9.49	9.70	PST_{INV}	189.8	194.0
RF_{FSINV}	1.30	1.34	FS_{INV}	26.1	26.9
Operating Level Rating Factors			Operating Level Rating		
RF	Interior Girder	Exterior Girder	RT (ton)	Interior Girder	Exterior Girder
RF_{FSOP}	2.18	2.24	FS_{OP}	43.6	44.9
RF_{PSTOP}	15.35	15.60	PST_{OP}	306.9	312.0

†Definitions of rating factors and ratings are provided in Table I.13.

Table I.33 Results of Load Rating Analysis E for Chandler Creek 60-ft Span

Inventory Level Rating Factors			Inventory Level Rating		
RF[†]	Interior Girder	Exterior Girder	RT[†] (ton)	Interior Girder	Exterior Girder
RF_{CC1}	10.40	9.26	CC_1	208.1	185.2
RF_{CC2}	7.38	6.53	CC_2	147.6	130.6
RF_{CT6}	1.30	1.29	CT_6	26.0	25.7
$RF_{CT7.5}$	1.48	1.45	$CT_{7.5}$	29.5	29.0
RF_{CT12}	2.01	1.94	CT_{12}	40.2	38.9
RF_{PSTINV}	9.78	9.27	PST_{INV}	195.7	185.4
RF_{FSINV}	1.46	1.39	FS_{INV}	29.1	27.8
Operating Level Rating Factors			Operating Level Rating		
RF	Interior Girder	Exterior Girder	RT (ton)	Interior Girder	Exterior Girder
RF_{FSOP}	2.43	2.32	FS_{OP}	48.7	46.4
RF_{PSTOP}	15.63	14.71	PST_{OP}	312.6	294.3

[†] Definitions of rating factors and ratings are provided in Table I.13.

Table I.34 Results of Load Rating Analysis E for Lake LBJ

Inventory Level Rating Factors			Inventory Level Rating		
RF[†]	Interior Girder	Exterior Girder	RT[†] (ton)	Interior Girder	Exterior Girder
RF_{CC1}	8.21	11.11	CC_1	164.1	222.1
RF_{CC2}	5.99	8.16	CC_2	119.9	163.3
RF_{CT6}	1.18	1.31	CT_6	23.6	26.1
$RF_{CT7.5}$	1.34	1.49	$CT_{7.5}$	26.8	29.8
RF_{CT12}	1.81	2.05	CT_{12}	36.2	41.0
RF_{PSTINV}	9.51	11.20	PST_{INV}	190.1	224.0
RF_{FSINV}	1.55	1.60	FS_{INV}	31.1	31.9
Operating Level Rating Factors			Operating Level Rating		
RF	Interior Girder	Exterior Girder	RT (ton)	Interior Girder	Exterior Girder
RF_{FSOP}	2.59	2.66	FS_{OP}	51.9	53.3
RF_{PSTOP}	14.83	17.41	PST_{OP}	296.6	348.2

[†] Definitions of rating factors and ratings are provided in Table I.13.

Table I.35 Results of Load Rating Analysis E for Lampasas River Bridge

Inventory Level Rating Factors			Inventory Level Rating		
RF[†]	Interior Girder	Exterior Girder	RT[†] (ton)	Interior Girder	Exterior Girder
RF_{CC1}	6.00	5.59	CC_1	120.1	111.7
RF_{CC2}	4.50	4.16	CC_2	90.0	83.1
RF_{CT6}	0.71	0.73	CT_6	14.2	14.6
$RF_{CT7.5}$	0.85	0.86	$CT_{7.5}$	17.0	17.1
RF_{CT12}	1.26	1.24	CT_{12}	25.1	24.8
RF_{PSTINV}	7.35	7.07	PST_{INV}	147.0	141.4
RF_{FSINV}	1.20	1.15	FS_{INV}	23.9	23.1
Operating Level Rating Factors			Operating Level Rating		
RF	Interior Girder	Exterior Girder	RT (ton)	Interior Girder	Exterior Girder
RF_{FSOP}	2.00	1.92	FS_{OP}	39.9	38.5
RF_{PSTOP}	11.99	11.46	PST_{OP}	239.9	229.1

[†] Definitions of rating factors and ratings are provided in Table I.13.

Table I.36 Results of Load Rating Analysis E for Willis Creek Bridge

Inventory Level Rating Factors			Inventory Level Rating		
RF[†]	Interior Girder	Exterior Girder	RT[†] (ton)	Interior Girder	Exterior Girder
RF_{CC1}	6.62	7.98	CC_1	132.4	159.7
RF_{CC2}	4.92	5.98	CC_2	98.3	119.6
RF_{CT6}	0.92	0.90	CT_6	18.5	18.0
$RF_{CT7.5}$	1.08	1.07	$CT_{7.5}$	21.6	21.4
RF_{CT12}	1.55	1.58	CT_{12}	31.1	31.6
RF_{PSTINV}	10.45	10.93	PST_{INV}	209.1	218.5
RF_{FSINV}	1.28	1.22	FS_{INV}	25.5	24.3
Operating Level Rating Factors			Operating Level Rating		
RF	Interior Girder	Exterior Girder	RT (ton)	Interior Girder	Exterior Girder
RF_{FSOP}	2.13	2.03	FS_{OP}	42.6	40.6
RF_{PSTOP}	17.12	17.91	PST_{OP}	342.4	358.1

[†] Definitions of rating factors and ratings are provided in Table I.13.

Table I.37 Results of Load Rating Analysis E for Wimberley Bridge

Inventory Level Rating Factors			Inventory Level Rating		
RF†	Interior Girder	Exterior Girder	RT† (ton)	Interior Girder	Exterior Girder
RF_{CC1}	13.53	17.77	CC_1	270.6	355.5
RF_{CC2}	9.34	12.25	CC_2	186.8	244.9
RF_{CT6}	2.37	2.82	CT_6	47.4	56.4
$RF_{CT7.5}$	2.58	3.06	$CT_{7.5}$	51.5	61.2
RF_{CT12}	3.19	3.78	CT_{12}	63.9	75.6
RF_{PSTINV}	15.38	18.05	PST_{INV}	307.6	360.9
RF_{FSINV}	2.21	2.25	FS_{INV}	44.2	45.0
Operating Level Rating Factors			Operating Level Rating		
RF	Interior Girder	Exterior Girder	RT (ton)	Interior Girder	Exterior Girder
RF_{FSOP}	3.69	3.76	FS_{OP}	73.8	75.1
RF_{PSTOP}	23.29	27.22	PST_{OP}	465.8	544.5

†Definitions of rating factors and ratings are provided in Table I.13.

I.7 LOAD RATING ANALYSIS F

Table I.38 Results of Load Rating Analysis F for Chandler Creek 40-ft Span

Inventory Level Rating Factors			Inventory Level Rating		
RF†	Interior Girder	Exterior Girder	RT† (ton)	Interior Girder	Exterior Girder
RF_{CC1}	16.73	14.21	CC_1	334.7	284.2
RF_{CC2}	11.53	9.75	CC_2	230.7	195.1
RF_{CT6}	1.88	1.75	CT_6	37.6	35.0
$RF_{CT7.5}$	2.10	1.95	$CT_{7.5}$	42.1	38.9
RF_{CT12}	2.78	2.55	CT_{12}	55.5	50.9
RF_{PSTINV}	11.64	10.52	PST_{INV}	232.8	210.4
RF_{FSINV}	1.60	1.46	FS_{INV}	32.0	29.2
Operating Level Rating Factors			Operating Level Rating		
RF	Interior Girder	Exterior Girder	RT (ton)	Interior Girder	Exterior Girder
RF_{FSOP}	2.67	2.43	FS_{OP}	53.4	48.7
RF_{PSTOP}	18.82	16.92	PST_{OP}	376.4	338.4

†Definitions of rating factors and ratings are provided in Table I.13.

Table I.39 Results of Load Rating Analysis F for Chandler Creek 60-ft Span

Inventory Level Rating Factors			Inventory Level Rating		
RF[†]	Interior Girder	Exterior Girder	RT[†] (ton)	Interior Girder	Exterior Girder
RF_{CC1}	12.17	11.11	CC_1	243.4	222.3
RF_{CC2}	8.63	7.83	CC_2	172.6	156.7
RF_{CT6}	1.52	1.54	CT_6	30.4	30.9
$\text{RF}_{\text{CT7.5}}$	1.73	1.74	$\text{CT}_{7.5}$	34.6	34.8
RF_{CT12}	2.35	2.33	CT_{12}	47.0	46.7
$\text{RF}_{\text{PSTINV}}$	11.44	11.12	PST_{INV}	228.9	222.5
RF_{FSINV}	1.70	1.67	FS_{INV}	34.1	33.4
Operating Level Rating Factors			Operating Level Rating		
RF	Interior Girder	Exterior Girder	RT (ton)	Interior Girder	Exterior Girder
RF_{FSOP}	2.85	2.79	FS_{OP}	56.9	55.7
RF_{PSTOP}	18.29	17.66	PST_{OP}	365.7	353.2

[†] Definitions of rating factors and ratings are provided in Table I.13.

Table I.40 Results of Load Rating Analysis F for Lake LBJ

Inventory Level Rating Factors			Inventory Level Rating		
RF[†]	Interior Girder	Exterior Girder	RT[†] (ton)	Interior Girder	Exterior Girder
RF_{CC1}	10.01	11.93	CC_1	200.2	238.6
RF_{CC2}	7.31	8.77	CC_2	146.2	175.4
RF_{CT6}	1.44	1.40	CT_6	28.8	28.1
$\text{RF}_{\text{CT7.5}}$	1.63	1.60	$\text{CT}_{7.5}$	32.7	32.0
RF_{CT12}	2.21	2.20	CT_{12}	44.2	44.0
$\text{RF}_{\text{PSTINV}}$	11.60	12.03	PST_{INV}	232.0	240.6
RF_{FSINV}	1.90	1.71	FS_{INV}	37.9	34.3
Operating Level Rating Factors			Operating Level Rating		
RF	Interior Girder	Exterior Girder	RT (ton)	Interior Girder	Exterior Girder
RF_{FSOP}	3.16	2.86	FS_{OP}	63.3	57.2
RF_{PSTOP}	18.09	18.70	PST_{OP}	361.8	374.0

[†] Definitions of rating factors and ratings are provided in Table I.13.

Table I.41 Results of Load Rating Analysis F for Lampasas River Bridge

Inventory Level Rating Factors			Inventory Level Rating		
RF[†]	Interior Girder	Exterior Girder	RT[†] (ton)	Interior Girder	Exterior Girder
RF_{CC1}	6.83	6.68	CC_1	136.5	133.6
RF_{CC2}	5.12	4.97	CC_2	102.4	99.4
RF_{CT6}	0.81	0.87	CT_6	16.2	17.4
$RF_{CT7.5}$	0.96	1.03	$CT_{7.5}$	19.3	20.5
RF_{CT12}	1.43	1.49	CT_{12}	28.6	29.7
RF_{PSTINV}	8.36	8.45	PST_{INV}	167.2	169.1
RF_{FSINV}	1.36	1.38	FS_{INV}	27.2	27.6
Operating Level Rating Factors			Operating Level Rating		
RF	Interior Girder	Exterior Girder	RT (ton)	Interior Girder	Exterior Girder
RF_{FSOP}	2.27	2.30	FS_{OP}	45.4	46.0
RF_{PSTOP}	13.64	13.70	PST_{OP}	272.8	274.1

[†] Definitions of rating factors and ratings are provided in Table I.13.

Table I.42 Results of Load Rating Analysis F for Willis Creek Bridge

Inventory Level Rating Factors			Inventory Level Rating		
RF[†]	Interior Girder	Exterior Girder	RT[†] (ton)	Interior Girder	Exterior Girder
RF_{CC1}	7.41	8.59	CC_1	148.2	171.7
RF_{CC2}	5.50	6.43	CC_2	110.1	128.6
RF_{CT6}	1.04	0.97	CT_6	20.7	19.4
$RF_{CT7.5}$	1.21	1.15	$CT_{7.5}$	24.2	23.0
RF_{CT12}	1.74	1.70	CT_{12}	34.8	33.9
RF_{PSTINV}	11.71	11.75	PST_{INV}	234.2	235.0
RF_{FSINV}	1.43	1.31	FS_{INV}	28.6	26.2
Operating Level Rating Factors			Operating Level Rating		
RF	Interior Girder	Exterior Girder	RT (ton)	Interior Girder	Exterior Girder
RF_{FSOP}	2.38	2.18	FS_{OP}	47.7	43.7
RF_{PSTOP}	19.17	19.26	PST_{OP}	383.5	385.1

[†] Definitions of rating factors and ratings are provided in Table I.13.

Table I.43 Results of Load Rating Analysis F for Wimberley Bridge

Inventory Level Rating Factors			Inventory Level Rating		
RF[†]	Interior Girder	Exterior Girder	RT[†] (ton)	Interior Girder	Exterior Girder
RF_{CC1}	16.02	16.87	CC_1	320.3	337.4
RF_{CC2}	11.05	11.62	CC_2	221.1	232.5
RF_{CT6}	2.81	2.67	CT_6	56.1	53.5
$RF_{CT7.5}$	3.05	2.90	$CT_{7.5}$	61.0	58.1
RF_{CT12}	3.78	3.59	CT_{12}	75.6	71.8
RF_{PSTINV}	18.20	17.13	PST_{INV}	364.0	342.6
RF_{FSINV}	2.62	2.14	FS_{INV}	52.3	42.7
Operating Level Rating Factors			Operating Level Rating		
RF	Interior Girder	Exterior Girder	RT (ton)	Interior Girder	Exterior Girder
RF_{FSOP}	4.37	3.56	FS_{OP}	87.3	71.3
RF_{PSTOP}	27.57	25.84	PST_{OP}	551.3	516.8

[†] Definitions of rating factors and ratings are provided in Table I.13.

I.8 LOAD RATING ANALYSIS G

Table I.44 Results of Load Rating Analysis G for Chandler Creek 40-ft Span

Inventory Level Rating Factors			Inventory Level Rating		
RF[†]	Interior Girder	Exterior Girder	RT[†] (ton)	Interior Girder	Exterior Girder
RF_{CC1}	11.67	11.03	CC_1	233.4	220.6
RF_{CC2}	8.04	7.57	CC_2	160.9	151.4
RF_{CT6}	1.31	1.36	CT_6	26.2	27.1
$RF_{CT7.5}$	1.47	1.51	$CT_{7.5}$	29.3	30.2
RF_{CT12}	1.94	1.98	CT_{12}	38.7	39.5
RF_{PSTINV}	8.12	8.17	PST_{INV}	162.3	163.3
RF_{FSINV}	1.12	1.13	FS_{INV}	22.3	22.6
Operating Level Rating Factors			Operating Level Rating Factors		
RF	Interior Girder	Exterior Girder	RT (ton)	Interior Girder	Exterior Girder
RF_{FSOP}	1.86	1.89	FS_{OP}	37.3	37.8
RF_{PSTOP}	13.13	13.13	PST_{OP}	262.5	262.7

[†] Definitions of rating factors and ratings are provided in Table I.13.

Table I.45 Results of Load Rating Analysis G for Chandler Creek 60-ft Span

Inventory Level Rating Factors			Inventory Level Rating		
RF[†]	Interior Girder	Exterior Girder	RT[†] (ton)	Interior Girder	Exterior Girder
RF_{CC1}	8.96	8.15	CC_1	179.2	163.0
RF_{CC2}	6.35	5.75	CC_2	127.1	114.9
RF_{CT6}	1.12	1.13	CT_6	22.4	22.6
$RF_{CT7.5}$	1.27	1.28	$CT_{7.5}$	25.4	25.5
RF_{CT12}	1.73	1.71	CT_{12}	34.6	34.2
RF_{PSTINV}	8.42	8.16	PST_{INV}	168.5	163.2
RF_{FSINV}	1.26	1.22	FS_{INV}	25.1	24.5
Operating Level Rating Factors			Operating Level Rating Factors		
RF	Interior Girder	Exterior Girder	RT (ton)	Interior Girder	Exterior Girder
RF_{FSOP}	2.09	2.04	FS_{OP}	41.9	40.9
RF_{PSTOP}	13.46	12.95	PST_{OP}	269.2	259.0

[†]Definitions of rating factors and ratings are provided in Table I.13.

Table I.46 Results of Load Rating Analysis G for Lake LBJ

Inventory Level Rating Factors			Inventory Level Rating		
RF[†]	Interior Girder	Exterior Girder	RT[†] (ton)	Interior Girder	Exterior Girder
RF_{CC1}	7.05	8.59	CC_1	141.0	171.8
RF_{CC2}	5.15	6.31	CC_2	103.0	126.3
RF_{CT6}	1.02	1.01	CT_6	20.3	20.2
$RF_{CT7.5}$	1.15	1.15	$CT_{7.5}$	23.0	23.1
RF_{CT12}	1.56	1.58	CT_{12}	31.1	31.7
RF_{PSTINV}	8.17	8.66	PST_{INV}	163.3	173.2
RF_{FSINV}	1.33	1.23	FS_{INV}	26.7	24.7
Operating Level Rating Factors			Operating Level Rating Factors		
RF	Interior Girder	Exterior Girder	RT (ton)	Interior Girder	Exterior Girder
RF_{FSOP}	2.23	2.06	FS_{OP}	2.23	2.06
RF_{PSTOP}	12.74	13.46	PST_{OP}	12.74	13.46

[†]Definitions of rating factors and ratings are provided in Table I.13.

Table I.47 Results of Load Rating Analysis G for Lampasas River Bridge

Inventory Level Rating Factors			Inventory Level Rating		
RF[†]	Interior Girder	Exterior Girder	RT[†] (ton)	Interior Girder	Exterior Girder
RF_{CC1}	5.28	4.80	CC_1	105.5	96.0
RF_{CC2}	3.95	3.57	CC_2	79.1	71.4
RF_{CT6}	0.63	0.63	CT_6	12.5	12.5
$RF_{CT7.5}$	0.75	0.74	$CT_{7.5}$	14.9	14.7
RF_{CT12}	1.10	1.07	CT_{12}	22.1	21.3
RF_{PSTINV}	6.46	6.07	PST_{INV}	129.2	121.5
RF_{FSINV}	1.05	0.99	FS_{INV}	21.0	19.8
Operating Level Rating Factors			Operating Level Rating Factors		
RF	Interior Girder	Exterior Girder	RT (ton)	Interior Girder	Exterior Girder
RF_{FSOP}	1.75	1.65	FS_{OP}	35.1	33.1
RF_{PSTOP}	10.54	9.84	PST_{OP}	210.8	196.9

[†] Definitions of rating factors and ratings are provided in Table I.13.

Table I.48 Results of Load Rating Analysis G for Willis Creek Bridge

Inventory Level Rating Factors			Inventory Level Rating		
RF[†]	Interior Girder	Exterior Girder	RT[†] (ton)	Interior Girder	Exterior Girder
RF_{CC1}	5.62	6.89	CC_1	112.3	137.9
RF_{CC2}	4.17	5.16	CC_2	83.4	103.3
RF_{CT6}	0.78	0.78	CT_6	15.7	15.6
$RF_{CT7.5}$	0.92	0.92	$CT_{7.5}$	18.4	18.5
RF_{CT12}	1.32	1.36	CT_{12}	26.4	27.3
RF_{PSTINV}	8.87	9.44	PST_{INV}	177.4	188.7
RF_{FSINV}	1.08	1.05	FS_{INV}	21.6	21.0
Operating Level Rating Factors			Operating Level Rating Factors		
RF	Interior Girder	Exterior Girder	RT (ton)	Interior Girder	Exterior Girder
RF_{FSOP}	1.81	1.75	FS_{OP}	36.1	35.1
RF_{PSTOP}	14.53	15.46	PST_{OP}	290.5	309.3

[†] Definitions of rating factors and ratings are provided in Table I.13.

Table I.49 Results of Load Rating Analysis G for Wimberley Bridge

Inventory Level Rating Factors			Inventory Level Rating		
RF[†]	Interior Girder	Exterior Girder	RT[†] (ton)	Interior Girder	Exterior Girder
RF_{CC1}	10.90	16.87	CC_1	218.0	337.4
RF_{CC2}	7.52	11.62	CC_2	150.4	232.5
RF_{CT6}	1.91	2.67	CT_6	38.2	53.5
$RF_{CT7.5}$	2.08	2.90	$CT_{7.5}$	41.5	58.1
RF_{CT12}	2.57	3.59	CT_{12}	51.4	71.8
RF_{PSTINV}	12.39	17.13	PST_{INV}	247.8	342.6
RF_{FSINV}	1.78	2.14	FS_{INV}	35.6	42.7
Operating Level Rating Factors			Operating Level Rating Factors		
RF	Interior Girder	Exterior Girder	RT (ton)	Interior Girder	Exterior Girder
RF_{FSOP}	2.97	3.56	FS_{OP}	59.4	71.3
RF_{PSTOP}	18.76	25.84	PST_{OP}	375.2	516.8

[†] Definitions of rating factors and ratings are provided in Table I.13.

I.9 LOAD RATING ANALYSIS H

Table I.50 Results of Load Rating Analysis H for Chandler Creek 40-ft Span

Inventory Level Rating Factors			Inventory Level Rating		
RF[†]	Interior Girder	Exterior Girder	RT[†] (ton)	Interior Girder	Exterior Girder
RF_{CC1}	13.64	13.10	CC_1	272.9	262.0
RF_{CC2}	9.40	8.99	CC_2	188.1	179.8
RF_{CT6}	1.53	1.61	CT_6	30.6	32.2
$RF_{CT7.5}$	1.71	1.79	$CT_{7.5}$	34.3	35.9
RF_{CT12}	2.26	2.35	CT_{12}	45.3	46.9
RF_{PSTINV}	9.49	9.70	PST_{INV}	189.8	194.0
RF_{FSINV}	1.30	1.34	FS_{INV}	26.1	26.9
Operating Level Rating Factors			Operating Level Rating Factors		
RF	Interior Girder	Exterior Girder	RT (ton)	Interior Girder	Exterior Girder
RF_{FSOP}	2.18	2.24	FSOP	43.6	44.9
RF_{PSTOP}	15.35	15.60	PSTOP	306.9	312.0

[†] Definitions of rating factors and ratings are provided in Table I.13.

Table I.51 Results of Load Rating Analysis H for Chandler Creek 60-ft Span

Inventory Level Rating Factors			Inventory Level Rating		
RF[†]	Interior Girder	Exterior Girder	RT[†] (ton)	Interior Girder	Exterior Girder
$\mathrm{RF}_{\mathrm{CC1}}$	10.40	9.26	CC_1	208.1	185.2
$\mathrm{RF}_{\mathrm{CC2}}$	7.38	6.53	CC_2	147.6	130.6
$\mathrm{RF}_{\mathrm{CT6}}$	1.30	1.29	CT_6	26.0	25.7
$\mathrm{RF}_{\mathrm{CT7.5}}$	1.48	1.45	$\mathrm{CT}_{7.5}$	29.5	29.0
$\mathrm{RF}_{\mathrm{CT12}}$	2.01	1.94	CT_{12}	40.2	38.9
$\mathrm{RF}_{\mathrm{PSTINV}}$	9.78	9.27	$\mathrm{PST}_{\mathrm{INV}}$	195.7	185.4
$\mathrm{RF}_{\mathrm{FSINV}}$	1.46	1.39	$\mathrm{FS}_{\mathrm{INV}}$	29.1	27.8
Operating Level Rating Factors			Operating Level Rating Factors		
RF	Interior Girder	Exterior Girder	RT (ton)	Interior Girder	Exterior Girder
$\mathrm{RF}_{\mathrm{FSOP}}$	2.43	2.32	FSOP	48.7	46.4
$\mathrm{RF}_{\mathrm{PSTOP}}$	15.63	14.71	PSTOP	312.6	294.3

[†] Definitions of rating factors and ratings are provided in Table I.13.

Table I.52 Results of Load Rating Analysis H for Lake LBJ

Inventory Level Rating Factors			Inventory Level Rating		
RF[†]	Interior Girder	Exterior Girder	RT[†] (ton)	Interior Girder	Exterior Girder
$\mathrm{RF}_{\mathrm{CC1}}$	8.21	11.11	CC_1	164.1	222.1
$\mathrm{RF}_{\mathrm{CC2}}$	5.99	8.16	CC_2	119.9	163.3
$\mathrm{RF}_{\mathrm{CT6}}$	1.18	1.31	CT_6	23.6	26.1
$\mathrm{RF}_{\mathrm{CT7.5}}$	1.34	1.49	$\mathrm{CT}_{7.5}$	26.8	29.8
$\mathrm{RF}_{\mathrm{CT12}}$	1.81	2.05	CT_{12}	36.2	41.0
$\mathrm{RF}_{\mathrm{PSTINV}}$	9.51	11.20	$\mathrm{PST}_{\mathrm{INV}}$	190.1	224.0
$\mathrm{RF}_{\mathrm{FSINV}}$	1.55	1.60	$\mathrm{FS}_{\mathrm{INV}}$	31.1	31.9
Operating Level Rating Factors			Operating Level Rating		
RF	Interior Girder	Exterior Girder	RT (ton)	Interior Girder	Exterior Girder
$\mathrm{RF}_{\mathrm{FSOP}}$	2.59	2.66	$\mathrm{FS}_{\mathrm{OP}}$	51.9	53.3
$\mathrm{RF}_{\mathrm{PSTOP}}$	14.83	17.41	$\mathrm{PST}_{\mathrm{OP}}$	296.6	348.2

[†] Definitions of rating factors and ratings are provided in Table I.13.

Table I.53 Results of Load Rating Analysis H for Lampasas River Bridge

Inventory Level Rating Factors			Inventory Level Rating		
$RF^{\dagger}$	Interior Girder	Exterior Girder	$RT^{\dagger}$ (ton)	Interior Girder	Exterior Girder
RF_{CC1}	6.00	5.59	CC_1	120.1	111.7
RF_{CC2}	4.50	4.16	CC_2	90.0	83.1
RF_{CT6}	0.71	0.73	CT_6	14.2	14.6
$RF_{CT7.5}$	0.85	0.86	$CT_{7.5}$	17.0	17.1
RF_{CT12}	1.26	1.24	CT_{12}	25.1	24.8
RF_{PSTINV}	7.35	7.07	PST_{INV}	147.0	141.4
RF_{FSINV}	1.20	1.15	FS_{INV}	23.9	23.1
Operating Level Rating Factors			Operating Level Rating		
RF	Interior Girder	Exterior Girder	RT (ton)	Interior Girder	Exterior Girder
RF_{FSOP}	2.00	1.92	FS_{OP}	39.9	38.5
RF_{PSTOP}	11.99	11.46	PST_{OP}	239.9	229.1

†Definitions of rating factors and ratings are provided in Table I.13.

Table I.54 Results of Load Rating Analysis H for Willis Creek Bridge

Inventory Level Rating Factors			Inventory Level Rating		
$RF^{\dagger}$	Interior Girder	Exterior Girder	$RT^{\dagger}$ (ton)	Interior Girder	Exterior Girder
RF_{CC1}	6.62	7.98	CC_1	132.4	159.7
RF_{CC2}	4.92	5.98	CC_2	98.3	119.6
RF_{CT6}	0.92	0.90	CT_6	18.5	18.0
$RF_{CT7.5}$	1.08	1.07	$CT_{7.5}$	21.6	21.4
RF_{CT12}	1.55	1.58	CT_{12}	31.1	31.6
RF_{PSTINV}	10.45	10.93	PST_{INV}	209.1	218.5
RF_{FSINV}	1.28	1.22	FS_{INV}	25.5	24.3
Operating Level Rating Factors			Operating Level Rating		
RF	Interior Girder	Exterior Girder	RT (ton)	Interior Girder	Exterior Girder
RF_{FSOP}	2.13	2.03	FS_{OP}	42.6	40.6
RF_{PSTOP}	17.12	17.91	PST_{OP}	342.4	358.1

†Definitions of rating factors and ratings are provided in Table I.13.

Table I.55 Results of Load Rating Analysis H for Wimberley Bridge

Inventory Level Rating Factors			Inventory Level Rating		
RF[†]	Interior Girder	Exterior Girder	RT[†] (ton)	Interior Girder	Exterior Girder
RF_{CC1}	13.53	17.77	CC_1	270.6	355.5
RF_{CC2}	9.34	12.25	CC_2	186.8	244.9
RF_{CT6}	2.37	2.82	CT_6	47.4	56.4
$RF_{CT7.5}$	2.58	3.06	$CT_{7.5}$	51.5	61.2
RF_{CT12}	3.19	3.78	CT_{12}	63.9	75.6
RF_{PSTINV}	15.38	18.05	PST_{INV}	307.6	360.9
RF_{FSINV}	2.21	2.25	FS_{INV}	44.2	45.0
Operating Level Rating Factors			Operating Level Rating		
RF	Interior Girder	Exterior Girder	RT (ton)	Interior Girder	Exterior Girder
RF_{FSOP}	3.69	3.76	FS_{OP}	73.8	75.1
RF_{PSTOP}	23.29	27.22	PST_{OP}	465.8	544.5

[†] Definitions of rating factors and ratings are provided in Table I.13.

APPENDIX J

Analysis of Prototype Beam for Determining Stress Ranges in the Strand for Fatigue Tests

As discussed in Chapter 5, the interior girder of the 60-ft span of the Chandler Creek bridge was selected as the prototype for this investigation. The analyses of the prototype beam using estimated in situ concrete compressive strengths are presented in this appendix. The results were used to determine the appropriate stress ranges in the strand for the fatigue tests.

The results from the analyses of the prototype beam using specified and quality control concrete compressive strengths are also presented. Similar results for the other bridges considered in this investigation are presented in Section J.3.

J.1 ANALYSIS OF INTERIOR BEAM OF CHANDLER CREEK BRIDGE

The analyses described in this section correspond to of the interior beam of the 60-ft span of the Chandler Creek bridge. Estimated in situ material and section properties were used in all calculations. The results from the analyses and stress ranges in the strand corresponding to index stress levels of $6\sqrt{f'_{ce}}$, $7.5\sqrt{f'_{ce}}$, and $12\sqrt{f'_{ce}}$ are presented.

J.1.1 Dimensions, Section Properties and Material Properties Used in Analysis

J.1.1.1 Material Properties Used in Analysis of Prototype Beam

Compressive Strength of Beam Concrete at Release, f'_{cei}	5500 psi
Modulus of Elasticity of Beam Concrete at Release, E_{cei}	4270 ksi
Estimated Compressive Strength of Beam Concrete In Situ, f'_{ce}	10,300 psi
Estimated Modulus of Elasticity of Beam Concrete In Situ, E_{ce}	5850 ksi
Estimated Compressive Strength of Slab Concrete In Situ, f'_{cse}	6200 psi
Estimated Modulus of Elasticity of Slab Concrete In Situ, E_{cei}	4540 ksi
Yield Strength of Strand, f_y	225 ksi
Breaking Strength of Strand, f_{pu}	250 ksi
Modulus of Elasticity of Strand, E_s	28,500 ksi
Modular Ratio at Release, $n_i = \dfrac{E_s}{E_{cei}}$	6.67
Modular Ratio In Situ, $n = \dfrac{E_s}{E_{ce}}$	4.87
Modular Ratio for Slab In Situ, $n_s = \dfrac{E_{cse}}{E_{ce}}$	0.78

J.1.1.2 Prestressing Information

Initial Effective Prestress, f_{pi}	175 ksi

J.1.1.3 Loading Information

The loads given in this section are the dead loads and include the self weight of the beam, weight of the tributary area of the slab based on a beam spacing of 8 ft, weight of the diaphragms, and superimposed dead loads applied to the composite beam. The superimposed dead loads include the weight of overlay and railings. The weight of the diaphragms and superimposed dead loads were taken from load ratings analyses provided by TxDOT.

Self Weight of Beam, w_{sw}	0.516 kip/ft
Moment Due to Self Weight of Beam, $M_{sw} = \frac{w_{sw}L^2}{8}$	2660 in.-kip
Weight of Slab, w_{sl}	0.725 kip/ft
Moment Due to Weight of Slab, $M_{sl} = \frac{w_{sl}L^2}{8}$	3730 in.-kip
Weight of Diaphragms, w_d	0.09 kip/ft
Moment Due to Diaphragms, $M_d = \frac{w_d L^2}{8}$	460 in.-kip
Superimposed Dead Load (SDL), w_{sdl}	0.088 kip/ft
Moment Due to Assumed SDL, $M_{sdl} = \frac{w_{sdl}L^2}{8}$	450 in.-kip

It was assumed that the self-weight of the beam, the weight of the slab, and the weight of the diaphragms were carried by the non-composite section. It was also assumed that the superimposed dead load was carried by the composite section. The total dead load moment carried by the composite section and non-composite section are as follows:

Total Non-Composite Dead Load, $M_{dl} = M_{sw} + M_{sl} + M_d$	6850 in.-kip
Total Composite Dead Load, $M_{dl\_c} = M_{sdl}$	450 in.-kip

J.1.1.4 Non-composite Beam Dimensions and Section Properties at Midspan

The non-composite beam dimensions and section properties at midspan are given in this section. The actual cross-section dimensions were changed to simplify the calculations. The assumed cross-section dimensions used are given in Figure J.1.

Gross Area of Concrete, A_{cb}	495.5 in.^{2}
Area of Prestressing Strand (30-⅜″ ϕ strands), A_{ps}	3.24 in.^{2}
Height of Beam, h_b	40 in.
Center of Gravity of Beam from bottom, y_b	17.07 in.
Center of Gravity of Beam from top, y_t	22.93 in.
Center of Gravity of Strand from bottom, y_{ps}	4 in.
Moment of Inertia of Beam, I_b	82,800 in.^{4}
Span Length, L	58.58 ft
Average Eccentricity of Prestressing strand, $e_m = y_b - y_{ps}$	13.07 in.

J.1.1.5 Composite Beam Dimensions and Section Properties at Midspan

Effective Slab Width, b_{eff}	94 in.
Slab Thickness, t_{sl}	7.25 in.
Height of Composite Beam, h_{b_comp}	47.25 in.
Center of Gravity of Composite Beam from bottom, y_{comp}	30.45 in.
Moment of Inertia of Composite Beam, I_{comp}	274,000 in.^{4}
Depth of Strand, d_p	43.25 in.

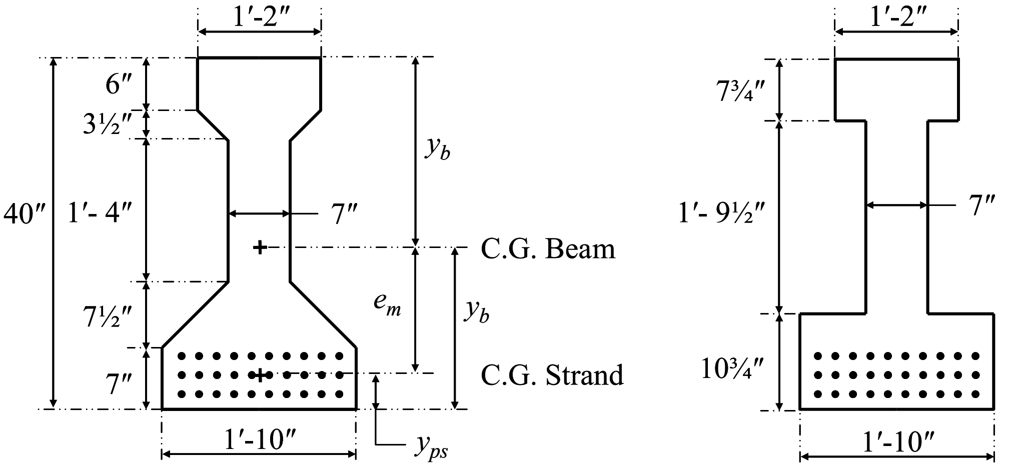

a) Dimensions of Interior Beam of Chandler Creek

b) Dimensions of Beam Assumed for Analysis

Figure J.1 Dimensions of Non-composite Beam

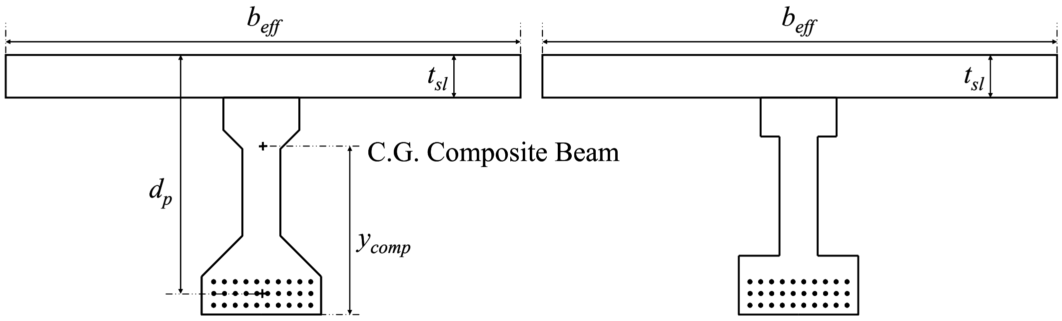

a) Interior Beam of Chandler Creek

b) Assumed Cross Section for Analysis

Figure J.2 Dimensions of Composite Beam

J.1.2 Calculation of Prestress Losses

Prestress losses were calculated as outlined in AASHTO LRFD (2003). Losses due to elastic shortening, shrinkage, creep and relaxation were calculated as follows.

Losses due to elastic shortening (*ES*):

$$ES = \frac{A_{ps} f_{pi} (I_b + e_m{}^2 A_{cb}) - e_m M_{sw} A_{cb}}{A_{ps}(I_b + e_m{}^2 A_{cb}) + \frac{A_{cb} I_b E_{cei}}{E_s}} \qquad \text{(J-1)}$$

$$ES = 11.6\,\text{ksi}$$

Losses due to shrinkage (*SH*):

$$SH = (17 - 0.15H) \qquad \text{(J-2)}$$

$$SH = 7.3\,\text{ksi}$$

where *H* is the average annual ambient relative humidity and was assumed to be 65%.

Losses due to creep (*CR*):

$$CR = 12 f_{gcp} - 7\Delta f_{cdp} \qquad \text{(J-3)}$$

$$CR = 16.1\,\text{ksi}$$

where f_{gcp} is the concrete stress at the center of gravity of prestressing steel at transfer and Δf_{cdp} is the change in concrete stress at the center of gravity of the prestressing steel due to permanent loads, with the exception of load applied at the time of transfer. These values are calculated using Equations J-4 and J-5.

$$f_{gcp} = \frac{A_{ps} f_p}{A_{cb}} + \frac{A_{ps} f_p e_m{}^2}{I_b} + \frac{M_{sw} e_m}{I_b} \qquad \text{(J-4)}$$

$$f_{gcp} = 1.73\,\text{ksi}$$

where f_p is typically assumed to be $0.65f_{pu}$ for pretensioned components with stress-relieved strand.

$$\Delta f_{cdp} = (M_{sdl} + M_{sl}) \frac{e_m}{I_b} \qquad \text{(J-5)}$$

$$\Delta f_{cdp} = 0.66\,\text{ksi}$$

Losses due to relaxation (R):

$$R = 20ksi - 0.4ES - 0.2(SH + CR) \qquad \text{(J-6)}$$

$$R = 10.7\,\text{ksi}$$

The total loss of prestress, which is the sum of the losses due to elastic shortening, shrinkage, creep, and relaxation, was 45.7 ksi. The effective prestress force, accounting for all losses is calculated using Equation J-7.

$$f_{peff} = f_{pi} - ES - SH - CR - R \qquad \text{(J-7)}$$

$$f_{peff} = 129.3\,\text{ksi}$$

J.1.3 Graphic Determination of Strand Stress Ranges

A plot of applied live load moment versus strand stress range was created by performing a section analysis at five levels of applied moment. In this dissertation, strand stress range is defined as the change in strand stress due to live loads. The five levels of applied moment considered were the full dead load state, the load when the strain at the bottom fiber of the composite section is zero, the load at which the neutral axis was located at the bottom surface of the web, the load at which the neutral axis was located at the bottom surface of the slab, and the load corresponding to the flexural capacity. Using these analyses, a plot of applied live load moment versus change in strand stress, as shown in Figure J.3, was developed. The full dead load state is condition of zero live load and full dead load. Therefore, this load level is the basis for determining the change in strand stress due to applied live load for subsequent analyses. As a result, the origin of the plot in Figure J.3 corresponds to the full dead load condition.

In Overman (1984), the analysis performed included the decompression load and the load at which the neutral axis was at the bottom fiber of the web. Therefore, these levels of loading were used in the analyses in this dissertation. The decision to use the point when the neutral axis is at the bottom of the slab was made for simplicity in the calculations and to provide an additional data point in the region between the decompression load and flexural capacity.

In addition to the five analyses described above, the non-composite dead load state was also analyzed. This level of load was analyzed because it is the state when the stress and the strain in the slab is zero and information from this analysis is used in subsequent analyses; however, it is not used in developing the plot of applied live load moment as a function of strand stress range.

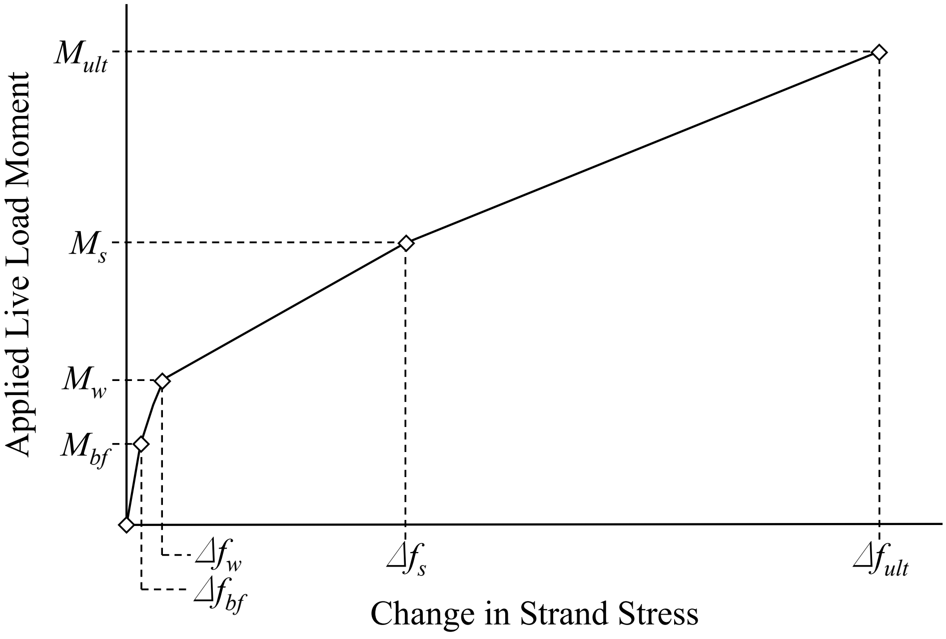

Figure J.3 Graphic Representation of Live Load as a Function of the Change in Strand Stress

J.1.3.1.1 Non-Composite Section Under Dead Load

The analysis at the non-composite dead load state assumes that all prestress losses occurred prior to composite action and includes the dead load due to self-weight of the beam, dead load due the slab assuming unshored construction, and the dead load of the diaphragms. Information from this analysis is used in subsequent analyses; however, it is not used in the development of the plot of applied live load moment as a function of strand stress range. The calculations performed are given below. The resulting strain and stress profiles for the dead load state are shown in Figure J.4. The stress in the strand and total moment for the non-composite dead load state are summarized in Table J.1.

Determine concrete stress at the bottom fiber of non-composite beam.

$$f_{b\_dl} = \frac{-f_{peff}A_{ps}}{A_b} + \frac{-f_{peff}A_{ps}e_m y_b}{I_b} + \frac{M_{dl}y_b}{I_b} \tag{J-8}$$

$f_{b\_dl} = \text{-0.562 ksi}$

Determine concrete strain at the bottom fiber of non-composite beam.

$$\varepsilon_{b\_dl} = \frac{f_{b\_dl}}{E_{ce}} \tag{J-9}$$

$\varepsilon_{b\_dl} = \text{-96}\,\mu\varepsilon$

Determine strand stress at the centroid of the strand.

$$f_{dl} = f_{peff} + \frac{nM_{dl}e_m}{I_b} \tag{J-10}$$

$f_{dl} = 135\text{ ksi}$

Determine concrete stress at CG of prestressing strand.

$$f_{ps\_dl} = \frac{-f_{peff}A_{ps}}{A_b} + \frac{-f_{peff}A_{ps}e_m^{\ 2}}{I_b} + \frac{M_{dl}e_m}{I_b} \tag{J-11}$$

$f_{ps\_dl} = \text{-0.629 ksi}$

Determine concrete strain at CG prestressing strand.

$$\varepsilon_{ps\_dl} = \frac{f_{ps\_dl}}{E_{ce}} \tag{J-12}$$

$\varepsilon_{ps\_dl} = \text{-107}\mu\varepsilon$

Determine concrete stress at the top fiber of non-composite beam.

$$f_{t\_dl} = \frac{-f_{peff} A_{ps}}{A_b} + \frac{f_{peff} A_{ps} e_m y_t}{I_b} - \frac{M_{dl} y_t}{I_b} \qquad \text{(J-13)}$$

$f_{t\_dl} = \text{-1.227 ksi}$

Determine concrete strain at the bottom fiber of non-composite beam.

$$\varepsilon_{t\_dl} = \frac{f_{t\_dl}}{E_{ce}} \qquad \text{(J-14)}$$

$\varepsilon_{t\_dl} = \text{-210}\ \mu\varepsilon$

Determine the curvature at the non-composite dead load state.

$$\phi_{dl} = \frac{\varepsilon_{b\_dl} - \varepsilon_{t\_dl}}{h_b} \qquad \text{(J-15)}$$

$\phi_{dl} = 2.84 \cdot 10^{-6}\,\text{/in.}$

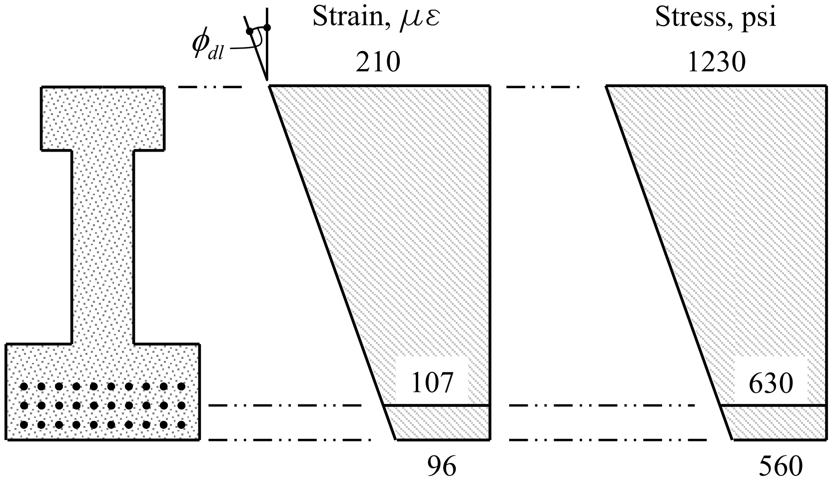

Figure J.4 Concrete Stress and Strain at Non-Composite Dead Load State

Table J.1 Summary of Analysis Results for Chandler Creek Using Estimated In Situ Material and Section Properties

Analysis	Total Moment (ft-kip)	Live Load Moment (ft-kip)		Stress in the Strand (ksi)	Strand Stress Range (ksi)	
Non-Composite Dead Load	571	—	—	134.6	—	—
Composite Dead Load	610	—	0	134.8	—	0
Decompression of Bottom Fiber	993	M_{bf}	383	137.0	Δf_{bf}	2.3
NA at Bottom of Web	1289	M_w	679	139.3	Δf_w	4.5
NA at Bottom of Slab	1941	M_s	1331	176.2	Δf_{sl}	41.4
Ultimate	2877	M_{ult}	2267	250.0	Δf_{ult}	115.2

J.1.3.1.2 Composite Section Under Dead Load

The analysis at the composite dead load state is the condition that will serve as the basis for the calculation of strand stress ranges and corresponding live load moments. The difference in loading between the non-composite dead load state and composite dead load state is the addition of the superimposed dead loads. For this analysis the non-composite section still resisted the non-composite dead loads, however, the composite cross section is assumed to resist the superimposed dead load. Therefore, gross, transformed composite section properties were used for calculating the changes in strain and stress from the non-composite dead load level due to the superimposed dead loads. The calculations performed are similar to the calculations performed at the non-composite dead load state; therefore, the equations are not repeated. The resulting strain and stress profiles for the composite dead load state are shown in Figure J.5. The stress in the strand and total moment for the composite dead load state are summarized in Table J.1.

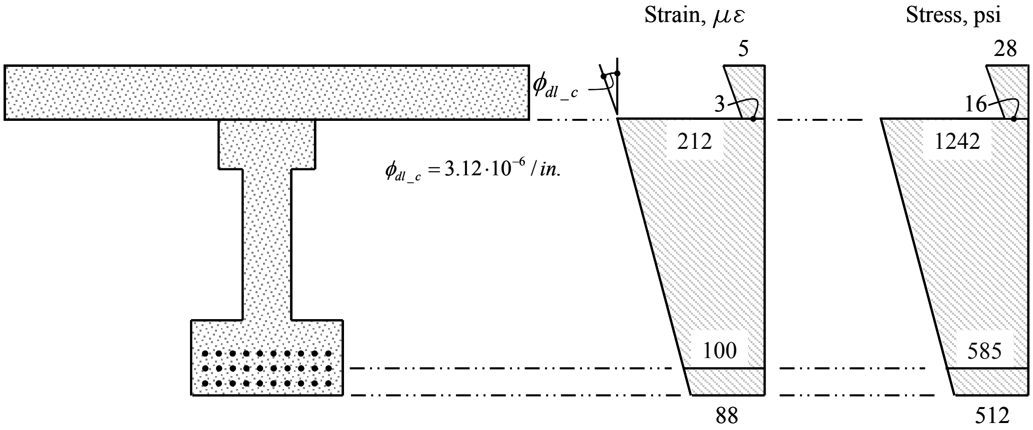

Figure J.5 Concrete Stress and Strain at Composite Dead Load State

J.1.3.1.3 Analysis of Section at Decompression of the Bottom Fiber

The live load moment required to produce zero stress at the bottom fiber is called the decompression moment, M_{bf}. The decompression moment is calculated using transformed, composite section properties as given in Eq. J-16. The resulting stress diagram is given in Figure J.6.

Determine decompression moment.

$$M_{bf} = f_{b\_dl\_c} \frac{I_{comp}}{y_{comp}} \tag{J-16}$$

$$M_{bf} = 383 \text{ ft - kip}$$

where $f_{b\_dl\_c}$ is the compressive stress at the bottom fiber of the section given in Figure J.5, and M_{bf} is the live load moment.

The stress in the prestressing strand is equal to the stress in the strand at the composite dead load state, plus the stress due to the decompression moment. This calculation is given in Eq. J-17. The corresponding strand stress range is calculated using Eq. J-18.

$$f_{bf} = f_{dl\_c} + M_{bf} \frac{(y_{comp} - y_{ps})}{I_{comp}} n \tag{J-17}$$

$$f_{bf} = 137 \text{ ksi}$$

$$\Delta f_{bf} = f_{bf} - f_{dl\_c} \tag{J-18}$$

$$\Delta f_{bf} = 2.3 \text{ ksi}$$

where f_{dl_c} is the stress in the strand at the composite dead load state as given in Table J.1.

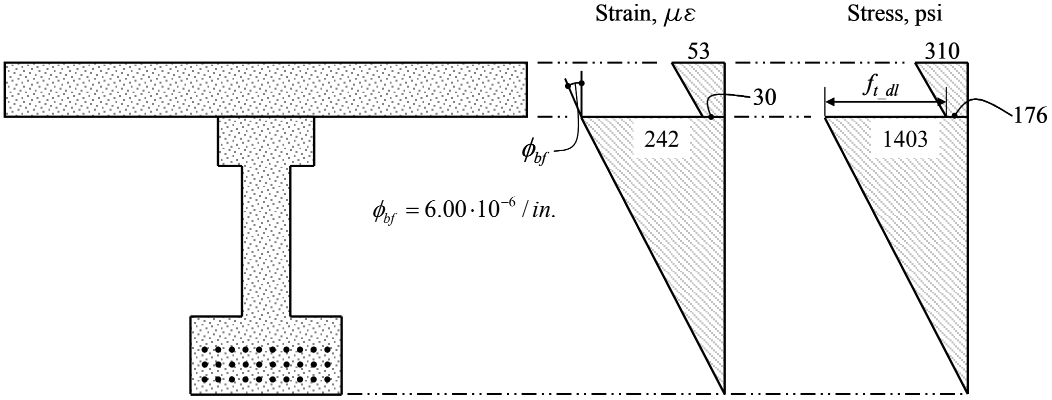

where f_{t_dl} is the compressive stress at the top of the girder given in Figure J.4.

Figure J.6 Stress Profile at Decompression of the Bottom Fiber

J.1.3.1.4 Analysis of Section When the Neutral Axis is at the Bottom of the Web

The analysis when the neutral axis is at the bottom of the web is an iterative process that assumes a linear stress profile as shown in Figure J.7. Equilibrium of the tension force in the strand and compressive forces in the concrete are achieved by iterating the curvature, while maintaining the compatibility condition that the strain at the bottom of the web is zero. Equilibrium for this analysis was achieved at a curvature of $8.65 \cdot 10^{-6}$/in.

For a given curvature, the stress in the strand is equal to the stress at the non-composite dead load state plus the stress due to the change in strain.

Determine stress in the strand.

$$f_w = f_{dl} + \left\lfloor (h_{bf} - y_{ps})\phi_{bw} - \varepsilon_{ps\_dl} \right\rfloor E_s \tag{J-19}$$

$$f_w = 139 \text{ ksi}$$

Determine change in strand stress from dead load state.

$$\Delta f_w = f_w - f_{dl\_c} \tag{J-20}$$

$$\Delta f_w = 5 \text{ ksi}$$

where f_{dl_c} is the stress in the strand at the composite dead load state as given in Table J.1.

Determine force in the strand.

$$T = f_w A_{ps} \tag{J-21}$$

$$T = 451.5 \text{ kip}$$

Based on the assumed curvature and a linear strain profile, the compression force in the concrete is calculated as follows.

Determine the compression force in the web.

$$C1 = \frac{h_w b_w}{2} \cdot E_{ce} \phi_w (h_w) \qquad C1 = 81.8 \text{ kip}$$

Determine the compression force in the top flange.

$$C2 = h_{tf} b_{tf} E_{ce} \phi_w h_w \qquad C2 = 118.0 \text{ kip}$$

$$C3 = \frac{h_{tf} b_{tf}}{2} E_{ce} \phi_w h_{tf} \qquad C3 = 21.3 \text{ kip}$$

Determine the compression force in the slab.

$$C4 = t_{sl} b_{eff} n_s [E_{ce} \phi_w (h_w + h_{tf}) - f_{t\_dl}] \qquad C4 = 133.5 \text{ kip}$$

$$C5 = \frac{t_{sl} b_{eff} n_s}{2} E_{ce} \phi_w t_{sl} \qquad C5 = 96.9\,\text{kip}$$

Calculate the total compressive force.

$$C = C1 + C2 + C3 + C4 + C5 \qquad C = 451.5\,\text{kip}$$

Determine the internal moment.

$$M_{C1} = \left[h_{bf} - y_{ps} + \frac{2h_w}{3} \right] C1 \qquad M_{C1} = 144\,\text{ft - kip}$$

$$M_{C2} = \left[h_{bf} + h_w - y.ps + \frac{h_{tf}}{2} \right] C2 \qquad M_{C2} = 316\,\text{ft - kip}$$

$$M_{C3} = \left[h_{bf} + h_w - y_{ps} + \frac{2h_{tf}}{3} \right] C3 \qquad M_{C3} = 59\,\text{ft - kip}$$

$$M_{C4} = \left[h_{bf} + h_w - y_{ps} + \frac{t_{sl}}{2} \right] C4 \qquad M_{C4} = 441\,\text{ft - kip}$$

$$M_{C5} = \left[h_{bf} + h_w + h_{tf} - y_{ps} + \frac{2t_{sl}}{3} \right] C5 \qquad M_{C5} = 330\,\text{ft - kip}$$

Calculate total internal moment.

$$M_{tot} = M_{C1} + M_{C2} + M_{C3} + M_{C4} + M_{C5} + M_{C6} + M_{C7}$$

$$M_{tot} = 1290\,\text{ft - kip}$$

Calculate live load moment.

$$M_w = M_{tot} - M_{dl} - M_{dl\_c}$$

$$M_w = 679\,\text{ft - kip}$$

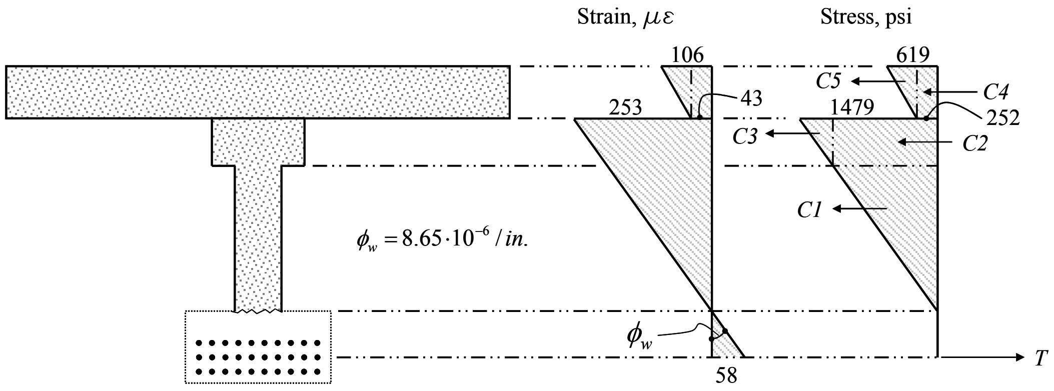

Figure J.7 Neutral Axis at Bottom of Web

J.1.3.1.5 Analysis of Section When Neutral Axis is at Bottom of Slab

When the section is loaded such that the neutral axis is at the bottom of the slab, the stress profile in the concrete is no longer linear. Therefore, an alternative method to those previously used had to be adopted. The method selected was the use of stress-block factors presented in Collins and Mitchell (1997). This method provides the means to analyze the section between the linear-elastic range and the flexural capacity of the member by using a rectangular stress-block. The stress and strain profiles for this portion of the analysis are shown in Figure J.8.

The neutral axis is assumed to be at the bottom of the slab. Therefore, *c* is equal to the depth of the slab, 7.25 in. For a concrete strength of 10,300 psi, which is used because transformed sections are being used, the strain at the maximum compressive stress, ε_c, is assumed to be 0.00256. This value of maximum compressive strain is the value suggested by Collins and Mitchell (1997). The solution requires iteration of the concrete strain at the top of the slab, ε_t, until equilibrium is reached. For this analysis, ε_t was determined to be $278\mu\varepsilon$.

The stress block factors are determined using Eq. J-22 and J-23, which are given in Collins and Mitchell (1997).

$$\beta_1 = \frac{4 - \frac{\varepsilon_t}{\varepsilon_c}}{6 - \frac{2\varepsilon_t}{\varepsilon_c}} \tag{J-22}$$

$$\beta_1 = 0.673$$

$$\alpha_1 \beta_1 = \frac{\varepsilon_t}{\varepsilon_c} - \frac{1}{3}\left(\frac{\varepsilon_t}{\varepsilon_c}\right)^2 \tag{J-23}$$

$$\alpha_1 \beta_1 = 0.105$$

$$\alpha_1 = 0.156$$

Using the stress block factors the compressive force, *C1*, is calculated using Eq. J-24.

$$C1 = f'_{ce} c b_{eff} n_s \alpha_1 \beta_1 \tag{J-24}$$

$$C1 = 571\,\text{kip}$$

Knowing the strain at the top of the slab and the location of the neutral axis, the strain in the prestressing strand can be calculated.

$$\varepsilon_{ps\_NA\_sl} = \frac{f_{ps\_dl}}{E_s} - \varepsilon_{ps\_dl} + \frac{\varepsilon_t}{c}(h_{b\_comp} - c - y_{ps}) \tag{J-25}$$

$$\varepsilon_{ps\_NA\_sl} = 0.00621$$

Because the stress in the strand is in the beyond the yield strength, the stress is calculated using the Ramberg-Osgood stress-strain profile given in Eq. J-26 and the calculated strain.

$$f_{ps\_NA\_sl} = E_s \varepsilon_{ps\_NA\_sl} \left[0.01 + \frac{1 - 0.1}{\left[1 + (120\varepsilon_{ps\_NA\_sl})^{10} \right]^{0.1}} \right] \tag{J-26}$$

$$f_{ps\_NA\_sl} = 176 \text{ ksi}$$

The corresponding force in the strand is:

$$T = f_{ps\_NA\_sl} A_{ps} \tag{J-27}$$

$$T = 571 \,\text{kip}$$

and the corresponding change in strand stress is:

$$\Delta f_{sl} = f_{ps\_NA\_sl} - f_{dl} \tag{J-28}$$

$$\Delta f_{sl} = 42 \,\text{ksi}$$

and the corresponding total internal moment is:

$$M_{NA\_sl} = C1(h_{b\_comp} - y_{ps} - 0.5\beta_1 c) \tag{J-29}$$

$$M_{NA\_sl} = 1941 \text{ ft} - \text{kip}$$

And the corresponding live load moment is:

$$M_s = M_{NA\_sl} - M_{dl} - M_{dl\_c} \tag{J-30}$$

$$M_s = 1331 \text{ ft} - \text{kip}$$

The curvature is calculated based on the top strain and strain in the prestressing strand as shown in Eq. J-31, and the corresponding curvature is:

$$\phi_s = \frac{\varepsilon_t + \frac{\varepsilon_t}{c}(h_{b\_comp} - c - y_{ps})}{h_{cg} - y_{ps}} \tag{J-31}$$

$$\phi_s = 38 \cdot 10^{-6} / in.$$

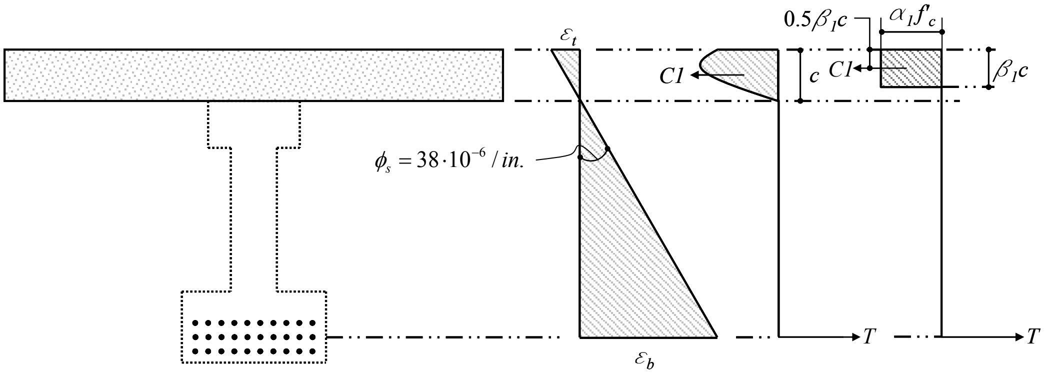

Figure J.8 Stress Diagram when NA is at Bottom Surface of Slab

J.1.3.1.6 Analysis of Section at Flexural Capacity

Determine flexural capacity.

$$M_{ult\_total} = A_{ps} f_{pu} \left[d_p - \frac{A_{ps} f_{pu}}{0.85 f_c b_{eff} n_s} \right] \tag{J-32}$$

$$M_{ult\_total} = 2877 \text{ ft - kip}$$

and the corresponding live load moment is:

$$M_{ult} = M_{ult\_total} - M_{dl} - M_{dl\_c} \tag{J-33}$$

$$M_{ult} = 2267 \text{ ft-kip}$$

and the corresponding change in stress in the strand is:

$$\Delta f_{ult} = f_{pu} - f_{dl} \tag{J-34}$$

$$\Delta f_{ult} = 115 \text{ ksi}$$

J.1.3.2 Live Load Moment at Each Index Stress Level

The live load moment for each index stress level is calculated using transformed, composite section properties.

Moment at index stress of $6\sqrt{f'_{ce}}$:

$$M_6 = (6\sqrt{f'_{ce}} - f_{b\_dl\_c})\frac{I_{comp}}{y_{comp}} \tag{J-35}$$

$$M_6 = 841 \text{ ft-kip}$$

Moment at index stress of $7.5\sqrt{f'_{ce}}$:

$$M_{7.5} = (7.5\sqrt{f'_{ce}} - f_{b\_dl\_c})\frac{I_{comp}}{y_{comp}} \tag{J-36}$$

$$M_{7.5} = 955 \text{ ft-kip}$$

Moment at index stress of $12\sqrt{f'_{ce}}$:

$$M_{12} = (12\sqrt{f'_{ce}} - f_{b\_dl\_c})\frac{I_{comp}}{y_{comp}} \tag{J-37}$$

$$M_{12} = 1298 \text{ ft-kip}$$

The results of the analyses are plotted in Figure J.9. Assuming a linear change in applied moment as a function of strand stress between the load levels analyzed, a backbone curve was developed from which the strand stress range was estimated.

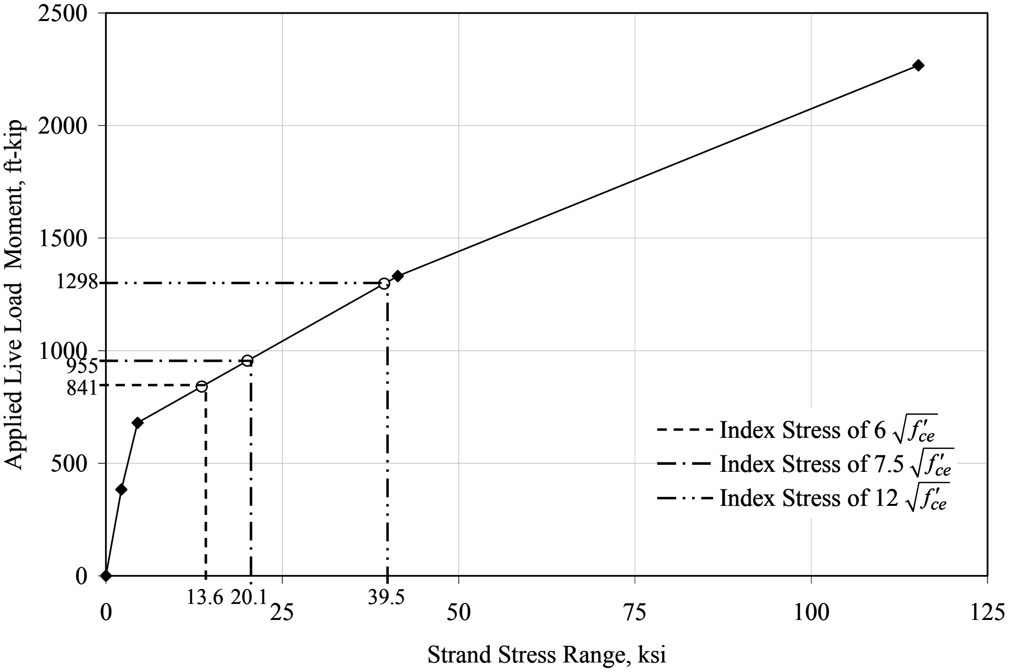

Figure J.9 Applied Moment as a Function of the Change in Strand Stress for Chandler Creek Interior Beam

J.2 Results of Analysis of Chandler Creek Interior Beam Using Specified and Quality Control Material and Section Properties

Table J.2 Summary of Analysis Results for Chandler Creek Using Specified Material and Section Properties

Analysis	Total Moment (ft-kip)	Live Load Moment (ft-kip)		Stress in the Strand (ksi)	Strand Stress Range (ksi)	
Non-Composite Dead Load	571	—	—	135.8	—	—
Full Dead Load	610	—	0	136.1	—	0
Decompression of Bottom Fiber	990	M_{bf}	380	139.1	Δf_{fs}	3.0
NA at Bottom of Web	1326	M_w	716	143.0	Δf_w	6.9
NA at Bottom of Slab	2363	M_{sl}	1753	214.7	Δf_{sl}	78.6
Ultimate	2831	M_{ult}	2221	250.0	Δf_{ult}	113.9

Table J.3 Summary of Analysis Results for Chandler Creek Using Quality Control Material and Section Properties

Analysis	Total Moment (ft-kip)	Live Load Moment (ft-kip)		Stress in the Strand (ksi)	Strand Stress Range (ksi)	
Non-Composite Dead Load	571	—	—	135.1	—	—
Full Dead Load	610	—	0	135.3	—	0
Decompression of Bottom Fiber	995	M_{bf}	385	137.7	Δf_{fs}	2
NA at Bottom of Web	1307	M_w	697	141.1	Δf_w	5.8
NA at Bottom of Slab	2022	M_{sl}	1412	183.5	Δf_{sl}	48.2
Ultimate	2869	M_{ult}	2259	250.0	Δf_{ult}	114.7

J.3 RESULTS OF ANALYSIS OF INTERIOR BEAM OF OTHER BRIDGES IN THIS STUDY USING ESTIMATED IN SITU MATERIAL AND SECTION PROPERTIES

Table J.4 Summary of Analysis Results for Chandler Creek 40-ft Span Using Estimated In Situ Material and Section Properties

Analysis	Total Moment (ft-kip)	Live Load Moment (ft-kip)		Stress in the Strand (ksi)	Strand Stress Range (ksi)	
Non-Composite Dead Load	222	—	—	135.8	—	—
Full Dead Load	238	—	0	136.1	—	0
Decompression of Bottom Fiber	533	M_{bf}	295	139.1	Δf_{fs}	2.9
NA at Bottom of Web	633	M_{w}	395	143.0	Δf_{w}	5.2
NA at Bottom of Slab	805	M_{sl}	567	214.7	Δf_{sl}	20.2
Ultimate	1365	M_{ult}	1127	250.0	Δf_{ult}	114.2

Table J.5 Summary of Analysis Results for Lake LBJ Using Estimated In Situ Material and Section Properties

Analysis	Total Moment (ft-kip)	Live Load Moment (ft-kip)		Stress in the Strand (ksi)	Strand Stress Range (ksi)	
Non-Composite Dead Load	673	—	—	132.3	—	—
Full Dead Load	718	—	0	132.6	—	0
Decompression of Bottom Fiber	1115	M_{bf}	397	134.8	Δf_{fs}	2.2
NA at Bottom of Web	1510	M_{w}	792	139.0	Δf_{w}	6.4
NA at Bottom of Slab	2412	M_{sl}	1694	185.4	Δf_{sl}	52.8
Ultimate	3387	M_{ult}	2668	250.0	Δf_{ult}	117.4

Table J.6 Summary of Analysis Results for Lampasas River Using Estimated In Situ Material and Section Properties

Analysis	Total Moment (ft-kip)	Live Load Moment (ft-kip)		Stress in the Strand (ksi)	Strand Stress Range (ksi)	
Non-Composite Dead Load	817	—	—	136.4	—	—
Full Dead Load	878	—	0	136.8	—	0
Decompression of Bottom Fiber	1020	M_{bf}	142	137.6	Δf_{fs}	0.8
NA at Bottom of Web	1473	M_{w}	595	141.8	Δf_{w}	5.0
NA at Bottom of Slab	2709	M_{sl}	1831	210.8	Δf_{sl}	74.0
Ultimate	3323	M_{ult}	2445	250.0	Δf_{ult}	113.2

Table J.7 Summary of Analysis Results for Willis Creek Using Estimated Material and Section Properties

Analysis	Total Moment (ft-kip)	Live Load Moment (ft-kip)		Stress in the Strand (ksi)	Strand Stress Range (ksi)	
Non-Composite Dead Load	559	—	—	136.6	—	—
Full Dead Load	605	—	0	136.8	—	0
Decompression of Bottom Fiber	795	M_{bf}	190	137.8	Δf_{fs}	1.0
NA at Bottom of Web	1140	M_{w}	535	141.7	Δf_{w}	4.9
NA at Bottom of Slab	2184	M_{sl}	1579	213.3	Δf_{sl}	76.5
Ultimate	2647	M_{ult}	2042	250.0	Δf_{ult}	113.2

Table J.8 Summary of Analysis Results for Wimberley Using Estimated In Situ Material and Section Properties

Analysis	Total Moment (ft-kip)	Live Load Moment (ft-kip)		Stress in the Strand (ksi)	Strand Stress Range (ksi)	
Non-Composite Dead Load	186	—	—	128.8	—	—
Full Dead Load	202	—	0	128.9	—	0.0
Decompression of Bottom Fiber	707	M_{bf}	505	133.1	Δf_{fs}	4.2
NA at Bottom of Web	835	M_w	633	136.6	Δf_w	7.7
NA at Bottom of Slab	1239	M_{sl}	1037	174.2	Δf_{sl}	45.3
Ultimate	1861	M_{ult}	1659	250	Δf_{ult}	121.1

APPENDIX K

Fatigue Specimen Material Properties

K.1 PROPERTIES OF CONCRETE USED IN FATIGUE TEST SPECIMENS

Two concrete mixtures were used to fabricate of the test specimens. The concrete placed in the web was a normal weight concrete, with a design compressive strength of 10,000 psi, a ¾-in. nominal maximum aggregate size and had the mixture proportions summarized in Table K.1. Two admixtures manufactured by Master Builders, Inc. were used to facilitate placement of the concrete. Rheobuild® 1000 was used to increase and maintain a high plasticity of the concrete during the placing process and conforms to ASTM C 494 requirements for Type A, water-reducing, and Type F, water-reducing and high-range, chemical admixtures. Pozzolith® 300R was used to retard the setting time of the concrete and conforms to ASTM C 494 requirements for Type B, retarding, and Type D, water-reducing and retarding, chemical admixtures.

The concrete placed in the slab was a normal weight concrete, with a design compressive strength of 5,000 psi, a ⅜-in. nominal maximum aggregate size and had the mixture proportions summarized in Table K.2. Pozzolith® 322N was used to increase and maintain the plasticity of the concrete during the placing process and conforms to ASTM C 494 requirements for Type A, water-reducing, chemical admixtures.

The web concrete was wet cured using moist burlap for twenty hours, at which time the concrete had achieved strength sufficient for release of the tension in the prestressing strand. After release, all formwork remained in place to allow for the placement of the slab. Approximately twenty-four hours after release of the prestressing strand, the slab concrete was placed. The slab concrete was wet cured using moist burlap until the beams were removed from their forms, which occurred approximately four days after placement of the slab concrete.

In addition to the temperature-controlled curing method described in Chapter 9, the Sure-Cure cylinders were cured with moist burlap for the same period of time as the web concrete. All other cylinders were cured in capped-plastic molds at the same ambient conditions as the beams until they were tested.

Table K.1 Mixture Proportions of Concrete Placed in Web of Test Specimens

Material	Quantity per Cubic Yard
Coarse Aggregate (¾ in. maximum aggregate)	2034 lb
Fine Aggregate	1232 lb
Portland Cement – Type 3	665 lb
Water	220 lb
High-Range Water Reducer (Rheobuild® 1000)	173 oz
Retarder (Pozzolith® 300R)	23 oz

Table K.2 Mixture Proportions of Concrete Placed in Slab of Test Specimens

Material	Quantity per Cubic Yard
Coarse Aggregate (⅜ in. maximum aggregate)	1625 lb
Fine Aggregate	1552 lb
Portland Cement – Type 1	564 lb
Water	180 lb
Water Reducer (Pozzolith® 322N)	17 oz

The unit weight of the concrete used in the web and slab of the specimens was measured for use in the analysis of the specimens. At various ages, four cylinders were weighed in order to determine the unit weight. These data are summarized in Table K.3. The measured unit weight of the concrete used in the web and slab were determined to be 150 lb/ft^3 and 145 lb/ft^3, respectively. The variation over time of these measured unit weights was less than 2%.

Table K.3 Unit Weight of Concrete used in Test Specimens

	Age (days)	Weight (lb)	Unit Weight (lb/ft^3)
Concrete in the Web	1*	8.86	152
		8.84	152
		8.86	152
		8.78	151
	41	8.78	151
		8.78	151
		8.82	152
		8.80	151
	140	8.78	151
		8.72	150
		8.74	150
		8.70	150
	Average	8.79	151
	Coefficient of Variation		1%
Concrete in the Slab	41	8.42	145
		8.42	145
		8.46	145
		8.40	144
	140	8.36	144
		8.42	145
		8.42	145
		8.42	145
	Average	8.42	145
	Coefficient of Variation		0.3%

* indicates Sure-Cure cylinder used to determine unit weight.

The cylinders made from each concrete mixture were used to evaluate the compressive strength and elastic modulus of the concrete. The compression tests were performed in accordance with ASTM C 39. The elastic modulus tests were performed in accordance with ASTM C 469. All the compression and elastic modulus tests were performed on a Forney model LT-0806-01 test machine at the Concrete Durability Center Laboratory located on the J.J. Pickle Research

Campus of the University of Texas at Austin. All cylinders were tested with non-bonded caps in accordance with ASTM C 1231.

The results of compressive strength tests on the Sure-Cure cylinders and standard cylinders made from concrete used in the web of the test specimens are summarized in Table K.4 and

Table K.5, respectively, and shown in Figure K.1. The Sure-Cure cylinder test results show that the concrete had achieved 61% of its design compressive strength after twenty hours. The results from the standard cylinders show that the concrete had achieved 108% of its design compressive strength at 28 days. The concrete continued to gain strength and after 190 days had achieved a compressive strength of 12,700 psi, 127% of its design compressive strength.

The results of compressive strength tests on the standard cylinders made from concrete used in the slab of the test specimens are summarized in Table K.6, and shown in Figure K.1. The results from the standard cylinders show that the concrete had achieved 124% of its design compressive strength at 26 days. The concrete continued to gain strength and after 188 days had achieved a compressive strength of 6800 psi, 136% of its design strength.

Table K.4 Compressive Strength Test Results of Concrete Placed in Web of Test Specimens using Sure-Cure Cylinders

Beam	Compressive Strength (psi)	
	Cylinder 1	Cylinder 2
1	††	6397
2	6419	6295
3	6247	**
4	6099	**
5	5871	6537
6	5254	5428
Average Strength at 20-hours (psi)		6072
Coefficient of Variation		7.6%

†† indicates cylinder was not suitable for compression testing.
** indicates that cylinder was used for an elastic modulus test.

Table K.5 Compressive Strength Test Results on Standard Cylinders from Concrete used in the Web of Fatigue Specimens

Cylinder ID	Date Tested	Elapsed Time From Placement (days)	Compressive Strength (psi)	Average Compressive Strength (psi)
1	5-Nov-02	7	9255	9200
2	5-Nov-02	7	9161	
4	12-Nov-02	14	10146	10100
5	12-Nov-02	14	10041	
6	19-Nov-02	20	9587	10200
7	19-Nov-02	20	10638	
8	19-Nov-02	20	10266	
9	26-Nov-02	28	10887	10800
10	26-Nov-02	28	10659	
11	3-Dec-02	35	10511	10700
12	3-Dec-02	35	10918	
13	12-Dec-02	44	11014	11000
14	12-Dec-02	44	10934	
15	4-Feb-03	98	11762	12000
16	4-Feb-03	98	12080	
19	5-Mar-03	127	11029	11600
20	5-Mar-03	127	12099	
21	18-Mar-03	139	12463	12600
22	18-Mar-03	139	12637	
25	7-May-03	190	12839	12700
26	7-May-03	190	12602	

Table K.6 Compressive Strength Test Results on Standard Cylinders from Concrete used in the Slab of Fatigue Specimens

Cylinder ID	Date Tested	Elapsed Time From Placement (days)	Compressive Strength (psi)	Average Compressive Strength (psi)
1	5-Nov-02	5	4909	4800
2	5-Nov-02	5	4763	
4	12-Nov-02	12	5565	5800
5	12-Nov-02	12	6007	
6	19-Nov-02	19	5574	5800
7	19-Nov-02	19	5894	
8	21-Nov-02	21	5955	5800
9	21-Nov-02	21	5445	
10	21-Nov-02	21	5878	
11	26-Nov-02	26	6348	6200
12	26-Nov-02	26	5986	
13	6-Dec-02	36	5951	6000
14	6-Dec-02	36	5960	
15	12-Dec-02	42	6306	6200
16	12-Dec-02	42	6026	
17	4-Feb-03	96	6416	6300
18	4-Feb-03	96	6181	
21	5-Mar-03	125	6785	6700
22	5-Mar-03	125	6713	
23	18-Mar-03	138	6755	6900
24	18-Mar-03	138	7028	
25	7-May-03	188	6945	6800
26	7-May-03	188	6637	

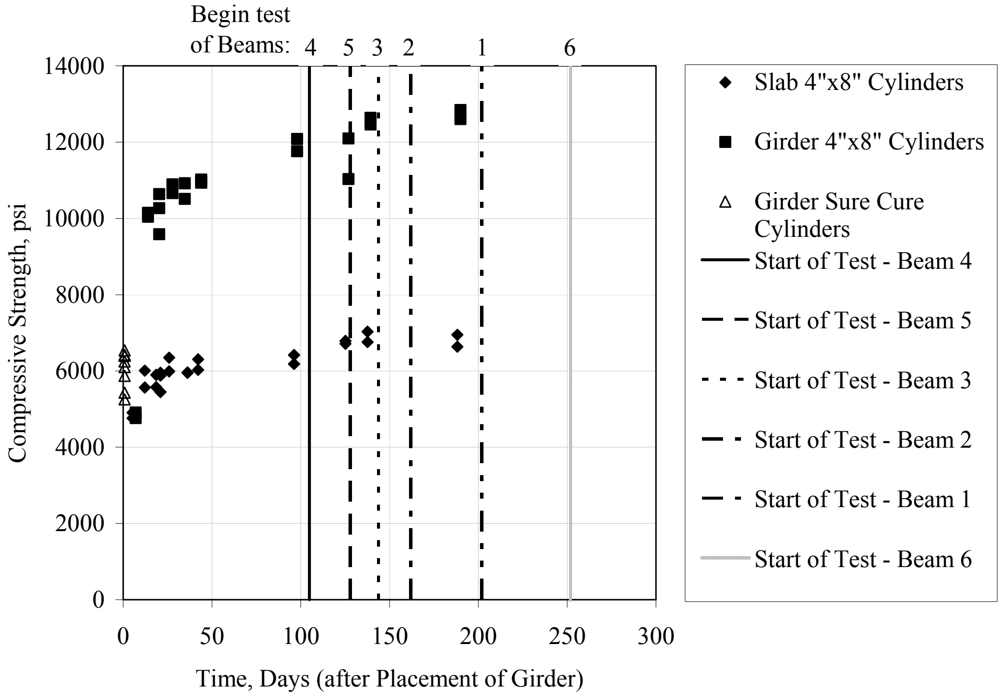

Figure K.1 Variation of Concrete Compressive Strength with Age

The measured modulus of elasticity was calculated using Equation K.1 as described in ASTM C 39.

$$E = \frac{(S_2 - S_1)}{\varepsilon_2 - \varepsilon_1} \qquad \text{(K.1)}$$

where:

E = chord modulus of elasticity, psi,

S_1 = measured stress corresponding to a longitudinal strain, ε_1, psi,

S_2 = measured stress corresponding to 40% of ultimate load, psi,

ε_1 = longitudinal strain of 0.00005, and

ε_2 = measured longitudinal strain produced by stress S_2.

Three loading cycles were run on each cylinder. Measured data and resulting modulus of elasticity on Sure-Cure cylinders and standard cylinders from concrete placed in the webs of the test specimens are summarized in Table K.7 and Table K.8, respectively. Measured data and resulting modulus of elasticity on standard cylinders from concrete placed in the slabs of the test specimens are summarized in Table K.9. These data are also shown graphically in Figure K.2.

Although the measured modulus of elasticity was used in all analysis on the test specimens, Equation K.2, from ACI 318-02, was used for comparative purposes.

$$E_{ACI} = 33\omega^{1.5}\sqrt{f'_c} \tag{K.2}$$

where:

E_{ACI} = ACI estimate of modulus of elasticity, ksi,

f'_c = compressive strength of the concrete at the time modulus test, psi,

ω = unit weight of the concrete, lb/ft^3.

Equation K.2 is a function of the unit weight of the concrete and compressive strength. The measured unit weights and results of compressive strength tests previously discussed were used in the calculations. The compressive strength used was the average measured compressive strength of tests conducted at the same time as the modulus test.

As expected, the elastic modulus increased as the compressive strength of the concrete increased. The measured modulus of elasticity was within 10% of the modulus calculated using the ACI equation.

Table K.7 Modulus of Elasticity Test Results from Sure-Cure Cylinders

Measured Value	Beam 3, Cylinder 2			Beam 4, Cylinder 2		
			Cycle 3			Cycle 3
S_1 (psi)	348	310	357	386	390	402
S_2 (psi)	2484	2484	2481	2467	2451	2463
ε_2	0.00045	0.00046	0.00046	0.00045	0.00045	0.00045
E (ksi)	5300	5250	5100	5300	5200	5200
Average Measured E (ksi)				5200		
Coefficient of Variation				1%		
ACI Estimate, E_{ACI} (ksi)				4700		
E/E_{ACI}				1.1		

Table K.8 Modulus of Elasticity Test Results from Standard Cylinders on Web Concrete

Cylinder ID	Age (days)	Cycle	S_1 (psi)	S_2 (psi)	ε_2	E (ksi)	Average Measured E (ksi)	ACI Estimate (ksi)
3	7	1	532	3728	0.00061	5717	5700	5800
		2	574	3718	0.00060	5717		
		3	510	3726	0.00061	5751		
17	98	1	414	4751	0.00078	5926	6000	6600
		2	374	4763	0.00078	5997		
		3	390	4760	0.00078	5971		
18	98	1	320	4775	0.00078	6087	6100	
		2	341	4770	0.00078	6052		
		3	334	4770	0.00078	6061		
23	172	1	421	5033	0.00078	6302	6300	6800
		2	409	5031	0.00079	6238		
		3	426	5050	0.00079	6241		
24	172	1	367	5036	0.00081	6150	6100	
		2	409	5050	0.00081	6113		
		3	445	5043	0.00081	6057		

Table K.9 Modulus of Elasticity Test Results from Standard Cylinders on Slab Concrete

Cylinder ID	Age (days)	Cycle	S_1 (psi)	S_2 (psi)	ε_2	E (ksi)	Average Measured E (ksi)	ACI Estimate (ksi)
3	5	1	369	1910	0.00061	4083	4100	4000
		2	343	1971	0.00060	4212		
19	96	1	322	2526	0.00050	4897	4900	4600
		2	313	2535	0.00050	4939		
		3	322	2521	0.00050	4887		
20	96	1	315	2519	0.00050	4897	5000	
		2	294	2533	0.00050	4976		
		3	268	2517	0.00050	4997		

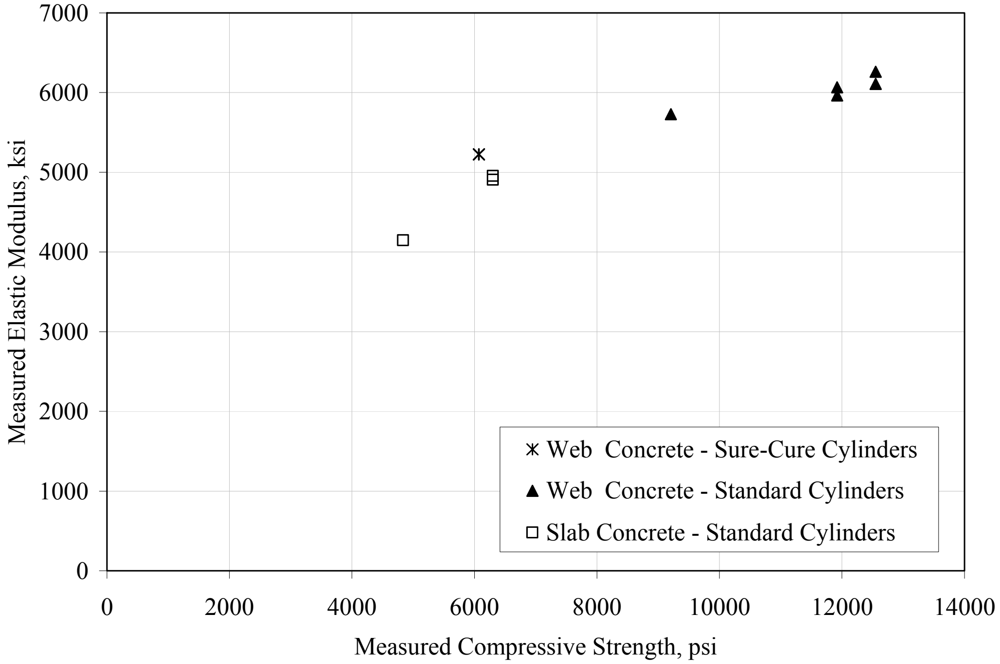

Figure K.2 Measured Modulus of Elasticity versus Measured Compressive Strength of Concrete used in Fatigue Specimens

K.2 MEASURED PROPERTIES OF STRAND USED IN FATIGUE TEST SPECIMENS

The data presented in this section are a summary of data previously reported by Heller (2003). Several types of tests were conducted on the seven-wire, ½-in. diameter, Grade 270 low-relaxation strand used to fabricate of the test specimens. The requirements for the prestressing steel are specified by ASTM A 416 and are summarized in Table K.10.

The tests included tensile strength tests, elastic modulus tests and fatigue tests. The tests were performed on an MTS 220-kip capacity load frame, model 311.31 using MTS TestStar software, version 4.0C.

As shown in Figure K.3 the prestressing strand used in the test specimens either met or exceeded the specified values in Table K.10. Then mean tensile strength, yield strength and percent elongation at rupture were 275 ksi, 245 ksi and 4.1%, respectively.

For use in the analysis of the fatigue specimens presented in Appendix N, a modified Ramberg-Osgood function was fit to the measured stress-strain relationship of the prestressing strand shown in Figure K.3. The general form of the modified Ramberg-Osgood function is shown in Equation K.3, where, f_{ps} is the stress in the prestressing strand, E_s is the measured modulus of elasticity of the prestressing strand, ε_{ps} is the axial strain in the strand that corresponds to f_{ps} and f_{pu} is the measured ultimate stress.

Values of 0.018, 115 and 8 for constants *A*, *B* and *C*, respectively resulted in the function given by Equation K.2. A comparison of the measured stress-strain relationship and the stress-strain relationship based on Equation K.2 is shown in Figure K.4.

$$f_{ps} = E_s \varepsilon_{ps} \left[A + \frac{1 - A}{\left[1 + (B\varepsilon_{ps})^C\right]^{1/C}} \right] \leq f_{pu} \qquad \text{(K.3)}$$

$$f_{ps} = E_s \varepsilon_{ps} \left[0.018 + \frac{1 - 0.18}{\left[1 + (115\varepsilon_{ps})^8\right]^{0.125}} \right] \leq f_{pu} \qquad \text{(K.4)}$$

Table K.10 ASTM A 416 Requirements for Prestressing Steel

Material Property	Requirement
Minimum Tensile Strength	270 ksi
Minimum Yield Stress*	245 ksi
Minimum Elongation at Rupture	3.5%
* Yield stress taken as the stress at an elongation of 1.0 %.	

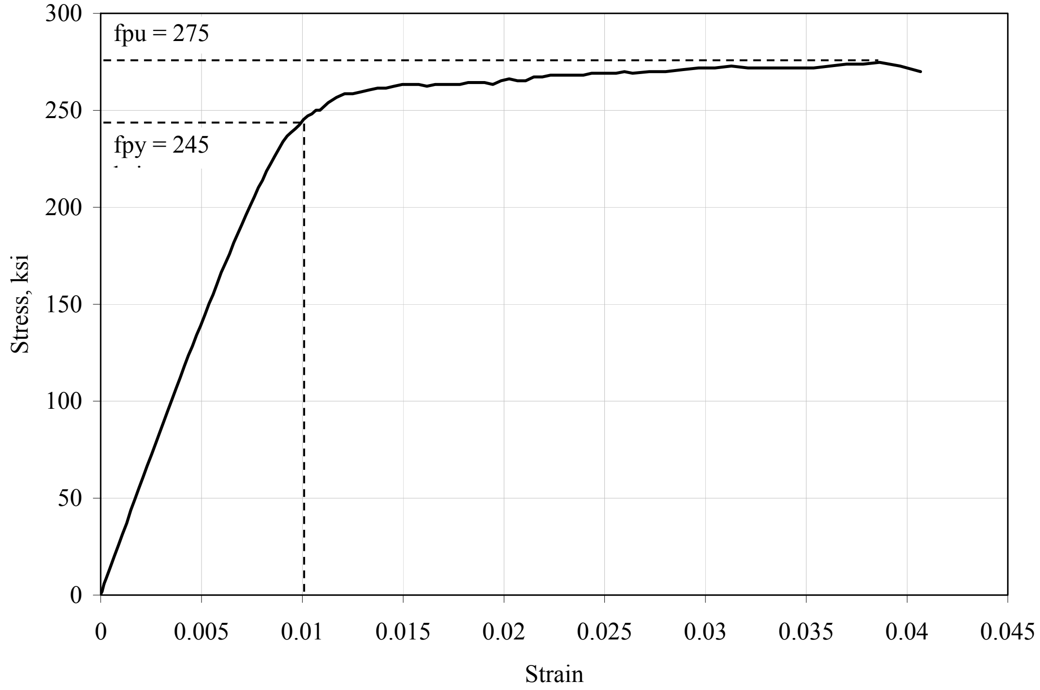

Figure K.3 Representative Tensile Test of Prestressing Strand

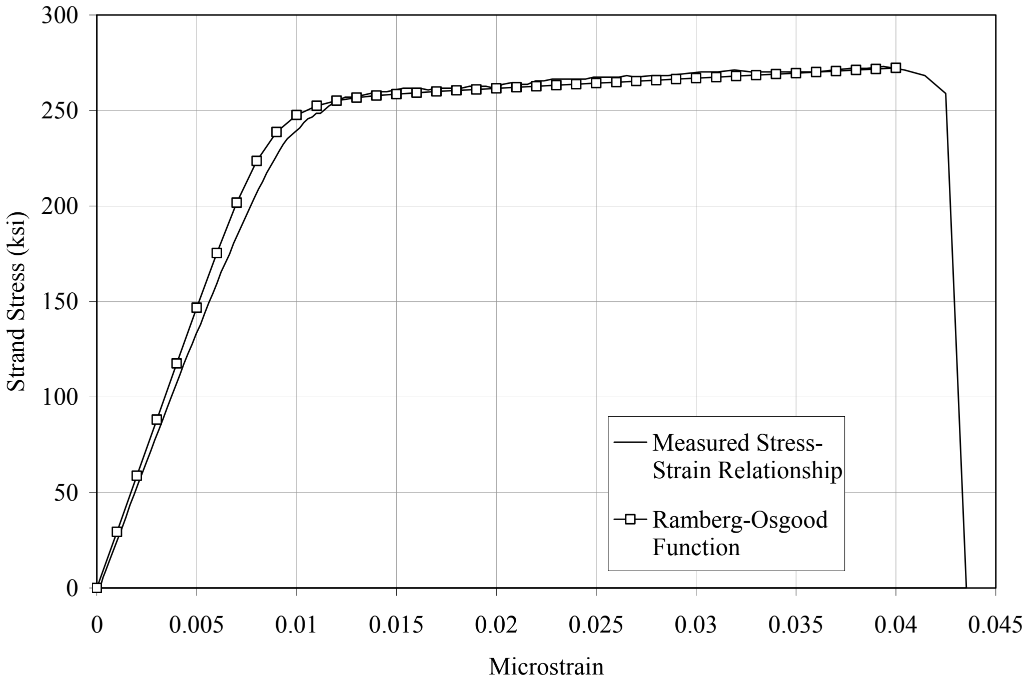

Figure K.4 Comparison of Measured Stress Strain Relationship with Modified Ramberg-Osgood Function

In addition to tensile tests, moduli of elasticity tests were conducted. During the fatigue testing, strain gages on the prestressing strand were used to monitor the effective prestress force and overall beam behavior. These gages were installed on individual wires on the exterior of the strand and were positioned parallel to the axis of the wire on which it was installed. The strain readings measured using these gages did not indicate the average strain parallel to the axis of the strand. The reason for this is the fact that the exterior wires of the strand are wrapped in a helical pattern around the center wire and therefore oriented at a pitch to the axis of the strand. As a result, the strain readings from these gages will be higher that the actual axial strain of the strand, resulting in an increased modulus of elasticity. Therefore, it was necessary to correlate this "apparent modulus" to the axial strand modulus of elasticity. Figure K.5 and

Figure K.6 present data from four test specimens on which these modulus tests were conducted. Both an external extensometer and strain gages were used during the modulus of elasticity tests. Based on the data collected, the inferred apparent modulus and modulus were approximately 31,200 ksi and 29,400 ksi, respectively.

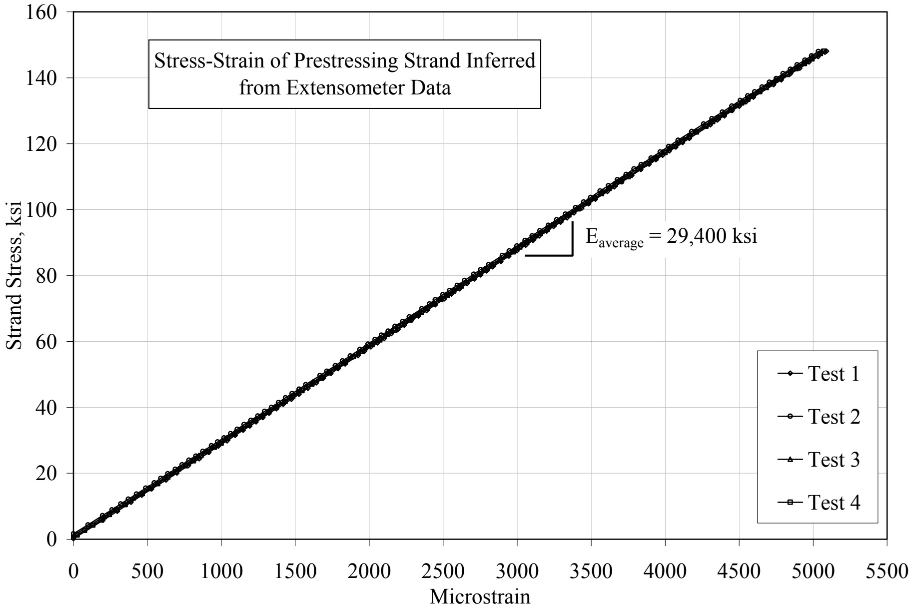

Figure K.5 Applied Axial Stress versus Axial Strain for Strand

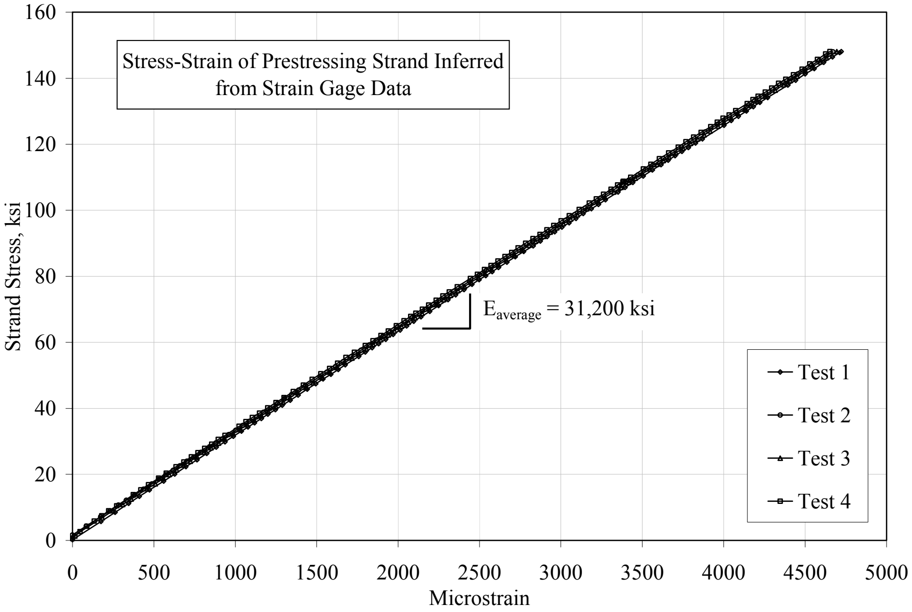

Figure K.6 Applied Axial Stress versus Strain Along the Axis of Wires for Strand

In order to characterize the fatigue behavior of the prestressing strand used in the test specimens, a series of fatigue tests were conducted on the strand. The specimens were tested in accordance with ASTM A 931. Details regarding the testing procedure and equipment used have been previously reported by Heller (2003).

The specimens tested were 4 ft in length, as measured between the grips, and were taken from the same reel as the strand used to fabricate of the beams. The results from these fatigue tests were compared with fatigue tests previously conducted by Paulson, et al. (1983). Figure K.7 clearly shows that the strand fatigue tests conducted at each stress range as part of this work fall within the expected number of cycles as those previously reported by Paulson, et al. (1983).

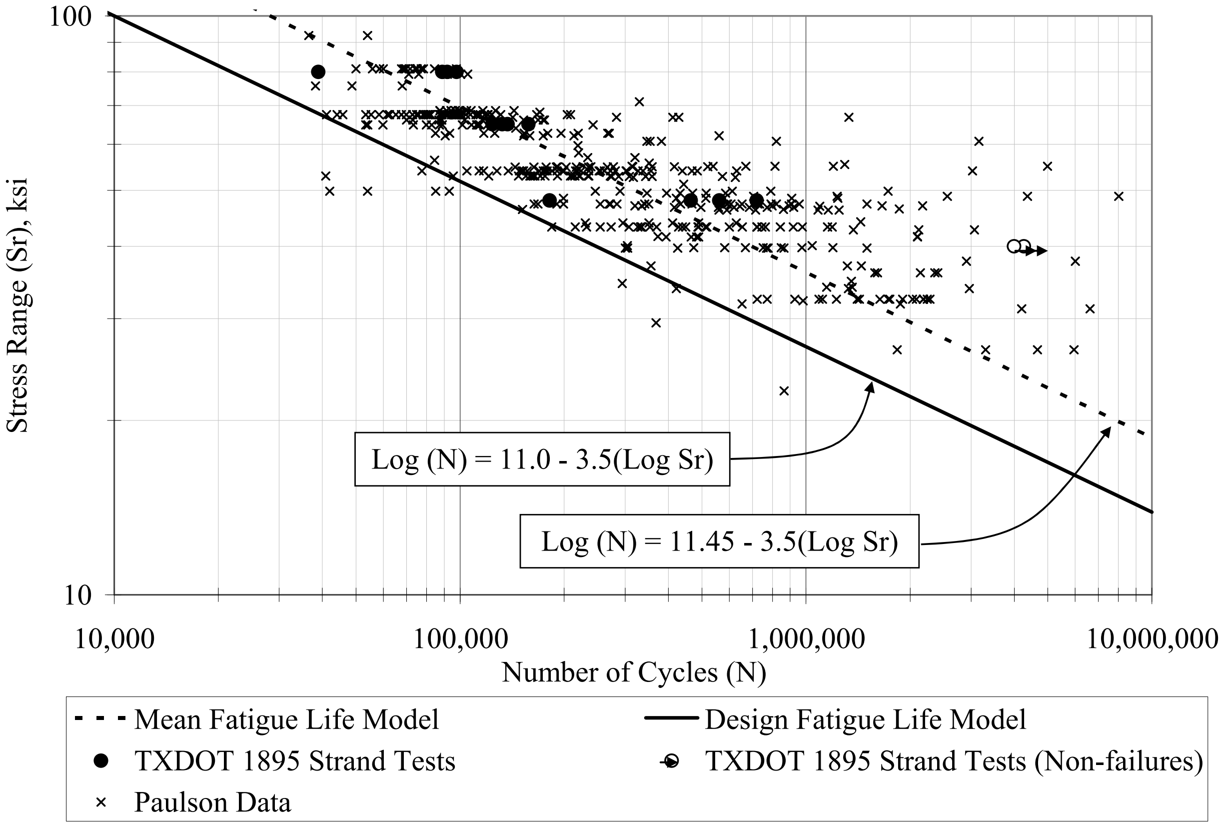

Figure K.7 Axial Fatigue Strength of Strand

APPENDIX L

Evaluation of Prestress Force in Fatigue Specimens

This appendix documents the measured response of the test specimens before the beams were loaded. This information was presented in Sections 5.6.1 and 5.6.2 for Beam 1. A comparison of the idealized response and measured response during load tests is presented in Section L.1. The calculation of prestress losses based on the procedures in the PCI Design Handbook (1992) is presented in Section L.2. A comparison of prestress losses inferred from measured and calculated data is presented in Section L.3.

L.1 COMPARISON OF IDEALIZED RESPONSE AND MEASURED RESPONSE DURING LOAD TESTS

The load test results for Beams 2 through 6 were similar to the results for Beam 1, which were discussed in Chapter 5. A summary of the differences between the idealized and measured response during the load tests is presented in Table L.1. Plots of the variation of strand strain as a function of inferred strand stress during the load tests for Beams 1 through 6 are provided in Figure L.1 through Figure L.3.

Table L.1 Comparison of Idealized and Measured Response during Load Tests for Determining Initial Prestress Force

Strand	Maximum Difference Between Idealized Strain and Measured Strain at During Load Test* ($\mu\varepsilon$)	Corresponding Strand Stress (ksi)
1	57	1.8
2	91	2.8
3	80	2.5
4	81	2.5
5	132	4.1
6	99	3.1
Average	90	2.8

* Value determined as shown in Figure L.1 for Beams 1 and 2. Values for Beams 3 through 6 were determined similarly.

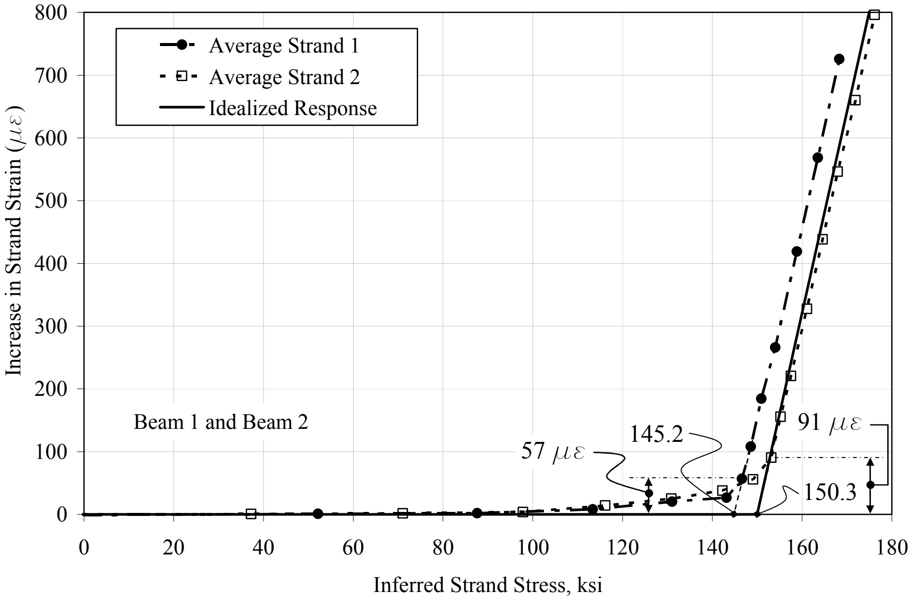

Figure L.1 Variation of Strand Strain and Inferred Strand Stress During Load Test of Strands in Beams 1 and 2

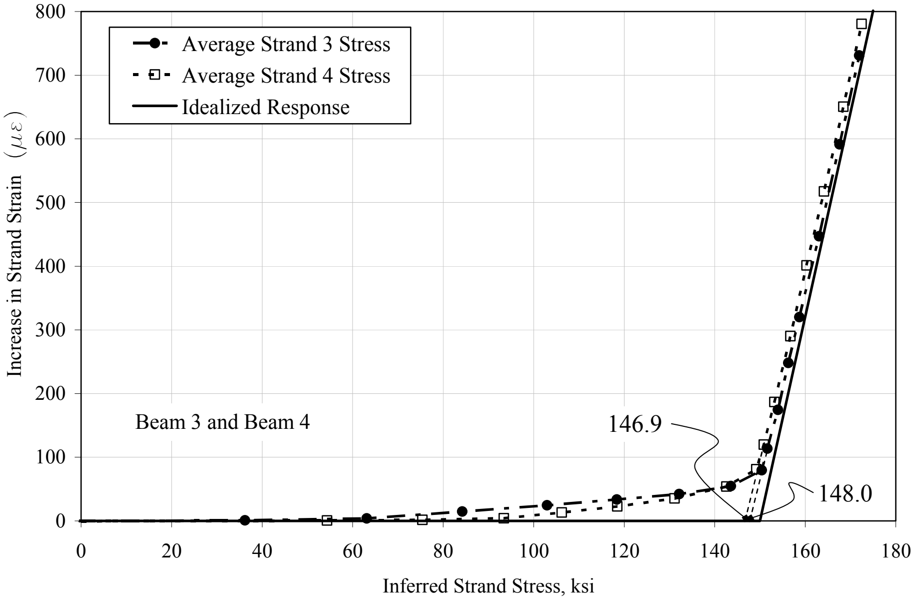

Figure L.2 Variation of Strand Strain and Inferred Strand Stress During Load Test of Strands in Beams 3 and 4

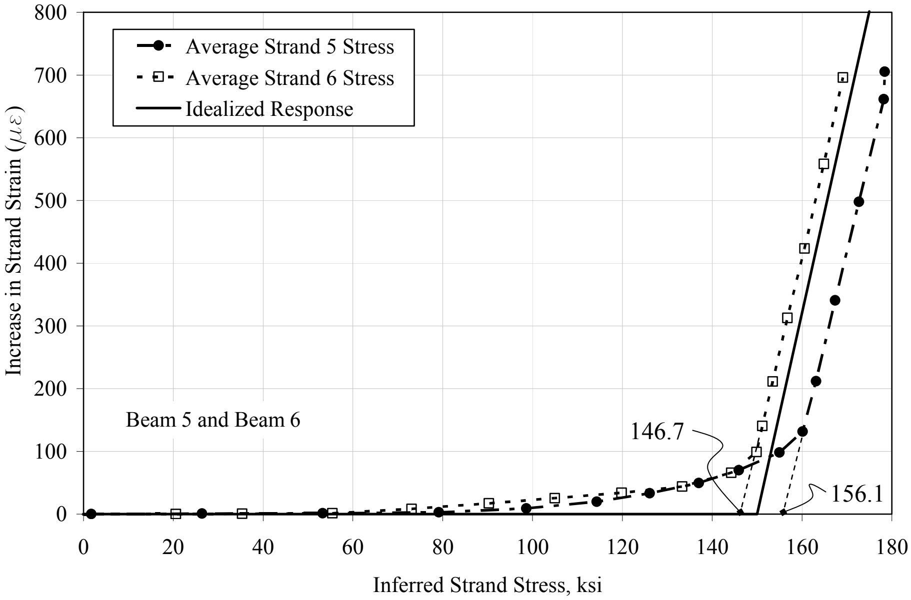

Figure L.3 Variation of Strand Strain and Inferred Strand Stress During Load Test of Strands in Beams 5 and 6

L.2 CALCULATION OF PRESTRESS LOSSES BASED ON AASHTO LRFD

As discussed in Section 5.7, prestress losses in the fatigue specimens were inferred from measured strain data. Prestress losses were calculated using the procedures provided in the PCI Design Handbook (1992). The prestress loss calculations for Beam 1 are documented in this appendix. The result of the analysis is an expression for prestress losses as a function of time. Results for all six test specimens are provided in the form of plots of inferred and calculated prestress losses as a function of time in Section L.3.

L.2.1 Calculation of Prestress Losses for Beam 1

L.2.1.1 Measured Material Properties Used in Prestress Loss Calculations for Beam 1

Beam Concrete Strength at Release, f'_{cmi}	6,070 psi
Modulus of Elasticity of Beam Concrete at Release, E_{cmi}	5,225 ksi
Beam Concrete Strength at Testing, f'_{cm}	12,800 psi
Modulus of Elasticity of Beam Concrete at Testing, E_{cm}	6,200 ksi
Slab Concrete Strength at Testing, f'_{csm}	6,800 psi
Modulus of Elasticity of Slab Concrete at Release, E_{csmi}	5,100 ksi
Yield Strength of Strand, f_{ym}	245 ksi
Breaking Strength of Strand, f_{pum}	275 ksi
Modulus of Elasticity of Strand, E_{sm}	29,400 ksi
Modular Ratio at Release, $n_i = \dfrac{E_{sm}}{E_{cmi}}$	5.62

Modular Ratio at Testing, $n = \frac{E_{sm}}{E_{cm}}$	4.74
Modular Ratio for Slab at Testing, $n_s = \frac{E_{cs}}{E_c}$	0.83

L.2.1.2 Prestressing Information

Area of Prestressing Strand (2-½″ ϕ strands), A_{ps}	0.306 in.^{2}
Measured Initial Effective Prestress, f_{pim}	148 ksi
Measured Initial Effective Prestress Force, P_{im}	45.9 kip

L.2.1.3 Loading Information

Self Weight of Beam, w_{sw}	0.054 kip/ft
Weight of Slab, w_{sl}	0.050 kip/ft
Effective Span Length, L	14.5 ft
Moment Due to Self Weight of Beam, $M_{sw} = \frac{w_{sw}L^2}{8}$	17 in.-kip
Moment Due to Weight of Slab, $M_{sl} = \frac{w_{sl}L^2}{8}$	16 in.-kip

L.2.1.4 Beam Dimensions and Section Properties at Midspan

Gross Area of Concrete, A_{cb}	50 in.^{2}
Center of Gravity of Beam from bottom, y_b	5 in.
Center of Gravity of Strand from bottom, y_{ps}	2 in.
Moment of Inertia of Beam, I_{cb}	417 in.^{4}
Average Eccentricity of Prestressing strand, $e_m = y_b - y_{ps}$	3 in.

L.2.1.5 Calculation of Prestress Losses for Beam 1

Instantaneous prestress losses were calculated based on procedures provided in the PCI Design Handbook (1992). The effects of anchorage set and friction were considered in the determination of the initial prestress force. Therefore, only the effects of elastic shortening are discussed in this section.

Losses due to elastic shortening (*ES*):

$$ES = \frac{K_{es} E_{sm} f_{cir}}{E_{cmi}} \tag{L-1}$$

where K_{es} = 1.0 for pretensioned members,

$$f_{cir} = K_{cir}\left[\frac{P_{im}}{A_{cb}} + \frac{P_{im} e_m{}^2}{I_{cb}}\right] - \frac{M_{sw} e_m}{I_{cb}},$$

K_{cir} = 0.9 for pretensioned members.

$ES = 9.0$ ksi for Beam 1 based on the above equations.

Losses due to shrinkage (*SH*) as a function of time:

$$SH(t) = K_{sh} \varepsilon_{sh} E_{sm}(1 - 0.06VS)\left[\frac{100 - RH}{100}\right] \tag{L-2}$$

where K_{sh} = 1.0 for pretensioned members,

$\varepsilon_{sh} = \frac{t}{35 + t}\varepsilon_{shu}$ (shrinkage strain at time, *t*),

ε_{shu} (nominal ultimate shrinkage strain) = $820\text{x}10^{-6}$, t = time in days from release,

VS = volume to surface ratio, and

RH (average ambient relative humitidy) = 65%.

Losses due to creep (*CR*) as a function of time:

$$CR(t) = C_t \left[\frac{E_{sm}}{E_{cm}} \right] f_{cgp} \qquad \text{(L-3)}$$

where $C_t = \frac{t^{0.6}}{10 + t^{0.6}} C_u$ (creep coefficient at time, *t*),

C_u (ultimate creep coefficient) = 2.35,

t = time in days from release, and

$$f_{gcp} = f_{cir} - \frac{(M_{sl})e_m}{I_{cb}}.$$

f_{gcp} is the concrete stress at the center of gravity of prestressing steel due to the effects of the initial prestress force and permanent loads.

Losses due to relaxation (*R*) as a function of time:

$$R(t) = \left[K_{re} - J(SH(t) + CR(t) + ES)\right]C \qquad \text{(L-4)}$$

where K_{re} = 5,000 for 270 Grade low-relaxation strand,

J = 0.040 for 270 Grade low-relaxation strand, and

C = 0.13 for f_{pi}/f_{pu} = 0.55.

Total losses as a function of time:

The change in effective prestress force as a function of time is calculated using Equation L-5.

$$\Delta f_{peff}(t) = ES + SH(t) + CR(t) + R(t) \tag{L-5}$$

For comparison with the measured losses, the change in strain due to the calculated prestress losses was calculated using Equation L-6.

$$\Delta \varepsilon_{ps}(t) = \frac{\Delta f_{peff}(t)}{E_{sm}} \tag{L-6}$$

L.3 COMPARISON OF INFERRED AND CALCULATED PRESTRESS LOSSES

The results for Beams 2 through 6 were similar to the results previously discussed for Beam 1. A summary of the difference between the changes in strain calculated based on the PCI Design Handbook (1992) and the measured change in strain is presented in Table L.2. Plots of the variation of strand strain and concrete strain at the center of gravity of the prestressing strands as a function of time are shown in Figure L.4 through Figure L.9 for Beams 1 to 6, respectively.

Table L.2 Comparison of Calculated and Measured Changes in Strain for Determining Prestress Losses

Beam	Time* (days)	Change in Strain		Measured as a Percent of PCI at Start of Fatigue Tests
		PCI ($\mu\varepsilon$)	Measured** ($\mu\varepsilon$)	
1	202	968	863	89%
2	162	949	793	84%
3	144	881	728	83%
4	105	841	640	76%
5	128	896	726	81%
6	252	958	769	80%

* From release to start of testing.

** Average of measured change in strain in concrete and steel at time of testing from Figures L.4 through L.9.

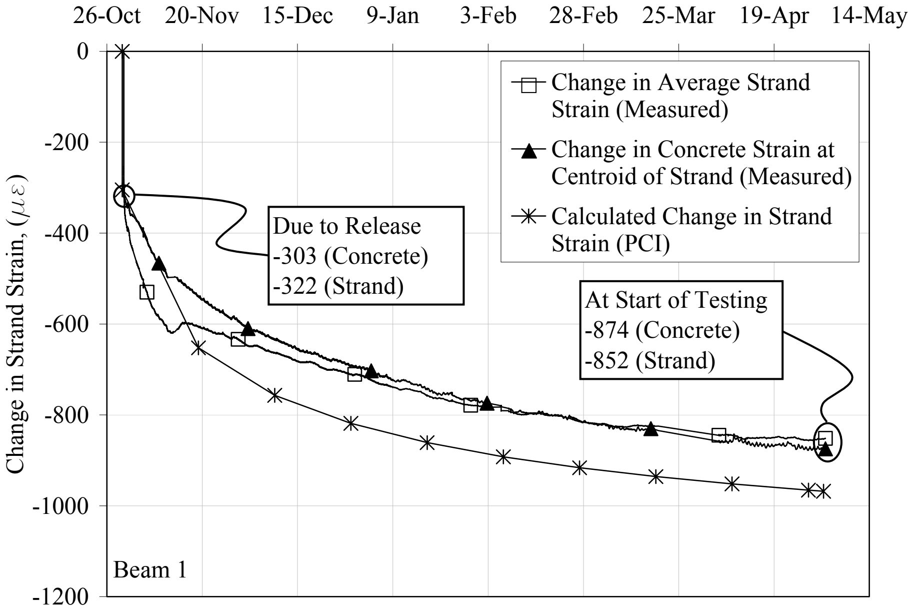

Figure L.4 Variation in Strand and Concrete Strain with Time for Beam 1

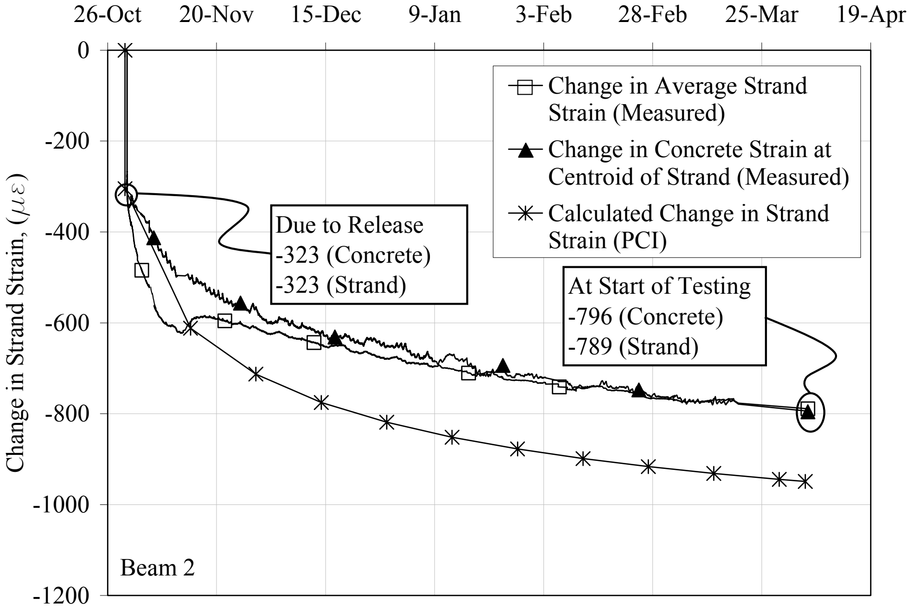

Figure L.5 Variation in Strand and Concrete Strain with Time for Beam 2

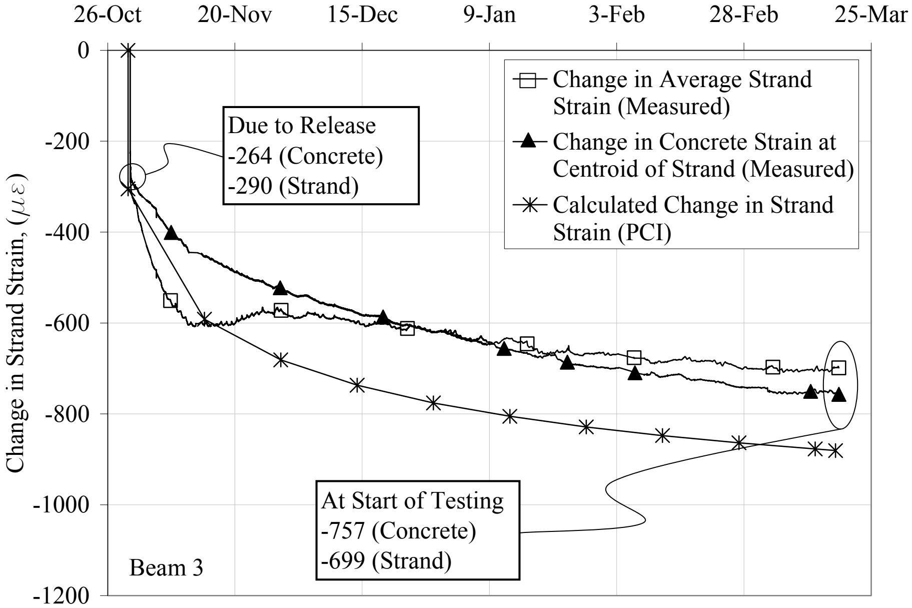

Figure L.6 Variation in Strand and Concrete Strain with Time for Beam 3

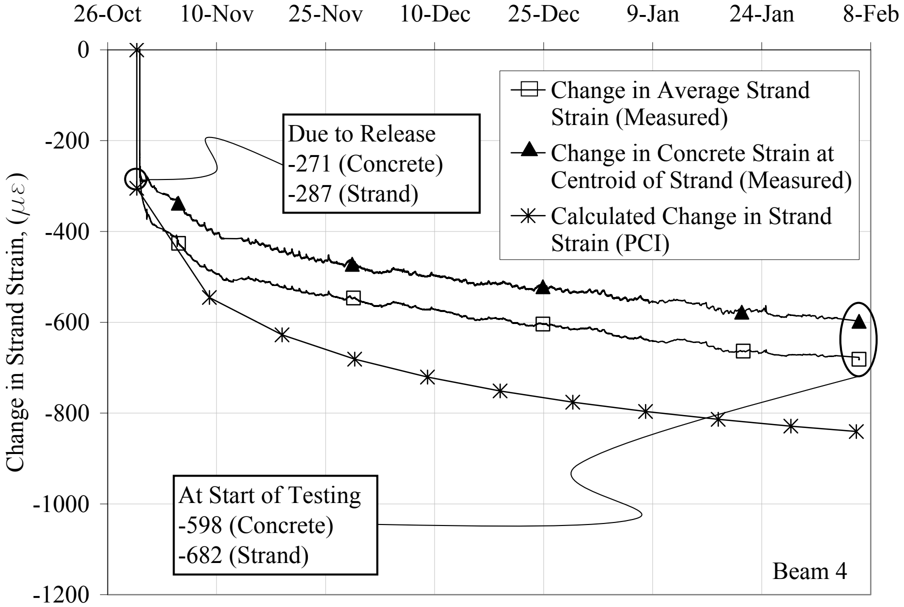

Figure L.7 Variation in Strand and Concrete Strain with Time for Beam 4

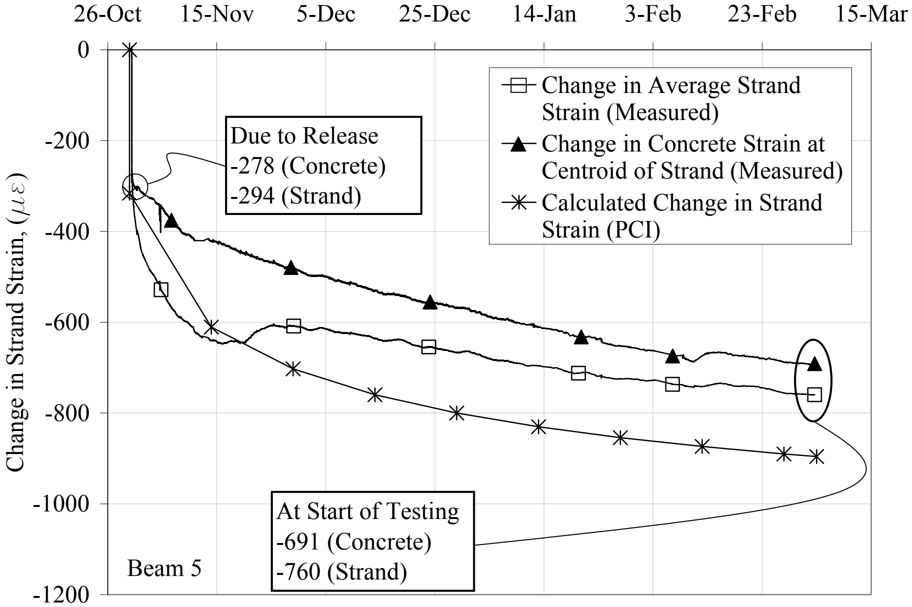

Figure L.8 Variation in Strand and Concrete Strain with Time for Beam 5

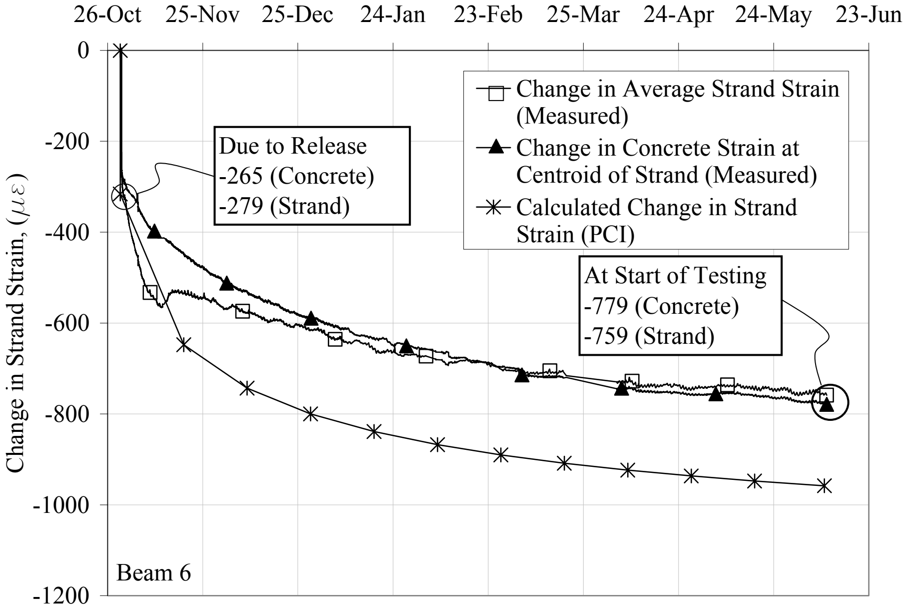

Figure L.9 Variation in Strand and Concrete Strain with Time for Beam 6

APPENDIX M

Analysis of Fatigue Test Specimens

As discussed in Chapter 5, the fatigue beams were analyzed to determine the load levels required to produce the desired median strand stress and strand stress range for the fatigue tests. The analyses of the fatigue specimens incorporated material properties and prestress losses inferred from measured data discussed in Appendices K and L, respectively. The approach to the analysis of the test specimens was similar to the approach used for the analysis of the Chandler Creek interior beams discussed in Appendix J.

For each beam, a plot of applied load versus change in strand stress range at midspan was developed. As discussed in Chapter 5, this plot was developed by performing section analyses at various levels of applied load: (1) the full dead load state, (2) the load when the strain at the bottom fiber of the composite section is zero, (3) the load at which the neutral axis was located at the center of gravity of the prestressing strands, (4) the load at which the neutral axis was located at the bottom surface of the slab, and (5) the load corresponding to the flexural capacity. These correspond to the same load levels that were used to analyze the prototype beam.

The analyses of Beam 4 are presented in Section M.1. Results from the other five beams are given in Section M.2.

M.1 ANALYSIS OF BEAM 4

M.1.1 Material Properties

The measured material properties used in the analyses of Beam 4 are summarized in Table M.1. Data from tests conducted to determine the material properties of the concrete and strand used in the test specimens are discussed in Appendix K.

Table M.1 Material Properties Used for the Analysis of Beam 4

Material Property	Symbol	Measured Value
Web Concrete Strength at Release	f_{ci}	6100 psi
Modulus of Elasticity of Web Concrete at Release	E_{ci}	5200 ksi
Web Concrete Strength at Testing	f_c	12,000 psi
Modulus of Elasticity of Web Concrete at Testing	E_c	6100 ksi
Slab Concrete Strength at From Removal	f_{csi}	4800 psi
Modulus of Elasticity of Slab Concrete at Form Removal	E_{csi}	4200 ksi
Slab Concrete Strength at Testing	f_{cs}	6300 psi
Modulus of Elasticity of Slab Concrete at Testing	E_{cs}	4900 ksi
Modulus of Elasticity of Strand	E_s	29,400 ksi
Apparent Modulus of Elasticity of Strand	E_{sa}	31,200 ksi
Modular Ratio at Release, Strand/Web Concrete	$n_i = E_s / E_{ci}$	5.63
Modular Ratio at Testing, Strand/Web Concrete	$n = E_s / E_c$	4.84
Modular Ratio at Testing, Slab/Web Concrete	$n_{si} = E_{csi} / E_c$	0.79
Modular Ratio at Testing, Slab/Web Concrete	$n_s = E_{cs} / E_c$	0.81

M.1.2 Prestressing Information

As discussed in Chapter 5, measured strains were used to evaluate the level of effective prestress force in each beam up to the time of testing. Table M.2 summarizes the prestressing information used in the analyses of Beam 4. Corresponding information for the five other beams was given in Table 5.12. The initial effective prestress was determined using the procedures discussed in Chapter 5 and Appendix L. The measured changes in strain are based on data recorded from the strain gages on the prestressing strand.

Table M.2 Prestressing Information Used in the Analysis of Beam 4

Measured Initial Effective Prestress	f_{pi}	147.5 ksi
Measured Change in Strain at Release	$\Delta\varepsilon_r$	$287\mu\varepsilon$
Measured Change in Strain at Testing	$\Delta\varepsilon_t$	$683\mu\varepsilon$

The baseline strain measurements for the values reported in Table M.2 correspond to the measured strains in the strand at the time that the concrete was placed.

M.1.3 Loading Information

Table M.3 summarizes the loading information used in the analyses of Beam 4. Using this information, moments due to dead loads and applied live loads were determined. The dead load moments due to the self-weight of the web, weight of the slab and weight of the spreader beam are calculated as shown in Eq. M.1 to M.3. The moment due to the applied load is calculated using Eq. M.4. The calculation of all dead load and live load moments assume the beam is simply supported with the effective span length assumed to be the distance from centerline to centerline of bearing pad.

Table M.3 Summary of Loading Information Used in the Analysis of Beam 4

Self Weight of Web*[†]	w_w	0.0544 kip/ft
Weight of Slab*[††]	w_{sl}	0.0498 kip/ft
Weight of Spreader Beam	W_{spr}	0.44 kip
Overall Beam Length	L	15 ft
Span Length	L_s	14.5 ft
Span Length of Spreader Beam	L_{spr}	4 ft

* Weight includes an allowance for the weight of reinforcement and was assumed to be 3% of the unit weight of the concrete.

[†] Based on measured unit weight of concrete in the web of 152 lb/ft^3.

[††] Based on measured unit weight of concrete in the slab of 145 lb/ft^3.

Moment Due to Weight of Web:
$$M_w = \frac{w_w L_s^2}{8} \tag{M.1}$$

$$M_w = 17.1 \text{ in.-kip}$$

Moment Due to Weight of Slab:
$$M_{sl} = \frac{w_{sl} L_s^2}{8} \tag{M.2}$$

$$M_{sl} = 15.7 \text{ in.-kip}$$

Moment Due to Spreader Beam:
$$M_{spr} = \frac{W_{spr}(L_s - L_{spr})}{4} \tag{M.3}$$

$$M_{spr} = 13.9 \text{ in.-kip}$$

Moment Due to Applied Load:
$$M_a = \frac{P_a(L_s - L_{spr})}{4} \tag{M.4}$$

where P_a is the applied load.

M.1.4 Specimen Dimensions and Section Properties at Midspan for Beam 4

The nomenclature used to describe the dimensions of the non-composite beam section and composite beam section is shown in Figure M.1. The corresponding dimensions are summarized in

Table M.4. Non-composite and composite section properties were calculated for use in the analyses, and are summarized in Table M.5 and Table M.6.

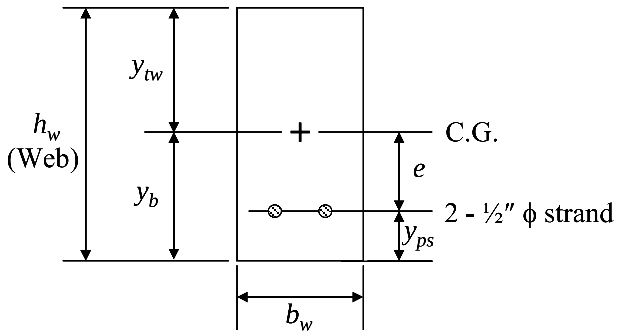

a) Non-composite Beam Section

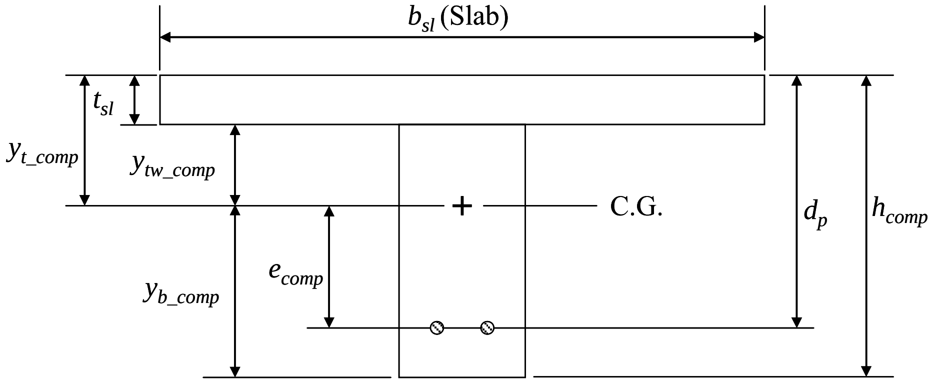

b) Composite Beam Section

Figure M.1 Nomenclature for Beam Dimensions

Table M.4 Dimensions of Fatigue Specimen

Width of Web	b_w	5 in.
Height of Web	h_w	10 in.
Thickness of Slab	t_{sl}	2 in.
Width of Slab	b_{sl}	24 in.
Height of Composite Beam	h_{comp}	12 in.
Depth of Strand	d_p	10 in.
Center of Gravity of Strand from Bottom	y_{ps}	2 in.
Area of Prestressing Strand (2-½″ ϕ strands)	A_{ps}	0.306 in.^{2}

Table M.5 Calculated Gross, Non-Composite Section Properties

Gross Area of Concrete, Web	A_w	50 in.^{2}
Center of Gravity of Web from Bottom	y_b	5 in.
Center of Gravity of Web from Top	y_{tw}	5 in.
Eccentricity of Strand	$e = y_b - y_{ps}$	3 in.
Moment of Inertia of Web	I_w	417 in.^{4}

Table M.6 Calculated Gross, Transformed, Composite Section Properties

Effective Slab Width	$b_{eff} = b_{sl} n_s$	19.5 in.
Area of Beam	A_{comp}	90.1 in.^{2}
Center of Gravity of Beam from Bottom of Web	y_{b_comp}	7.55 in.
Center of Gravity of Beam from Top of Slab	y_{t_comp}	4.45 in.
Center of Gravity of Beam from Top of Web	y_{tw_comp}	2.45 in.
Moment of Inertia of Beam	I_{comp}	1226 in.^{4}
Eccentricity of Strand	$e_{comp} = y_{b\_comp} - y_{ps}$	5.55 in.

M.1.5 Measured Prestress Losses

As discussed in Chapter 5, the change in strain was monitored with strain gages located on the axis of the exterior wires of the prestressing strand. Based on these measured data, the change in the effective prestress was calculated. Equations M.5 and Eq. M.6 were used to calculate the change in effective prestress at release of the prestressing force and prior to the start of fatigue testing.

Change in prestress at release:
$$\Delta f_{ps\_r} = f_{pi} - \Delta\varepsilon_r E_{sa} \tag{M.5}$$
$$\Delta f_{ps\_r} = 9.0\,\text{ksi}$$

Change in prestress at testing:
$$\Delta f_{ps\_t} = f_{pi} - \Delta\varepsilon_t E_{sa} \tag{M.6}$$
$$\Delta f_{ps\_t} = 21.3\,\text{ksi}$$

M.1.6 Analysis of Section at Release

Based on data collected during the removal of the fatigue specimens from their formwork, it is believed that friction between the formwork and the test specimens reduced the effects of the prestress force at release.

The change in strain at the center of gravity of the strands as a function of time, as measured by the embedded strain gage, is shown in Figure M.2. The fatigue specimens were removed from the formwork between 1 pm and 3 pm on November 4, 2002 As highlighted in Figure M.2 a sudden decrease in strand strain was observed during the removal operation for each beam. Figure M.3 is a plot of the same data shown in Figure M.2, however, only the data collected at the time of removal is shown. The time of the change in strain recorded for each beam corresponds with the order in which the beams were removed from the formwork. This order is noted in Figure M.3. Based on the analyses presented in Section 5.6, it was determined that Beams 1 and 2 were likely not restrained by the formwork during removal, however, Beams 3 through 6 were restrained.

To account for this effect, an analysis was performed based on the measured change in strain at the center of gravity of the strands due to the release of the prestressing strands for Beams 3 through 6. The analysis for Beam 4 and results for Beams 3, 5, and 6 are given in Section M.1.6.1. The analysis used for Beams 1 and 2 is given in Section M1.6.2.

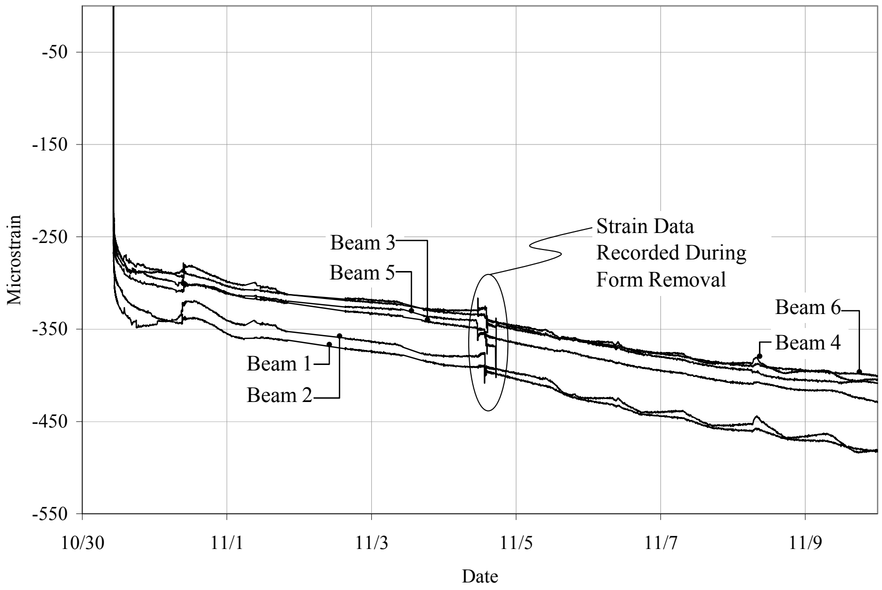

Figure M.2 Change in Strain Measured by Embedded Concrete Gage At Center of Gravity of Prestressing Strands

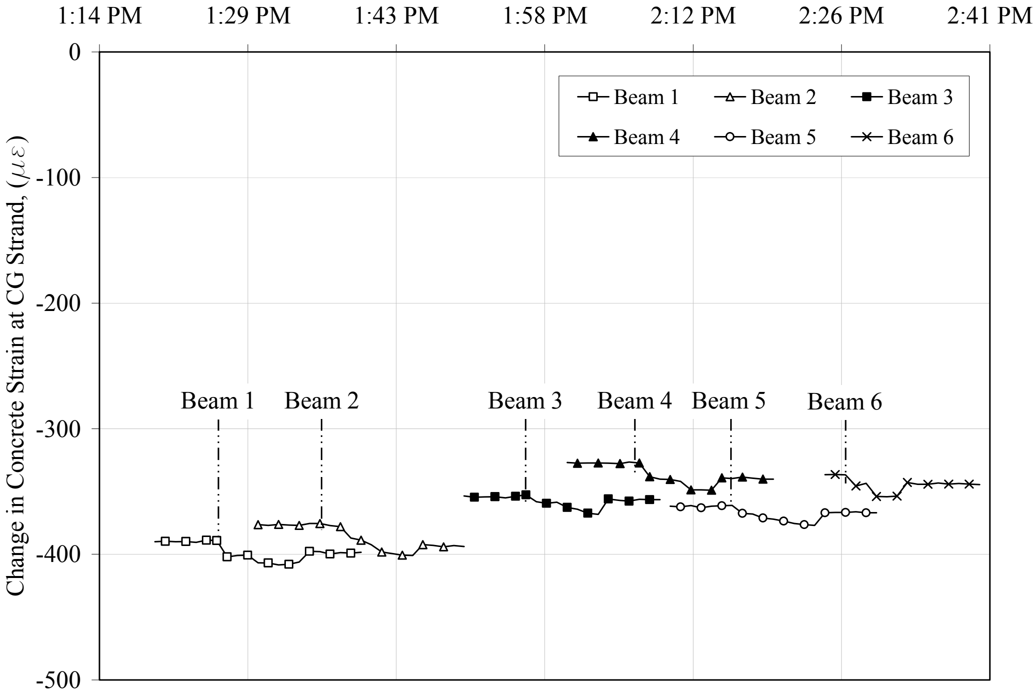

Figure M.3 Measured Change in Strain During Removal of Beams from Forms on November 4, 2002

M.1.6.1 Analysis Used for Beams 1 and 2 at Release

For Beams 1 and 2, the stresses and corresponding strains at release were calculated using the gross section properties of the non-composite beam and the measured initial effective prestress force. The equations used for this analysis are given below. These equations were used because it was likely that Beams 1 and 2 were not restrained by the formwork.

Determine the concrete stress and strain at the bottom fiber of the web.

$$f_{b\_r} = \frac{-f_{pi}A_{ps}}{A_w} + \frac{-f_{pi}A_{ps}ey_b}{I_w} + \frac{M_{sw}y_b}{I_w} \tag{M.20}$$

$$\varepsilon_{b\_r} = \frac{f_{b\_r}}{E_{ci}} \tag{M.21}$$

Determine the concrete stress and strain at the top fiber of the web.

$$f_{tw\_r} = \frac{-f_{pi}A_{ps}}{A_w} + \frac{f_{pi}A_{ps}ey_{tw}}{I_w} - \frac{M_{sw}y_{tw}}{I_w} \tag{M.22}$$

$$\varepsilon_{tw\_r} = \frac{f_{tw\_r}}{E_{ci}} \tag{M.23}$$

Determine the concrete strain at the center of gravity of the prestressing strand and corresponding stress in the prestressing strand.

$$\varepsilon_{ps\_r} = \varepsilon_{b\_r} - \frac{(\varepsilon_{b\_r} - \varepsilon_{tw\_r})y_{ps}}{h_w} \tag{M.24}$$

$$f_{ps\_r} = f_{pi} + \varepsilon_{ps\_r}E_s \tag{M.25}$$

M.1.6.2 Analysis of Beam 4 at Release

Because it is likely that Beam 4 was restrained by the formwork during release the following analysis was performed to account for the effects of the restraint. This method of analysis was also used for Beams 3,5, and 6 because it is likely they were also restrained.

Using the assumed strain profile shown in Figure M.4, equilibrium and compatibility equations were developed from which the moment in the section could be determined. This moment is due to the restraining effect of the formwork and dead load of the web.

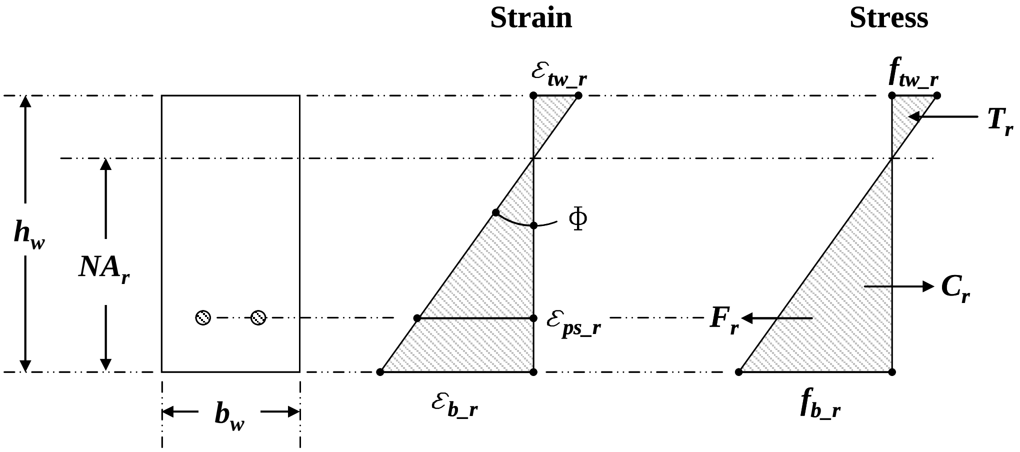

Figure M.4 Strain and Stress Profiles of Test Specimen at Release

Applied Force at Release: $F_r = (f_{pi} - \Delta\varepsilon_r E_s))A_{ps}$ (M.7)

$F_r = 42.4\,\text{kip}$

Compatibility relationships: $\Phi = \dfrac{\varepsilon_{ps\_r}}{NA_r - y_{ps}}$ (M.8)

$$\Phi = \frac{\varepsilon_{tw\_r}}{10 - NA_r} \quad \text{(M.9)}$$

$$\Phi = \frac{\varepsilon_{b\_r}}{NA_r} \quad \text{(M.10)}$$

Based on equilibrium, the applied force, F_r, must equal the sum of the compressive and tensile forces in the concrete. This leads to Eq. M.11 through Eq. M.17.

Equilibrium equations: $$C_r = f_{tw\_r}\frac{b_w(h_w - NA_r)}{2} \quad \text{(M.11)}$$

$$f_{tw\_r} = \varepsilon_{tw\_r}E_{ci} \quad \text{(M.12)}$$

$$C_r = \varepsilon_{tw\_r}E_{ci}\frac{b_w(h_w - NA_r)}{2} \quad \text{(M.13)}$$

$$T_r = f_{b\_r}\frac{b_w NA_r}{2} \quad \text{(M.14)}$$

$$f_{b\_r} = \varepsilon_{b\_r}E_{ci} \quad \text{(M.15)}$$

$$T_r = \varepsilon_{b\_r}E_{ci}\frac{b_w NA_r}{2} \quad \text{(M.16)}$$

$$F_r = C_r - T_r \quad \text{(M.17)}$$

Substituting the compatibility equations, Equations M.8 through M.10, into Euations M13 and M.16 results in equations where the only unknown variable is *NA$_r$*. Eq. M.18 is then written by substituting these new equations into Eq. M.17 and solving for the neutral axis location.

$$NA_r = \frac{1}{2}\frac{-2P_r y_{ps} + \varepsilon_{ps\_r}E_{ci}b_w h_w{}^2}{-F_r + \varepsilon_{ps\_r}E_{ci}b_w h_w} \quad \text{(M.18)}$$

$NA_r = 8.42$ in.

The internal moment at release, M_r, is then calculated using Eq. M.19.

$$M_r = C_r(\frac{1}{3}NA_r - y_{ps}) - T_r(h_w - y_{ps} - \frac{1}{3}(h_w - NA_r)) \quad \text{(M.19)}$$

$$M_r = 23.8 \text{ in.-kip}$$

For use in subsequent analyses of Beam 4, the top and bottom fiber stresses and strains are calculated using Eq. M.11, M.12, M.14, and M.15.

$f_{b\_r} = -2.08 \text{ ksi}$ $\qquad$ $f_{tw\_r} = 0.39 \text{ ksi}$

$\varepsilon_{b\_r} = -399\mu\varepsilon$ $\qquad$ $\varepsilon_{tw\_r} = 75\mu\varepsilon$

M.1.7 Analysis of Section at Full Dead Load State

The analysis of the section at the full dead load state uses the results of the analysis at release as the basis for the calculations. The measured change in strain of the prestressing strand and the change in applied loads are used to calculate the changes in stress and strain in the section and are added to the results from the analysis at release. The results of the analysis at the full dead load state will serve as the basis for subsequent analyses.

For Beams 3 through 6, the change in applied moment between release and dead load prior to testing is calculated using Eq. M.26. The result of this calculation for Beam 4 is shown. The change in moment is the difference between the dead load due to the self-weight of the web, weight of the slab, and weight of the spreader beam, and the internal moment at release previously calculated.

Determine the change in moment from release to the full dead load state:

$$\Delta M = M_{sw} + M_{sl} + M_{spr} - M_r \qquad \text{(M.26)}$$

$$\Delta M = 22.9 \text{ in - kip}$$

For Beams 1 and 2, the change in moment was calculated in a similar manner. Because there was no restraint provided by the formwork and the self-weight was included in the calculations at release, the change in moment for Beams 1 and 2 is due to only the weight of the slab and the spreader beam. The change in moment for Beams 1 and 2 was calculated as follows:

$$\Delta M = M_{sl} + M_{spr} \tag{M.27}$$

The change in prestress force from release to the full dead load state is calculated using the measured strain data given in Table M.2 and was the same for all the beams. The calculation and result for Beam 4 is as follows:

$$\Delta F = (\Delta\varepsilon_r - \Delta\varepsilon_t)E_{sa}A_{ps} \tag{M.28}$$

$$\Delta F = -3.8 \text{ kip}$$

The corresponding effective prestress in the strand at the full dead load state is calculated as follows:

$$f_{ps\_dl} = f_{pi} - (\Delta\varepsilon_t E_{sa}) \tag{M.29}$$

$$f_{ps\_dl} = 126 \text{ ksi}$$

The change in stress and strain in the section are calculated using the change in moment and prestress force using gross, transformed composite section properties as follows. The resulting stain and stress profile is given in Figure M.5.

Determine the stress and strain at the bottom fiber of the web:

$$f_{b\_dl} = f_{b\_r} - \frac{\Delta P}{A_{comp}} - \frac{\Delta P e_{comp} y_{comp}}{I_{comp}} + \frac{(\Delta M) y_{comp}}{I_{comp}} \tag{M.30}$$

$f_{b\_dl} = \text{-}1.77\text{ ksi}$

$$\varepsilon_{b\_dl} = \varepsilon_{b\_r} + \frac{f_{b\_dl} - f_{b\_r}}{E_c} \tag{M.31}$$

$\varepsilon_{b\_dl} = \text{-}348\mu\varepsilon$

Determine the stress and strain at the top fiber of the web:

$$f_{tw\_dl} = f_{t\_r} - \frac{\Delta P}{A_{comp}} + \frac{\Delta P e_{comp} (y_{wt\_comp})}{I_{comp}} + \frac{(\Delta M) y_{wt\_comp}}{I_{comp}} \tag{M.32}$$

$f_{tw\_dl} = 0.346\text{ ksi}$

$$\varepsilon_{tw\_dl} = \varepsilon_{tw\_r} + \frac{f_{tw\_dl} - f_{tw\_r}}{E_c} \tag{M.33}$$

$\varepsilon_{tw\_dl} = 67\mu\varepsilon$

Determine the stress and strain in the bottom fiber of the slab:

$$f_{bs\_dl} = \frac{-\Delta P}{A_{comp}} - \frac{\Delta P e_{comp} y_{tw\_comp}}{I_{comp}} - \frac{(\Delta M) y_{tw\_comp}}{I_{comp}} \tag{M.34}$$

$f_{bs\_dl} = 0.046\text{ ksi}$

$$\varepsilon_{bs\_dl} = \frac{f_{bs\_dl}}{E_c} \tag{M.35}$$

$\varepsilon_{bs\_dl} = 7.6\mu\varepsilon$

Determine the stress and strain in the top fiber of the slab:

$$f_{t\_dl} = \frac{-\Delta P}{A_{comp}} + \frac{\Delta P e_{comp}(y_{t\_comp})}{I_{comp}} + \frac{(\Delta M) y_{t\_comp}}{I_{comp}} \qquad \text{(M.36)}$$

$$f_{t\_dl} = 0.118 \text{ ksi}$$

$$\varepsilon_{t\_dl} = \frac{f_{t\_dl}}{E_c} \qquad \text{(M.37)}$$

$$\varepsilon_{t\_dl} = 19\mu\varepsilon$$

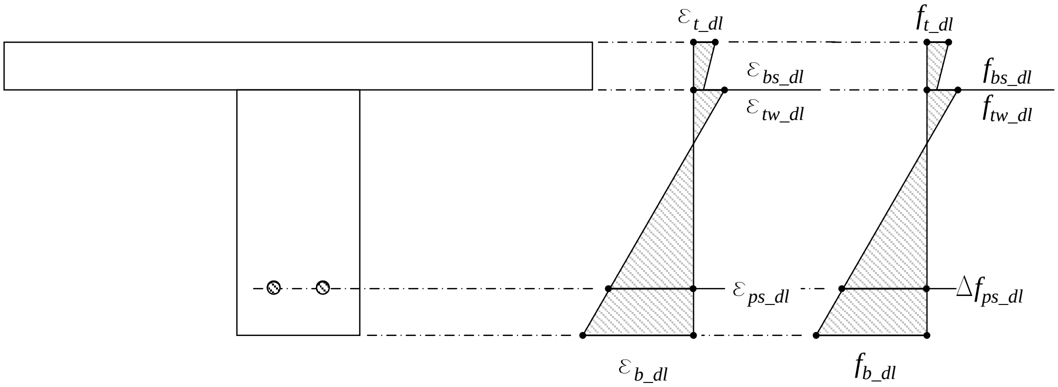

Figure M.5 Strain and Stress Profiles under Full Dead Load

M.1.8 Analysis of Section When the Neutral Axis is at Bottom Fiber

Assuming the linear stress profile shown in Figure M.6, the equilibrium condition when the total compression force equals the tension in the strand was determined by iterating to find the curvature, Φ_{bf_o}, and the corresponding level of applied load at decompression of the bottom fiber. For Beam 4, equilibrium was satisfied at a curvature of $5.3 \cdot 10^{-6} \frac{1}{\text{in.}}$.

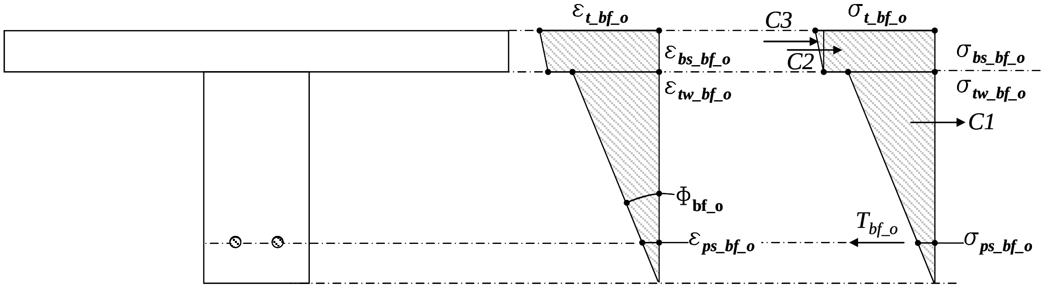

Figure M.6 Stress Diagram when NA is at Bottom Fiber

The tensile force in the strand at decompression is equal to the tensile force in the strand at the full dead load state plus the change in force from the dead load state to decompression of the bottom fiber. The change in force is calculated using the strain at the center of gravity of the prestressing strand at the dead load state, and the strain at decompression using the strain profile in Figure M.6. The tensile force is calculated as follows:

$$T_{bf\_o} = [f_{ps\_dl} + (\varepsilon_{ps\_dl} - \Phi_{bf\_o} y_{ps}) E_s] A_{ps} \tag{M.38}$$

$$T_{bf\_o} = 40.9\ \text{kip}$$

The corresponding change in prestress from the dead load state is calculated as follows:

$$\Delta f_{bf\_o} = \frac{T_{bf\_o}}{A_{ps}} - f_{ps\_dl} \tag{M.39}$$

$$\Delta f_{bf\_o} = 7.48 \text{ ksi}$$

Using the strain profile from Figure M.6 and the curvature, equilibrium can be confirmed by calculating the compressive force in the section.

Compression force in the web:

$$C1 = \Phi_{\mathrm{bf\_o}} h_w E_c \frac{b_w h_w}{2} \tag{M.40}$$

$$C1 = 8.0 \text{ kip}$$

Compression forces in the slab:

$$C2 = [\Phi_{bf\_o} h_w + (\varepsilon_{tw\_dl} - \varepsilon_{bs\_dl})] E_c A_{sl\_eff} \tag{M.41}$$

$$C2 = 30.3 \text{ kip}$$

$$C3 = \Phi_{\mathrm{bf\_o}} t_{sl} E_c \frac{A_{sl\_eff}}{2} \tag{M.42}$$

$$C3 = 2.6 \text{ kip}$$

Total compressive force:

$$C = C1 + C2 + C3 \tag{M.43}$$

$$C = 40.9 \text{ kip}$$

The internal moment can then be calculated by summing the moments in the section about the centroid of the prestressing strand as follows:

Internal moment:

$$M_{C1} = \left[\frac{2}{3} h_w - y_{ps} \right] C1 \tag{M.44}$$

$$M_{C1} = 37 \text{ in.-kip}$$

$$M_{C2} = \left[h_{comp} - y_{ps} - \frac{t_{sl}}{2} \right] C2 \tag{M.45}$$

$$M_{C2} = 272 \text{ in.-kip}$$

$$M_{C3} = \left[h_{comp} - y_{ps} - \frac{t_{sl}}{3} \right] C3 \tag{M.46}$$

$$M_{C3} = 25 \text{ in.-kip}$$

Total internal moment:

$$M_{bf\_o} = M_{C1} + M_{C2} + M_{C3} \tag{M.47}$$

$$M_{bf\_o} = 334 \text{ in.-kip}$$

The live load moment, which is the moment due to the applied force from the ram, required to produce the decompression condition is calculated by subtracting the applied dead loads from the total internal moment, M_{bf_o}.

Moment that results in the decompression condition:

$$M_{ram\_bf\_o} = M_{bf\_o} - M_w + M_{sl} + M_{spr} \tag{M.48}$$

$$M_{ram\_bf\_o} = 287 \text{ in.-kip}$$

The corresponding force in the ram is calculated as follows:

$$P_{ram\_bf\_o} = \frac{4M_{ram\_bf\_o}}{L_s - L_{spr}} \tag{M.49}$$

$$P_{ram\_bf\_o} = 9.1\,\text{kip}$$

M.1.9 Analysis of Section When the Neutral Axis is at CG of Strand

The analysis of the section when the neutral axis is at the center of gravity of the prestressing strand is similar to the analysis performed for the decompression condition. Assuming the linear stress profile shown in Figure M.7, the equilibrium condition when the total compression force equals the tension in the strand was determined by iterating to find the curvature, Φ_{ps_o}, and the corresponding level of applied load when the neutral axis of the section was at the center of gravity of the prestressing strand. For Beam 4, equilibrium was satisfied at a curvature of $7.0 \cdot 10^{-6}\,\dfrac{1}{\text{in.}}$. A cracked section was assumed; therefore, it was assumed that the stress was zero in the concrete below the neutral axis.

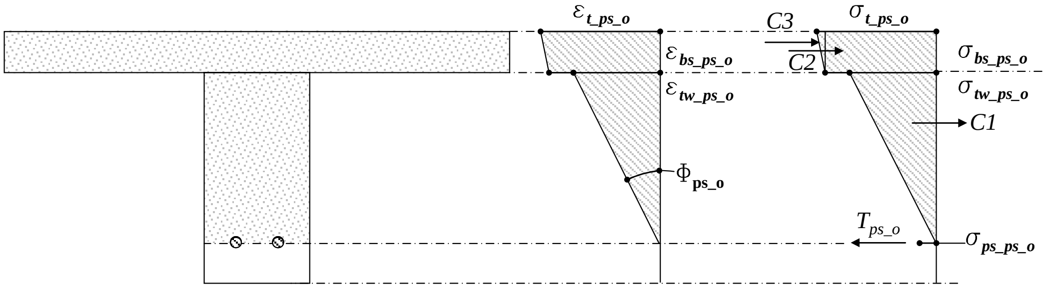

Figure M.7 Stress Diagram when NA is at CG of Strand

Because the calculations are similar to the calculations performed for the decompression condition, they are not repeated. However, the change in strand stress due to the applied load from the ram and required ram load to produce the condition are as follows:

Change in strand stress from full dead load state to the condition when the neutral axis was at the center of gravity of the prestressing strand:

$\Delta f_{ps\_o} = 7.33\,\text{ksi}$

Required applied load to produce the condition when the neutral axis was at the center of gravity of the prestressing strand:

$P_{ram\_ps\_o} = 9.3\,\text{kip}$

M.1.10 Analysis of Section When Neutral Axis is at Bottom of Slab

The calculations when the neutral axis is at the top of the web are similar to the calculations performed at the previous load levels. Assuming the stress and strain profiles shown in Figure M.8, the equilibrium condition when the total compression force equals the tension in the strand was determined by iterating to find the curvature, Φ_{sl}, and the corresponding level of applied load when the neutral axis of the section was at the bottom surface of the slab. For Beam 4, equilibrium was satisfied at a curvature of $131.5 \cdot 10^{-6}\,\frac{1}{\text{in.}}$. A cracked section was assumed; therefore, the stress in the concrete below the neutral axis was assumed to be zero. A critical difference between this analysis and the previous analyses is that the stress-strain relationship for the prestressing strand at this level of load is no longer linear. Therefore, the Ramberg-Osgood stress-strain profile developed for the strand used in the specimens was used in determining the stress in the strand. The data used to develop this relationship are given in Appendix K.

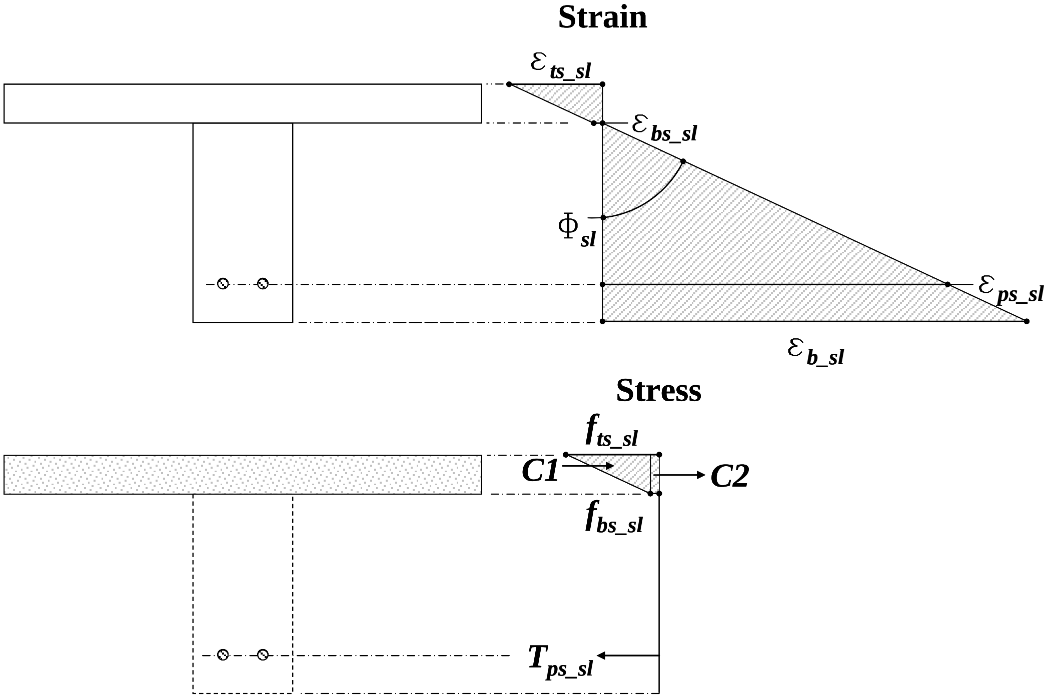

Figure M.8 Stress and Strain Diagrams for Analysis when NA is at the Top of the Web

Using the dead load state as the basis for calculation and the strain profile given in Figure M.8, the strain at the bottom of the slab is equal to the difference between the strains at the bottom of the slab and at the top of the web at the dead load state. This is calculated as follows:

$$\varepsilon_{bs\_sl} = \varepsilon_{bs\_dl} - \varepsilon_{tw\_dl} \qquad \text{(M.50)}$$

$$\varepsilon_{bs\_sl} = -75\mu\varepsilon$$

Similarly, the strain at the top of the slab is calculated as follows:

$$\varepsilon_{ts\_sl} = \varepsilon_{bs\_sl} + \Phi_{sl} t_{sl} + (\varepsilon_{bs\_dl} - \varepsilon_{t\_dl}) \tag{M.51}$$

$$\varepsilon_{ts\_sl} = -350\mu\varepsilon$$

Based on the above strains, the stresses at the top and bottom of the slab are calculated.

$$f_{ts\_sl} = E_{cs}\varepsilon_{ts\_dl} \tag{M.52}$$

$$f_{ts\_sl} = -1.724 \text{ ksi}$$

$$f_{bs\_sl} = E_{cs}\varepsilon_{bs\_dl} \tag{M.53}$$

$$f_{bs\_sl} = -0.370 \text{ ksi}$$

It is important to note that the stresses in the slab are below 40% of the compressive strength of the concrete in the slab. Therefore, the assumption that the stress-strain behavior is still linear is valid.

The compressive force in the slab is then calculated using the stresses calculated in Eq. 52 and 53.

Compression force in the slab:

$$C1 = (f_{ts\_sl} - f_{bs\_sl})\frac{b_{sl}t_{sl}}{2} \qquad C1 = -32.5 \text{ kip}$$

$$C2 = f_{bs\_sl} b_{sl} t_{sl} \qquad C2 = -17.8 \text{ kip}$$

The dead load state is used as the basis for calculating the total strain in the prestressing strand as follows:

$$\varepsilon_{ps\_sl} = \frac{f_{ps\_dl}}{E_s} - \varepsilon_{ps\_dl} + \Phi_{sl}(h_w - y_{ps}) \tag{M.54}$$

$$\varepsilon_{ps\_sl} = 5607\mu\varepsilon$$

The corresponding stress in the strand is calculated using the Ramberg-Osgood stress-strain profile. The shape of the Ramberg-Osgood stress-strain profile was determined based on data collected during tensile tests of the strand.

$$f_{ps\_sl} = E_s \varepsilon_{ps\_sl} \left[0.018 + \frac{1 - 0.018}{\left[1 + (115\varepsilon_{ps\_sl})^8 \right]^{0.125}} \right] \tag{M.55}$$

$$f_{ps\_sl} = 164\,\text{ksi}$$

The corresponding force in the strand is as follows:

$$T = f_{ps\_sl} A_{ps} \tag{M.56}$$

$$T = 50.3\,\text{kip}$$

The corresponding change in strand stress due to the applied live load is calculated as follows:

$$\Delta f_{sl} = f_{ps\_sl} - f_{ps\_dl} \tag{M.57}$$

$$\Delta f_{NA\_sl} = 38\,\text{ksi}$$

Similarly to previous calculations, the internal moment is calculated by summing the moments about the center of gravity of the prestressing strand, from which the required applied load is calculated. The required load for Beam 4 was determined to be:

$P_{ram\_sl} = 13.2 \text{ kip}$

M.1.11 Analysis of Section at Flexural Capacity

Determine the live load moment corresponding to the flexural capacity of the composite cross section.

$$M_{ult} = A_{ps} f_{pu} \left[d_p - \frac{A_{ps} f_{pu}}{0.85 f_c b_{sl} n_s} \right] \tag{M.58}$$

$M_{ult} = 823 \text{ in - kip}$

Determine change in strand stress from dead load state.

$$\Delta f_{ult} = f_{pu} - f_{ps\_dl} \tag{M.59}$$

$\Delta f_{ult} = 149 \text{ ksi}$

Required Force:

$$P_{ram\_ult} = \frac{4(M_{ult} - M_{sw} - M_{sl} - M_{spr})}{L_s - L_{spr}} \tag{M.60}$$

$P_{ram\_ult} = 24.7 \text{ kip}$

M.2 SUMMARY OF RESULTS OF ANALYSES FOR BEAMS

As discussed in Chapter 5, the results of the analyses were used to develop plots of applied load as a function of strand stress range. For each beam, the strand stress, strand stress range, and applied load are summarized in Tables M.8 through M.13. Corresponding plots of applied load as a function of the stress range in the strand is are given in Figures M.10 through M.15. Table M.7 provides a key to the tables and plots provided in this section.

Table M.7 Description of Analysis Points for Fatigue Specimens

Point	Description
1	Full dead load state
2	Decompression of bottom fiber
3	Neutral axis at center of gravity of strand
4	Neutral axis at top of web
5	Flexural Capacity
A	Minimum applied load for fatigue test
B	Maximum applied load for fatigue test

Table M.8 Results from Analyses of Beam 1

Point	Strand Stress, ksi	Strand Stress Range, ksi	Load, kip
1	121.2	0.0	0.0
2	129.4	8.2	9.2
3	129.6	8.4	9.4
4	145.7	24.5	11.5
5	275.0	153.8	24.7
Fatigue Loads			
A	138.1	7.1	10.5
B	145.2		11.4

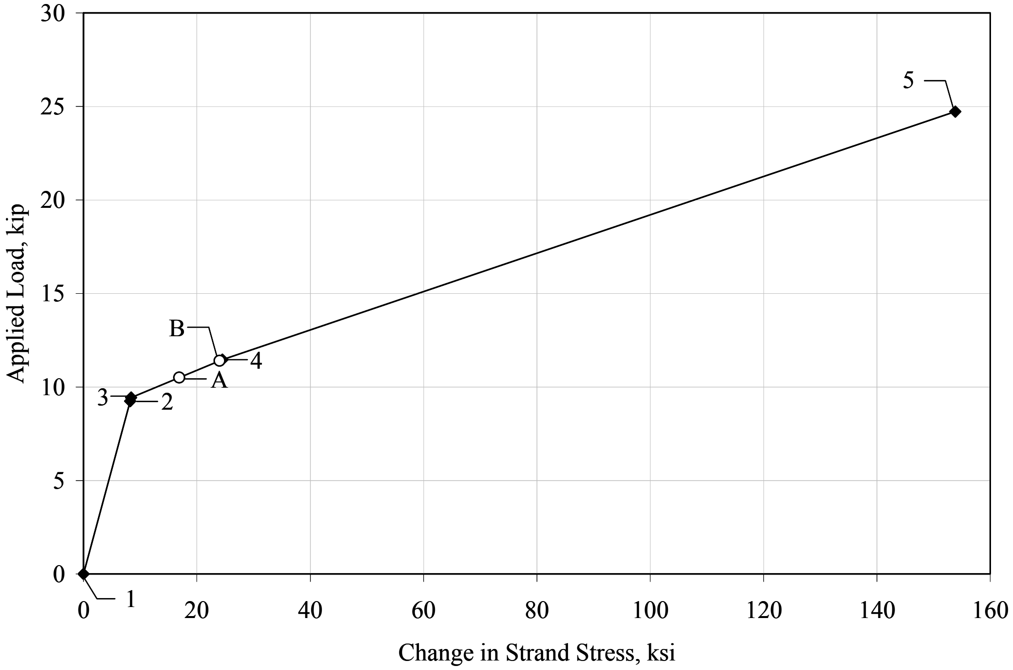

Figure M.9 Load Plotted as a Function of Stress Range in the Strand for Beam 1

Table M.9 Results from Analyses of Beam 2

Point	Strand Stress, ksi	Strand Stress Range, ksi	Load, kip
1	123.1	0.0	0.0
2	131.4	8.3	9.4
3	131.6	8.5	9.6
4	149.2	26.1	11.8
5	275.0	151.9	24.7
Fatigue Loads			
A	126.1	22.4	3.4
B	148.5		11.7

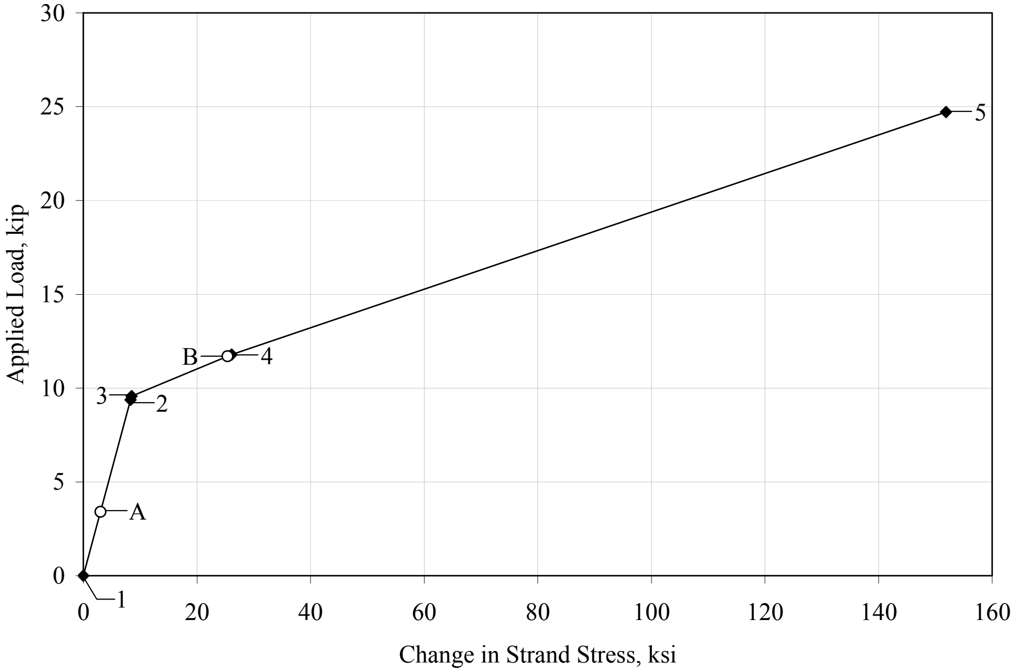

Figure M.10 Load Plotted as a Function of Stress Range in the Strand for Beam 2

Table M.10 Results from Analyses of Beam 3

Point	Strand Stress, ksi	Strand Stress Range, ksi	Load, kip
1	125.6	0.0	0.0
2	133.2	7.6	9.3
3	133.4	7.8	9.5
4	158.2	32.6	12.7
5	275.0	149.4	24.7
Fatigue Loads			
A	127.5	24.8	2.3
B	152.2		11.9

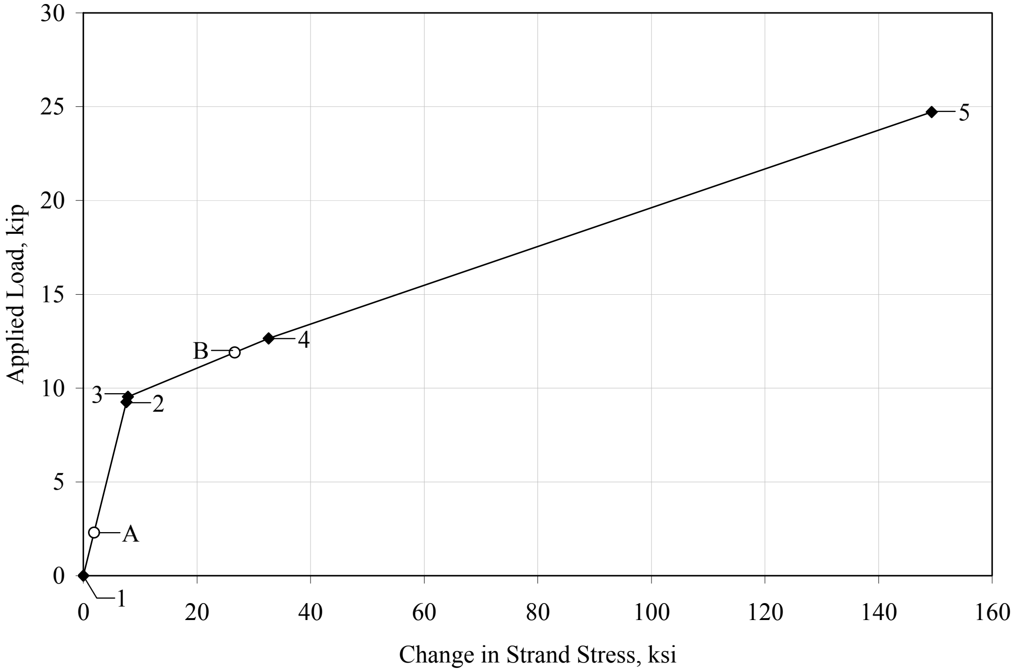

Figure M.11 Load Plotted as a Function of Stress Range in the Strand for Beam 3

Table M.11 Results from Analyses of Beam 4

Point	Strand Stress, ksi	Strand Stress Range, ksi	Load, kip
1	126.1	0.0	0.0
2	133.6	7.5	9.1
3	133.9	7.8	9.5
4	164.2	38.1	13.2
5	275.0	148.9	24.7
Fatigue Loads			
A	127.1	46.6	1.2
B	173.7		14.2

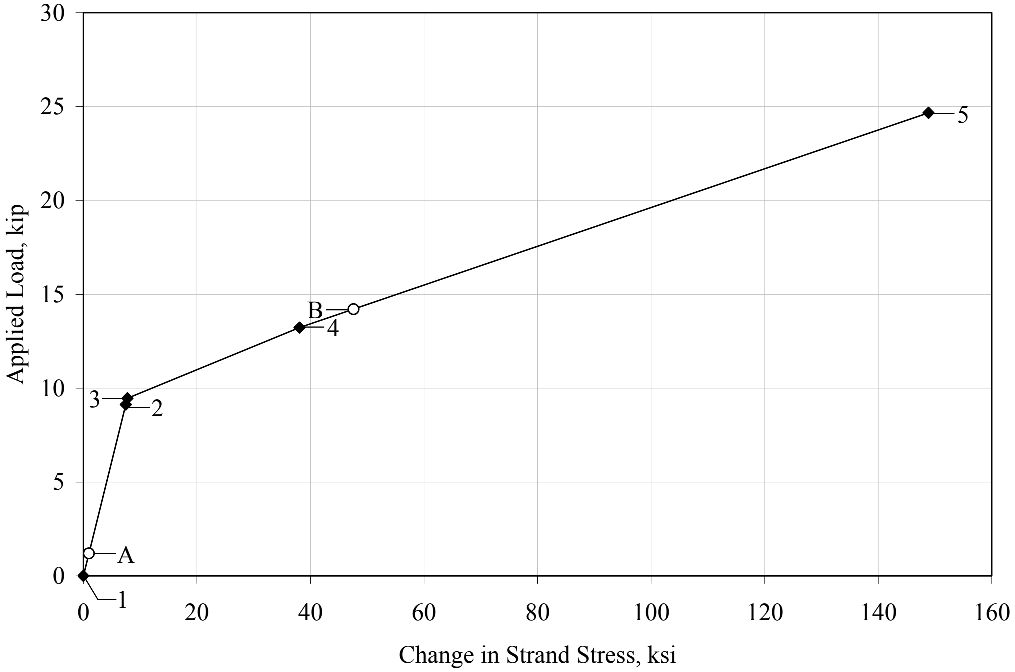

Figure M.12 Load Plotted as a Function of Stress Range in the Strand for Beam 4

Table M.12 Results from Analyses of Beam 5

Point	Strand Stress, ksi	Strand Stress Range, ksi	Load, kip
1	123.7	0.0	0.0
2	131.1	7.4	9.1
3	131.5	7.8	9.5
4	165.4	41.7	13.7
5	271.0	147.3	24.7
Fatigue Loads			
A	124.2	46.7	0.6
B	170.9		14.3

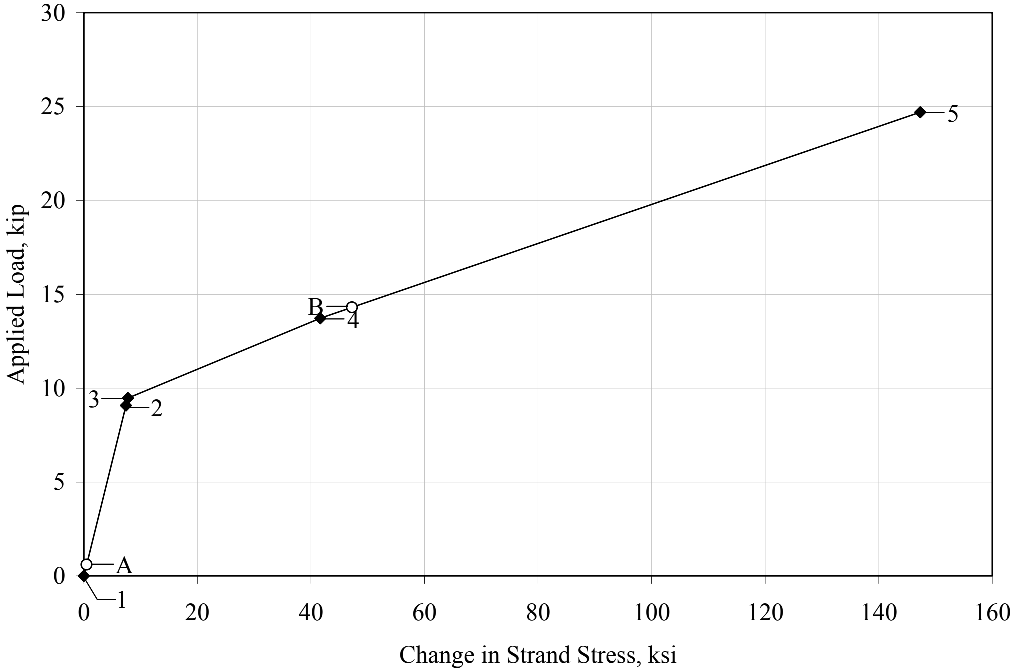

Figure M.13 Load Plotted as a Function of Stress Range in the Strand for Beam 5

Table M.13 Results from Analyses of Beam 6

Point	Strand Stress, ksi	Strand Stress Range, ksi	Load, kip
1	127.7	0.0	0.0
2	135.0	7.3	9.0
3	135.4	7.7	9.4
4	171.1	43.4	13.9
5	275.0	147.3	24.7
Fatigue Loads			
A	132.2	14.3	5.5
B	146.5		10.8

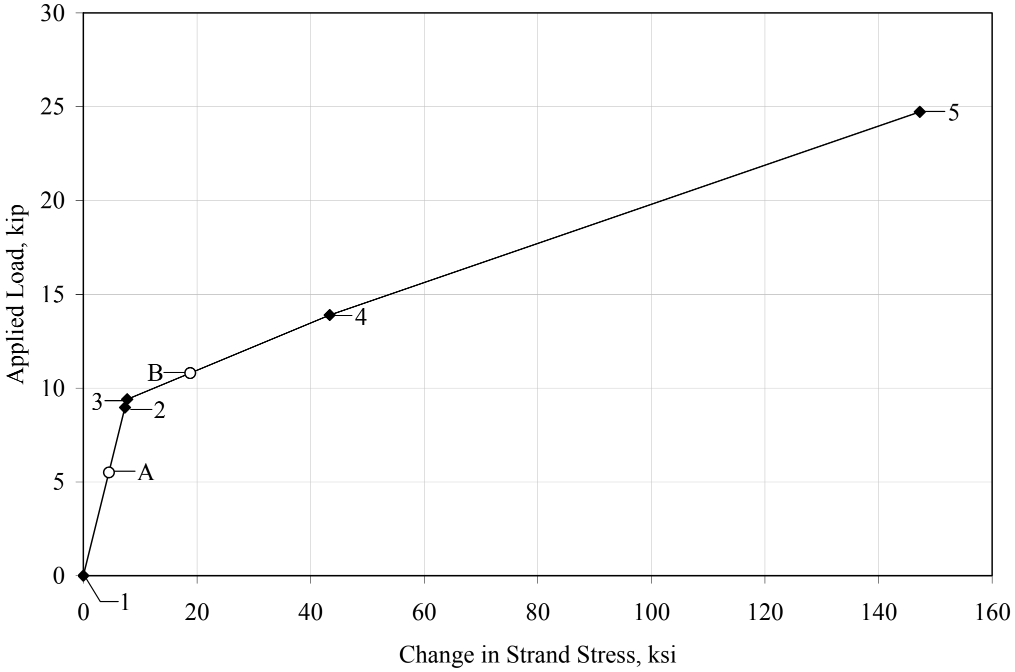

Figure M.14 Load Plotted as a Function of Stress Range in the Strand for Beam 6

Appendix N

Additional Results from Laboratory Fatigue Tests

Additional results from the laboratory fatigue tests are presented in this appendix. Additional decompression load data for Beams 1 through 6 are presented in Section N.1. This information has been previously discussed in Chapter 6. Additional photographs documenting the wire failures in Beam 6 are shown in section N.2. Section N.3 includes additional fatigue response data for Beams 1 and 6 that are not pertinent to the discussion in this dissertation; however, it is presented to compliment information that has been previously reported in Heller (2003) on Beams 2, 3, 4 and 5. Section N.4 summarizes measured strain data from static tests performed on the fatigue test specimens.

N.1 ADDITIONAL DECOMPRESSION LOAD DATA FOR BEAMS 1 THROUGH 6

As discussed in Chapter 6 of this dissertation, the decompression load was inferred from the measured response of the beams. Table 6.4 is a summary of the data presented here and has been previously discussed in Section 6.1.2. Therefore, the reader is referred to Section 6.1.2 for a complete discussion of the analysis used to approximate the decompression load and the results of those analyses.

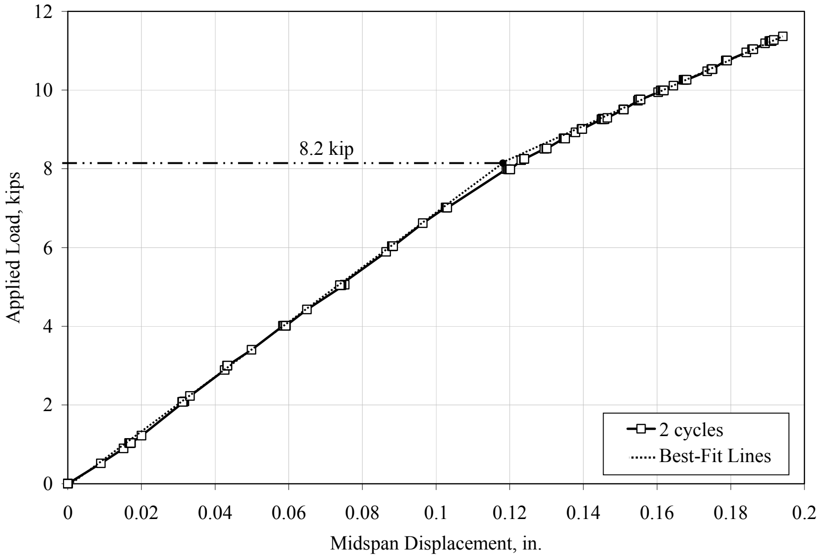

Figure N.1 Estimated Decompression Load of Beam 1 Using Midspan Displacement

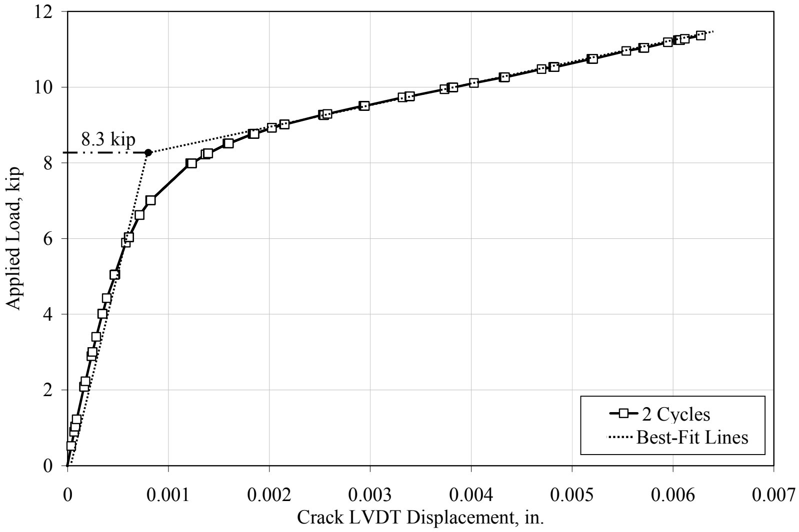

Figure N.2 Estimated Decompression Load of Beam 1 Using Crack LVDT Displacement

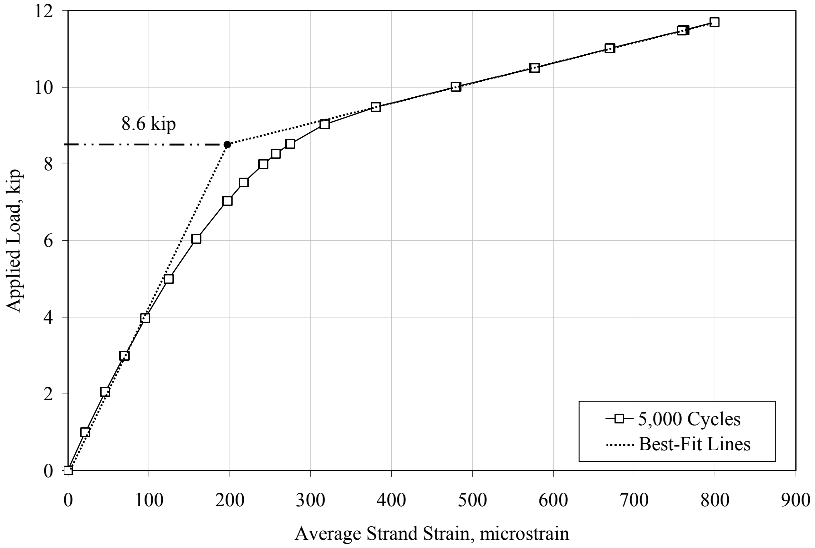

Figure N.3 Estimated Decompression Load of Beam 2 Using Average Strand Strain

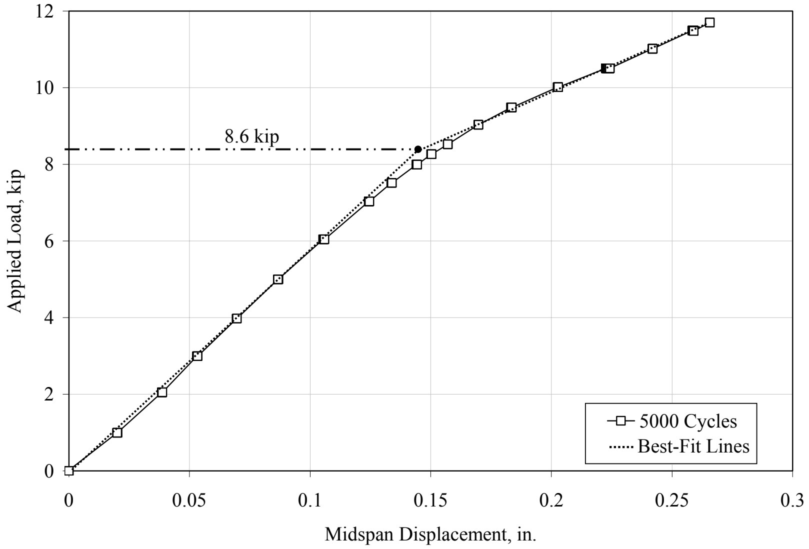

Figure N.4 Estimated Decompression Load of Beam 2 Using Midspan Displacement

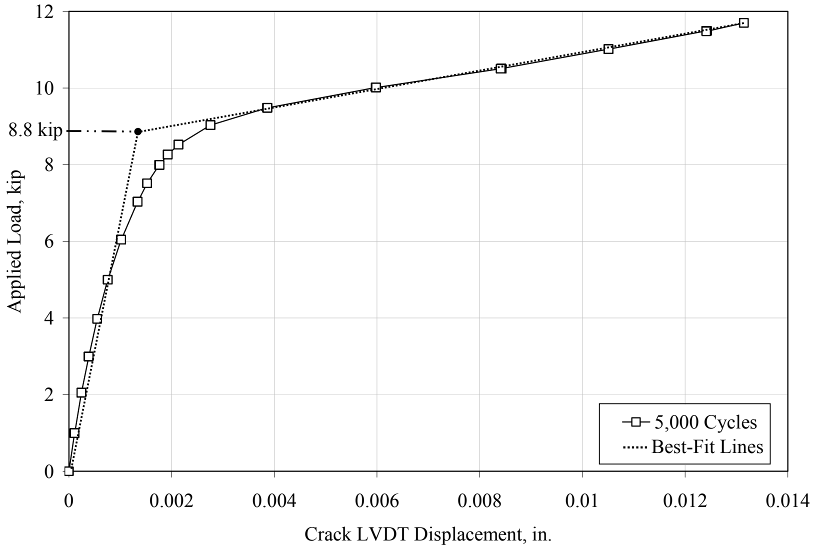

Figure N.5 Estimated Decompression Load of Beam 2 Using Crack LVDT Displacement

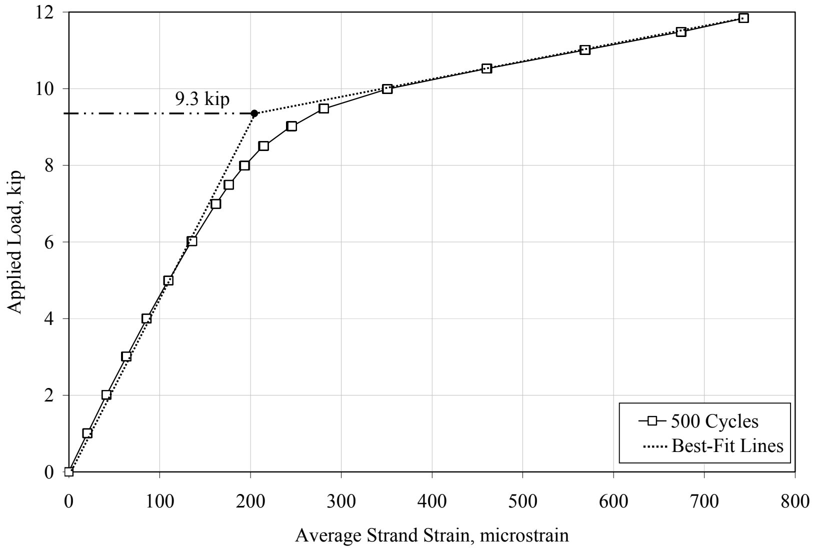

Figure N.6 Estimated Decompression Load of Beam 3 Using Average Strand Strain

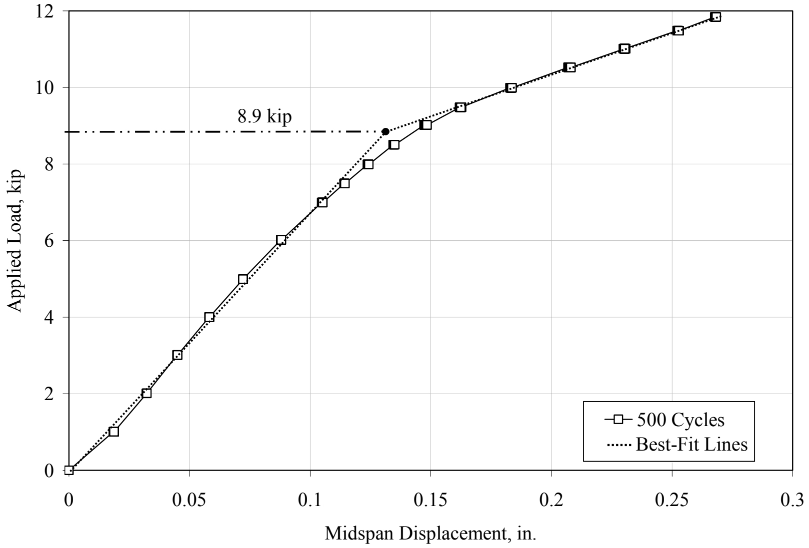

Figure N.7 Estimated Decompression Load of Beam 3 Using Midspan Displacement

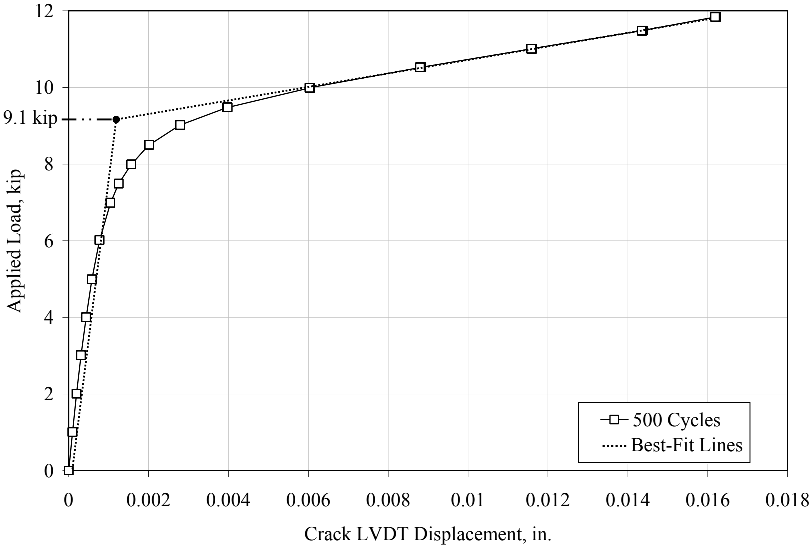

Figure N.8 Estimated Decompression Load of Beam 3 Using Crack LVDT Displacement

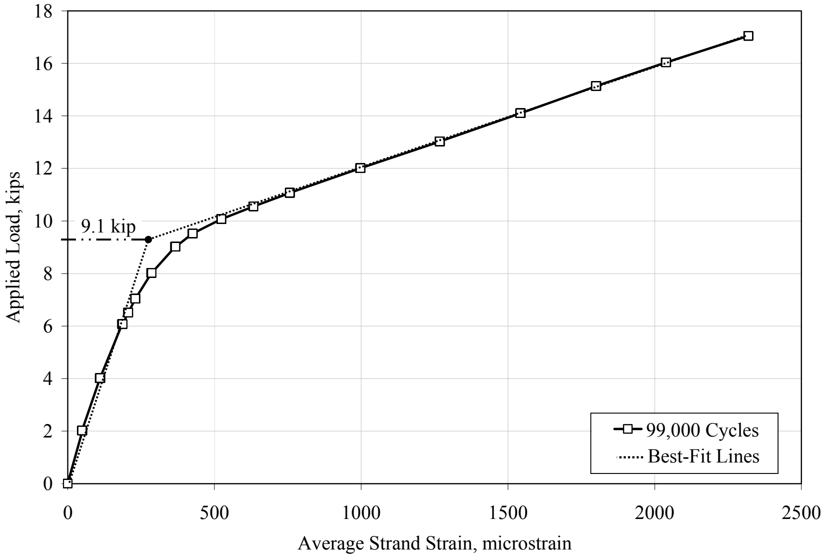

Figure N.9 Estimated Decompression Load of Beam 4 Using Average Strand Strain

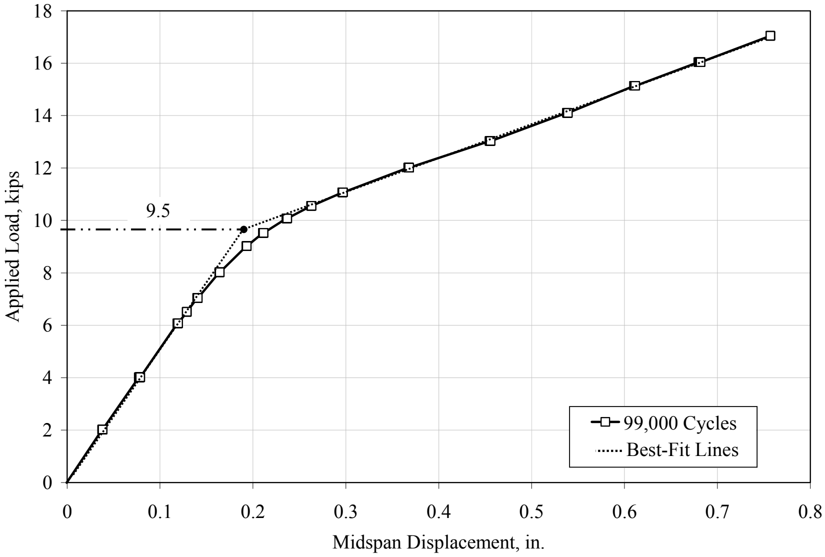

Figure N.10 Estimated Decompression Load of Beam 4 Using Midspan Displacement

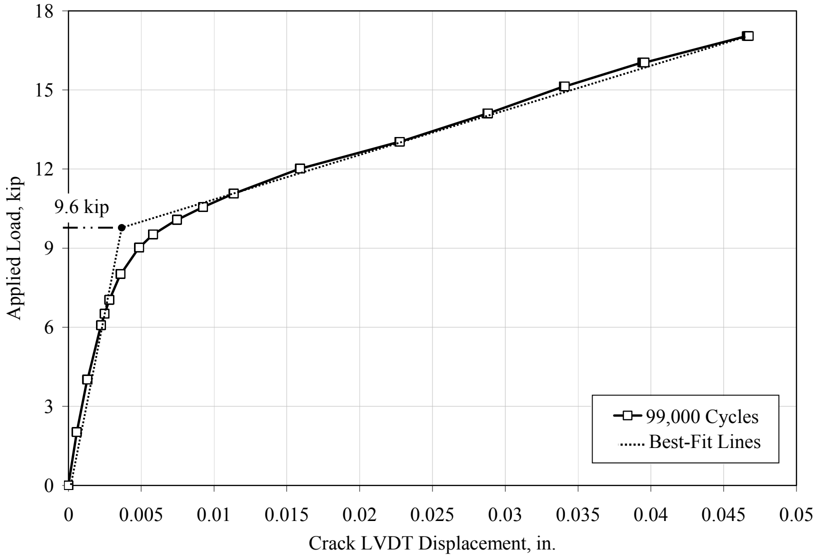

Figure N.11 Estimated Decompression Load of Beam 4 Using Crack LVDT Displacement

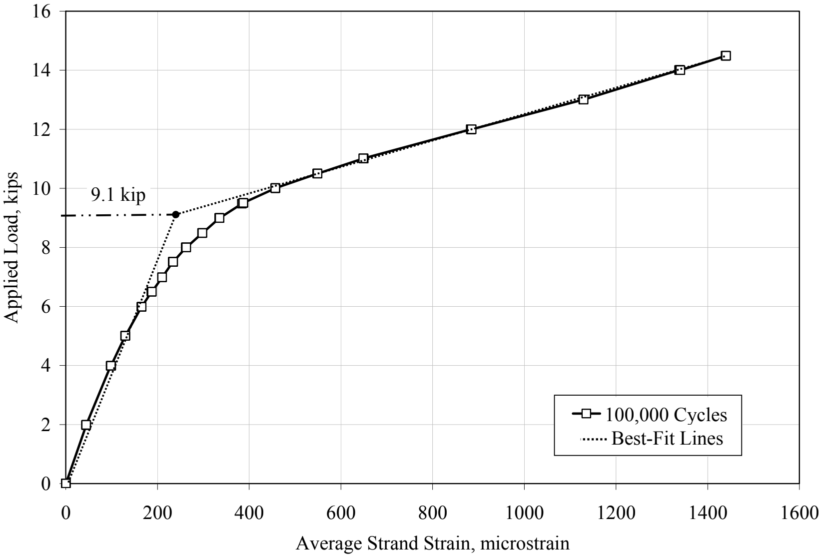

Figure N.12 Estimated Decompression Load of Beam 5 Using Average Strand Strain

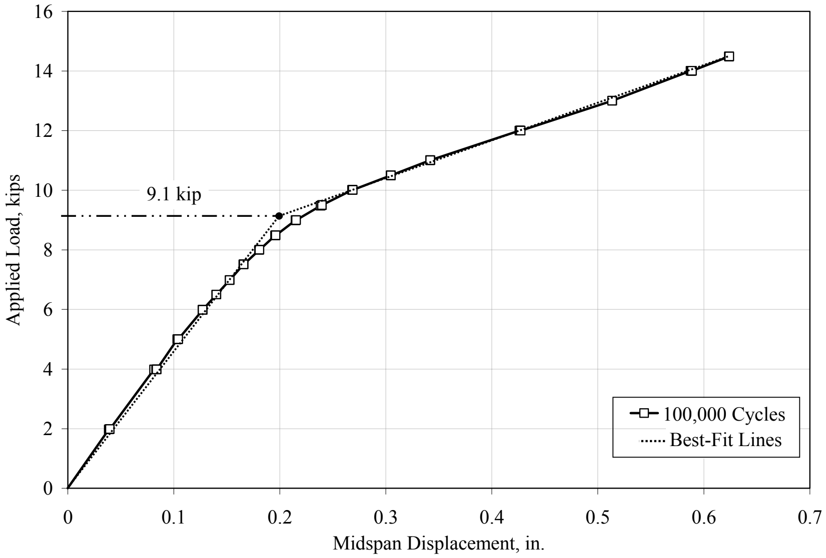

Figure N.13 Estimated Decompression Load of Beam 5 Using Midspan Displacement

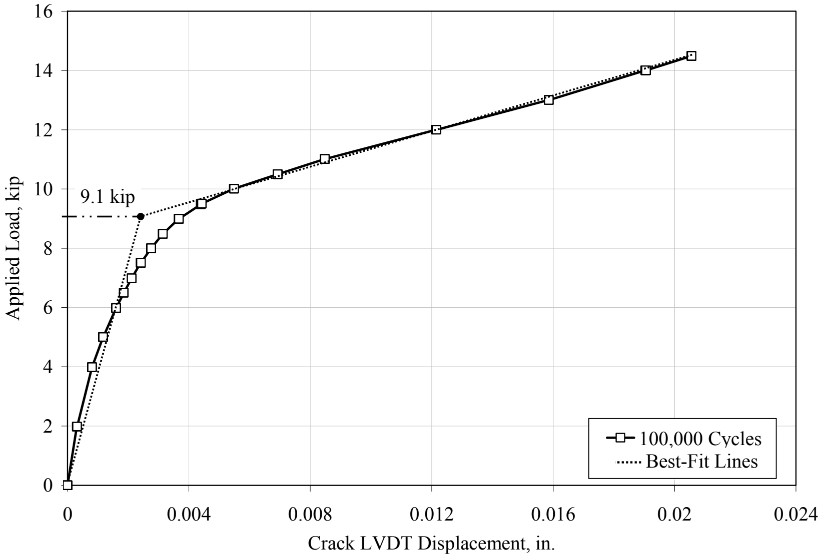

Figure N.14 Estimated Decompression Load of Beam 5 Using Crack LVDT Displacement

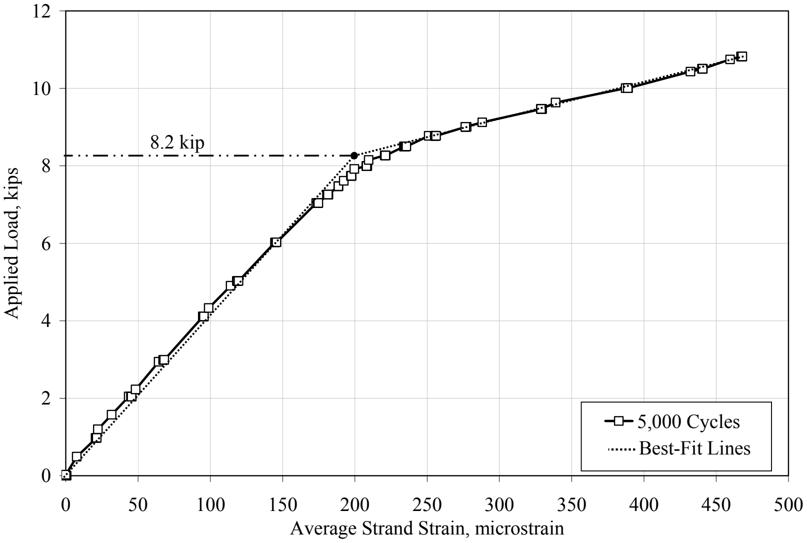

Figure N.15 Estimated Decompression Load of Beam 6 Using Average Strand Strain

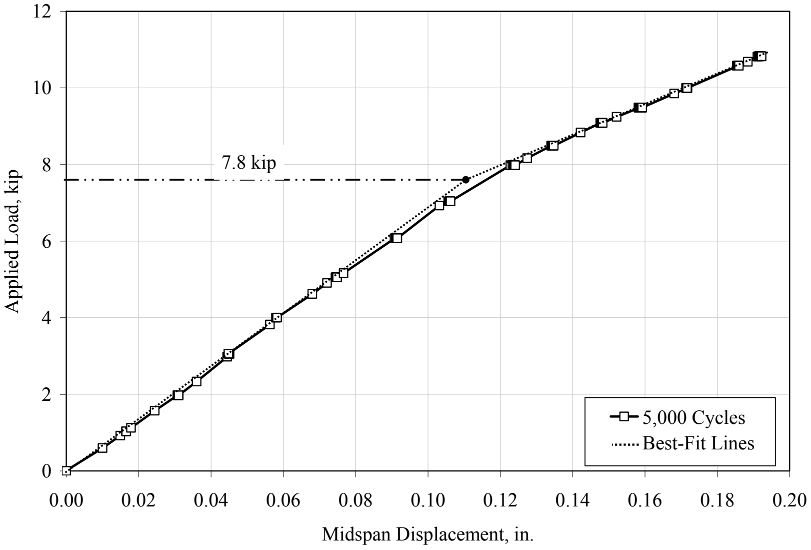

Figure N.16 Estimated Decompression Load of Beam 6 Using Midspan Displacement

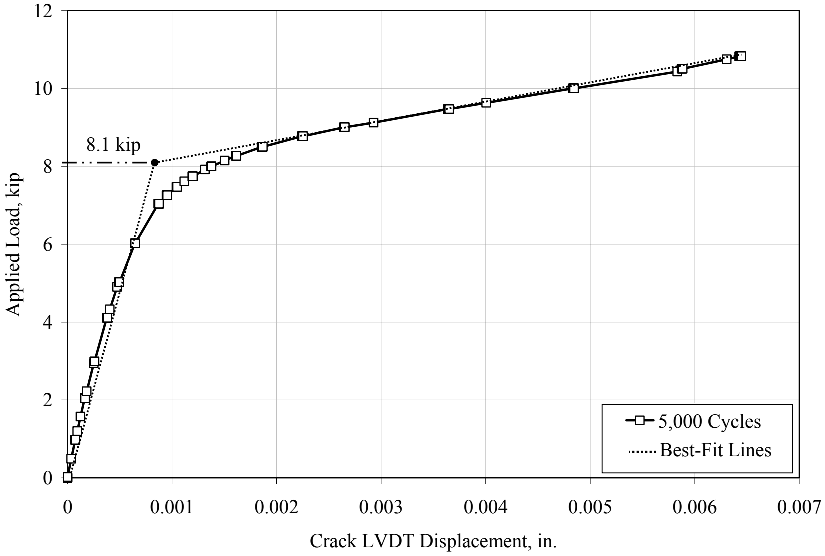

Figure N.17 Estimated Decompression Load of Beam 6 Using Crack LVDT Displacement

N.2 ADDITIONAL PHOTOGRAPHS FROM POST MORTEM INVESTIGATION OF BEAM 6

Additional photos of the wire fatigue failures in Beam 6 are included in this section. As noted in Chapter 8, the locations indicated correspond to the locations designated in Figure 8.69.

Figure N.18 Photo of Wire Failures in Beam 6 – Location A

Figure N.19 Photo of Wire Failures in Beam 6 – Location B

Figure N.20 Photo of Wire Failures in Beam 6 – Location C

N.3 ADDITIONAL FATIGUE RESPONSE DATA FOR BEAMS 1 AND 6

Additional fatigue response data for Beams 1 and Beam 6 are presented in this section. As previously discussed, these data are included to compliment the data for Beams 2, 3, 4 and 5 previously reported in Heller (2003).

N.3.1 Variation of Measured Concrete Strain at CG of Strand

As discussed in Chapter 3, a concrete strain gage was embedded in each beam at the center of gravity of the prestressing strand and was positioned at the midspan of the test specimen. Figure N.21 is a plot of applied load versus concrete strain for each static test performed on Beam 1 during the fatigue test at the strand stress range of 7 ksi. A significant change in strain occurred after the first and second static tests as a result of flexural cracking in the beam. After 5,000 cycles, no significant change occurred during all subsequent static tests performed at the strand stress range of 7 ksi. Corresponding data for Beam 6 at the strand stress range of 14 ksi are shown in Figure N.22. The trends in the data are similar to those for Beam 1. These trends indicate that no significant deterioration of the concrete in the proximity of the strain gage occurred during the fatigue cycles performed after the initial cracking occurred.

Figure N.23 is a plot of applied load versus concrete strain at the center of gravity of the prestressing strand for each static test performed on Beam 1A during the fatigue test at the strand stress range of 41 ksi. A significant increase in strain occurred after approximately 700,000 cycles at this index stress. This trend in the data does not correspond with the trends reported in Heller (2003) for Beams 4 and 5, which were also tested at a similar strand stress range. The trend in the data for Beams 4 and 5 was a decrease in measured strain for a given applied load.

Figure N.24 is a plot of applied load versus concrete strain at the center of gravity of the prestressing strand for each static test performed on Beam 6 during the fatigue test at the strand stress range of 45 ksi. There is no clear trend in the data as the number of fatigue cycles increases. Therefore, no comparison can be made with other beams tested at similar strand stress ranges.

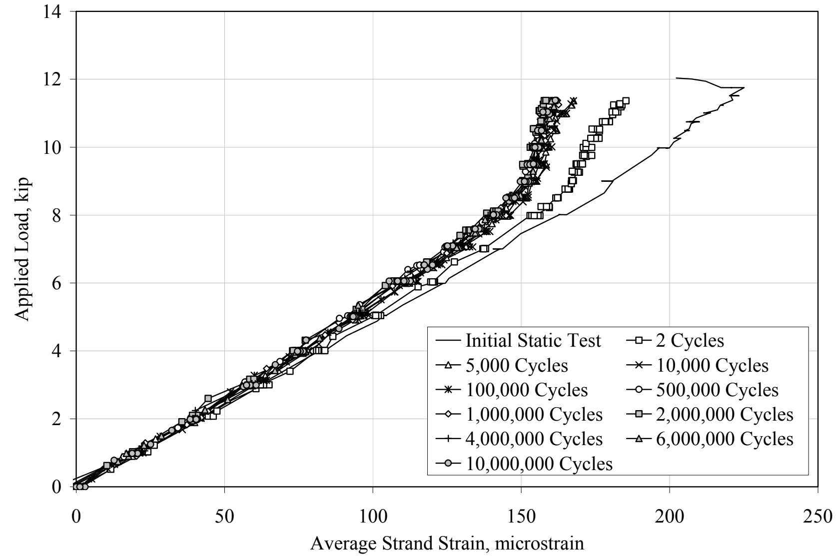

Figure N.21 Variation of Concrete Strain at Center of Gravity of Strand During Fatigue Tests for Beam 1 at a Strand Stress Range of 7 ksi

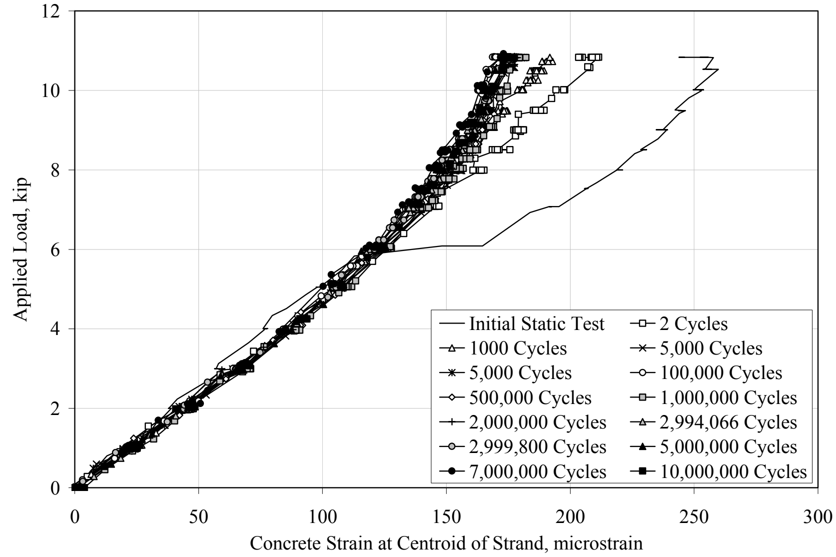

Figure N.22 Variation of Concrete Strain at Center of Gravity of Strand During Fatigue Tests for Beam 6 at a Strand Stress Range of 14 ksi

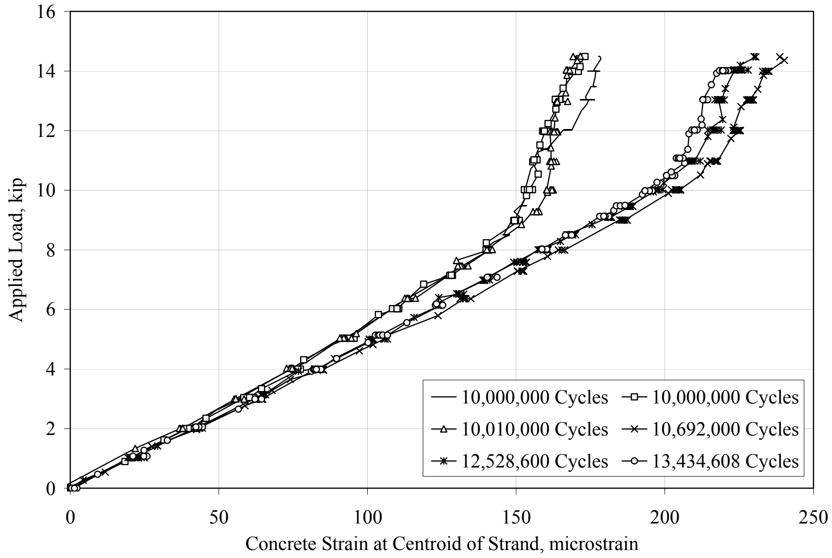

Figure N.23 Variation of Concrete Strain at Center of Gravity of Strand During Fatigue Tests for Beam 1A at a Strand Stress Range of 41 ksi

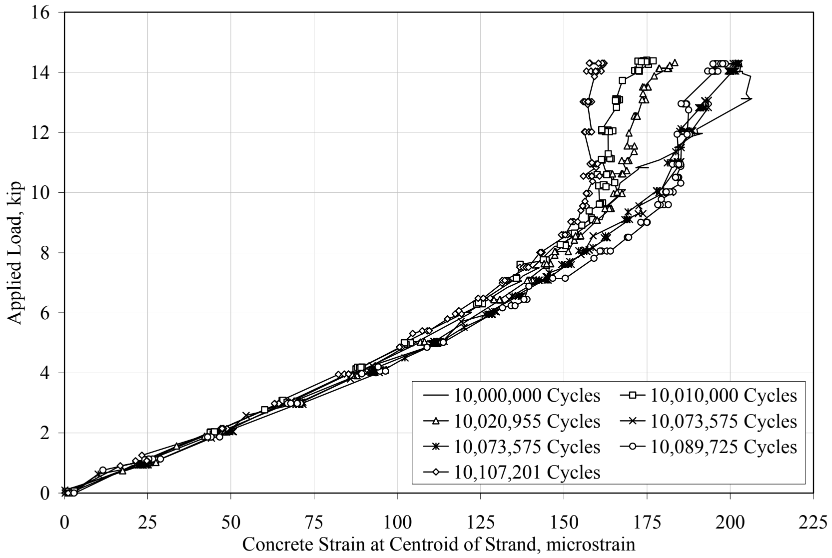

Figure N.24 Variation of Concrete Strain at Center of Gravity of Strand During Fatigue Tests for Beam 6A at a Strand Stress Range of 45 ksi

N.3.2 Comparison of Strand Strain and Concrete Strain at CG of Strand

Figure N.25 is a comparison of strand and concrete strain for static test 1 and static test 2 performed on Beam 1 at a strand stress range of 7 ksi. Below the decompression load, the steel and concrete strains are very similar; however they are dramatically different above the decompression load. This is anticipated because above the decompression load, cracks in the concrete begin to open and the behavior of the strand and surrounding concrete differ. The corresponding data for Beam 6 at a strand stress range of 14 ksi, and for Beam 1A and 6A at a strand stress range of approximately 43 ksi are shown in Figure N.26, Figure N.27 and Figure N.28, respectively. The trends exhibited in these data are similar to the trends exhibited by data from Beam 1 at a strand stress range of 7 ksi. Similar trends in the corresponding data for Beams 2, 3, 4 and 5 are reported in Heller (2003).

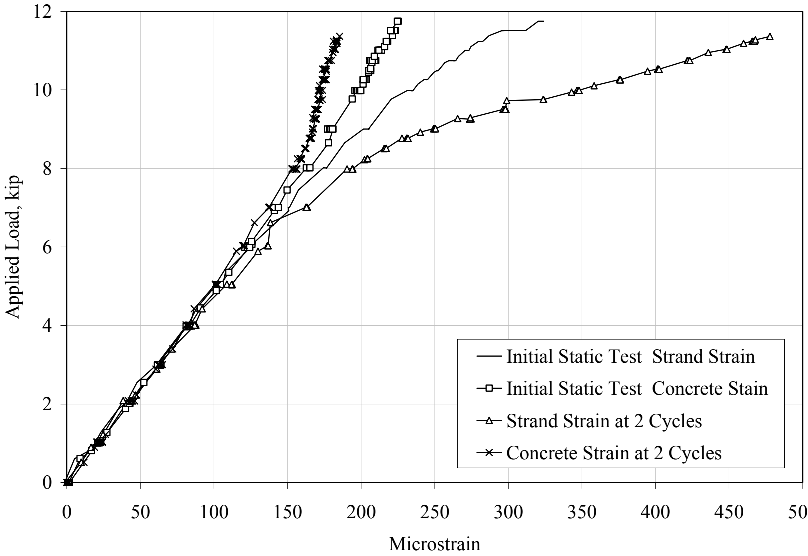

Figure N.25 Comparison of Strand Strain and Concrete Strain for Beam 1 a Strand Stress Range of 7 ksi

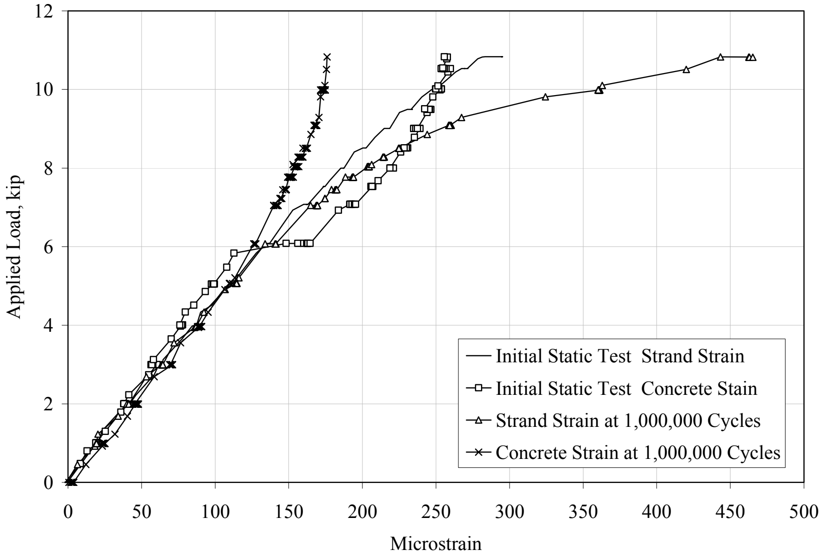

Figure N.26 Comparison of Strand Strain and Concrete Strain for Beam 6 a Strand Stress Range of 14 ksi

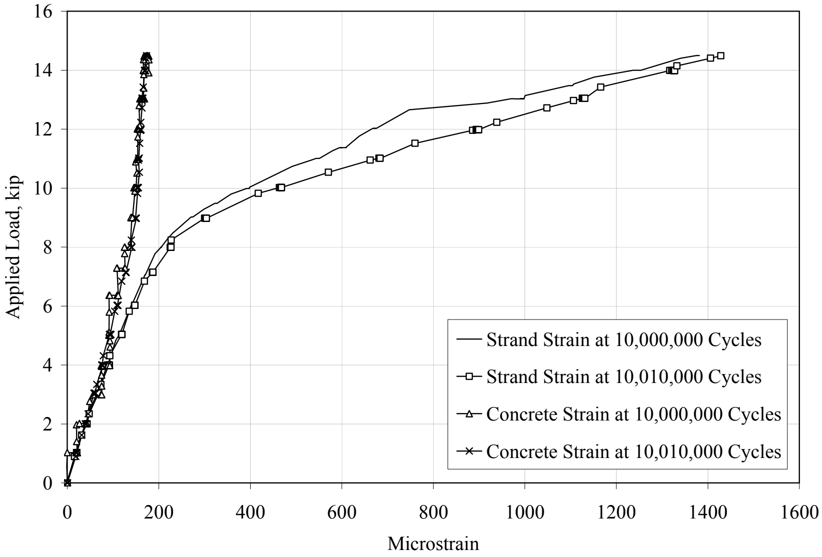

Figure N.27 Comparison of Strand Strain and Concrete Strain for Beam 1A at a Strand Stress Range of 41 ksi

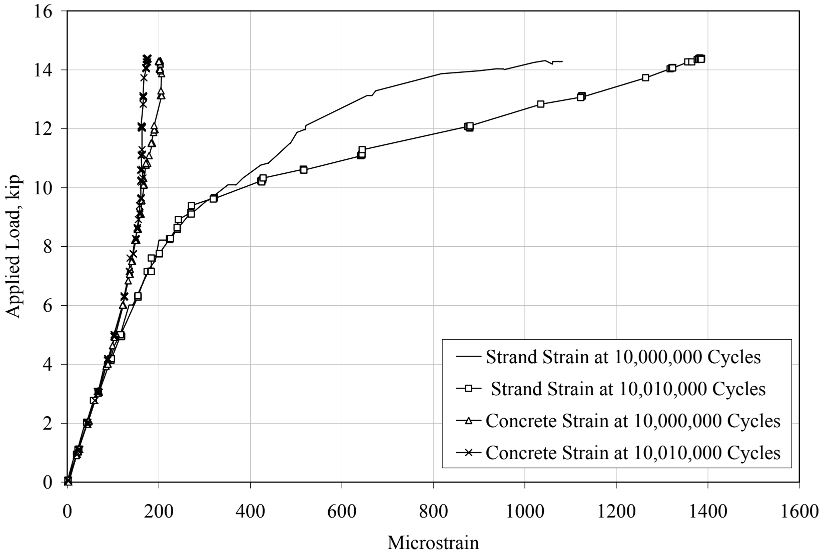

Figure N.28 Comparison of Strand Strain and Concrete Strain for Beam 6A at a Strand Stress Range of 45 ksi

N.3.3 Variation of Measured Surface Concrete Strains

Prior to testing the beams under fatigue loads, two, 60-mm strain gages were attached to the bottom surface of each beam. These strain gages were applied on each side of the most prominent crack after the initial static tests. The variation of measured strains from these gages is discussed in this section.

Plots of applied load versus surface concrete strain on each side of the crack for Beam 1 at a strand stress range of 7 ksi are shown in Figure N.29 and Figure N.30. The behavior of the concrete on each side of the crack was similar throughout the fatigue testing. As the number of cycles increased the maximum measured strain on each side of the crack decreased. This is most likely due an increase in the length of debonding between the strand and concrete on each side of the crack. The corresponding data for Beam 6 at a strand stress range of 14 ksi are shown in Figure N.31 and Figure N.32. The trend in these data is similar to the trend exhibited by Beam 1 at a similar strand stress range.

Plots of applied load versus surface concrete strain on each side of the crack for Beam 1A at a strand stress range of 41 ksi are shown in Figure N.33 and Figure N.34. As the number of cycles increased, the maximum measured strain on each side of the crack decreased. Again, this is most likely due an increase in the length of debonding between the strand and concrete on each side of the crack. Additionally, it is noted that during tests after approximately 700,000 cycles, at loads above the decompression load, the strain gages begin to read a decrease in tension. One possible explanation for this is a decrease in bond between the strand and surrounding concrete near the crack, causing the concrete to "slip" relative to the strand and indicate recompression of the concrete. The corresponding data for Beam 6A at the same index stress are shown in Figure N.35 and Figure N.36. The gage on the east side of the crack (Figure N.35), failed between the fifteenth and sixteenth static tests and therefore provides no insight into the behavior of the beam beyond 10,000,000 cycles. The behavior of the gage on the west side of the crack is similar to that for Beam 1A at the same strand stress range.

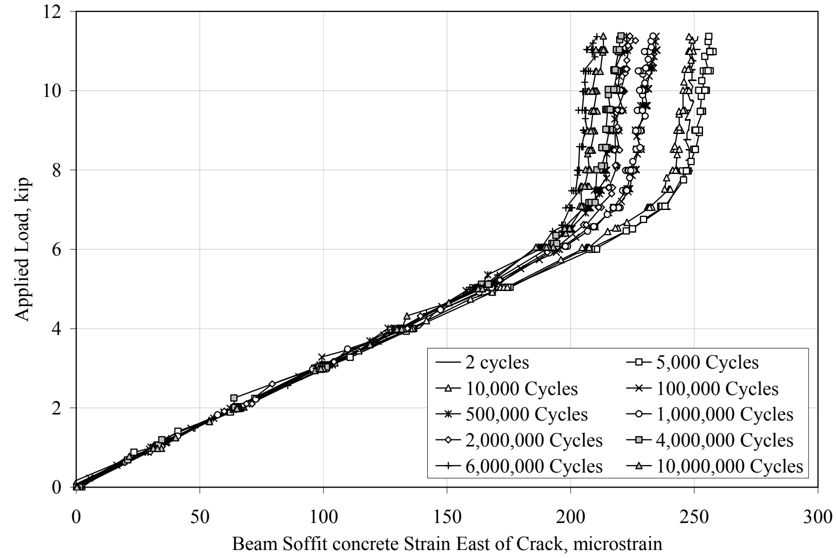

Figure N.29 Variation of Beam Soffit Strain East of Crack During Fatigue Tests for Beam 1 at Strand Stress Range of 7 ksi

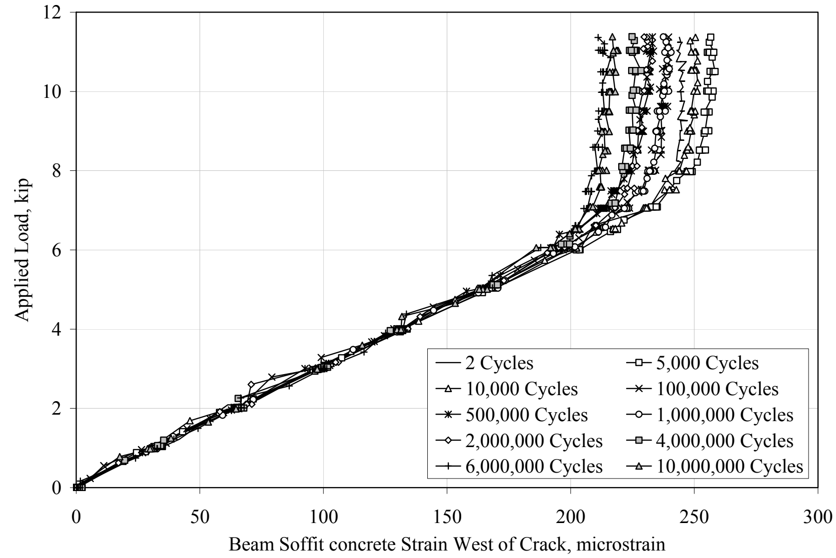

Figure N.30 Variation of Beam Soffit Strain West of Crack During Fatigue Tests for Beam 1 at a Strand Stress Range of 7 ksi

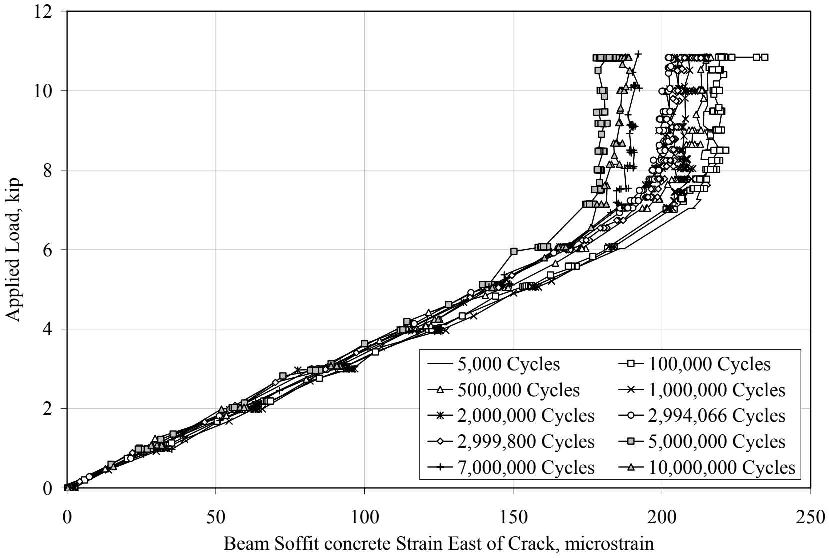

Figure N.31 Variation of Beam Soffit Strain East of Crack During Fatigue Tests for Beam 6 at a Strand Stress Range of 14 ksi

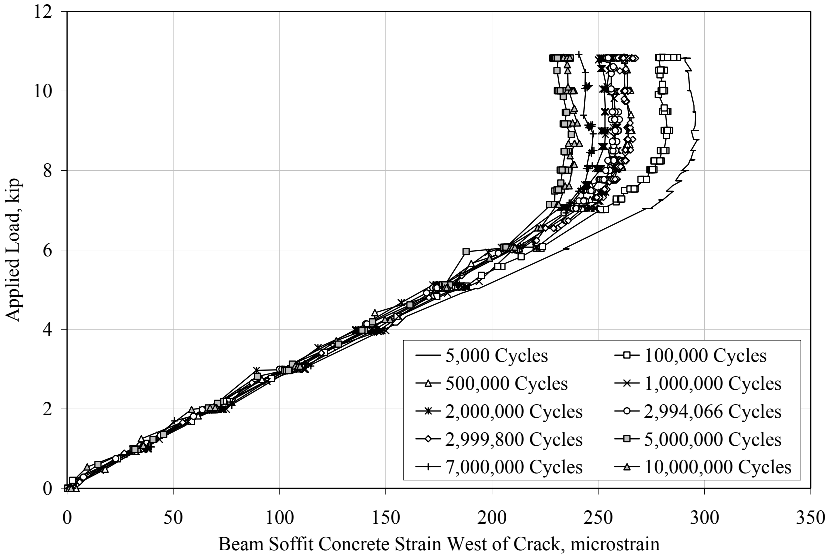

Figure N.32 Variation of Beam Soffit Strain West of Crack During Fatigue Tests for Beam 6 at a Strand Stress Range of 14 ksi

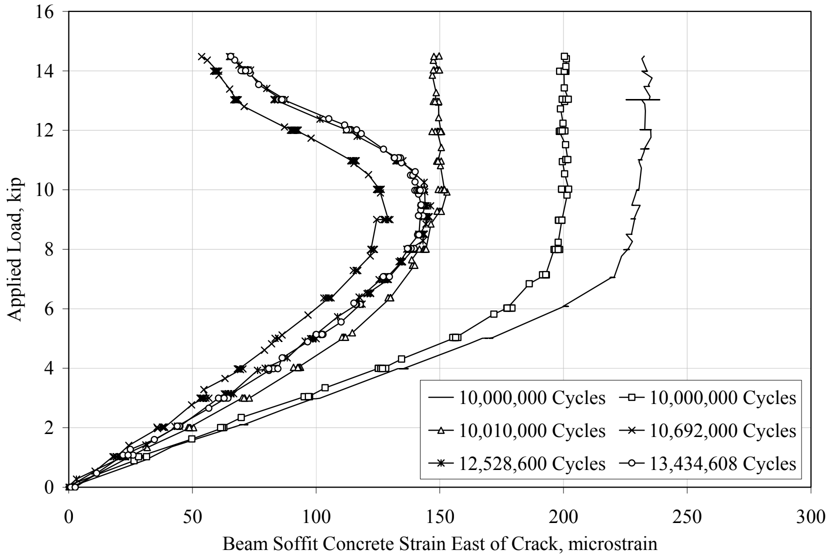

Figure N.33 Variation of Beam Soffit Strain East of Crack During Fatigue Tests for Beam 1A at a Strand Stress Range of 41 ksi

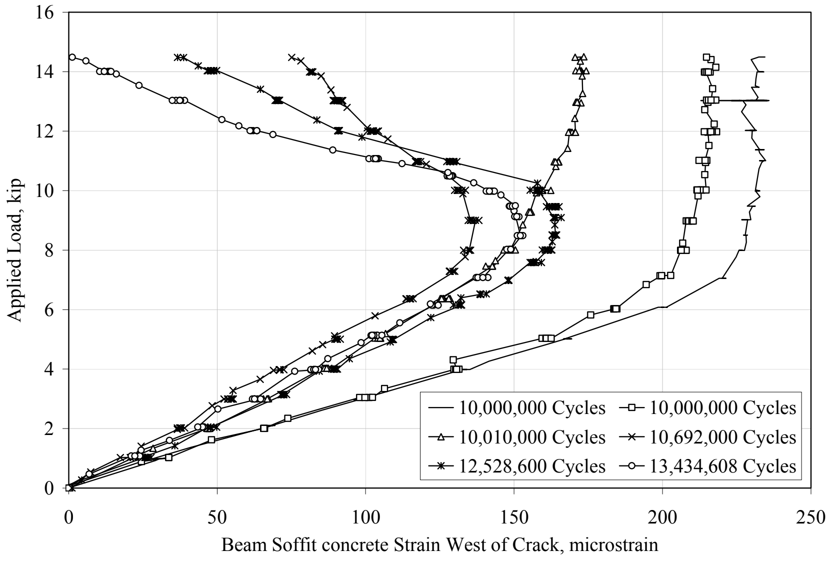

Figure N.34 Variation of Beam Soffit Strain West of Crack During Fatigue Tests for Beam 1A at a Strand Stress Range of 41 ksi

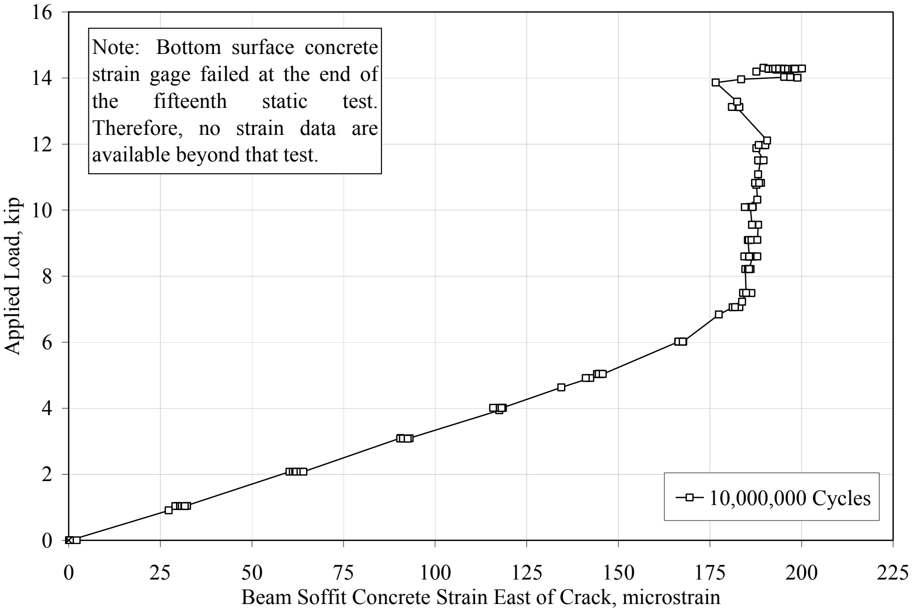

Figure N.35 Variation of Beam Soffit Strain East of Crack During Fatigue Tests for Beam 6A at a Strand Stress Range of 45 ksi

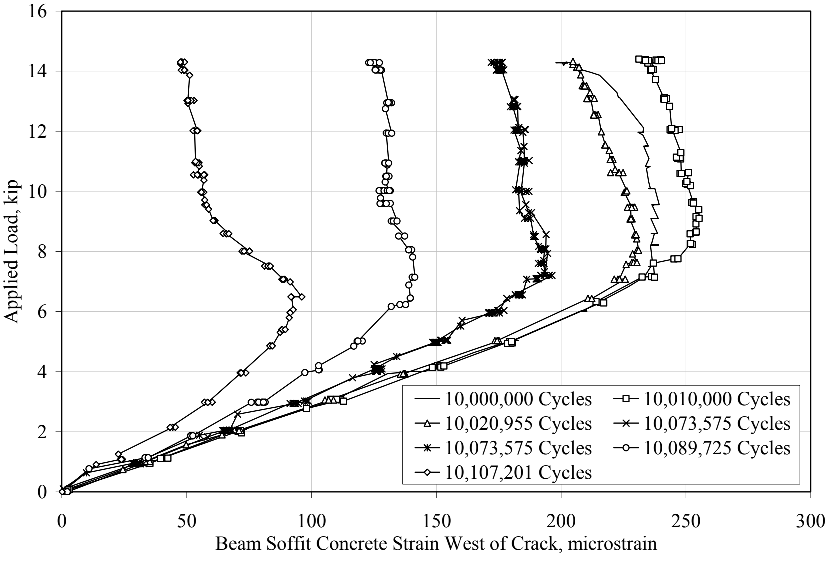

Figure N.36 Variation of Beam Soffit Strain West of Crack During Fatigue Tests for Beam 6A at a Strand Stress Range of 45 ksi

N.4 SUMMARY OF MEASURED STRAND STRAINS FOR BEAMS 1 THROUGH 6

The maximum, minimum and average measured strains at the maximum and minimum applied fatigue loads are summarized in Table N.1 and Table N.2. Strain values were taken from the static test performed at the number of fatigue cycles indicated in the tables and occurred when strand strain results were repeatable.

Table N.1 Summary of Measured Strand Strain at Minimum Applied Fatigue Load

Beam ID	Strand Stress Range	Number of Fatigue Cycles†	Minimum Applied Fatigue Load	Maximum Measured Strand Strain	Minimum Measured Strand Strain	Average Measured Strand Strain
	ksi		kip	$\mu\varepsilon$	$\mu\varepsilon$	$\mu\varepsilon$
1	7	2	10.5	523	174	351
1A	41	10,000*	10	670	425	538
1B	44	1**	0.7	100	59	74
2	22	100	3.4	94	71	77
3	25	100	2.3	58	43	49
4	47	2	1.2	34	25	29
5	47	2	0.6	14	12	13
6	14	5,000	5.5	132	119	126
6A	45	10,000*	2.7	63	58	60

† Number of fatigue cycles at the strand stress range listed.

* Number of cycles is in addition to the total number of cycles at a strand stress range of approximately 10 ksi.

** Number of cycles is in addition to the total number of cycles at the index stress of 7 ksi and 41 ksi.

Table N.2 Summary of Measured Strand Strain at Maximum Applied Fatigue Load

Beam ID	Strand Stress Range	Number of Fatigue Cycles†	Maximum Applied Fatigue Load	Minimum Measured Strand Strain	Maximum Measured Strand Strain	Average Measured Strand Strain
	ksi		kip	$\mu\varepsilon$	$\mu\varepsilon$	$\mu\varepsilon$
1	7	2	11.4	646	283	466
1A	41	10,000*	14.5	1883	1609	1749
1B	44	1**	13.5	1639	1017	1222
2	22	100	11.7	692	380	586
3	25	100	11.9	884	569	718
4	47	2	14.2	1436	1000	1310
5	47	2	14.3	1509	1144	1347
6	14	5,000	10.8	579	356	479
6A	45	10,000*	14.3	1414	1321	1370

† Number of fatigue cycles at the strand stress range listed.

* Number of cycles is in addition to the total number of cycles at a strand stress range of approximately 10 ksi.

** Number of cycles is in addition to the total number of cycles at the index stress of 7 ksi and 41 ksi.

References

Abendroth, R.E.; Klaiber, F.W. and Shafer, M.W. "Diaphragm Effectiveness in Prestressed-Concrete Girder Bridges." *Journal of Structural Engineering,* September 1995, pp. 1362-1369.

Abeles, P.W., Brown, E.I, II, and Hu, C.H. (1974). "Behavior of Under-Reinforced Prestressed Concrete Beams Subjected to Different Stress Ranges." *Abeles Symnposium on Fatigue of Concrete, SP-41, American Concrete Institute,* Detroit 1974, pp. 279-299.

ACI Committee 209 (1997). "Prediction of Creep, Shrinkage, and Temperature Effects in Concrete Structures." ACI Manual of Concrete Practice.

ACI Committee 215 (1997). "Considerations for Design of Concrete Structures Subjected to Fatigue Loading." ACI Manual of Concrete Practice.

American Association of State Highway and Transportation Officials. *Standard Specifications for Highway Bridges, 17th Edition*. Washington, D.C., 2002.

American Association of State Highway and Transportation Officials. *2003 Interim AASHTO LRFD Bridge Design Specifications, Second Edition*. Washington, D.C., 2000.

American Association of State Highway and Transportation Officials. *2003 Interim Manual for Condition Evaluation of Bridges, Second Edition*. Washington, D.C., 2000.

ASTM C 39/C 39M (2001). "Standard Test Method for Compressive Strength of Cylinder Concrete Specimens." American Society for Testing and Materials, West Conshohocken, PA.

ASTM C 469 (2002). "Standard Test Method for Static Modulus of Elasticity and Poisson's Ratio of Concrete in Compression." American Society for Testing and Materials, West Conshohocken, PA.

Barr, P.J.; Eberhard, M.O., and Stanton, J.F. "Live-Load Distribution Factors in Prestressed Concrete Girder Bridges." *Journal of Bridge Engineering*, September/October 2001, pp. 298-306.

Brooks, C.R., and Choudhury, A. (2002). Failure Analysis of Engineering Materials. The McGraw-Hill Company, Inc., New York, NY.

Chen, Yohchia, and Aswad, Alex. "Stretching Span Capability of Prestressed Concrete Bridges Under AASHTO LRFD." *Journal of Bridge Engineering,* August 1996, pp. 112-120.

Collins, M.P. and Mitchell, D. (1997). Prestressed Concrete Structures. Response Publications, Toronto, Canada.

Hurst, M.K. *Prestressed Concrete Design, Second Edition.* Routledge, New York, New York, 1998.

Heller, Bryan. "Fatigue Response of Pretensioned Concrete Beams." M.S.E. Thesis, The University of Texas at Austin, August 2003.

Muller, J.F., and Dux, P.F. (1994). "Fatigue of Prestressed Concrete Beams with Inclined Strands." Journal of Structural Engineering, Vol. 120, No. 4, April, 1994, pp. 1122-1139.

Nordby, G.M., and Venuti, W.J. (1957). "Fatigue and Static Tests of Steel Strand Prestressed Beams of Expanded Shale Concrete and Convential Concrete." Journal of the American Concrete Institute, August 1957, pp. 141-160.

Onyemelukwe, Okey (1999). "Long-term Measurement of Time-Dependent Prestressed Losses in the Westbound Gandy Bridge Project (Phase II)." Final Report, Florida Department of Transportation.

Overman, T.R. (1984). "Flexural Fatigue Behavior of Pretensioned Concrete Girders." M.S. Thesis, Department of Civil Engineering, The University of Texas at Austin.

Ozell, A.M. (1962). "Fatigue Tests of Prestressed Concrete I-Beams with Depressed Strands." Fourth congress, Federation Internationale de la precontrainte, 1962, pp. 128-135.

Ozell, A.M., and Ardaman, E. (1956). "Fatigue Tests of Pre-Tensioned Prestressed Beams." Journal of the American Concrete Institute, 1956, pp. 413-424.

Ozell, A.M., and Diniz, J.F. (1958). “Composite Prestressed Concrete Beams Under Repetitive Loading.” Prestressed Concrete Institute Journal, March 1958, pp. 19-27.

PCI (1992). PCI Design Handbook, Precast and Prestressed Concrete, 4th Edition. Precast/Prestressed Concrete Institute, U.S.A.

Paulson, C., Frank, K., and Breen, J. (1983). “A Fatigue Study of Prestressing Strand.” Research Report 300-1, Center for Transportation Research, Bureau of Engineering Research, The University of Texas at Austin, Austin, TX, April, 1983.

Rabbat, B.G., Karr, P.H., Russel, H.G., and Bruce, N.G. (1978). “Fatigue Tests of Full Size Prestressed Girders.” Research Report 113, Portland Cement Association, June, 1978.

Rao, C., and Frantz, G.C. (1996). “Fatigue Tests of 27-Year-Old Prestressed Concrete Bridge Box Beams.” PCI Journal, Vol. 41, No. 5, September-October, 1996, pp. 74-83.

Roller, J.J., Russell, H.G., Bruce, R.N., and Martin, B.T. (1995). “Long-Term Performance of Prestressed, Pretensioned High Strength Concrete Bridge Girders.” PCI Journal, Vol. 40, No. 6, November-December, 1995, pp. 48-59.

Russell, B.W., and Burns, N.H. (1993). “Static and Fatigue Behavior of Pretensioned Composite Bridge Girders Made with High Strength Concrete.” PCI Journal, Vol. 38, No. 3, May-June, 1993, pp. 116-128.

Shahawi, M.E., and Batchelor, B.D. (1986). “Fatigue of Partially Prestressed Concrete.” Journal of Structural Engineering, Vol. 112, No. 3, March, 1986, pp. 524-537.

Texas Department of Transportation. “Bridge Inventory, Inspection, and Appraisal Program (BRINSAP) Database.” May 2002.

Wagener, Patrick. “Load Testing of Prestressed Concrete Girder Bridges in Texas.” M.S.E. Thesis, The University of Texas at Austin, May 2002.

Warner, R.F., and Hulsbos, C.L. (1966). “Probable Fatigue Life of Prestressed Concrete Beams.” Prestressed Concrete Institute Journal, April 1966, pp. 337-352.

VITA

Michael John Hagenberger was born in Schertz, Texas on December 22, 1969, the son of Eileen Hagenberger and Frederick Hagenberger. After graduating from Bucknell University in May 1992, he entered the Graduate School at Cornell University in August 1992. He received the degree of Master of Engineering in May 1993. From June 1993 to August 1999, he was employed as a structural design engineer in New York State, where he earned his professional engineering license. In August 1999, he entered the Graduate School of the University of Texas at Austin to pursue his Ph.D. degree.

Permanent Address: 122 Woodview Drive
Valparaiso, IN 46383

This dissertation was typed by the author.